



University of HUDDERSFIELD

University of Huddersfield Repository

Lee, Samuel P.

MIXED FLOW TURBINE HOUSING DEVELOPMENT FOR A FIXED GEOMETRY
TURBOCHARGER APPLICATION

Original Citation

Lee, Samuel P. (2018) MIXED FLOW TURBINE HOUSING DEVELOPMENT FOR A FIXED GEOMETRY TURBOCHARGER APPLICATION. Doctoral thesis, University of Huddersfield.

This version is available at <http://eprints.hud.ac.uk/id/eprint/34776/>

The University Repository is a digital collection of the research output of the University, available on Open Access. Copyright and Moral Rights for the items on this site are retained by the individual author and/or other copyright owners. Users may access full items free of charge; copies of full text items generally can be reproduced, displayed or performed and given to third parties in any format or medium for personal research or study, educational or not-for-profit purposes without prior permission or charge, provided:

- The authors, title and full bibliographic details is credited in any copy;
- A hyperlink and/or URL is included for the original metadata page; and
- The content is not changed in any way.

For more information, including our policy and submission procedure, please contact the Repository Team at: E.mailbox@hud.ac.uk.

<http://eprints.hud.ac.uk/>

MIXED FLOW TURBINE HOUSING
DEVELOPMENT FOR A FIXED GEOMETRY
TURBOCHARGER APPLICATION

Samuel P. Lee

A thesis submitted to the University of Huddersfield
in partial fulfilment of the requirements for the degree of
Doctor of Philosophy

The University of Huddersfield
July 2018

ABSTRACT

This thesis investigates the impact of volute design on the performance of a mixed flow turbine. Both computational and experimental methods were used to assess performance. All computational work was conducted in CFX under both steady state and unsteady pulsating conditions with the models including inlet, volute, rotor and outlet volumes. Both the mixing plane and sliding mesh approaches were implemented and the results compared. The $k - \omega$ SST turbulence model was implemented throughout this thesis with the exceptions of chapters 8 and 9 where the SAS SST model was used in an attempt to accurately capture secondary flows. Further SBES simulations were included for flow validation.

It was found that pulse shape had a significant impact on the instantaneous performance while the cycle averaged performance remained largely insensitive to the changes. Further thorough analysis showed, under a range of pulse frequencies, loads and amplitudes, significant variations in LE incidence over the pulse cycle. Furthermore, the spanwise distribution of the incidence also changed considerably over the pulse due to volute secondary flow development.

As result of the initial analysis both volute tilt and aspect ratio (and a combination of the two) were assessed. A new tilted volute was introduced which resulted in a performance improvement of up to 2.356% in cycle averaged rotor efficiency and 2.171% improvement in cycle average stage efficiency. This improvement reduced when volute A/r was reduced. The impact of volute aspect ratio showed that the MFP varied by up to 4.3%. Furthermore, volute secondary flows were significantly impacted by aspect ratio with smaller aspect ratios resulting in strong vortices that persisted around the volute. Increasing the aspect ratio removed these vortices. However, the span-wise distribution of LE incidence was only slightly improved with increasing aspect ratio. The maximum efficiency improvement measured over the aspect ratio range was 1.47% for the turbine stage. Combining both tilt and aspect ratio showed a maximum performance variation between the worst performing design, radial $AR=0.5$ and the best performing design tilted $AR=2$ of 3.00% in the rotor region and 2.87% over the entire stage.

Extensive experimental testing under steady state and pulsating flows was conducted at Imperial College, London to validate the computational work. It was observed that the tilted volute resulted in pulsating efficiency improvements at 48krpm and 56krpm. This trend was found to increase as pulse frequency increased. However, steady state testing only showed efficiency improvements at 30krpm for the tilted volute.

PUBLICATIONS

Journal papers –

- Lee, S. P., Jupp, M. L., Barrans, S. M., & Nickson, A. K. (2018). Analysis of leading edge flow characteristics in a mixed flow turbine under pulsating flows. *Proceedings of the Institution of Mechanical Engineers, Part A: Journal of Power and Energy*, 0957650918778661.
- Lee, S. P., Barrans, S. M., Jupp, M. L., & Nickson, A. K. (2017). The Impact of Volute Aspect Ratio on the Performance of a Mixed Flow Turbine. *Aerospace*, 4(4), 56.
- Lee, S. P., Rezk, A., Jupp, M., & Nickson, K. (2017). The influence of pulse shape on the performance of a mixed flow turbine for turbocharger applications. *International Journal of Mechanical Engineering and Robotics Research*.

Conference papers –

- Lee, S. P., Barrans, S. M., Jupp, M. L., & Nickson, A. K. Investigation into the Impact of Span-wise flow Distribution on the Performance of a Mixed Flow Turbine (2018). In *ASME Turbo Expo 2018: Turbomachinery Technical Conference and Exposition*. American Society of Mechanical Engineers (ASME). In Press
- Lee, S. P., S. M., Jupp, M. L., Allport, J., & Nickson, A. K. Analysis of a tilted turbine housing volute design under pulsating inlet conditions. In *ASME Turbo Expo 2017: Turbomachinery Technical Conference and Exposition* (pp. V02CT44A016-V02CT44A016). American Society of Mechanical Engineers (ASME).
- Lee, S. P., S. M., Jupp, M. L., & Nickson, A. K. The influence of secondary flow structures in a turbocharger turbine housing in steady state and pulsating flow conditions. In *Mechanical and Aerospace Engineering (ICMAE), 2016 7th International Conference on* (pp. 154-159). IEEE.
- Lee, S. P., S. M., Jupp, M. L., & Nickson, A. K. The introduction of a tilted volute design for operation with a mixed flow turbine for turbocharger applications.

In Mechanical and Aerospace Engineering (ICMAE), 2016 7th International Conference on (pp. 165-170). IEEE.

ACKNOWLEDGEMENTS

Firstly, I would like to thank my supervisors Dr Simon Barrans, Dr Martyn Jupp and Professor John Allport who have provided invaluable support throughout this thesis. Their efforts to ensure the quality of the work produced and to support my development is very much appreciated. I would especially like to thank Dr Simon Barrans for agreeing to take the role of primary supervisor after the departure of Dr Marytn Jupp from the university. Taking up this task was a huge commitment, for which I am extremely grateful. I would like to wish the best to Dr Marytn Jupp in his new venture and thank him for all of his earlier support in guiding the direction of this research.

I would also like to thank Dr Keith Nickson at BorgWarner for his industrial perspective, facilitating the transfer of data and geometry, and over seeing the manufacture of components. I would like to thank Pawel Bakula at BorgWarner for the time he spent liaising with me on volute geometry development and production.

Thanks must also go to Professor Ricardo Martinez-Botas at Imperial College London for his support with experimental testing and to Jose Francisco Cortell Fores for his technical support and extensive knowledge of experimental performance and testing.

To the team at the TRI Sidharath Sharma, MD shams Tabriz, Mahir Alani, Ahmed Ali, Ahmed Rezk and Goodarz Khodabakhshi who I shared an office with for three years, thank you for making the experience so enjoyable. I will miss the debates on everything from cricket to the rising of the AI's.

Finally, I would like to thank my wife, Natasha Lee, for putting up with me over the last three years and for pretending to listen to the endless PhD related monologues. Despite this, she still agreed to marry me midway through the experience. I promise to be less distracted from now on.

COPYRIGHT STATEMENT

The following notes on copyright and the ownership of intellectual property rights must be included as written below:

i. The author of this thesis (including any appendices and/ or schedules to this thesis) owns any copyright in it (the “Copyright”) and s/he has given The University of Huddersfield the right to use such Copyright for any administrative, promotional, educational and/or teaching purposes.

ii. Copies of this thesis, either in full or in extracts, may be made only in accordance with the regulations of the University Library. Details of these regulations may be obtained from the Librarian. Details of these regulations may be obtained from the Librarian. This page must form part of any such copies made.

iii. The ownership of any patents, designs, trademarks and any and all other intellectual property rights except for the Copyright (the “Intellectual Property Rights”) and any reproductions of copyright works, for example graphs and tables (“Reproductions”), which may be described in this thesis, may not be owned by the author and may be owned by third parties. Such Intellectual Property Rights and Reproductions cannot and must not be made available for use without permission of the owner(s) of the relevant Intellectual Property Rights and/or Reproductions.

CONTENTS

| | |
|---|-------------|
| ABSTRACT | III |
| PUBLICATIONS | V |
| ACKNOWLEDGEMENTS | VII |
| COPYRIGHT STATEMENT | VIII |
| CONTENTS | IX |
| LIST OF TABLES:..... | XIII |
| LIST OF FIGURES:..... | XIV |
| NOMENCLATURE: | XXV |
| | |
| 1 INTRODUCTION..... | 29 |
| 1.1 INTRODUCTION AND MOTIVATION | 29 |
| 1.2 TURBOCHARGER COMPONENTS..... | 31 |
| 1.2.1 <i>Turbine operating Environment</i> | 31 |
| 1.2.2 <i>Mixed Flow Turbine Definition</i> | 34 |
| 1.3 TURBINE PERFORMANCE PARAMETERS..... | 38 |
| 1.4 RESEARCH AIMS | 40 |
| | |
| 2 LITERATURE REVIEW | 41 |
| 2.1 PULSED FLOW TURBOCHARGING RESEARCH | 41 |
| 2.2 MIXED FLOW TURBINE RESEARCH | 48 |
| 2.3 VOLUTE FLOWS | 57 |
| 2.4 LITERATURE REVIEW SUMMARY | 67 |
| | |
| 3 COMPUTATIONAL FLUID DYNAMICS METHODOLOGY..... | 70 |
| 3.1 COMPUTATIONAL FLUID DYNAMICS OVER VIEW | 70 |
| 3.1.1 <i>Governing Equations</i> | 70 |
| 3.1.2 <i>The Transport Equations</i> | 72 |
| 3.1.3 <i>Numerical Approach's to CFD</i> | 72 |
| 3.1.3.1 <i>Finite Volume Method</i> | 73 |
| 3.1.4 <i>Spatial Discretization of the Domain</i> | 74 |
| 3.1.5 <i>Temporal Discretization</i> | 76 |
| 3.1.6 <i>Turbulence</i> | 76 |
| 3.1.6.1 <i>k-ε</i> | 79 |

| | | |
|----------|---|------------|
| 3.1.6.2 | k- ω | 80 |
| 3.1.6.3 | k- ω SST..... | 81 |
| 3.1.7 | <i>Near Wall Modelling</i> | 81 |
| 3.2 | CFD FOR TURBINE SIMULATIONS | 84 |
| 3.2.1 | <i>Steady State and Transient Simulations</i> | 84 |
| 3.2.2 | <i>Domain Rotation</i> | 86 |
| 3.2.3 | <i>Turbulence Modeling</i> | 88 |
| 3.3 | CFD SET-UP..... | 90 |
| 3.4 | MESH STUDY | 91 |
| 3.4.1 | <i>Computational domain</i> | 91 |
| 3.4.2 | <i>Mesh Refinement</i> | 91 |
| 3.4.3 | <i>Volute Mesh Study</i> | 92 |
| 3.4.4 | <i>Rotor Mesh Refinement</i> | 97 |
| 3.4.5 | <i>Outlet Mesh Refinement</i> | 99 |
| 3.4.6 | <i>Boundary Layer Mesh Refinement</i> | 101 |
| 3.4.7 | <i>Final Mesh</i> | 102 |
| 3.5 | TIME STEP STUDY..... | 106 |
| 3.6 | COMPARISON OF FROZEN ROTOR AND SLIDING MESH METHODS | 108 |
| 3.7 | IMPACT OF ROTOR POSITION | 111 |
| 3.8 | EXPERIMENTAL VALIDATION..... | 114 |
| 3.9 | CHAPTER CONCLUSIONS..... | 116 |
| 4 | IMPACT OF PULSE SHAPE | 117 |
| 4.1 | MIXED FLOW TURBINE GEOMETRY..... | 117 |
| 4.2 | BOUNDARY CONDITIONS | 119 |
| 4.3 | RESULTS AND DISCUSSION..... | 120 |
| 4.4 | CHAPTER CONCLUSIONS | 133 |
| 5 | ANALYSIS OF A MIXED FLOW TURBINE UNDER PULSATING FLOW CONDITIONS | 135 |
| 5.1 | INVESTIGATED PULSE FORMS | 135 |
| 5.2 | RESULTS AND DISCUSSION – IMPACT OF PULSE FREQUENCY | 137 |
| 5.2.1 | <i>Cycle Averaged Performance</i> | 147 |
| 5.2.2 | <i>Circumferential Averaging</i> | 148 |
| 5.2.3 | <i>Comparison of Flow angles throughout pulse</i> | 150 |
| 5.3 | IMPACT OF PULSE LOAD | 162 |
| 5.4 | IMPACT OF PULSATION NUMBER..... | 168 |
| 5.5 | CHAPTER CONCLUSIONS..... | 174 |

| | | |
|-----------|--|------------|
| 6 | ANALYSIS OF TILTED VOLUTE HOUSING | 175 |
| 6.1 | DEFINITION OF THE TILTED HOUSING DESIGN | 175 |
| 6.2 | MODELLING OF THE TILTED HOUSING DESIGN..... | 177 |
| 6.3 | PERFORMANCE COMPARISONS STEADY STATE | 179 |
| 6.4 | PERFORMANCE COMPARISON PULSATING FLOWS | 183 |
| 6.4.1 | <i>Pulsation Frequency</i> | 183 |
| 6.4.2 | <i>Pulsation Number</i> | 205 |
| 6.4.3 | <i>Pulsation Load</i> | 209 |
| 6.5 | THE IMPACT OF VOLUTE A/R AND HOUSING TILT ON PERFORMANCE | 212 |
| 6.5.1 | <i>Volute Secondary Flows</i> | 219 |
| 6.6 | CHAPTER CONCLUSIONS..... | 228 |
| 7 | THE IMPACT OF ROTOR LE FLOW DISTRIBUTION..... | 229 |
| 7.1 | METHODOLOGY..... | 229 |
| 7.2 | THE IMPACT OF ROTOR INLET FLOW FROM THE RADIAL HOUSING..... | 231 |
| 7.3 | TILTED PASSAGE PERFORMANCE | 239 |
| 7.4 | CHAPTER CONCLUSION | 244 |
| 8 | IMPACT OF VOLUTE ASPECT RATIO | 246 |
| 8.1 | TURBULENCE MODELLING APPROACH..... | 246 |
| 8.2 | ASPECT RATIO MODELS | 246 |
| 8.3 | 4.1. IMPACT OF VOLUTE ASPECT RATIO ON MFP..... | 247 |
| 8.4 | 4.2. ASPECT RATIO EFFECT WITH CONSTANT MFP..... | 249 |
| 8.5 | SECONDARY FLOW STRUCTURES | 254 |
| 8.6 | SCALE RESOLVING TURBULENCE APPROACH | 271 |
| 8.7 | CHAPTER CONCLUSIONS..... | 275 |
| 9 | COMBINING HOUSING TILT AND ASPECT RATIO | 277 |
| 9.1 | INTRODUCTION..... | 277 |
| 9.2 | TURBINE PERFORMANCE RESULTS | 278 |
| 9.3 | VOLUTE FLOW ANALYSIS | 282 |
| 9.4 | CHAPTER CONCLUSIONS..... | 292 |
| 10 | EXPERIMENTAL INVESTIGATION AND FURTHER VALIDATION | 294 |
| 10.1 | INTRODUCTION TO TEST SET-UP..... | 294 |
| 10.2 | EQUIVALENT PERFORMANCE PARAMETERS | 296 |
| 10.3 | EXPERIMENTAL FACILITY INSTRUMENTATION | 297 |
| 10.3.1 | <i>Mass Flow Steady State Hardware</i> | 297 |

| | | |
|-------------------|---|------------|
| 10.3.2 | <i>Unsteady Mass Flow</i> | 299 |
| 10.3.2.1 | Hot Wire calibration | 299 |
| 10.3.2.2 | Unsteady Mass Flow Uncertainty | 300 |
| 10.3.3 | <i>Pressure Steady Flow</i> | 301 |
| 10.3.4 | <i>Unsteady Pressure</i> | 301 |
| 10.3.5 | <i>Steady State Temperature</i> | 302 |
| 10.3.6 | <i>Unsteady Temperature</i> | 302 |
| 10.3.7 | <i>Rotational Speed</i> | 302 |
| 10.3.8 | <i>Steady Flow Torque</i> | 303 |
| 10.3.9 | <i>Unsteady Flow Torque</i> | 303 |
| 10.3.9.1 | Torque Uncertainty | 303 |
| 10.4 | UNCERTAINTY ANALYSIS | 304 |
| 10.5 | DATA PROCESSING OF UNSTEADY MEASUREMENTS | 307 |
| 10.6 | TURBINE HARDWARE..... | 308 |
| 10.6.1 | <i>Volute</i> | 308 |
| 10.7 | STEADY STATE RADIAL HOUSING VS TILTED | 311 |
| 10.7.1 | <i>Steady State Computational Validation and Analysis</i> | 315 |
| 10.8 | UNSTEADY PERFORMANCE ANALYSIS | 322 |
| 10.8.1 | <i>Unsteady Turbine Mass Flow Parameter</i> | 322 |
| 10.8.2 | <i>Unsteady Turbine Efficiency Analysis</i> | 328 |
| 10.8.3 | <i>Lambda Parameter</i> | 334 |
| 10.8.4 | <i>Pulsating Validation</i> | 337 |
| 10.9 | CHAPTER CONCLUSIONS..... | 343 |
| 11 | CONCLUSIONS..... | 344 |
| 11.1 | CONTRIBUTIONS | 347 |
| 11.2 | <i>Scholarly output</i> | 348 |
| 11.3 | FUTURE WORK..... | 349 |
| 12 | REFERENCES..... | 351 |
| APPENDIX A | -V-CONE CALIBRATION DOCUMENT | 358 |
| APPENDIX B | - EXPERIMENTAL INLET PRESSURE PULSE | 359 |

LIST OF TABLES:

| | |
|---|-----|
| TABLE 1.1: STAGE NUMBERING SYSTEM | 38 |
| TABLE 3.1: VOLUTE MESH CONVERGENCE VALUES NORMALISED BY FINEST MESH VALUE | 92 |
| TABLE 3.2: VOLUTE GCI | 95 |
| TABLE 3.3: ROTOR MESH CONVERGENCE VALUES NORMALISED BY THE FINEST MESH VALUES | 98 |
| TABLE 3.4: ROTOR GCI RESULTS..... | 99 |
| TABLE 3.5: OUTLET MESH CONVERGENCE VALUES NORMALISED BY THE FINEST MESH VALUES | 100 |
| TABLE 3.6: BOUNDARY LAYER MESH CONVERGENCE VALUES NORMALISED BY THE FINEST GRID VALUE | 101 |
| TABLE 3.7: NUMBER OF CELLS IN STAGE PER DOMAIN AND TOTAL | 102 |
| TABLE 3.8: COMPARISON OF FINAL OPTIMISED MESH AND HIGHLY REFINED MESH. | 103 |
| TABLE 4.1: CYCLE AVERAGED PERFORMANCE RESULTS FOR EACH PULSE NORMALISED BY THE SINUSOIDAL WAVE RESULTS | 131 |
| TABLE 5.1: CYCLE AVERAGED PERFORMANCE RESULTS AT 20HZ, 40HZ AND 60HZ PULSE FREQUENCIES..... | 148 |
| TABLE 5.2: CYCLE-AVERAGED PERFORMANCE RESULTS FOR THREE LOAD CONDITIONS AT 40HZ PULSE FREQUENCY | 165 |
| TABLE 5.3: CYCLE AVERAGED PERFORMANCE RESULTS FOR 50, 75, 100 AND 125 PULSATION NUMBER AT 40HZ PULSE FREQUENCY..... | 171 |
| TABLE 6.1: TILTED VOLUTE (TV) VS RADIAL VOLUTE (RV) PERFORMANCE PARAMETERS | 186 |
| TABLE 6.2: TILTED (TV) VS RADIAL (RV) VOLUTE PERFORMANCE PARAMETER OVER RANGE OF PULSATION NUMBERS..... | 206 |
| TABLE 6.3: TILTED (TV) VS RADIAL (RV) VOLUTE PERFORMANCE PARAMETER OVER RANGE OF PULSE LOADS..... | 209 |
| TABLE 6.4: CYCLE AVERAGED PERFORMANCE DIFFERENCE BETWEEN RADIAL (RV) AND TILTED VOLUTE (TV) DESIGNS OVER A RANGE OF VOLUTE A/R'S | 216 |
| TABLE 7.1: PERCENTAGE EFFICIENCY CHANGE FROM THE REALISTIC VARIATION SPAN-WISE DISTRIBUTION | 239 |
| TABLE 8.1: NORMALISED PERFORMANCE OF EACH ASPECT RATIO HOUSING DESIGN AT 20HZ, 40HZ AND 60HZ PULSE FREQUENCY | 252 |
| TABLE 9.1: RADIAL AND TILED VOLUTES, AR=0.5 AND AR=2, RELATIVE PERFORMANCE | 281 |
| TABLE 9.2: COMPARISON OF THE IMPACT OF VOLUTE TILT ON CYCLE AVERAGED PERFORMANCE AT ASPECT RATIOS OF 0.5 AND 2 | 281 |
| TABLE 9.3: COMPARISON OF THE IMPACT OF ASPECT RATIO ON CYCLE AVERAGED PERFORMANCE IN A RADIAL AND TILTED VOLUTE | 282 |
| TABLE 10.1: PARAMETER SENSITIVITY COEFFICIENTS | 305 |
| TABLE 10.2: EXPERIMENTAL ERRORS 30KRPM | 307 |
| TABLE 10.3: EXPERIMENTAL ERRORS 48KRPM | 307 |
| TABLE 10.4: EXPERIMENTAL ERRORS 56KRPM | 307 |

LIST OF FIGURES:

| | |
|---|-----|
| FIGURE 1.1: CO ₂ EMISSIONS DATA FOR 2014 (IEA, 2016) | 29 |
| FIGURE 1.2: ROTOR INLET VELOCITY TRIANGLES UNDER PULSATING FLOW | 32 |
| FIGURE 1.3: IMPACT OF INLET FLOW ANGLES ON PASSAGE FLOWS | 34 |
| FIGURE 1.4: RADIAL STACKING OF BLADE FIBRES FOR ZERO AND NON-ZERO BLADE ANGLES..... | 35 |
| FIGURE 1.5: FLOW CONE ANGLE (Δ FLOW), BLADE CONE ANGLE (Λ) AND CAMBER ANGLE (Φ)..... | 35 |
| FIGURE 1.6: INLET FLOW IN RADIAL, AXIAL AND MIXED FLOW TURBINES (LEONARD ET AL., 2013) | 36 |
| FIGURE 1.7: PASSAGE FLOWS IN A MIXED FLOW TURBINE WITH NON-ZERO BLADE ANGLE | 37 |
| FIGURE 2.1: PULSATING PERFORMANCE MEASURED BY (DALE AND WATSON, 1986) | 42 |
| FIGURE 2.2: IMPERIAL COLLEGE TEST FACILITY INLET PULSE FORM FROM CHOPPER PLATES (PADZILLAH ET AL., 2015) | 45 |
| FIGURE 2.3: MIXED FLOW TURBINE PERFORMANCE CHARACTERISTICS. LEFT – COMPARISON OF OPTIMAL RADIAL AND MIXED FLOW PERFORMANCE (WATSON AND JANOTA, 1982). RIGHT – COMPARISON OF RADIAL AND AXIAL PERFORMANCE SHOWING HOW MIXED FLOW TURBINES CAN BRIDGE THE GAP BETWEEN THE TWO TYPES (WHITFIELD AND BAINES, 1990). | 48 |
| FIGURE 2.4: LEFT - LE BLADE DISTRIBUTIONS. RIGHT – LE SPAN-WISE BLADE ANGLE (ZHANG ET AL., 2011) | 50 |
| FIGURE 2.5: SINGLE ENTRY VOLUTE DESIGN, LEFT. DOUBLE ENTRY VOLUTE DESIGN, RIGHT (CHOU AND GIBBS, 1989)..... | 50 |
| FIGURE 2.6: FLOW SEPARATION FROM SHROUD CURVATURE (CHOU AND GIBBS, 1989). | 52 |
| FIGURE 2.7: VOLUTE DESIGNS COMPARED BY ARCOUMANIS ET AL. (1997). LEFT OLD DESIGN. RIGHT - NEW DESIGN..... | 52 |
| FIGURE 2.8: LE INCIDENCE ANGLE DISTRIBUTION FROM LDA STUDY BY KARAMANIS ET AL. (2001). | 54 |
| FIGURE 2.9: TWO VOLUTE CROSS SECTIONAL SHAPES FOR A RADIAL TURBINE (YANG ET AL., 2014) | 61 |
| FIGURE 2.10: ENTROPY DISTRIBUTION FOR VOLUTE A AND B AT 0° AZIMUTH ANGLE (YANG ET AL., 2014)..... | 63 |
| FIGURE 2.11 - SECONDARY FLOW AT 0° AZIMUTH ANGLE (YANG ET AL., 2014) | 63 |
| FIGURE 2.12: COUNTER ROTATING DEAN VORTICES (HELLSTROM, 2010)..... | 65 |
| FIGURE 2.13: DEAN VORTEX DEVELOPMENT IN TWIN ENTRY VOLUTE DESIGN..... | 66 |
| FIGURE 3.1: EXAMPLE OF 2-DIMENSIONAL FINITE VOLUME CELL | 75 |
| FIGURE 3.2: REPRESENTATION OF LAMINAR TO TURBULENT TRANSITION (VAN DYKE AND VAN DYKE, 1982) | 77 |
| FIGURE 3.3: REPRESENTATION OF THE NEAR WALL FLOWS (ANSYS, 2009b) | 83 |
| FIGURE 3.4: COMPUTATIONAL DOMAIN..... | 91 |
| FIGURE 3.5: VOLUTE MESH REFINEMENT EFFICIENCY PLOT..... | 92 |
| FIGURE 3.6: SECONDARY FLOW STRUCTURES IN THE VOLUTE AT THREE MESH DENSITIES | 96 |
| FIGURE 3.7: VOLUTE MESH REFINEMENT TOTAL PRESSURE LOSS COEFFICIENT..... | 97 |
| FIGURE 3.8: ROTOR MESH REFINEMENT EFFICIENCY PLOT NORMALISED BY THE FINEST MESH VALUES | 98 |
| FIGURE 3.9: OUTLET MESH REFINEMENT EFFICIENCY PLOT | 100 |
| FIGURE 3.10: BOUNDARY LAYER MESH REFINEMENT EFFICIENCY PLOT NORMALISED BY THE FINEST GRID VALUE | 102 |
| FIGURE 3.11 - STRUCTURED ROTOR MESH | 104 |
| FIGURE 3.12 - RESULTING VOLUTE MESH | 105 |
| FIGURE 3.13 - IMPACT OF TIME STEP ON ROTOR TORQUE..... | 106 |

| | |
|--|-----|
| FIGURE 3.14 - IMPACT OF TIME STEP SIZE ON ROTOR EFFICIENCY | 107 |
| FIGURE 3.15: LOW MASS FLOW COMPARISON OF ABSOLUTE FLOW ANGLE AT VOLUTE EXIT USING THE FROZEN ROTOR AND SLIDING MESH APPROACHES. (A) - 54°, (B) - 90°, (C) - 126°, (D) - 198° AND (E) - 270° | 109 |
| FIGURE 3.16: HIGH MASS FLOW COMPARISON OF ABSOLUTE FLOW ANGLE AT VOLUTE EXIT USING THE FROZEN ROTOR AND SLIDING MESH APPROACHES. (A) - 54°, (B) - 90°, (C) - 126°, (D) - 198° AND (E) - 270° | 110 |
| FIGURE 3.17 - IMPACT OF ROTOR RELATIVE POSITION TO VOLUTE TONGUE ON PERFORMANCE..... | 112 |
| FIGURE 3.18 - PRESSURE PLOTS THROUGH VOLUTE PASSAGE AND AT MID BLADE STREAMWISE POSITION | 112 |
| FIGURE 3.19: COMPARISON OF STEADY STATE COMPUTATIONAL AND GAS STAND EFFICIENCY (T-s) | 115 |
| FIGURE 3.20: COMPARISON OF STEADY STATE COMPUTATIONAL AND GAS STAND MFP | 116 |
| FIGURE 4.1: MIXED FLOW ROTOR..... | 117 |
| FIGURE 4.2: ROTOR LE SPAN-WISE CAMBER ANGLE VARIATION | 118 |
| FIGURE 4.3: BASE RADIAL VOLUTE DESIGN WITH $A/R=23$ SHOWN LEFT AND THE VARIATION IN A/R AROUND THE VOLUTE AZIMUTH ANGLE SHOWN RIGHT. | 118 |
| FIGURE 4.4: INLET MASS FLOW PULSES SHAPES..... | 119 |
| FIGURE 4.5: REALISTIC WAVE FORM AND IT SIMPLIFIED PULSES. | 120 |
| FIGURE 4.6: VOLUTE MASS ACCUMULATION RESULTING FROM THE FOUR TESTED INLET PULSE SHAPES | 121 |
| FIGURE 4.7: SINUSOIDAL TURBINE INLET PULSE AND CORRESPONDING ROTOR INLET PULSE | 122 |
| FIGURE 4.8: TRIANGULAR TURBINE INLET PULSE AND CORRESPONDING ROTOR INLET PULSE..... | 123 |
| FIGURE 4.9: REALISTIC TURBINE INLET PULSE AND CORRESPONDING ROTOR INLET PULSE | 123 |
| FIGURE 4.10: SQUARE TURBINE INLET PULSE AND CORRESPONDING ROTOR INLET PULSE | 124 |
| FIGURE 4.11: INSTANTANEOUS ROTOR TORQUE FOR EACH INLET PULSE SHAPE | 125 |
| FIGURE 4.12: INSTANTANEOUS MFP FOR EACH INLET PULSE SHAPE | 126 |
| FIGURE 4.13: INSTANTANEOUS ROTOR EFFICIENCY (T-s) FOR EACH INLET PULSE SHAPE | 127 |
| FIGURE 4.14: CHANGE IN LEADING EDGE INCIDENCE PLOTTED AGAINST VELOCITY RATIO FOR THE FOUR TESTED INLET PULSE SHAPES | 128 |
| FIGURE 4.15: MIXED FLOW TURBINE VELOCITY TRIANGLES | 128 |
| FIGURE 4.16: CHANGE IN LEADING EDGE INCIDENCE OVER NORMALISED TIME FOR THE FOUR TESTED INLET PULSE SHAPES. | 130 |
| FIGURE 4.17: ROTOR VELOCITY RATIO THROUGH THE INLET PULSATION..... | 132 |
| FIGURE 4.18: ENERGY AVAILABLE WITHIN EACH ROTOR U/CS RANGE. | 133 |
| FIGURE 5.1: INLET MASS FLOW AND TOTAL TEMPERATURE PULSES AT 20HZ, 40HZ AND 60HZ FREQUENCIES..... | 136 |
| FIGURE 5.2: INLET MASS FLOW PULSES AT 40 HZ LEFT - LOW, MEDIUM AND HIGH LOAD. RIGHT – 0.5, 0.75, 1 AND 1.25 INLET PULSATION NUMBER PULSES..... | 136 |
| FIGURE 5.3: STAGE INLET AND ROTOR INLET MASS FLOW AT 20HZ, 40HZ AND 60HZ PULSE FREQUENCIES | 138 |
| FIGURE 5.4: VOLUTE MASS ACCUMULATION AT 20HZ, 40HZ AND 60HZ. | 139 |
| FIGURE 5.5: MFP VS PRESSURE RATIO FOR STEADY STATE, 20HZ, 40HZ AND 60HZ INLET CONDITIONS | 140 |
| FIGURE 5.6: RESULTING ROTOR TORQUE AT 20HZ, 40HZ AND 60HZ PULSE FREQUENCIES..... | 141 |
| FIGURE 5.7: INSTANTANEOUS ROTOR EFFICIENCY AT 20HZ, 40HZ AND 60HZ PULSE FREQUENCIES | 141 |

| | |
|---|-----|
| FIGURE 5.8: ROTOR VELOCITY RATIO THROUGH THE INLET PULSATION | 142 |
| FIGURE 5.9: ENERGY AVAILABLE WITHIN EACH ROTOR U/c_3 RANGE. | 143 |
| FIGURE 5.10: INLET BOUNDARY CONDITIONS OF MASS FLOW AND TOTAL TEMPERATURE | 143 |
| FIGURE 5.11: VOLUTE INLET AND OUTLET FLOW PARAMETERS AT 40HZ FREQUENCY. (A) - MASS FLOW, (B) - STATIC TEMPERATURE, (C) - STATIC PRESSURE, (D) - DENSITY AND (E) - NORMAL VELOCITY..... | 145 |
| FIGURE 5.12: 20HZ FREQUENCY ISENTROPIC ENERGY AND INCIDENCE ANGLE | 146 |
| FIGURE 5.13: 40HZ FREQUENCY ISENTROPIC ENERGY AND INCIDENCE ANGLE | 147 |
| FIGURE 5.14: 60HZ FREQUENCY ISENTROPIC ENERGY AND INCIDENCE ANGLE | 147 |
| FIGURE 5.15: VELOCITY AND PRESSURE DISTRIBUTION AROUND THE VOLUTE THROUGH THE PULSE | 149 |
| FIGURE 5.16: VARIATION IN STATIC PRESSURE AROUND THE VOLUTE OUTLET CIRCUMFERENCE OVER PULSE PERIOD..... | 150 |
| FIGURE 5.17: MASS FLOW AVERAGED LEADING EDGE INCIDENCE ANGLE THROUGHOUT PULSE AT 20HZ, 40HZ AND 60HZ PULSE FREQUENCIES | 151 |
| FIGURE 5.18: LEADING EDGE FLOW CONE ANGLE AT THREE POINTS OVER THE BLADE SPAN DURING THE 40HZ INLET PULSE | 152 |
| FIGURE 5.19: LEADING EDGE BLADE ANGLE AT THREE POINTS IN THE PULSE AT 20HZ..... | 153 |
| FIGURE 5.20: LEADING EDGE BLADE ANGLE AT THREE POINTS IN THE PULSE AT 40HZ | 153 |
| FIGURE 5.21: LEADING EDGE BLADE ANGLE AT THREE POINTS IN THE PULSE AT 60HZ | 154 |
| FIGURE 5.22: LEADING EDGE INCIDENCE OVER THE BLADE SPAN AT THE MINIMUM INCIDENCE RUNNING POINT AT 20HZ, 40HZ AND 60HZ PULSE FREQUENCIES | 155 |
| FIGURE 5.23: LEADING EDGE INCIDENCE OVER THE BLADE SPAN AT THE -10° INCIDENCE RUNNING POINT AT 20HZ, 40HZ AND 60HZ PULSE FREQUENCIES | 156 |
| FIGURE 5.24: LEADING EDGE INCIDENCE OVER THE BLADE SPAN AT THE MAXIMUM INCIDENCE RUNNING POINT AT 20HZ, 40HZ AND 60HZ PULSE FREQUENCIES | 156 |
| FIGURE 5.25: VARIATION IN CIRCUMFERENTIAL VELOCITY AT THE BLADE LEADING EDGE AT 40HZ..... | 157 |
| FIGURE 5.26: VARIATION IN MERIDIONAL VELOCITY AT THE BLADE LEADING EDGE AT 40HZ | 157 |
| FIGURE 5.27: STREAM LINES AND RADIAL VELOCITY CONTOURS AT PLANES AROUND THE VOLUTE CIRCUMFERENCE. LEFT - MINIMUM INCIDENCE RUNNING POINT. RIGHT - MAXIMUM INCIDENCE RUNNING POINT | 159 |
| FIGURE 5.28: CONTOURS OF STATIC ENTROPY AND VELOCITY VECTORS ON A CONSTANT STREAMWISE PLANE AT 5% AND 15% CHORD. PASSAGE POSITION IS 180° FROM TONGUE. LEFT - MINIMUM INCIDENCE RIGHT - MAXIMUM INCIDENCE | 159 |
| FIGURE 5.29: LEADING EDGE INCIDENCE AROUND THE VOLUTE CIRCUMFERENCE AT MINIMUM INCIDENCE DURING THE 40HZ PULSE | 161 |
| FIGURE 5.30: LEADING EDGE INCIDENCE AROUND THE VOLUTE CIRCUMFERENCE AT MAXIMUM INCIDENCE DURING THE 40HZ PULSE | 161 |
| FIGURE 5.31: MFP VS PRESSURE RATIO FOR STEADY STATE, LOW, MEDIUM AND HIGH LOAD AT 40HZ PULSE FREQUENCY | 162 |
| FIGURE 5.32: VOLUTE MASS ACCUMULATION AT LOW, MEDIUM AND HIGH LOAD. | 163 |
| FIGURE 5.33: ROTOR TORQUE OF THE 40HZ PULSE AT THREE LOAD CONDITIONS | 164 |
| FIGURE 5.34: INSTANTANEOUS ROTOR TORQUE AT THREE LOAD CONDITIONS AT THE 40HZ PULSE FREQUENCY | 164 |
| FIGURE 5.35: LEADING EDGE INCIDENCE OVER THE 40HZ PULSE AT THREE LOAD CONDITIONS | 165 |

| | |
|--|-----|
| FIGURE 5.36: LEADING EDGE INCIDENCE OVER THE BLADE SPAN AT MINIMUM INCIDENCE UNDER THREE LOAD CONDITIONS AT 40HZ PULSE FREQUENCY | 166 |
| FIGURE 5.37: LEADING EDGE INCIDENCE OVER THE BLADE SPAN AT MAXIMUM INCIDENCE UNDER THREE LOAD CONDITIONS AT 40HZ PULSE FREQUENCY | 166 |
| FIGURE 5.38: MFP VS PRESSURE RATIO FOR STEADY STATE, 50, 75, 100 AND 125 PULSATION NUMBERS AT 40HZ PULSE FREQUENCY..... | 168 |
| FIGURE 5.39: VOLUTE MASS ACCUMULATION AT 0.5, 0.75, 1 AND 1.25 PULSATION NUMBER | 169 |
| FIGURE 5.40: ROTOR TORQUE OVER THE PULSE AT 50, 75, 100 AND 125 PULSATION NUMBERS AT 40HZ PULSATION FREQUENCY | 170 |
| FIGURE 5.41: PULSE ENERGY DISTRIBUTION OVER RANGE OF PULSATION NUMBERS | 170 |
| FIGURE 5.42: LEADING EDGE INCIDENCE OVER THE PULSE AT 50, 75, 100 AND 125 PULSATION NUMBERS AT 40HZ PULSE FREQUENCY..... | 172 |
| FIGURE 5.43: LE INCIDENCE OVER THE BLADE SPAN AT MINIMUM INCIDENCE UNDER FOUR PULSATION NUMBERS AT 40HZ PULSE FREQUENCY..... | 173 |
| FIGURE 5.44: LE INCIDENCE OVER THE BLADE SPAN AT MAXIMUM INCIDENCE UNDER FOUR PULSATION NUMBERS AT 40HZ PULSE FREQUENCY..... | 173 |
| FIGURE 6.1: TILTED VOLUTE DEFINITION AND CUT PLANE OF RESULTING FLOW PASSAGE OF BOTH RADIAL AND TILTED VOLUTES. | 176 |
| FIGURE 6.2: COMPARISON OF RADIAL AND TILTED VOLUTE DESIGNS INTERFACE BETWEEN STATIONARY AND ROTATING DOMAINS | 178 |
| FIGURE 6.3: NORMALISED STEADY STATE STAGE EFFICIENCY AT 70KRPM..... | 179 |
| FIGURE 6.4: NORMALISED STEADY STATE STAGE EFFICIENCY AT 90KRPM..... | 179 |
| FIGURE 6.5: NORMALISED STEADY STATE STAGE EFFICIENCY AT 110KRPM..... | 180 |
| FIGURE 6.6: STEADY STATE ROTOR EFFICIENCY AT 90KRPM | 180 |
| FIGURE 6.7: VOLUTE TOTAL PRESSURE LOSS COEFFICIENT PLOTTED AGAINST ROTOR VELOCITY RATIO AT 90KRPM | 181 |
| FIGURE 6.8: PERCENTAGE MFP DIFFERENCE BETWEEN RADIAL AND TILTED DESIGNS AT 70KRPM, 90KRPM AND 110KRPM | 182 |
| FIGURE 6.9: MFP VS PRESSURE RATIO AT 20HZ, 40HZ AND 60HZ..... | 183 |
| FIGURE 6.10: EFFICIENCY PLOTTED AGAINST VELOCITY RATIO 20HZ | 184 |
| FIGURE 6.11: EFFICIENCY PLOTTED AGAINST VELOCITY RATIO 40HZ | 184 |
| FIGURE 6.12: EFFICIENCY PLOTTED AGAINST VELOCITY RATIO 60HZ | 185 |
| FIGURE 6.13: INSTANTANEOUS LE INCIDENCE ANGLE AND NORMALISED ROTOR EFFICIENCY VS. NORMALISED TIME 20HZ PULSE FREQUENCY..... | 187 |
| FIGURE 6.14: INSTANTANEOUS LE INCIDENCE ANGLE AND NORMALISED ROTOR EFFICIENCY VS. NORMALISED TIME 40HZ PULSE FREQUENCY..... | 187 |
| FIGURE 6.15: INSTANTANEOUS LE INCIDENCE ANGLE AND NORMALISED ROTOR EFFICIENCY VS. NORMALISED TIME 60HZ PULSE FREQUENCY..... | 188 |
| FIGURE 6.16: LE FLOW CONE ANGLE IN THE RADIAL AND TILTED VOLUTE VARIANTS AT MINIMUM AND MAXIMUM INCIDENCE RUNNING POINTS | 188 |

| | |
|--|-----|
| FIGURE 6.17: LE BLADE ANGLE IN THE RADIAL AND TILTED VOLUTE VARIANTS AT MINIMUM AND MAXIMUM INCIDENCE RUNNING POINTS..... | 189 |
| FIGURE 6.18: LE INCIDENCE AT MINIMUM AND MAXIMUM INCIDENCE IN THE RADIAL AND TILTED VOLUTE VARIANTS 20Hz..... | 191 |
| FIGURE 6.19: LE INCIDENCE AT MINIMUM AND MAXIMUM INCIDENCE IN THE RADIAL AND TILTED VOLUTE VARIANTS 40Hz..... | 191 |
| FIGURE 6.20: LE INCIDENCE AT MINIMUM AND MAXIMUM INCIDENCE IN THE RADIAL AND TILTED VOLUTE VARIANTS 60Hz..... | 192 |
| FIGURE 6.21: VOLUTE SECONDARY FLOW STRUCTURES AROUND VOLUTE CIRCUMFERENCE. RADIAL AND 20° TILTED VOLUTE DESIGN 40HZ PULSE FREQUENCY MINIMUM INCIDENCE | 194 |
| FIGURE 6.22: VOLUTE SECONDARY FLOW STRUCTURES AROUND VOLUTE CIRCUMFERENCE. RADIAL AND TILTED 20° VOLUTE DESIGN 40HZ PULSE FREQUENCY MAXIMUM INCIDENCE..... | 195 |
| FIGURE 6.23: VOLUTE PRESSURE DISTRIBUTION IN THE RADIAL AND 20° TILTED VOLUTES AT MINIMUM AND MAXIMUM INCIDENCE RUNNING POINTS | 196 |
| FIGURE 6.24: STREAMLINE AND CONTOUR PLOTS AT 72° AND 90° PLANES SHOWING THE DEVELOPMENT OF VOLUTE FLOWS OVER THE PULSE PERIOD. | 198 |
| FIGURE 6.25: BLADE PASSAGE REGIONS..... | 199 |
| FIGURE 6.26: PASSAGE ENTROPY GENERATION MINIMUM U/c_s RUNNING POINT 20HZ PULSE FREQUENCY | 201 |
| FIGURE 6.27: PASSAGE ENTROPY GENERATION MINIMUM U/c_s RUNNING POINT 40HZ PULSE FREQUENCY | 201 |
| FIGURE 6.28: PASSAGE ENTROPY GENERATION MINIMUM U/c_s RUNNING POINT 60HZ PULSE FREQUENCY | 202 |
| FIGURE 6.29: VECTORS ON BLADE TO BLADE PLANE 10% OF PASSAGE WIDTH FROM BLADE SS. MINIMUM U/c_s 40HZ. LEFT - RADIAL HOUSING. RIGHT - TILTED HOUSING | 202 |
| FIGURE 6.30: FLOW ANALYSIS PLANE POSITIONS..... | 203 |
| FIGURE 6.31: STATIC ENTROPY ON CONSTANT SPAN-WISE PLOT AT 50% SPAN, MINIMUM U/c_s RUNNING POINT 40HZ PULSE FREQUENCY. LEFT - RADIAL HOUSING. RIGHT TILTED HOUSING DESIGN | 203 |
| FIGURE 6.32: CONSTANT STREAM-WISE PLOTS OF STATIC ENTROPY AND VECTORS AT THREE CHORD POSITIONS. LEFT - RADIAL HOUSING. RIGHT – TILTED HOUSING | 205 |
| FIGURE 6.33: ROTOR EFFICIENCY, RADIAL AND TILTED VOLUTES. PULSATING NUMBER = 0.5 | 207 |
| FIGURE 6.34: ROTOR EFFICIENCY, RADIAL AND TILTED VOLUTES. PULSATING NUMBER = 0.75 | 207 |
| FIGURE 6.35: ROTOR EFFICIENCY, RADIAL AND TILTED VOLUTES. PULSATING NUMBER = 1 | 208 |
| FIGURE 6.36: ROTOR EFFICIENCY, RADIAL AND TILTED VOLUTES. PULSATING NUMBER = 1.25 | 208 |
| FIGURE 6.37: ROTOR EFFICIENCY, RADIAL AND TILTED VOLUTES. LOW LOAD | 210 |
| FIGURE 6.38: ROTOR EFFICIENCY, RADIAL AND TILTED VOLUTES. MID LOAD | 210 |
| FIGURE 6.39: ROTOR EFFICIENCY, RADIAL AND TILTED VOLUTES. HIGH LOAD..... | 211 |
| FIGURE 6.40: VOLUTE A/R PROGRESSION | 212 |
| FIGURE 6.41: MFP VS PRESSURE RATIO PLOTS FOR THE RADIAL AND TILTED VOLUTE DESIGNS AT A/R=20, A/R=23 AND A/R=26 | 213 |
| FIGURE 6.42: ROTOR EFFICIENCY FOR RADIAL AND TILTED VOLUTES A/R=20 | 214 |
| FIGURE 6.43: ROTOR EFFICIENCY FOR RADIAL AND TILTED VOLUTES A/R=23 | 215 |
| FIGURE 6.44: ROTOR EFFICIENCY FOR RADIAL AND TILTED VOLUTES A/R=26 | 215 |

| | |
|--|-----|
| FIGURE 6.45: COMPARISON OF ROTOR AND STAGE EFFICIENCY FOR THE RADIAL AND TILTED VOLUTE DESIGNS OVER A RANGE OF A/R'S | 216 |
| FIGURE 6.46: ENTROPY GENERATION THROUGH ROTOR REGION FOR RADIAL AND TILTED VOLUTE. A/R=20 | 217 |
| FIGURE 6.47: ENTROPY GENERATION THROUGH ROTOR REGION FOR RADIAL AND TILTED VOLUTE. A/R=23 | 217 |
| FIGURE 6.48: ENTROPY GENERATION THROUGH ROTOR REGION FOR RADIAL AND TILTED VOLUTE. A/R=26 | 218 |
| FIGURE 6.49: MERIDIONAL VELOCITY CONTOURS AND STREAMLINES AT MIN INCIDENCE. A/R=20, RADIAL AND 20° TILTED VOLUTES. | 220 |
| FIGURE 6.50: MERIDIONAL VELOCITY CONTOURS AND STREAMLINES AT MIN INCIDENCE. A/R=23 RADIAL AND 20° TILTED VOLUTES. | 220 |
| FIGURE 6.51: MERIDIONAL VELOCITY CONTOURS AND STREAMLINES AT MIN INCIDENCE. A/R=26 RADIAL AND 20° TILTED VOLUTES. | 221 |
| FIGURE 6.52: MERIDIONAL VELOCITY CONTOURS AND STREAMLINES AT MAX INCIDENCE. A/R=20 RADIAL AND 20° TILTED VOLUTES. | 221 |
| FIGURE 6.53: MERIDIONAL VELOCITY CONTOURS AND STREAMLINES AT MAX INCIDENCE. A/R=23 RADIAL AND 20° TILTED VOLUTES. | 222 |
| FIGURE 6.54: MERIDIONAL VELOCITY CONTOURS AND STREAMLINES AT MAX INCIDENCE. A/R=26 RADIAL AND 20° TILTED VOLUTES. | 222 |
| FIGURE 6.55: VOLUTE EXIT ABSOLUTE FLOW ANGLE AT MIN INCIDENCE A/R=20. LEFT - RADIAL HOUSING. RIGHT - TILTED HOUSING. | 224 |
| FIGURE 6.56: VOLUTE EXIT ABSOLUTE FLOW ANGLE AT MIN INCIDENCE A/R=23. LEFT - RADIAL HOUSING. RIGHT - TILTED HOUSING. | 224 |
| FIGURE 6.57: VOLUTE EXIT ABSOLUTE FLOW ANGLE AT MIN INCIDENCE A/R=26. LEFT - RADIAL HOUSING. RIGHT - TILTED HOUSING. | 224 |
| FIGURE 6.58: VOLUTE EXIT ABSOLUTE FLOW ANGLE AT MAX INCIDENCE A/R=20. LEFT - RADIAL HOUSING. RIGHT - TILTED HOUSING. | 225 |
| FIGURE 6.59: VOLUTE EXIT ABSOLUTE FLOW ANGLE AT MAX INCIDENCE A/R=23. LEFT - RADIAL HOUSING. RIGHT - TILTED HOUSING. | 225 |
| FIGURE 6.60: VOLUTE EXIT ABSOLUTE FLOW ANGLE AT MAX INCIDENCE A/R=26. LEFT - RADIAL HOUSING. RIGHT - TILTED HOUSING. | 225 |
| FIGURE 6.61: SPAN-WISE INCIDENCE DISTRIBUTION AT MINIMUM AND MAXIMUM INCIDENCE RUNNING POINTS FOR RADIAL AND TILTED VOLUTE. A/R=20 | 226 |
| FIGURE 6.62: SPAN-WISE INCIDENCE DISTRIBUTION AT MINIMUM AND MAXIMUM INCIDENCE RUNNING POINTS FOR RADIAL AND TILTED VOLUTE. A/R=23 | 227 |
| FIGURE 6.63: SPAN-WISE INCIDENCE DISTRIBUTION AT MINIMUM AND MAXIMUM INCIDENCE RUNNING POINTS FOR RADIAL AND TILTED VOLUTE. A/R=26 | 227 |
| FIGURE 7.1: SINGLE PASSAGE RADIAL COMPUTATIONAL DOMAIN | 230 |
| FIGURE 7.2: VOLUTE RADIAL VELOCITY CONTOURS AND EXIT ABSOLUTE FLOW ANGLE..... | 231 |

| | |
|---|-----|
| FIGURE 7.3: LE RELATIVE FLOW ANGLE FOR ALL TESTED INLET SPAN-WISE DISTRIBUTIONS | 232 |
| FIGURE 7.4: LE INCIDENCE ANGLE FOR ALL TESTED INLET SPAN-WISE DISTRIBUTIONS | 233 |
| FIGURE 7.5: LE BLADE ANGLE FOR ALL TESTED INLET SPAN-WISE DISTRIBUTIONS | 233 |
| FIGURE 7.6: BLADE LE CAMBER ANGLE..... | 234 |
| FIGURE 7.7: LE FLOW CONE ANGLE FOR ALL TESTED INLET SPAN-WISE DISTRIBUTIONS..... | 234 |
| FIGURE 7.8: NORMALISED MASS FLOW ACROSS LE SPAN..... | 235 |
| FIGURE 7.9: STATIC ENTROPY CONTOURS AND VECTORS PLOTTED ON CONSTANT STREAMWISE PLANES IN BOTH THE UNIFORM INLET VELOCITY DISTRIBUTION AND REALISTIC DISTRIBUTION MODELS..... | 236 |
| FIGURE 7.10: BETWEEN BLADE PLOT 5% OF PASSAGE OFF SUCTION SURFACE..... | 237 |
| FIGURE 7.11: ROTOR PASSAGE CONTROL VOLUMES | 238 |
| FIGURE 7.12: ENTROPY GENERATION IN ROTOR PASSAGE REGIONS | 238 |
| FIGURE 7.13: LE RELATIVE FLOW ANGLE RADIAL AND TITLED PASSAGE | 240 |
| FIGURE 7.14: LE BLADE ANGLE RADIAL AND TITLED PASSAGE | 241 |
| FIGURE 7.15: LE INCIDENCE RADIAL AND TITLED PASSAGE | 241 |
| FIGURE 7.16: STATIC ENTROPY CONTOURS AND VECTORS PLOTTED ON CONSTANT STREAMWISE PLANES IN BOTH THE UNIFORM INLET VELOCITY DISTRIBUTION AND REALISTIC DISTRIBUTION CASES. TILTED PASSAGE..... | 242 |
| FIGURE 7.17: BETWEEN BLADE PLOT 5% OF PASSAGE OFF SS. TILTED PASSAGE | 243 |
| FIGURE 8.1: ASPECT RATIO DESIGNS, AR=0.5, AR=1 AND AR=2 | 247 |
| FIGURE 8.2: MFP VS PRESSURE RATIO FOR VOLUTE ASPECT RATIO DESIGNS WITH CONSTANT A/R. (A) - 20Hz, (B) 40Hz AND (C) 60Hz | 249 |
| FIGURE 8.3: VARIATION IN LE INCIDENCE BETWEEN DESIGNS AT CONSTANT A/R..... | 249 |
| FIGURE 8.4: VOLUTE A/R DISTRIBUTIONS TO MATCH MFP..... | 250 |
| FIGURE 8.5: MFP VS PRESSURE RATIO FOR EACH OF THE VOLUTE ASPECT RATIO DESIGN WITH MODIFIED A/R DISTRIBUTIONS.. | 250 |
| FIGURE 8.6: TURBINE ROTOR EFFICIENCY. (A) - 20Hz, (B) - 40Hz AND (C) - 60Hz | 251 |
| FIGURE 8.7: BREAKDOWN OF PASSAGE INTO SECTION FOR LOSS ANALYSIS | 253 |
| FIGURE 8.8: ENTROPY GENERATION IN ROTOR PASSAGE AT MINIMUM INCIDENCE | 254 |
| FIGURE 8.9: ENTROPY GENERATION IN ROTOR PASSAGE AT MAXIMUM INCIDENCE..... | 254 |
| FIGURE 8.10: SURFACE STREAMLINES AT PLANES AROUND THE TURBINE VOLUTE AND CONTOURS OF RADIAL VELOCITY AT 40Hz MINIMUM INCIDENCE RUNNING POINT | 256 |
| FIGURE 8.11: LAMBDA 2 PARAMETER TO SHOW THE VORTEX CORE DEVELOPMENT AROUND AR=0.5 VOLUTE. (A) – MINIMUM INCIDENCE ANGLE. (B) MAXIMUM INCIDENCE ANGLE..... | 257 |
| FIGURE 8.12: LAMBDA 2 PARAMETER TO SHOW VORTEX CORE DEVELOPMENT AROUND VOLUTE AT MINIMUM INCIDENCE (A) – AR=1. (B) AR=2..... | 258 |
| FIGURE 8.13: VARIATION IN ABSOLUTE FLOW ANGLE ACROSS THE VOLUTE EXIT SPAN AT THE MINIMUM AND MAXIMUM INCIDENCE RUNNING POINTS | 259 |
| FIGURE 8.14: LE INCIDENCE AT 20Hz FREQUENCY. LEFT -MINIMUM INCIDENCE RUNNING POINT. RIGHT- MAXIMUM INCIDENCE RUNNING POINT..... | 261 |

| | |
|--|-----|
| FIGURE 8.15: LE INCIDENCE AT 40Hz FREQUENCY. LEFT -MINIMUM INCIDENCE RUNNING POINT. RIGHT- MAXIMUM INCIDENCE RUNNING POINT..... | 261 |
| FIGURE 8.16: LE INCIDENCE AT 60Hz FREQUENCY. LEFT -MINIMUM INCIDENCE RUNNING POINT. RIGHT- MAXIMUM INCIDENCE RUNNING POINT..... | 261 |
| FIGURE 8.17: VORTEX DEVELOPMENT AND VOLUTE EXIT ABSOLUTE FLOW ANGLE DISTRIBUTION IN AR=0.5 VOLUTE THROUGH PULSE PERIOD..... | 263 |
| FIGURE 8.18: MERIDIONAL VELOCITY ACROSS VOLUTE PASSAGE CENTRE 54°. LEFT - MINIMUM INCIDENCE RIGHT - MAXIMUM INCIDENCE | 264 |
| FIGURE 8.19: MERIDIONAL VELOCITY ACROSS VOLUTE PASSAGE CENTRE 72°. LEFT - MINIMUM INCIDENCE RIGHT - MAXIMUM INCIDENCE | 265 |
| FIGURE 8.20: MERIDIONAL VELOCITY ACROSS VOLUTE PASSAGE CENTRE 90°. LEFT - MINIMUM INCIDENCE RIGHT - MAXIMUM INCIDENCE | 265 |
| FIGURE 8.21: MERIDIONAL VELOCITY ACROSS VOLUTE PASSAGE CENTRE 180°. LEFT - MINIMUM INCIDENCE RIGHT - MAXIMUM INCIDENCE | 265 |
| FIGURE 8.22: MERIDIONAL VELOCITY ACROSS VOLUTE PASSAGE CENTRE 270°. (LEFT - MINIMUM INCIDENCE RIGHT - MAXIMUM INCIDENCE | 266 |
| FIGURE 8.23: MERIDIONAL VELOCITY AT VOLUTE EXIT 54°. (A) - MINIMUM INCIDENCE (B) - MAXIMUM INCIDENCE..... | 267 |
| FIGURE 8.24: MERIDIONAL VELOCITY AT VOLUTE EXIT 90°. (A) - MINIMUM INCIDENCE (B) - MAXIMUM INCIDENCE..... | 267 |
| FIGURE 8.25: MERIDIONAL VELOCITY AT VOLUTE EXIT 198°. (A) - MINIMUM INCIDENCE (B) - MAXIMUM INCIDENCE..... | 267 |
| FIGURE 8.26: MERIDIONAL VELOCITY AT VOLUTE EXIT 270°. (A) - MINIMUM INCIDENCE (B) - MAXIMUM INCIDENCE..... | 268 |
| FIGURE 8.27: MERIDIONAL VELOCITY PERCENTAGE VARIATION AT VOLUTE EXIT 90° (A) - MINIMUM INCIDENCE (B) - MAXIMUM INCIDENCE | 269 |
| FIGURE 8.28: CIRCUMFERENTIAL VELOCITY PERCENTAGE VARIATION AT VOLUTE EXIT 90° (A) - MINIMUM INCIDENCE (B) - MAXIMUM INCIDENCE | 269 |
| FIGURE 8.29: MERIDIONAL VELOCITY PERCENTAGE VARIATION AT VOLUTE EXIT 270° (A) - MINIMUM INCIDENCE (B) - MAXIMUM INCIDENCE | 270 |
| FIGURE 8.30: CIRCUMFERENTIAL VELOCITY PERCENTAGE VARIATION AT VOLUTE EXIT 270° (A) - MINIMUM INCIDENCE (B) - MAXIMUM INCIDENCE | 270 |
| FIGURE 8.31: DEAN NUMBER AROUND THE VOLUTE FOR THE MINIMUM AND MAXIMUM INCIDENCE RUNNING POINTS | 271 |
| FIGURE 8.32: ROTOR EFFICIENCY PLOT COMPARING SST, SAS-SST AND SBES APPROACHES..... | 273 |
| FIGURE 8.33: STREAMLINES AND LAMBDA 2 CRITERION THROUGH VOLUTE PASSAGE AT MINIMUM AND MAXIMUM INCIDENCE FOR THREE APPROACHES..... | 274 |
| FIGURE 8.34: COMPARISON OF LE INCIDENCE IN AR=0.5 VOLUTE USING SST, SAS-SST AND SBES APPROACHES | 275 |
| FIGURE 9.1: TILT VOLUTE DESIGNS WITH AR=0.5 (BLACK) AND AR=2 (BLUE)..... | 277 |
| FIGURE 9.2: MFP HYSTERESIS FOR RADIAL AND TILTED HOUSING AT AR=0.5 AND AR=2 | 278 |
| FIGURE 9.3: ROTOR EFFICIENCY 20Hz..... | 279 |
| FIGURE 9.4: ROTOR EFFICIENCY 40Hz..... | 279 |

| | |
|---|-----|
| FIGURE 9.5: ROTOR EFFICIENCY 60HZ..... | 280 |
| FIGURE 9.6: SURFACE STREAMLINES AND CONTOURS OF MERIDIONAL VELOCITY AT PLANES AROUND THE VOLUTE FOR THE 20° TILTED VOLUTE AR=0.5 AND AR=2 AT MINIMUM AND MAXIMUM INCIDENCE. (40Hz) | 283 |
| FIGURE 9.7: LAMBDA 2 CRITERION IN THE VOLUTE FOR THE TITLED VOLUTE WITH AR=0.5. (A) - MINIMUM INCIDENCE. (B) MAXIMUM INCIDENCE. (40Hz) | 284 |
| FIGURE 9.8: VORTEX DEVELOPMENT IN AR=0.5 20° TILTED VOLUTE THROUGH PULSE PERIOD (40Hz) | 285 |
| FIGURE 9.9: MERIDIONAL VELOCITY ACROSS VOLUTE PASSAGE CENTRE 54°. (A) - MINIMUM INCIDENCE (B) - MAXIMUM INCIDENCE | 286 |
| FIGURE 9.10: MERIDIONAL VELOCITY ACROSS VOLUTE PASSAGE CENTRE 72°. (A) - MINIMUM INCIDENCE (B) - MAXIMUM INCIDENCE | 287 |
| FIGURE 9.11: MERIDIONAL VELOCITY ACROSS VOLUTE PASSAGE CENTRE 90°. (A) - MINIMUM INCIDENCE (B) - MAXIMUM INCIDENCE | 287 |
| FIGURE 9.12: MERIDIONAL VELOCITY ACROSS VOLUTE PASSAGE CENTRE 180°. (A) - MINIMUM INCIDENCE (B) - MAXIMUM INCIDENCE | 287 |
| FIGURE 9.13: MERIDIONAL VELOCITY ACROSS VOLUTE PASSAGE CENTRE 270°. (A) - MINIMUM INCIDENCE (B) - MAXIMUM INCIDENCE | 288 |
| FIGURE 9.14: VOLUTE EXIT ABSOLUTE FLOW ANGLE FOR THE RADIAL VOLUTE AT MINIMUM INCIDENCE. LEFT AR=0.5. RIGHT AR=2..... | 289 |
| FIGURE 9.15: VOLUTE EXIT ABSOLUTE FLOW ANGLE FOR THE TILTED VOLUTE AT MINIMUM INCIDENCE. LEFT AR=0.5. RIGHT AR=2..... | 289 |
| FIGURE 9.16: VOLUTE EXIT ABSOLUTE FLOW ANGLE FOR THE RADIAL VOLUTE AT MAXIMUM INCIDENCE. LEFT AR=0.5. RIGHT AR=2..... | 290 |
| FIGURE 9.17: VOLUTE EXIT ABSOLUTE FLOW ANGLE FOR THE TILTED VOLUTE AT MAXIMUM INCIDENCE. LEFT AR=0.5. RIGHT AR=2..... | 290 |
| FIGURE 9.18: LE INCIDENCE AT THE MINIMUM INCIDENCE RUNNING POINT IN TILTED AND RADIAL VOLUTE CONFIGURATIONS WITH AR=0.5 AND AR=2 | 291 |
| FIGURE 9.19: LE INCIDENCE AT THE MAXIMUM INCIDENCE RUNNING POINT IN TILTED AND RADIAL VOLUTE CONFIGURATIONS WITH AR=0.5 AND AR=2 | 292 |
| FIGURE 10.1: IMPERIAL COLLEGE TEST FACILITY LAYOUT (PADZILLAH, 2014)..... | 294 |
| FIGURE 10.2: IMPERIAL COLLEGE TEST FACILITY CHOPPER PLATES (NEWTON, 2014)..... | 296 |
| FIGURE 10.3: V-CONE FLOW METER LAYOUT. OPERATION AND MAINTENANCE MANUAL, MCCROMETER 2013 | 298 |
| FIGURE 10.4: HOT WIRE CALIBRATION DATA. LEFT – RADIAL HOUSING RIGHT – RADIAL HOUSING..... | 300 |
| FIGURE 10.5: RADIAL AND TILTED VOLUTES. LEFT - RADIAL. RIGHT - TILTED..... | 309 |
| FIGURE 10.6: MIXED FLOW TURBINE WHEEL AND SHAFT..... | 309 |
| FIGURE 10.7: SCHEMATIC OF THE TESTED TURBINE GEOMETRIES. LEFT -RADIAL HOUSING. RIGHT - TILTED HOUSING..... | 310 |
| FIGURE 10.8: TEST LAYOUT | 311 |
| FIGURE 10.9: MFP COMPARISON OF RADIAL AND TILTED VOLUTE DESIGNS AT 30KRPM | 312 |

| | |
|--|-----|
| FIGURE 10.10: MFP COMPARISON OF RADIAL AND TILTED VOLUTE DESIGNS AT 48KRPM | 313 |
| FIGURE 10.11: MFP COMPARISON OF RADIAL AND TILTED VOLUTE DESIGNS AT 56KRPM | 313 |
| FIGURE 10.12: EFFICIENCY COMPARISON OF RADIAL AND TILTED VOLUTE DESIGNS AT 30KRPM | 314 |
| FIGURE 10.13: EFFICIENCY COMPARISON OF RADIAL AND TILTED VOLUTE DESIGNS AT 48KRPM | 314 |
| FIGURE 10.14: EFFICIENCY COMPARISON OF RADIAL AND TILTED VOLUTE DESIGNS AT 56KRPM | 315 |
| FIGURE 10.15: 30KRPM STEADY STATE EFFICIENCY COMPARISON EXPERIMENTAL VS CFD | 316 |
| FIGURE 10.16: 48KRPM STEADY STATE EFFICIENCY COMPARISON EXPERIMENTAL VS CFD | 317 |
| FIGURE 10.17: 56KRPM STEADY STATE EFFICIENCY COMPARISON EXPERIMENTAL VS CFD | 317 |
| FIGURE 10.18: 30KRPM STEADY STATE MFP COMPARISON EXPERIMENTAL VS CFD..... | 318 |
| FIGURE 10.19: 48KRPM STEADY STATE MFP COMPARISON EXPERIMENTAL VS CFD..... | 319 |
| FIGURE 10.20: 56KRPM STEADY STATE MFP COMPARISON EXPERIMENTAL VS CFD..... | 319 |
| FIGURE 10.21: COMPARISON OF TURBINE EFFICIENCY AT 56KRPM BETWEEN CFD WITH STEP INCLUDED AND EXPERIMENTAL.. | 320 |
| FIGURE 10.22: IMPACT OF BACK FACE STEP ON ROTOR FLOW FIELD. (A) – RADIAL VOLUTE NO STEP, (B) TITLED VOLUTE NO STEP, (C) RADIAL VOLUTE WITH STEP, (D) TILTED VOLUTE WITH STEP..... | 321 |
| FIGURE 10.23: CYCLE AVERAGED MFP 30KRPM 20HZ | 324 |
| FIGURE 10.24: CYCLE AVERAGED MFP 30KRPM 40HZ | 324 |
| FIGURE 10.25: CYCLE AVERAGED MFP 30KRPM 60HZ | 325 |
| FIGURE 10.26: CYCLE AVERAGED MFP 48KRPM 20HZ | 326 |
| FIGURE 10.27: CYCLE AVERAGED MFP 48KRPM 40HZ | 326 |
| FIGURE 10.28: CYCLE AVERAGED MFP 48KRPM 60HZ | 327 |
| FIGURE 10.29: CYCLE AVERAGED MFP 56KRPM 20HZ | 327 |
| FIGURE 10.30: CYCLE AVERAGED MFP 56KRPM 40HZ | 328 |
| FIGURE 10.31: CYCLE AVERAGED MFP 56KRPM 60HZ | 328 |
| FIGURE 10.32: CYCLE AVERAGED EFFICIENCY 30KRPM 20HZ | 329 |
| FIGURE 10.33: CYCLE AVERAGED EFFICIENCY 30KRPM 40HZ | 330 |
| FIGURE 10.34: CYCLE AVERAGED EFFICIENCY 30KRPM 60HZ | 330 |
| FIGURE 10.35: CYCLE AVERAGED EFFICIENCY 48KRPM 20HZ | 331 |
| FIGURE 10.36: CYCLE AVERAGED EFFICIENCY 48KRPM 40HZ | 331 |
| FIGURE 10.37; CYCLE AVERAGED EFFICIENCY 48KRPM 60HZ | 332 |
| FIGURE 10.38: CYCLE AVERAGED EFFICIENCY 56KRPM 20HZ | 333 |
| FIGURE 10.39: CYCLE AVERAGED EFFICIENCY 56KRPM 40HZ | 333 |
| FIGURE 10.40: CYCLE AVERAGED EFFICIENCY 56KRPM 60HZ | 334 |
| FIGURE 10.41: 30KRPM LAMBDA PARAMETER RADIAL VS TILTED VOLUTE DESIGN | 335 |
| FIGURE 10.42: 48KRPM LAMBDA PARAMETER RADIAL VS TILTED VOLUTE DESIGN | 336 |
| FIGURE 10.43: 56KRPM LAMBDA PARAMETER RADIAL VS TILTED VOLUTE DESIGN | 337 |
| FIGURE 10.44: UNSTEADY ISENTROPIC WORK CFD VS EXPERIMENTAL FOR THE RADIAL VOLUTE DESIGN | 338 |
| FIGURE 10.45: UNSTEADY ISENTROPIC WORK CFD VS EXPERIMENTAL FOR THE TILTED VOLUTE DESIGN | 338 |

| | |
|---|-----|
| FIGURE 10.46: COMPARISON OF ROTOR TORQUE BETWEEN EXPERIMENTAL AND CFD AT 20HZ, 40HZ AND 60HZ. (A) RADIAL VOLUTE, (B) TILTED VOLUTE..... | 339 |
| FIGURE 10.47: GENERATED ROTOR TORQUE USING FROZEN ROTOR AND SLIDING MESH METHODS 40HZ | 340 |
| FIGURE 10.48: VOLUTE EXIT ABSOLUTE FLOW ANGLE USING FROZEN ROTOR AND SLIDING MESH APPROACH AROUND AZIMUTH ANGLE AT MINIMUM MASS FLOW POINT OF PULSE AT 40HZ FREQUENCY | 341 |
| FIGURE 10.49: VOLUTE EXIT ABSOLUTE FLOW ANGLE USING FROZEN ROTOR AND SLIDING MESH APPROACH AROUND AZIMUTH ANGLE AT MAXIMUM MASS FLOW POINT OF PULSE AT 40HZ FREQUENCY | 342 |

NOMENCLATURE:

| | |
|-----------|---|
| \bar{a} | Sonic Velocity |
| A | Area |
| AR | Aspect Ratio |
| A/r | Ratio of Cross Sectional Area to Radius |
| B | Blockage Factor |
| C | Absolute Velocity |
| CFD | Computational Fluid Dynamics |
| C_H | Absolute Velocity at High Mass Flow |
| C_L | Absolute Velocity at Low Mass Flow |
| C_p | Specific Heat at Constant Pressure |
| C_v | Specific Heat at Constant Volume |
| d | Diameter |
| De | Dean Number |
| f | Frequency |
| F_S | Safety Factor |
| GCI | Grid Convergence Index |
| h | Grid Spacing |
| i | Internal Energy |
| i_{LE} | Leading Edge Incidence |
| k | Thermal Conduction Coefficient |
| K_{PL} | Total Pressure Loss Coefficient |
| L | Characteristic Length |
| LES | Large Eddy Simulation |
| LDA | Laser Doppler Anemometry |
| LE | Leading Edge |

| | |
|------------------|--|
| \dot{m} | Mass Flow |
| \dot{m}_{Load} | Mass Flow pulse load |
| \dot{m}_{no} | Mass Flow Pulsation Number |
| M_{acc} | Mass accumulation |
| n | Number of Nodes |
| N | Rotational Speed |
| N_i | Shape Function |
| $PMSt$ | Pressure Wave Modified Strouhal Number |
| P | Pressure |
| PR | Pressure Ratio |
| PS | Pressure Surface |
| \vec{r} | Upwind Vector |
| r | Volute Radius |
| r_i | Mesh Refinement Factor |
| R | Gas Constant |
| $RANS$ | Reynolds Averaged Navier Stokes |
| R_C | Radius of Curvature |
| Re_D | Reynolds Number Based on Diameter |
| RMS | Root Mean Squared |
| S | Swirl Factor |
| S_m | Momentum Source Term |
| S_i | Internal Energy Source Term |
| SAS | Scaled Adaptive Simulation |
| SS | Suction Surface |
| SST | Shear Stress Transport |
| S_t | Strouhal Number |

| | |
|-----------|--|
| t | Time |
| TE | Trailing Edge |
| T | Inlet Total Temperature |
| u | Bulk Velocity |
| \bar{u} | Time Averaged Velocity |
| u' | Instantaneous Velocity |
| u^+ | Non-Dimensional Velocity |
| U | Blade Speed |
| U/c_s | Velocity Ratio |
| URANS | Unsteady Reynolds Averaged Navier Stokes |
| V | Volume |
| W | Relative Velocity |
| x | Volute Axial Position |
| y^+ | Non-Dimensional Wall Distance |

Greek Letters

| | |
|------------------|-------------------------|
| α | Absolute Flow Angle |
| β | Relative Flow Angle |
| β_B | Blade Angle |
| β_f | Blending Factor |
| θ | Volute Tilt Angle |
| \emptyset | Exhaust Valve Parameter |
| λ_{flow} | Flow Cone Angle |
| Λ | Blade Cone Angle |
| η | Efficiency |
| Φ | Dissipation Function |

| | |
|------------|--------------------------|
| Γ | Diffusion Coefficient |
| ϕ | Blade Camber Angle |
| ρ | Density |
| τ | Torque |
| τ_w | Viscous Stress |
| δ_v | Viscous Length Scale |
| μ_t | Eddy Viscosity |
| μ | Dynamic Viscosity |
| u_τ | Frictional Velocity |
| γ | Ratio of Specific Heats |
| ω | Rotational Speed (Rad/s) |

Subscripts

| | |
|--------|-----------------------------------|
| ip | Integration Point |
| up | Upwind Point |
| $meri$ | Meridional |
| ref | Reference Value |
| u | Tangential |
| T-T | Total to Total |
| T-s | Total to Static |
| 0 | Parameter total |
| 1 | Volute Inlet Station |
| 1.5 | Volute Outlet/Rotor Inlet Station |
| 2 | Rotor LE Station |
| 2.5 | Rotor TE station |
| 3 | Stage Outlet Station |

1 INTRODUCTION

1.1 INTRODUCTION AND MOTIVATION

Environmental issues have, over recent years, become increasingly important. Government legislation has aimed to reduce emissions in many industries. Data taken from the International Energy Agency IEA, (2016) showed that transport contributes to 23% of the world's CO₂ emissions in 2014, furthermore, 75% of this figure comes from road transport alone (see figure 1.1 for breakdown). Therefore approximately 17% of the worlds CO₂ emissions come from road transport alone. The European Union (EU) is aiming is to reduce CO₂ emissions by 20% of that in 1990 by the year 2020 and by 80% by 2050 European-Commission, (2011). To achieve this, it is estimated that the transport sector must reduce its greenhouse emissions by 54%-67% by the year 2050.

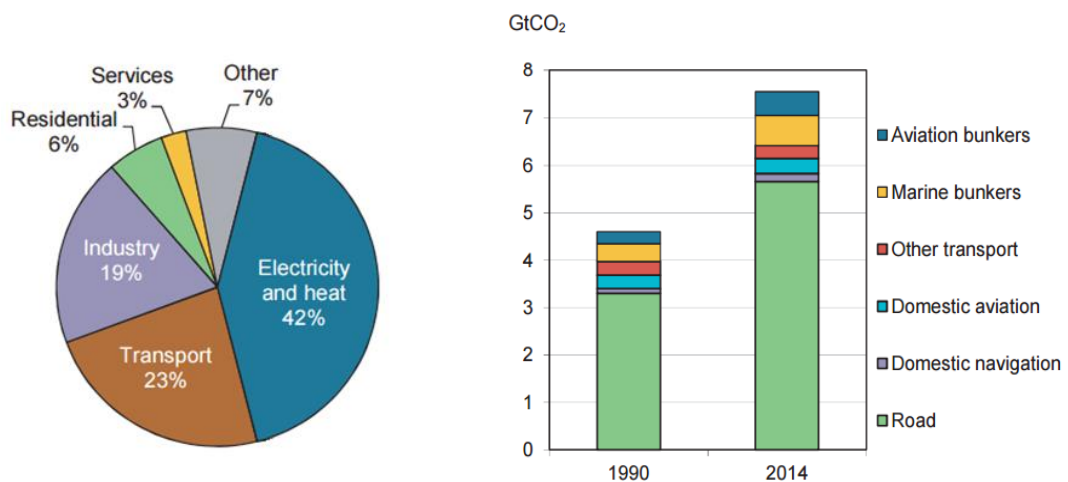


Figure 1.1: CO₂ Emissions data for 2014 (IEA, 2016).

For the automotive industry to achieve these strict emission guidelines, the efficiency of the power plant must be improved. Engine downsizing is a key method in achieving this goal as it reduces inertial mass and space requirements. However, for a downsized engine to maintain overall performance the power density of the engine must be increased. As a result, turbocharging has become an increasingly desirable, not only in diesel powered engines, but in gasoline engines too.

As the internal combustion engine is an air breathing machine, the flow of oxygen into and out of the engine is vital for work output. Turbochargers can enhance the breathing capabilities of an engine by increasing the cylinder inlet air density, thus increasing the engine output power and torque. This process is achieved by employing a compressor ahead of the cylinder, to compressor the inlet air. The compressor is driven by the turbine positioned downstream of the combustion process that extracts energy from the otherwise wasted exhaust gas.

1.2 TURBOCHARGER COMPONENTS

Turbochargers usually consist of a centrifugal compressor stage, into which ambient air enters axially into the compressor wheel. The driven rotation of the wheel does work on the fluid increasing the flow velocity. The flow is then diffused through the compressor and volute increasing air density ahead of combustion.

The compressor wheel is driven by a common shaft from the turbine. High energy flow enters into the turbine volute from the engine cylinder which is accelerated and directed into the turbine rotor. The primary design parameter of the volute is its area to radius ratio (A/r). The volute A/r determines the angle in which the flow exits the volute into the rotor and the swallowing capacity of the stage.

The turbine rotor extracts shaft work from the flow directed by the volute. This is achieved by accelerating and turning of the flow through the wheel resulting in a reduction in angular momentum and therefore a rotor torque is generated. Automotive turbochargers almost exclusively employ the use of radial flow turbines to drive the compressor stage. This is mainly due to the fact that a radial turbine can offer a greater specific power than the axial alternative. This is because there is a change in blade speed in a radial rotor from inlet to outlet, adding to the work extraction. Therefore, fewer stages or a smaller turbine can be implemented (Japikse and Baines, 1994). The flow is then diffused ahead of the exhaust to a required back pressure.

1.2.1 TURBINE OPERATING ENVIRONMENT

The operation of the turbocharger turbine is further complicated due to the nature of the reciprocating engine. As the engine turns the movement of each cylinder will produce a pulse of exhaust flow. This effect results in a highly unsteady, pulsating flow at the turbine inlet and therefore the turbine must be capable of operating efficiently over a wide range of flow conditions.

The form of the inlet pulse is dependent on the engine geometry, speed and valve timing. Changing any one of these factors will affect pulse propagation through the

exhaust system and hence the flow that the turbine encounters (Watson and Janota, 1982). Variable valve timing also has an impact on pulse propagation as it influences the scavenging of the engine as engine speed is changed. As a result it is impossible to characterise a single pulse form that the turbine experiences. Therefore, it is necessary to analyse turbine performance over a range of pulse characteristics such as frequency, amplitude, load and shape to encompass the full turbine operating envelope.

Figure 1.2 illustrates the impact of pulsating flows on the rotor leading edge (LE) velocity components and flow angles through the pulse while blade speed remains constant due to rotor inertia. A significant change in inlet relative flow angle (β) from highly negative, at low mass flows, to highly positive, at high mass flows is experienced through the pulse. These excessive flow angles result in LE flow separation. C_H and C_L represent the absolute velocity of gas leaving the volute at high and low flow rates respectively, and W_H and W_L represent the relative flow velocities at high and low mass flow respectively. U is the LE blade velocity.

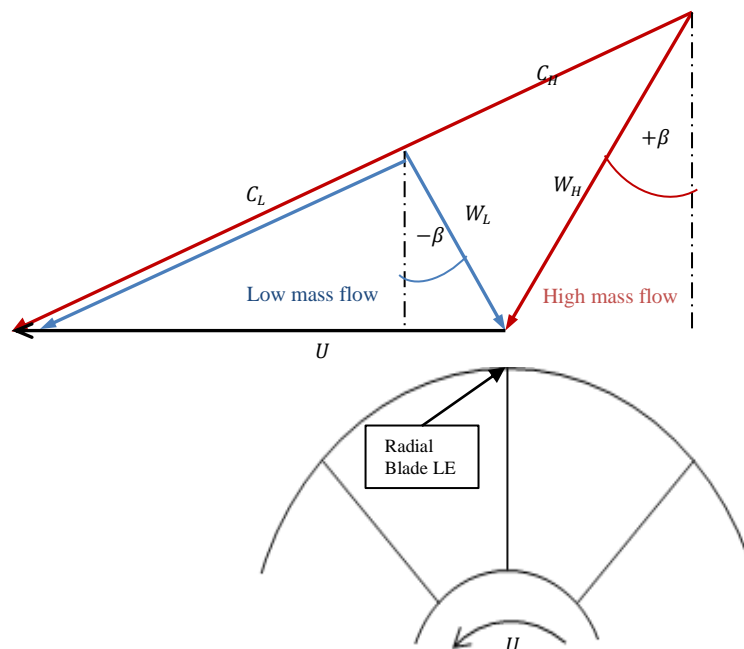


Figure 1.2: Rotor inlet velocity triangles under pulsating flow

Furthermore, with varying inlet flow conditions the energy available within the flow also changes. Maximum available energy is present at the mass flow peak where stage pressure ratio is maximised. The velocity ratio (U/c_s) can be defined as an important turbine performance parameter which is inversely proportional to pressure ratio -

$$\frac{U}{c_s} = \frac{U}{\sqrt{2C_p T_{01} \left(1 - \left(\frac{P_2}{P_{01}}\right)^{\gamma-1/\gamma}\right)}} \quad (1)$$

Where U is blade speed, c_s is the isentropic spouting velocity, C_p is the specific heat at constant pressure, T_{01} is inlet total temperature, P_2 is the outlet static pressure, P_{01} is the inlet total pressure and γ is the ratio of specific heats.

The need for a turbine to operate efficiently at higher energy, low velocity ratio running points is vital for optimal pulse energy extraction. Radial turbines, despite their many advantages in turbocharging applications, have limited flexibility in dealing with such low velocity ratio running points. The optimal inlet flow angles in radial flow turbines is usually between -10 and -40 degrees due to the existence of the Coriolis force resulting in cross passage flows (Japikse and Baines, 1994). The flow through a radial turbine passage at different inlet conditions is presented in figure 1.3. At high velocity ratios (a), the highly negative flow angles result in pressure surface separation at the leading edge. At the high energy, low velocity ratio running points (c) the highly positive flow angles result in separation from the suction surface of the rotor. Optimal performance occurs at point (b) where the inlet flow angles are slightly negative (-10° to -40°).

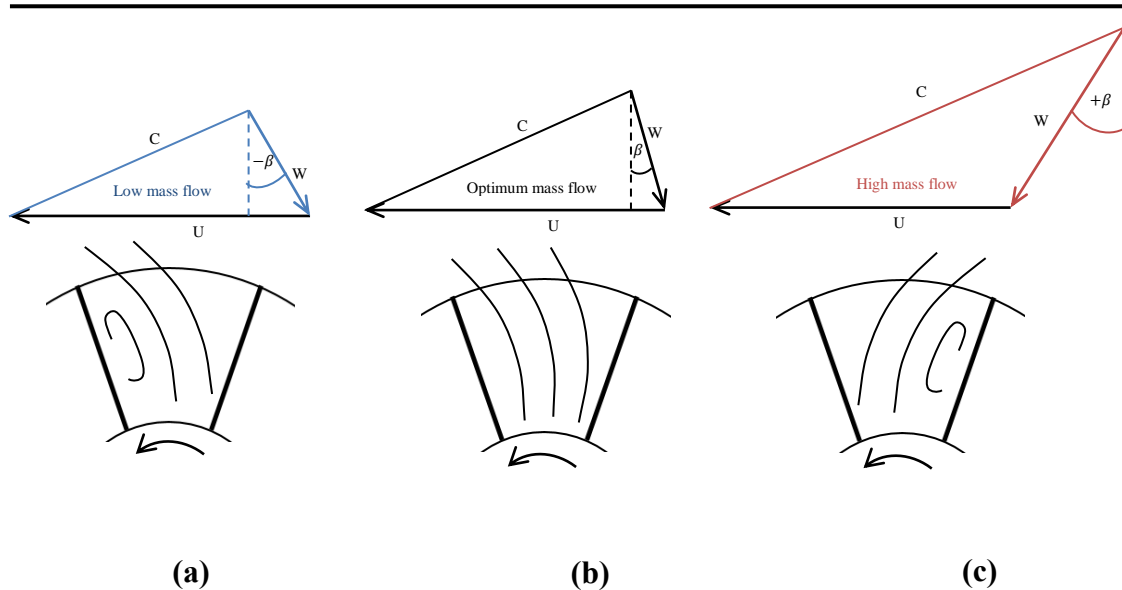


Figure 1.3: Impact of inlet flow angles on passage flows

At the low velocity ratio running points the inlet flow angles are increasingly positive and as the blade angle is fixed at 0° due to mechanical constraints, blade incidence is equal to the inflow angle. Incidence, i , is defined as –

$$i = \beta + \beta_B \quad (2)$$

Where β is the relative flow angle and β_B is the blade angle.

The fixed value of blade angle means that the rotor cannot be modified to improve incidence. Alternately, mixed flow turbines can be implemented which have the ability to achieve non-zero blade angles and thereby improve incidence at off design conditions.

1.2.2 MIXED FLOW TURBINE DEFINITION

While radial turbines must have a 0° blade angle to maintain radial stacking of the blade fibres, mixed flow turbines overcome this constraint through fundamental changes to the blade design. The stacking of blade fibres is demonstrated in figure 1.4. Any violation of this stacking results in excessive stresses in the rotor and inevitably, wheel failure due to the high rotational speeds.

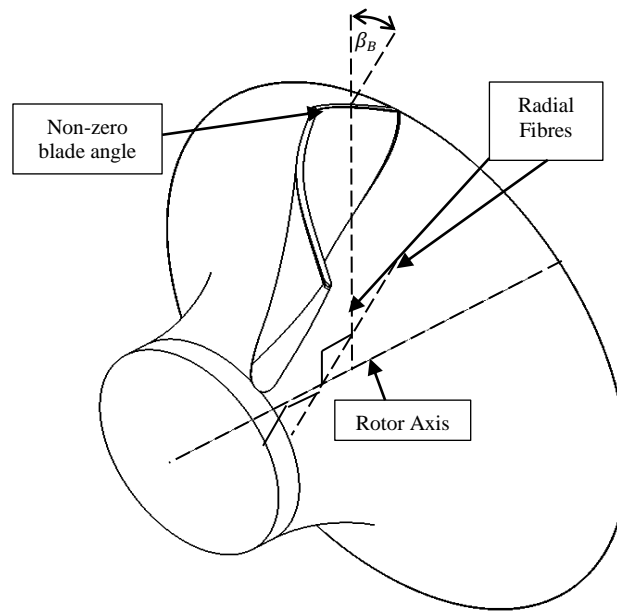


Figure 1.4: Radial stacking of blade fibres for zero and non-zero blade angles

Mixed flow turbines achieve non-zero blade angles while maintaining radial stacking of the blades fibres through the addition of cone (Λ) and camber angles (φ), both of which are defined in figure 1.5. It should be noted that the definition of camber angle is positive in the direction of wheel rotation, in figure 1.5 the wheel contains negative camber, giving rise to a negative blade angle, effectively a swept back configuration.

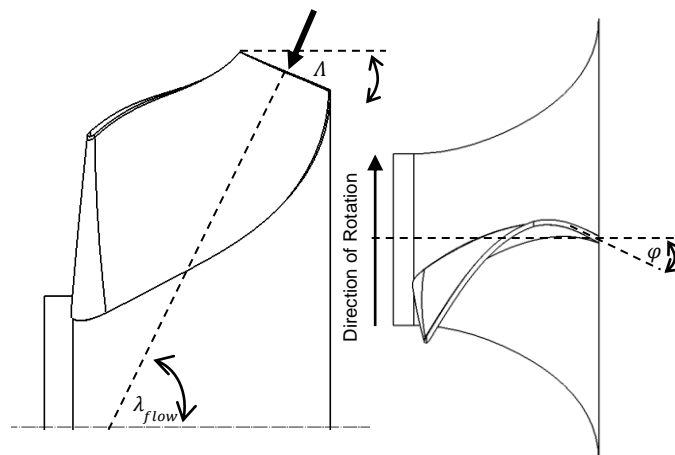


Figure 1.5: Flow cone angle (λ_{flow}), blade cone angle (Λ) and camber angle (φ)

How the combination of these two angles can result in a non-zero blade without violation of the radial stacking of blade fibers is illustrated in figure 1.6. Where β_B denotes the blade angle, φ the blade camber angle and λ_{flow} the flow cone angle.

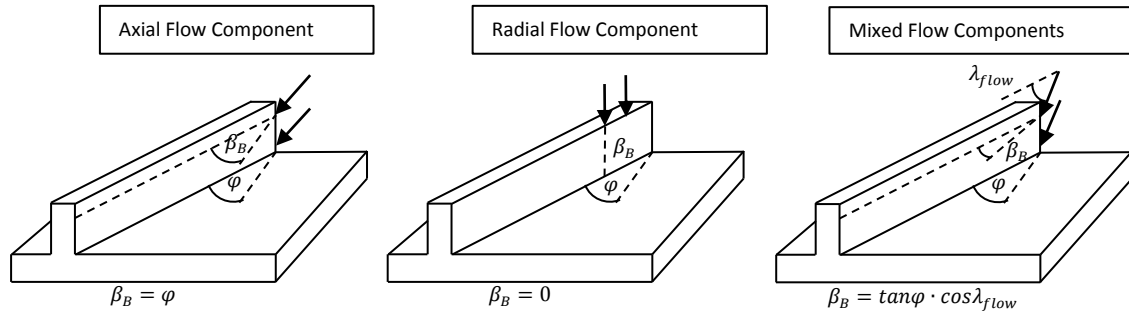


Figure 1.6: Inlet flow in radial, axial and mixed flow turbines (Leonard et al., 2013)

In the axial flow case, the blade angle is equal to the camber angle of the blade. The blade angle in the radial case is independent of the camber angle and remains at zero degrees. Finally, in the mixed flow case, the blade angle is dependent on both the camber and cone angles. The resulting blade angle is given by equation 3.

$$\tan\beta_B = \tan\varphi \cdot \cos\lambda_{flow} \quad (3)$$

The resulting non-zero blade angle can reduce the flow incidence between the incoming relative flow angle (β) and the blade resulting in reduced flow separation at low velocity ratio running points by effectively producing swept back blades as demonstrated in figure 1.7. Here the existence of a positive flow angle results in improved incidence.

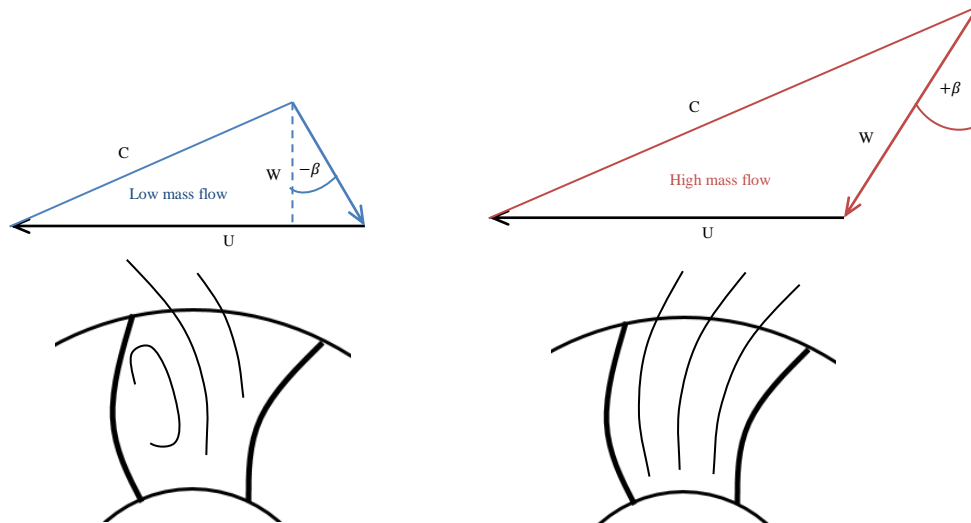


Figure 1.7: passage flows in a mixed flow turbine with non-zero blade angle

Not only can the mixed flow turbine reduce inlet flow loss but the removal of blade mass due to the blade cone angle can have a significant impact on the inertia of the wheel resulting in improved transient response. The combination of these effect makes the introduction of mixed rotor highly desirable particularly when considering the nature of pulsating flows. However, fundamental changes to the turbine geometry must be taken into account during volute design. If a mixed flow turbine is not supplied with an axial flow component the mixed flow effect cannot take place and the reduction in incidence isn't achieved. Also, the added degree of freedom of the blade angle requires detailed knowledge about leading edge flows throughout the pulse for optimal performance to be achieved.

1.3 TURBINE PERFORMANCE PARAMETERS

It is important to define the positions through the turbine with the numbering system used throughout this thesis. The positions through the turbine and there numbering is given in table 1.1 -

| <i>Position</i> | <i>number</i> |
|----------------------------------|---------------|
| <i>Volute Inlet</i> | 1 |
| <i>Volute outlet/rotor inlet</i> | 1.5 |
| <i>Rotor LE</i> | 2 |
| <i>Rotor TE</i> | 2.5 |
| <i>Stage outlet</i> | 3 |

Table 1.1: stage numbering system

Baines & Whitfield, (1990) showed that the behavior of a turbine is dependent on numerous basic parameters. In turbocharging applications there is usually only one turbine stage and the kinetic energy available downstream of the rotor is wasted. As such the total pressure at the exit is replaced with static pressure. This results in -

$$f(d_2, N, \dot{m}, P_{01}, P_3, T_{01}, T_{03}, R, \gamma, \mu) = 0 \quad (4)$$

Where d_2 is the rotor inlet diameter, N is the rotation speed, \dot{m} is mass flow, P_{01} is inlet total pressure, P_3 is outlet static pressure, T_{01} is inlet total pressure, T_{03} is outlet total temperature, R is the gas constant, γ is the ratio of specific heats and μ is dynamic viscosity.

These variables can be reduced to a number of dimensionless parameters using Buckingham Pi theory. As the parameters expressed in equation 4 are of four different fundamental dimensions, length, time, mass and temperature; the 10 variables can be reduced to 6 dimensionless π terms resulting in -

$$f\left(\frac{Nd_2}{\sqrt{RT_{01}}}, \frac{\dot{m}d_2^2\sqrt{RT_{01}}}{P_{01}}, \frac{P_3}{P_{01}}, \frac{T_{03}}{T_{01}}, \gamma, \frac{\mu\sqrt{RT_{01}}}{P_{01}d_2}\right) = 0 \quad (5)$$

Usually the Reynold number term (the final term within the brackets) is ignored as it has very little impact on turbine performance unless the size difference of the turbines compared is significant. The ratio of specific heats is also often assumed to be constant. This produces just four non-dimensional parameters -

$$f\left(\frac{Nd_2}{\sqrt{RT_{01}}}, \frac{\dot{m}d_2^2\sqrt{RT_{01}}}{P_{01}}, \frac{P_3}{P_{01}}, \frac{T_{03}}{T_{01}}\right) = 0 \quad (6)$$

The expression can be further simplified by replacing the total temperature ratio with the total to static isentropic efficiency which is expressed as -

$$\eta_{T-s} = \frac{\dot{W}_{actual}}{\dot{W}_{isentropic}} = \frac{\dot{m}C_p(T_{01} - T_{03})}{\dot{m}C_p(T_{01} - T_{03is})} = \frac{\tau \cdot \omega}{\dot{m}C_p \cdot T_{01} \cdot \left(1 - \left(\frac{P_3}{P_{01}}\right)^{\frac{\gamma-1}{\gamma}}\right)} \quad (7)$$

Where C_p is the specific heat at constant pressure. Furthermore, the gas constant R can be ignored and if the same turbine wheel is used, so can the rotor inlet diameter d_2 . This results in the final relationship -

$$f\left(\frac{N}{\sqrt{T_{01}}}, \frac{\dot{m}\sqrt{T_{01}}}{P_{01}}, \frac{P_3}{P_{01}}, \eta_{T-s}\right) = 0 \quad (8)$$

Where $\frac{N}{\sqrt{T_{01}}}$ is the specific speed and $\frac{\dot{m}\sqrt{T_{01}}}{P_{01}}$ is the mass flow parameter (MFP). These two terms are no longer non-dimensional but pseudo non-dimensional. The remaining two terms, pressure ratio $\left(\frac{P_3}{P_{01}}\right)$ and total to static efficiency (η_{T-s}) are non-dimensional. These four parameters describe the performance of a turbine. The operating point of the turbine will be fixed if two of these parameters are constant. The resulting turbine performance can then be plotted on two figures, MFP vs pressure ratio and efficiency vs pressure. It is common practise to plot the efficiency against isentropic velocity ratio (equation 1) instead of pressure ratio. These two plots show the overall performance of any turbine stage.

1.4 RESEARCH AIMS

The aim of this work is to gain a better understanding of the impact of the turbine volute design on overall mixed flow turbine performance. In the past, a number of studies have investigated the effects of volute design on radial turbine performance. Furthermore, many authors have examined mixed flow turbine rotor performance. However, there are only a limited number of studies that focus on the volute requirements specifically for a mixed flow turbines. Therefore, this work aims to provide a better understanding of volute flow physics and how to optimise the volute exit flow conditions specifically for a mixed flow turbine. As explained in the previous section, the inlet characteristics of mixed flow turbines differs significantly from that of radial turbines. Therefore, special attention to the volute design is require specifically for mixed flow stages. Furthermore, the addition of flow cone and camber angles can allow the blade angle to vary over the LE span. Correct match of rotor and volute is therefore vital to optimal performance.

2 LITERATURE REVIEW

This section provides an overview of the work to date that is relevant to the current investigation. This focuses on advancement in pulsating flows in turbines, mixed flow turbine optimisation and investigation into volute flow development.

2.1 PULSED FLOW TURBOCHARGING RESEARCH

The first published study investigating the true effects of pulsating inlet flow on turbine performance was conducted by Wallace & Blair, (1965) . The authors investigated a wide range of parameters on turbine performance including pulse frequency, pulse form, pulse amplitude, turbine speed, nozzle angle, pipe length and pipe area. Despite the large under taking of work, the authors were unable to draw solid conclusions from this work. This was soon followed by work by Benson & Scrimshaw, (1965) who investigated the impact of pulse frequency on performance, Kosuge et al., (1975) looked at the impact of pulse amplitude and Strouhal number and Benson, (1974), who again investigated the impact of pulse shape. These studies all agreed that the pulsating performance deviated from the previously accepted quasi-steady approach. However, the level of deviation from the steady state performance found was inconsistent with Wallace & Blair, (1965) and Benson, (1974) reporting an increase in mass flow rate and power output under pulsating conditions and Benson & Scrimshaw, (1965) and Kosuge et al., (1975) reporting a reduction.

One of the main difficulties with investigating the impact of pulsating flow is the need to record instantaneous performance parameters including temperature, rotational speed, mass flow rate and rotor torque. In the early studies mentioned, only time averaged performance could be measure due to technical limitations. This low fidelity data acquisition led to significant variations in the results obtained and the lack of consistency.

Dale & Watson, (1986) published the first work completed on the pulsed flow test rig at Imperial College London. This facility provided instantaneous

measurements of rotor torque and mass flow while the instantaneous temperature was calculated from the measured pressure by assuming adiabatic conditions. Szymko, (2006) later showed this approach to give accurate results for temperature. The average rotor torque was obtained through the use of an eddy-current dynamometer, while the instantaneous fluctuations of torque were obtained through precise measurement of the rotor speed. Summing these two values gave the total instantaneous torque. The instantaneous mass flux was obtained through hot wire anemometry. The presented results showed, for the first time the hysteresis present in turbine performance under pulsating flow conditions, as shown in figure 2.1 for the mass flow rate.

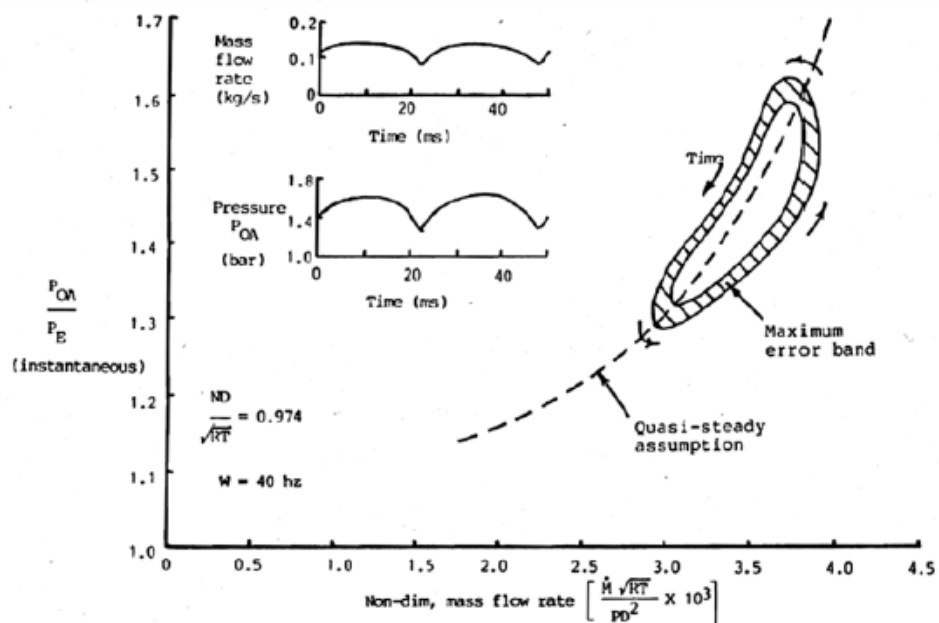


Figure 2.1: Pulsating performance measured by (Dale and Watson, 1986)

A few years later Dale, (1990) presented more experimental results of the unsteady performance of a twin entry turbine. This again showed the performance hysteresis and the authors also proposed that the impact was the result of flow acceleration and deceleration into the volute. Baines, (2010) identified this filling and emptying behavior as one of the major findings from the work conducted at Imperial College London.

Yeo & Baines, (1990) used the same test rig as Dale, (1990) at Imperial College London to investigate the internal flow of the turbine. This was done using laser two focus velocimetry. Measurements of the velocity components at numerous positions at the rotor inlet and outlet were taken, but under unsteady flows, only one position was measured at the rotor inlet. The authors found that the velocity components measured under unsteady operation were similar to those at steady state operating points. From this they concluded that the rotor operates in a quasi-steady manor. The quasi-steady assumption of the turbine assumes that at any point in time, under pulsating inlet conditions, the turbine will perform the same as it would under corresponding steady conditions. Therefore, the cycle averaged quasi-steady performance can be obtained by integrating the steady state performance of the turbine over the range of flow conditions experience in the pulse.

Baines et al., (1994) used this knowledge along with the provided by Dale, (1990) to develop an unsteady turbine model based on the filling and emptying behaviour. Baines found good agreement with experimental data further supporting this conclusion.

Szymko et al., (2002) presented the work completed at Imperial College to improve the test facility. A new eddy current dynamometer was added that was capable of giving a much greater range of loading on the turbine. This is particularly important when investigating pulsating flow as the range of operation will often extend beyond the normal range of steady state maps. Therefore, to compare the pulsating performance in these regions with the equivalent quasi-steady performance the steady state map must be extended.

During testing, the data measured at the stage inlet is acquired at a different spatial location to the turbine torque recorded. As such it takes a finite amount of time for the conditions observed at the stage inlet to propagate to the rotor. Therefore, it is necessary to phase shift the isentropic conditions measured at the inlet to account for the time delay. A number of methods have been attempted to achieve this. Arcoumanis et al., (1995) used the sonic velocity, while Winterbone et

al., (1991) and Baines et al., (1994) used the bulk flow velocity. Alternately, Szymko et al., (2005) using the sum of the sonic and bulk velocities found good agreement. More recently Cerdoun & Ghenaiet, (2015) simulated pulsating flows through a twin entry volute and found the performance was highly dependent on the phase shift method used. The authors stated that there is a non-constant time shift between isentropic and actual power during the pulse and this can be dependent of pulse frequency, amplitude and temporal gradient of mass flow not just flow velocity. In all cases where pulsating performance is investigated the time shifting method used is a potential area for error and needs to be done with care.

Szymko, (2006) also made contributions to the understanding of the unsteady performance of turbochargers under pulsating flows. He characterised the impact of unsteadiness on performance using the Strouhal number, (St). The Strouhal number is defined in equation 9 and relates the travel time of the flow to the time period of the flow disturbance.

$$St = \frac{f_{ref} L_{ref}}{v_{ref}} \quad (9)$$

Where f_{ref} is the reference frequency, L_{ref} is the reference length and v_{ref} is the reference velocity.

From this Szymko defined a normalised Strouhal number that accounts for the length of the pulse cycle in which the pulse is present. For instance a 4 stroke engine operating at 1200rpm results in 600 pulse cycles each minute and therefore, a frequency of 10Hz. However, the exhaust valve is typical only open for 1/3 of the of the cycle and so the parameter ϕ was introduced to account for this, $\phi = 1/3$. The factor of $\frac{1}{2}$ was also introduced to the formula as the pulse event only accounts for half of the wave length in the experimental facilities at Imperial college, see figure 2.2. This means that the normalised Strouhal number is defined as -

$$St^* = \frac{f_{ref} L_{ref}}{v_{ref}} \frac{1}{2\phi} \quad (10)$$

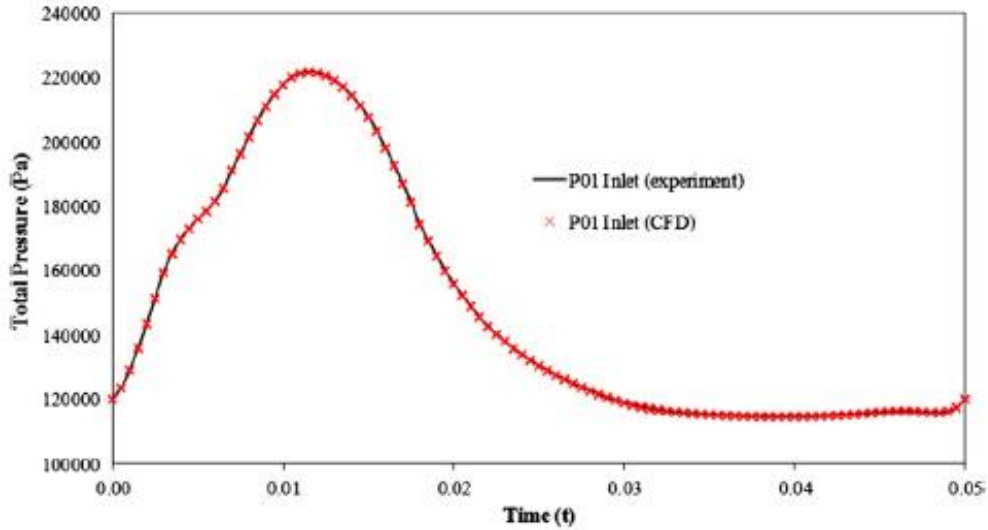


Figure 2.2: Imperial College test facility inlet pulse form from chopper plates (Padzillah et al., 2015)

Szymko then went onto define the Pressure wave modified normalised Strouhal number, ($PMSt$), using the pressure wave propagation velocity which is equal to the sum of the bulk flow velocity and sonic velocity ($\bar{u} + \bar{a}$) as the reference value. This is defined in equation 11.

$$PMSt = \frac{f_{ref} L_{ref}}{\bar{u} + \bar{a}} \frac{1}{2\phi} \quad (11)$$

Three modes of turbine operation were then defined. The first stage of unsteadiness where $St^* < 0.1$, is the quasi-steady operation mode. The second stage where $St^* > 0.1 > PMSt$, is dominated by the by filling and emptying effects of the volute. The final wave action mode occurs when $PMSt > 0.1$. In this mode, wave dynamics in the volute contribute to the unsteadiness and the pressure wave will experience significant changes in shape. Although Syzkmo didn't demonstrate the

first mode the latter two were and the impact of increased unsteadiness was investigated.

Copeland et al., (2012) used the Imperial College test facility to investigate the performance of a double entry turbine. He found that pulse amplitude can have more of an effect on turbine performance than pulse frequency. The method of calculating unsteadiness proposed by Szymko (2006) was therefore questioned as this method only accounts for the pulse frequency. Copeland et al., (2012) introduced a new parameter that quantified the magnitude of the change in mass flow rate with respect to the rate of mass traveling in and out of the domain. Summing this parameter and the Strouhal number produced a measure of overall unsteadiness. It was shown that when there is a significant discrepancy between mass flowing in and out of the domain, the system is not quasi-steady. The impact of the new parameter on turbine unsteadiness was quantified by Padzillah et al., (2015) showing good agreement with the proposed patterns by Copeland et al., (2012). Newton, (2014) compared the unsteadiness present using both the method proposed by Copeland et al., (2012) and by measuring the mass flow imbalance in the volute. He concluded that the omega value consistently over predicted the level of unsteadiness in the turbine measured by the mass imbalance method.

Accurate measurement of mass flow in and out of the volute experimentally is extremely difficult and therefore can only realistically be used in computational simulations. Roclawski et al., (2014) also used the mass imbalance in the volute to determine the level of unsteadiness and found that the variation in imbalance over the pulse was clearly influenced by the local gradient of pressure in the pulse. Therefore, the shape of the inlet pulse will also impact on the level of turbine unsteadiness.

While pulse shape is very difficult to control experimental, computationally the pulse characteristics are easily changeable. Computational modelling of unsteady turbine performance has been attempted by numerous authors using different pulse shapes. Galindo et al., (2014) and Lee et al., (2016) used a sinusoidal wave form.

Galindo et al., (2014) stated that as the inlet pressure pulse can be decomposed into a sum of sinusoidal wave forms as demonstrated by Costall & Martinez-Botas, (2007), therefore the turbine behaviour under a sinusoidal pulse is of particular importance. Alternately, Roclawski et al., (2014) and Hellstrom & Fuchs, (2009) simulated turbine operation using inlet pulses generated from one dimensional engine simulation tools. Yang et al., (2014) and Padzillah et al., (2015) used the pulse form generated from the experimental test facility at Imperial College, which uses a chopper plate to create the pulse. Extensive experimental validation was therefore available for the computational method used. The pulse shape generated from a chopper plate is not necessarily representative of that found on engine. In reality, the turbine inlet pulse is dependent on the exhaust manifold geometry, valve and injection timing and operating conditions of the engine and is therefore very difficult to fully characterise. Furthermore, as stated by Hakeem et al., (2007b), achieving independent control of pulse shape and frequency is very difficult experimentally, hence limiting practical investigation of the impact of pulse shape. To date the impact of pulse shape on turbine performance has not been satisfactorily established although numerous authors have implemented different approaches.

2.2 MIXED FLOW TURBINE RESEARCH

As discussed in the introductory section, mixed flow turbines can achieve non-zero blade angles, thereby potentially shifting optimal operation to lower velocity ratio running points. This is illustrated in figure 2.3 showing the optimum velocity ratios for radial, axial and mixed flow turbine designs. Furthermore, the removal of blade material from the wheel extremity reduces the rotor inertia improving transient response. Due to the potential performance benefits, a large number of studies have investigated the performance of mixed flow turbines. This section will give an overview of the research in this field to date.

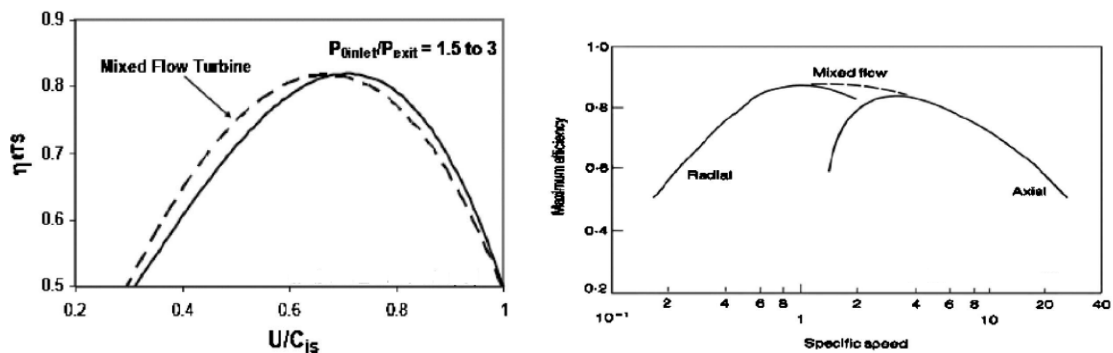


Figure 2.3: Mixed flow turbine performance characteristics. Left - comparison of optimal radial and mixed flow performance (Watson and Janota, 1982). Right - comparison of radial and axial performance showing how mixed flow turbines can bridge the gap between the two types (Whitfield and Baines, 1990).

Wallace & Blair, (1965) completed one of the earliest published experimental studies on the performance of a mixed flow turbine for automotive turbocharging applications. The authors introduced a parametric design process to produce a mixed flow wheel and compared its performance against a base radial design. The authors observed a 25% increase in mass flow rate and a small increase in efficiency. Specifically, the improvement in efficiency were found at higher speed and pressure ratio running points where the radial design experienced a significant drop off in performance. Later Baines et al., (1979) used a similar mixed flow design approach to produce two mixed flow turbines and compared their performance. The authors found similar results to those documented by Wallace & Blair, (1965).

Abidat et al., (1992) extended the work on mixed flow turbine design to include the impact of blade incidence on performance. The authors design two rotors, one with constant blade angle the other with constant incidence, i.e. varying LE blade angle to produce constant span-wise incidence. The constant incidence design was produced assuming constant meridional inlet flow, and that the circumferential velocity was given by the free vortex equation. Therefore, the blade was designed to account for the varying tip speed of the mixed flow rotor. It was found that the peak efficiency achieved was greatest for the constant blade angle design. However, the authors concluded that the simple assumptions made about the upstream flow were questionable based on the analysis. Furthermore, the axial length of the two investigated rotors were not constant and therefore the impact of flow diffusion on performance could have been a contributing factor to the performance differences measured.

Similarly, Zhang et al., (2011) numerically investigated the impact of LE sweep on the performance of a mixed flow turbine while ensuring all other blade geometries remained constant. The resulting LE blade angle of the two tested turbines (A and B) is presented in figure 2.4 alongside images of the two blade designs for clarity. The average difference in sweep between the two turbines is approximately 10° and the span-wise distribution in both cases remains constant. In this study no volute was included and so the rotor inlet flow conditions were assumed to be idealised. The authors observed up to a 2% improvement in cycle averaged efficiency for rotor B and no noticeably change in mass flow rate. The efficiency improvement was shown to be due to reduced LE separation from the increased mixed flow nature of rotor B.

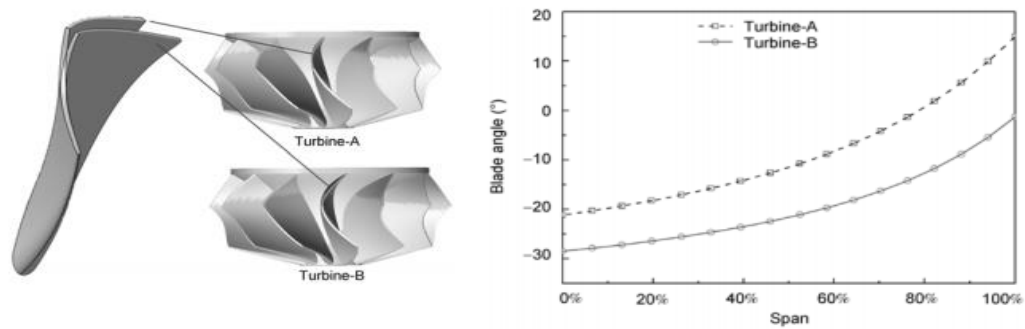


Figure 2.4: Left - LE blade distributions. Right - LE span-wise blade angle (Zhang et al., 2011)

Following the initial published work on mixed flow turbines, emphasis was then placed on the implementation into engine environments, for example - Yamaguchi et al., (1984) Chou & Gibbs (1989), Naguib, (1986) and Minegashi et al., (1995).

Chou & Gibbs, (1989) developed two new mixed flow turbine designs, one with a double volute design and one single. Interestingly the authors specifically designed the divided volute for the mixed flow turbine, something which is not discussed in the available literature despite the differing requirements of mixed flow turbine compared to their radial counterpart. The volute designs are shown in figure 2.5, the twin entry design is angled towards the bearing housing in an attempt to improve inflow into the rotor. Unfortunately, the volute design is not discussed nor is the impact of this tilted volute design isolated and studied. Comparison were only made between the full mixed flow and radial stages. Engine test showed up to 14% increase in mass flow rate and an 8% increase in efficiency for the mixed flow designs over the radial alternatives.

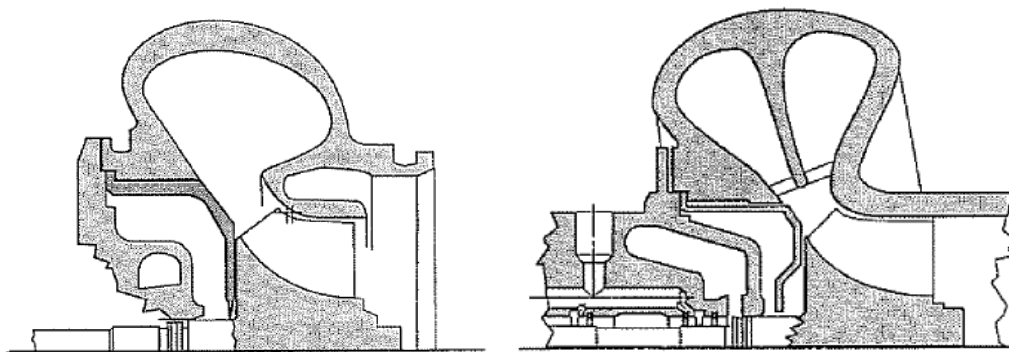


Figure 2.5: single entry volute design, left. Double entry volute design, right (Chou and Gibbs, 1989).

Likewise, Yamaguchi et al., (1984) designed a tilted housing design in a similar study comparing mixed flow and radial turbines on engine. In this case the application was for a large 23.2 litre engine. Again, the tilted nature of the design was not discussed only shown in schematics. Neither was the impact of the volute angle isolated and investigated.

While a tiled type volute design was implemented in both these studies, neither focused on volute design, or made any efforts to understand its impact. The comparisons were done in terms of whole stage performance to illustrate the advancements of the mixed flow turbine performance. In both cases the volute was designed specifically for the mixed flow application as appose to simple adaption of a radial volute which is common. The aim of the housing tilt is clearly to align the flow passage with the rotor LE. If housing tilt is not implemented and no guide vanes present, the flow is expected to turn into the axial direction through the small nozzle-less region ahead of the blade. If the axial turning is not achieved the mixed flow effect cannot be achieved as explain in the introduction section. Achieving significant turning in such a short distance would require extreme curvature along the hub and shroud contours and potentially induce flow separation ahead of the blade. In fact, this very issue has been reported in radial turbines along the shroud contour due to excessive curvature, as illustrated in figure 2.6. Palfreyman & Martinez-Botas, (2002) have suggested that one the advantages of the mixed flow turbines is reduced turning of the blade shroud contour thereby alleviating this issue. However, if the volute is radially positioned, the flow through the stage is still turning 90° and hence the turning of the shroud would not be reduced, it would merely be focused ahead of the LE. The shroud curvature could be reduced in such an application by increasing the length of the nozzle-less region giving a longer passage to turn the flow into the rotor. However, this would require an increase in the radial size of the design and result in increased package size which is undesirable. This leaves housing tilt as the only method to reduce passage turning to align the volute flows with the rotor and maintain a compact design. Tilting the volute does result in the volute encroaching on the bearing housing and therefore the bearing housing would require redesign to

accommodate this, which is perhaps one of the reasons volute tilt is not commonly seen in mixed flow applications. The extent of this issue is dependent on the desired tilt angle.

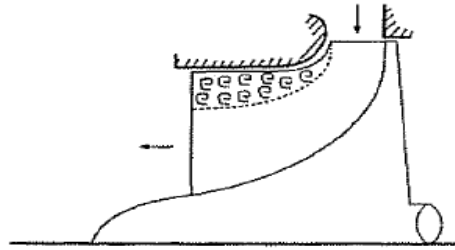


Figure 2.6: Flow separation from shroud curvature (Chou and Gibbs, 1989).

Work by Arcoumanis et al., (1997) introduced a new volute design and compared the “new” design (volute b) with the “old” design (volute a), referring to a volute designed by Abidat et al., (1992). It was observed that the new volute had a larger swallowing capacity and higher efficiencies, particularly at lower rotational speeds. The two designs are shown in figure 2.7. Clear improvements to the volute design are apparent in terms of passage refinement with an obvious reduction in the sharp turning of the shroud. Furthermore, the hub side of the volute shows good alignment with the LE of the blade to ensure well directed flow. At the shroud, while the curvature is improved, the turning of the housing is still substantial.

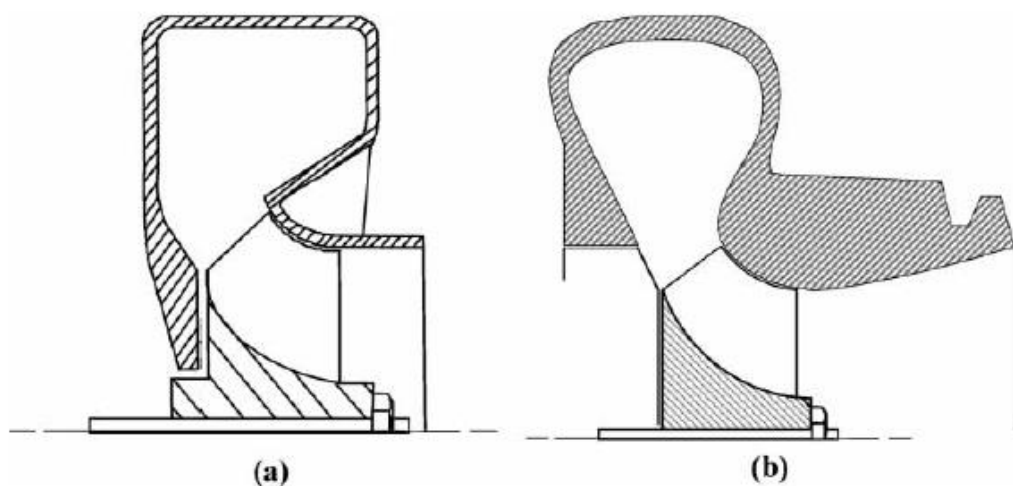


Figure 2.7: Volute designs compared by Arcoumanis et al. (1997). Left old design. right - New design

The comparison of the two volute designs was extended by Hakeem et al., (2007a) to account for pulsating inlet flow. Improved efficiency at lower rotational speeds was observed in the new volute, creating a more compact efficiency curve, hence, a reduced sensitivity to rotational speeds, and an improvement in transient response. Overall, the new volute design produced a 5.8% increase in mean cycle efficiency relative to the old volute. This work further supported the conclusions of Arcoumanis et al., (1997) that “the geometry of the volute plays a critical role in the overall performance of a mixed flow turbine”. However, the volute design used in both cases was based on a radial turbine volute and no attempt to isolate the impact of specific volute feature was made.

Karamanis et al., (2001) completed an experimental study using Laser Doppler Anemometry (LDA) to investigate the LE and trailing edge (TE) flow components of a mixed flow turbine. The authors obtained distributions of the velocity components over the rotor LE span at two steady state running points. The steady state velocity distributions showed the complex flow patterns at the rotor LE as illustrated in figure 2.8. The figure shows contours of LE incidence angle at two rotational speeds, the x and y axis show normalised span-wise and circumferential distance. The contours show substantial span-wise and circumferential variation over the blade LE. However, a lack of knowledge of the volute flow physics enabled only limited conclusions to be drawn. It was clear that the rotor was fed with highly non-uniform flow from the nozzle-less volute, but without data of the volute flows, the exact mechanism causing such variation was not possible. Furthermore, under pulsating flow the velocity measurements were limited to only the LE mid span and therefore the flow distribution over the span was not investigated.

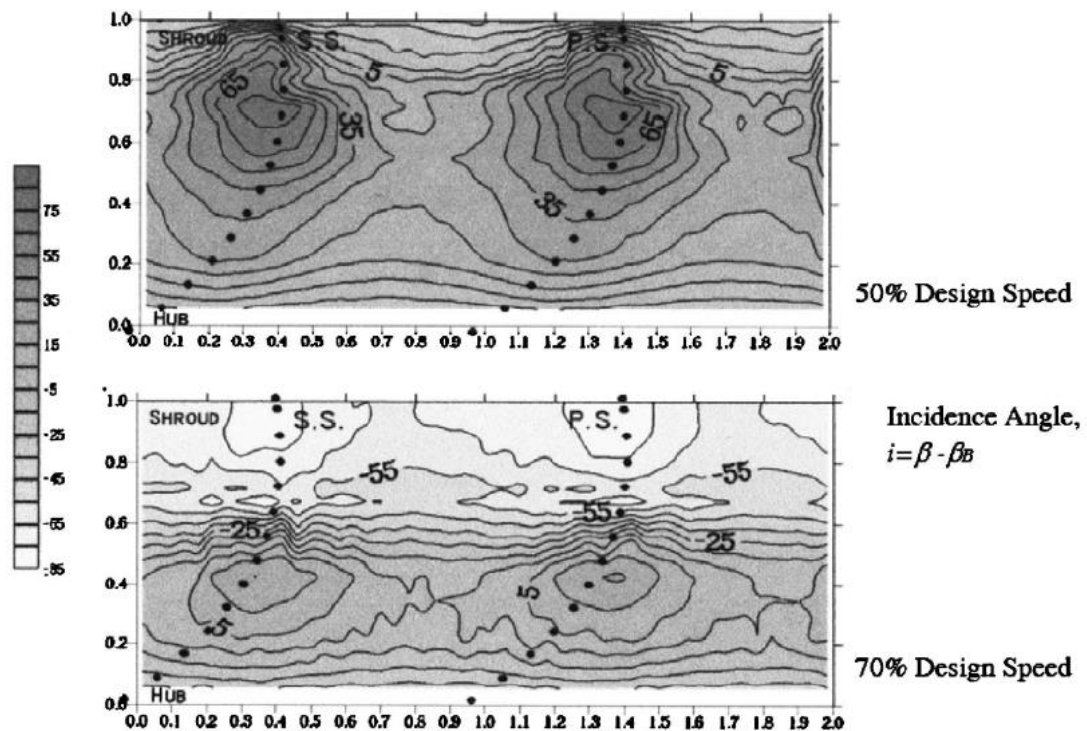


Figure 2.8: LE incidence angle distribution from LDA study by Karamanis et al. (2001).

Based on the findings of Karamanis et al. (2001), Palfreyman & Martinez-Botas, (2004) conducted a computational investigation into the flows within a mixed flow turbine and compared the results with that of a radial turbine. The authors found that the flow was poorly guided ahead of the rotor in agreement with the findings of Karamanis et al. (2001). However, the study did not focus on volute flows and therefore an explanation of the rotor inlet flow variation in terms of flow development prior to the rotor is missing. Despite this, the authors reported significant differences in flow characteristics between the mixed flow and radial designs including reduce shroud separation in the mixed flow design and a characteristic hub separation in the mixed flow case that was not observed in the radial design.

Leonard et al., (2014) completed a study on a range of mixed flow rotor design with different cone and camber angles and compared performance. The authors noted that the axial velocity component at the LE of the rotor was very poor and showed significant variation from hub to shroud, thereby limiting the mixed flow

effect. No further work to investigate this effect, its impact or how to improve the performance was conducted. Morrison et al., (2016) investigated the impact of rotor inlet velocity components on a mixed flow rotor. The authors analysed rotor flows and LE incidence angles created over a range of inlet conditions. The authors reported some interesting findings with regards to the impact of span-wise flow distributions on the rotor performance. However, a significant draw back with both of these studies was the lack of the presence of a volute. Therefore, the idealised meridional flow assumption, questioned by Abidat et al. (1992), was still used. Furthermore, when Morrison et al., (2016) investigated the impact of the axial flow component; the rotor passage design remained constant with a radial nozzle-less space. As such the impact of the axial flow component meant the flow was miss aligned with the rotor passage. As such the performance loss observed in the stage was not necessarily the result of the axial flow component but the poor flow alignment.

The impact of span-wise flow on turbine performance is an interesting area of investigation as stated by Rajoo & Martinez-Botas, (2008). The authors concluded that the poorly guided flow into the rotor shown by Karamanis et al. (2001) and that shown in the computational work by Palfreyman & Martinez-Botas, (2002), demonstrates that nozzleless volutes are not adequate in directing rotor inlet flow. The authors went on to develop guide vanes for mixed flow application aiming to reduce non-uniformity of the flow. However, due to the added expense of nozzle guide vanes and the potential limitation to the range of operation associated with them, nozzleless volutes are still widely used according to Japikse & Baines, (1994).

In nozzleless designs, span-wise non-uniformity in mixed flow turbines can arise through two methods –

- The varying LE diameter results in varying LE tip linear speed. The resulting blade incidence will therefore vary from hub to shroud. This effect was studied in detail by Morrison et al., (2016).

-
- The flows exiting the volute can show significant variation in velocity components both in the circumferential and span-wise sense. Thereby resulting in significant incidence variation.

While the first point is inherent of mixed flow turbines the second, is also present in radial turbines. However, the ability of a mixed flow turbine to achieve non-zero blade angles at the LE makes understanding the variation important to optimisation. Furthermore, the need for an axial flow component at the rotor LE increases the need for better flow guidance into the rotor of a mixed flow turbine, without which the efforts of mixed flow blade design are wasted. Correct matching between volute and blade LE profile could improve incidence at desired running points. It is therefore apparent that a better understanding of the volute flow physics is necessary, particularly in the nozzleless mixed flow turbines.

2.3 VOLUTE FLOWS

As outlined in the previous section, the variation in flow distribution at the LE of the rotor in nozzleless designs is significant. While the variation in the span-wise sense is important in both radial and mixed flow turbines, the added freedom to manipulate the blade angle, as well as the fact that the inlet flow conditions dictate the resulting mixed flow effect, make it a particularly interesting area for study in mixed flow turbine applications. This is supported by the work by Abidat et al. (1992) discussed in the previous section. The author's attempts to optimise the span-wise blade angle of a mixed flow turbine failed due to such effects. Understanding the flow conditions delivered to the rotor is therefore vital for both blade optimisation and improving volute design to reduce such variation. In particular, volute designs that address the specific requirements of mixed flow turbines are not present in the published literature and therefore understanding the impact of the volute on LE flows is the first step to better matching of the two components.

The volute is tasked with supplying the rotor with flow. Ideally the flow enters the rotor in a uniform fashion with optimal flow angles. The flow angle is defined primarily by the volute A/r . Turbine volutes can take a number of different configurations, including single or dual entry and vaned or nozzleless. This project focuses on a single entry nozzleless set-up. Bhinder, (1969) stated that nozzleless volutes could result in a 2-3% efficiency loss when compared to vaned volutes. Similar findings were observed by Baines & Lavy, (1990) and Romagnoli et al., (2010). In contrast, experimental work by Spence et al., (2007) and the corresponding numerical analysis Simpson et al., (2009) found that the nozzleless configuration suffered smaller pressure losses and therefore resulted in better efficiencies. Spence et al., (2007) base their investigation on equivalent flow capacity conditions for two volutes, whereas Romagnoli et al., (2010) kept A/r constant. Therefore Simpson et al., (2009) were able to conclude that a well-designed nozzleless volute can deliver better efficiencies. One advantage of a nozzleless volute is that a flatter efficiency curve is achieved as the turbine does not experience the same efficiency drop off as in vanned configuration (Japikse and Baines, 1994).

The Conventional approach to turbine volute design is to assume 1D and free vortex flow. This approach is well documented in literature (Baines and Whitfield, 1990); (Watson and Janota, 1982))

Starting with the free vortex assumption -

$$rc_u = \mathbf{Constant} = k \quad (12)$$

Where: r is radius and c_u is tangential velocity in the absolute frame of reference. Given the continuity equation -

$$\dot{m}_\theta = \rho_\theta A_\theta c_{u\theta} \quad (13)$$

Where: \dot{m}_θ is mass flow, ρ_θ is density and A_θ is area all at a given at the volute azimuth angle θ . This can be written for uniform distribution of mass flow around the volute -

$$\dot{m}_\theta = \dot{m} \times \frac{\theta}{2\pi} \quad (14)$$

Combining equations 12, 13 and 14 and rearranging yields -

$$\frac{A_\theta}{r_\theta} = \frac{\dot{m}}{\rho_\theta} \frac{1}{k} \frac{\theta}{2\pi} \quad (15)$$

If the flow is assumed to be incompressible, the ratio of A/r should be a linear function of the azimuth angle. If the mass flow rate and velocity around the volute exit are constant, the rotor inlet angle can be given by -

$$\mathbf{tana}\alpha_{1.5} = \frac{c_{u1.5}}{c_{m1.5}} \quad (16)$$

Where subscript 1 represents the volute inlet and 1.5 represents the volute outlet. Substituting in equations 12 and 13 from volute inlet (1) to outlet (1.5) yields -

$$\mathbf{tana}\alpha_{1.5} = \frac{\rho_{1.5}}{\rho_1} \left(\frac{A_{1.5}/r_{1.5}}{A_1/r_1} \right) \quad (17)$$

If the flow is assumed to be incompressible and as $A_{1.5}$ and $r_{1.5}$ are fixed by rotor dimensions, the flow angle is driven solely by the by inlet area A_1 and inlet radius r_1 . The results of this 1D analysis are as follows –

- A/r must decrease linearly with azimuth angle to give constant volute exit (rotor inlet) conditions.
- Value of A/r determines the volute outlet flow angle.

This relationship is based on assumptions of one-dimensional, incompressible and free vortex flow. While numerous studies have shown the inaccuracies of these assumptions ((Benisek, 1987); (Gu et al., 2001); (Hussain and Bhinder, 1984); (Scrimshaw, 1984)) this approach is still widely used.

Loss coefficients and factors can be added to account for some of the further complexity of the volute flow. One example is the blockage factor that can be introduced into the continuity equation to account for boundary layer growth and secondary flow developments –

$$M_\theta = \rho_\theta A_\theta (1 - B) c_\theta \quad (18)$$

Where B is the blockage factor which is defined empirically and is approximately between 0-0.1. Other examples include pressure loss coefficient K_{PL} (equation 19) and swirl loss that can be introduced into the free vortex equation (equation 20).

$$K_{PL} = \frac{P_{01} - P_{01.5}}{P_{01.5} - P_{1.5}} \quad (19)$$

$$c_{\theta 1.5} r_{1.5} = S c_{\theta 1} r_1 \quad (20)$$

Where: S is the swirl coefficient, the value lies between 0.85 and 0.95. The pressure loss coefficient generally lies between 0.05-0.15 (Japikse and Baines, 1994).

A significant draw back with the 1D approach is that the flow equations are only satisfied at the mean flow line and not in the regions nearer the walls (Chen, 1996). Therefore discrepancies between the intended design parameters and test results should be expected, as experienced by Scrimshaw, (1981)

In an attempt to overcome some of these limitations, Chapple et al., (1980) proposed a 2D method for volute design that fully defined the volute dimensions. A flow field of both radial and tangential vectors was generated by specifying a width to radius ratio. The method led to an improved volute design with an almost uniform blade inlet state, and thus significantly improved stage efficiency.

All of the volute design approaches mentioned here are based on the free vortex assumption. The validity of the free vortex assumption has been brought into question by a number of authors. Hussain & Bhinder, (1984), Whitfield & Noor, (1994) and Martinez-Botas et al., (1996) all found significant variation between results from the free vortex predictions and experimental results. Martinez-Botas et al., (1996) compared the free vortex assumption with both a 3D Navier Stokes solver and experimental results. It was observed that the Navier Stokes approach had better correlation with experimental results than the free vortex method. It was therefore proposed that volutes designed through the free vortex method require further 3D computational analysis and optimisation.

Recent advancements in CFD approaches allow in depth 3D analysis of the flows within the volute. One of the early full CFD investigations was that conducted by Martinez-Botas et al., (1996) using a 3D Navier Stokes solver coupled with the higher Reynolds number $k - \epsilon$ turbulence model. This work presented both experimental and 3D CFD results. The authors found that secondary flow structures became stronger between azimuth angles of 45deg and 270deg, as well as being stronger at the top and bottom of the volute cross section. Furthermore, low momentum energy was measured at the sharp corners around the volute exit, leading to high total pressure losses. In the axial direction, an almost constant static pressure was measured. It was concluded that the computational approach used was ideal for the

study of the volute flow field and to allow for geometry modification to be carried out. Simpson et al., (2009) completed full stage CFD simulations and managed to capture detailed secondary flow structures within the volute. Within the trapezoid cross sectional shaped volute, two counter rotating vortices were found to form at approximately 90° azimuth angle and continued to persist around the volute. Increased losses due to the existence of the secondary flows were found only around end walls. Furthermore, for the nozzleless volutes tested it was found that volute pressure distribution was symmetrical despite the non-symmetrical pressure distribution at the rotor inlet.

Work conducted at Imperial College on a radial flow volute geometry by Yang et al., (2014) looked into the effect of volute cross sectional design on turbine performance. Figure 2.9 shows the two volute designs tested. The volutes have the same A/r but different cross sectional shapes. The volute aspect ratio (b/h) is the ratio of the volute height to its width. For volute A the aspect ratio ranges from 0.8 at 0° azimuth angle to 2.6 at 360° azimuth angle. The aspect ratio for volute B remains constant at 1.7 for all values of azimuth angle.

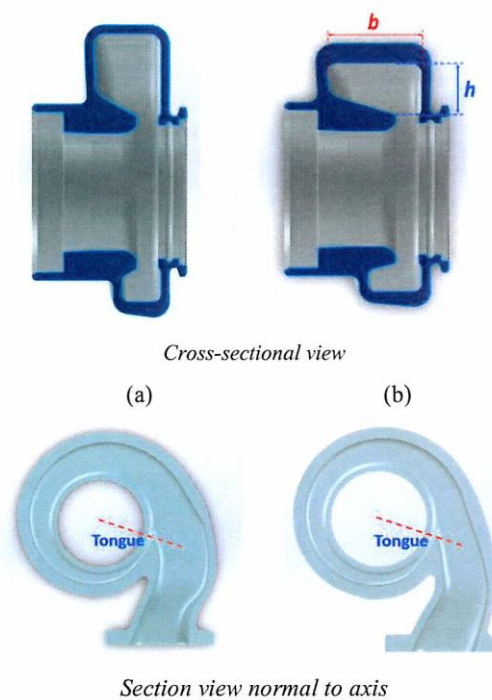


Figure 2.9: Two volute cross sectional shapes for a radial turbine (Yang et al., 2014)

Figure 2.10 shows the entropy distribution in the volute cross section for both designs. A high entropy region occurs at the shroud side of the blade inlet in both cases. The magnitude of the entropy increase is significantly larger in volute B. This is due to the increase in volute width and the sharper flow turning into the blade. The result of these geometrical parameters caused distinct secondary flow patterns shown in figure 2.11. In both volutes, vortex structures are formed, causing flow to move across the plane. In volute B there are two very distinct, large vortices; one positioned vertically and the other horizontally. These two vortex structures are much less distinct in volute A. The secondary flow structures in the volute clearly affect the flow delivered into the rotor, therefore affecting the rotor efficiency. In other words, the difference in efficiency between the two designs is not solely a result of efficiency gains in the volute. It was concluded that volute A sees a cycle averaged efficiency increase of an average of 1.8 points over all tested frequencies and loads. Transient testing showed that the major increase in efficiency came from the improvement of volute A's emptying ability. Furthermore, volute B's poor emptying abilities made it more sensitive to the pulsating effects. From figure 2.11, it is clear that the flow across the plane is not symmetrical. The effect of the non-symmetrical cross section on the volute exit flow was not investigated by Yang et al., (2014). Those authors did, however investigate how the flow angle around the azimuth angle differs in both volutes and the effect under steady and unsteady conditions. For the most part, the flow angle remained constant. However, in volute B, significant differences were measured in flow angles between the steady and unsteady results near to the shroud. This was put down to volute B's larger aspect ratio, making it more sensitive to unsteady effects.

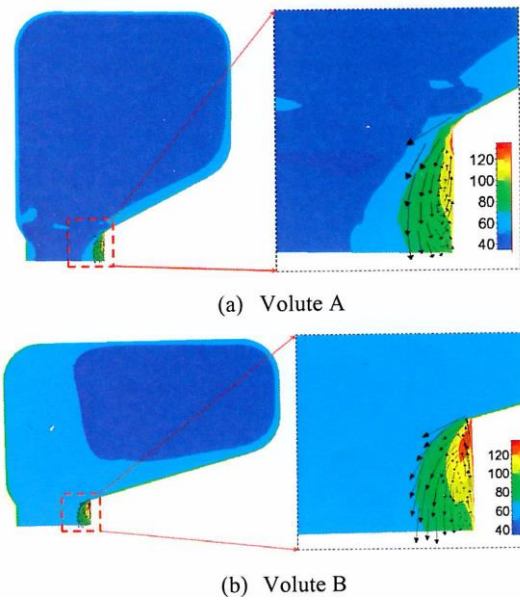


Figure 2.10: Entropy distribution for volute A and B at 0° azimuth angle (Yang et al., 2014)

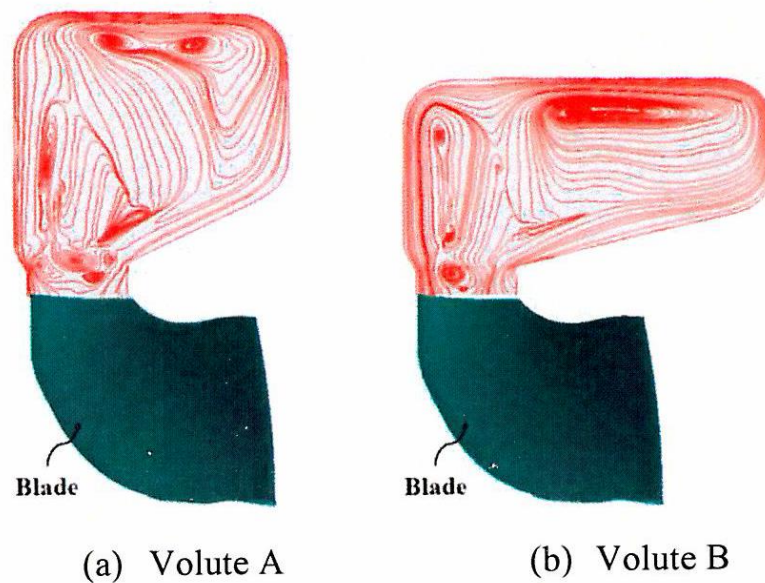


Figure 2.11 - Secondary Flow at 0° azimuth angle (Yang et al., 2014)

A similar study was conducted by Meghine et al., (2017). In this case asymmetrical housing designs were once again used with four variants. However, whereas the Yang et al., (2014) study was conducted on a radial turbine, Meghine et al., (2017) used a mixed flow rotor. The authors observed clear vortex generation in each housing design and concluded that the volute can be occupied by one or more vortices and that the volute volume is critical in decreasing the number of vortices.

This study did not investigate the impact of cross sectional shape on span-wise and circumferential variation of incidence. While both of these studies show complex secondary flow structures no explanation is provided regarding their formation. Furthermore, the asymmetry of the volute introduced added complexity to the flow physics and no similar published studies are available for symmetrical volute designs.

Kalpakli Vester, (2014) investigated the development of secondary flow structures in a 90° pipe bend. The flow conditions were set to replicate that of engine exhaust flow. Development of the secondary flows incurred through the pipe bend were therefore be used to replicate the flow field that develops in the exhaust manifold ahead of the turbocharger turbine. The authors showed the development of Dean vortices within the pipe which could be expected to occur upstream of the turbine stage in an engine environment.

Dean vortices were first observed by Dean, (1927) and Dean, (1928). The secondary flow structures shown in figure 2.12 (Dean vortices), are the result of the central passage flow having greater inertia than that close to the walls. When the flow encounters a bend the low inertia flow at the walls turns readily into the radial direction with the pipe. However, the higher inertia flow in the passage center does not turn as readily resulting in the development of counter rotation vortices with flow moving radially downwards at the wall and upwards in the passage center creating two “D” shaped vortices known as Dean vortices. The Dean number represents the strength of said vortices and is expressed as –

$$De = 4 \sqrt{\frac{D}{R_c}} Re_D = 4 \sqrt{\frac{\rho \bar{R}_c u^2 / \bar{R}_c^2 \times \rho u^2}{\mu u / D}} \approx \frac{\sqrt{\text{centripetal forces} \times \text{inertial forces}}}{\text{viscous forces}} \quad (21)$$

Equation 21 represents the Dean number as a balance of forces responsible for their development. Where: $\rho \bar{R}_c u^2 / \bar{R}_c^2$ is an approximation of the force to produce centripetal acceleration, ρu^2 represents the fluid inertia and $\mu u / D$ represents the viscous forces (Doorly and Sherwin, 2009). De is the Dean Number, D is the pipe

diameter, R_C is the radius of curvature, Re_D is the Reynolds number based on the pipe diameter, μ is viscosity, ρ is density and u is bulk velocity.

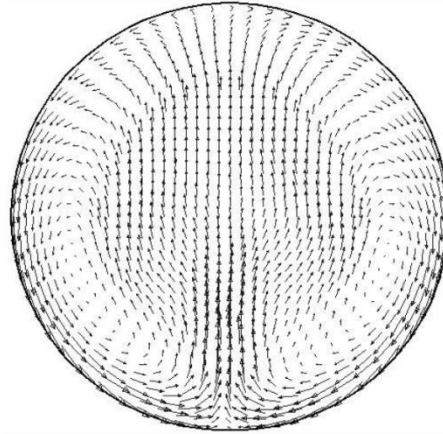


Figure 2.12: counter rotating dean vortices (Hellstrom, 2010)

Hellstrom & Fuchs, (2009) investigated the effect of the upstream geometry on the performance of a radial turbine. This simulation work used Large Eddy Simulation (LES) tools to resolve the turbulence accurately and the model included the manifold geometry. The authors concluded that the manifold had a significant impact on turbine inlet flow conditions. Hellstrom & Fuchs, (2008) also investigated the impact of Dean vortices and swirling flow conditions at the inlet of the turbine stage applied as boundary conditions. The authors showed how such conditions impact volute flow structures and rotor performance. These works provided improved knowledge of the impact of upstream secondary flows. However, the impact of the volute geometry itself was not investigated nor was the design optimised to deal with such conditions.

Turbine volutes are a particularly interesting example of a curved pipe as both radius of curvature and diameter decrease with progression of azimuth angle. In addition to the complex geometry, a substantial pressure gradient exists driving the flow into the turbine rotor that has a significant impact on the volute flow.

Cerdoun & Ghenaiet, (2016) completed an investigation into volute secondary flows in a twin entry volute. The authors observed secondary flows that were attributed to a Dean-type effect within the volute. The Dean number through the pulse was calculated and the vortex development visualised. The authors found that the secondary flows result in variation in LE incidence at around 180° from the tongue. Figure 2.13 shows the vortices present around the volute at four points during the inlet pulse, A, B, C and D. In this instance the shroud side of the volute is fed with flow leading to greater development of secondary flows in the hub side. It can be seen that the vortices are most prominent at the 90° position before decaying further around the volute. However, this work was limited to a twin entry volute where complex interaction between the two sides occur that impact the development of secondary flows. Furthermore, the authors did not investigate the span-wise variation induced at the rotor leading edge in detail.

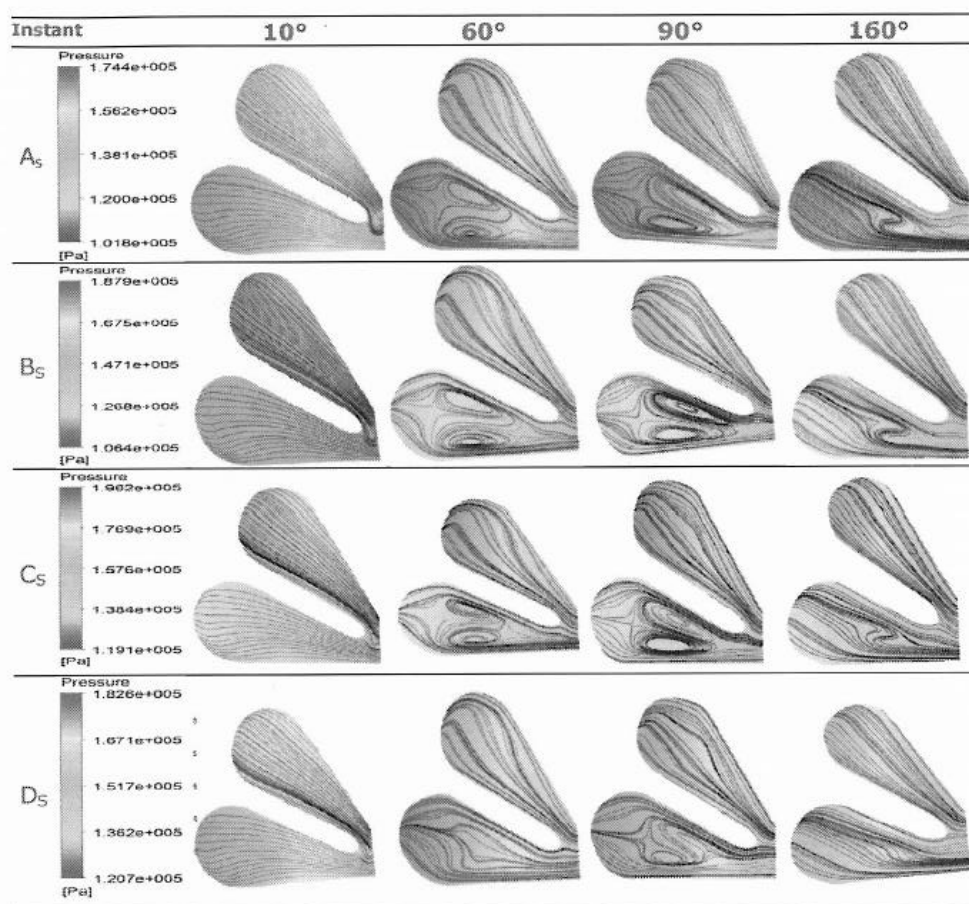


Figure 2.13: Dean vortex development in twin entry volute design.

2.4 LITERATURE REVIEW SUMMARY

The literature review presented in this section has discussed the computational and experimental works to date that investigate the performance of mixed flow turbines. Investigations involving the effects of the volute on turbine performance have been highlighted as it is clear that there is a limited knowledge on the impact that volute design can have on rotor inlet conditions. From the literature survey three main areas of interest to the thesis have been identified –

1. The impact that pulsation shape may have on turbine performance requires more detailed analysis with a range of pulse shapes and operating conditions.
2. While tilted designs can be seen in the literature, no systematic investigation of the impact of these designs has been published.
3. The impact of volute design on volute flow structures and the subsequent impact on rotor inlet flow conditions appears to be a neglected area.

Point 1

It is extremely difficult to experimentally measure exhaust pulsations accurately. Furthermore, pulse shape will vary with engine speed, load, valve timings and manifold design. It is therefore important to understand the impact of pulse shape and how a turbine will operate under a range of applications. Understanding this effect will add to the theoretical understanding of the unsteady performance of a mixed flow turbines and what mechanisms influence stage unsteadiness.

In order to address this point multiple mass flow pulse shapes will be implemented and the impact on turbine performance studied. Particular attention will be paid to the impact on stage unsteadiness and the range of operation of the rotor as a result.

Point 2

The application of tilted housings is something seen in the literature but never discussed in detail. Neither has the impact of such a design ever been directly studied. Morrison et al., (2016) investigated the impact of the axial flow component, but the lack of a turbine volute and inlet pulsation limit this investigation. As explained in the literature review the miss alignment of flow and passage brings into question the conclusions of this paper. Furthermore, the lack of a volute in that study means that the flow was not guided using any realistic means.

Although many works have investigated the performance of mixed flow rotors, no published studies discuss the design of a volute specifically for mixed flow applications despite the differing inlet flow requirements. To improve mixed flow turbine performance, it is important to understand the impact the volute has on these flows and how to optimise them specifically for mixed flow applications. Understanding the impact of tilt is a logical starting point of this.

To address this point, the impact on a mixed flow turbine with and without volute tilt will be investigated. In depth analysis of the resulting performance and flow physics will be included to provide better understanding. The resulting axial flow component, that was shown by Leonard et al., (2014) to be unsatisfactory will be compared in both designs.

Point 3

While point two focusses on the impact of volute tilt to improve the axial flow component and reduce shroud turning, further volute design parameters require investigation. The work of Karamanis et al. (2001) showing the existence of substantial span-wise flow variation and the inability of Abidat et al. (1992) to optimise the span-wise blade distributions illude to signifcant flow structures that originate in the volute that are not fully understood. Rajoo & Martinez-Botas, (2008) state that the poorly guided flow into the rotor shown by Karamanis et al. (2001) and that shown in the computational work by Palfreyman & Martinez-Botas, (2002), demonstrates that nozzleless volutes are not adequate in directing rotor inlet flow. However the added expense and limitation of guide vanes means they are not allways

the best solution. It is therefore necessary to understand the impact the volute can have on reducing such variation.

As discussed in the literature review Yang et al., (2015) and Meghni et al. (2017) studied the impact of volute cross sectional shape on performance. However, the understanding of these parameters is still not fully explored. In fact Yang et al., (2015) stated further investigation is necessary to understand these effects. Neither of these studies investigated the symmetrical designs which are widely used. Volute symmetry can potentially simplify the secondary flow structures leading to more solid conclusions. The impact of such flows are of great interest in this thesis as optimisation of the mixed flow turbine requires good knowledge of the upstream flows.

To address this point, firstly an in-depth analysis of the volute flows will be conducted under pulsating flow conditions. Investigation of the span-wise flow variation at the volute exit will be included comparing how the flows vary during the pulse. Understanding the impact that this has on turbine performance will allow potential improvements to be identified.

The impact of the aspect ratio of the symmetrical volute will then be studied. Investigating this fundamental design feature will not only give information to designers with regard to the trade of between performance and packaging size; but will also provide a basis for volute improvement. Understanding how this parameter effects secondary flow development, and in turn, effects outlet span-wise flow variation will further the knowledge of volute design. Any reduction in span-wise distribution can then be fed into the blade design process for future optimisation.

3 COMPUTATIONAL FLUID DYNAMICS METHODOLOGY

This section describes the computational approach used throughout this thesis. This includes an overview of the computational approach, the mesh development, the boundary conditions implemented and the convergence criteria used. Throughout this thesis ANSYS CFX is used for all CFD simulation.

3.1 COMPUTATIONAL FLUID DYNAMICS OVER VIEW

Computational Fluid Dynamics (CFD) is widely used in turbomachinery applications to gain a better understanding of the flow physics occurring within the machine. This is particularly important in the turbine stages as experimental flow measurement within the high temperature, rotating environment is extremely difficult.

CFD codes solve the partial differential flow equations, namely the continuity equation for conservation of mass, the Navier-Stokes equations that defines the conservation of momentum and the energy equation from the first law of thermodynamics. The approach of CFD is to discretize the flow domain, and numerically solve the flow field based on these equations. In this section a brief overview of the governing principles will be given. Versteeg & Malalasekera, (2007) provide an in-depth derivation of the governing equations as well as further information on the numerical methods employed within CFD codes.

3.1.1 GOVERNING EQUATIONS

The continuity equation defines the conservation of mass. It simple states that the rate of increase of mass in a fluid element is equal to the net rate of flow of mass into the fluid element. The continuity equation is given in its compact vector notation in equation 22.

$$\frac{\partial \rho}{\partial t} + \mathit{div}(\rho \mathbf{u}) = 0 \quad (22)$$

Where ρ is density, t is time and u is velocity. The momentum transport equations describes the conservation of momentum within a fluid element. This can be explained by Newton's second law, the rate of increase of momentum of a fluid particle is equal to the sum of the forces acting on that fluid particle. For Newtonian fluids, where the viscous stresses are proportional to the rates of deformation, we obtain the Navier-Stokes equations which are given in equations 23-25 for the x , y and z components respectively.

$$\frac{\partial(\rho u)}{\partial t} + \text{div}(\rho u u) = -\frac{\partial p}{\partial x} + \text{div}(\mu \text{grad } u) + S_{Mx} \quad (23)$$

$$\frac{\partial(\rho v)}{\partial t} + \text{div}(\rho v u) = -\frac{\partial p}{\partial y} + \text{div}(\mu \text{grad } v) + S_{My} \quad (24)$$

$$\frac{\partial(\rho w)}{\partial t} + \text{div}(\rho w u) = -\frac{\partial p}{\partial z} + \text{div}(\mu \text{grad } w) + S_{Mz} \quad (25)$$

Where u , v and w denote velocity in the x , y and z directions, μ is the dynamics viscosity p is pressure and S_M is the momentum source term. The conservation of energy equation is derived from the first law of thermodynamics, that energy cannot be created or destroyed. Using the Newtonian fluid model for the viscous stresses again, the energy equation can be obtained in the form given in equation 26.

$$\frac{\partial(\rho i)}{\partial t} + \text{div}(\rho i u) = -p \text{div } u + \text{div}(k \text{grad } T) + \Phi + S_i \quad (26)$$

Where i is internal energy, k is the thermal conduction coefficient, T is temperature, Φ is the dissipation function and S_i is the internal energy source term. The result is that the motion of a fluid can be described by five partial differential equations, the conservation of mass (equation 22), the momentum equations in X, Y and Z (equations 23, 24 and 25) and energy equation (equation 26). Within the equation are the four thermodynamic variables ρ , p , i and T . Assuming

thermodynamic equilibrium, these variables can be related through the two equations of state. For a perfect gas these are –

$$p = \rho RT \quad (27)$$

$$i = C_v T \quad (28)$$

Where C_v is the specific heat at constant volume. Adding the two equation of state to the 5 partial differential equations gives a system of seven equation. This results in seven unknowns and seven equations and is therefore a mathematically closed system.

3.1.2 THE TRANSPORT EQUATIONS

There are clear commonalities between the given governing equations of fluid motion. By introducing a general variable ϕ the conservation form of all governing equations can be written as the general transport equation –

$$\frac{\partial(\rho\phi)}{\partial t} + \mathit{div}(\rho\phi\mathbf{u}) = \mathit{div}(\Gamma \mathit{grad} \phi) + S_\phi \quad (29)$$

On the left, this equation shows the rate of increase of the fluid variable ϕ within the fluid element, plus the net rate of flow of the variable ϕ out of the fluid element. This is equated to the rate of increase of ϕ due to diffusion, plus the rate of increase of ϕ due to sources on the right.

This equation forms the basis of most finite volume CFD codes by setting ϕ equal to $1, u, v, w$ and i or T and h_0 and selecting the appropriate values for the diffusion coefficient Γ and sources term S_ϕ .

3.1.3 NUMERICAL APPROACH'S TO CFD

As the transport equation given in equation 29 is non-linear and is dependent on both space and time, it cannot not be solved analytically. Therefore, numerical

methods must be employed to solve the problem. There are three available numerical methods, namely the finite difference method, the finite element method and the finite volume method. It is the latter method that is commonly used in CFD packages and is used throughout this thesis.

3.1.3.1 FINITE VOLUME METHOD

The finite volume method is employed by ANSYS CFX. This approach requires the discretisation of the domain into a number of control volumes or cells, where the variables of interest are located at the cell centres. The governing equations are then integrated over the entire control volume ensuring conservation. As the conservation of the variables are ensured over each cell, global conservation of the variables is also ensured. Inter-population profiles are used to give the variation of the physical variables between neighbouring cells.

The integration of the general transport equation over a given control volume yields –

$$\int_{CV} \frac{\partial(\rho\phi)}{\partial t} dV + \int_{CV} \mathbf{div}(\rho\phi\mathbf{u})dV = \int_{CV} \mathbf{div}(\Gamma \mathbf{grad} \phi)dV + \int_{CV} S_{\phi} dV \quad (30)$$

Gauss's divergence theorem is then implemented into the convective and diffusive terms of equation 30. Gauss's theorem shows that the volume integral can be related to an equivalent surface integral and is described as -

$$\int_{CV} \mathbf{div} \mathbf{a} dV = \int_A \mathbf{n} \cdot \mathbf{a} dA \quad (31)$$

Where \mathbf{n} is the unit vector normal to the control surface and $\mathbf{n} \cdot \mathbf{a}$ represents the flux of variable \mathbf{a} through the surface. Applying Gauss's theorem to equation 30 results in -

$$\int_{CV} \frac{\partial(\rho\phi)}{\partial t} dV + \int_A \mathbf{n} \cdot (\rho\phi\mathbf{u})dA = \int_A \mathbf{n} \cdot (\Gamma \mathbf{grad} \phi)dA + \int_{CV} S_{\phi} dV \quad (32)$$

Finally, to include time dependence, equation 29 must also be integrated over the time interval Δt . This results in the most general form of the transport equation used in finite volume methods such as that employed by ANSYS CFX –

$$\int_{\Delta t} \frac{\partial}{\partial t} \left(\int_{CV} \frac{\partial(\rho\phi)}{\partial t} dV \right) dt + \int_{\Delta t} \int_A \mathbf{n} \cdot (\rho\phi\mathbf{u}) dA dt \quad (33)$$

$$= \int_{\Delta t} \int_A \mathbf{n} \cdot (\Gamma \mathbf{grad} \phi) dA dt + \int_{\Delta t} \int_{CV} S_\phi dV dt$$

3.1.4 SPATIAL DISCRETIZATION OF THE DOMAIN

Spatial discretization of the fluid domain is a fundamental part of finite volume method. The entire domain must be divided into small control volumes for the numerical methods to be employed. In reality this is done in 3-dimensions, however, for simplicity a 2-dimensional case will be discussed here (full 3-dimensional discretization can be found in Versteeg & Malalasekera, (2007)). Figure 3.1 illustrates a 2-dimension CFD grid. A control volume is shown in grey with the volume center shown as the large black dot. Eight further cell centroids surround this central cell. The central cell is subdivided into four quadrants. Each of the quadrants along with quadrants from other surrounding cells make up an element, one of which is showed by the solid black boarder. The center of the elements are shown by the red dots. In the center, between each of the segments that make up the element is an integration point shown as the small black point.

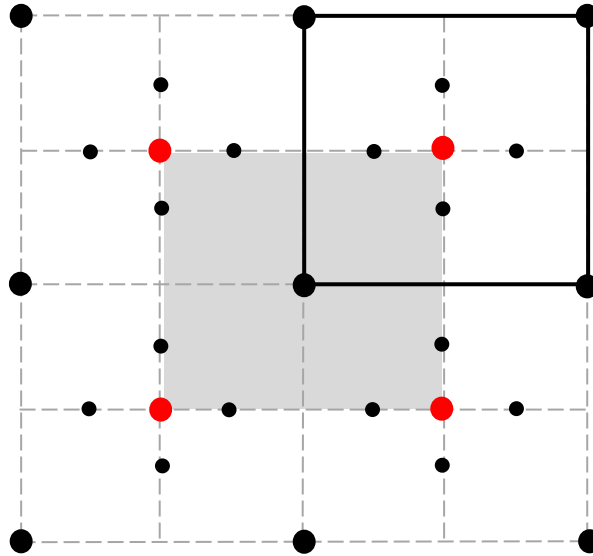


Figure 3.1: Example of 2-dimensional finite volume cell

The variables are stored at the points at the center of each control volume. To compute the governing equations, the gradients of the variables are required on the surfaces of the volume, at the shown integrations points formed by the additional elements. ANSYS CFX does this using finite element shape functions to approximate the variables across the control volume to neighbouring nodes. This variation is given by -

$$\phi = \sum_{i=1}^n N_i \phi_i \quad (34)$$

N_i is the shape function and ϕ_i is the value of the considered variable at node i , and n is the number of nodes at the element boundary. The value of the variable is therefore dependent on the surrounding values at all neighboring nodes. The shape functions applied result in each surrounding node having an equal effect on the value of the variable under consideration with respect to distance from the integration point.

The diffusion of scalar quantities within fluid flows occurs on a molecular scale and is dependent on the gradient of the quantity in any given direction. This process is not affected by the bulk fluid flow. Therefore, calculating the diffusion terms based on all surrounding is physically sound.

The advection term is dependent on the bulk flow and therefore the influence of the surrounding nodes will vary. For example, the impact of an upstream node is expected to have a greater impact than one downstream. Therefore, the method described above is not used in the calculation of the advection term. CFX has several schemes that can compute the advection term that all follow the general form of -

$$\phi_{ip} = \phi_{up} + \beta_f \nabla \phi \cdot \Delta \vec{r} \quad (35)$$

Where ϕ_{ip} is the value of the variable at the integration point, ϕ_{up} is the value at the upwind node, β_f is a blending factor, $\nabla \phi$ denotes the gradient of the variable using the shape function approach and $\Delta \vec{r}$ is the vector from the upwind point to the integration point. The blending factor used can vary between 0 and 1 where 0 denotes an upwind scheme and 1 central differencing. The approach used in this thesis is the “High-Resolution Scheme” in CFX which calculates a value of the blending factor between 0 and 1 at each point depending on the fluid properties. Further details of the process implemented by ANSYS CFX can be found in Ansys, (2009a).

3.1.5 TEMPORAL DISCRETIZATION

For all unsteady simulations the second order backwards Euler scheme was used for temporal discretization. This is an implicit scheme and is therefore robust with no time step size limitations.

3.1.6 TURBULENCE

Fluid flows can be broken down into two main regimes, laminar and turbulent. Figure 3.2 depicts the development of flow from laminar, through transition to turbulent flow. Laminar flow is characterised by parallel layers producing smooth streamlines, as seen to the left of the image. As Reynolds number increases to a critical value, the flow transitions to turbulent, which in contrast to laminar flow, is characterised by chaotic fluctuations in pressure and velocity. This is shown on to the right of the images as the streamlines break down into chaotic mixing.

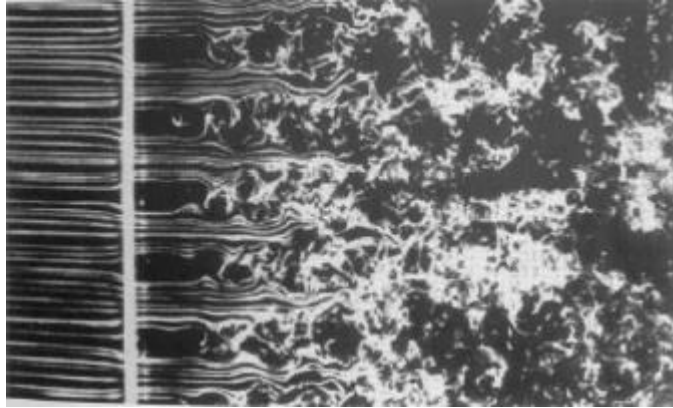


Figure 3.2: Representation of laminar to turbulent transition (Van Dyke and Van Dyke, 1982)

The chaotic fluctuations of pressure and velocity in turbulent flow fields cause the flow velocity to fluctuate around a mean value. To separate out the mean and fluctuating velocity components the Reynolds decomposition can be used –

$$\mathbf{u} = \bar{\mathbf{u}} + \mathbf{u}' \quad (36)$$

Where \mathbf{u}' is the instantaneous velocity and $\bar{\mathbf{u}}$ is time averaged velocity.

The velocity, pressure and other scalar quantities in the governing equations, and the general transport equation can be replaced to incorporate the mean and fluctuating components. Adding the decomposed components to the governing equations for incompressible flow yields the Reynolds Averaged Navier-Stokes (RANS) equations. As this thesis focusses on the compressible flow regime (where density cannot be assumed to be constant) the compressible version of the equations are shown here. If compressibility is included the equations are named the Favre-Averaged Navier-Stokes equations and are expressed as –

$$\frac{\partial \bar{\rho}}{\partial t} + \mathit{div}(\bar{\rho} \tilde{\mathbf{U}}) = \mathbf{0} \quad (37)$$

$$\begin{aligned}
\frac{\partial(\bar{\rho}\tilde{U})}{\partial t} + \mathit{div}(\bar{\rho}\tilde{U}\tilde{u}) & \quad (38) \\
& = -\frac{\partial\bar{p}}{\partial x} + \mathit{div}(\mu \mathit{grad} \tilde{U}) \\
& \quad + \left[-\frac{\partial\overline{\rho u'^2}}{\partial x} - \frac{\partial\overline{\rho u'v'}}{\partial y} - \frac{\partial\overline{\rho u'w'}}{\partial z} \right] + S_{Mx}
\end{aligned}$$

$$\begin{aligned}
\frac{\partial(\bar{\rho}\tilde{V})}{\partial t} + \mathit{div}(\bar{\rho}\tilde{V}\tilde{u}) & \quad (39) \\
& = -\frac{\partial\bar{p}}{\partial y} + \mathit{div}(\mu \mathit{grad} \tilde{V}) \\
& \quad + \left[-\frac{\partial\overline{\rho u'v'}}{\partial x} - \frac{\partial\overline{\rho v'^2}}{\partial y} - \frac{\partial\overline{\rho v'w'}}{\partial z} \right] + S_{My}
\end{aligned}$$

$$\begin{aligned}
\frac{\partial(\bar{\rho}\tilde{W})}{\partial t} + \mathit{div}(\bar{\rho}\tilde{W}\tilde{u}) & \quad (40) \\
& = -\frac{\partial\bar{p}}{\partial z} + \mathit{div}(\mu \mathit{grad} \tilde{W}) \left[-\frac{\partial\overline{\rho u'w'}}{\partial x} - \frac{\partial\overline{\rho v'w'}}{\partial y} - \frac{\partial\overline{\rho w'^2}}{\partial z} \right] \\
& \quad + S_{Mz}
\end{aligned}$$

$$\begin{aligned}
\frac{\partial(\bar{\rho}\tilde{\phi})}{\partial t} + \mathit{div}(\bar{\rho}\tilde{\phi}\tilde{u}) & \quad (41) \\
& = \mathit{div}(\Gamma_{\phi} \mathit{grad} \tilde{\phi}) + \left[-\frac{\partial\overline{\rho u'\phi'}}{\partial x} - \frac{\partial\overline{\rho v'\phi'}}{\partial y} - \frac{\partial\overline{\rho w'\phi'}}{\partial z} \right] \\
& \quad + S_{\phi}
\end{aligned}$$

The set of equations given are similar to those shown in 22-26 with the obvious addition of the Reynolds stress terms within the square brackets. In this set of equations, the number of unknown values now exceeds the number of equations, this is known as the closure problem. A further model is therefore necessary to solve the Reynolds stress terms.

The most common approach to modelling turbulence is through the assumption that the process of the Reynolds stress is analogous to that of dynamics viscosity.

Boussinesq Proposed that the Reynolds stress is proportional to the mean rate of strain (Pope, 2001)-

$$\tau_{ij} = -\rho \overline{u'_i u'_j} = \mu_t \left(\frac{\partial U_i}{\partial x_j} + \frac{\partial U_j}{\partial x_i} \right) - \frac{2}{3} \rho k \delta_{ij} \quad (42)$$

The turbulence model is then tasked with obtaining a value for the eddy viscosity μ_t .

Throughout this thesis the $k - \omega$ Shear Stress Transport (SST) model is used as well as the Shear Stress Transport Scale Adaptive Simulation SST SAS model. The selection of these models is discussed in section 3.2. A full description of these models and other methods of modelling turbulence can be found in Versteeg & Malalasekera, (2007). Here a brief description of the $k - \omega$ SST model is given.

The $k - \omega$ SST model was proposed and developed by (Menter, 1992a); (Menter, 1992b); (Menter, 1994); (Menter, 1997)). Menter, (1992b) noted that the $k - \varepsilon$ worked well in the free stream flow but was unsatisfactory in the near wall regions. He therefore proposed a hybrid model that used $k - \varepsilon$ in the full turbulent free stream and $k - \omega$ in the near wall region.

3.1.6.1 $k - \varepsilon$

The $k - \varepsilon$ model calculates the eddy viscosity as -

$$\mu_t = \frac{\rho C_\mu k^2}{\varepsilon} \quad (43)$$

Where C_μ is a dimensionless constant. The following transport equations define the parameters for k and ε .

$$\frac{\partial(\rho k)}{\partial t} + \text{div}(\rho k \mathbf{u}) = \text{div} \left[\frac{\mu_t}{\sigma_k} \text{grad } k \right] + 2\mu_t S_{ij} \cdot S_{ij} - \rho \varepsilon \quad (44)$$

$$\frac{\partial(\rho\varepsilon)}{\partial t} + \mathit{div}(\rho\varepsilon\mathbf{u}) = \mathit{div} \left[\frac{\mu_t}{\sigma_\varepsilon} \mathit{grad} \varepsilon \right] + C_{1\varepsilon} \frac{\varepsilon}{k} 2\mu_t S_{ij} \cdot S_{ij} - C_{2\varepsilon} \rho \frac{\varepsilon^2}{k} \quad (45)$$

As shown by Versteeg & Malalasekera (2007) the equation in words state -

| | | | | |
|--|---|--|--|---|
| Rate of change of k or ε | + Transport of k or ε by convection | = Transport of k or ε by diffusion | + Rate of production of k or ε | - Rate of destruction of k or ε |
|--|---|--|--|---|

The equations contain 5 constants. The standard values of these constants are $C_\mu = 0.09$, $\sigma_k = 1$, $\sigma_\varepsilon = 1.3$, $C_{1\varepsilon} = 1.44$ and $C_{2\varepsilon} = 1.92$.

3.1.6.2 $k - \omega$

The $k - \omega$ model calculates the eddy viscosity as -

$$\mu_t = \frac{\rho k}{\omega} \quad (46)$$

The following transport equations define the parameters for k and ω .

$$\frac{\partial(\rho k)}{\partial t} + \mathit{div}(\rho k \mathbf{u}) = \mathit{div} \left[\left(\mu + \frac{\mu_t}{\sigma_k} \right) \mathit{grad} (k) \right] + P_k - \beta^* \rho k \omega \quad (47)$$

$$\begin{aligned} \frac{\partial(\rho \omega)}{\partial t} + \mathit{div}(\rho \omega \mathbf{u}) \\ = \mathit{div} \left[\left(\mu + \frac{\mu_t}{\sigma_\omega} \right) \mathit{grad} (\omega) \right] \\ + \gamma_1 \left(2\rho S_{ij} \cdot S_{ij} - \frac{2}{3} \rho \omega \frac{\partial U_i}{\partial x_i} \delta_{ij} \right) - \beta_1 \rho \omega^2 \end{aligned} \quad (48)$$

In words this equation states -

| | | | | |
|---|--|---|---|--|
| Rate of change of k or ω | + Transport of k or ω by convection | = Transport of k or ω by diffusion | + Rate of production of k or ω | - Rate of destruction of k or ω |
|---|--|---|---|--|

The equations contain 5 constants. The standard values of these constants are $\sigma_k = 2$, $\sigma_\omega = 2$, $\gamma_1 = 0.553$ and $\beta_1 = 0.075$ and $\beta^* = 0.09$.

3.1.6.3 $k - \omega$ SST

The $k - \omega$ SST model uses the $k - \varepsilon$ approach in the free stream flow and the $k - \omega$ method in the near wall regions. The k equation used is the same in the $k - \omega$ and the $k - \omega$ SST models but the ε equation is transformed into the ω equation by substituting $\varepsilon = k\omega$ to allow transition between the two methods resulting in -

$$\begin{aligned} & \frac{\partial(\rho\omega)}{\partial t} + \mathit{div}(\rho\omega\mathbf{u}) \\ & = \mathit{div} \left[\left(\mu + \frac{\mu_t}{\sigma_\omega} \right) \mathit{grad}(\omega) \right] + \gamma_1 \left(2\rho S_{ij} \cdot S_{ij} - \frac{2}{3}\rho\omega \frac{\partial U_i}{\partial x_i} \delta_{ij} \right) \\ & \quad - \beta_1 \rho \omega^2 + 2 \frac{\rho}{\sigma_{w,2}\omega} \frac{\partial k}{\partial x_k} \frac{\partial \omega}{\partial x_k} \end{aligned} \quad (49)$$

3.1.7 NEAR WALL MODELLING

At any wall boundary, the flows are significantly impacted due to the no slip condition at the wall. This results in large gradients of velocity in this region. Therefore, near wall modelling can significantly impact the numerical result as the region is the greatest source of turbulence and vorticity. As this thesis is involved with internal flows, near wall modelling is of importance to ensure accurate numerical results.

A non-dimensional wall distance and velocity can be defined for near wall flows. Very close to the wall, the kinematic viscosity and wall shear stress are important scaling parameters. The shear stress (τ) in the y direction (i.e. flow along a flow plate) can be expressed as -

$$\tau = \mu \left(\frac{dU}{dy} \right) - \rho \overline{uv} \quad (50)$$

At the wall, the Reynolds stress term equals zero due to the no slip condition. Therefore, the wall shear stress is purely a result of the viscous stresses -

$$\tau_w = \mu \frac{du}{dy} \quad (51)$$

Through dimensional analysis the shear stress can be equated to the density multiplied by the velocity squared. As such the frictional velocity (u_τ) can be defined -

$$u_\tau = \sqrt{\frac{\tau_w}{\rho}} \quad (52)$$

The viscous length scale (δ_v) can also be defined as -

$$\delta_v = \frac{\nu}{u_\tau} \quad (53)$$

Where ν is the kinematic viscosity. From this the non-dimensional velocity and wall distances can be defined -

$$u^+ = \frac{u}{u_\tau} \quad (54)$$

$$y^+ = \frac{y}{\delta_v} \quad (55)$$

Many experiments have gained information about the flows in the near wall region. Figure 3.3 shows how this region can be broken down into three separate regions, the viscous sublayer, the buffer region and the fully turbulent or log law region. Note the values are plotted in terms of the non-dimensional velocity and wall distance. The first region known as the viscous sublayer is where molecular viscosity is a major factor and the flows is almost laminar. In the turbulent region, turbulence

is a major factor contributing to the flow development. The buffer region sits between the two regions where both the molecular viscosity and turbulence are important and blends the physics of the two regions.

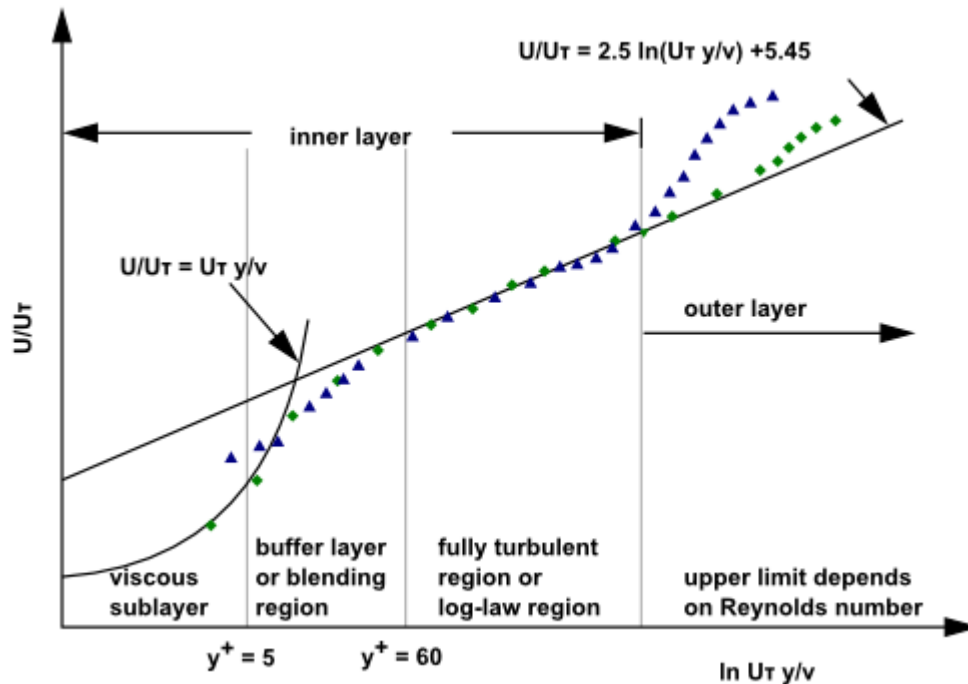


Figure 3.3: Representation of the near wall flows (Ansys, 2009b)

Accurately capturing the boundary layer region is an important consideration during the meshing process. The y^+ of the first cell is an important parameter in terms of the resolution of the boundary layer. Some turbulence models cannot resolve the flow through the viscous dominated regions. Instead a larger y^+ value is needed, and semi-empirical formulas are implemented to bridge the gap between the resolved flow and the wall. Alternately, some turbulence models can resolve the flow right down to the wall. One such model is the $k - \omega$ SST model used in this thesis.

In ANSYS CFX the $k - \omega$ SST model uses automatic near wall treatment. This approach means that the viscous region of the boundary layer will be resolved where the mesh is sufficiently refined or wall models will be implemented where the mesh is too coarse. This is done automatically allowing y^+ insensitive refinement of meshes without convergence issues. In this thesis the y^+ of the mesh was kept below

3 in all cases. This ensures that the flow is resolved up to the wall for accurate modelling of the wall bounded flows.

3.2 CFD FOR TURBINE SIMULATIONS

The previous section gave an overview of the computational approach used in this thesis. There are further considerations, specific to turbine simulations that also require discussion. These include, dealing with the rotation of the wheel, implementation of turbulence models, ensuring convergence, time stepping and development of the mesh.

Baines, (2010) gave a thorough overview of the computational approach for turbine modelling in 1D, 2D and 3D. Here an overview and the consideration made in the CFD set-up is given.

3.2.1 STEADY STATE AND TRANSIENT SIMULATIONS

A steady state approach assumes that flow is constant with respect to time and removes the time derivative from the Navier-Stokes equations. This has a significant effect on the complexity and computational requirements. However, the steady state assumption means that transient effects such as that occurring between the rotor and stator are not accounted for. Furthermore, a transient simulation can be used to account for the pulsed inlet flow associated with turbine operation where as a steady state approach cannot.

The first published work conducted for transient calculations of the 3D Navier Stokes equations were by Lam et al., (2002) . This study compared steady, unsteady and experimental results. While the unsteady set-up accounted for pulse effect, the rotor was modeled using a frozen rotor approach (see section 3.2.2). Lam et al., (2002) found that steady state efficiency only deviated a small amount from the instantaneous efficiencies. However, as stated by Baines, (2010), the use of the frozen rotor model may obscure this result and further investigation was necessary. Palfreyman & Martinez-Botas, (2004) noted much larger differences between steady

and unsteady simulations than previously found by Lam et al., (2002). In this case a sliding mesh approach was used, as opposed to the frozen rotor, which could better account for transient effects and perhaps indicates that a transient simulation of the rotor is necessary. Hellstrom & Fuchs, (2009) raised the point that Palfreyman & Martinez-Botas, (2004) tested a nozzleless turbine, whereas Lam et al., (2002) tested a vanned turbine. As the former may result in greater flow variations at the turbine inlet, an increase in variation between steady and unsteady results could be expected and may not be the result of the frozen rotor method. Abidat & Hachemi, (2005) also completed transient simulation and their findings supported that of Lam et al., (2002) for the rotor domain. They concluded that as fluctuations in rotor mass flow at the inlet and outlet were similar the quasi steady rotor approach which is a valid approximation.

Galindo et al., (2014) found a significant difference between the steady and transient results for a turbine at off design conditions. In this instance, inlet pulsing was not taken into consideration and the turbine consisted of guide vanes, therefore indicating that the discrepancies are a result of transient effects caused by the rotor stator interaction.

Multiple unsteady, pulsed flow simulations have successfully shown that a hysteresis loop is created due to the filling and emptying of the volute, Lam et al., (2002) Abidat et al., (2008a). These results agree with observations from earlier experimental works such as those by Baines & Yeo, (1991) and Winterbone et al., (1991) on a radial turbine and Arcoumanis et al., (1995) and Karamanis & Martinez-Botas, (2002) on a mixed flow turbine. This effect has been found to cause a significant difference in steady and unsteady results. Abidat et al., (2008a) performed both steady and unsteady pulsed computations. They concluded that while the steady state efficiency predictions showed reasonable agreement with experimental data, the unsteady results were a clear improvement with the development of a hysteresis loop that accounted for the difference in performance. Similar conclusions were drawn by Karamanis & Martinez-Botas, (2002) and Hakeem et al., (2007b). Karamanis & Martinez-Botas, (2002) noted that the pulsed flow conditions deviated

from the steady state results but as the pulsed frequency increased they tended to the steady state values. Hakeem et al., (2007b) also found that the instantaneous performance differed substantially between a fully transient pulsed cases and that of a steady state case. They concluded that the steady flow assumption was unsatisfactory for efficiency measurements in highly pulsed operating environments. Chiong et al., (2012) concluded that the quasi-steady assumption is only valid if the volume of the region is much smaller than the overall volume of the stage. Therefore, the quasi-steady assumption in the rotor region, which has a very small volume in comparison to the whole turbine stage, is valid but the same cannot be said for the volute, which requires a finite time to fill and empty, resulting in the creation of the hysteresis loop.

Previous work has demonstrated the necessity to capture the unsteady pulsating effects on turbine performance. While the quasi steady assumption of the rotor may be valid due to its small volume. As this thesis focusses on the impact of the volute it is important to capture the flow development within this domain over the course of a pulsation.

3.2.2 DOMAIN ROTATION

To simulate the rotor motion, there are two common approaches taken, the Multiple Reference Frame (MRF) approach and the sliding mesh approach. The MRF method does not require the mesh to move, instead the flow parameters are set relative to the rotating reference frame (Ansys, 2009a). There are two MRF approaches available in CFX, the ‘frozen rotor method’ and the ‘mixing plane approach’. The mixing plane approach circumferentially averages the flow parameters at the interface, whereas the frozen rotor approach passes the wakes and secondary flows downstream but with the rotor in only one stationary position. In turbocharger applications the frozen rotor method is commonly used in the literature ((Roclawski et al., 2012); (Roclawski et al., 2014); (Yang et al., 2017b)).

The advantage of the MRF approach is a significant reduction in computational cost compared to the sliding mesh alternative. However, the MRF approach cannot

account for transient effects such as the interaction between the rotating and stationary parts. Galindo et al., (2014) compared the MRF frozen rotor and sliding mesh approaches for a vanned radial turbine. While the sliding mesh approach used is fully transient, as opposed to the MRF approach, neither approaches took into account pulsed inlet flow. Galindo et al., (2014) investigated the performance of a radial turbine with guide vanes under the frozen rotor and sliding mesh approaches and compared the results with experimental data. The authors concluded that a MRF approach was accurate at design conditions but started to deviate at low expansion ratios due to stronger interaction between the stator vanes and the rotor. The maximum variation between the sliding mesh and MRF approach is 11% at the lowest expansion ratio tested (~ 1.5). However, the narrow range of experimental data limits validation of either computational approach; particularly at low expansion ratios where no experimental data was available. Furthermore, this investigation only considered a vanned turbine. Alternately, a nozzleless configuration will encounter less rotor stator interactions. Therefore, the deviation in the two approaches, that was said to be the result of stator-rotor interactions, will reduce in a nozzleless configuration. Hence, the added computational requirements of a sliding mesh method may not be particularly beneficial.

Yang et al., (2017b) used the MRF approach for one such nozzleless configuration and found good agreement with experimental results under both steady state and pulsating flows. The only discrepancies between experimental and computational results noted by the authors was the magnitude of the hysteresis loop formed. This was attributed to the impact of the volute tongue on the flow distribution that is not accurately modelled with the frozen rotor method. Yang et al., (2017a) compared the frozen rotor and sliding mesh method in detail for a nozzleless configuration. The authors found that the circumferential variations in rotor inlet conditions and rotor torque were well predicted by the frozen rotor method. Discrepancies between the two methods were only seen in a detail study of the passage secondary flows downstream of the LE due to the difference in time scales of the secondary flow development caused by the tongue and that of the rotation of the wheel.

Furthermore, analysis of secondary flows in the rotor passage away from the volute tongue showed no noticeable differences in flow development.

The focus of the current study is in the impact that volute secondary flows have on rotor inlet conditions. As such, accurate modelling of the effects of the blade passing the tongue is deemed of secondary importance, furthermore the lack of guide vanes in the current geometry is assumed to reduce the impact of the frozen rotor approach on performance. The detailed validation of the frozen rotor approach presented by Yang et al., (2017a) and Yang et al., (2017b) along with further validation carried out in this thesis (see section 3.7) means that the frozen rotor approach is used throughout this thesis reducing the computational time required per simulation by up to a factor of 10.

3.2.3 *TURBULENCE MODELING*

A common turbulence model used for turbomachinery application is the $k - \omega$ shear stress transport (SST) and is used throughout this work. The model is discussed in section 3.1.5. This model accounts for the transport of turbulent shear stress and is capable of predicting flow separation under adverse pressure conditions accurately (Ansys, 2009a).

While $k - \varepsilon$ requires less computational resources and has been used in the past by a number of authors Abidat et al., (2008b), Padzillah et al., (2015), Newton, (2014), the SST model is more appropriate for complex flows, such as those present in turbine operations Abidat et al., (2008b). Other RANS based turbulence models have also been used by other authors, Zhang et al., (2011) and Yang et al., (2015) both used the one equation Spallart Allmares model; while Abidat et al., (2006) implemented the Renormalization Group $k - \varepsilon$ (RNG) $k - \varepsilon$ as an improvement to the basic $k - \varepsilon$ model.

Abidat et al., (2008b) noted that the SST model is more appropriate for complex flows such as those present in turbines despite using the $k - \varepsilon$. However, the SST model has been used extensively in turbomachinery applications (Galindo et al., 2014); (Leonard et al., 2014); (Morrison et al., 2016); (Roelawski et al., 2014)).

Simpson et al., (2009) found good agreement with experimental results for both vanned and nozzleless turbines. Extensive validation of this model with the frozen rotor approach for pulsating flow was also completed by Yang et al., (2017a).

Hellstrom, (2010) completed Large Eddy Simulations (LES) to resolve the true turbulence in the large scales while small scale turbulence is modelled. Such a method accurately computes the turbulence present in the unsteady regions instead of using the Reynolds Averaging approach which can lead to inaccuracies in such unsteady regions. Despite the advantage of this approach a significant increase in computational resources are required.

Alternatively, the Scale Adaptive Simulation approach can be used to improve the modelling of unsteady regions without extensive computational requirements. This approach introduces the Von Karman length scales into the URANS computation to resolve the turbulent spectrum in the unsteady flow regions. The method detects the resolved unsteady flow structures computed through the URANS approach, and adjusts them based on the Von Karman length scale computation added into the model producing LES like results in the unsteady regions Ansys, (2009a). This modelling approach can therefore result in more accurate predictions in highly unsteady separated or vortical regions. Therefore, in addition to the SST model used in this thesis the Shear Stress Transport Scale-Adaptive simulation (SST-SAS) model is also implement in some of the more refined computational works. Full details of the turbulence computation can be found in Menter & Egorov, (2005).

3.3 CFD SET-UP

In this thesis both steady state non-pulsed and fully transient pulsating simulations were used. The steady state approach, although not realistic to the engine environment, can provide a solid basis for comparison. In the pulsating flow simulation, the frozen rotor was used throughout, due to the excessive computational resources necessary for fully sliding mesh simulations. This allows a greater number of simulations to be complete within the time period of the project. Furthermore, this project focusses on nozzleless turbine configurations. As such the interaction between the stator and rotor is minimised with the non-uniformity occurring being that caused by the tongue.

In the pulsating simulations, the inlet conditions supplied are of mass flow and total temperature. The impact of multiple pulse forms has been included within the thesis. The pulse shape used in the work is also an area of discussion as outlined from the literature review. Furthermore, multiple pulse frequencies and pulsation numbers have been included to fully quantify the impact of pulsating flow on the turbine stage.

The $k - \omega$ SST turbulence model was implemented throughout this thesis with the exceptions of chapters 8 and 9 where the SAS SST model was used in an attempt to accurately capture secondary flows. The implementation of this model and its effect is discussed in chapter 8.

In all simulations convergence was judged to be sufficient when the root mean squared residuals fell below $1e10^{-4}$. In the majority of simulations the residuals fell below $1e10^{-5}$.

3.4 MESH STUDY

3.4.1 COMPUTATIONAL DOMAIN

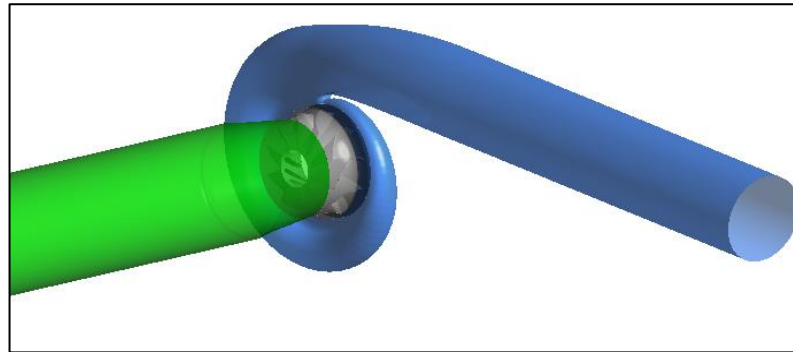


Figure 3.4: Computational domain

Figure 3.4 shows the computational domain which consists of the turbine volute, rotor and the outlet region. The inlet section is extended to allow flow development ahead of the volute spiral. The inlet pipe work is straight, unlike what might be expected in true engine installations. This simplification is accepted as the focus of this thesis is to investigate the performance of the turbine stage only. In the current case no guide vanes were present (nozzleless configuration) and so the volute connects directly to the rotating domain at the volute-rotor interface. The outlet region then connects to the rotating region just downstream of the TE of the wheel. The outlet plane has a static pressure boundary and is positioned approximately 15 wheel diameters downstream. This is done to ensure no flow reversal at the outlet plane at the low mass flow running points. A discussion of the impact of this was given by Serrano et al., (2017).

3.4.2 MESH REFINEMENT

A full domain specific mesh study was completed, similar to that recommended by Galindo et al., (2014) and was extended to include a boundary mesh independence study. The volute and outlet region domains used an unstructured tetrahedral mesh developed in ICEM CFD. The rotor region used a structured hexahedral mesh completed in ANSYS TurboGrid. This section shows the results of the mesh independence studies conduct for each domain. As this thesis focuses on the impact

of volute geometry, particular attention has been paid to the impact of the mesh is this region.

3.4.3 VOLUTE MESH STUDY

The volute mesh analysis was done in both a quantitative and qualitative manor. The initial part of the analysis looked at the impact of progressive mesh refinement on the efficiency of the turbine stage, presented in table 3.1 and figure 3.5 where the values are normalised by the most refined grid values. The resultant behaviour shows that the stage efficiency tends towards an asymptote. While the refinement between 2.73 and 9.44 million cells only results in a 0.67% variation in stage efficiency it is important to ensure that the volute flows are accurately captured.

| <i>No. Cells</i> | <i>Eff</i> |
|------------------|------------|
| 2732545 | 99.33% |
| 3203381 | 99.52% |
| 4587206 | 99.76% |
| 5828768 | 99.86% |
| 8173549 | 99.96% |
| 9440683 | 100.00% |

Table 3.1: volute mesh convergence values normalised by finest mesh value

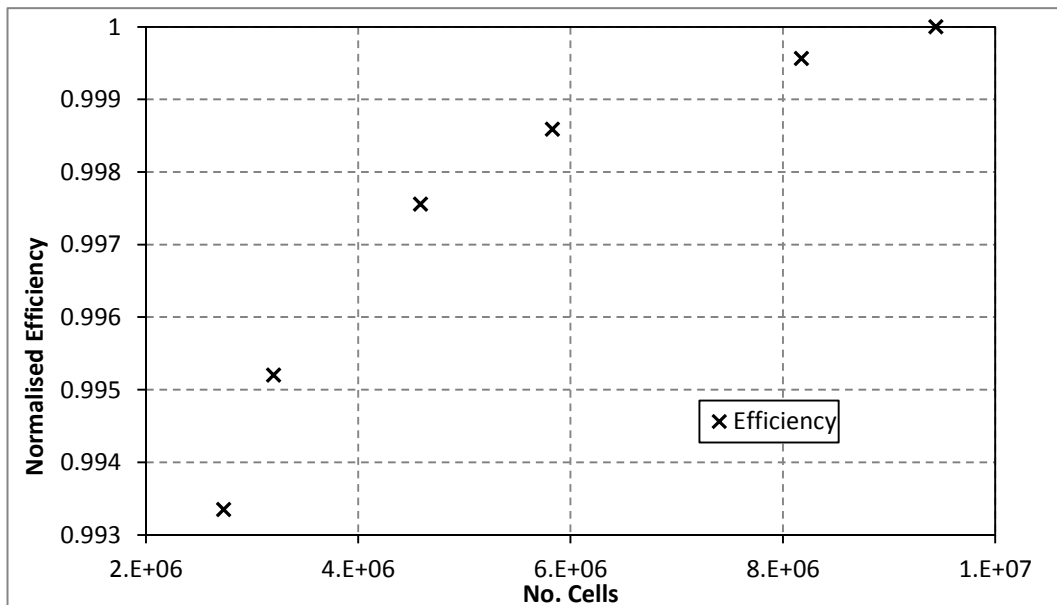


Figure 3.5: Volute mesh refinement efficiency plot

The Grid Convergence Index (GCI) technique introduced by Roach, (1997) is a method used to investigate the discretisation errors. Celik et al., (2008) and Slater, (2008) also provide detailed descriptions of how to implement the method. Cerdoun & Ghenaiet, (2018) showed the use of the method for a radial turbine for turbocharger applications similar to that in this thesis. The approach uses a Richardson extrapolation to calculate the continuum result and reports the error of the mesh with respect to this value. The method is briefly described here.

The method is done over three mesh densities of progressive refinement. Firstly, a representative grid spacing (h) must be calculated to produce a refinement factor (r).

$$h_i = \sqrt[3]{V/n} \quad (56)$$

$$r_i = \frac{h_i}{h_{i+1}} \quad (57)$$

Where –

$$h_i < h_{i+1} \quad (58)$$

Where h_i and h_{i+1} are the grid spacings on the i^{th} and i^{th+1} grids, V is the domain volume and n is the number of cells. r_i is then the refinement factor between the two successive grids.

The order of convergence (P) is then calculated using an iterative method for equations 59-62.

$$P = \frac{1}{\ln(r_i)} |\ln|\varepsilon_{i+1}/\varepsilon_i| + q(p)| \quad (59)$$

$$\varepsilon = f_{i+1} - f_i \quad (60)$$

$$q(p) = \ln \left(\frac{r_i^p - s}{r_{i+1}^p - s} \right) \quad (61)$$

$$s = \text{sgn}(\varepsilon_{i+1}/\varepsilon_i) \quad (62)$$

Where f is the solution parameter being investigated, i.e. efficiency.

Richardson extrapolation is used to obtain the continuum approximation from the asymptotic solution.

$$f_{h=0} = \frac{r_i^p f_i - f_{i+1}}{r_i^p - 1} \quad (63)$$

The relative difference between solutions is then given by –

$$e_r^i = \frac{f_i - f_{i+1}}{f_i} \quad (64)$$

The relative difference between the solution and the continuum value is given by

–

$$e_{ext}^i = \frac{f_{h=0} - f_{i+1}}{f_{h=0}} \quad (65)$$

Finally, the convergence index between two grids can be obtained through equation 66.

$$GCI = \frac{F_S e_r^i}{r_i^p - 1} \quad (66)$$

Where F_S is a safety factor. Roach, (1997) suggested using a value 1.25 in studies using 3 levels of grid refinement. The resulting values are presented in table 3.2 for the volute mesh using the mesh size of 2.7, 4.6 and 9.4 million cells.

Table 3.2: Volute GCI

| | h | f | r | P | $f_{h=0}$ | e_r^i | e_{ext}^i | GCI |
|----------------------|----------|-------|-------|------|-----------|---------|-------------|--------|
| Coarsest Mesh | 0.000651 | 0.989 | | 5.31 | 1.001 | | 1.221% | |
| | 0.000511 | 0.996 | 1.274 | | | 0.886% | 0.338% | 0.424% |
| Finest Mesh | 0.000401 | 1 | 1.272 | | | 0.244% | 0.094% | 0.118% |

The resulting GCI calculations in table 3.2 show that the approximated errors for the middle and finest meshes are 0.424% and 0.118% respectively and the relative errors to the continuum approximation are 0.338% and 0.094% respectively. From this analysis the middle mesh represents an acceptable level of accuracy for the global performance parameters. In addition to the analysis of the global performance parameters the mesh must be capable of capturing the complex secondary flow structures within the volute for detailed analysis. Figure 3.6 shows the contours of radial velocity and streamlines at the volute plane 90° from the tongue for the 2.73, 5.85 and 9.44 million cell cases. The position of the plane was selected as a significant amount of secondary flow activity was observed in this region, allowing detailed comparison of the modelled flows. The position of this plane is also shown in figure 3.7 for clarity. Clearly the coarsest of the meshes results in significant recirculation of the flow within the volute. As the mesh is progressively refined this behaviour is reduced and the streamlines show similar flow structures in the 5.85 and 9.44 million element meshes. Between these two mesh densities the stage efficiency variation was only 0.14% The radial velocity contours show a similar trend with a ring of low radial velocity existing in the finer two mesh cases. The low radial velocity present in the 2.73 million element case encompasses a larger area in the centre of the volute.

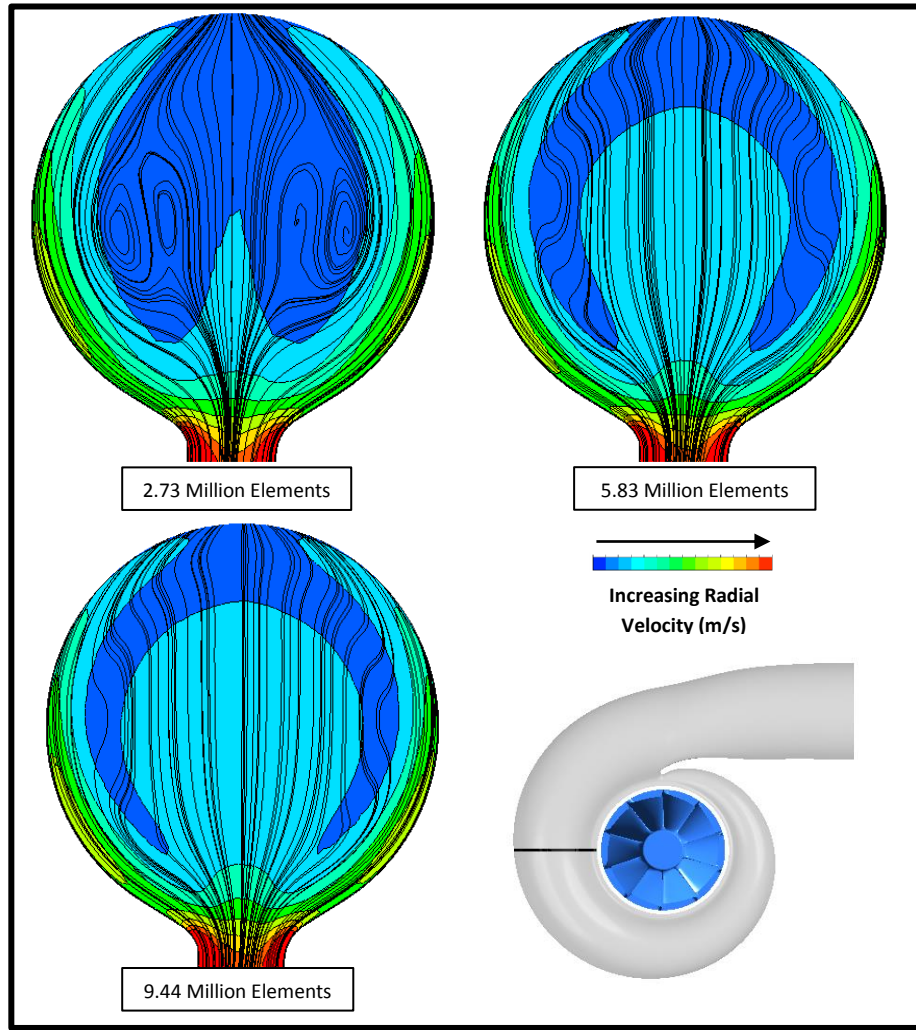


Figure 3.6: Secondary flow structures in the volute at three mesh densities

To analysis the impact of the volute mesh density further, the impact on the volute total pressure loss coefficient can be plotted. The total pressure loss coefficient is defined as –

$$K_{PL} = \frac{P_{01} - P_{01.5}}{\frac{1}{2}\rho_{1.5}u_{1.5}^2} = \frac{P_{01} - P_{01.5}}{P_{01.5} - P_{1.5}} \quad (67)$$

Where P_{01} is total pressure at the stage inlet, $P_{01.5}$ is total pressure at the volute outlet, $P_{1.5}$ is the static pressure at the volute exit, $\rho_{1.5}$ is density at the volute exit and $u_{1.5}$ is velocity at the volute exit. The total pressure loss coefficient is therefore the

loss in total pressure through the volute normalised by the dynamic pressure at the volute exit. Comparing the mesh densities using this parameter allows the impact of the mesh purely on the performance of the volute to be assessed as appose to the impact on stage efficiency, to which the volute has only a small impact due to its relatively small losses compared with the rotor. The total pressure loss plotted is normalised by the finest mesh value.

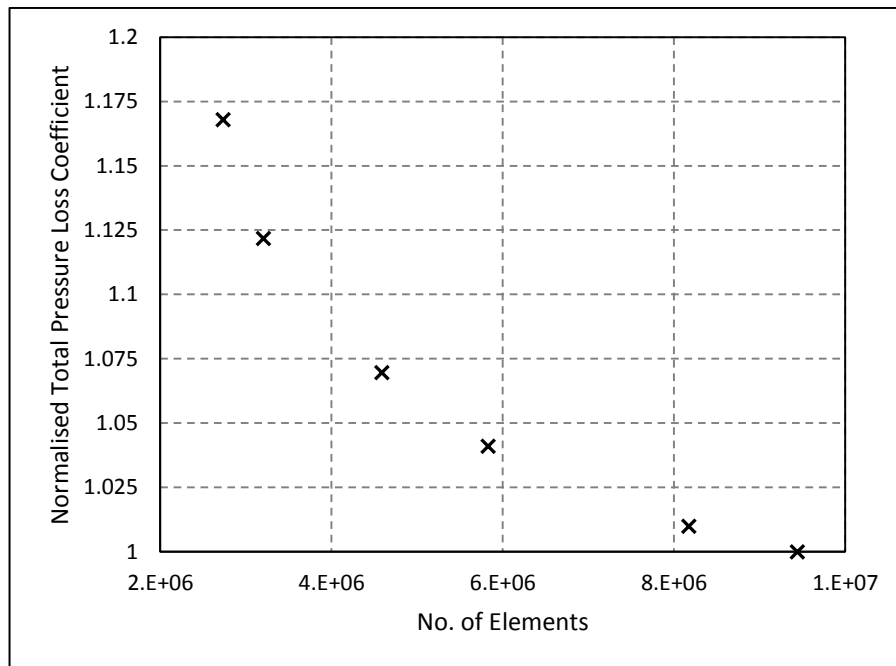


Figure 3.7: Volute mesh refinement total Pressure loss coefficient

Figure 3.7 shows that the refinement of the grid results in lower total pressure loss coefficients. Based on the contour plots presented in figure 3.7 this logically follows that the courser mesh densities over predicts the existence of secondary flow structures which lead to increases in total pressure loss.

From the mesh density analysis conducted it was deemed that the 5.8 million mesh density is necessary to accurately capture the volute secondary flows and account for volute losses. As this thesis is focussed on the impact of volute design it is important to ensure a high resolution of the predicted flows. Therefore, this highly refined volute mesh density is implemented though out.

3.4.4 ROTOR MESH REFINEMENT

While the volute and outlet regions were meshed using an unstructured mesh in ICEM CFD, the rotor was meshed with a hexahedral structured mesh developed in TurboGrid. This meshing tool is specific for turbomachinery applications producing high accuracy meshes with minimal required elements. TurboGrid also allows the number of cells in the blade tip to shroud gap to be specified. In the current work this value was set to 20 elements and remained constant for all cases to ensure tip leakage flow was accurately captured.

| <i>Rotor Cells</i> | <i>TG Eff</i> | <i>TG Mass Flow</i> |
|--------------------|---------------|---------------------|
| 1286460 | 99.71% | 0.193688 |
| 1990390 | 100.24% | 0.192287 |
| 2579400 | 100.36% | 0.191992 |
| 3540000 | 100.32% | 0.191987 |
| 4517970 | 100.19% | 0.192088 |
| 5411760 | 100.11% | 0.19215 |
| 6455680 | 100.02% | 0.19225 |
| 7059370 | 100.00% | 0.1923 |

Table 3.3: Rotor mesh convergence values normalised by the finest mesh values

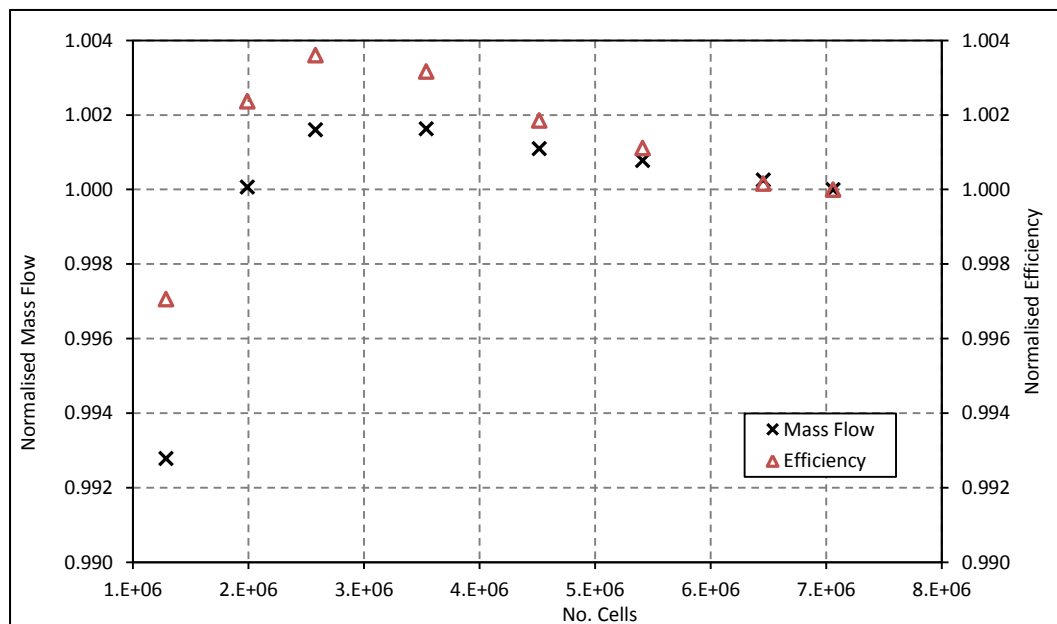


Figure 3.8: Rotor mesh refinement efficiency plot normalised by the finest mesh values

The stage efficiency and mass flow values for each of the mesh densities are presented in figures 3.8 and table 3.3 where the values are normalised by the most refined grid values. The rotor mesh independence plot shows an under damped trend. When the mesh density falls below 1.99 million the accuracy of the predicted efficiency and mass flow suffers greater inaccuracies. In terms of the measured efficiency, further refinement shows that the predicted efficiency begins to increase again showing an over damped type trend. The corresponding plot of stage mass flows shows a much more modest change with progressive refinement beyond 2.44 million elements. Beyond the mesh size of 3.5 million cells, the mesh shows good levels of convergence with less than 0.4% variation in efficiency and less than 0.2% in mass flow.

The GCI method was again applied to analyse the accuracy of the meshes. The results are presented in table 3.4 for the 1.3, 3.5 and 7.1 million cell grids.

Table 3.4: Rotor GCI Results

| | h | f | r | P | $f_{h=0}$ | e_r^i | e_{ext}^i | GCI |
|----------------------|----------|-------|-------|------|-----------|---------|-------------|--------|
| Coarsest Mesh | 0.000780 | 0.997 | | 2.18 | 0.995 | | 0.193% | |
| | 0.000557 | 1.003 | 1.401 | | | 0.609% | 0.807% | 0.698% |
| Finest Mesh | 0.000442 | 1.000 | 1.259 | | | 0.317% | 0.488% | 0.607% |

The calculated GCI values for the two finest meshes are 0.698% and 0.607% respectively. While this value is larger than in the volute, it is still an acceptable level of uncertainty. It should be noted that the reduced relative error of the coarsest mesh with respect to the approximated continuum value is the result of the under damped trend observed in the mesh study and not an indication of a greater accuracy of the coarse mesh. Due to the considerable increase in computational time for further refinement of the grid the middle mesh size, containing 3.5 million cells was deemed satisfactory.

3.4.5 OUTLET MESH REFINEMENT

In the outlet domain, the flow is diffused to atmospheric pressure at the stage outlet. Table 3.5 and figure 3.9 present the impact of the mesh density in this region where the values are normalised by the most refined grid values. As this region only acts to diffuse the flow the impact of the mesh refinement in this domain has a smaller impact on the measured performance of the turbine stage. Again, the behavior in this region shows an over damped type trend. Between the 1.54 million element mesh and the 14.01 million elements mesh the variation in stage efficiency is less than 0.15%. As a result, the 1.54 million element mesh was used throughout this thesis.

| <i>No. Cells</i> | <i>Eff</i> |
|------------------|------------|
| 500000 | 99.77% |
| 1008445 | 99.90% |
| 1540135 | 100.04% |
| 4053050 | 100.15% |
| 9660358 | 100.03% |
| 14012136 | 100% |

Table 3.5: Outlet mesh convergence values normalised by the finest mesh values

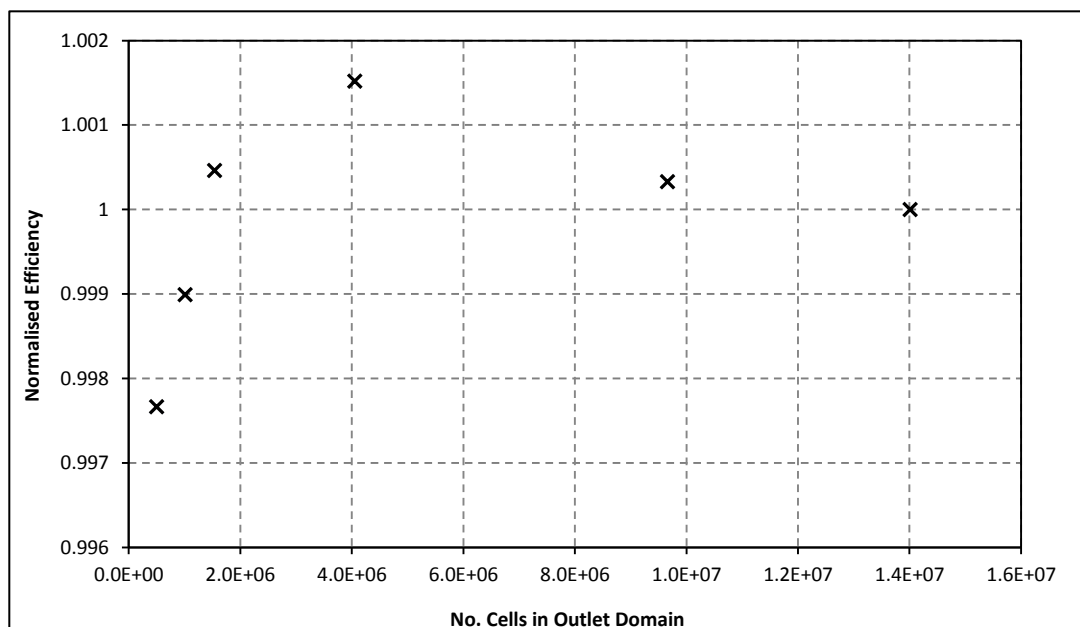


Figure 3.9: Outlet mesh refinement efficiency plot

3.4.6 BOUNDARY LAYER MESH REFINEMENT

As discussed in section 3.1.6, the boundary layer consists of large velocity gradients causing difficulties in accurately capturing the flows in this region. Within the boundary layer, prism mesh layers produce an ordered mesh close to the wall to capture these gradients.

In all cases the initial cell height is specified at 0.01mm, this cell height ensures that the stage Y^+ remains below 3 throughout the stage. The inflation layer ratio is also held constant at 1.25. With these two parameters kept constant the boundary layer study investigated the impact of the number of prim layers used. Increasing the number of layers for a constant expansion ratio increases the height of the boundary layer mesh region. Increasing or decreasing the number of prim layers has a substantial impact on the total number of elements in the mesh and hence computational time. Efficiently capturing the boundary layer is therefore vital. The results of the study are shown in table 3.6 and figure 3.10.

| <i>No. Cells</i> | <i>Eff</i> |
|------------------|------------|
| 7 | 98.85% |
| 9 | 99.89% |
| 11 | 99.96% |
| 13 | 100% |

Table 3.6: Boundary layer mesh convergence values normalised by the finest grid value

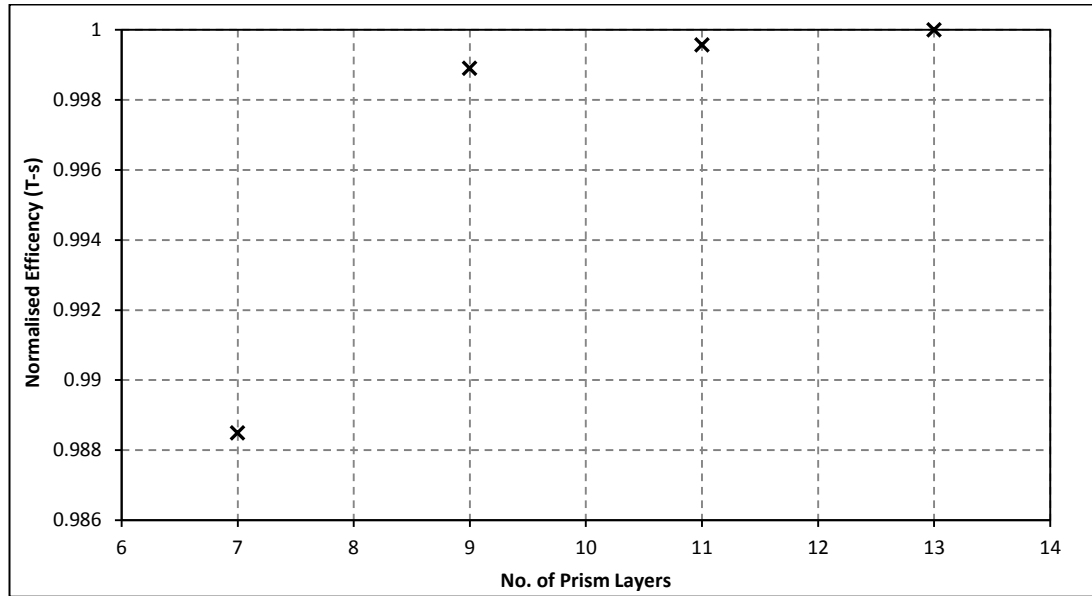


Figure 3.10: Boundary layer mesh refinement efficiency plot normalised by the finest grid value

From the results of the boundary layer mesh study, 9 prism layers were deemed capable of resolving the boundary layer to an acceptable level of accuracy. Further refinement results in a small increase in measured efficacy but with this, run times increase significantly.

3.4.7 FINAL MESH

The resulting number of cells in each domain and the stage total is given in table 3.7. The number of cells present varies slightly between volute designs in this thesis. However, in all cases the mesh set-up remains constant and the resulting change in element count was the result of the greater surface area or internal volume.

| <i>Domain</i> | <i>No. cells</i> |
|---------------|------------------|
| <i>Volute</i> | 5,828,768 |
| <i>Rotor</i> | 3,540,020 |
| <i>Outlet</i> | 1,540,135 |
| <i>Total</i> | 10,734,823 |

Table 3.7: Number of cells in stage per domain and total

A mesh study conducted on a domain specific basis can results in the measured errors accumulating over the stage. Summing the relative uncertainties of the mesh in each of the studies regions results in an overall uncertainty level of approximately

0.65% in efficiency. To assess this accumulative uncertainty, the final mesh was compared with a that of a complete mesh consisting of the finest domain meshes constructed. The resulting variation in performance parameters is plotted in table 3.8. The results show that the uncertainty measured in each specific domain does not accumulate to result in a larger discrepancy. Indeed, the final uncertainty is much lower than that of the summed domain specific uncertainty. The small discrepancy between the final mesh and the highly refined version, gives confidence in the accuracy of the final optimised mesh.

| <i>Parameter</i> | <i>Percentage change</i> |
|-------------------------|--------------------------|
| <i>Mass flow</i> | 0.09% |
| <i>Rotor Torque</i> | 0.33% |
| <i>Stage Efficiency</i> | 0.24% |

Table 3.8: Comparison of final optimised mesh and highly refined mesh.

Figure 3.11 shows the resulting rotor structured mesh and figure 3.12 shows the volute mesh. The structured mesh in the rotor ensures that the regions around the blade are highly refined and ordered to capture the flows. This mesh structure also improves mesh quality around the complex blade geometry where as an unstructured mesh can lead to poor quality cells. The volute mesh shows local refinement in regions close to the volute exit where the flow is accelerated in the rotor. The boundary layer mesh is also shown at the volute edge plane.

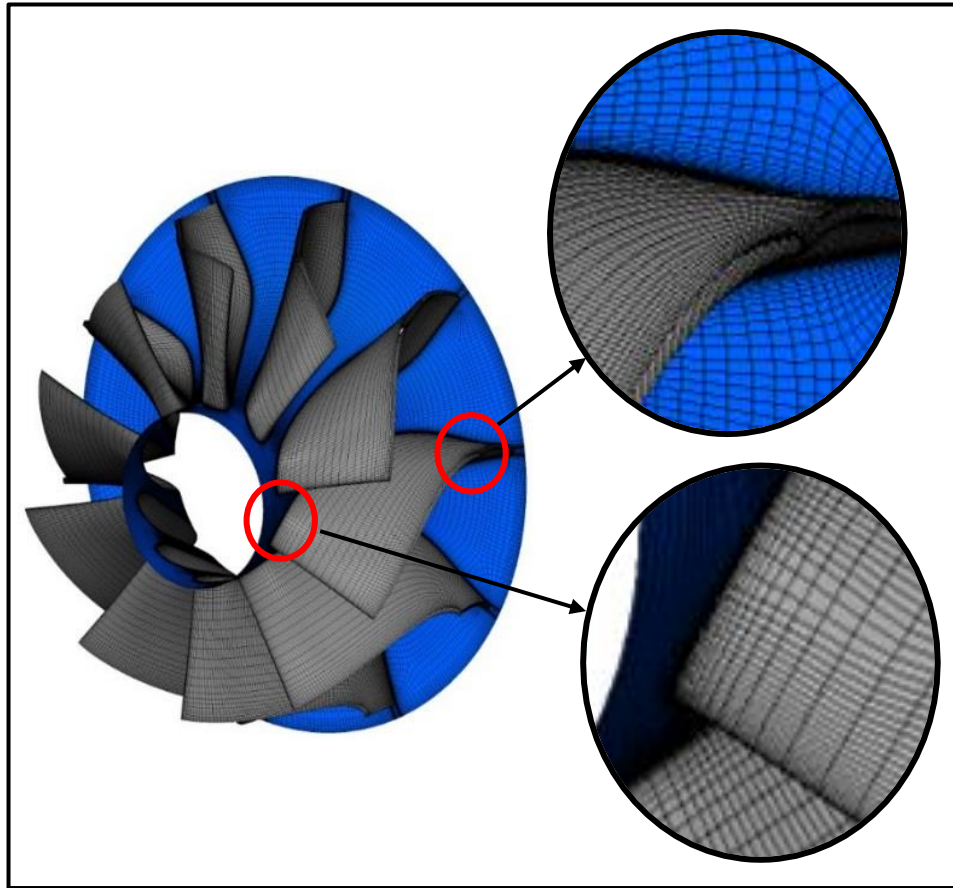


Figure 3.11 - Structured rotor mesh

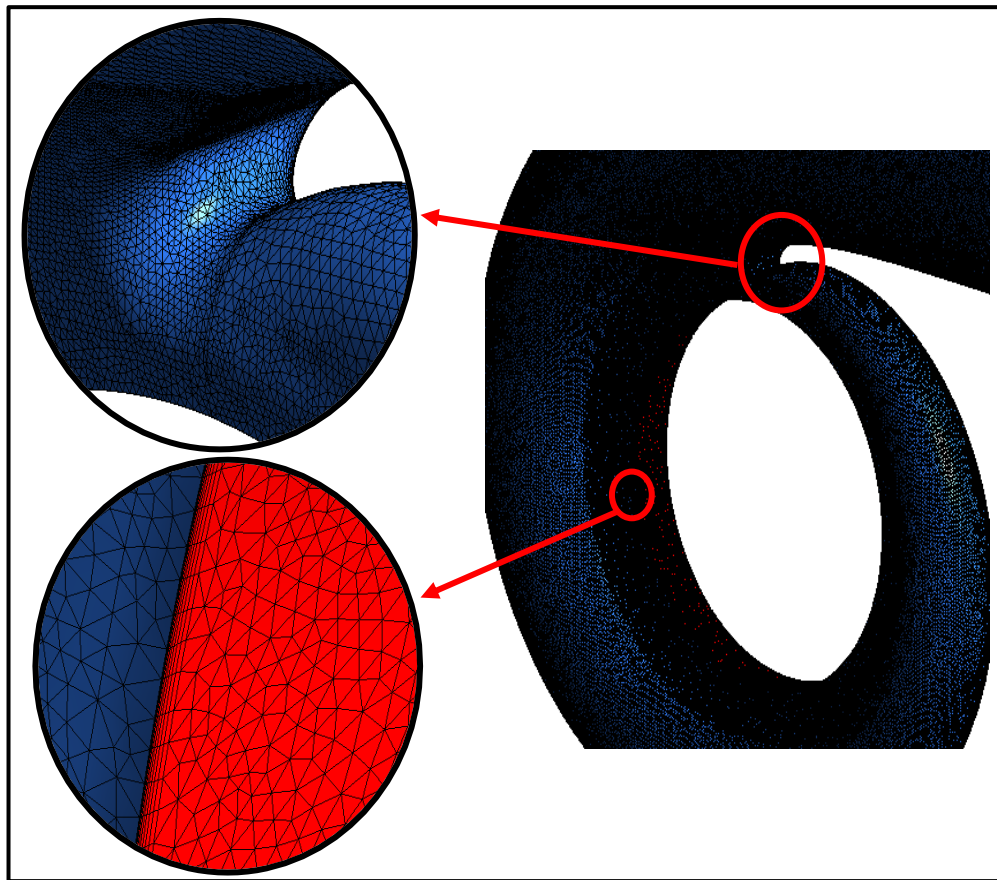


Figure 3.12 - Resulting volute mesh

3.5 TIME STEP STUDY

Convergence of the simulations was deemed to be achieved when the residuals fell below $1e^{-4}$ within the inner iteration loops of the transient simulations. In all cases a minimum of 200 points per pulse were implemented to ensure high resolution of the pulsating flow. In addition to this the time step was further refined to investigate the impact on performance.

Figure 3.13 shows the rotor torque generated in two simulations, one with a time step half of the original. The impact of the reduced time step which required twice the computational time to compute, is very small in terms of measure rotor torque. The cycle average change in torque performance was found to be only 0.025%. The resulting rotor efficiency achieved for both time steps is also presented in figure 3.14. In this case the cycle averaged variation was only 0.0002% between the two cases. This result demonstrates that the time step sized used in this study is sufficient and the transient effects are successfully captured with 200 time steps per pulse. Further reducing the time step led to convergence issues with flow reversal occurring at the outlet plane.

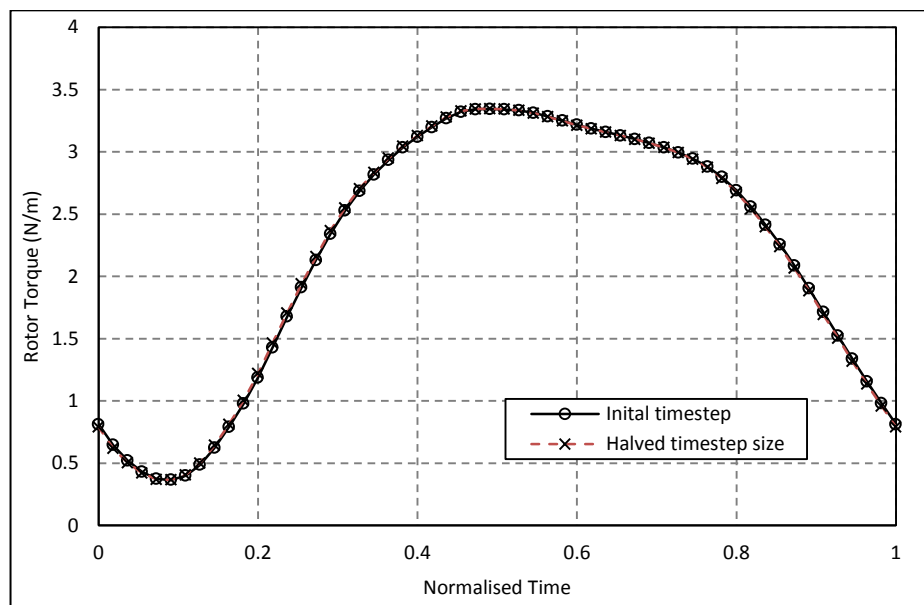


Figure 3.13 - Impact of time step on rotor torque

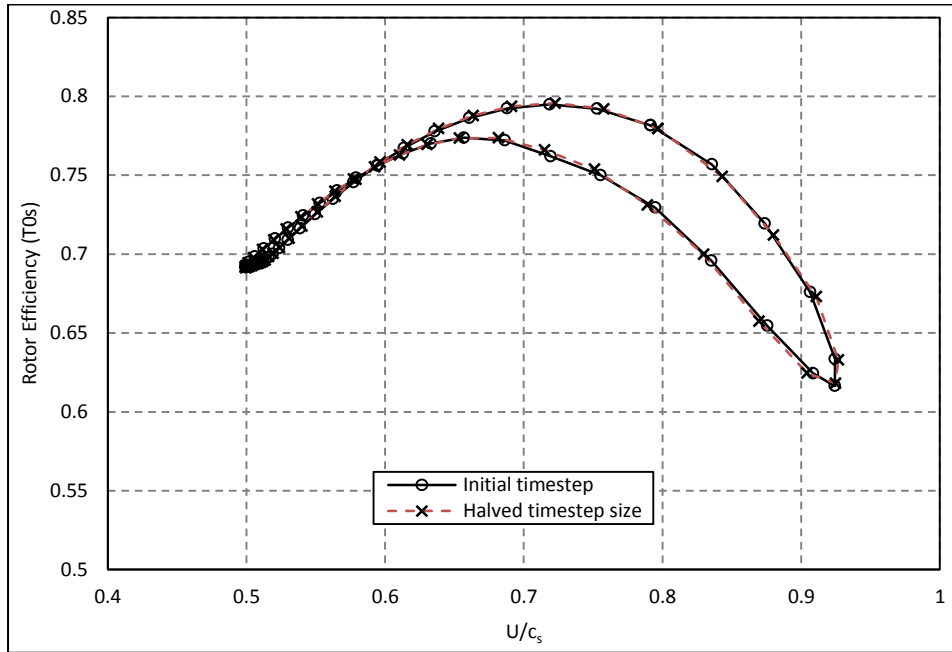


Figure 3.14 - Impact of time step size on rotor efficiency

3.6 COMPARISON OF FROZEN ROTOR AND SLIDING MESH METHODS

The geometry studied in the current investigation is that of a nozzleless mixed flow turbine (no stator guide vanes). Therefore, the only circumferential non-uniformity present was that of the volute tongue. The impact of the frozen rotor approach was assessed, as it was deemed necessary to validate the capability of the frozen rotor approach to predict the volute exit flows. The frozen rotor method was compared with that of the sliding mesh approach under non-pulsating flows at two inlet mass flows, a low mass flow corresponding to the minimum pulse mass flow and a high mass flow corresponding to a maximum pulse mass flow. The time step size in the sliding mesh simulations was equivalent to 4° of rotor rotation and the results averaged over multiple rotations. In the sliding case the rotor torque fluctuates as each rotor blade passes the volute tongue, while the constant position of the rotor in the frozen rotor approach results in a constant torque. The variation in rotor torque, averaged over multiple rotor rotations between the sliding and frozen rotor approaches was found to be 1.02% and 0.52% in the low and high mass flow cases respectively. A greater deviation at low mass flows can be expected due to increased unsteadiness and so the impact of blade passing increases. Figures 3.15 and 3.16 presents the absolute flow angles at the volute exit at 5 circumferential locations at both the low and high mass flow running points. In both cases the trends in absolute flow angle are in agreement and the variation around the volute circumference matches. However, the frozen rotor approach consistently over predicts the peak absolute flow angle by a small amount.

As the variation between the two approaches was small and the frozen rotor method was found to be capable of predicting turbine performance and the volute exit flow conditions, the frozen rotor approach was used throughout. Implementation of the frozen rotor approach significantly reduces the computational time required.

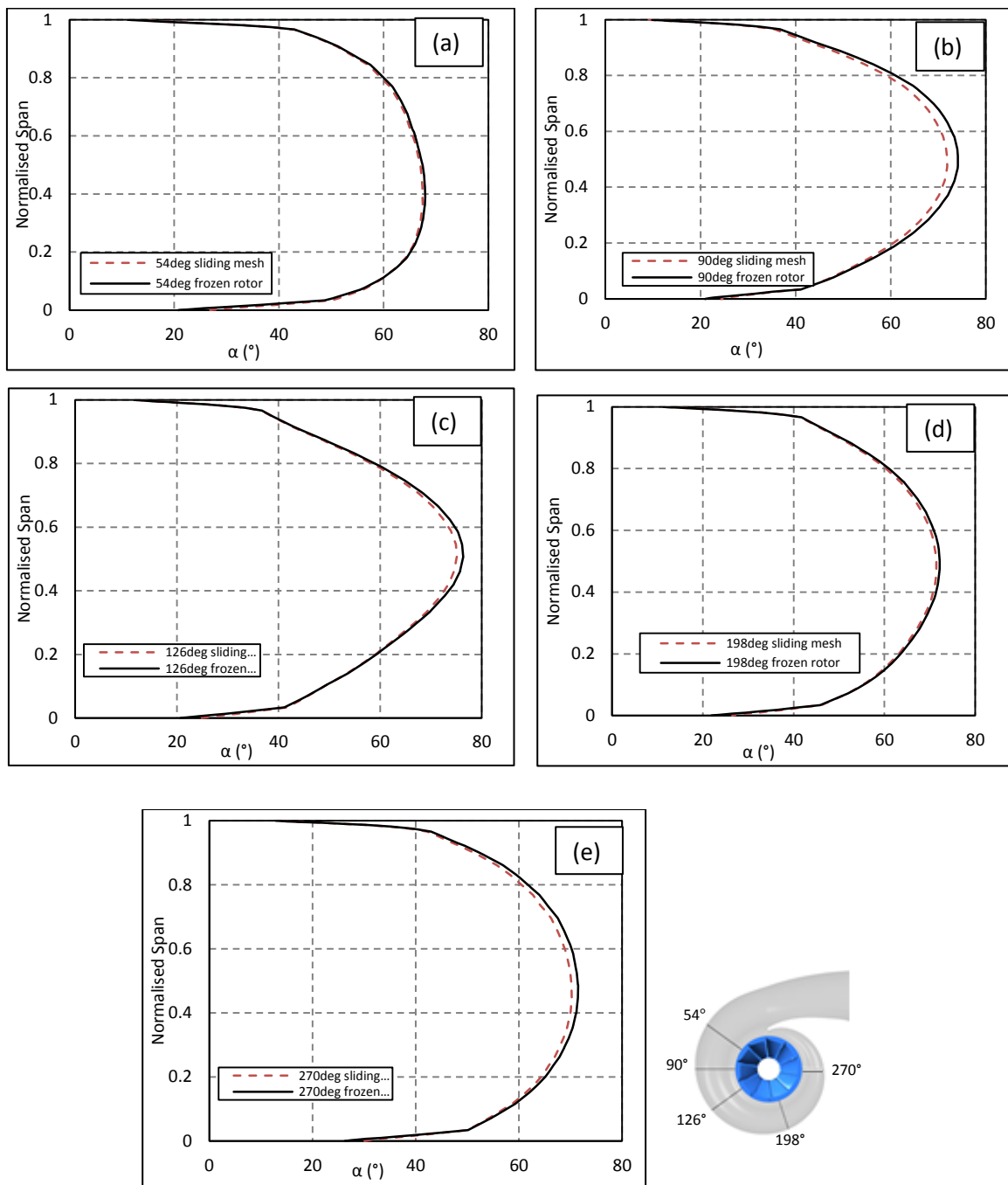


Figure 3.15: Low mass flow comparison of absolute flow angle at volute exit using the frozen rotor and sliding mesh approaches. (a) - 54°, (b) - 90°, (c) - 126°, (d) - 198° and (e) - 270°

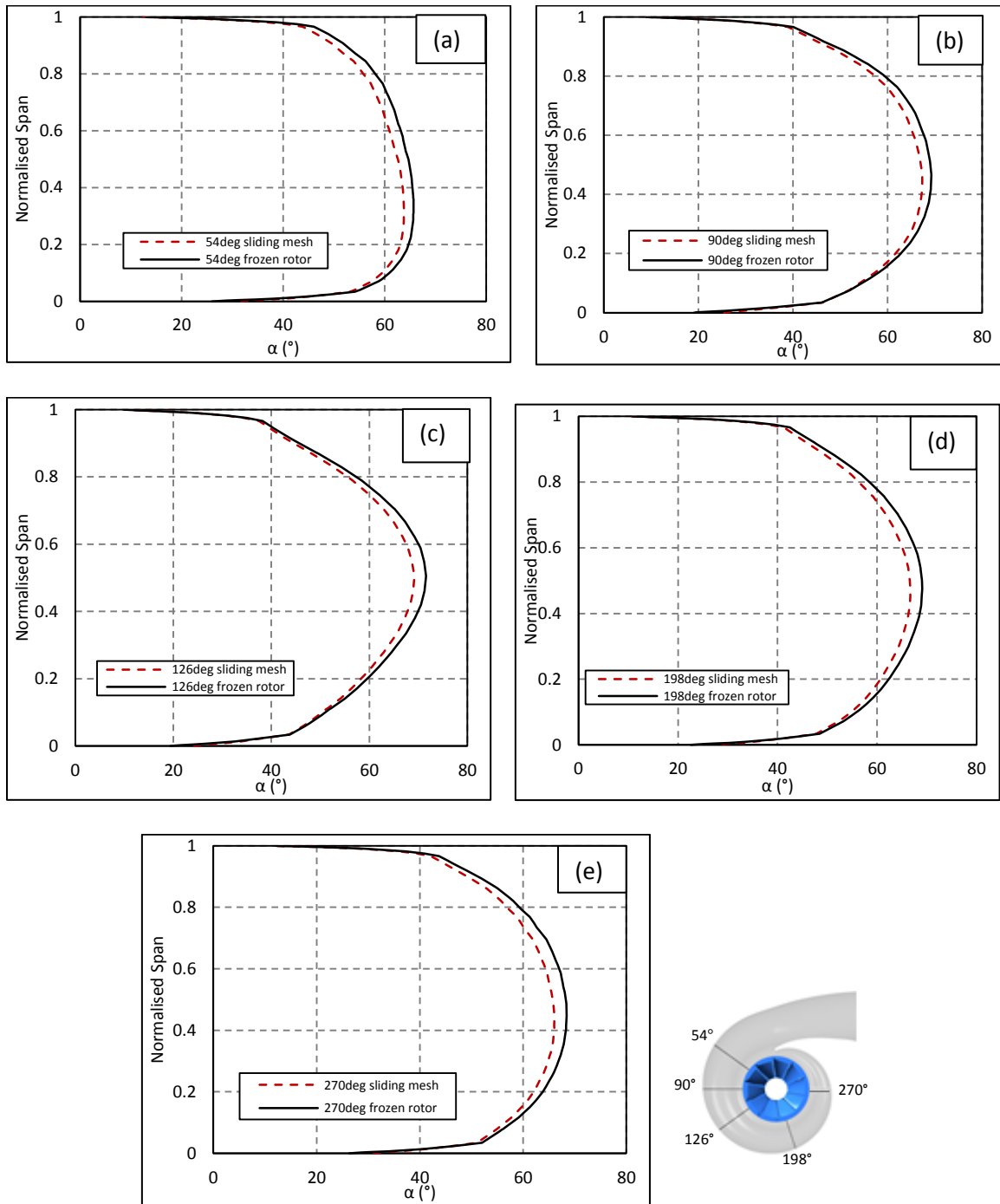


Figure 3.16: High mass flow comparison of absolute flow angle at volute exit using the frozen rotor and sliding mesh approaches. (a) - 54°, (b) - 90°, (c) - 126°, (d) - 198° and (e) - 270°

3.7 IMPACT OF ROTOR POSITION

Throughout this work the frozen rotor approach was implemented to account for the relative rotation of the wheel. The validity of this selection has been demonstrated in the previous literature which is thoroughly discussed in section 3.2.2 and section 3.6 shows the validation completed in this work supporting the choice of this method.

The turbine stages analyzed in this work are all nozzleless designs. Therefore, the volute tongue provides the only non-uniformity in the circumferential direction. As the frozen rotor approach results in the position of the wheel remaining constant with respect to the volute this introduces an inaccuracy due to the rotor's relative position to the tongue. In reality the rotor rotates relative to the volute and the blade pass the tongue. In vanned designs this effect is increased as the guide vanes introduces a greater non-uniformity.

Walkingshaw et al., (2015) studied the impact of the rotor position relative to the volute for a double scroll application. Such a design increases the impact of rotor position due to the presence of two tongues. The authors observed a variation in efficiency of up to 5.5% and almost 3% in MFP.

The impact of the relative rotor position was also studied for the mixed flow stage used in this work. Figure 3.17 shows the impact in stage efficiency and mass flow. As the rotor contains 10 blades the rotor was moved in 6° increments resulting in 6 rotor positions being tested. The resulting variation in efficiency and mass flow is less than 0.5% and 0.35% respectively. This finding gives further confidence in the frozen rotor approach.

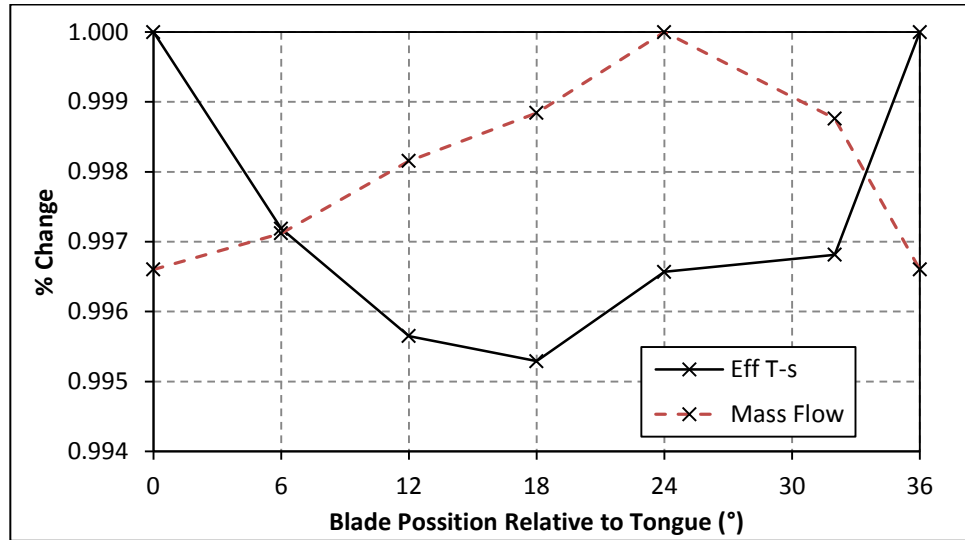


Figure 3.17 - Impact of rotor relative position to volute tongue on performance

Figure 3.18 presents static pressure contour plots through the centre of the volute passage and rotor wheel in both the 0° and 18° relative positions from the tongue. While the volute pressure distribution is almost constant in both cases a discrepancy around the tongue region can be observed due to the effect of the blade proximity to the tongue. The most notable impact is seen within the rotor region, where higher static pressure can be seen downstream of the volute tongue in the 18° case in passage 10. Other than the change in pressure distribution in the three labelled passages, 1, 2 and 10; no significant changes exist in the rotor region.

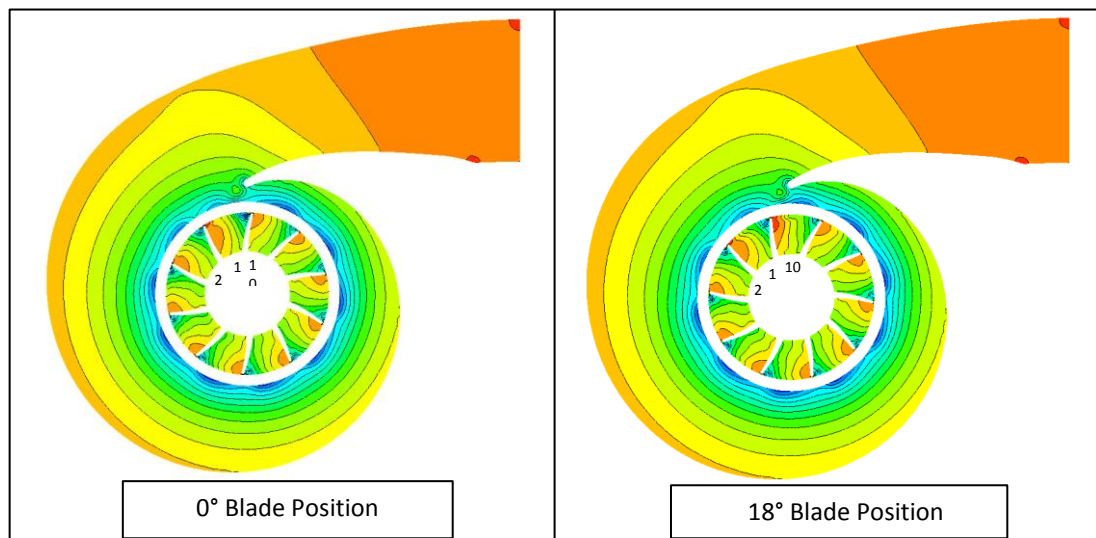


Figure 3.18 - Pressure plots through volute passage and at mid blade streamwise position

From both the quantitative and qualitative analysis, it was found that the relative position of the rotor and tongue has minimal effect on performance. Furthermore, any effects are limited to the first three blade passage. In-depth analysis of the rotor flow physics should be completed outside of this region to remove the impact of tongue proximity on flow structures.

3.8 EXPERIMENTAL VALIDATION

The computational approach used in the current work was validated against steady state gas stand tests to assess the accuracy of the CFD method. This was done over a range of three turbine speeds of 70krpm, 90krpm and 110krpm to assess the accuracy of the predictions over a wide range of turbine operation. The boundary conditions applied in the computations were total pressure and temperature at the inlet and static pressure at the outlet. The aim of the validation was to assess the ability of the computational model to predict the performance trends of the mixed flow turbine. Figures 3.19 and 3.20 present the efficiency and mass flow obtained.

The predicted turbine mass flow shows good agreement with that measured by gas stand testing with the CFD starting to show slightly higher mass flow values at the 110krpm speed line only. The turbine efficiency characteristics are also well predicted by the CFD model. While the efficiency trends show good correlation, it can be observed that the CFD does consistently over predict the maximum efficiency achieved. The predicted peak efficiency was found to occur at lower pressure ratios than that measured on the gas stand and the efficiency drop off also occurred at lower pressure ratios resulting in an extension to the operating range.

The discrepancies in absolute efficiency values measured could be the result of the adiabatic assumption applied in the computational work. While the gas stand pipe work is insulated to reduce the impact of thermal losses, inevitably loss still occurs where the rig is not fully insulated. Furthermore, experimental measurement of the turbine outlet pressure, where the flow contains a large swirling component is extremely difficult potentially leading to further discrepancies. It should also be noted that the CFD method is not fluid driven, hence any fluctuation in turbine speed that occur experimentally cannot be replicated computationally.

Despite the variation in absolute measured efficiency the characteristics of turbine performance are accurately captured over the range of operations. As stated by Simpson et al., (2009), CFD methods are capable of replicating the performance trends of the turbine but deviation in the absolute values should be expected due to a

number of assumptions in the CFD set-up, including smooth surfaces, rotation strategy and the adiabatic assumption. The impact of the adiabatic assumption was assessed by Zimmermann et al., (2015) and the authors showed a significant improvement in gas stand map replication under cold flow conditions where thermal losses were minimised. Hence this assumptions can account for a sizable portion of discrepancies in the absolute values of the gas stand and CFD data. The accurate replication of the turbine performance trends provides a level of confidence in the computational approach used throughout this study.

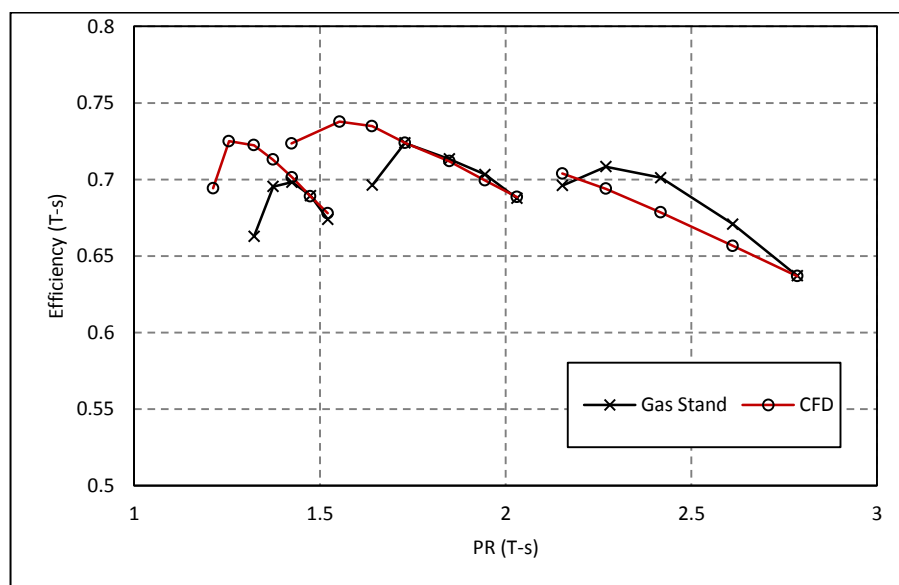


Figure 3.19: Comparison of steady state computational and gas stand efficiency (T-s)

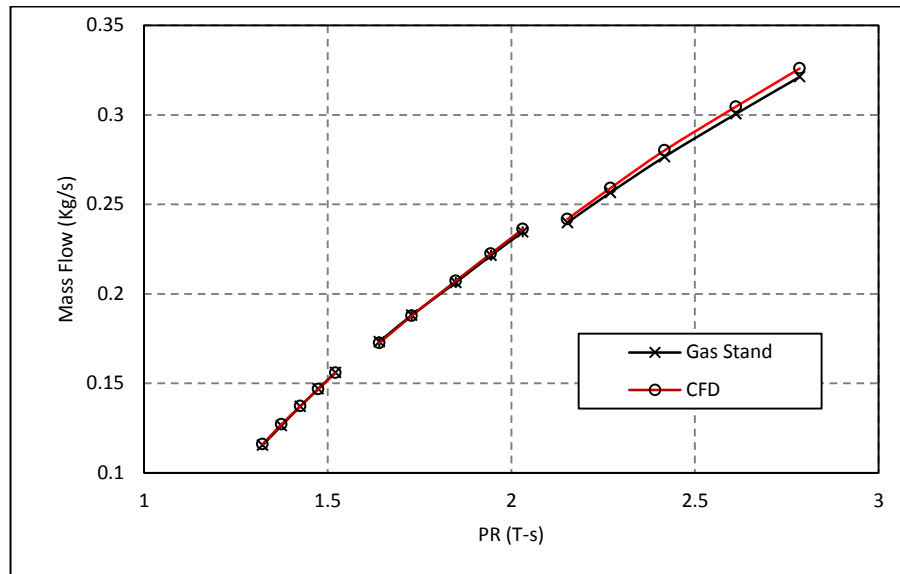


Figure 3.20: Comparison of steady state computational and gas stand MFP

3.9 CHAPTER CONCLUSIONS

This chapter has discussed the various challenges in modelling turbine performance. A thorough discussion of the various methods that can be implemented and their limitations has been included. From this a robust approach to computational modelling of the turbine has been outlined. Thorough validation has been conducted and reported to ensure that performance comparisons throughout this thesis are accurate. These included a full mesh study, time step investigation and comparison of the rotor rotational method.

The ability of the approach to predict turbine performance has also been investigated by comparing the computational results with that of experimental data. The results showed good agreement in performance for the turbine efficiency and mass flow parameter proving the general validity of the approach implemented.

4 IMPACT OF PULSE SHAPE

As discussed in the introduction and literature sections of this thesis, the turbine operates under highly pulsating conditions introduced by the nature of the reciprocating engine. The literature section also discussed the various methods used in the previous studies to account for the pulse. Numerous authors have used different methods to replicate the engine pulse with varying levels of accuracy. Furthermore, the pulse shape will depend on engine geometry and engine operating point. As a result, no one engine pulse shape is fully representative.

This chapter investigates the effect that a number of pulse shapes have on turbine performance.

4.1 MIXED FLOW TURBINE GEOMETRY

Throughout this thesis a single mixed flow wheel is used as the basis for the investigation, a schematic of which is presented in figure 4.1. This is a production mixed flow rotor used in commercial applications containing 10 blades with a mean rotor radius of 35.1mm.

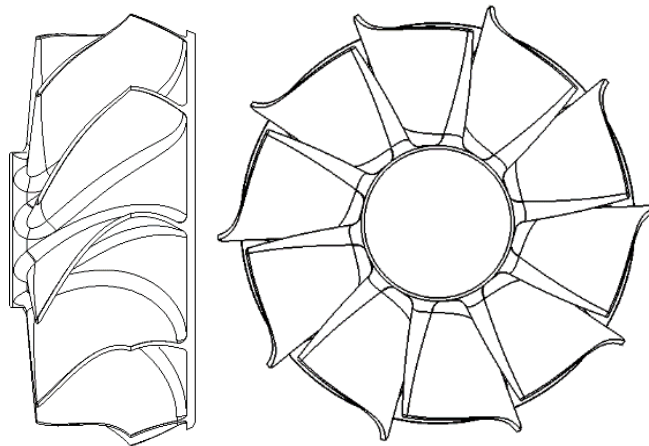


Figure 4.1: Mixed Flow Rotor

This wheel contains a camber angle varying from approximately -27° at the hub to 13° at the shroud tip and a blade cone angle of 20° , the variation in LE camber is presented in figure 4.2.

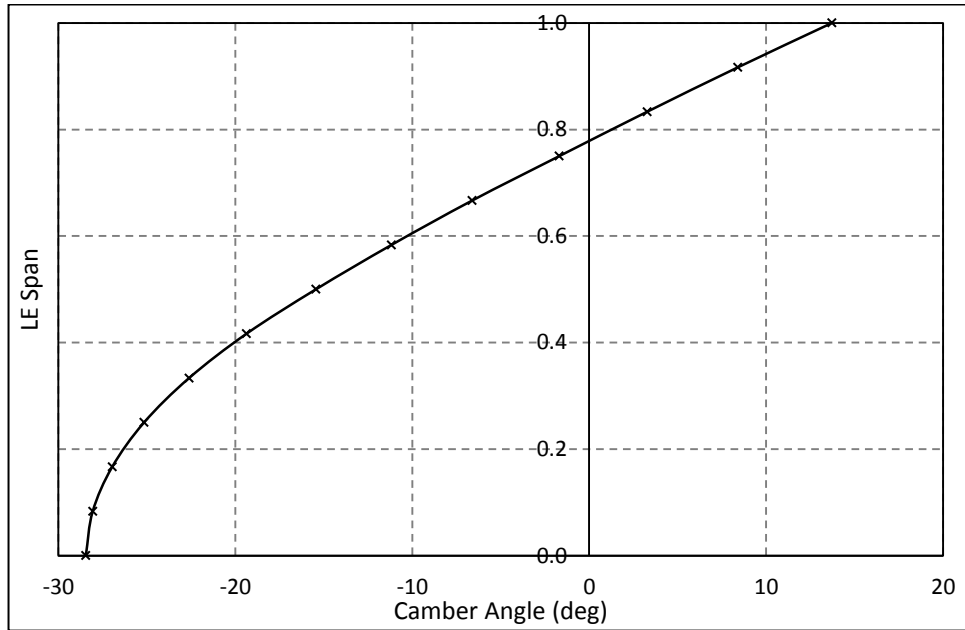


Figure 4.2: Rotor LE span-wise camber angle variation

The base volute used in this thesis is a nozzleless, single entry design with a circular cross section and an $A/r=23$. Figure 4.3 shows the A/r distribution around the volute azimuth angle and a cut plane view of the volute.

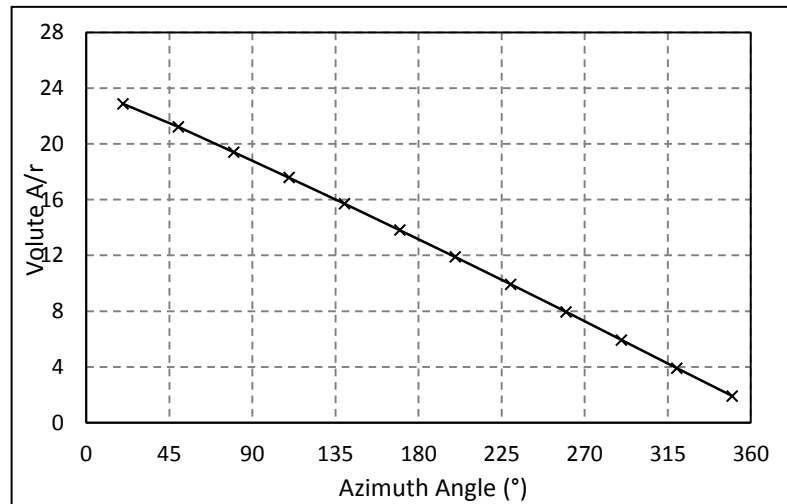
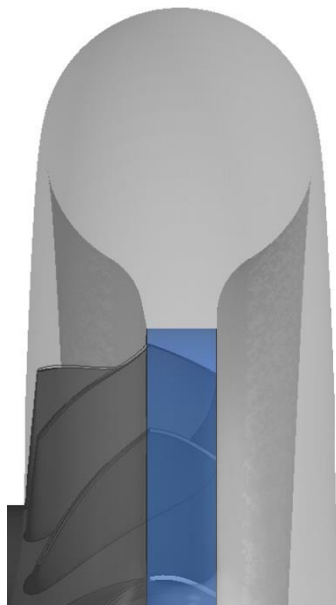


Figure 4.3: Base radial volute design with $A/r=23$ shown left and the variation in A/r around the volute azimuth angle shown right.

4.2 BOUNDARY CONDITIONS

The inlet mass flow pulse shapes used in this study are presented in figure 4.4. In all cases the integration of the mass flow over the pulse remains the same and the inlet total temperature is kept constant at 923K.

The inlet wave forms implemented include sinusoidal, triangular and square, as well as a pulse shape that was determined by a one dimensional engine model using a similar approach to Roclawski et al., (2014) and Hellstrom & Fuchs, (2009) and is considered to be a realistic wave form.

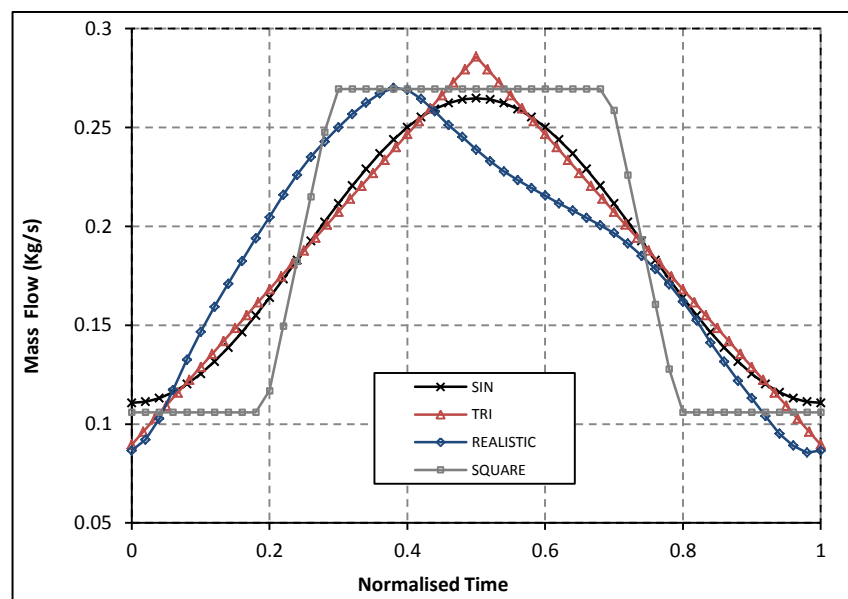


Figure 4.4: Inlet Mass Flow Pulses Shapes

As shown by Costall and Martinez-Botas Costall & Martinez-Botas, (2007) any wave form can be decomposed into a series of sinusoidal waves. As such the realistic wave used in this work can be decomposed through a Fourier transform and its harmonics found. From this data the pulse can be recreated from a specified number of harmonics resulting in a simplified wave. Figure 4.5 shows the full realistic wave, its fundamental harmonic, the wave formed by its first two harmonics, and the wave formed by its first three harmonics for comparison. The realistic wave is not accurately represented until the third harmonic is included. Furthermore, the simple fundamental harmonic, is the same as the sinusoidal wave included in this study. This

allows comparisons to be made between a significantly simplified pulse shape and that of a more realistic shape. Both the triangular and square waves can be created in the same way and are formed through the sum of the odd harmonics.

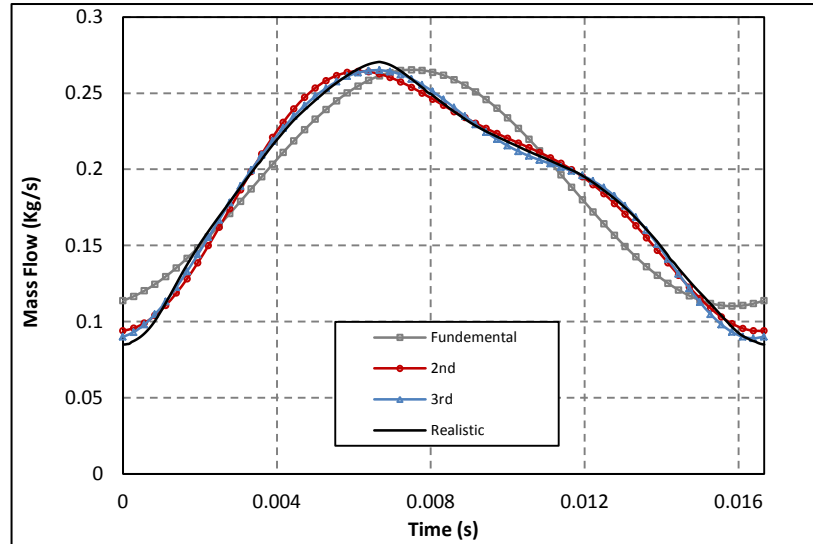


Figure 4.5: Realistic Wave Form and its Simplified Pulses.

4.3 RESULTS AND DISCUSSION

The impact of the inlet pulse on the unsteadiness within the volute can be assessed through the mass accumulation, M_{acc} . The definition of which is given in equation 68 -

$$M_{acc} = \frac{\dot{m}_1 - \dot{m}_2}{\dot{m}_{mean}} \quad (68)$$

Where \dot{m}_1 is the mass flow at the volute inlet, $\dot{m}_{1.5}$ is mass flow at the volute exit and \dot{m}_{mean} is the pulse mean mass flow. Greater mass accumulation within the system results in further deviation from quasi-steady performance. Conversely, the relatively small volume of the rotor region has been shown by a number of authors to behave in a quasi-steady manner (Newton, 2014), (Roclawski et al., 2014) Figure 4.6

shows the mass accumulation within the turbine volute for the four pulse shapes tested. The square wave results in significantly greater accumulation than the other tested shapes. This effect can be explained by the pulse duty cycles parameter introduced by Szymko, (2006). This parameter suggests that the pulse frequency should be taken only over the pulse event and is discussed in the literature review section of this thesis. In this case, the square wave would be said to have a frequency of nearly twice that of the other pulse shapes. The remaining three pulse shapes also show a variation in the filling and emptying characteristics. It is clear that the inlet pulse gradient has a significant effect on the filling and emptying of the volute.

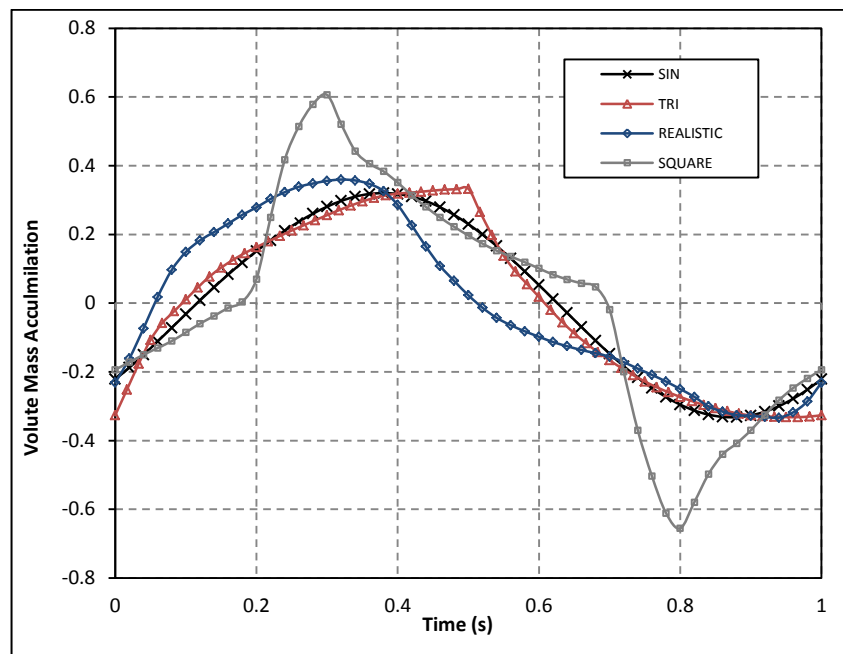


Figure 4.6: Volute Mass Accumulation Resulting from the Four Tested Inlet Pulse Shapes

Figures 4.7 - 4.10 show the turbine inlet mass flow pulse and the mass flow pulse at the rotor inlet for the sinusoidal, triangle, realistic and square pulse shapes respectively. The sinusoidal wave form shows a phase shift in the peak mass flow and a damping of the pulse amplitude, but the pulse shape is maintained. Both the triangular and realistic waves also see a shifting and damping of the wave amplitude. Furthermore, both pulses exhibit a significant shape change through the volute passage, becoming more sinusoidal in nature. The square wave experiences a significant change in shape as it passes through the volute but with less damping of

the peak pulse amplitude. It can be seen from Figure 4.10 that the step change in mass flow is not present at the rotor inlet. Instead the mass flow increases gradually over approximately 40% of the pulse time. The change in mass flow pulse shape is caused by gas dynamics effects within the volute. Pulse shapes that exhibit greater gradients of mass flow, or regions of the pulse with larger mass flow gradients, therefore experience a greater change in pulse shape.

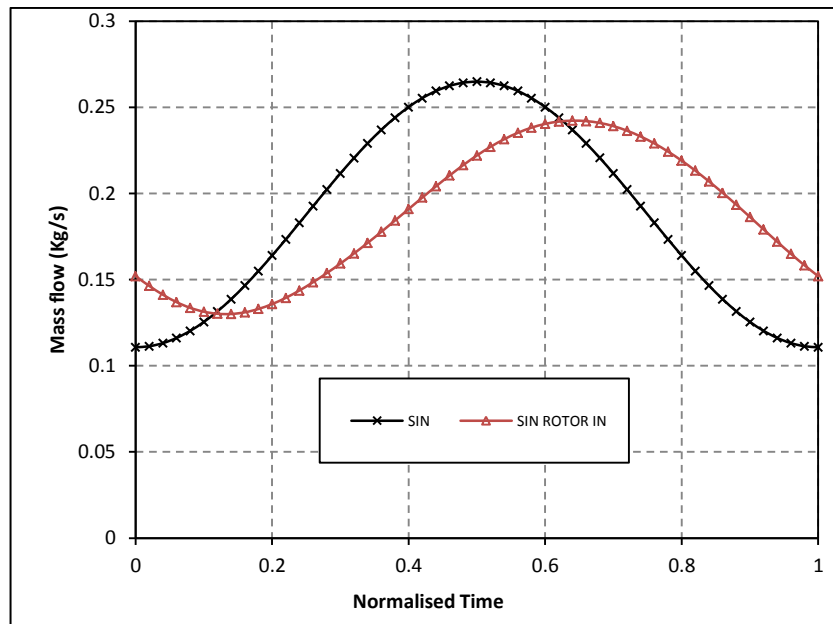


Figure 4.7: Sinusoidal Turbine Inlet Pulse and Corresponding Rotor Inlet Pulse

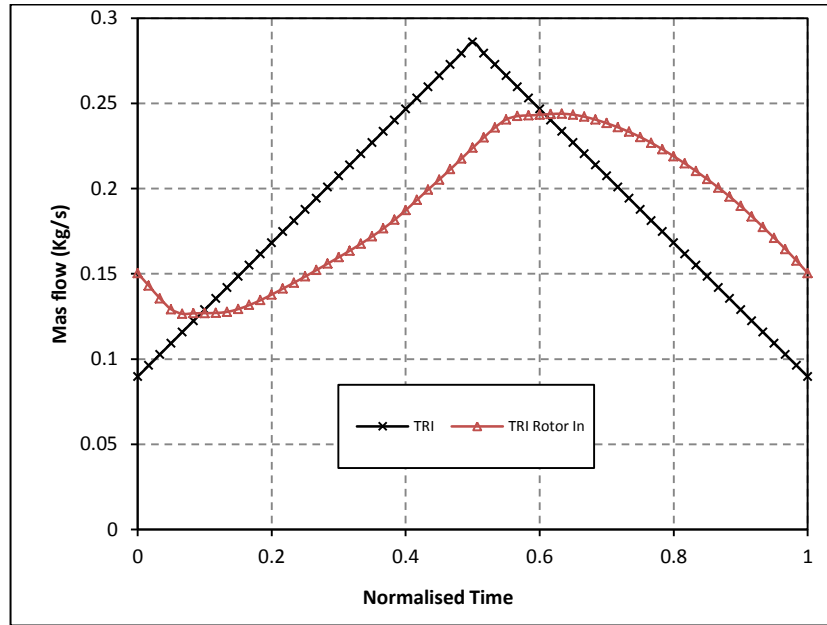


Figure 4.8: Triangular Turbine Inlet Pulse and Corresponding Rotor Inlet Pulse

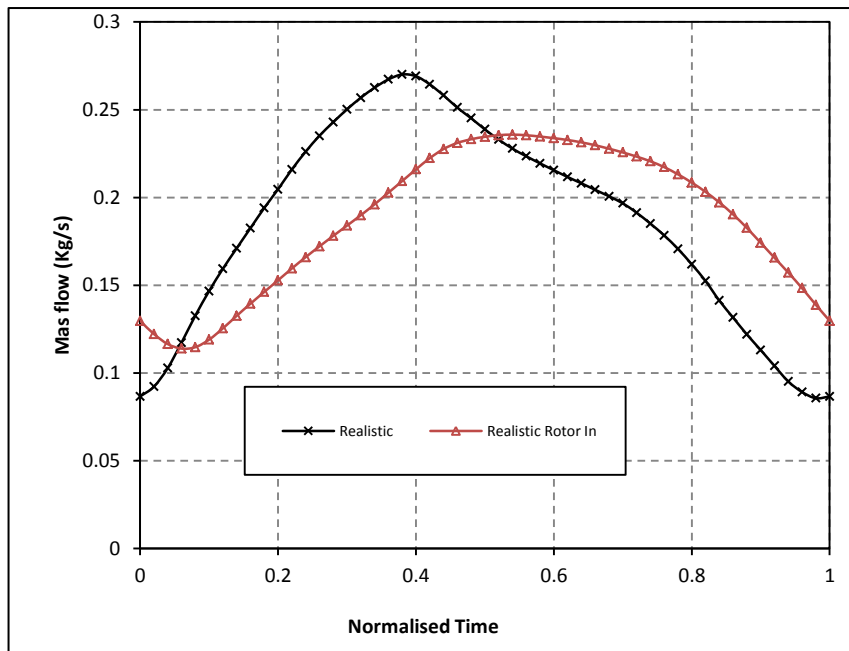


Figure 4.9: Realistic Turbine Inlet Pulse and Corresponding Rotor Inlet Pulse

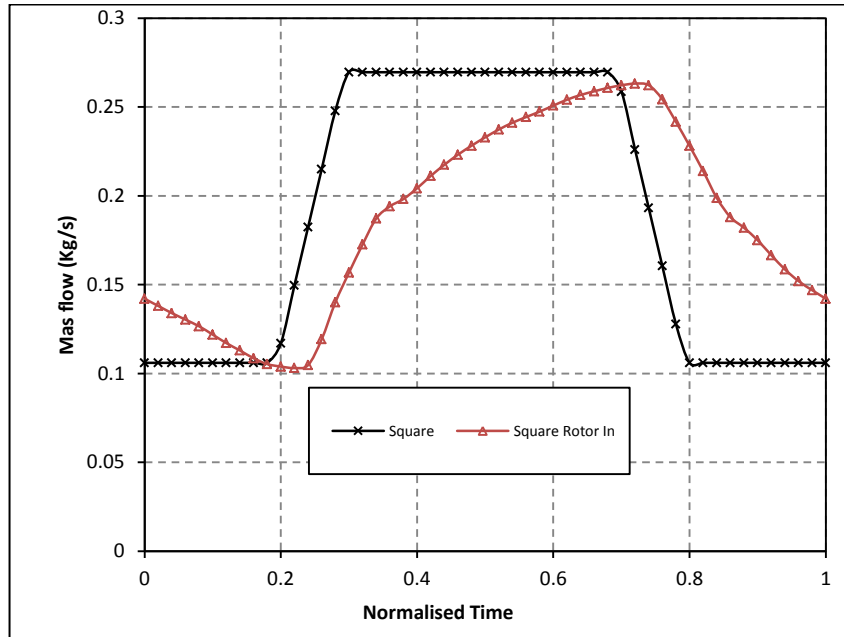


Figure 4.10: Square Turbine Inlet Pulse and Corresponding Rotor Inlet Pulse

The impact of the rotor input pulses can be seen in the rotor torque presented in Figure 4.11. In all cases, the variation in rotor torque over the pulse cycle is similar in shape to the variation in mass flow at the rotor inlet. The rotor torque generated by the square pulse has the greatest variation over the cycle. While the realistic pulse results in the lowest peak torque production, a plateau at the peak occurs, maintaining a constant maximum torque for approximately a third of the cycle. The resulting torque produced by both the sinusoidal and triangular wave forms are very similar, as are the rotor inlet mass flows due to damping of the triangular wave in the volute.

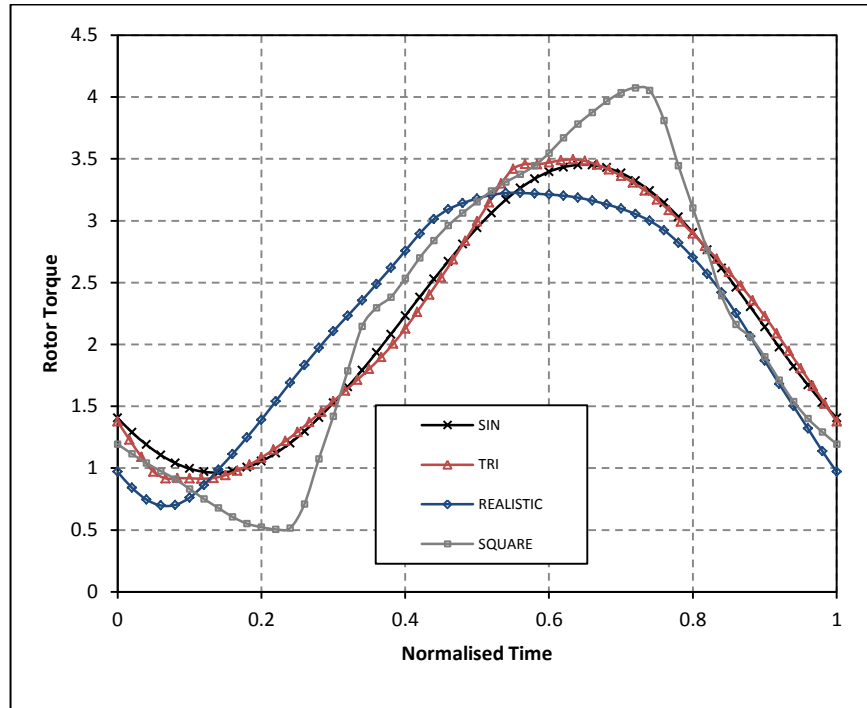


Figure 4.11: Instantaneous Rotor Torque for Each Inlet Pulse Shape

Figure 4.12 shows that the MFP hysteresis of the square pulse is significantly larger than the others with the hysteresis forming a rhomboid shape around the steady state results. Both the sinusoidal and triangular shapes show similar results, but the triangular wave shows a slight increase in hysteresis in localised regions. The realistic wave results in a larger pressure ratio range than the sinusoidal or triangular pulses with the pressure ratio reducing down to 1.4. Furthermore, the MFP hysteresis also shows a significant change in shape at the higher pressures ratios when compared to that of the sinusoidal and triangular waves. The steadily varying mass flow of the sinusoidal wave results in a smaller performance hysteresis than the other wave forms which contain greater rates of change of mass flow.

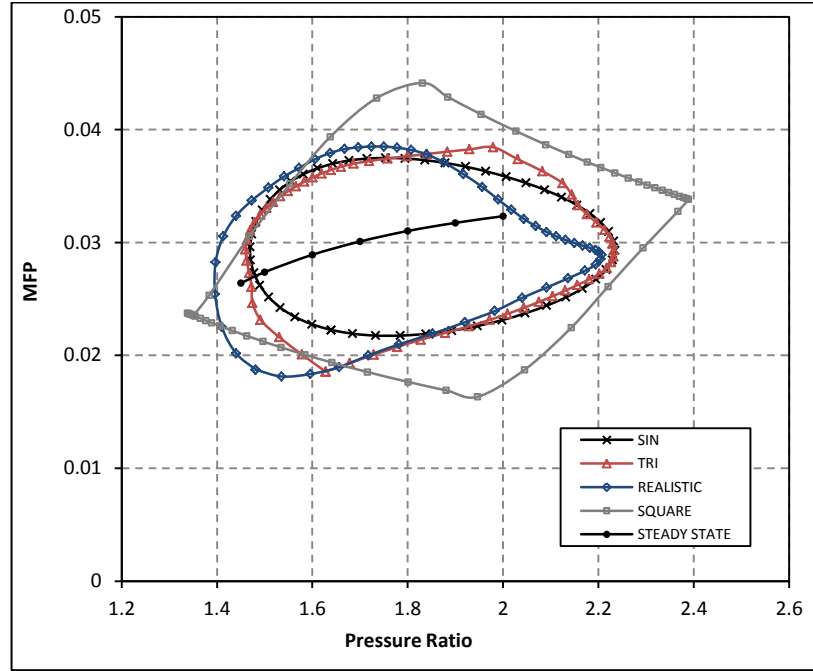


Figure 4.12: Instantaneous MFP for Each Inlet Pulse Shape

The resulting instantaneous rotor efficiency is presented in figure 4.13 against rotor U/c_s . The instantaneous rotor efficiency is defined in equation 69.

$$\eta_{rotor} = \frac{\tau \cdot \omega}{\dot{m}_{1.5} \cdot C_p \cdot T_{01.5} \cdot \left(1 - \left(\frac{P_3}{P_{01.5}}\right)^{\frac{\gamma-1}{\gamma}}\right)} \quad (69)$$

Where τ is rotor torque, ω is the rotor angular velocity and $\dot{m}_{1.5}$ is the rotor inlet mass flow.

From figure 4.13 it is clear that the range of velocity ratios that the blade encounters was greatest under the square inlet wave, with both the maximum and minimum velocity ratio limits extending, resulting in a U/c_s range of 0.469 to 0.856. The realistic wave form also results in an increased maximum velocity ratio achieved when compared to that of the sinusoidal or triangular wave forms. However, the minimum velocity ratio achieved under the realistic pulse is slightly higher than that of the sinusoidal or triangular cases. Both the sinusoidal and triangular waves result in similar velocity ratio ranges which is expected as the rotor inlet mass flow pulses were very similar. In all cases, a greater rotor performance hysteresis was seen at

higher rotor velocity ratios, with the square wave form exhibiting the greatest hysteresis.

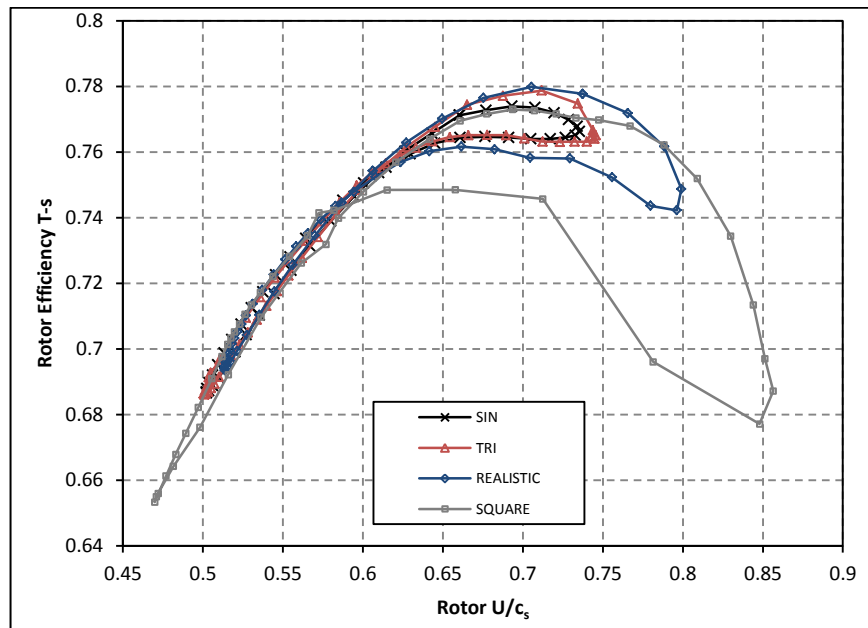


Figure 4.13: Instantaneous Rotor Efficiency (T-s) for Each Inlet Pulse Shape

The resulting variation in rotor leading edge incidence against rotor velocity ratio is presented in figure 4.14 for all four inlet pulse shapes. The blade LE Incidence is determined using equation 2 where the blade angle is calculated from equation 3. Mass flow averaged velocity components around the rotor LE circumference were used to calculate the relative flow angle (β) and flow cone angle (λ_{flow}). The span-wise averaged blade LE camber angle (φ) is taken from the blade geometry. It should be noted that care must be taken to correctly calculate the relative flow angle in mixed flow turbines. For radial turbines, the blade LE has no cone angle. As such the absolute and relative flow angles can be easily calculated from the radial component of velocity. In a mixed flow turbine, the rotor LE contains a blade cone angle. Therefore, the relative flow angle must be calculated using the meridional component of velocity (C_{meri}) that is perpendicular to the LE, this is shown in figure 4.15.

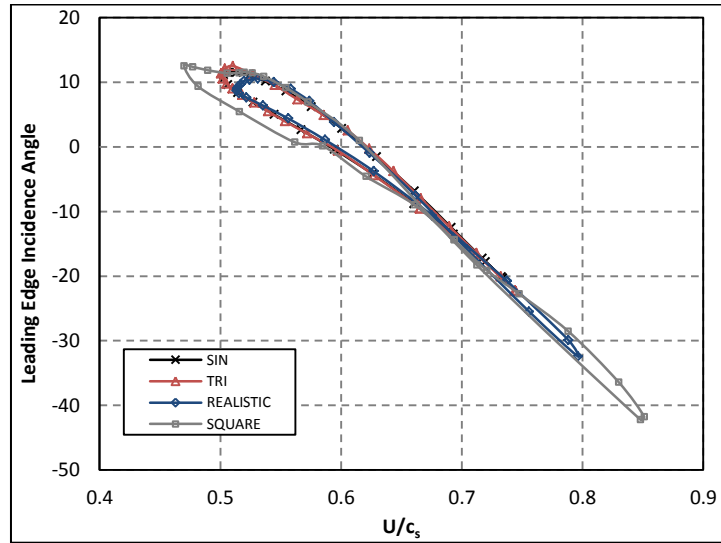


Figure 4.14: Change in leading edge incidence plotted against velocity ratio for the four tested inlet pulse shapes

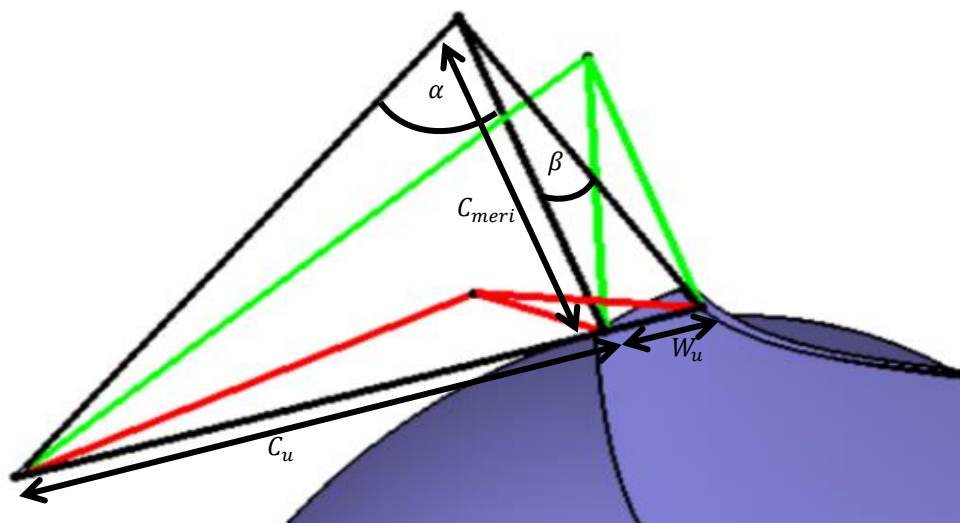


Figure 4.15: Mixed flow turbine velocity triangles

Figure 4.15 shows the velocity components at the LE of a mixed flow turbine. The radial velocity components are shown in green, the axial components in red and the meridional components in black. The meridional velocity components are dependent on both the radial and axial velocities. The relative and absolute flow angles for a mixed flow turbine are therefore given by -

$$\beta = \tan^{-1} \frac{w_u}{C_{meri}} \quad (70)$$

$$\alpha = \tan^{-1} \frac{C_u}{C_{meri}} \quad (71)$$

As with the efficiency curves, plotted in Figure 4.13, the sinusoidal and triangular waves result in very similar leading incidence angle distributions with only localised variation at peak incidence. In comparison, the realistic wave reached more negative incidence angles at the higher velocity ratios achieved and the square wave resulted in even greater negative incidence at velocity ratios as high as 0.85. The peak incidence angle of the realistic wave was the lowest of the four tested, at only 10.6°. The sinusoidal and triangular waves peaked at 11.5° and 12.5° respectively. Despite the square wave reaching the lowest velocity ratio, the maximum incidence achieved was only 11.6° and at the peak incidence angle, the distribution shows clear deviation from the trends experienced by the other pulse shapes.

In addition, figure 4.16 presents the variation in LE incidence plotted against normalised time. This plot shows how rapidly incidence varies with time over the pulse. In all cases a plateau at maximum incidence occurs resulting in an almost constant value for a significant period of the pulse. At the lowest incidence angles, the variation occurs much more rapidly, and no plateau occurs. In the realistic wave case, the peak plateau exists over approximately 40% of the pulse. Both the sinusoidal and triangular waves result in the lowest rate of change of incidence throughout the pulse and the smallest range in LE incidence. On the other hand, the variation in incidence angle occurs much more rapidly under the square wave with the increase in incidence from the minimum to maximum occurring over approximately 10% of the pulse.

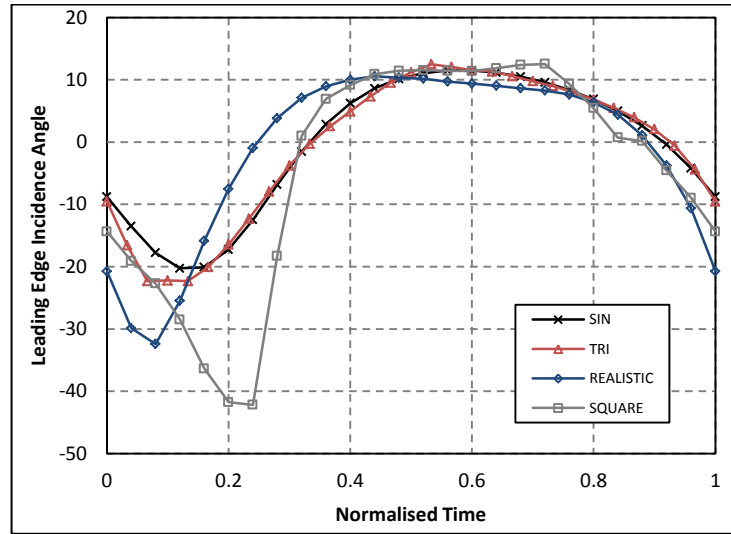


Figure 4.16: Change in leading edge incidence over normalised time for the four tested inlet pulse shapes.

Table 4.1 shows the cycled averaged stage efficiencies and MFP's of the turbine under each of the investigated pulse shapes. The definitions of the cycle averaged efficiency, η_{cyc} , and cycle averaged mass flow parameter, MFP_{cyc} , are presented in equations 72 and 73 respectively.

$$\eta_{cyc} = \frac{\int_0^T (\tau \cdot \omega) dt}{\int_0^T \left(m_1 \cdot C_p \cdot T_{01} \cdot \left(1 - \left(\frac{P_3}{P_{01}} \right)^{\frac{\gamma-1}{\gamma}} \right) \right) dt} \quad (72)$$

$$MFP_{cyc} = \frac{\int_0^T MFP dt}{T} \quad (73)$$

Where C_p is the specific heat at constant pressure, T_{01} is the total temperature at the stage inlet, P_3 is the static pressure at the stage outlet, P_{01} is the total pressure at the stage inlet and γ is the ratio of specific heats.

There is little variation between the sinusoidal, triangular and realistic wave forms in both efficiency and MFP. However, the square wave shows a significant

reduction in cycle averaged MFP of 2.33% and a reduction in efficiency of 1.37%. This result shows that, at least in the cycle-averaged sense, pulse shape only has a small impact on performance.

| | <i>SIN</i> | <i>TRI</i> | <i>Realistic</i> | <i>Square</i> |
|---|------------|------------|------------------|---------------|
| Normalised Stage η_{cyc} | 100.00% | 99.87% | 99.74% | 98.63% |
| Normalised MFP_{cyc} | 100.00% | 99.67% | 99.50% | 97.77% |

Table 4.1: Cycle averaged performance results for each pulse normalised by the sinusoidal wave results

To better understand the impact of the instantaneous performance of the rotor on cycle averaged performance the relative time spent at each velocity ratio, and the available isentropic work can be plotted. These plots are presented in figures 4.17 and 4.18 respectively. The relative time plot shows how long the turbine rotor operates within a certain velocity ratio range. The available isentropic energy plot shows the relative energy available in each region over the pulse period. Combining the trends in figure 4.13 and figure 4.18 explains the resulting cycle averaged performance achieved. Displaying the data in this manor shows the impact of the low velocity ratio running points on cycle averaged performance. As the available energy in this region is so large, it is necessary to target performance improvements in this region of operation to maximise energy extraction. Alternately, differences in performance at the high velocity ratios have little impact on the cycle averaged performance.

Again, the increased velocity ratio range resulting from the square wave form is obvious in both figures 4.17 and 4.18. Figure 4.17 shows that the peak isentropic work availability occurs in the 0.5-0.55 range for the realistic wave. This peak is the greatest of all the pulse forms. The square wave form shows the opposite trend with the pulse energy spread over a wider range of velocity ratios.

The sinusoidal and triangular waves result in very similar behaviour at the low end of the velocity ratio range. However, at the high velocity ratios the triangular

wave shows a more distinct peak. However relative to the magnitude seen at the low velocity ratios this difference will result in only small changes to cycle averaged performance.

While the cycle averaged performance differences between the pulse shapes are small, it is clear that the actual operating points within the pulse differ across all the tested shapes. Therefore, optimisation of the design requires knowledge of the energy availability to improve performance.

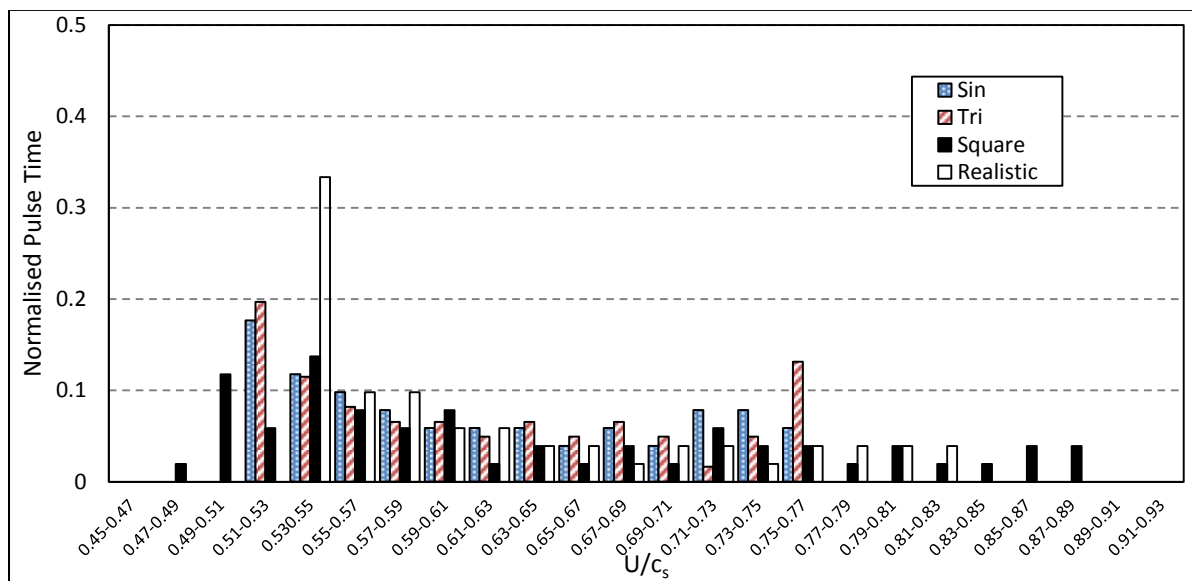


Figure 4.17: Rotor velocity ratio through the inlet pulsation

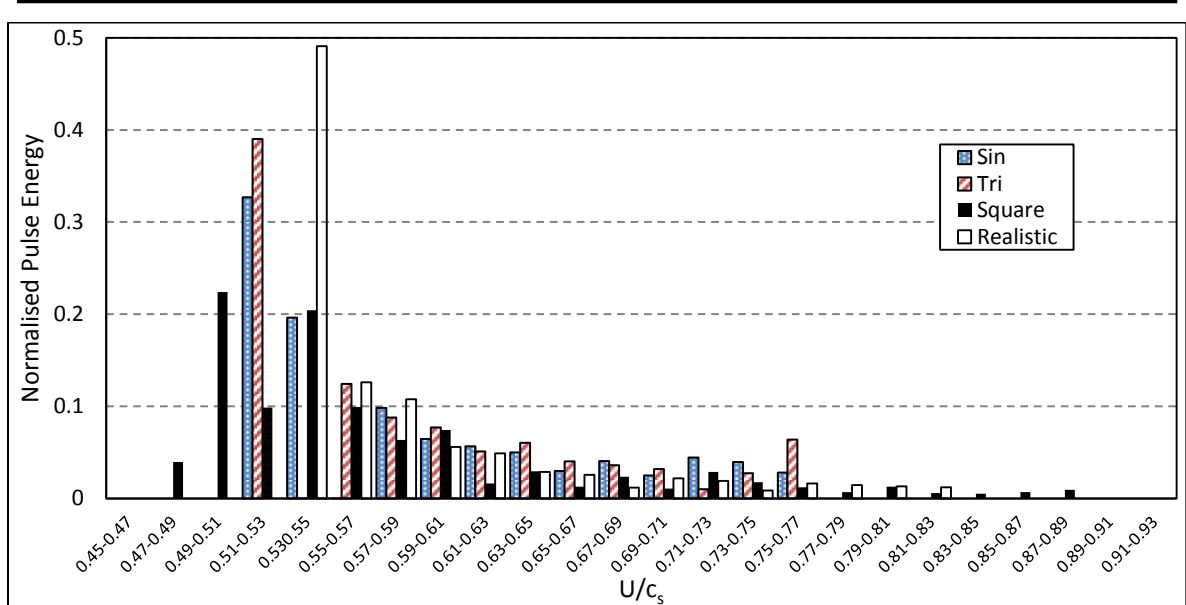


Figure 4.18: Energy available within each rotor U/c_s range.

4.4 CHAPTER CONCLUSIONS

This chapter investigated the performance of a mixed flow turbine operating under unsteady pulsating flow conditions. From the four pulse shapes investigated, only the square wave showed a significant variation in cycle-averaged turbine performance. This deviation can be explained by the change in effective frequency as defined by Szymko, (2006). However, the instantaneous performance differs significantly for all pulse shapes. This result shows that while pulse shape only has a small impact on performance in a gross, cycle-averaged sense, it is important with regards to any in-depth analysis of the turbine flow physics. Therefore, whilst a simplified sinusoidal wave form can be used for investigations of global performance trends, for more detailed studies into the flow physics and loss mechanisms within the pulse, matching the pulse shape is vital.

The results of this section led to the selection of the realistic pulse shape being used for pulsating flow simulations throughout this thesis. While the shape may not be completely representative of a true engine pulse as it was supplied by a 1D engine model, it is more accurate than the other shapes. As it is extremely difficult to accurately measure engine pulses experimentally with a high level of accuracy no

experimental pulse shapes were available for the engine configuration likely to be match with this turbine.

5 ANALYSIS OF A MIXED FLOW TURBINE UNDER PULSATING FLOW CONDITIONS

This chapter discusses the results of an in depth computational analysis of the performance of a mixed flow rotor within a radial flow housing under a range of pulse forms. The base pulse shape used is the “realistic” wave shape as presented in the previous chapter. The impact of pulse frequency, load and pulsation number are all investigated and the resulting performance of the stage investigated.

As discussed in the literature review section, work by (Karamanis et al. 2001) showed the presence of significant span-wise flow variation experimentally. Despite this observation, little work has investigated this effect in detail. Particular attention has been paid to the development of span-wise variation over the pulse period and how this effect links back to volute secondary flow structures.

5.1 INVESTIGATED PULSE FORMS

The impact of the inlet pulse was investigated at three pulse frequencies (20Hz, 40Hz and 60Hz), three pulse loads, \dot{m}_{Load} , (73%, 100% and 127%) and four pulsation numbers, $\dot{m}_{no.}$, (0.5, 0.75, 1 and 1.25). The pulse load and pulsation number are defined in equations 74 and 74 respectively –

$$\dot{m}_{Load} = \int_0^T \frac{\dot{m}}{T} dt \quad (74)$$

$$\dot{m}_{no.} = \frac{\dot{m}_{max} - \dot{m}_{min}}{\dot{m}_{Load}} \quad (75)$$

Where \dot{m} is mass flow rate, T is the pulse duration \dot{m}_{max} is the maximum pulse mass flow rate and \dot{m}_{min} is the minimum pulse mass flow rate.

The resulting pulses implemented in the study are presented in Figures 5.1 and 5.2. The magnitude of the temperature pulse remained constant throughout the study but the pulse frequency was changed to match the frequency of the corresponding inlet mass flow pulse.

The three pulse frequencies were tested at a pulsation number of 1 and a pulse load of 100%. The three pulse loads were investigated at 40Hz frequency and a pulsation number of 0.5, further increases in the pulsation number would have led to low mass flows, flow reversal and therefore convergence issues. The four pulsation numbers tested were analysed at 40Hz frequency and a pulse load of 100%. In all cases the temperature pulse load and pulsation number were kept constant. The resulting pulse are displayed in figures 5.1 and 5.2.

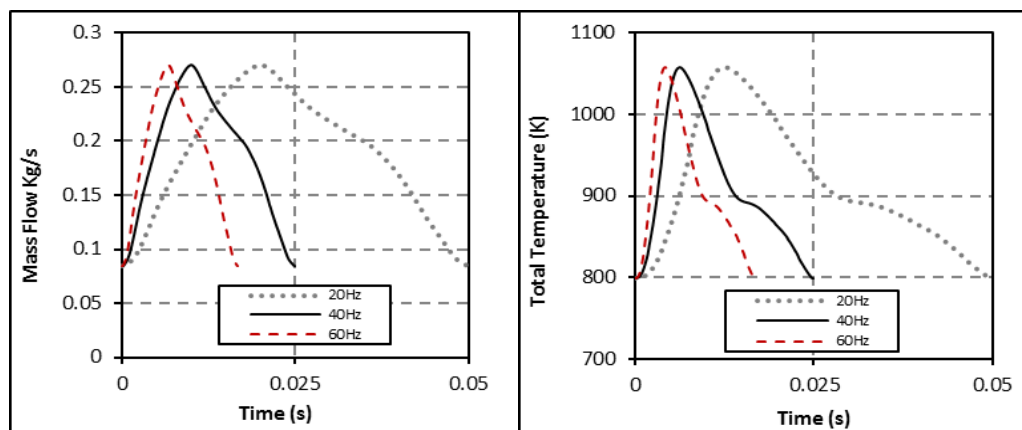


Figure 5.1: Inlet mass flow and total temperature pulses at 20Hz, 40Hz and 60Hz frequencies

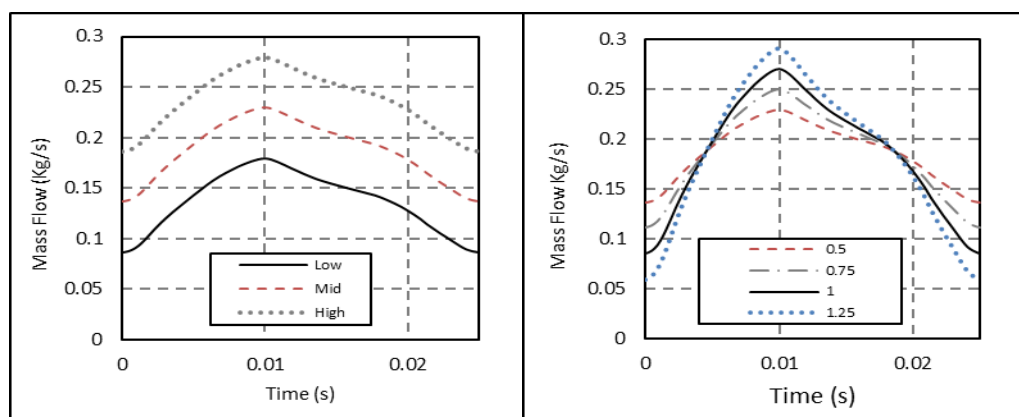


Figure 5.2: Inlet mass flow pulses at 40 Hz Left - low, medium and high load. Right - 0.5, 0.75, 1 and 1.25 inlet pulsation number pulses.

The turbine rotor used in this investigation, was shown in figure 4.1. This wheel contains a camber angle varying from approximately -27° at the hub to 13° at the shroud tip and a blade cone angle of 20° , the variation in LE camber was presented in figure 4.2. Thus, there is a variation in blade angle from hub to shroud. As is the nature of mixed flow turbines, the tip speed varies from hub to shroud due to the cone angle. This variation, due to the conservation of angular momentum, has been shown to result in a variation in LE incidence by Morrison et al., (2016). Furthermore, the LE incidence in mixed flow turbines is heavily dependent on the axial flow component at the LE of the rotor and the distribution of flow angle at the volute exit. As the blade camber and flow cone angles can be used to manipulate the LE blade angle, a thorough understanding of the impact that pulsating flow has on rotor incidence over the LE span is necessary for further performance optimisation.

5.2 RESULTS AND DISCUSSION – IMPACT OF PULSE FREQUENCY

Figure 5.3 presents the mass flow at the stage inlet and rotor inlet against normalised time for 20Hz, 40Hz and 60Hz pulse frequencies. The figures are normalised in this manner to make the three inlet pulses identical leading to a clearer comparison of the effects of frequency. The mass flow range measured at the rotor inlet shows a gradual reduction with increasing frequency. This is the result of increased mass flow damping through the volute at higher frequencies. Increasing frequency resulted in flattening of the pulse peak leading to a plateau at peak mass flow in the 60Hz case spanning approximately 30% of the pulse. This result is caused by the gas dynamics within the volute. As was experienced in the pulse shape investigation, pulses and regions of pulses containing larger gradients experience a more significant gas dynamic effect and therefore a greater shape change through the volute passage.

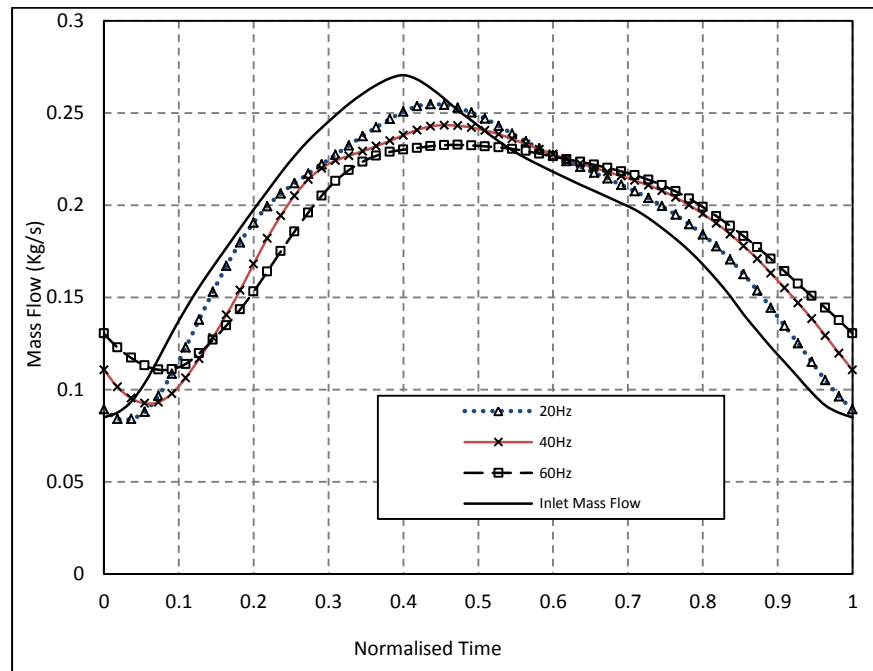


Figure 5.3: Stage inlet and rotor inlet mass flow at 20Hz, 40Hz and 60Hz pulse frequencies

Figure 5.4 shows the mass accumulation in the volute at the three tested pulse frequencies. The approach allows the turbine unsteadiness to be investigated in computational domains as mass flow can be extracted at numerous locations.

From figure 5.4 it is clear that the unsteadiness of the turbine increases with pulse frequency. During the volute filling the accumulation is positive and during volute emptying it is negative. The maximum accumulation of mass achieved was 0.28 in the 60Hz case, this reduced to only 0.12 maximum in the 20Hz case. Interestingly, two positive peaks occur due to the change in mass flow pulse shape through the volute. Comparison of the position of the mass flow pulse peaks at volute inlet and exit in figure 5.3 explains the source of this effect.

Pulse Frequency

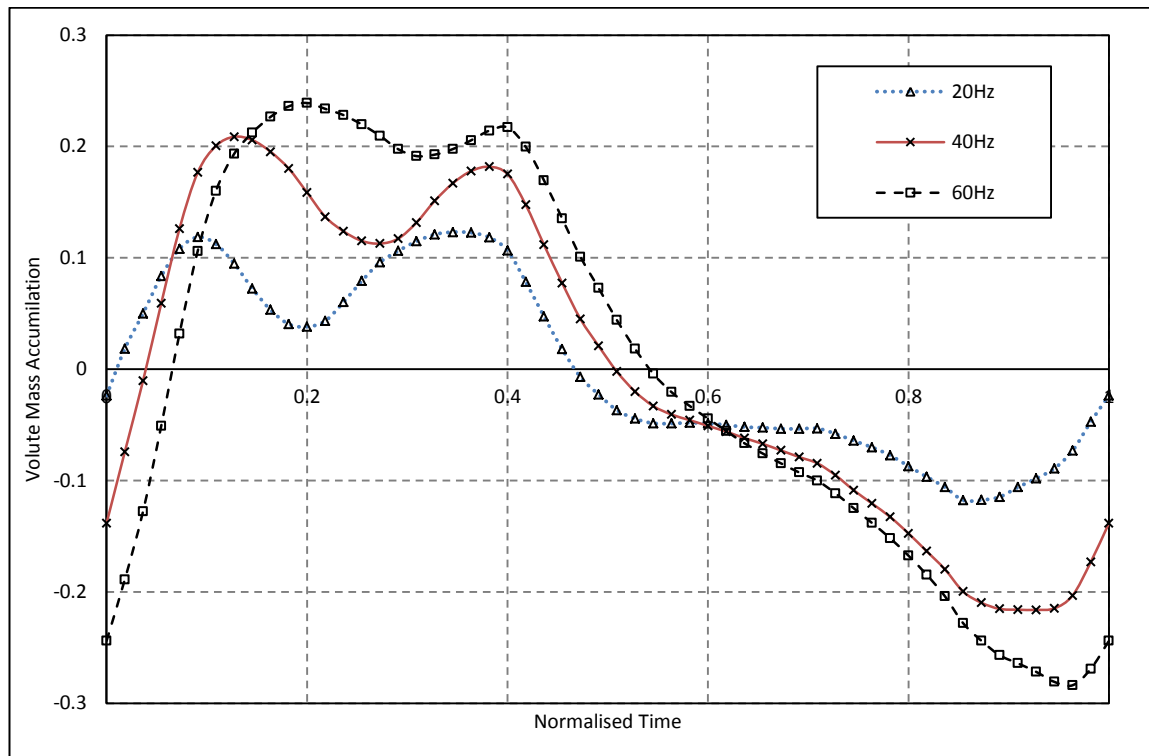


Figure 5.4: Volute mass accumulation at 20Hz, 40Hz and 60Hz.

The turbine Mass Flow Parameter (MFP) hysteresis is presented in figure 5.5 for each of the tested frequencies. With increasing frequency, the deviation in MFP from the steady state results increases and the range of pressure ratios experienced reduces from 1.25-2.35 at 20Hz, to 1.29-2.31 at 40Hz and 1.38-2.23 at 60Hz. The hysteresis formed around the steady state performance line greatly increases with pulsating frequency. Notably, in the 60Hz case the peak MFP is achieved in the middle of the pressure ratio range and begins to reduce while the pressure ratio continues to increase. This effect can be attributed to the reflected pressure wave traveling back through the volute to the measurement plane.

Pulse Frequency

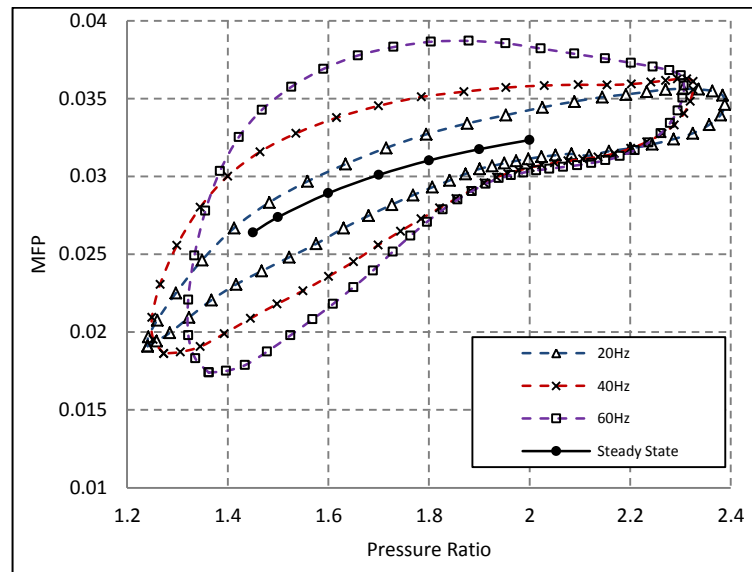


Figure 5.5: MFP vs pressure ratio for steady state, 20Hz, 40Hz and 60Hz inlet conditions

The resulting rotor torque, presented in figure 5.6, resembles the corresponding rotor inlet mass flow at each frequency. With increasing frequency, the torque range reduces and the shape of the curve towards the peak sees a change resulting in a reduction in the gradients in that region.

The rotor efficiency from the three pulse frequencies presented in figure 5.7 shows that the maximum velocity ratio experienced under the 20Hz pulse was the greatest, reaching a peak U/c_s of 0.99, while the 40Hz and 60Hz cases reached U/c_s 's of 0.93 and 0.83 respectively. The minimum velocity ratio achieved in all cases was approximately 0.45. While the range of rotor operation was significantly reduced with increasing frequency, the efficiency curve at a given U/c_s converged for all frequencies and as the U/c_s increased, the hysteresis formed reduced.

Pulse Frequency

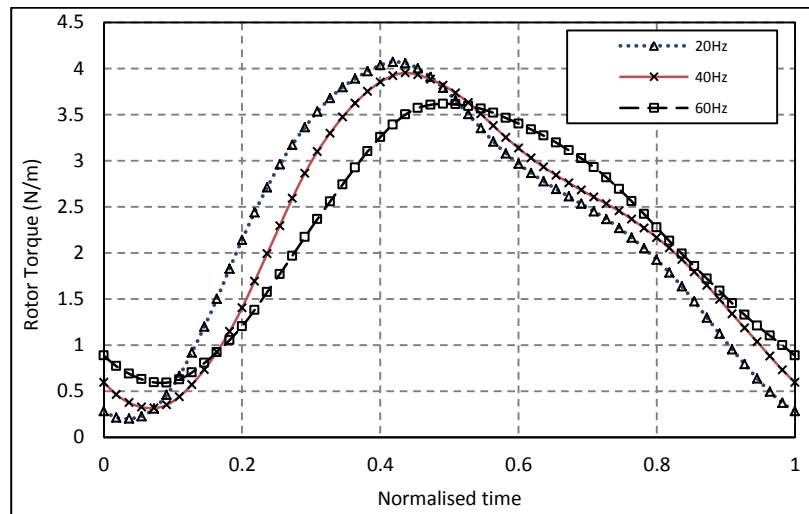


Figure 5.6: Resulting rotor torque at 20Hz, 40Hz and 60Hz pulse frequencies

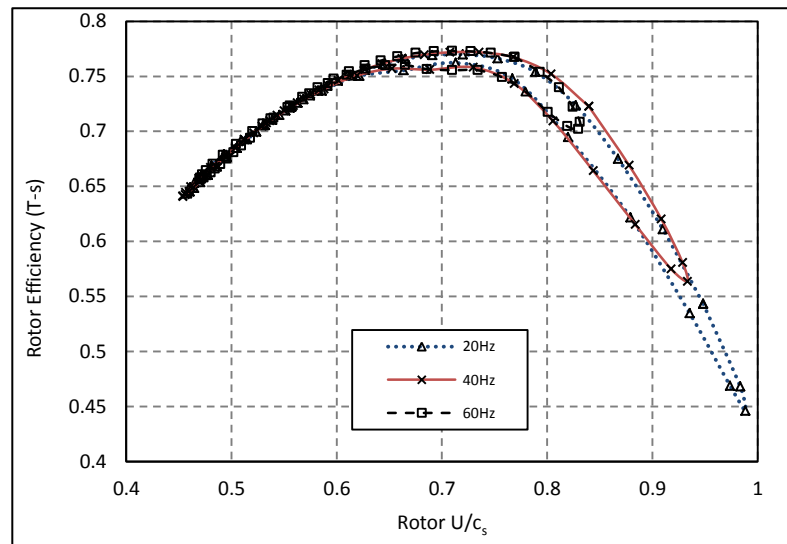


figure 5.7: Instantaneous rotor efficiency at 20Hz, 40Hz and 60Hz pulse frequencies

The impact of pulsating frequency on rotor U/c_s is better presented in figure 5.8, where the percentage time spent within discrete U/c_s ranges is presented. With increasing frequency, the range of rotor velocity ratios decreases. This occurs at the high end of the U/c_s spectrum. This can be explained by the non-linear relationship between velocity ratio and pressure ratio i.e. as U/c_s is a ratio of blade speed to the isentropic spouting velocity, progressively reducing U/c_s requires increasingly large spouting velocities (driven by larger pressure ratios) to achieve the same U/c_s reduction. Although the minimum velocity ratio achieved is not significantly

Pulse Frequency

impacted by pulse frequency it can be observed that as frequency is increased, less percentage time is spent within the lowest velocity ratio range. This is supported by the cycle averaged velocity ratio values given in table 5.1 where a decrease in cycle averaged velocity ratio with decreasing pulsation frequency can be observed. It is also noteworthy that under the tested pulse, the rotor spends more time operating at the low end of the U/c_s range, which is again supported by the fact that the cycle averaged velocity ratio in each case is below 0.6 despite a range of 0.45-1.

In addition, the low velocity ratio operating points have a greater impact on cycle averaged performance due to the greater available energy. The effect of this is illustrated in figure 5.9 which shows the energy available within each U/c_s range. This value is calculated from the time spent in each discrete velocity ratio range and the isentropic work available within. In this case the impact of low velocity ratio running points have a larger effect on performance and hence optimisation in this region of operation is required for performance benefits under all tested frequencies. Increasing frequency tends to reduce the value of the most influential velocity ratio range on performance with the 60Hz frequency showing the greatest peak between 0.475-0.525.

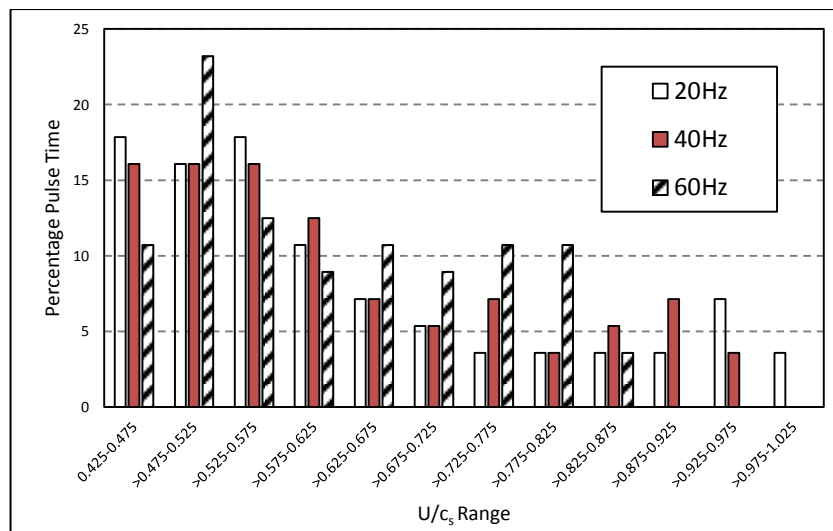


Figure 5.8: Rotor velocity ratio through the inlet pulsation

Pulse Frequency

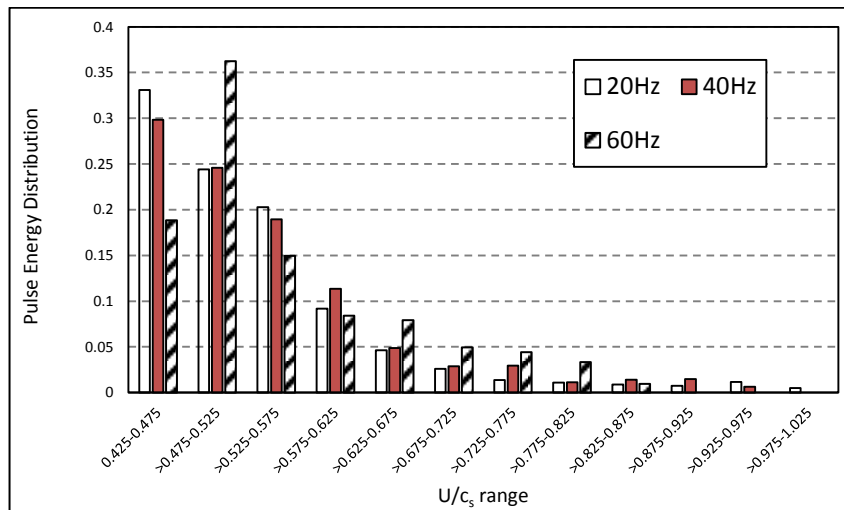


Figure 5.9: Energy available within each rotor U/c_s range.

Figure 5.10 presents the inlet boundary conditions of mass flow and total temperature. The fact that the mass flow and total temperature are out of phase impacts on the fluid propagation through the volute. The same out of phase behaviour of mass flow and total temperature from GT power engine simulations were also evident in work by Roclawski et al., (2014) but the impact of this effect was not discussed.

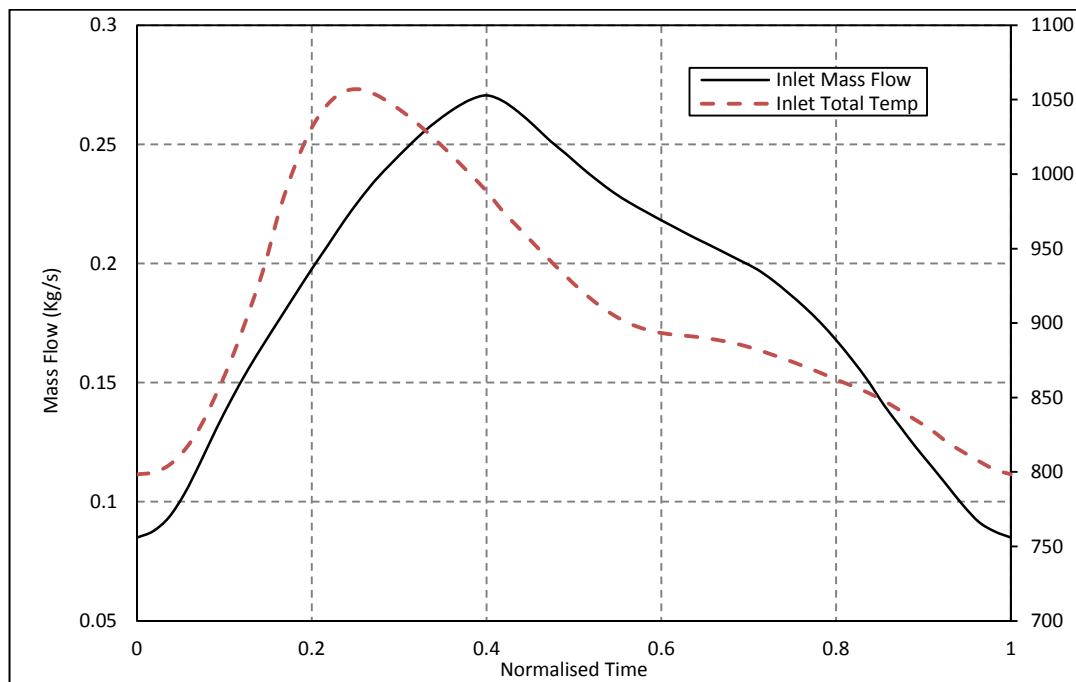
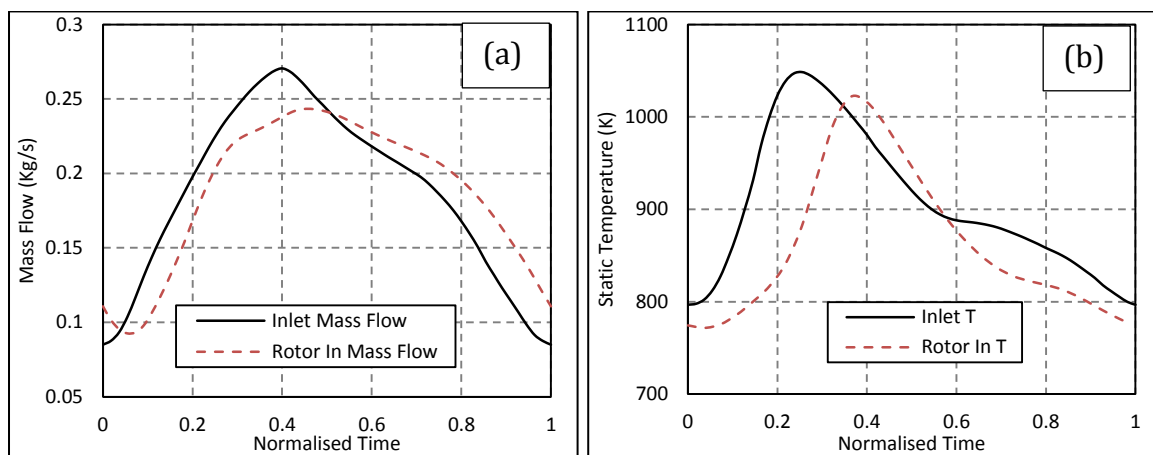


Figure 5.10: Inlet boundary conditions of mass flow and total temperature

Figure 5.11 compares the mass flow, static temperature, static pressure, density and normal velocity at the volute inlet and outlet stations. The time lag between the inlet and outlet stations is due to the speed of propagation of the relevant property. The greatest time lag occurs in the static temperature and velocity cases. The lag in mass flow is slightly less and lag in pressure is very small. The observation of the temperature travelling slower than mass flow and both slower than pressure was made by Roclawski et al., (2014). The authors then went on to say this shows the travelling pulse is dominated by two effects, the convection of temperature and mass flow, and the propagation of pressure waves. The authors did not mention the time difference in the relative properties at the stage inlet that was clear in their plots, as is the case in the current study (figure 5.10). As the temperature and mass flow boundary conditions are out of phase and all the parameters plotted in figure 5.11 are interdependent through the ideal gas equation and mass flow equation; each parameter is slightly out of phase with each other at the stage inlet. Each of the parameters experiences a shift in normalised time due to the propagation time required through the volute, but the parameters remain out of phase at the rotor inlet.



Pulse Frequency

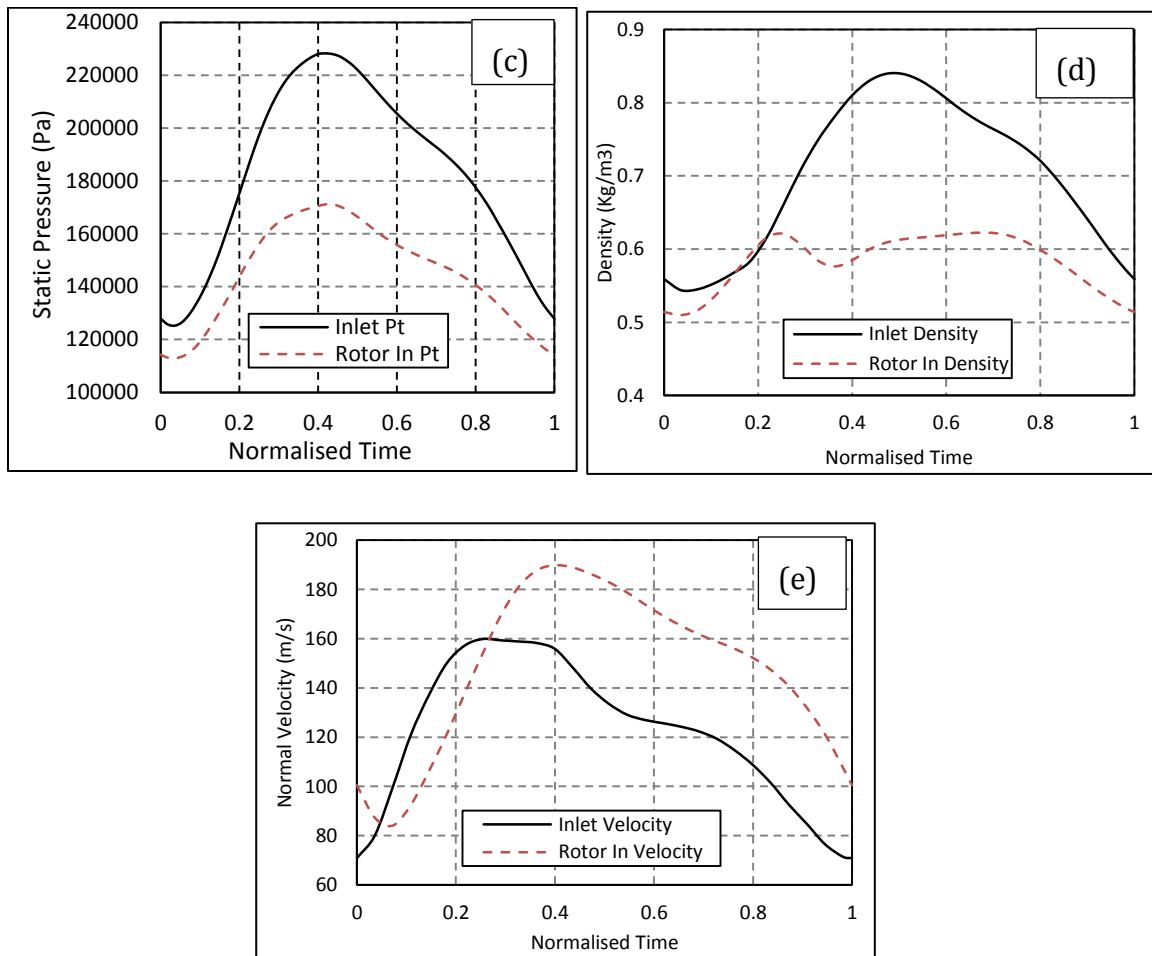


Figure 5.11: Volute inlet and outlet flow parameters at 40Hz frequency. (a) - mass flow, (b) - Static Temperature, (c) - Static Pressure, (d) - Density and (e) - Normal Velocity

The interesting result of this observation comes from the isentropic energy and incidence pulses. It has already been stated that maximum energy is available at the peak of the pulse. However, as the isentropic energy is dependent on the mass flow, total temperature and pressure and these are all out of phase, the peak isentropic energy is available at some mean point. Furthermore, the incidence angle is only dependent on the rotor inlet velocity (U/c_s), and is a source of significant loss within the rotor passage at peak operation due to excessively positive values. The resulting variations of isentropic energy and incidence are shown in figures 5.12-5.14 for each tested frequency.

The phase difference between the isentropic energy and incidence angle is clearly dependent on pulse frequency. The phase difference is greatest at 20Hz and reduces as frequency increases until the 60Hz case where they are nearly in phase. The result of this effect is that at lower frequencies the incidence angle is slightly lower when peak energy is available. Therefore, potentially the peak energy can be extracted more efficiently due to reduced LE separation at the peak isentropic energy running point. However, the reduction in incidence experienced was small as incidence does not reduce rapidly after the peak under the current pulse form.

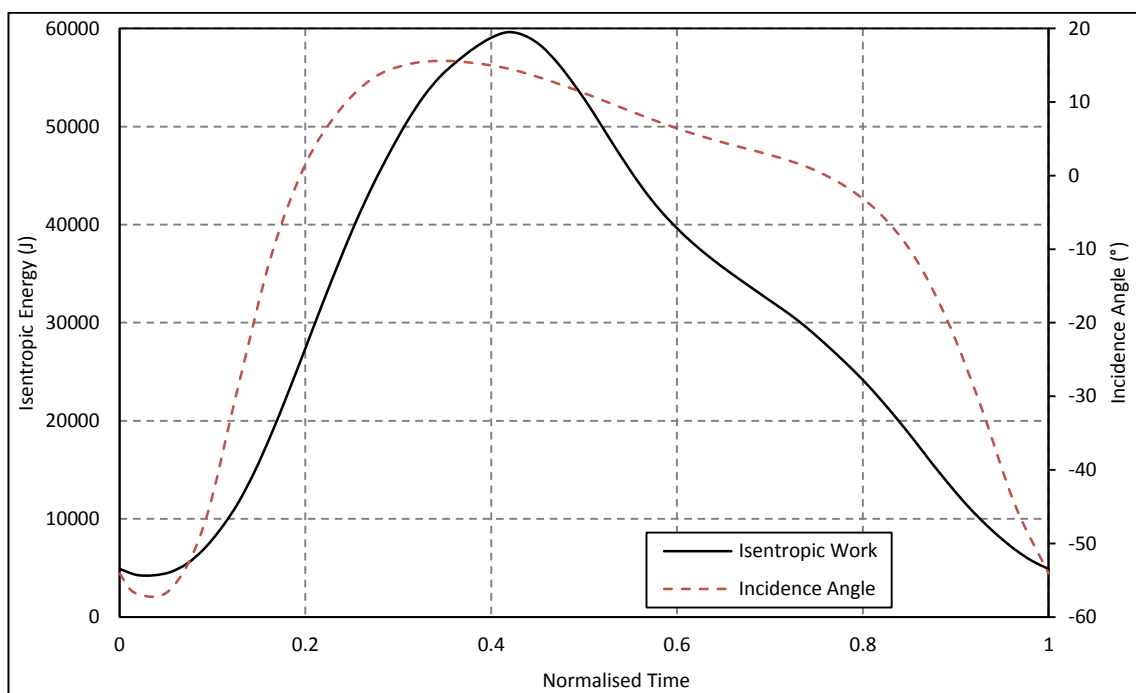


Figure 5.12: 20Hz frequency isentropic energy and incidence angle

Pulse Frequency

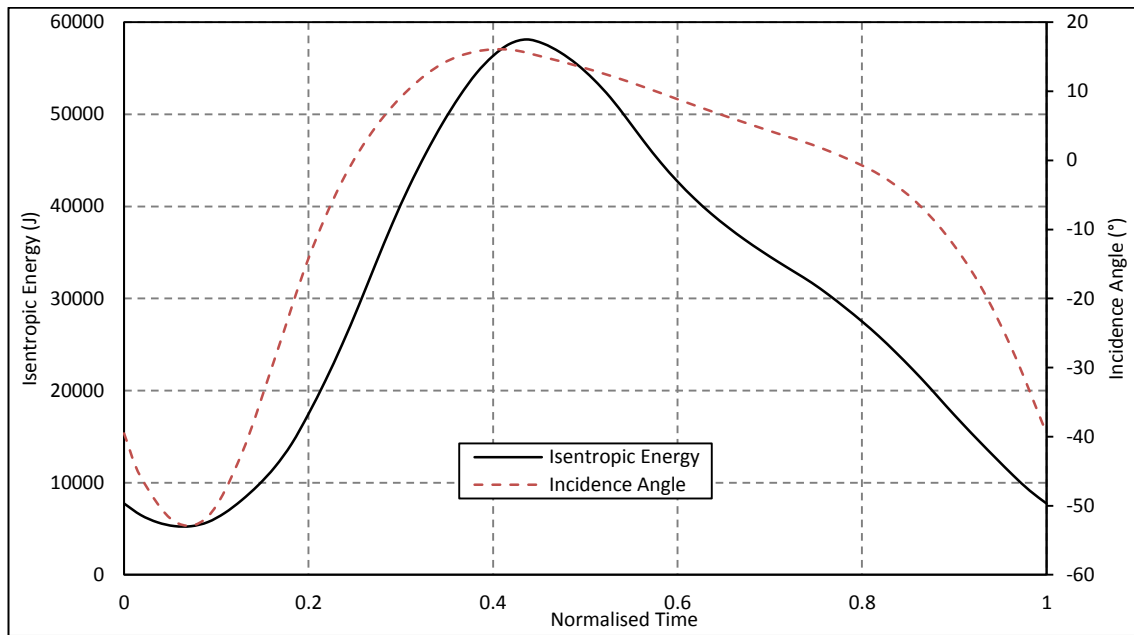


Figure 5.13: 40Hz frequency isentropic energy and incidence angle

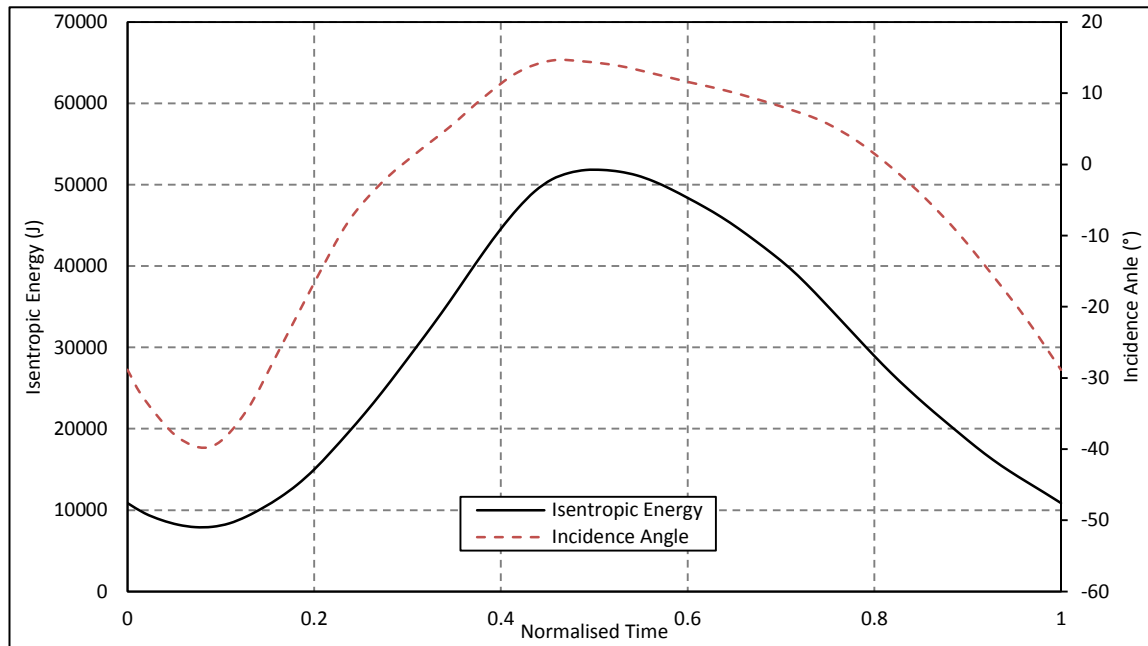


Figure 5.14: 60Hz frequency isentropic energy and incidence angle

5.2.1 CYCLE AVERAGED PERFORMANCE

The cycle averaged performance values are presented in table 5.1 for all tested frequencies. With increasing frequency, the rotor efficiency, stage efficiency and stage swallowing capacity increased. Despite this the cycle averaged rotor torque

decreased. This effect is the result of a cycle averaged decrease in velocity ratio due to the higher pressure ratios required to pass the specified mass flow at low frequencies. Furthermore, the volute loss coefficient was found to decrease slightly as frequency increased.

| <i>Frequency (Hz)</i> | <i>20</i> | <i>40</i> | <i>60</i> |
|-----------------------------------|-----------|-----------|-----------|
| <i>Normalised Rotor Eff</i> | 98.00% | 98.60% | 100% |
| <i>Volute K_{PL}</i> | 100% | 98.99% | 97.99% |
| <i>Normalised Stage Eff</i> | 96.87% | 98.20% | 100% |
| <i>Normalised MFP</i> | 98.67% | 99.14% | 100% |
| <i>Normalised Torque</i> | 100% | 99.20% | 97.90% |
| <i>Rotor U/c_s</i> | 0.5761 | 0.5785 | 0.5816 |

Table 5.1: Cycle averaged performance results AT 20hz, 40hz and 60hz pulse frequencies

5.2.2 CIRCUMFERENTIAL AVERAGING

At the volute exit plane the pressure and mass flow can be assumed to be circumferential constant with respect to the time dependent inlet conditions i.e. the circumferential variation in the flow, due the time dependent inlet conditions was negligible. While a finite amount of time is required for the fluid to travel from the stage inlet to rotor inlet, this is not the case around the volute circumference. This assumption allows the volute outlet parameters to be taken as the outlet circumferential average and the LE incidence to be taken as the circumferential average at the rotor LE as no variation occurs due to the pulse. The evidence for this assumption is given in figures 5.15. In this figure both static pressure and velocity are plotted at the central plane at three points during the pulse. In each case local variation at the volute outlet can be observed due to the proximity of the blades. However, the variation around the circumference at any given time is negligible compared to the variation over the pulse. This is represented graphically in figure 5.16 which shows the relative static pressure around the volute exit at each of the three time steps. The volute tongue is positioned at 90° in this case. The LE of the blades have a distinct impact on the pressure as too does the volute tongue. However,

variation around the circumference does not show a change from blade passage to blade passage. This shows that the time taken for the fluid parameters to propagate around the rotor outlet is negligible supporting the application of circumferential averaging. Circumferential averaging is therefore, used throughout the data analysis to compare the impact of pulse conditions on the rotor LE characteristics.

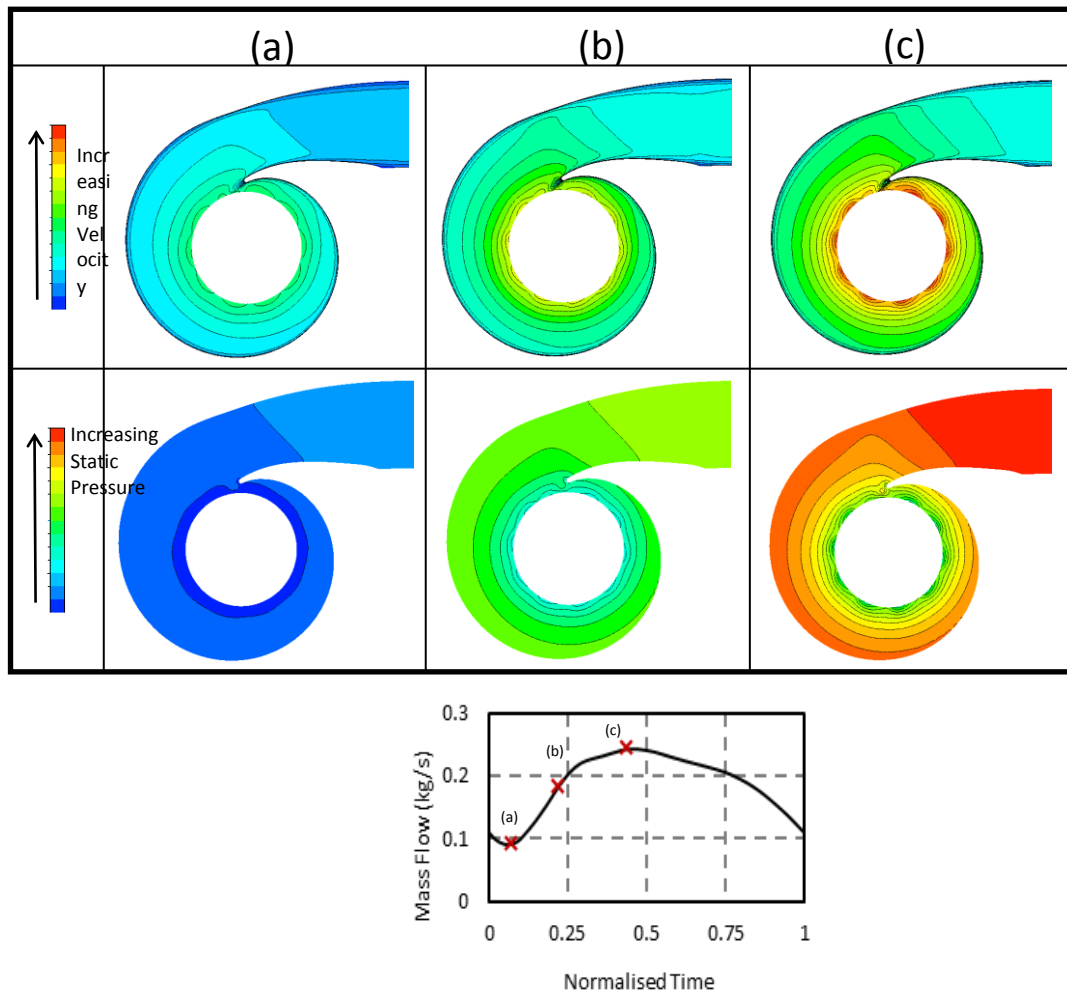


Figure 5.15: Velocity and pressure distribution around the volute through the pulse

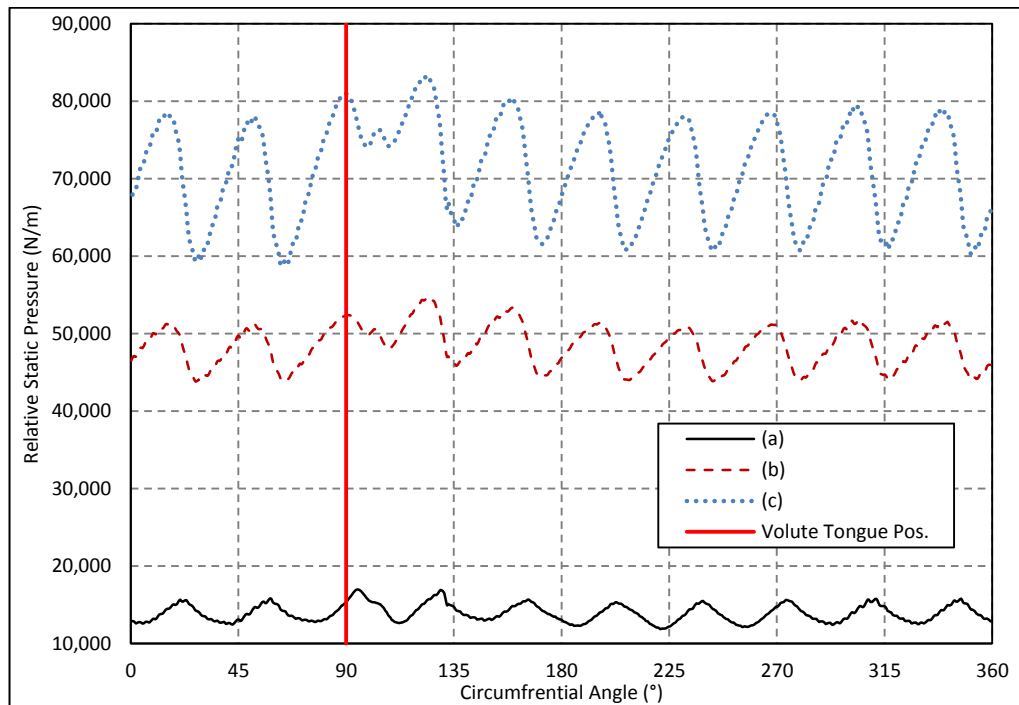


Figure 5.16: variation in static pressure around the volute outlet circumference over pulse period.

5.2.3 COMPARISON OF FLOW ANGLES THROUGHOUT PULSE

Figure 5.17 presents the span-wise and circumferentially averaged incidence angles at the blade LE (i_{LE}) at points in time over the pulse duration. The average blade LE Incidence is calculated from the mass flow velocity components averaged around the rotor LE circumference and the span-wise averaged blade LE camber angle (φ). As frequency is increased the minimum incidence angles achieved reduce in magnitude significantly. The maximum incidence angles achieved do not vary significantly with pulse frequency despite the variation in rotor inlet mass flow. Alternately, the maximum incidence angles achieved do not vary significantly with pulse frequency. While the mass flow pulses, shown in figure 13, show a greater variation at the pulse minimum, a significant variation in the peak also exists. However, the LE incidence evidently doesn't experience the same variation. The increased impact of the mass flow variation on incidence angle at lower angles can be visualised through the velocity triangles as shown in figure 2. At low mass flow operation (negative incidence) a reduction in the velocity component C , will have a

greater impact of the resulting relative flow angle than the same absolute increase would have at maximum mass flow operation. Hence, how the incidence angle range change with frequency does not necessarily follow the same trend as the mass flow.

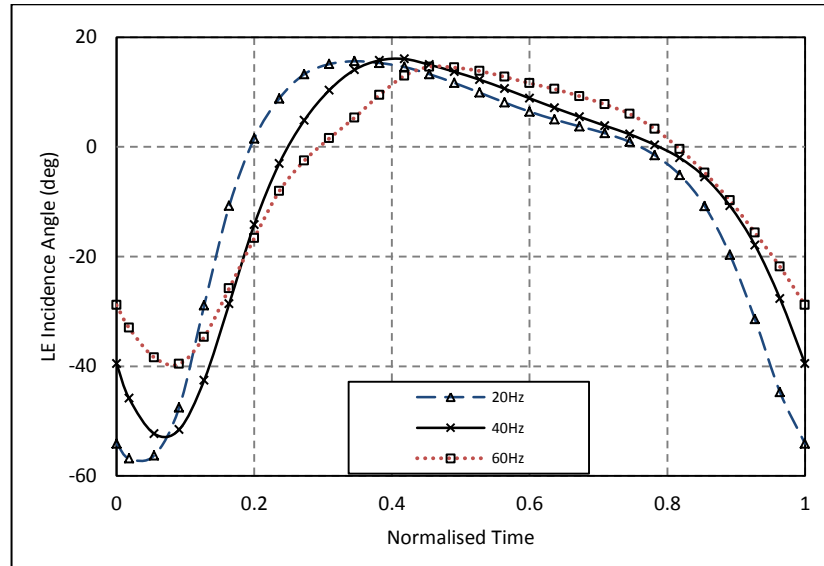


Figure 5.17: Mass flow averaged leading edge incidence angle throughout pulse at 20Hz, 40Hz and 60Hz pulse frequencies

As previously discussed, the incidence angle in a mixed flow turbine is dependent on the volute exit flow angles and the blade angle achieved. The mixed flow rotor used in this case has varying LE camber and therefore the blade angle from hub to shroud is not constant. However, for this to be implemented successfully it is necessary to understand the span-wise variation in flow conditions under pulsating conditions.

Firstly, the span-wise variation in flow cone angle is assessed. This is presented in figure 5.18 for the 40Hz pulse frequency at three points in time over the pulse duration: minimum incidence, -10° LE incidence during the emptying phase of the pulse and maximum incidence. These three points are extracted from figure 5.17 and plotted against normalised span where 0% is the rotor hub and 100% the shroud. In all cases the flow cone angle is greater than the 70° required for flow to enter the rotor normal to the LE, indicating a lack of flow turning ahead of the rotor. This is particularly evident at the minimum incidence running point where the flow cone

angle remains above 80° over 85% of the LE. However, as this running point corresponds to highly negative incidence, the addition of the mixed flow effect is not beneficial at this point in the pulse. At the -10° and maximum incidence running points, the flow cone angle achieved is significantly smaller. Poor flow turning at the hub is particularly evident, and the variation from hub to shroud is substantial in both cases.

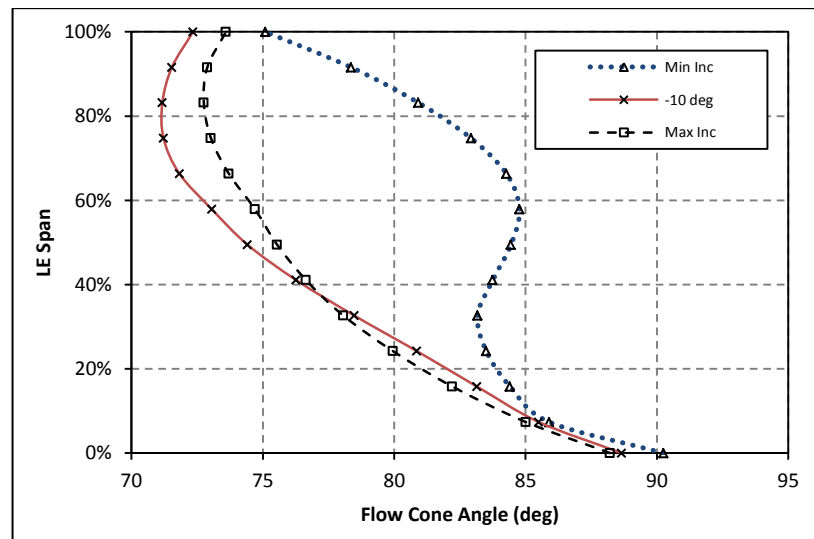


Figure 5.18: Leading edge Flow cone angle at three points over the blade span during the 40Hz inlet pulse

The resulting blade angles achieved from the combination of the LE camber angle and flow cone angle are presented in figures 5.19-5.21 for the 20Hz, 40Hz and 60Hz cases respectively. In all cases, a significant variation in blade LE angle is observed over the blade span. The maximum magnitude achieved is only -4.9° at the maximum incidence running point for all tested frequencies. In all cases the blade angle becomes increasingly positive towards the shroud due to positive blade camber present in this region. While the blade angles at -10° and maximum incidence appear to be independent of pulse frequency, significant variations in the LE blade angle at minimum incidence are apparent. At 20Hz, the blade LE angle reaches a maximum negative magnitude of only -2.5° at 20% span. However, with increasing frequency the deviation of the blade angle at the minimum incidence running point reduces. This effect is the result of the lower mass flow achieved under lower frequency.

Pulse Frequency

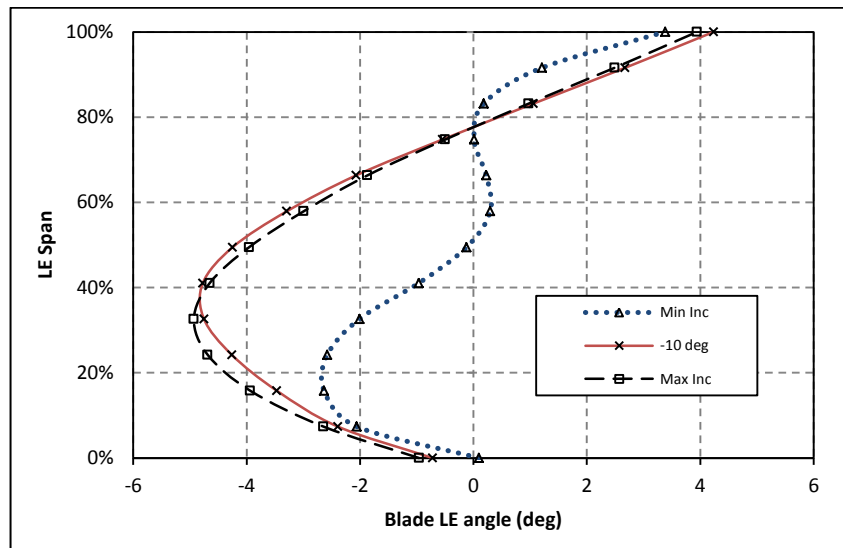


Figure 5.19: Leading edge blade angle at three points in the pulse at 20Hz

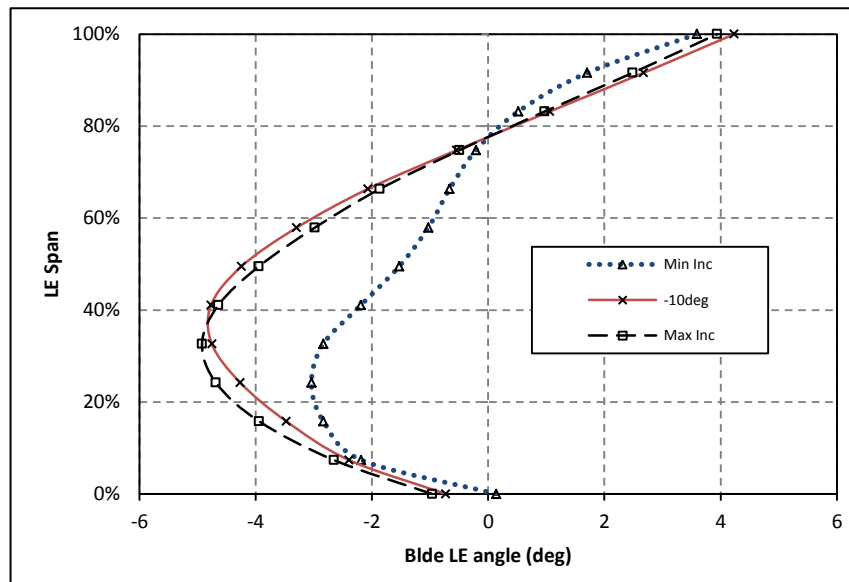


Figure 5.20: Leading edge blade angle at three points in the pulse at 40hz

Pulse Frequency

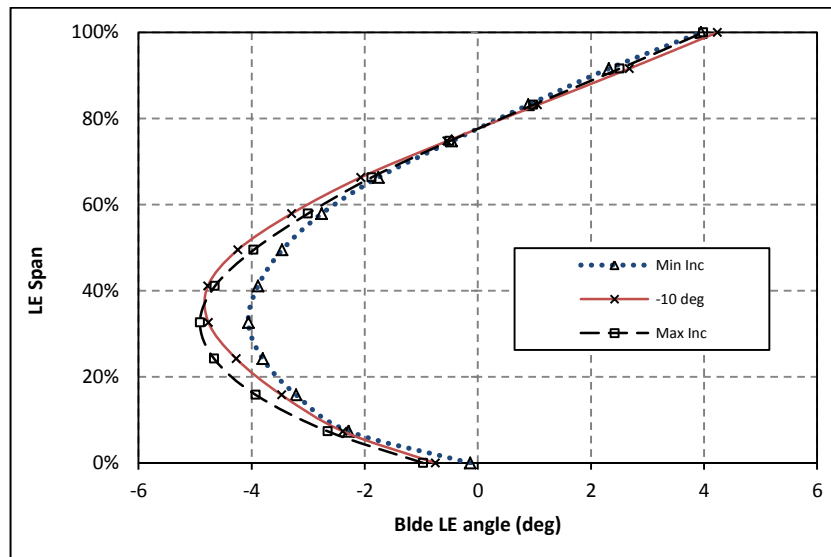


Figure 5.21: leading edge blade angle at three points in the pulse at 60Hz

The resulting LE incidence is plotted in figures 5.22–5.24 for the minimum, -10° and maximum incidence running points respectively at all tested pulse frequencies. The variation in incidence over the rotor span is large in all cases. At minimum incidence, the lowest flow angles are achieved at the rotor hub, increasing to a maximum at approximately 20% chord. Incidence reaches a local minimum at centre span before increasing again to a maximum at the shroud side. While the distribution of incidence at the LE remains similar for all pulse frequencies, the distribution shifts to a more negative mean as the pulse frequency is reduced. The impact of pulse frequency on the mean incidence was not observed at the maximum LE incidence running point. The velocity ratio at this point corresponds to the minimum velocity ratio and as shown in figure 5.7, frequency has little impact on U/c_s at this end of the range. However, at the minimum incidence running point, which corresponds to the maximum velocity ratio, a notable difference in the values was achieved when pulse frequency was varied.

At -10° incidence, the minimum incidence over the blade span is achieved at the hub and increases to a maximum at around the centre of the LE before decreasing again towards the shroud at a more gradual rate. At this operating point, the frequency does not have a significant impact on the distribution of incidence.

At the maximum incidence point, a distribution with a parabolic-like shape is formed at all pulsed frequencies with the maximum incidence achieved in the centre of the LE. Again, for all tested frequencies, the distribution and mean incidence angles are very similar.

The resulting span-wise variation in incidence angle is clearly heavily influenced by inlet pulsations. While Morrison et al., (2016) noted the impact of varying blade speed at the LE of a mixed flow turbine as a source of incidence variation, this effect is not observed in the current study. This is put down to the fact that the span-wise variation of the velocity components exiting from the volute (which were not accounted for by Morrison et al., (2016)) has a such substantial impact on the blade LE incidence that any impact of varying tip speed is masked, Furthermore, with a mild blade cone angle of only 20° , the variation in LE radius is not as substantial.

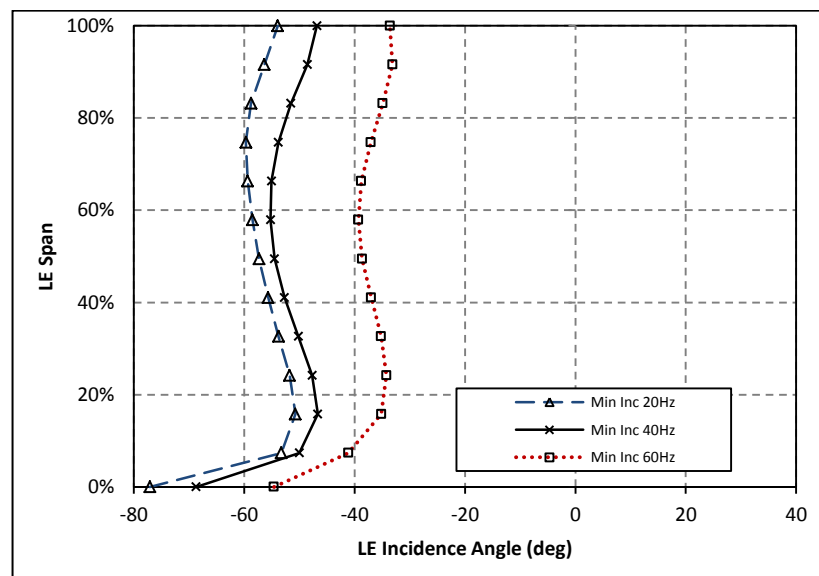


Figure 5.22: Leading edge incidence over the blade span at the minimum incidence running point at 20Hz, 40Hz and 60Hz pulse frequencies

Pulse Frequency

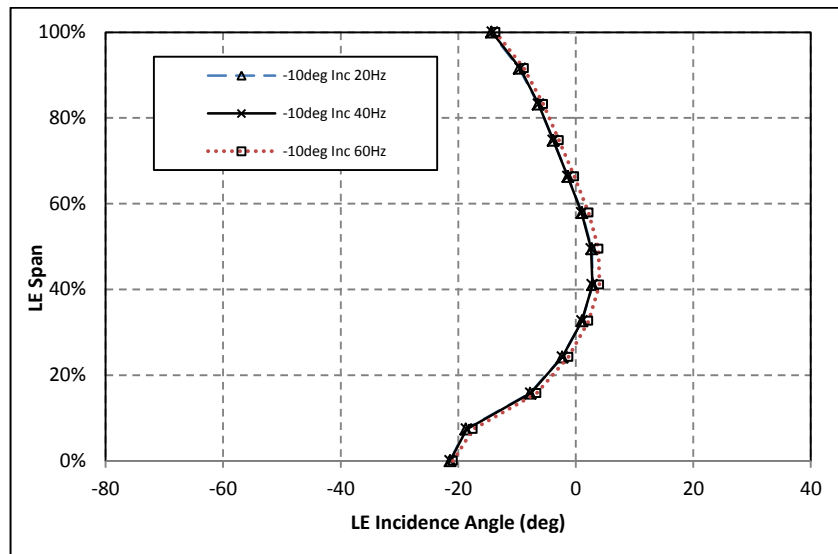


Figure 5.23: Leading edge incidence over the blade span at the -10° incidence running point at 20Hz, 40Hz and 60Hz pulse frequencies

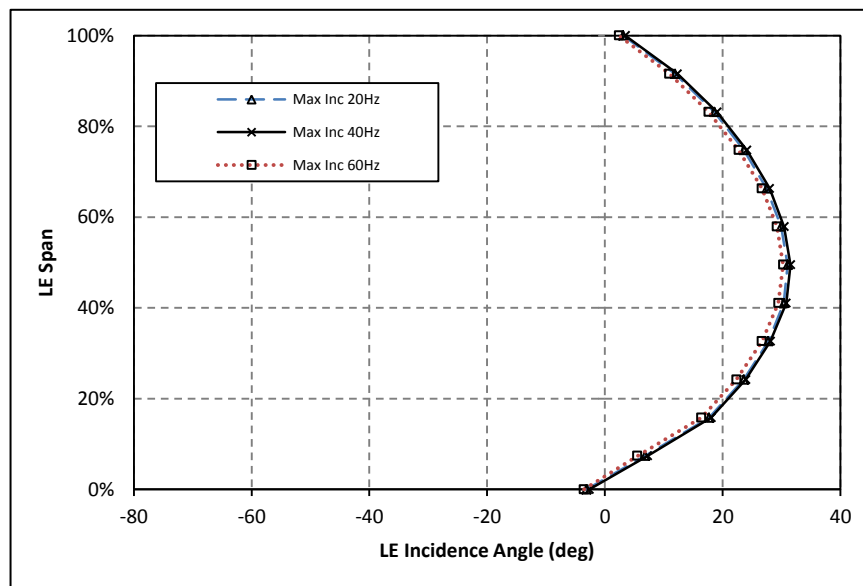


Figure 5.24: Leading edge incidence over the blade span at the maximum incidence running point at 20Hz, 40Hz and 60Hz pulse frequencies

The variation in relative circumferential velocity with respect to the mean velocity is presented in figure 5.25 at minimum, -10° and maximum incidence. In all cases the general shape of the distribution represents that of fully developed pipe flow which can be expected due to the flow development within the volute. Towards the hub the circumferential velocity becomes increasingly positive due to the

proximity of blade hub surface. Towards the shroud the velocity becomes increasingly negative due to the relative movement of the shroud surface with respect to the passage. The central 60% of the span sees a more constant circumferential velocity distribution, but as incidence increases, so does the variation over this region.

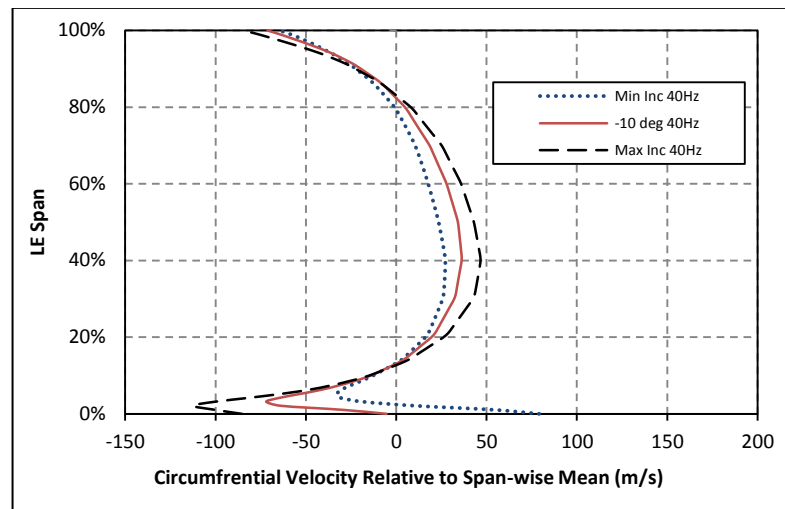


Figure 5.25: Variation in circumferential velocity at the blade leading edge at 40Hz

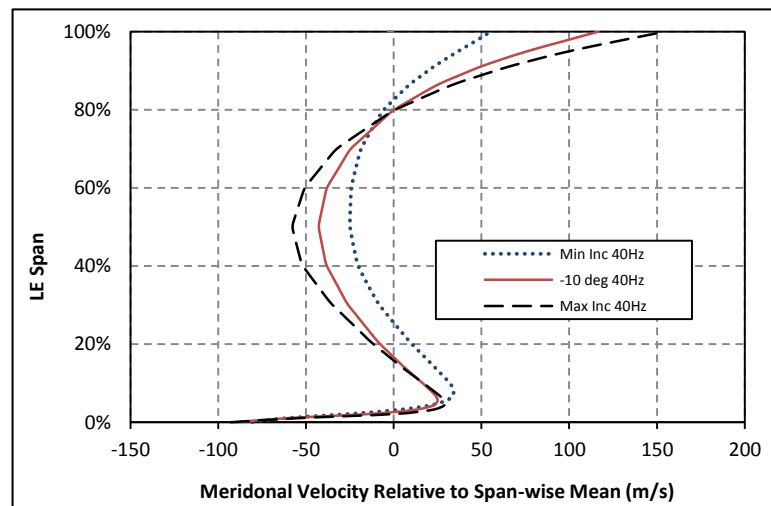


Figure 5.26: Variation in meridional velocity at the blade leading edge at 40Hz

Figure 5.26 shows the variation in meridional velocity from the mean over the same three running points as in figure 5.25. In all cases a local minimum radial velocity occurs in the centre of the LE (excluding that occurring very close to the hub

surface) and the velocity increases towards both the hub and shroud. This trend becomes more pronounced with increasing incidence angle as the peak of the inlet pulse is approached.

This behaviour is the result of the development of flows within the volute and was discussed previously by Lee et al., (2016). Figure 5.27 shows contours of radial velocity and surface streamlines on six planes around the volute at 40Hz pulse frequency at both the minimum and maximum incidence running points. The position of the six planes are 54° , 72° , 90° , 126° , 198° and 270° .

At the minimum incidence running point in the 72° plane, two pairs of counter rotating vortices form on each side of the volute. The higher vortices rotate clockwise and lower vortices in the counter-clockwise direction. These flow structures develop as a result of the Dean effect, where the high velocity central passage flow with higher inertia is more resistant to radial turning compared with the lower inertia flow adjacent to the volute walls (this effect is described in equation 21). As a result, the flow near the walls turns radially in more readily than the bulk central flow. The variation in radial velocity across the volute passage exit is the result of this mechanism. At the 90° plane, the vortices no longer exist but a distinct deviation in the streamlines low in the volute can be observed. While the vortex structures do not persist further around the volute a clear variation in radial velocity from the contour plots is visible around the volute passage and is particularly evident at the volute exit.

At the maximum incidence running point, no distinct vortex regions were observed. Despite this, the variation in radial velocity shown in the contour plot is still large. The lack of vortex formation is attributed to the positive pressure gradient pushing the flow into the rotor; this driving force suppresses any potential flow reversal. The same effect explains the rapid breakdown of the vortices at the minimum incidence running point as volute area reduces. Despite the lack of vortices a significant variation in radial velocity over the volute cross section is evident at all plotted positions.

Pulse Frequency

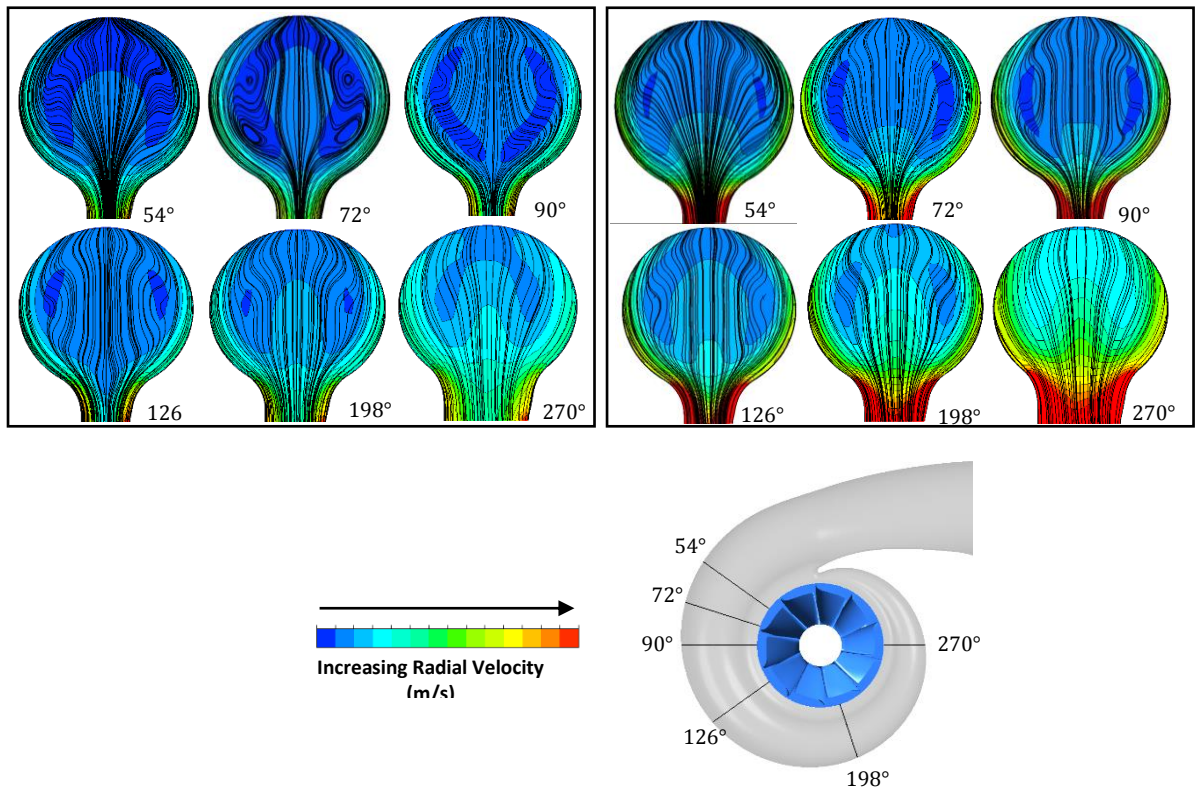


Figure 5.27: Stream lines and radial velocity contours at planes around the volute circumference. Left - minimum incidence running point. Right - maximum incidence running point

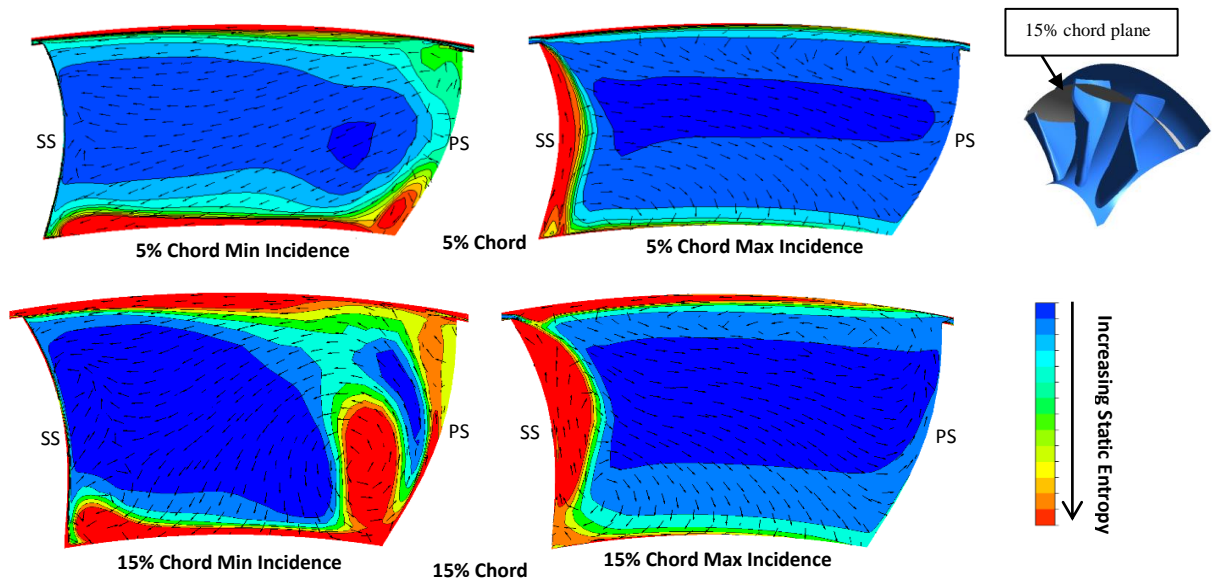


Figure 5.28: Contours of static entropy and velocity vectors on a constant streamwise plane at 5% and 15% chord. Passage position is 180° from tongue. Left - Minimum incidence right - maximum incidence

Figure 5.28 illustrates the flow losses as they develop in the rotor passage using contours of static entropy. The planes are orientated to look downstream from the LE

to the TE. The planes are positioned in the blade passage 180° from the volute tongue to minimise any impact of the tongue on the flow distribution. At the minimum incidence running point, a clear separation region exists on the pressure surface (PS) towards the hub at both chord positions. The development of this loss is the result of the negative inlet flow angles and the coriolis effect occurring within the passage. The loss region initiates close to the hub at the 5% chord position and grows to the 15% chord position. The region also moves away from the PS due to the cross-passage pressure gradient. There are also significant loss regions at the shroud due to the relative movement at the surface.

At the maximum incidence running point, separation from the suction surface (SS) is evident at the blade span centre and reduces towards both the hub and shroud. This compares favourably with the incidence distribution shown in figure 5.24. The high entropy region at the shroud is the result of the relative movement of the shroud and the interaction with tip leakage.

The variation in incidence over the LE span at five points around the volute circumference (54° , 90° , 126° , 198° and 270°) are shown in figures 5.29 and 5.30 for the minimum and maximum incidence points respectively. Incidence was extracted at these positions as they are located midway between the rotor blades (18° from both neighbouring LE's). This is done to minimise the upstream effect on the flow distribution and therefore focus on that produced by the volute. While circumferential location was found to have minimal impact on the propagation of fluid parameters, the variation in the LE incidence over the rotor span was found to be influenced by circumferential position. At the 54° position, the incidence across the span remains the most consistent in both cases. The greatest variation in incidence is then experienced at 126° from the tongue in both cases. However, this effect makes the flow increasingly negative at the span centre in the minimum incidence case and increasingly positive at the span centre in the maximum incidence case. Beyond the 126° position the variation reduces in both cases and then remains almost constant at the 198° and 270° positions.

Pulse Frequency

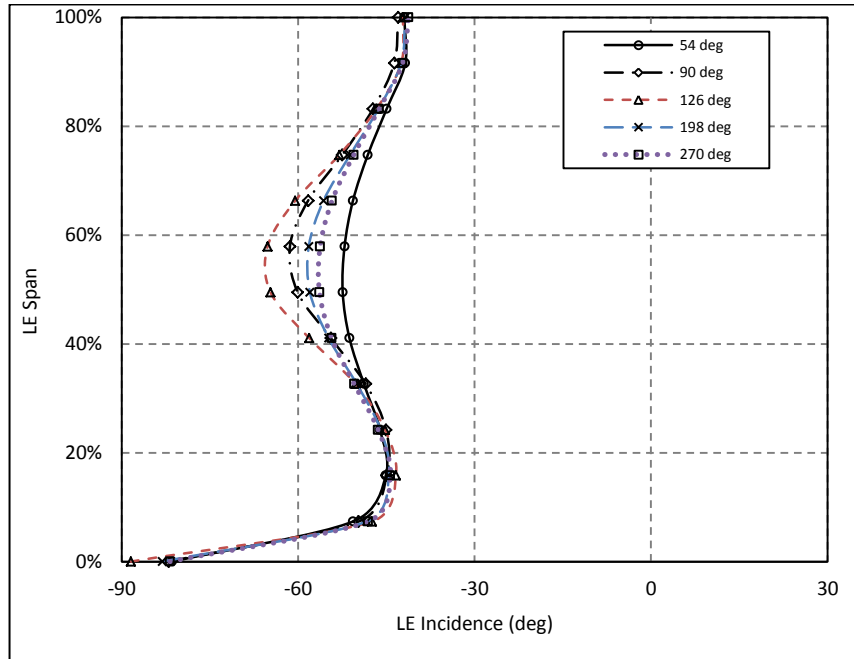


Figure 5.29: Leading edge incidence around the volute circumference at minimum incidence during the 40Hz pulse

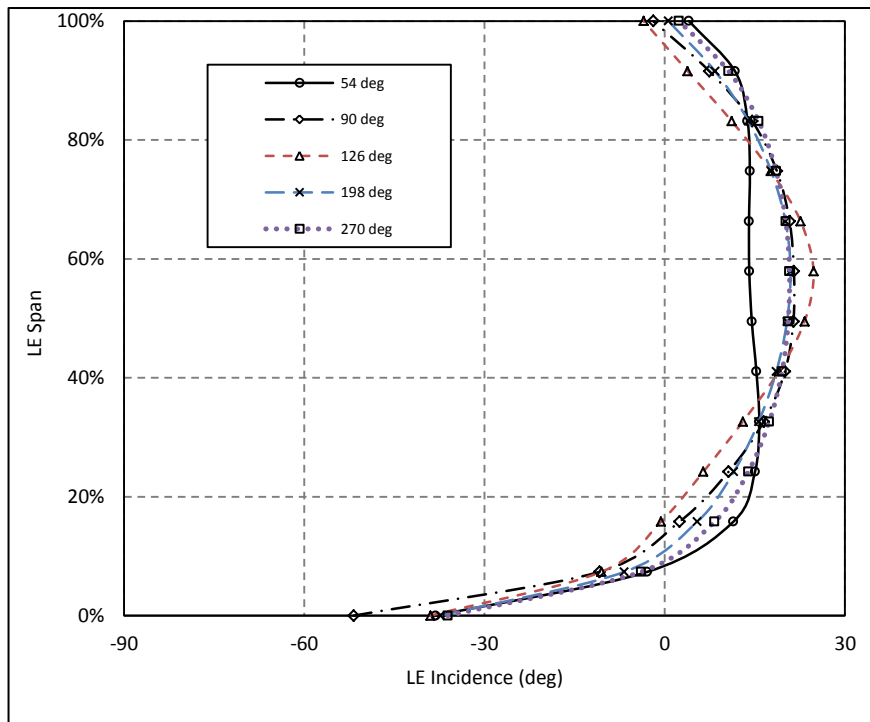


Figure 5.30: Leading edge incidence around the volute circumference at maximum incidence during the 40Hz pulse

5.3 IMPACT OF PULSE LOAD

In this study, three mass flow pulse loads (low load – 73%, mid load 100% and high load – 127%) were tested. The resulting MFP is plotted against stage pressure ratio in figure 5.31. All loads were tested at 40Hz pulse frequency and pulsation number of 0.5. There is a clear change in the shape of the hysteresis with changing pulse load. Also, the hysteresis increases with load, resulting in greater deviation from the steady state results at higher loads. The range of the stage pressure ratio over the pulse also increased with increasing load. This behaviour was the result of the increasing inlet mass flow. As the stage approaches the choked condition larger pressure ratios are necessary to achieve further increases in mass flow resulting in a reduction of the MFP range over the pulse and an increase in the pressure ratio range.

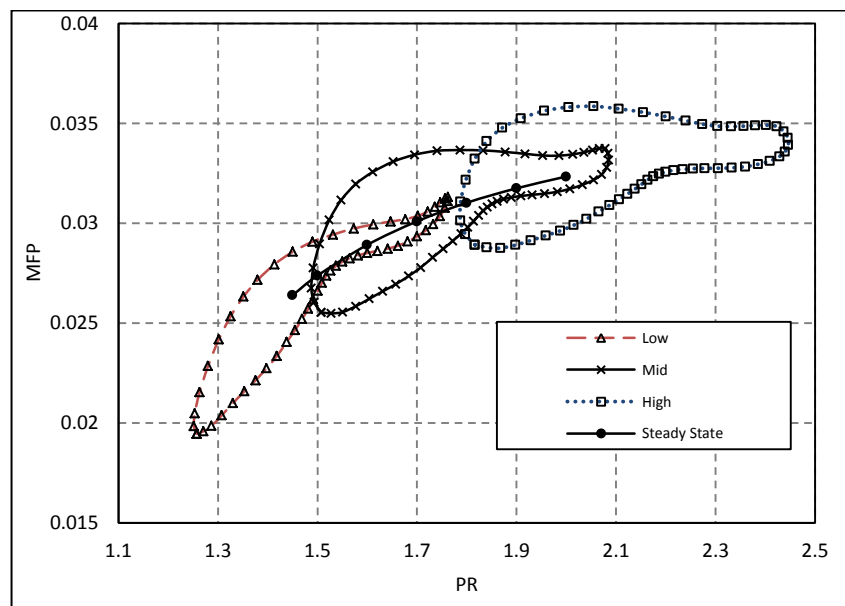


Figure 5.31: MFP vs pressure ratio for steady state, low, medium and high load at 40Hz pulse frequency

Figure 5.32 shows the mass accumulation in the volute at the three tested pulse loads. With increasing pulse load the mass accumulation reduced, and hence turbine unsteadiness reduced. This can be attributed to the lower flow velocities at low pulse loads, hence the propagation of the mass through the volute reduced. This resulted in greater mass accumulation over the pulse period.

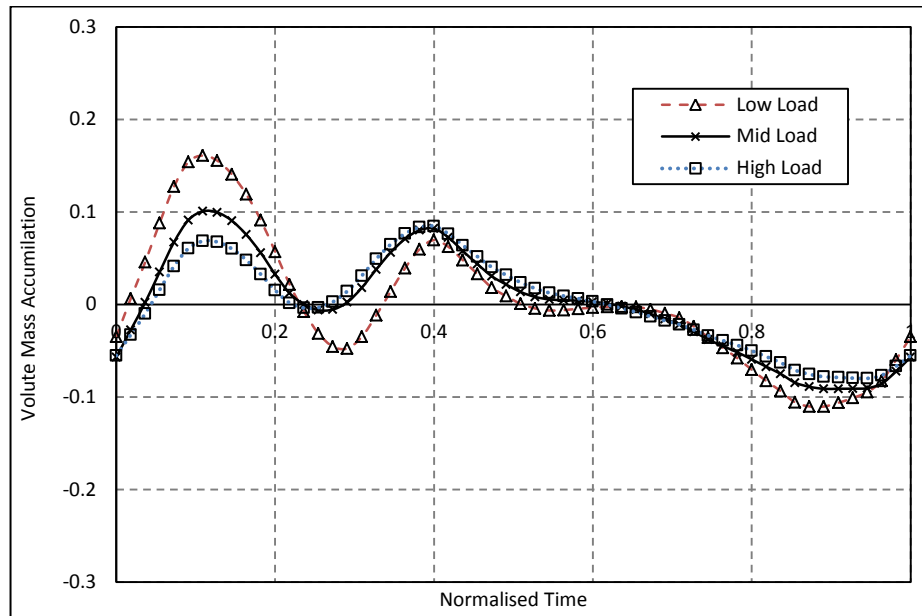


Figure 5.32: Volute mass accumulation at low, medium and high load.

The resulting rotor torque is presented in figure 5.33. While the pulse frequency had a significant impact on the shape of the turbine torque generated over the course of the pulse, the turbine load has little impact on this. However, the torque mean experiences a distinct shift up with increasing turbine load which is to be expected.

The resulting rotor efficiency for each turbine load presented in figure 5.34 shows that the mean rotor velocity ratio shifts to lower values with an increase in load and that the rotor velocity range significantly reduces. The resulting efficiencies, particularly at low velocity ratios, collapse onto a single line demonstrating the quasi steady performance of the rotor. However, as with varying frequency the hysteresis in performance increased at high velocity ratios.

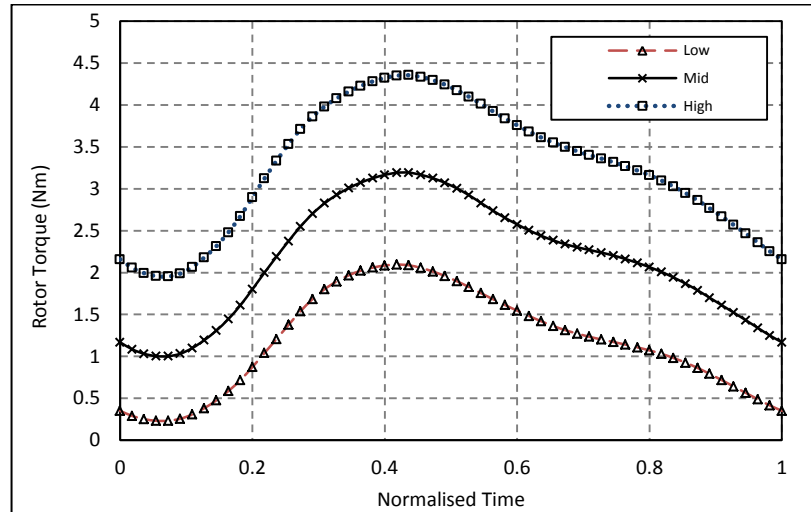


Figure 5.33: Rotor torque of the 40Hz pulse at three load conditions

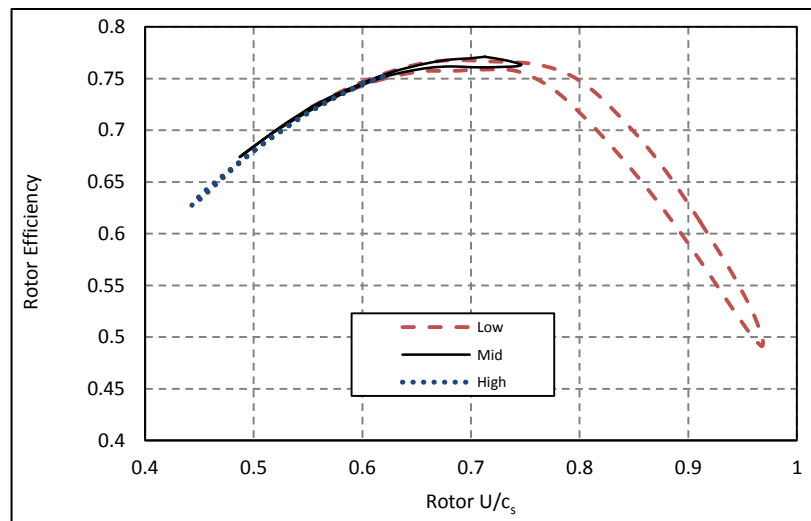


Figure 5.34: Instantaneous rotor torque at three load conditions at the 40Hz pulse frequency

The turbine performance parameters achieved under each load are presented in table 5.2. In the current case the lowest tested turbine load achieves the greatest rotor and stage efficiencies. While increasing load results in a considerable increase in torque produced, the energy demands required are also much higher. Increased aerodynamic loss associated with the higher pressure running points result in a reduction in efficiency as the turbine performs over a more inefficient range of operation. Conversely it was found that the volute loss coefficient reduces with increasing load.

| <i>Pulse Load</i> | <i>Low</i> | <i>Mid</i> | <i>High</i> |
|-----------------------------------|------------|------------|-------------|
| <i>Normalised Rotor Eff</i> | 100% | 98.14% | 92.73% |
| <i>Volute K_{PL}</i> | 100% | 96.79% | 86.10% |
| <i>Normalised Stage Eff</i> | 100% | 98.64% | 93.71% |
| <i>Normalised MFP</i> | 81.72% | 93.79% | 100% |
| <i>Normalised Torque</i> | 36.24% | 66.08% | 100% |
| <i>Rotor U/c_s</i> | 0.6918 | 0.5842 | 0.5162 |

Table 5.2: Cycle-averaged performance results for three load conditions at 40Hz pulse frequency

The resulting rotor LE incidence is plotted in figure 5.35. Increasing the turbine load increased the mean incidence over the pulse cycle. Furthermore, the range of incidence decreased significantly as the load was increased which is predominantly the result of changes to the minimum incidence range. Under the maximum load pulse, incidence ranged from -5.1° to 15.6° , at the middle load from -24.1° to 14.8° and under the lowest load pulse from -55.8° to 7.3° . The results show that at higher loads, incidence was less sensitive to mass flow changes.

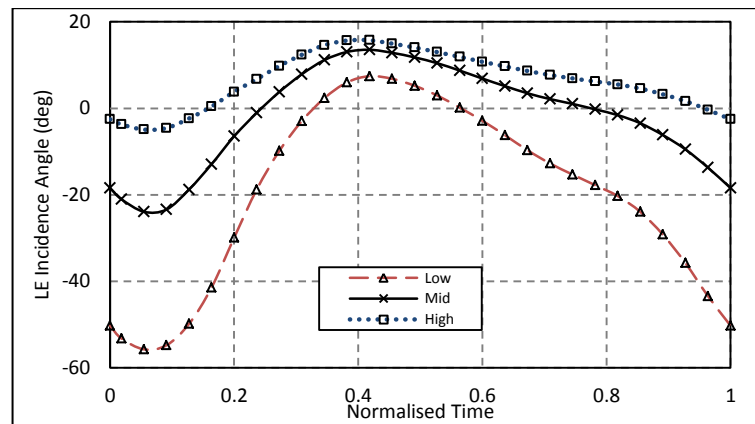


Figure 5.35: Leading edge incidence over the 40Hz pulse at three load conditions

The variation in incidence over the rotor LE span is presented at minimum incidence in figure 5.36 for the three test pulse loads. At the minimum incidence angle running point, the incidence over the span between the three pulse loads exhibit different profiles. At the lowest load, minimum incidence occurred at the hub

wall increasing to a maximum at 15% span, then reduced to a local minimum at the centre and a moderate increase towards the shroud. The middle load resulted in an almost constant distribution from the 20% span position to the shroud side. This running point of the middle load pulse corresponds to peak rotor efficiency where mean incidence was approximately -20° . The high load point shows the opposite distribution to that observed at low load. The most positive values occurred at the centre of the blade span and decreased towards both the hub and shroud.

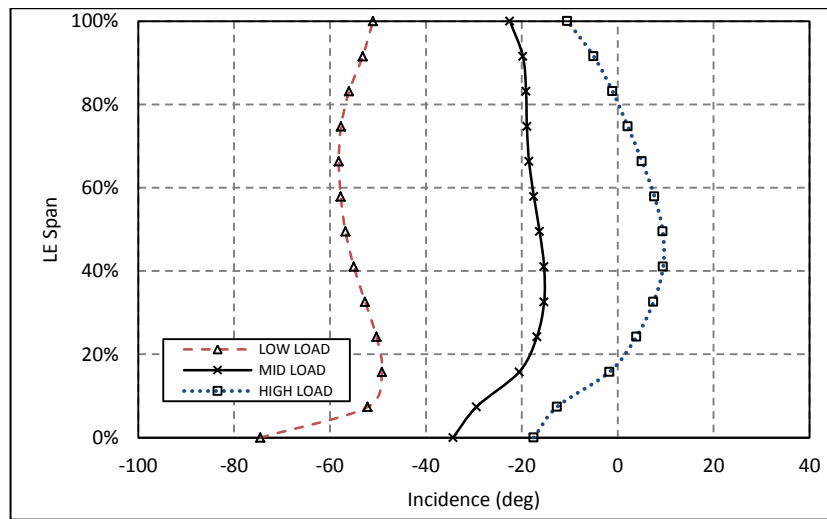


Figure 5.36: Leading edge incidence over the blade span at minimum incidence under three load conditions at 40Hz pulse frequency

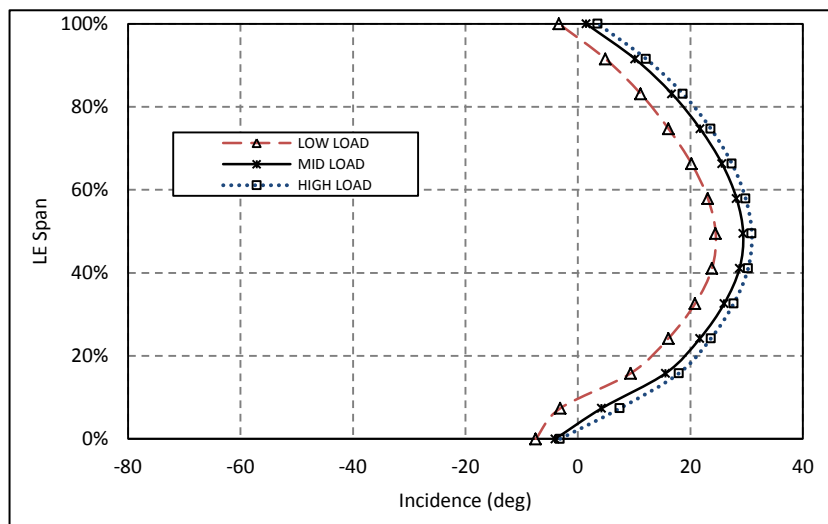


Figure 5.37: Leading edge incidence over the blade span at maximum incidence under three load conditions at 40Hz pulse frequency

At the maximum incidence running points shown in figure 5.37, incidence over the span shows similar distribution for all three loads. At the lowest tested load, the incidence remained approximately 5° less than that of the middle and high load pulses over the entire span but the distribution shape is similar. The variation between the middle and high load pulses was negligible despite both points having significantly different mass flows. This finding illustrates that the mean incidence and incidence distribution is approximately constant beyond a certain mass flow value.

5.4 IMPACT OF PULSATION NUMBER

Four pulsation numbers were tested (0.5, 0.75, 1 and 1.25) at 40Hz frequency and a pulse load of 100%. The resulting stage MFP plots for the four pulses are presented in figure 5.38. As the pulsation number increases, the MFP hysteresis and stage pressure ratio range increase, however, the shape of the hysteresis loop is similar.

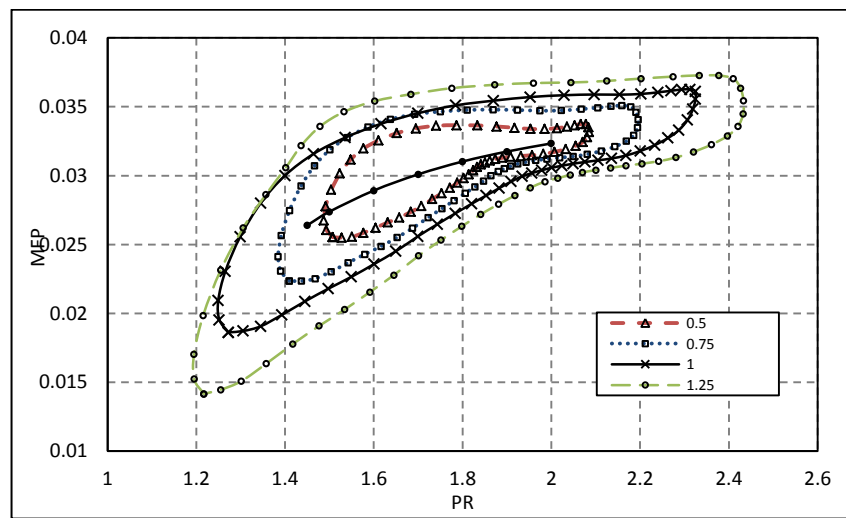


Figure 5.38: MFP vs pressure ratio for steady state, 50, 75, 100 and 125 pulsation numbers at 40Hz pulse frequency

Figure 5.39 shows the mass accumulation at the four tested pulsation numbers. With increasing pulsation number, the accumulation of mass within the volute increased and therefore the unsteadiness in the stage increased. The maximum accumulation observed was 0.28 in the 1.25 pulsation number case, this reduced to only 0.09 in the 0.5 case. With increasing pulsation number, the shape of the accumulation was not observed to change unlike the impact of increasing pulse frequency.

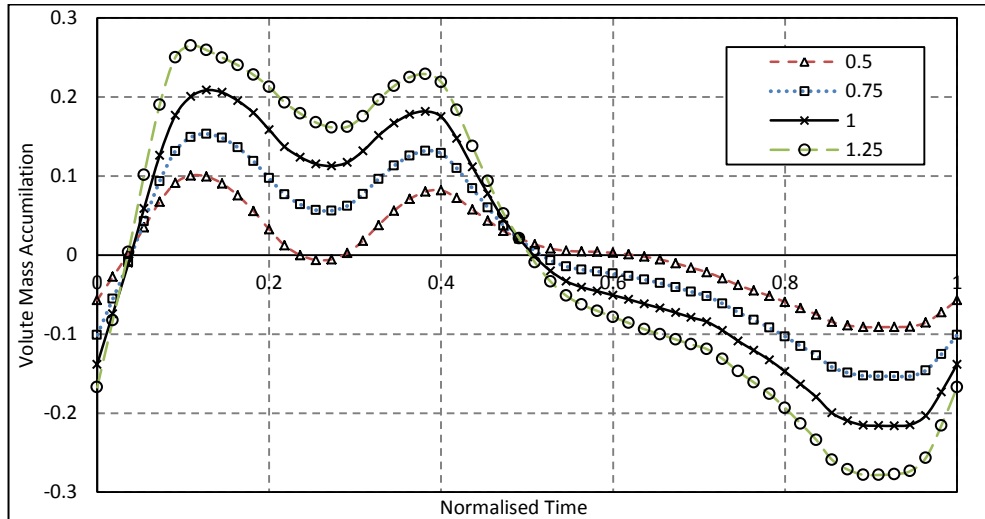


Figure 5.39: Volute mass accumulation at 0.5, 0.75, 1 and 1.25 pulsation number

The resulting rotor torque is plotted in figure 5.40. The range of rotor torque achieved increased with increasing pulsation number resulting in a significant increase in the rate of change with respect to time. The range of rotor velocity ratio also increased significantly with increasing pulsation number. The energy distribution available over the velocity ratio range is presented in figure 5.41. As the pulsation number increases the maximum rotor velocity ratio achieved was found to increase significantly, however due to the low energy availability in this region, this has negligible impact on cycle averaged performance. The impact on the U/c_s at the low end of the range is less distinct, but an increase in available energy at the low velocity ratios was observed as pulsation number is increased. This is supported by the reduction in cycle averaged velocity ratio as pulsation number increases as shown in table 5.3.

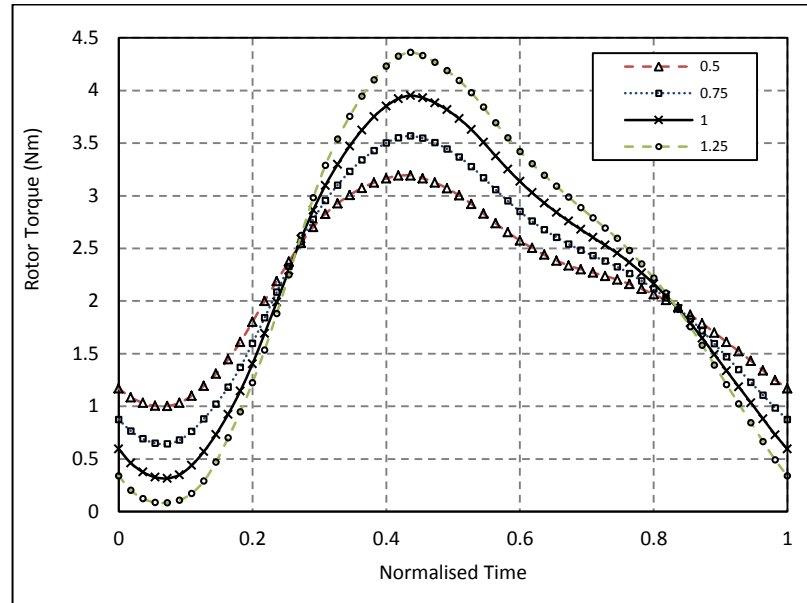


Figure 5.40: Rotor torque over the pulse at 50, 75, 100 and 125 pulsation numbers at 40Hz pulsation frequency

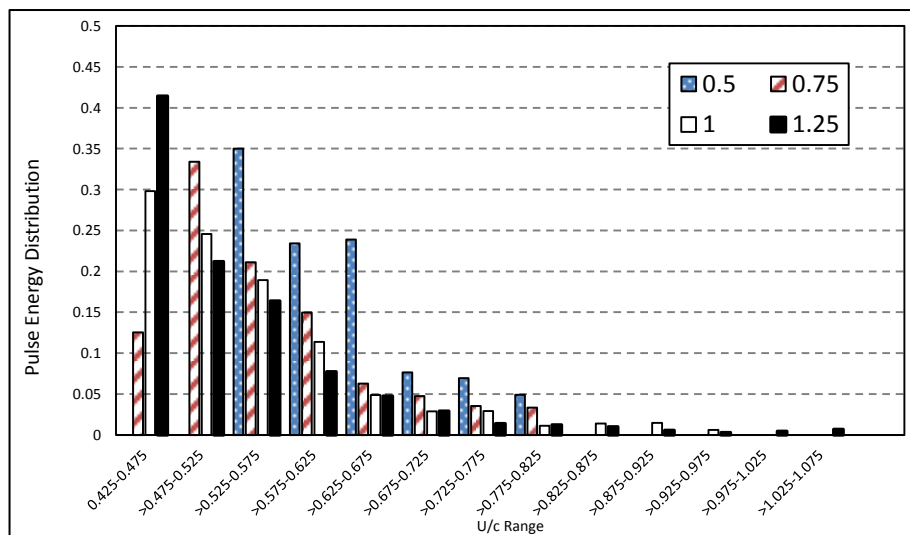


Figure 5.41: Pulse energy distribution over range of pulsation numbers

Table 5.3 presents the cycle-averaged performance for each of the tested pulsation numbers. With increasing pulsation number, the stage and rotor efficiency decreased. This was the result of the increased range of operation causing the turbine to operate at increasingly off design conditions. It was also observed that the volute total pressure loss coefficient decreased with increasing pulsation number. Throughout this study it has been apparent that volute losses reduce when the

turbine operates away from the low mass flow running points where secondary flow structures more commonly form as shown in figure 5.27.

| <i>Pulsation No.</i> | 0.5 | 0.75 | 1 | 1.25 |
|-----------------------------------|------------|-------------|----------|-------------|
| <i>Normalised Rotor Eff</i> | 100% | 98.24% | 96.08% | 93.78% |
| <i>Volute K_{Pl}</i> | 100% | 98.83% | 97.22% | 89.95% |
| <i>Normalised Stage Eff</i> | 100% | 98.68% | 97.03% | 95.33% |
| <i>Normalised MFP</i> | 100% | 98.76% | 96.98% | 94.39% |
| <i>Normalised Torque</i> | 94.49% | 95.76% | 97.46% | 100% |
| <i>Rotor U/c_s</i> | 0.5842 | 0.5819 | 0.5785 | 0.5739 |

Table 5.3: Cycle averaged performance results for 50, 75, 100 and 125 pulsation number at 40Hz pulse frequency

The resulting LE incidence over the pulse cycle is presented figure 5.42. The peak incidence angle was not significantly impacted by the pulsation number with maximum incidence ranging between 16.71° and 13.36° for the 1.25 and 0.5 pulsation number pulses. However, the pulsation number did have a significant impact on the minimum incidence angle achieved with minimum incidence angles of -24.09° , -37.88° , -52.39° and -62.44° achieved for the 0.5, 0.75, 1 and 1.25 pulsation number pulses respectively. This effect is similar to that experience under the range of tested frequencies. The reason for this is that to further increase the incidence to positive values, the absolute velocity (C) must exponentially increase. Alternately, to reduce incidence to more negative value requires smaller changes in absolute velocity (C), refer to figure 1.3.

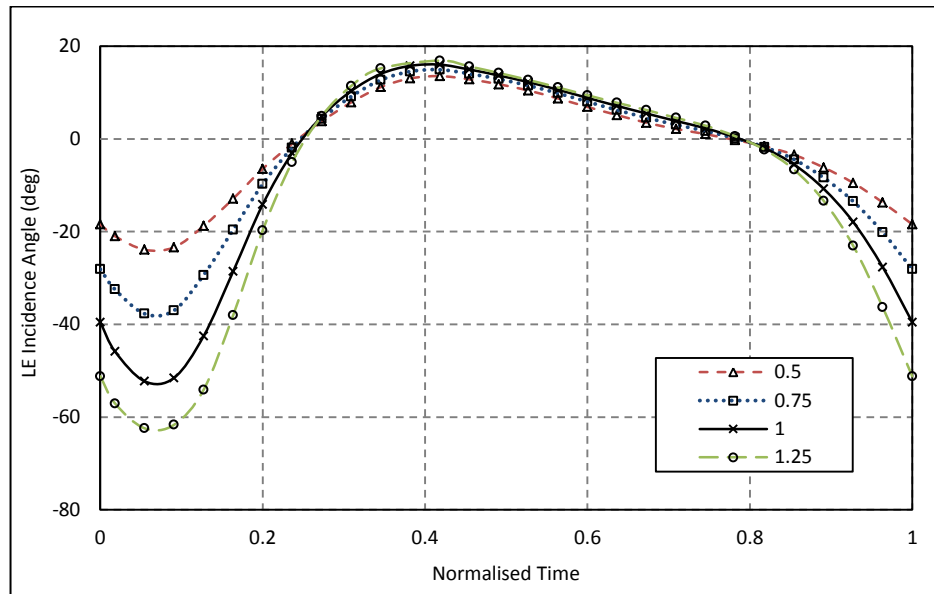


Figure 5.42: Leading edge incidence over the pulse at 50, 75, 100 and 125 pulsation numbers at 40Hz pulse frequency

The variation in incidence over the rotor span at both the minimum and maximum incidence running points for the four tested pulsation numbers are plotted in figures 5.43 and 5.44. As was shown over the range of pulse loads, the variation in LE incidence at the minimum incidence running point exhibited significant changes with pulsation number. The lowest pulsation number, resulted in almost constant incidence from 20% span to the shroud. With increasing pulsation number, the variation over the span increases, with the incidence at the centre of the span tending towards more negative values. This effect was due to the circumferential velocity shifting from negative values towards positive, changing the resulting incidence distribution. The exception is the 1.25-pulsation number case, the variation across the span changes significantly with the incidence at the hub less negative. The cause of this behaviour was hub separation occurring at the low mass flow running point encountered under the large pulsation number. At the maximum incidence running point the distribution over the span remained almost constant in all cases.

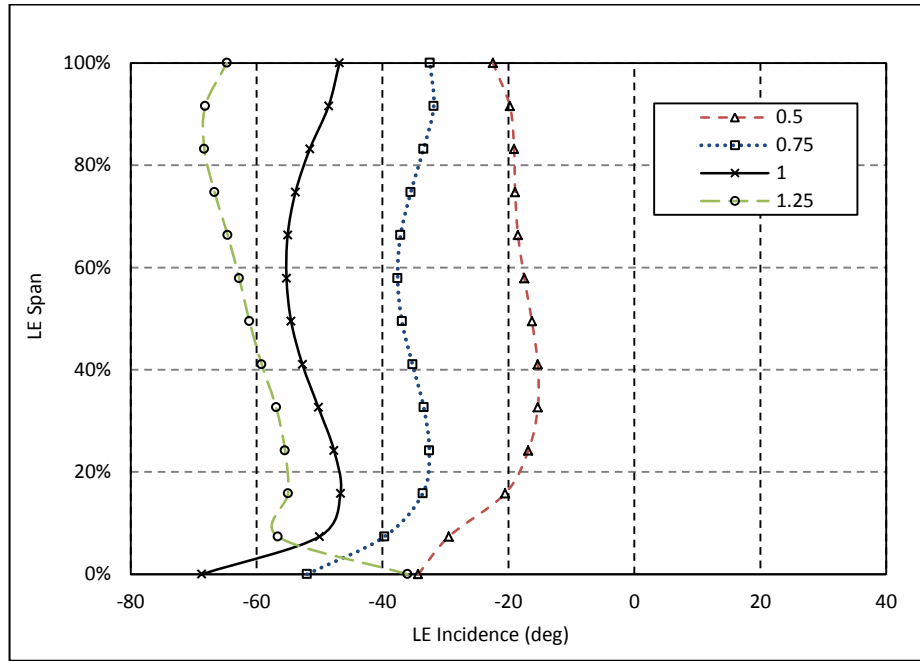


Figure 5.43: LE incidence over the blade span at minimum incidence under four pulsation numbers at 40Hz pulse frequency

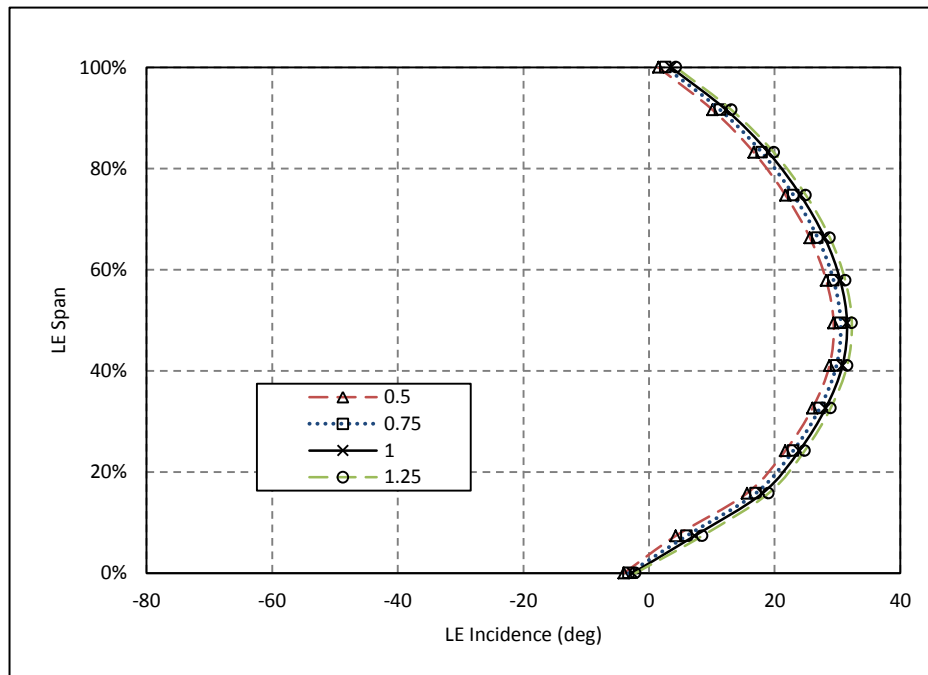


Figure 5.44: LE incidence over the blade span at maximum incidence under four pulsation numbers at 40Hz pulse frequency

5.5 CHAPTER CONCLUSIONS

This chapter has presented the results of a study investigating the impact of pulsation frequency, load and pulsation number on a mixed flow turbine within a radial flow housing. Particular focus was placed on the impact of pulsating inlet flow conditions on LE incidence. It was found that LE incidence varies significantly over the blade span and that the variation changes over the course of the inlet pulse. At low pressure ratio points within the pulse, complex secondary flow structures were found to develop early in the volute. However, at high mass flow running points such secondary flow structures were suppressed. Despite this, significant span-wise incidence variation was still observed.

It was also shown that the phase difference between inlet mass flow and total temperature resulted in rotor inlet phase differences between relevant flow properties. This resulted in the isentropic energy available at the rotor inlet being out of phase with the incidence angle. Therefore, the maximum LE loss did not necessarily occur at the peak energy availability. This effect was also found to be dependent on pulse frequency. As the boundary condition was extracted from a one-dimensional engine model, the phase difference between the inlet properties is only as accurate as the 1D modelling approach. However, the same phase shift was also present in a study by Roclawski et al., (2014) using a validated engine model. However, the authors did not note the difference, nor did they explore its impact.

Pulsation frequency, load and pulsation number resulted in significant changes to the magnitude and distribution of incidence over the LE span at low mass flow running points. However, towards the pulse peak the magnitude of LE incidence and its span distribution was almost constant under all frequencies, loads and pulsation numbers. Therefore, optimisation of a mixed flow rotor for such conditions may provide optimal performance over a wide range of pulsating operations.

6 ANALYSIS OF TILTED VOLUTE HOUSING

From the literature survey it was concluded that the impact of volute tilt has not been satisfactorily studied in the available literature. While tilted volutes have appeared, no works attempted to isolate the impact of tilting the volute to investigate the impact on performance. Furthermore, in the previous chapter, investigation into the performance of a mixed flow rotor in a radial volute housing showed clear signs of poor flow turning ahead of the rotor limiting the mixed flow effect achieved.

This chapter first defines a tilted housing design. The performance of this design is then compared against that of a radial volute under both steady state and pulsating flow conditions over a range of pulsating conditions and volute A/r 's.

6.1 DEFINITION OF THE TILTED HOUSING DESIGN

Volute design is driven by the ratio of the cross sectional area to the radius of the volute passage centre (A/r ratio). The A/r ratio controls the rotor inlet flow angle and usually varies linearly around the volute passage (Chapple et al., 1980); (Gu et al., 2001)). This relationship is based on assumptions of one-dimensional, incompressible and free vortex flow. And is discussed in section 2.1.3.

The volute designed for use with a mixed flow rotor incorporates a tilt angle. The aim in introducing housing tilt was to reduce flow turning, particularly along the shroud contour, reducing loss and providing a reduced flow cone angle.

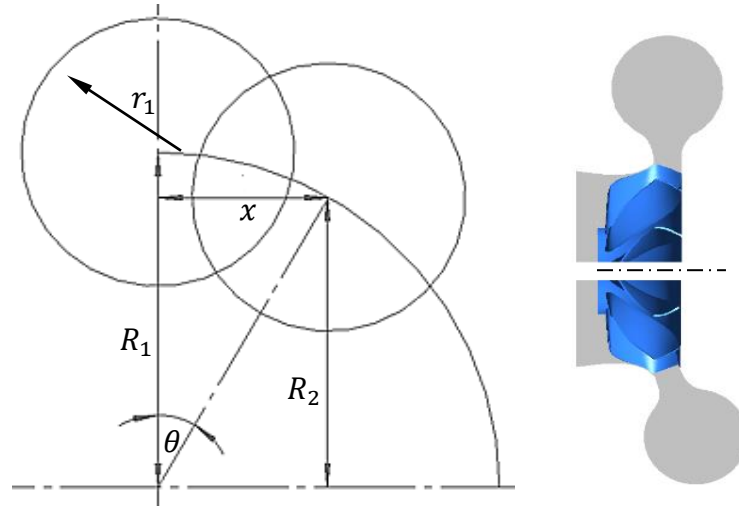


Figure 6.1: tilted volute definition and cut plane of resulting flow passage of both radial and tilted volutes

Figure 6.1 presents the new tilted volute design. The tilted volute is positioned at an angle of θ to the radial volute. The axial (x) and radial (R_2) positions of the tilted housing in relation to the radial housing at the base section are defined as:

$$x = \sin\theta R_1 \quad (76)$$

$$R_2 = \cos\theta R_1 \quad (77)$$

With progression around the volute azimuth angle the axial position (x) changes expressed as -

$$x^* = \sin\theta r_1 - (r_1 - r^*) \quad (78)$$

Where x^* is the axial distance at a given azimuth angle, r_1 is the volute cross sectional radius at the base section and r^* is the volute cross sectional radius at a given azimuth angle. This method produces a spiralled volute centroid. The tilt angle introduced here is 20° to match the blade cone angle and improve the mixed flow effect.

Tilting the volute reduces the radius from R_1 to R_2 as illustrated in Fig. 6.1. The implication of this is that the volute A/r increases. From a design perspective, this can mean one of two things:

- That the volute area can be reduced correspondingly to maintain a constant A/r for a smaller housing area.
- The volute area can remain constant resulting in a larger A/r for a given volute area. Hence allowing A/r manipulation without increasing the radial dimension of the turbine

The tilted volute design has therefore introduced an extra degree of freedom. In the current study, the volute A/r was kept constant in an attempt to maintain a constant MFP. This ensures aerodynamic similarity between the two designs allowing for a fair comparison. However, exploring the use of tilt to manipulate volute A/r is another aspect that could be explored in future work in an attempt to produce a more compact volute with equal A/r .

6.2 MODELLING OF THE TILTED HOUSING DESIGN

The volute tilt adds a degree of complexity into the computational modelling of the stage. Tilting the housing changes the shape and size of the nozzleless region in the tilted design. Therefore, the position of the interface between the stationary volute domain and the rotating rotor domain shifts. Figure 6.2 illustrates the position of the two interfaces. The position of the interface ensures that the area remains constant and the volute passage length is constant as the entire volute is simply tilted. This results in the nozzleless space in the rotating domain reducing due to the encroaching volute. The domain interface is therefore closer to the blade LE in the tilted design.

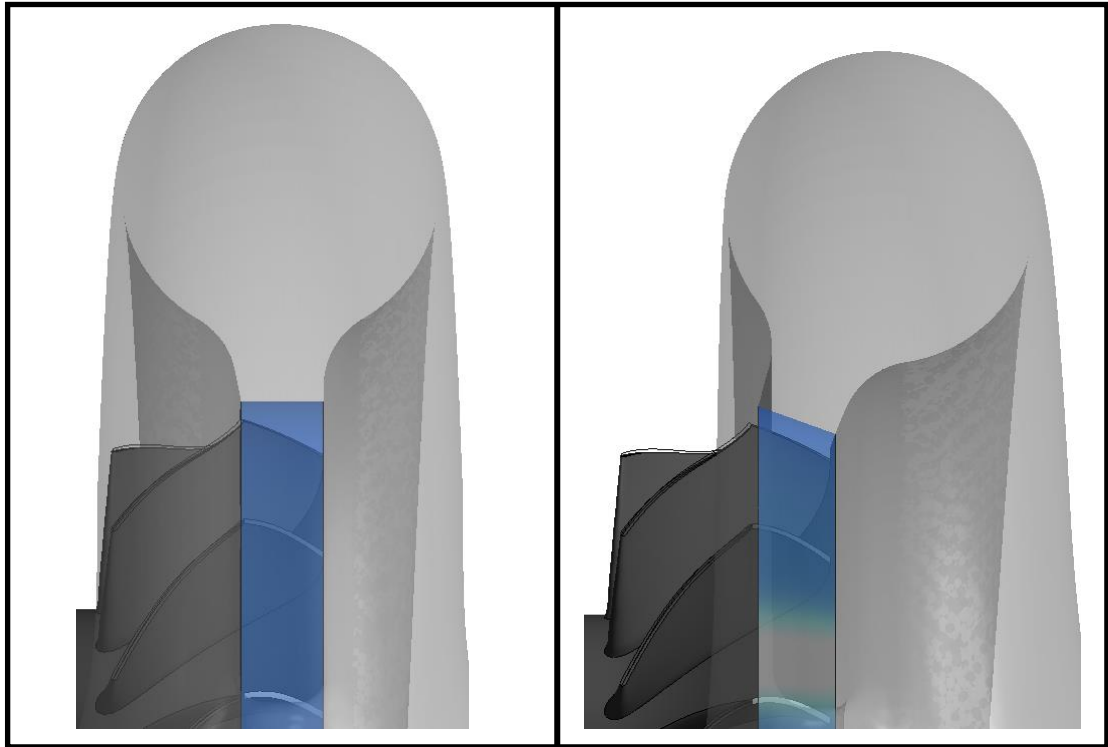


Figure 6.2: Comparison of radial and tilted volute designs interface between stationary and rotating domains

The impact of the interface LE proximity was studied to ensure fair comparisons of the two designs. The tilted volute design was simulated with the tilted interface plane and a comparable radially positioned plane with the same LE proximity as the radial volute design. The results of this comparison showed that the impact of the tilted interface resulted in less than 0.15% variation in efficiency. Furthermore, in terms of domain development and meshing, the tilted interface reduces complexity due to the normal position of the plane with respect to the volute passage. This geometrical constraint improves the mesh quality in the interface region. The impact of the tilted interface was deemed to be small and comparisons of the two designs fair despite the change in interface position.

6.3 PERFORMANCE COMPARISONS STEADY STATE

The stage efficiency results for both the radial and tilted volute designs are presented in figures 6.3-6.5 for the three tested turbine speeds of 70kRPM, 90kRPM and 110kRPM. For all tested turbine speeds, the tilted housing design results in an improvement in stage efficiency. The greatest percentage improvement measured was 1.64% at a turbine speed of 90kRPM. In all cases the performance improvement measure in the presence of volute tilt reduced at lower velocity ratio running points. In addition, no shift in peak efficiency to lower velocity ratios running points was observed. This result indicates that the mixed flow effect has not been substantially increased through tilting the volute despite the measured efficiency improvement.

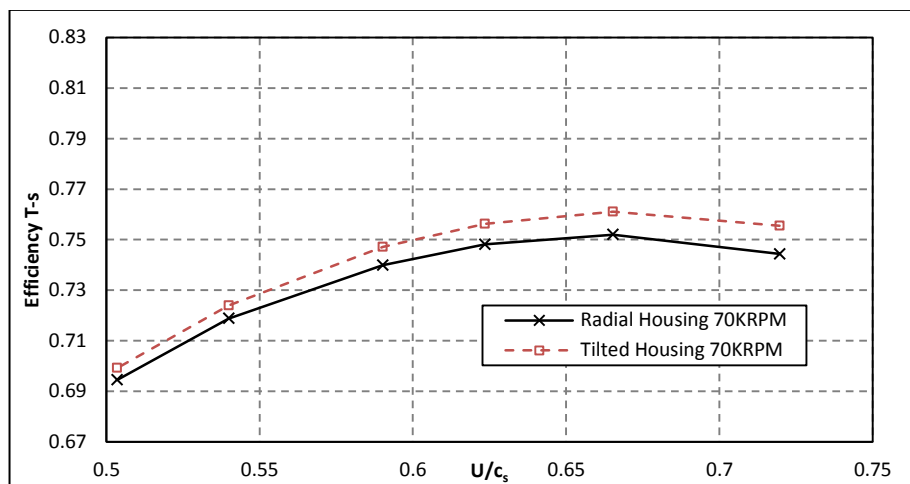


Figure 6.3: Normalised steady state stage efficiency at 70kRPM

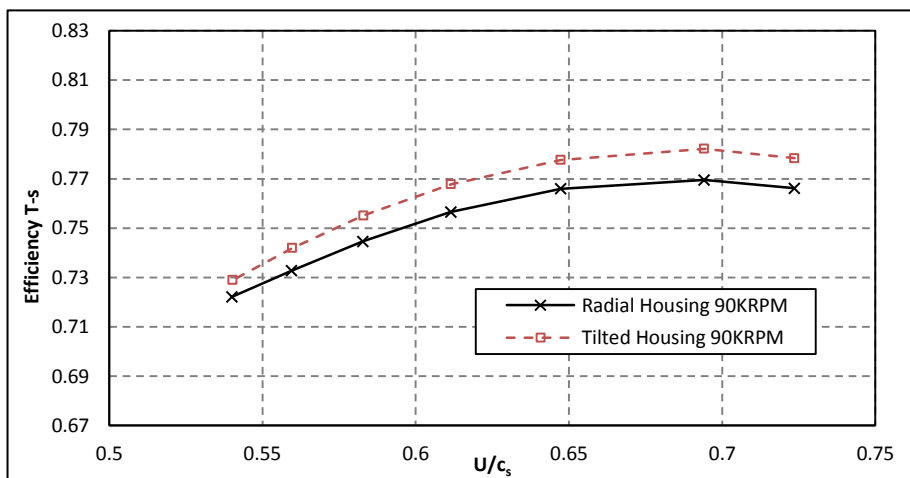


Figure 6.4: Normalised steady state stage efficiency at 90kRPM

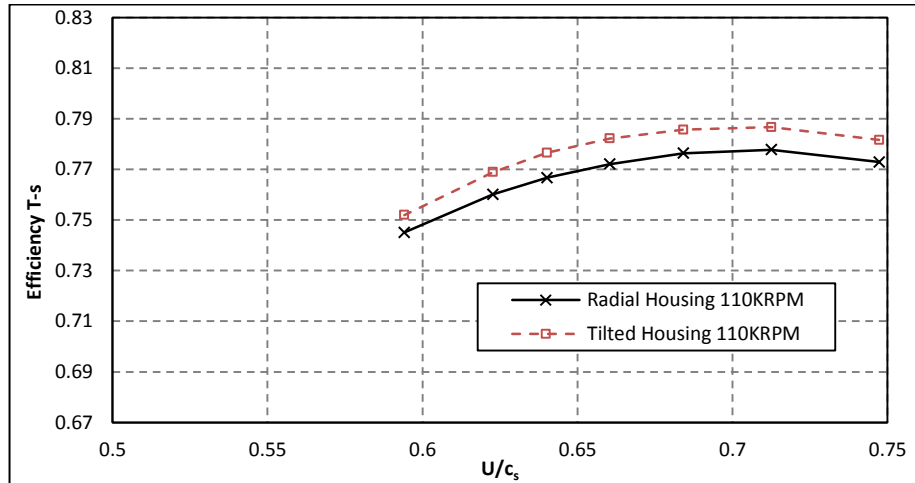


Figure 6.5: Normalised steady state stage efficiency at 110kRPM

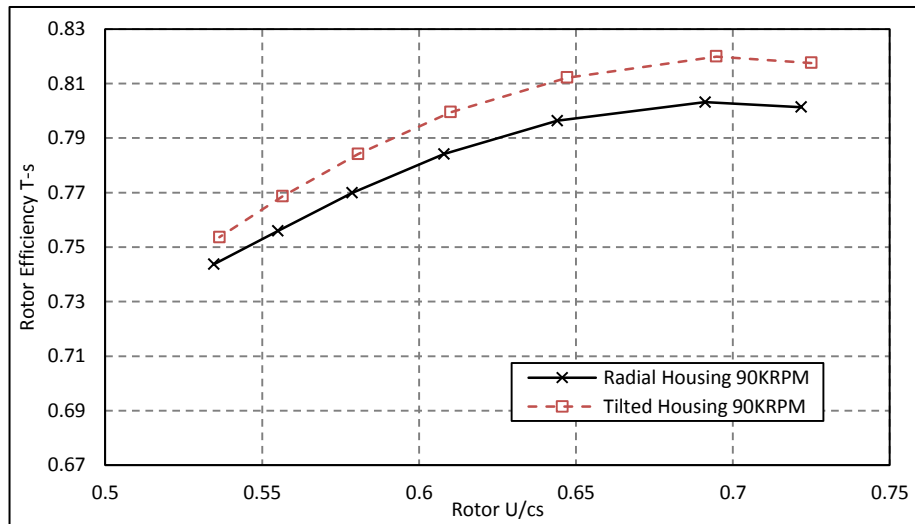


Figure 6.6: Steady state rotor efficiency at 90kRPM

Figure 6.6 compares only the rotor efficiency of the radial and tiled housing designs. In this instance, the difference between the two designs increases to 2.67% for the tilted design over the radial. It is clear that the volute is generating an increased loss in the tilted design, reducing the stage efficiency improvement.

The losses within the volute can be calculated from the volute total pressure loss coefficient which is given in equation 79 -

$$K_{PL} = \frac{P_{01} - P_{01.5}}{P_{01.5} - P_{1.5}} \tag{79}$$

Where P_{01} is the total pressure at the volute inlet, $P_{01.5}$ the total pressure at the volute outlet and $P_{1.5}$ is the static pressure at the volute outlet. Therefore, the total pressure loss coefficient is simply the total pressure loss, normalised by the dynamic pressure at the volute outlet. Figure 6.7 plots the volute total pressure loss coefficient against velocity ratio for both designs. In both cases, as the velocity ratio decreases, the total pressure loss coefficient also reduces indicating better volute performance at lower velocity ratios. The tilted housing design resulted in an increased volute loss compared to the radial volute. The mean increase in pressure loss coefficient over the plotted range is 7%. However, the percentage difference in total pressure loss between the two volutes increases with velocity ratio resulting in a range of 6%-8% over the tested range. Although the change in efficiency in the volute is large, the impact of volute performance on the stage efficiency is small due to the much greater impact of the rotor. As such the greater improvement in the rotor region in the presence of volute tilt, makes up for the increased volute loss and still results in a stage efficiency improvement.

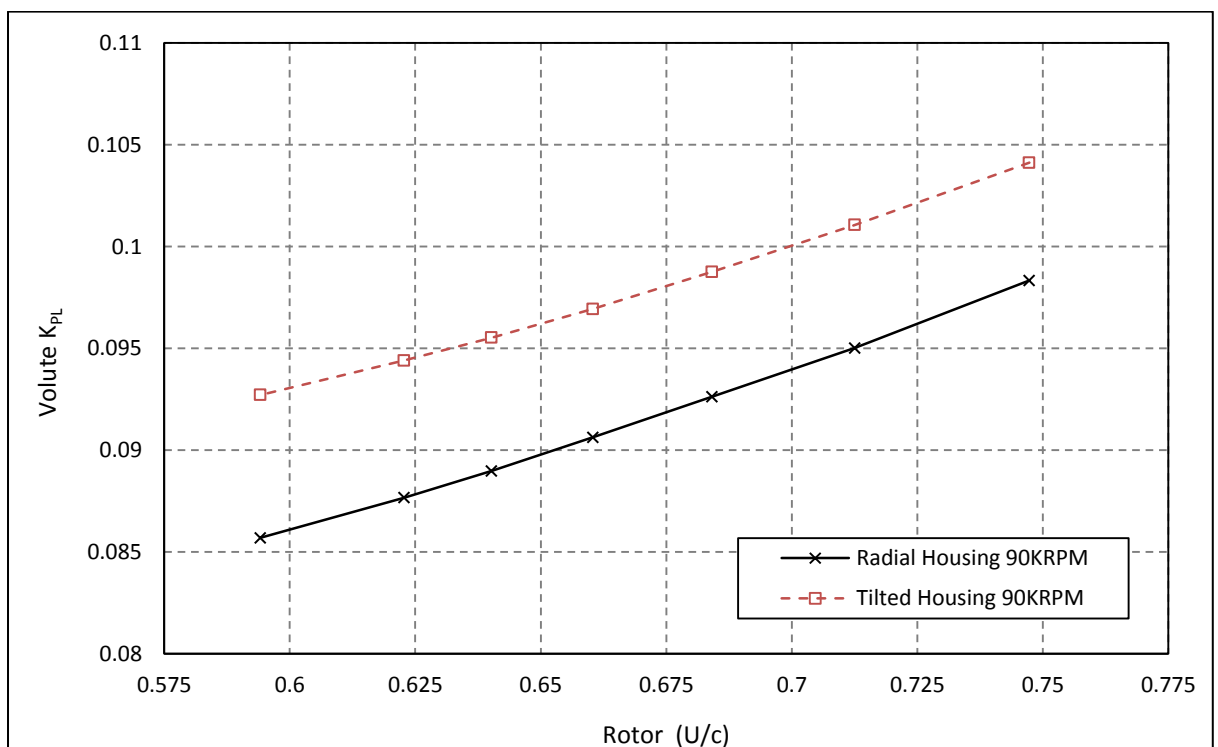


Figure 6.7: Volute total pressure loss coefficient plotted against rotor velocity ratio at 90KRPM

Further to the improvement in efficiency, a small increase in swallowing capacity was observed for the tilted housing design at all tested turbine speeds. The variation in turbine MFP over each of the steady state speed lines is presented in figure 6.8

As stated previously, the volute A/r was kept constant for both designs. This was done to ensure the effect of tilt angle was isolated and to control MFP. However, in the current study a small increase in MFP was found. As A/r is held constant, this variation must be a direct result of the volute tilt angle. However, the variation in MFP was less than 0.5% in all cases and the impact of such a small change was deemed negligible. Therefore, the stages can be said to aerodynamically similar for the purpose of performance comparison.

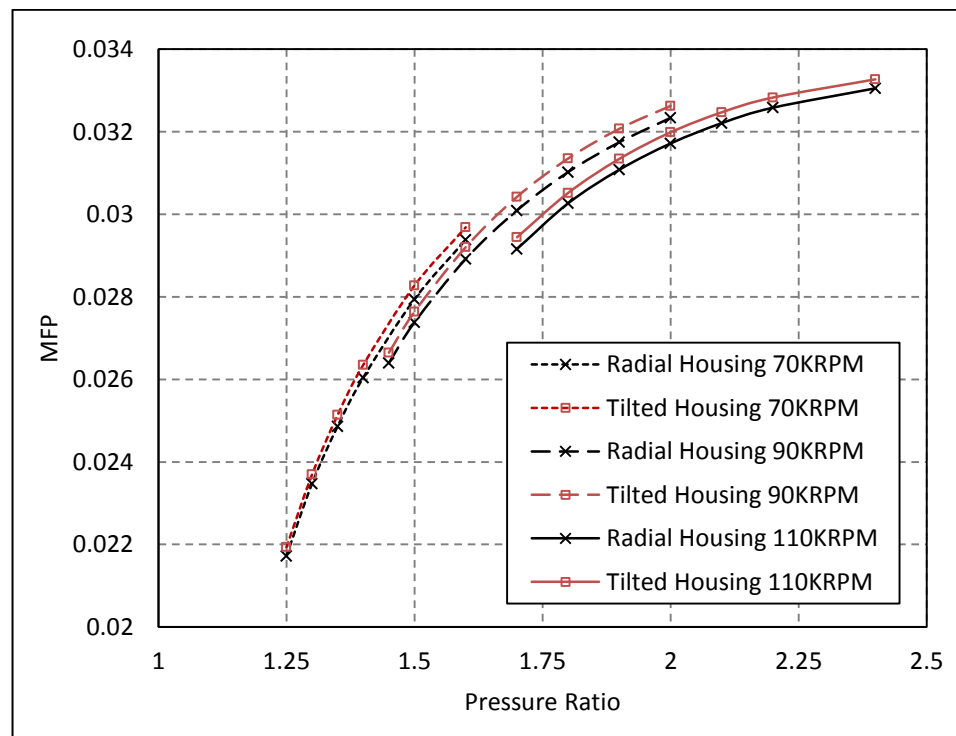


Figure 6.8: percentage MFP difference between radial and tilted designs at 70kRPM, 90kRPM and 110kRPM

6.4 PERFORMANCE COMPARISON PULSATING FLOWS

Similar to the analysis undertaken in chapter 5, the tilted housing design was tested at a range of frequencies, pulsation numbers and pulse loads. The frequencies tested were, 20Hz, 40Hz and 60Hz. The pulsation numbers tested were 0.5, 0.75, 1 and 1.25. The tested pulse loads were low, medium and high (73%, 100% and 127%). At each condition the results of the tilted volute design were compared with those of the aerodynamically similar radial volute.

6.4.1 PULSATION FREQUENCY

Figure 6.9 presents the MFP hysteresis loops under each of the tested pulse frequencies. At all frequencies, the cycle averaged variation in MFP between the three designs was maintained below 0.5% under pulsating conditions to ensure fair comparison.

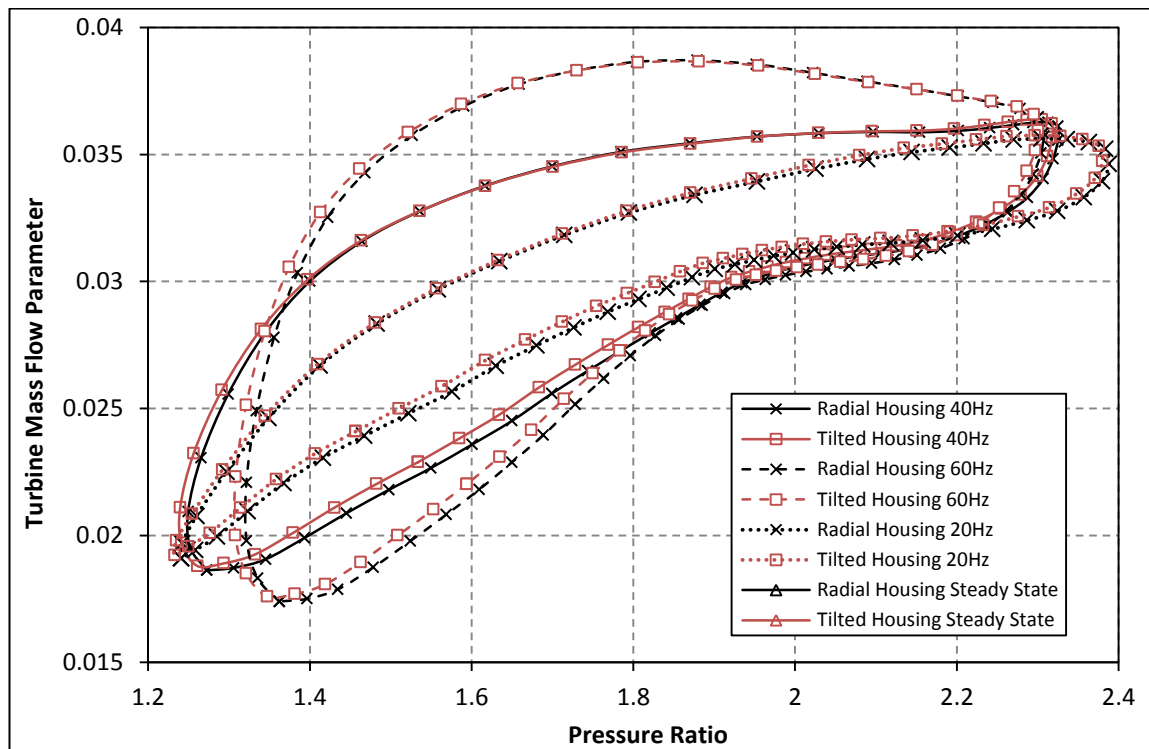


Figure 6.9: MFP vs Pressure Ratio at 20Hz, 40Hz and 60Hz

Figures 6.10 – 6.12 present the rotor efficiency of the radial and tilted volute designs at the three tested pulse frequencies of 20Hz, 40Hz and 60Hz. At all tested

frequencies an increase in efficiency is measured when the housing tilt is present. However, the improvement reduces at all frequencies as the velocity ratio is increased. As the maximum energy is available at lower velocity ratios, performance improvements in these regions would be more beneficial in terms of energy extraction and cycle averaged performance. Meanwhile the increased improvement with the tilt present at higher velocity ratio operating points has little impact on cycle averaged efficiency due to the reduction in available energy.

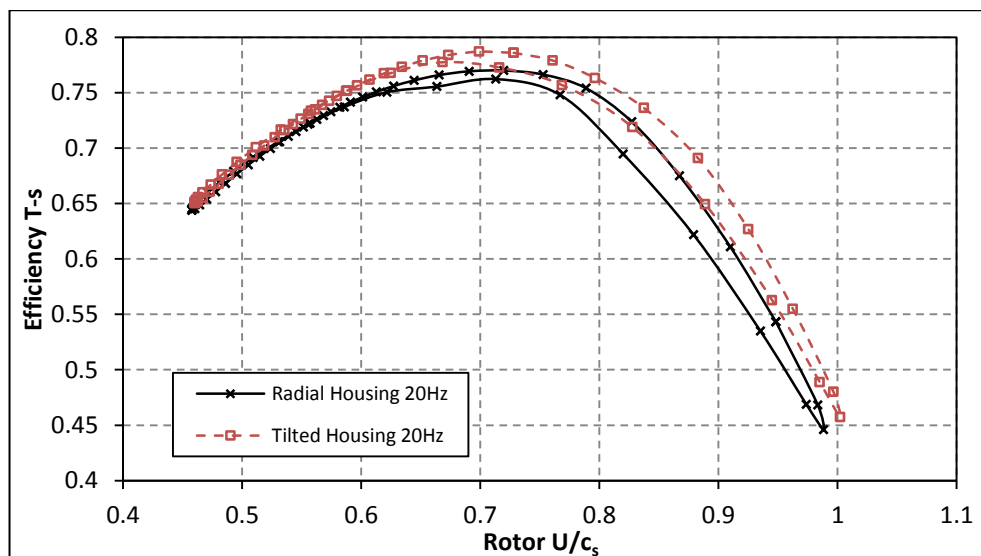


Figure 6.10: Efficiency plotted against velocity ratio 20Hz

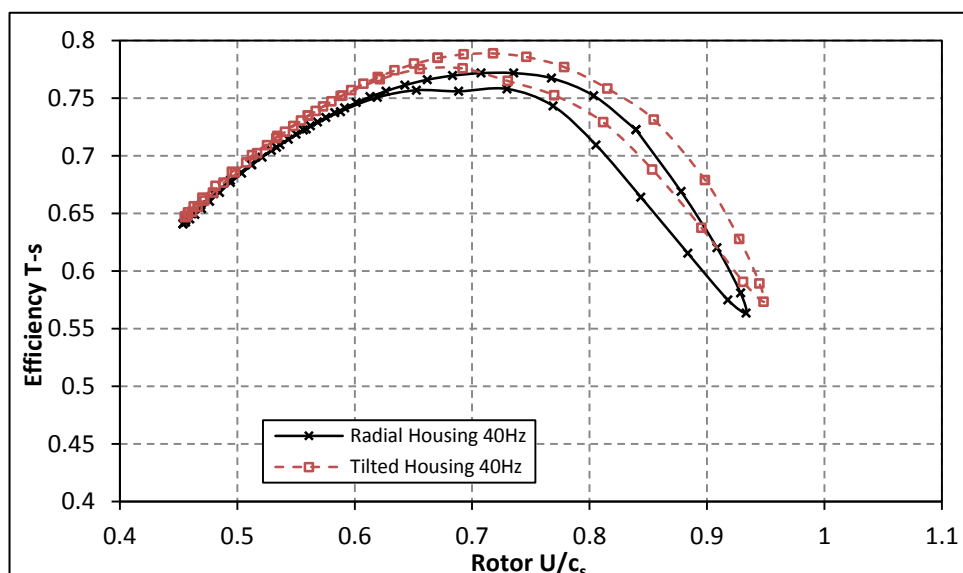


Figure 6.11: Efficiency plotted against velocity ratio 40Hz

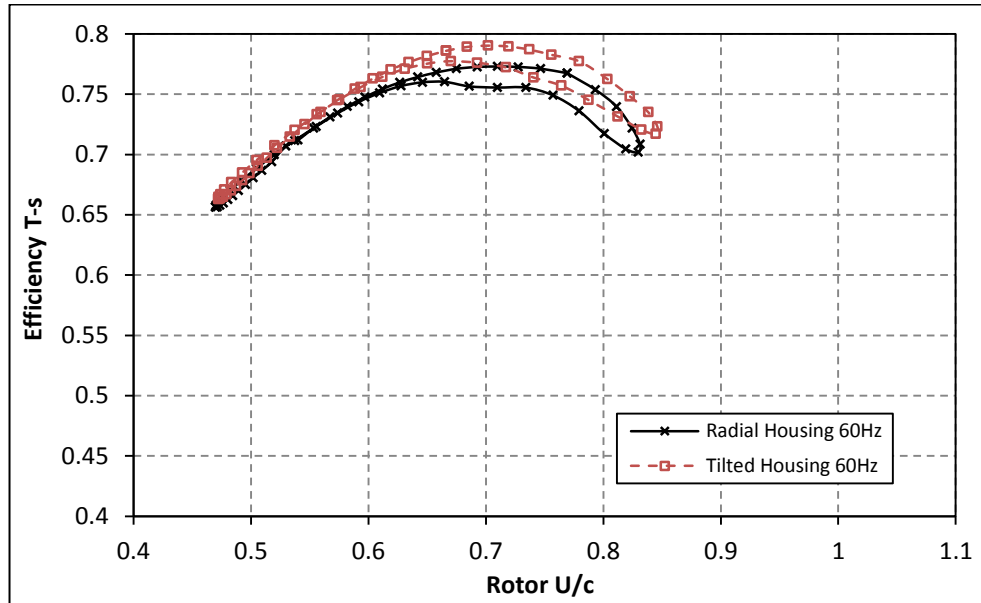


Figure 6.12: Efficiency plotted against velocity ratio 60Hz

In all cases a shift in rotor velocity ratio can be observed with the tilted design operating under a higher range of velocity ratios. This effect is particularly evident at the high end of the velocity ratio spectrum due to the non-linear effect of pressure ratio on velocity ratio. The shift in velocity ratio is the result of lower total pressure at the rotor inlet in the tilted design. This is primarily caused by an increase in total pressure loss through the tilted volute which is quantified in table 6.1 showing up to a 11.38% increase in total pressure loss coefficient in the volute at 60Hz.

Table 6.1 illustrates the efficiency improvement in each case at the peak efficiency velocity ratio and minimum velocity ratio, as well as the improvement in cycle averaged rotor and stage efficiency observed. The maximum improvement in cycle averaged stage and rotor efficiency was 1.160% and 1.450% percent respectively at the 20Hz frequency. The improvement in efficiency at the minimum velocity ratio was found to be approximately 1% at all frequencies.

| | <i>Frequency</i> | | |
|---|------------------|-----------|-----------|
| | <i>20</i> | <i>40</i> | <i>60</i> |
| <i>Cycle Avg Rotor Eff increase (TV-RV)</i> | 1.450% | 1.421% | 1.397% |
| <i>Cycle Avg Stage Eff increase (TV-RV)</i> | 1.160% | 1.145% | 1.152% |
| <i>Peak rotor Eff increase (TV-RV)</i> | 2.163% | 2.167% | 2.192% |
| <i>Eff at min U/c increase (TV-RV)</i> | 1.005% | 1.035% | 1.019% |
| <i>K_{PL} (TV-RV)</i> | 9.27% | 10.62% | 11.38% |

Table 6.1: Tilted volute (TV) vs radial volute (RV) performance parameters

Figures 6.13 – 6.15 present the rotor LE incidence angles alongside the instantaneous rotor total-to-static efficiency. The incidence angles in the tilted design are consistently lower than those in the radial design. This is beneficial at low velocity ratio running points where there is a large positive incidence. At high velocity ratios, increasingly negative incidence angles are a disadvantage. Despite this, the tilted housing achieves greater rotor efficiency over the entire pulse.

With increasing frequency, the range of both LE incidence and rotor efficiency reduce in a similar manner in both the radial and tilted cases. The same is also evident for the resulting pulse shapes. Therefore, it appears that the volute tilt has no significant effect on the primary pulse propagation through the volute.

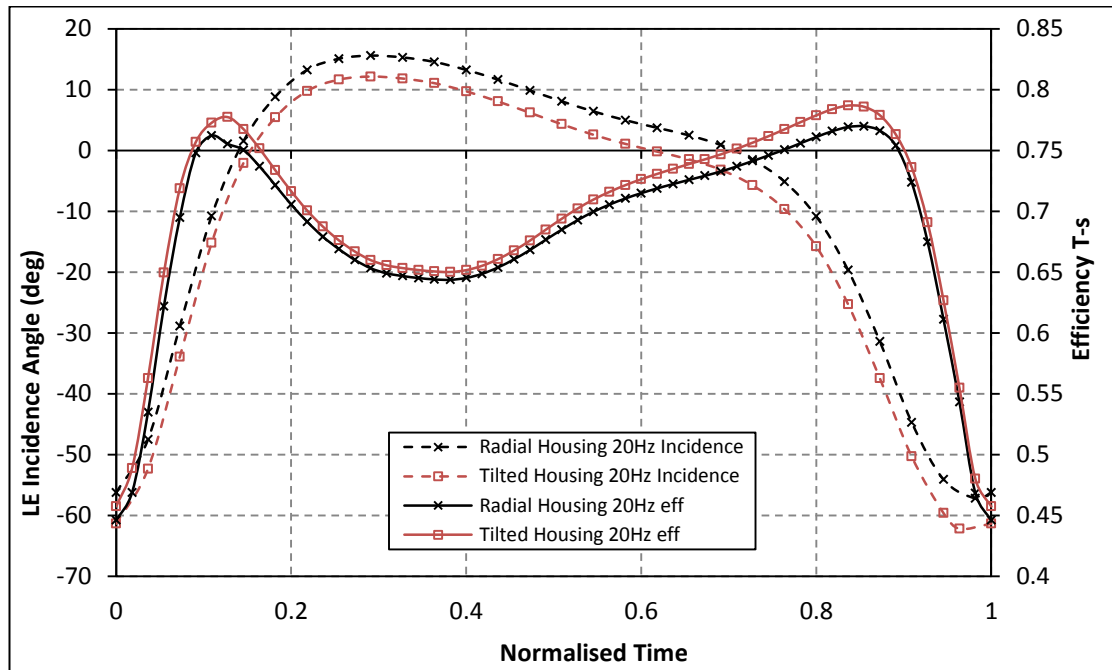


Figure 6.13: Instantaneous LE incidence angle and normalised rotor efficiency vs. normalised time 20Hz pulse frequency

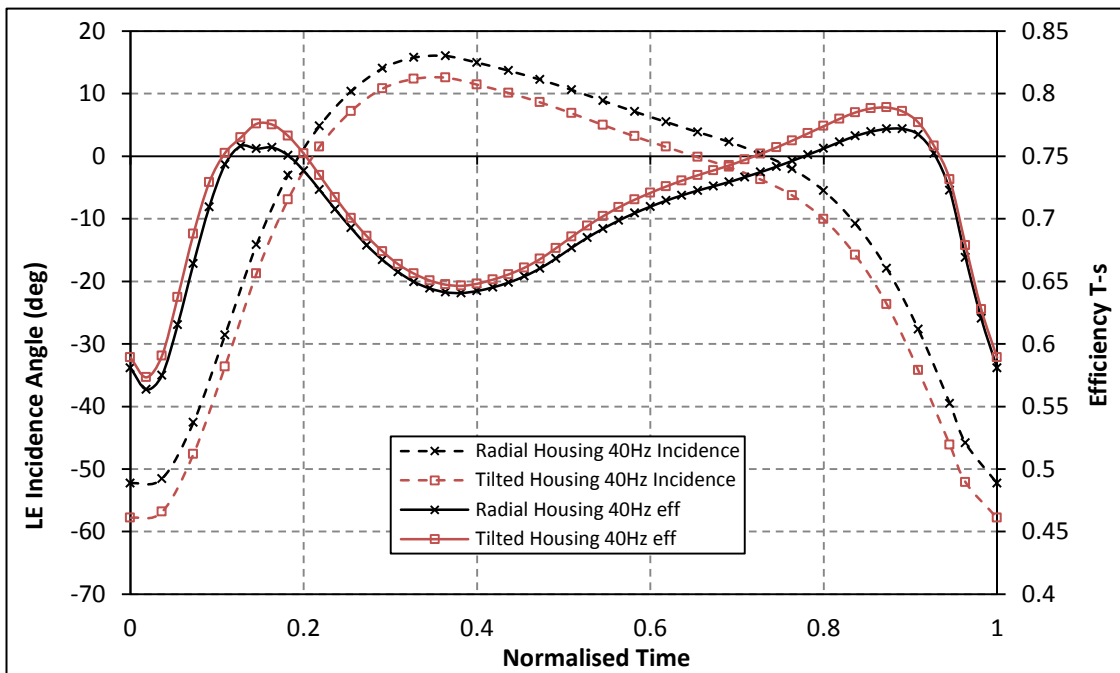


Figure 6.14: Instantaneous LE incidence angle and normalised rotor efficiency vs. Normalised time 40Hz pulse frequency

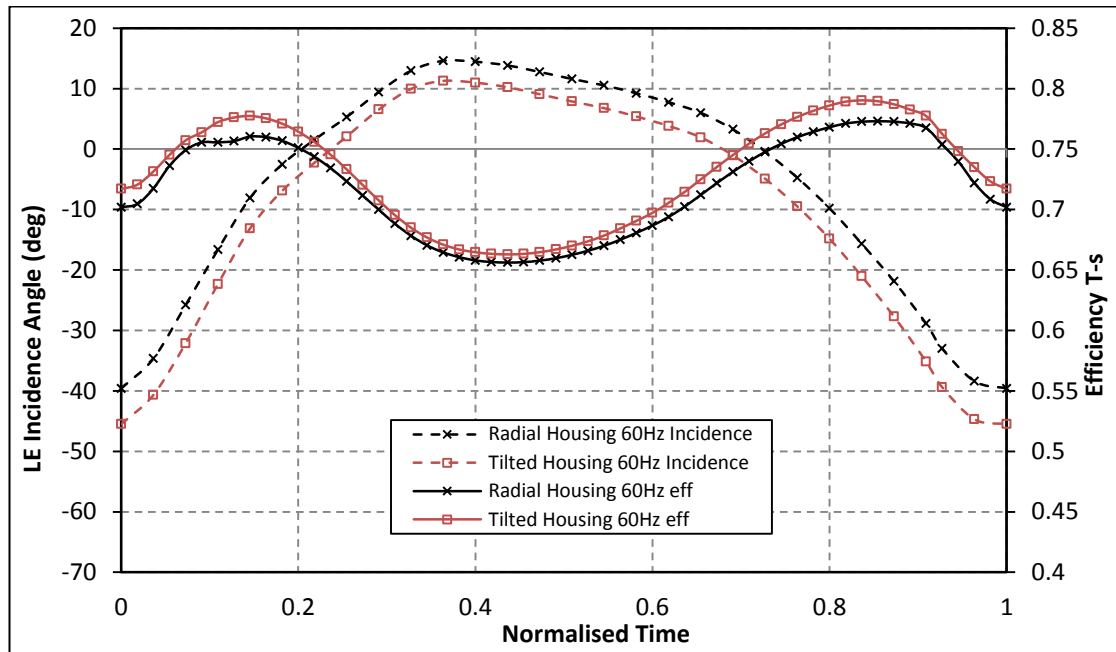


Figure 6.15: Instantaneous LE incidence angle and normalised rotor efficiency vs. Normalised time 60Hz pulse frequency

One of the aims of the tilted volute design was to improve the LE flow distribution in terms of the axial flow component achieved. It was observed in the standard volute design that the flow cone angle was less than satisfactory and that a significant variation from hub to shroud existed (see section 5.2.2). This limits the extent of the mixed flow effect. Figures 6.13-6.15 show that the tilted housing resulted in a reduction in LE incidence between 3°-7° over the pulse.

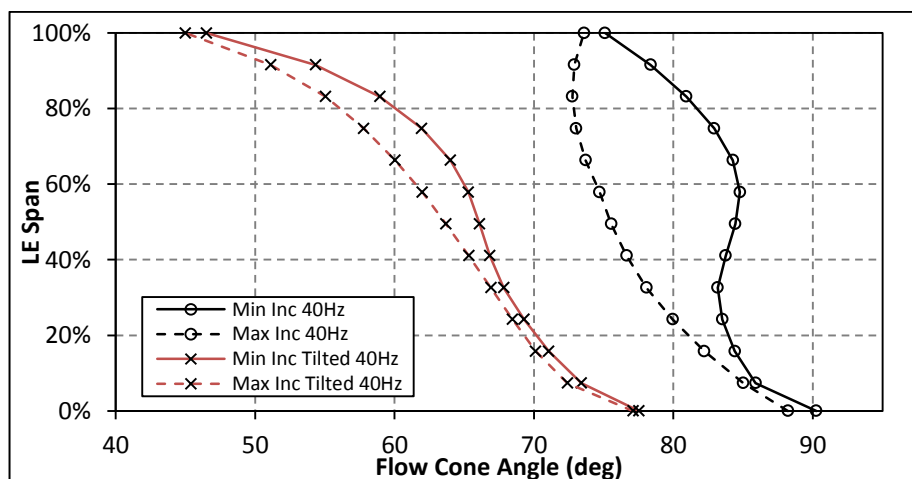


Figure 6.16: LE flow cone angle in the radial and tilted volute variants at minimum and maximum incidence running points

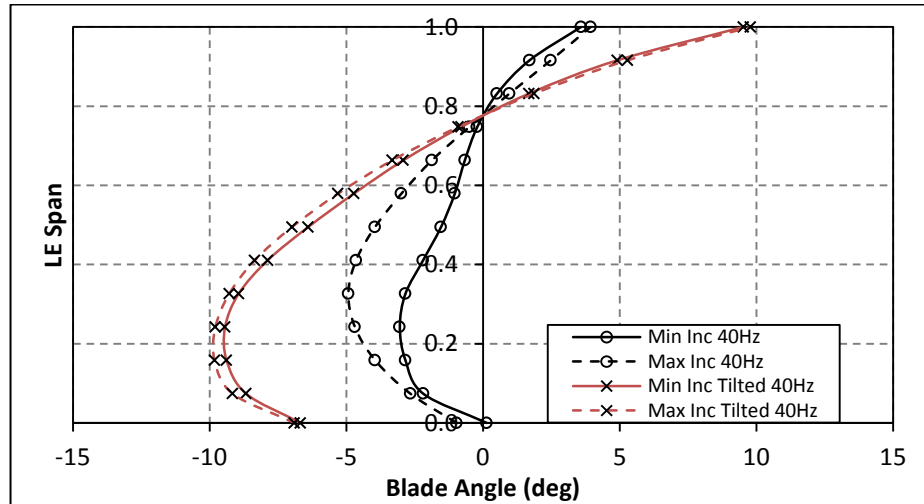


Figure 6.17: LE blade angle in the radial and tilted volute variants at minimum and maximum incidence running points

Figure 6.16 compares the flow cone angle over the LE span at minimum and maximum incidence points within the pulse for the radial and tilted volute designs. The tilted housing design produces a much greater axial flow component but the span-wise variation in flow angles is also greater. In the radial case the flow turning at the hub is very poor, but this increases towards the shroud. In the tilted design the flow cone angle across the span is significantly smaller. The increased variation from hub to shroud results in cone angles as low as 45° occurring close to the shroud. The variation in flow cone angle between the minimum and maximum incidence running points is also smaller in the tiled housing design. This is because the radial housing does not act to turn the flow into the rotor, instead the pressure difference acting into the rotor acts to turn the flow. Therefore, as the pressure ratio changes the amount of flow turning also changes resulting in a notable change over the pulse. Alternately, as the tilted design passage turns the flow, the reliance on pressure ratio to produce the flow turning is reduced.

The resulting blade angles are presented in figure 6.17. At the maximum incidence running point, the tilted housing design achieved a minimum blade angle of approximately -10° and -9.5° at minimum incidence. In comparison, the radial turbine achieved blades angles of only -5° and -3° at the maximum and minimum incidence running point respectively due to the reduced flow turning ahead of the LE. The impact

of the varying camber is obvious as the blade angle varies from negative at the hub to positive at the shroud, this effect is more significant in the tilted volute case as the flow cone angle is smaller across the entire LE span. At peak incidence, negative blade angles are favourable, to reduce incidence and reduce suction surface (SS) separation. The reverse is true at minimum incidence. However, as the maximum pulse energy is available to peak incidence running points, improvements in this region are more beneficial in terms of cycle averaged performance.

The LE incidence achieved by both designs is presented in figure 6.18-6.20 for each of the pulse frequencies. The result of the change in blade angle causes the incidence from the hub up to 75% span in the minimum incidence case and 65% in the maximum incidence case, to be lower when the housing tilt is present. The only exception is the incidence very close to the hub surface in the 20Hz and 40Hz cases at minimum incidence. The change in the distribution at this local point can be explained by the increased hub separation present in the tilted design. Towards the shroud, as the negative LE camber reduces, and eventually becomes positive, the reduction in incidence achieved from the tilt reduces and eventually gives rise to an incidence increase. At maximum incidence, the peak angle occurs at a larger span position in the tilted case (approximately 60% span) while the incidence distribution is symmetrical in the radial case. This effect can be attributed to the asymmetry introduced by the housing tilt and the blade angle distribution making the incidence more negative towards the hub. At the minimum incidence operating point, the passage minimum incidence angles occurred at lower span-wise positions in the tilted case. Again, this effect can be explained by the blade angle distribution with the more negative blade angle in this case shifting the peak negative incidence angles to lower span positions.

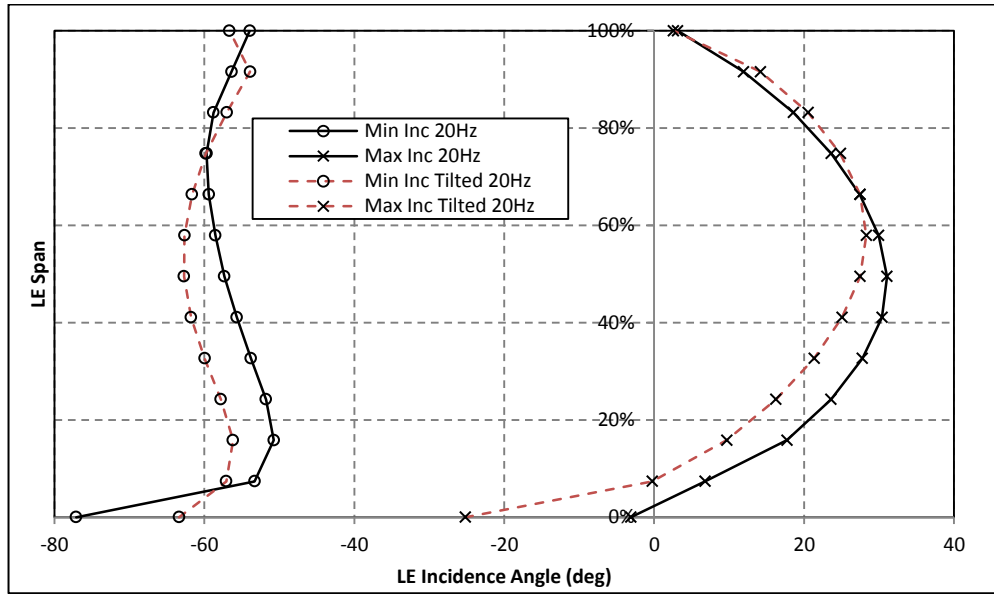


Figure 6.18: LE incidence at minimum and maximum incidence in the radial and tilted volute variants 20Hz

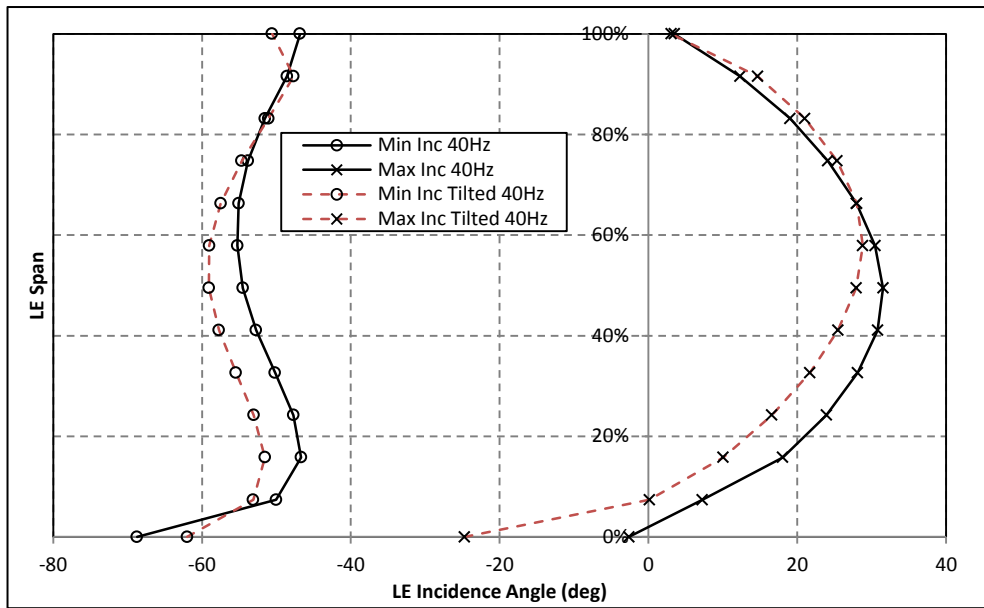


Figure 6.19: LE incidence at minimum and maximum incidence in the radial and tilted volute variants 40Hz

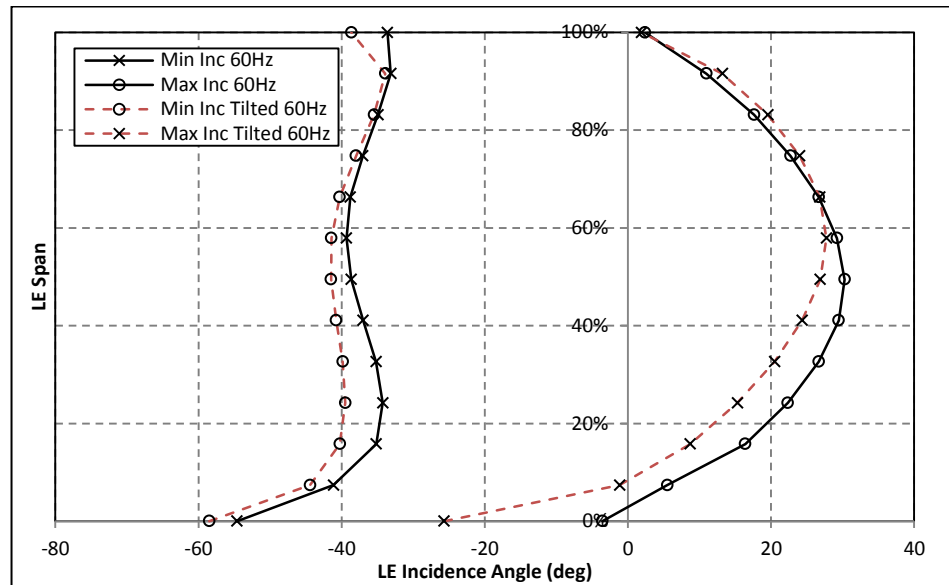


Figure 6.20: LE incidence at minimum and maximum incidence in the radial and tilted volute variants 60Hz

The variation in LE incidence over the blade span is the result of flow development in the volute as was explained in chapter 5. Figures 6.21 and 6.22 compare the development of volute flows in the radial and tilted volute designs at minimum and maximum incidence. The contours are plotted on planes cut through the volute passage showing the difference between the radial volute internal geometry, and the tilted volute geometry which is angled 20° in the anticlockwise direction. The contour plots represent the meridional component of velocity. In the radial case this means radial velocity but in the tilted volute design this is the velocity component acting normal to the volute exit plane (20° to the radial component).

The secondary flow development is more prevalent in at the minimum incidence running point in both designs. The flow structures at this running point in the tilted housing design show clear asymmetry with two vortices forming towards the hub side of the volute in the 90° plane. The contour plot in the tilted design shows significantly greater meridional velocities towards the hub side of the volute wall. This effect can be attributed to the housing tilt influencing the Dean effect as the volute walls in the tilted case turn the flow axially. The greater velocity gradient between the wall and central passage velocities towards the hub side of the volute span leads to greater vortex development. The reduced wall velocities on the shroud

side of the volute span result in lower velocity gradients and hence there is no vortex development.

In comparison, the vortices in the radial volute show span-wise symmetry due to the symmetry in the passage velocities. Furthermore, the vortices in this case develop earlier in the volute and clear vortices breakdown ahead of the 90° plane.

At the maximum incidence running point, no vortex development occurred in either volute design despite the significant variation in meridional velocity present across the volute span. The significant asymmetry of meridional velocity at the volute exit in the tilted case at this running point is the cause of the shift in peak incidence towards higher span positions shown in figures 6.18-6.20.

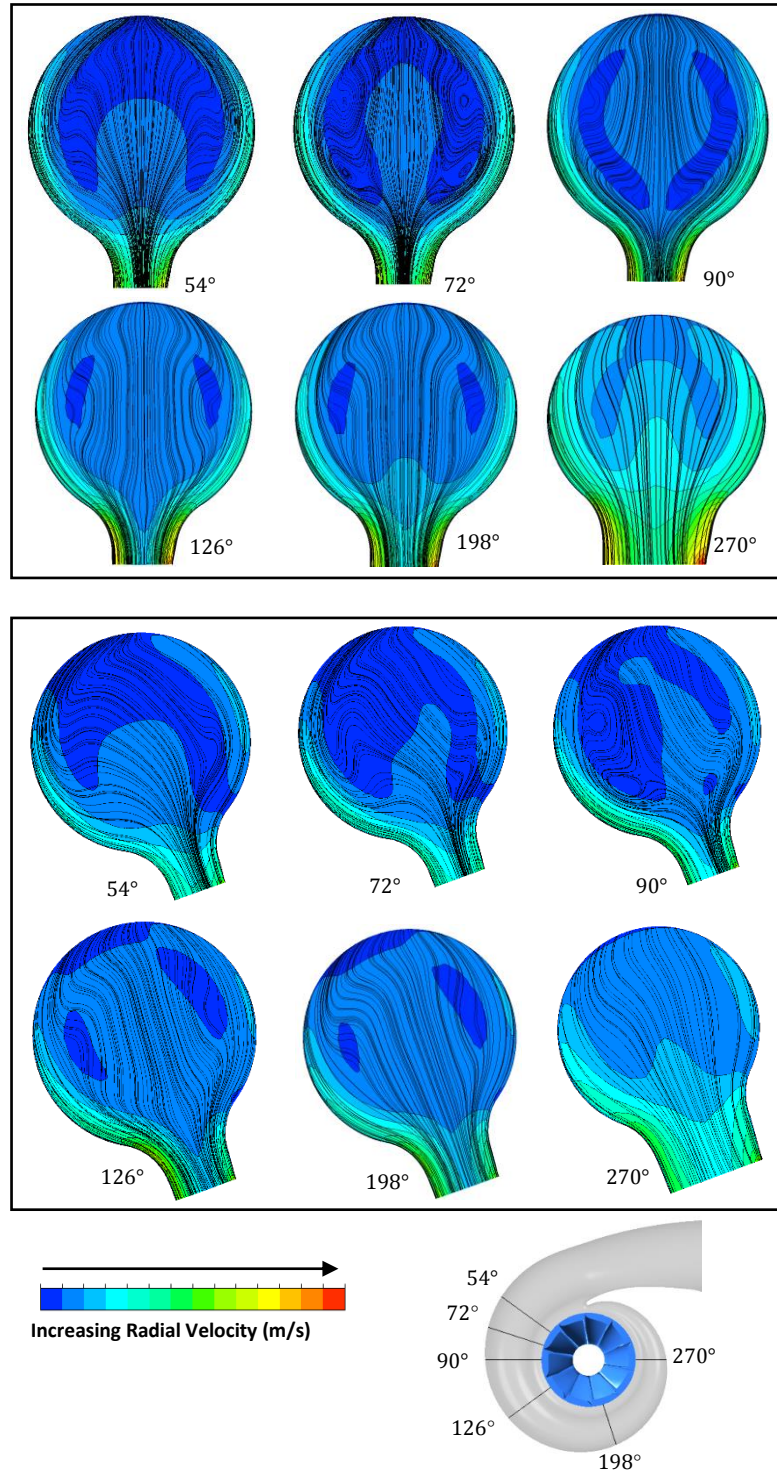


Figure 6.21: Volute secondary flow structures around volute circumference. Radial and 20° tilted volute design 40Hz pulse frequency minimum incidence

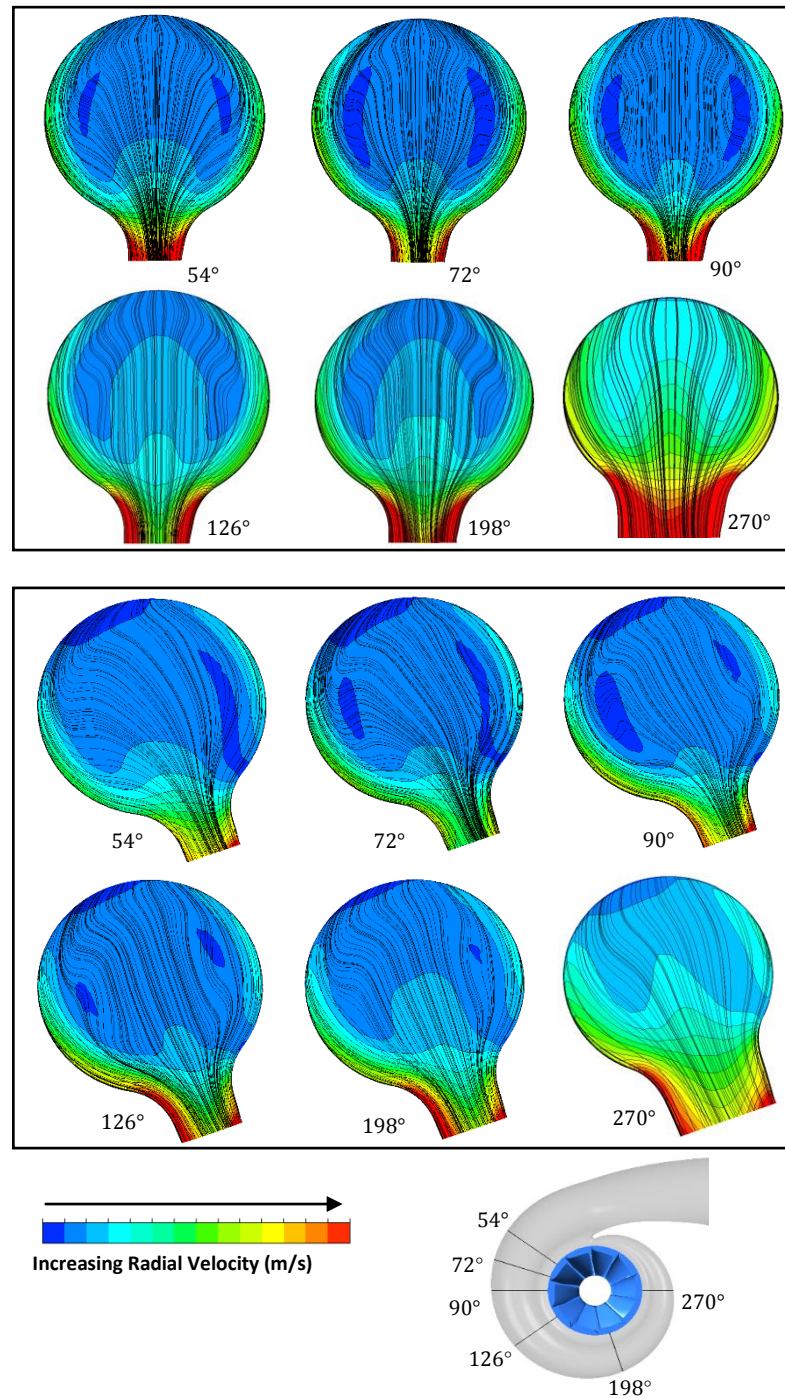


Figure 6.22: Volute secondary flow structures around volute circumference. Radial and tilted 20° volute design 40Hz pulse frequency maximum incidence

In the tilted housing design, the Dean effect is evident, as in the radial case. The centripetal force exerted on the flow acts radial inwards from the outer radius of the volute. In the tilted design the maximum radial point is not positioned on the plane of

symmetry. The position of this point is where the streamlines develop from in figures 6.21 and 6.22. This leads to notable changes in the streamline paths from the volute outer position to the volute exit around the hub and shroud sides of the volute. This results in a notable change in the flow acceleration around the volute walls between the two cases.

The pressure distribution in the volute shown in figure 6.23 is similar in both the radial and tilted volute designs. In both cases the pressure distribution acts radially inward over most of the volute passage. Towards the volute outlet the pressure distribution in the titled housing turns in the axial direction producing the axial flow component and hence, the increased mixed flow effect. The combination of both the pressure and Dean effect acting radially, in the tilted passage results in the introduction of asymmetrical flow development. Furthermore, the axial movement of the passage through the volute spiral means that the flow volute outer walls turn the flow axially causing an acceleration over the volute span further contributing the asymmetry of the volute flows.

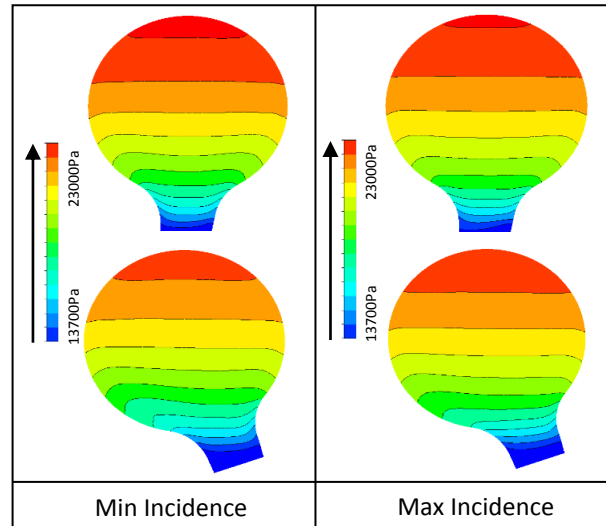


Figure 6.23: Volute pressure distribution in the radial and 20° tilted volutes at minimum and maximum incidence running points

The development of the volute secondary flows is shown in more detail over the pulse period in figure 6.24. Vortices are present in both the radial and tilted volute designs at points 1 and 2 within the pulse, which correspond to minimum mass flow

and during the volute filling process. The vortices present in the radial volute occur only at the 72° plane and breakdown ahead of the 90° plane. Alternately, in the tilted case the vortices are only present in the 90° plane. A clear lack of symmetry of the streamline is clear at all points within the pulse in the tilted variant.

Comparing points 2 and 4 shows that despite a constant volute outlet mass flow, the flow structures within the volute can differ significantly in both the radial and tilted volute designs. This effect is due to the volute hysteresis. During the volute filling process (point 2) secondary flow structures clearly form in the volute at the 72° plane in the radial design and at the 90° plane in the tilted design. However, during the volute emptying process (point 4) when flow is accelerating out of the volute into the rotor, the presence of secondary flow structures reduces.

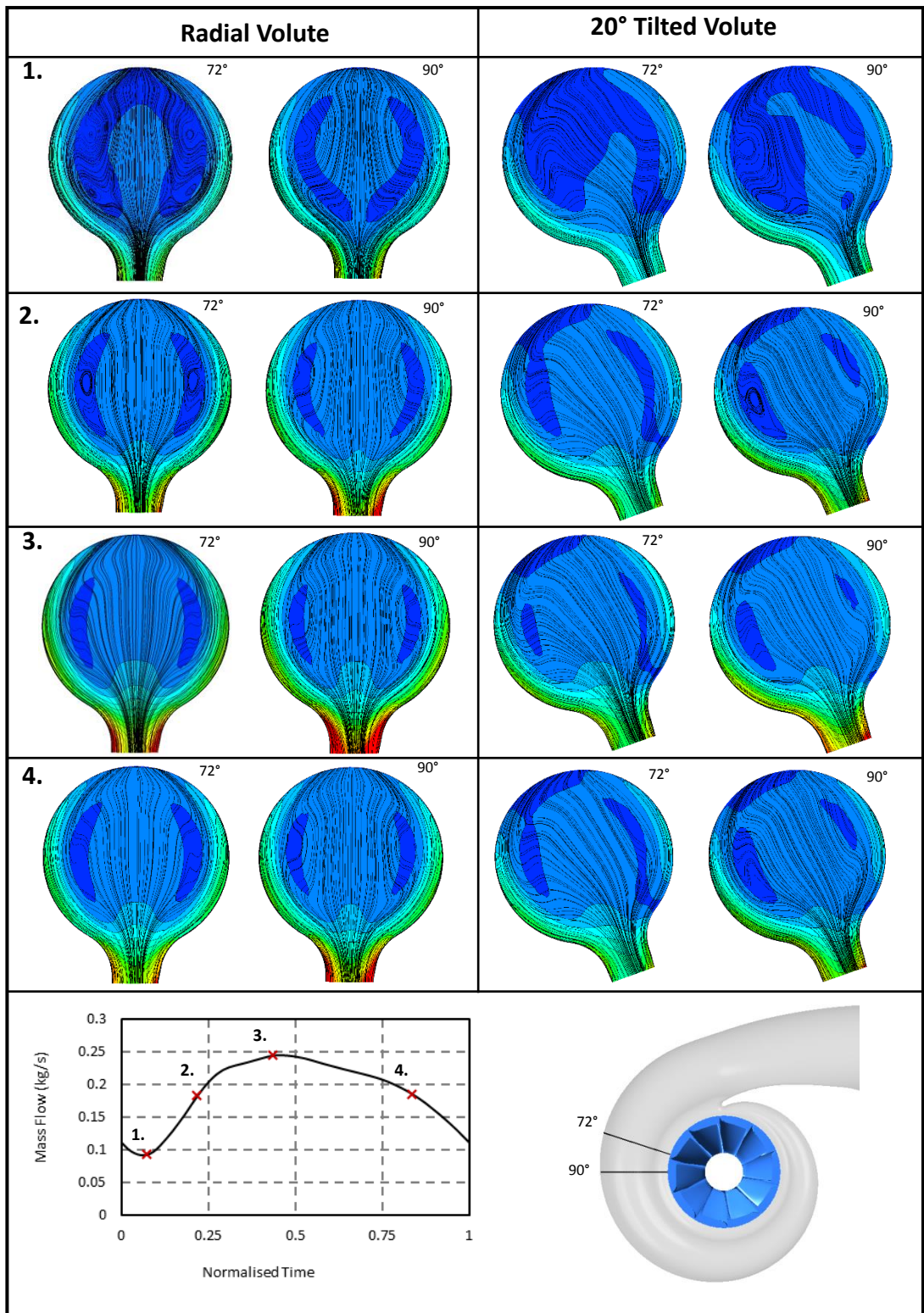


Figure 6.24: Streamline and contour plots at 72° and 90° planes showing the development of volute flows over the pulse period.

To assess the loss mechanisms within the rotor region, entropy generation through the passage was investigated using a similar approach to that implemented by Newton, (2014). The loss within each region can be attributed to a dominant mechanism giving a greater understanding of the physics behind the performance improvements.

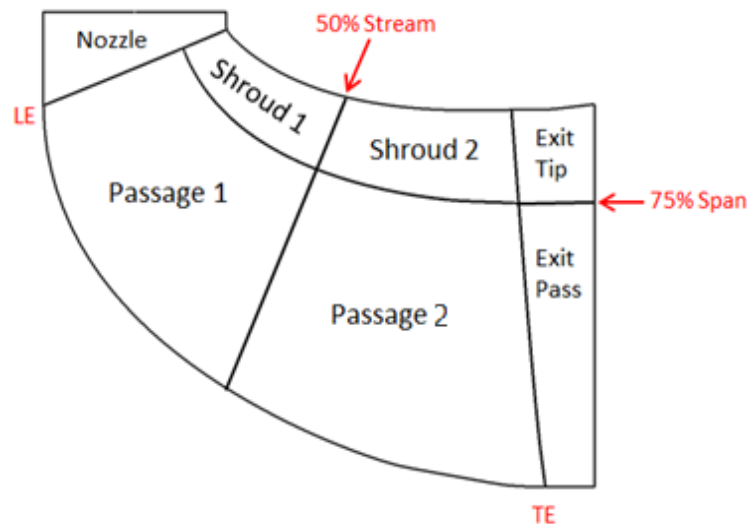


Figure 6.25: Blade passage regions

Figure 6.25 shows the control volumes used in the entropy generation calculation. The entropy increase was determined from the net entropy flux through the surfaces bounding the volumes. Denton, (1993) showed that the use of entropy generation through the stage in this way is the most reliable method of measuring fluid loss, particularly in adiabatic systems where entropy generation is irreversible. As stated by Newton, (2014), in cases such as these, entropy generation is purely a result of a loss of kinetic energy, which in turn leads to a loss in total pressure which is the more traditional measure of loss.

To ensure accuracy with this method, it's vital to ensure that the control volumes are "water tight", therefore accurate creation of the surfaces was paramount. For this method of analysis it is assumed that the rotor is quasi steady which is not strictly due. However, the small volume of the region makes this assumption a good approximation.

Figures 6.26-6.28 present the entropy generation through the rotor at the point within the pulse where the minimum velocity ratio was achieved for the 20Hz, 40Hz and 60Hz pulse frequencies. This running point occurs close to the peak energy availability and is therefore highly influential in energy extraction and cycle averaged performance. The rotor operating velocity ratio is also approximately constant for both designs ensuring a fair comparison of loss. At all tested frequencies the distribution of the losses in the rotor remains similar. The greatest loss occurs in the Suction Surface (SS) Passage 1 region. The cause of this behaviour is the occurrence of large positive incidence angles at the LE. At all tested frequencies, the tilted housing results in marginally less entropy generation due to the small reduction in incidence shown in figures 6.18-6.20.

The greatest differences in entropy generation is achieved in the SS shroud 1 and 2 regions. The main loss in these regions is attributed to blade tip leakage and shroud surface separation. This effect is illustrated in Figure 6.29 which shows velocity vectors and static entropy contours on a blade-to-blade surface 10% of the passage width from the SS. The position of this plane is shown in figure 6.30 along with the positions of both the constant stream-wise and constant span-wise plane positions. There is a clear increase in shroud separation in the radial housing design leading to greater flow losses along the shroud. The reduction of this loss mechanism in the tilted case is the result of reduced shroud curvature. Figure 6.29 also shows an increase in loss along the hub contour in the tilted housing design. Loss at the rotor hub is a characteristic of mixed flow turbines and was reported by Palfreyman & Martinez-Botas, (2002). The current work shows that housing tilt increases this loss due to flow being directed away from the hub relative to that in the radial volute case.

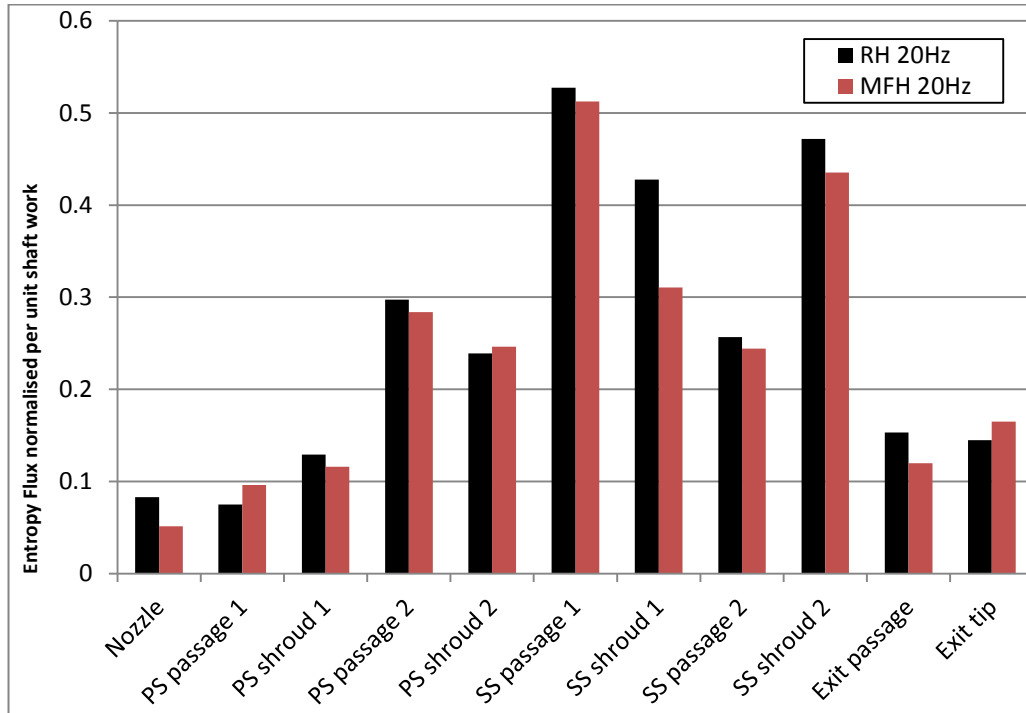


Figure 6.26: Passage entropy generation minimum U/c_s running point 20Hz pulse frequency

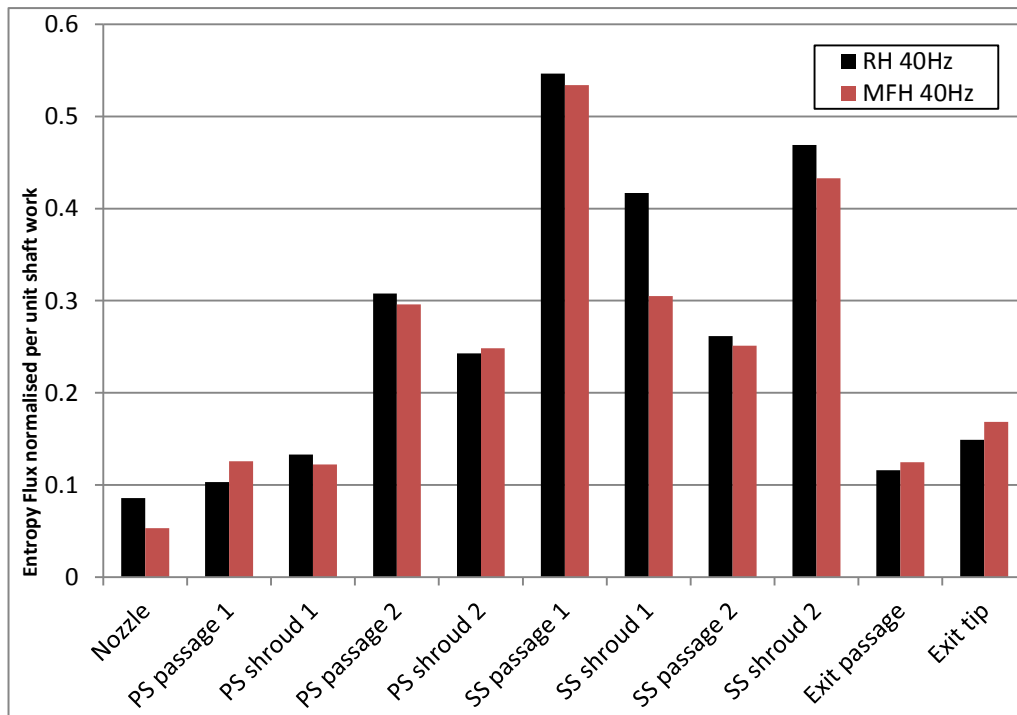


Figure 6.27: Passage entropy generation minimum U/c_s running point 40Hz pulse frequency

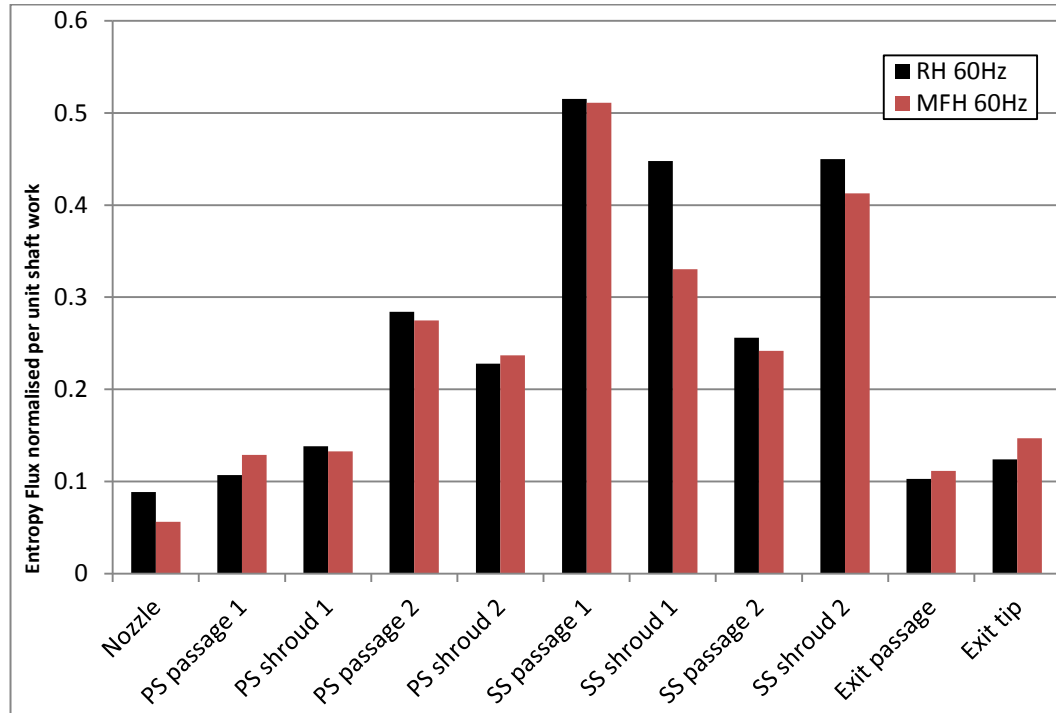


Figure 6.28: Passage entropy generation minimum U/c_s running point 60Hz pulse frequency

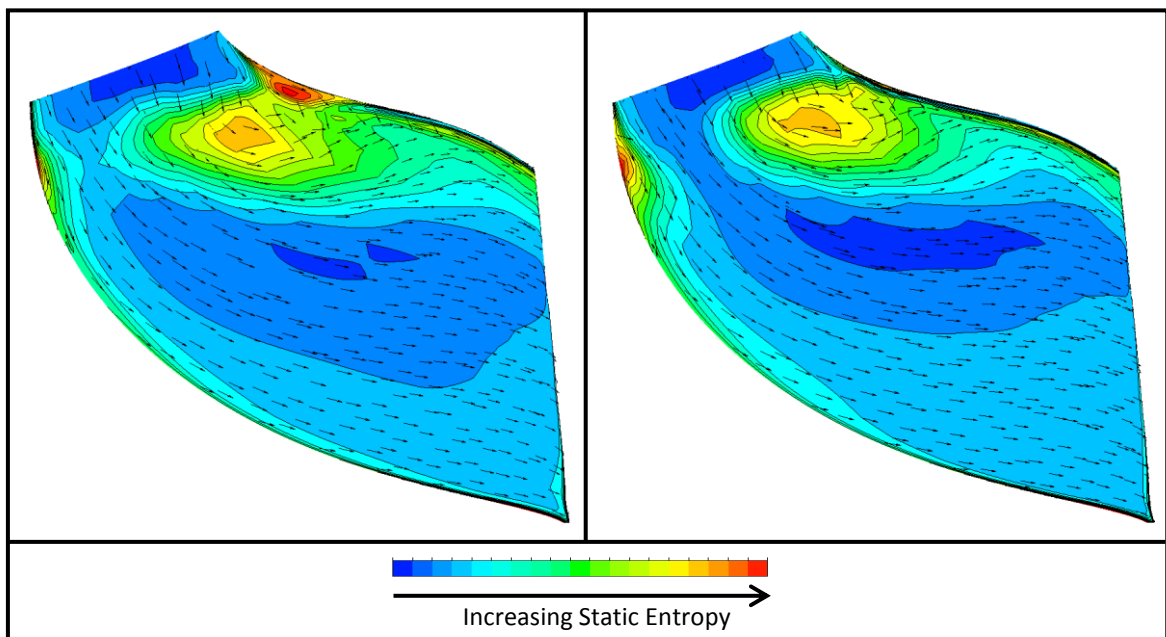


Figure 6.29: Vectors on blade to blade plane 10% of passage width from blade ss. minimum U/c_s 40Hz. Left - radial housing. Right - tilted housing

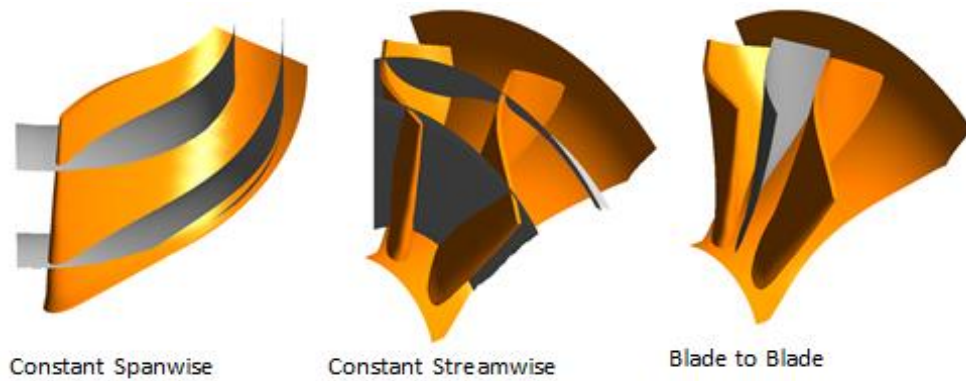


Figure 6.30: Flow analysis plane positions

Figure 6.31 shows the span-wise (see figure 6.30) static entropy contour plot at the 40Hz pulse frequency for both designs at the minimum velocity ratio running point. The contour plots show the loss caused by LE separation due to highly positive incidence. The loss region on the blade SS shows a slight reduction in size in the tilted design case. The improvement seen is small due to a reduction of only 3.5° in LE incidence in the tilted case. The quantitative effect of this marginal reduction in loss over the LE span, is represented in figures 6.26-6.28 by the small reduction in entropy generation in the SS Passage 1 region in the tilted design.

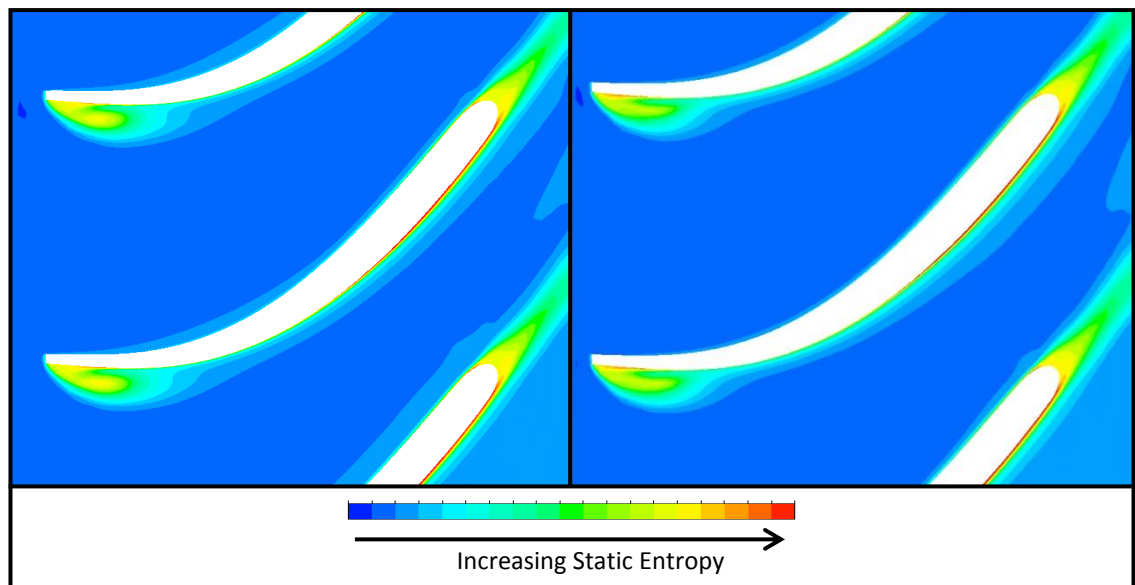


Figure 6.31: Static entropy on constant span-wise plot at 50% span, minimum U/c_s running point 40Hz pulse frequency.
Left - radial housing. Right tilted housing design

Figure 6.32 shows entropy contours and vectors plotted on constant stream-wise planes (see figure 6.30). The planes are orientated such that the observer is looking downstream towards the trailing edge (TE) and the blades are rotating in the clockwise direction. These planes complete a 3D analysis of the flow physics within the blade passage. Between the two designs, there is a distinct difference in the development of flow near the SS shroud gap. A loss region shown by “X” is present in the radial case that is not observed in the tilted design. This region can be attributed to the shroud surface separation and the resulting interaction with the tip leakage flow. At the 25% plane, a deflection of the tip leakage flow due to this added loss is clear, with the tip flow traveling down the passage in the radial design as opposed to across the passage in the tilted case. The result is that the loss region spans a greater percentage of the blade span in the radial case at the 25% plane.

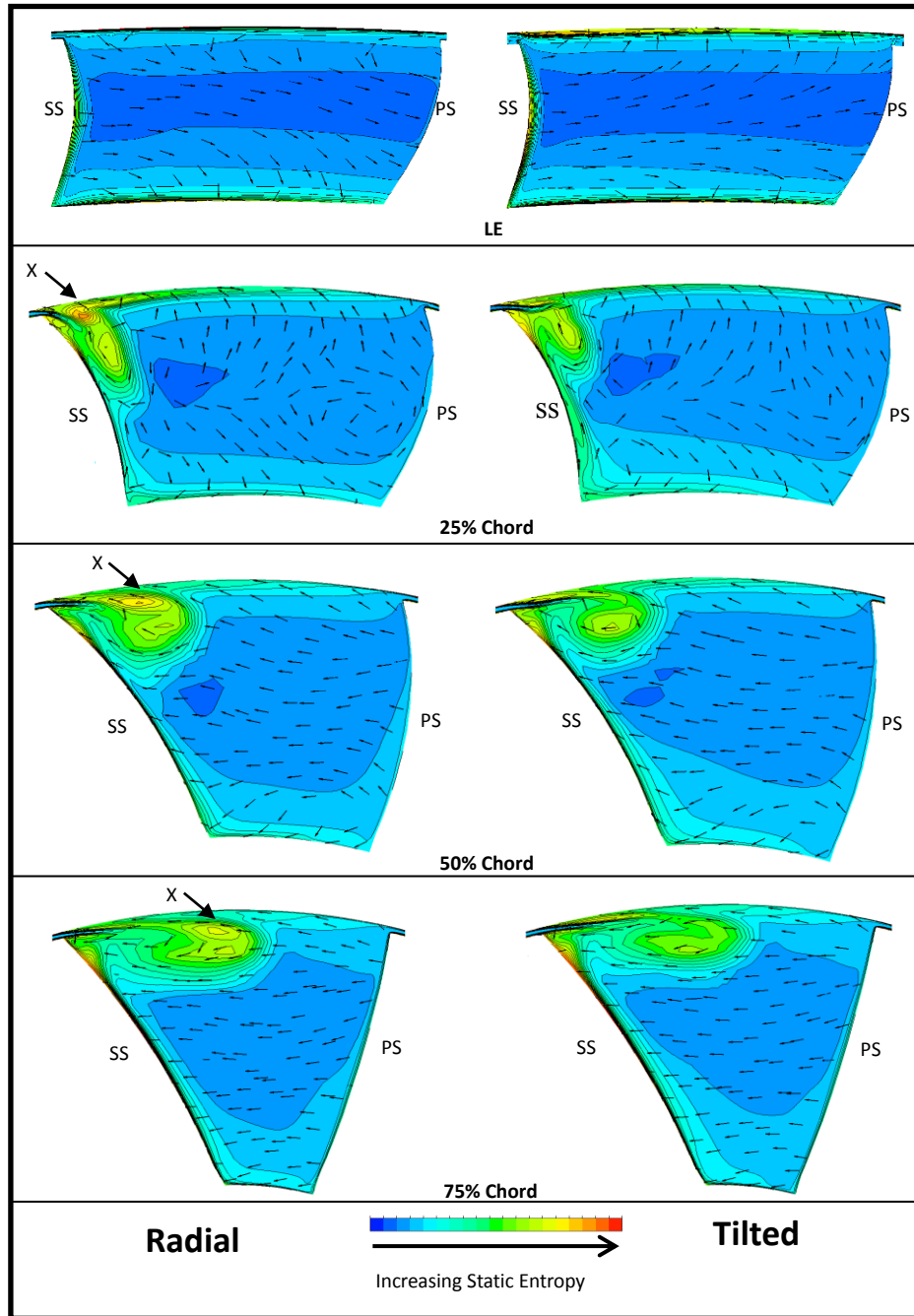


Figure 6.32: Constant stream-wise plots of static entropy and vectors at three chord positions. Left - radial housing. Right - tilted housing

6.4.2 PULSATION NUMBER

The impact of the volute tilt was further analyzed at a range of pulsation numbers (0.5, 0.75, 1 and 1.25). This analysis was included to investigate the impact of tilt over a wide range of operation.

The resulting rotor efficiencies of both designs are plotted against rotor velocity ratio for each case in figures 6.33-6.36. Tables 6.2 gives an overview of the performance differences under each operating pulse.

With decreasing pulsation number, the cycle averaged stage and rotor efficiency improvement experienced increased. However, the peak instantaneous efficiency improvement was lowest in the 0.5 pulsation number case. This was due to the higher velocity ratio running points not being achieved under this pulse as the velocity ratio range was reduced. Similarly, the reduced range meant that the lowest velocity ratios were also not encountered. As has been shown, under these conditions the improvement of the tilted volute reduces, and due to the large energy availability at these operating points, the cycle averaged values are significantly impacted.

At the pulsation number of 1.25, the maximum velocity ratio encountered differed significantly between the two designs resulting in the tilted volute design achieving lower minimum efficiencies than the radial alternative. As previously mentioned this is caused by the increased total pressure loss in the tilted volute design. As the pulsation number was increased, loss in the tilted volute further increased, this combined with the non-linear effect of total pressure on velocity ratio, resulting a variation of 0.05 between the two designs and with this a reduction in efficiency.

Other than the reduced efficiency of the tilted design in the 1.25 case at maximum velocity ratio, the tilted design consistently resulted in increased rotor efficiencies over the tested range of pulsation numbers.

| | <i>Pulsation no.</i> | | | |
|--|----------------------|-------------|----------|-------------|
| | <i>0.5</i> | <i>0.75</i> | <i>1</i> | <i>1.25</i> |
| <i>Cycle Avg Rotor Eff increase (TV-RV)</i> | 1.64% | 1.51% | 1.42% | 1.30% |
| <i>Cycle Avg Stage Eff increase (TV-RV)</i> | 1.35% | 1.22% | 1.15% | 1.03% |
| <i>Peak efficiency increase (TV-RV)</i> | 2.04% | 2.17% | 2.17% | 2.12% |

Table 6.2: Tilted (TV) vs radial (RV) volute performance parameter over range of pulsation numbers

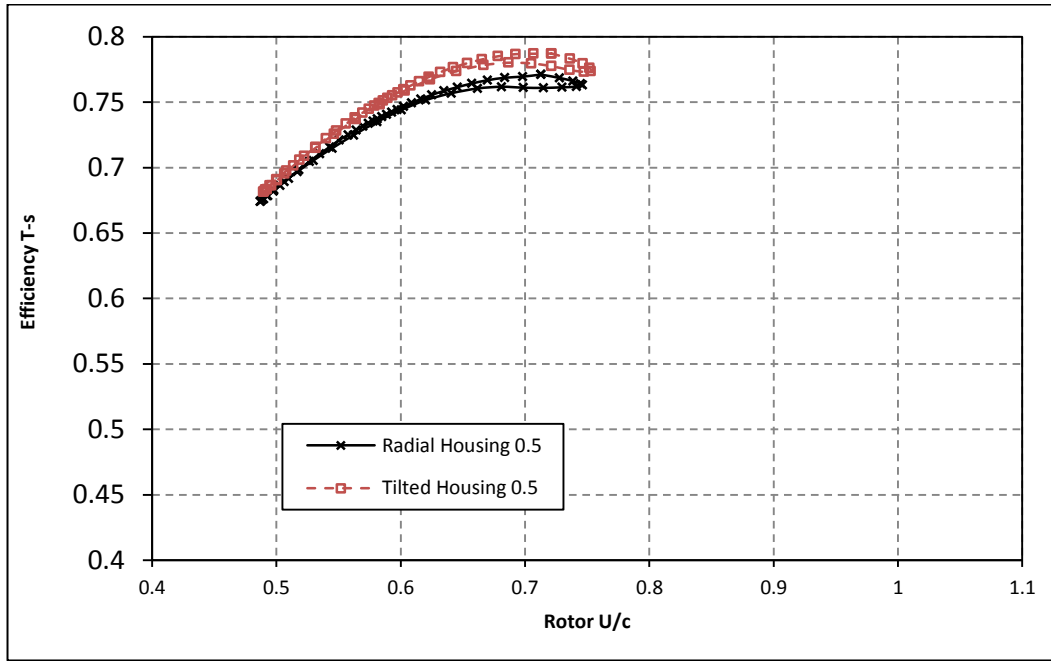


Figure 6.33: Rotor efficiency, radial and tilted volutes. Pulsating number = 0.5

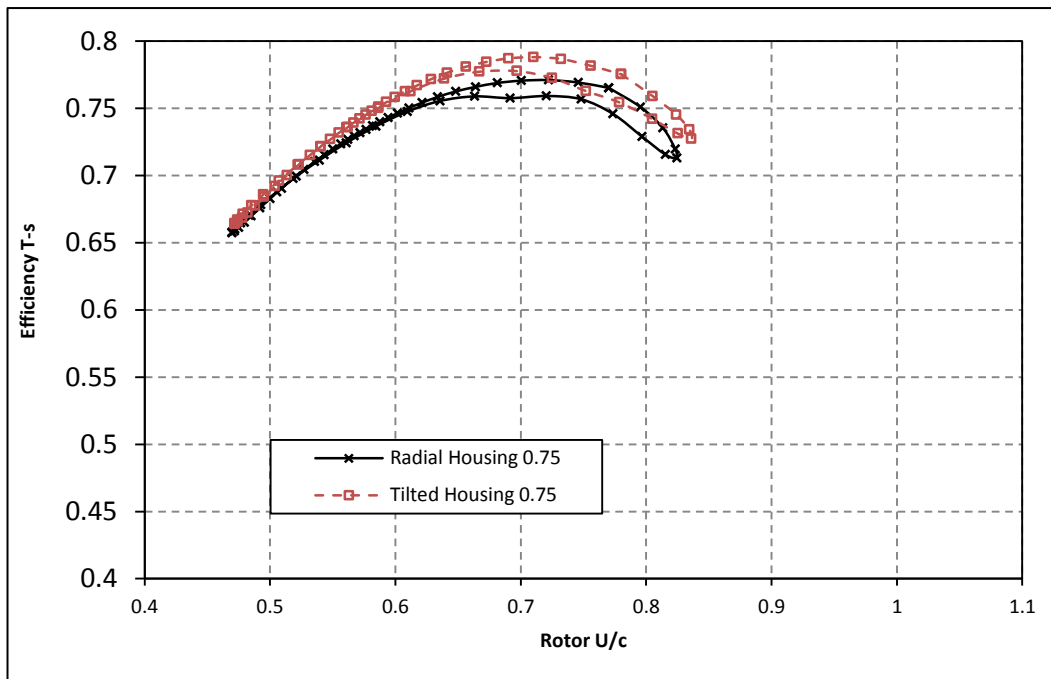


Figure 6.34: Rotor efficiency, radial and tilted volutes. Pulsating number = 0.75

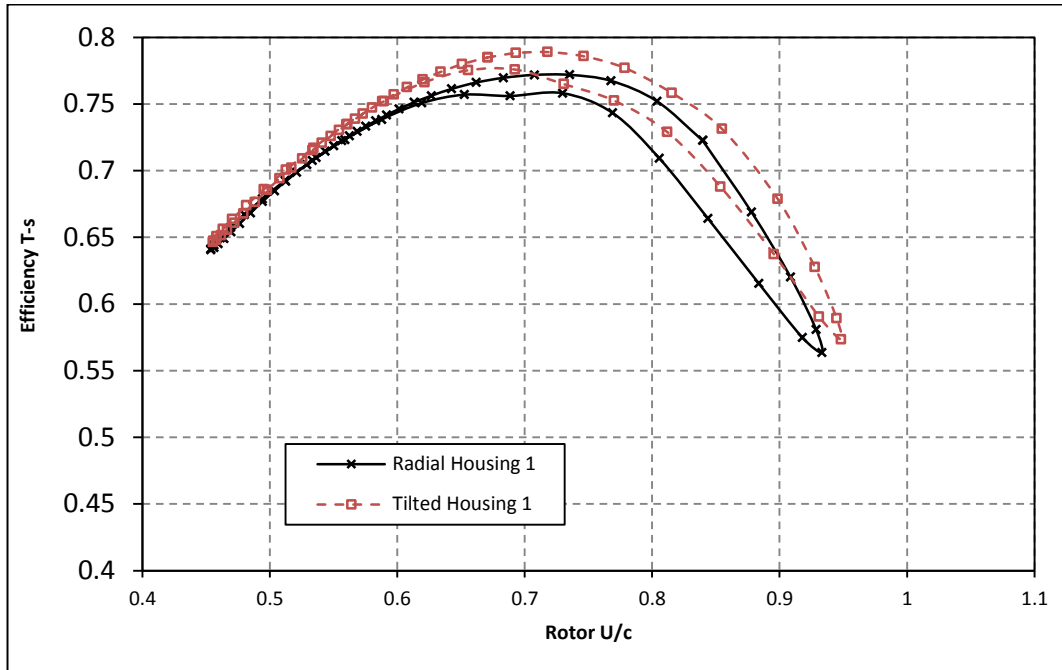


Figure 6.35: Rotor efficiency, radial and tilted volutes. Pulsating number = 1

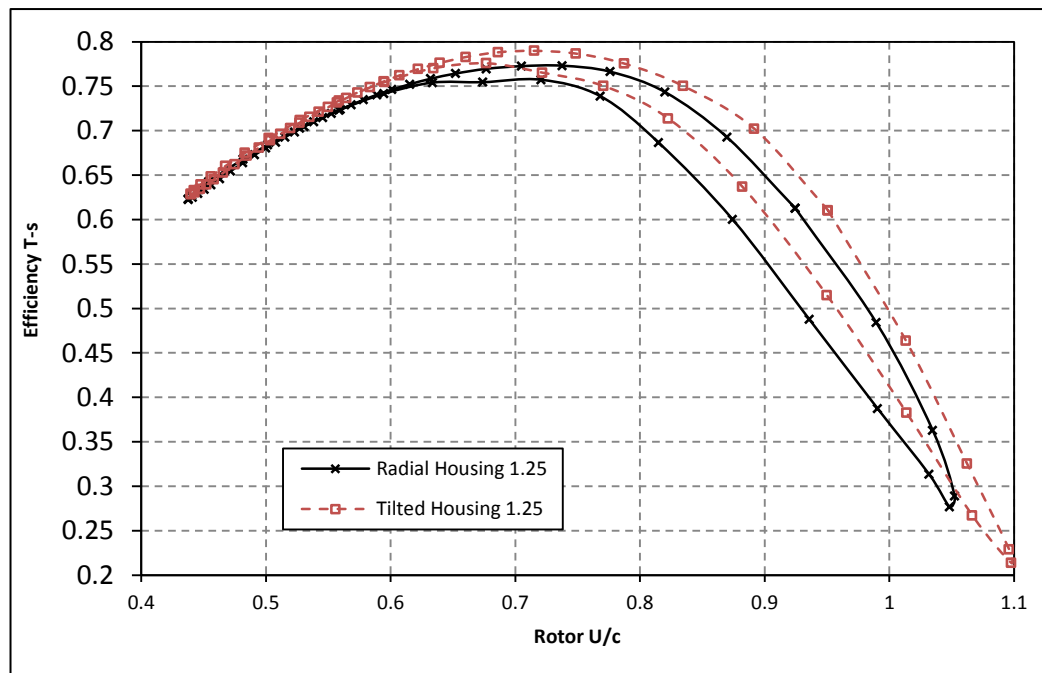


Figure 6.36: Rotor efficiency, radial and tilted volutes. Pulsating number = 1.25

6.4.3 PULSATION LOAD

The impact of pulse load was also investigated on the radial and tilted volute designs. Three pulse loads included were Low load – 73%, middle load – 100% and high load – 127% at 40Hz and a pulsation number of 1. The resulting rotor efficiencies are plotted against rotor velocity ratio in figures 6.37-6.39. Table 6.3 gives an over view of the cycle averaged performance under each pulse load.

With increasing pulse load the turbine operation range changes, with increasing load leading to lower velocity ratio ranges. As a result, the cycle averaged stage and rotor efficiencies are higher at the lower loads where the tilted design results in greater performance benefits. Similar to the impact of pulsation number, as the rotor velocity ratio reduces the performance improvement due to the tilt also reduces. This reduced to only a 0.5% increase in rotor efficiency at the minimum velocity ratio at the high load condition.

| | <i>Load</i> | | |
|--|-------------|------------|-------------|
| | <i>Low</i> | <i>Mid</i> | <i>High</i> |
| <i>Cycle Avg Rotor Eff increase (TV-RV)</i> | 2.13% | 1.64% | 1.29% |
| <i>Cycle Avg Stage Eff increase (TV-RV)</i> | 1.76% | 1.35% | 1.07% |
| <i>Peak rotor Eff increase (TV-RV)</i> | 2.272% | 2.039% | 2.195% |

Table 6.3: Tilted (TV) vs radial (RV) volute performance parameter over range of pulse loads

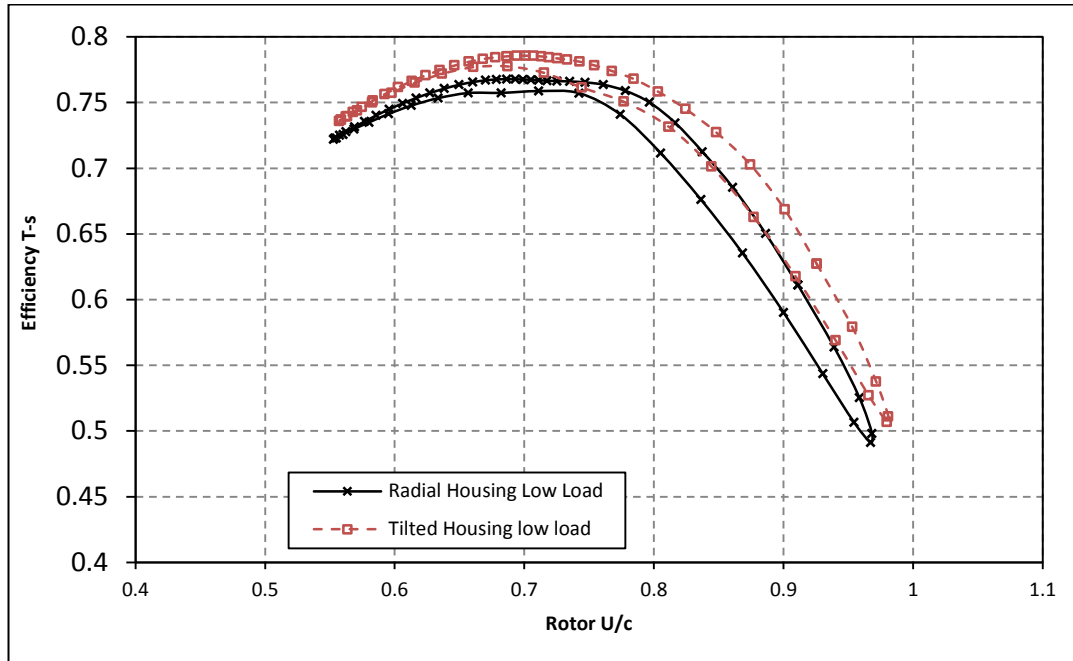


Figure 6.37: Rotor efficiency, radial and tilted volutes. Low load

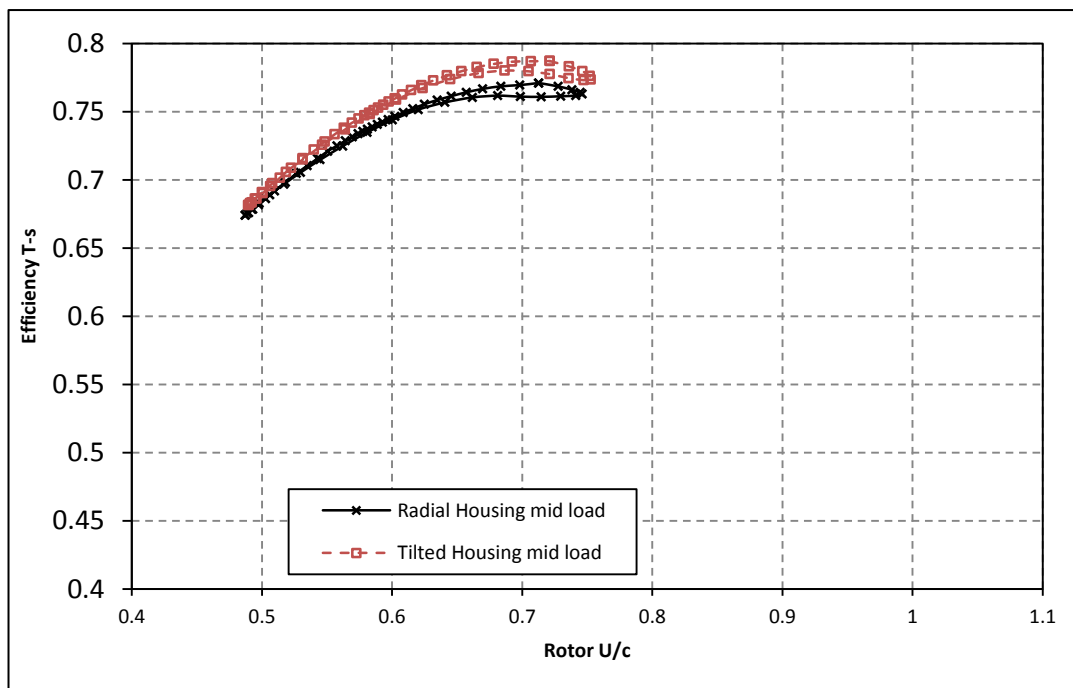


Figure 6.38: Rotor efficiency, radial and tilted volutes. Mid load

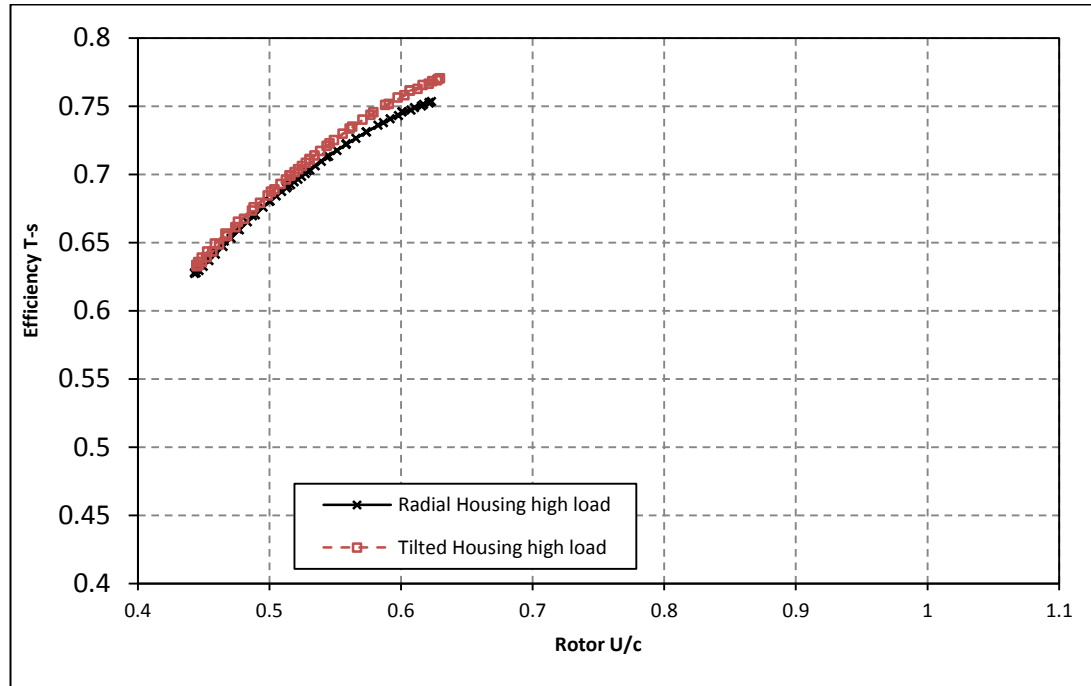


Figure 6.39: Rotor efficiency, radial and tilted volutes. High load

6.5 THE IMPACT OF VOLUTE A/R AND HOUSING TILT ON PERFORMANCE

The impact of housing tilt was investigated over a range of volute A/r's. The volute A/r is one of the main geometrical parameters in volute design and controls the volute exit flow angle and turbine mass flow parameter (see section 2.1.3 for more details). The A/r's tested were 20, 23 and 26 which is defined at the 20° position. Where the A/r=23 is the base design used throughout the analysis up to this point. As discussed previously, the volute A/r plays a critical role in delivering the rotor with the required flow. It is therefore common for A/r to be changed to ensure correct engine matching. As A/r plays such a critical role in volute design, the volute tilt was analysed over this range to ensure that the improvement is consistent over a viable spectrum of products. Comparisons were completed at 40Hz pulse frequency, 100% load and a pulsation number of 1. The variation in A/r with azimuth angle for each of the designs is plotted in figure 6.40.

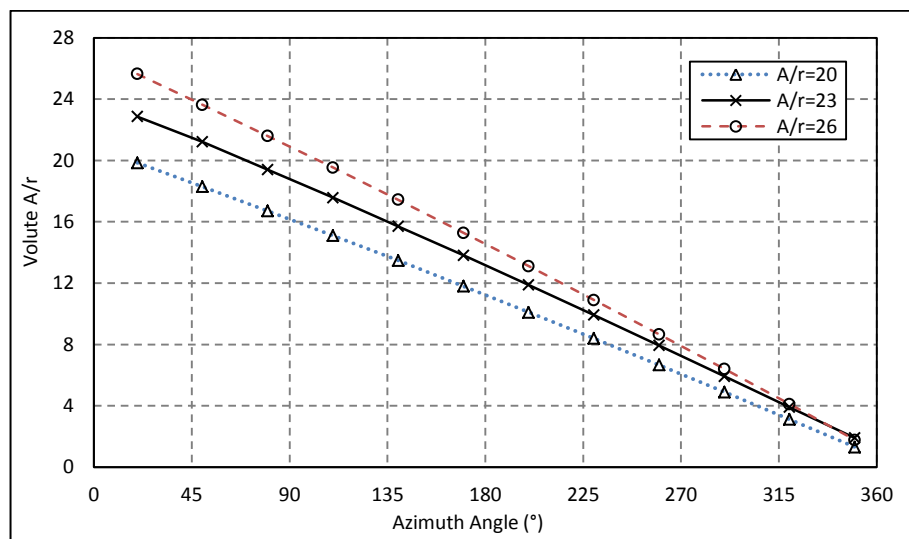


Figure 6.40: Volute A/r progression

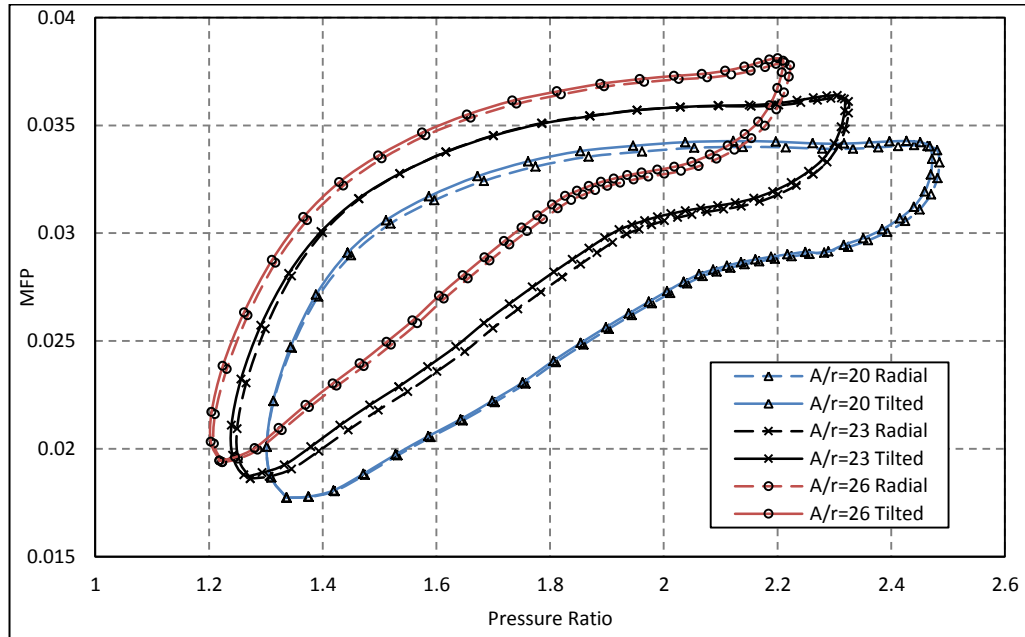


Figure 6.41: MFP vs pressure ratio plots for the radial and tilted volute designs at A/r=20, A/r=23 and A/r=26

Stage MFP is plotted against pressure ratio in figure 6.41 showing the hysteresis in each design. The change in cycle averaged MFP between the three A/r designs is 10%. The variation between the radial and tilted volute designs at a given A/r remains less than 0.5% in all cases and therefore aerodynamic similarity between the variants was achieved.

The efficiency curves for each of the tested volutes is presented in figures 6.42-6.44 for both the radial and tilted designs. In all cases the tilted design results in an increase in rotor performance over the radial counterpart. The impact of A/r can be observed as the range of rotor velocity ratios shifts to higher values as the A/r reduces. This is due to the fact that higher stage pressure ratios are necessary in the small volute designs to pass the same mass flow. This also causes a change in the degree of reaction (DoR) defined as –

$$DoR = \frac{P_2 - P_3}{P_1 - P_3} \quad (80)$$

A low degree of reaction implies a greater acceleration in the turbine volute while a high degree of reaction implies greater acceleration in the rotor. Increasing

volute A/r acts to increase the stage degree of reaction, this was investigated by Roclawski et al., (2014). This effect results in a considerable change in stage flows and hence loss mechanisms.

Figures 6.42-6.44 also show that the improvement in efficiency with volute tilt tends to increase with volute A/r. This effect is not purely the result of shifting the operating range to higher velocity ratios, where the improvement with volute tilt has already been observed to be greater. As comparing the radial and tilted rotor efficiencies across the volute A/r range at a constant velocity ratio, still shows an increase with A/r. This effect is most significant at lower velocity ratios which are more influential to cycle averaged performance.

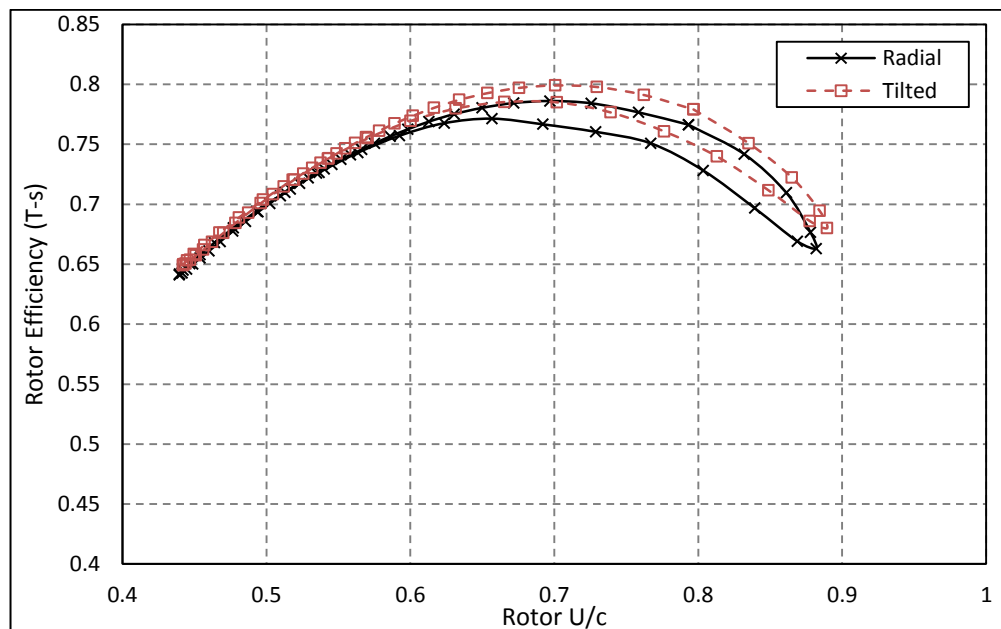


Figure 6.42: Rotor efficiency for radial and tilted volutes A/r=20

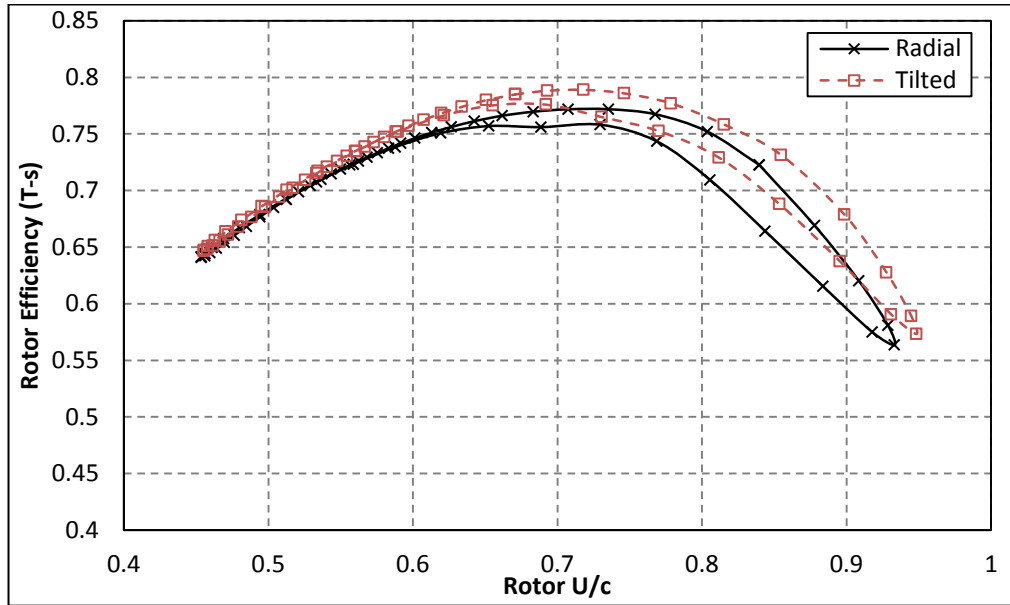


Figure 6.43: Rotor efficiency for radial and tilted volutes A/r=23

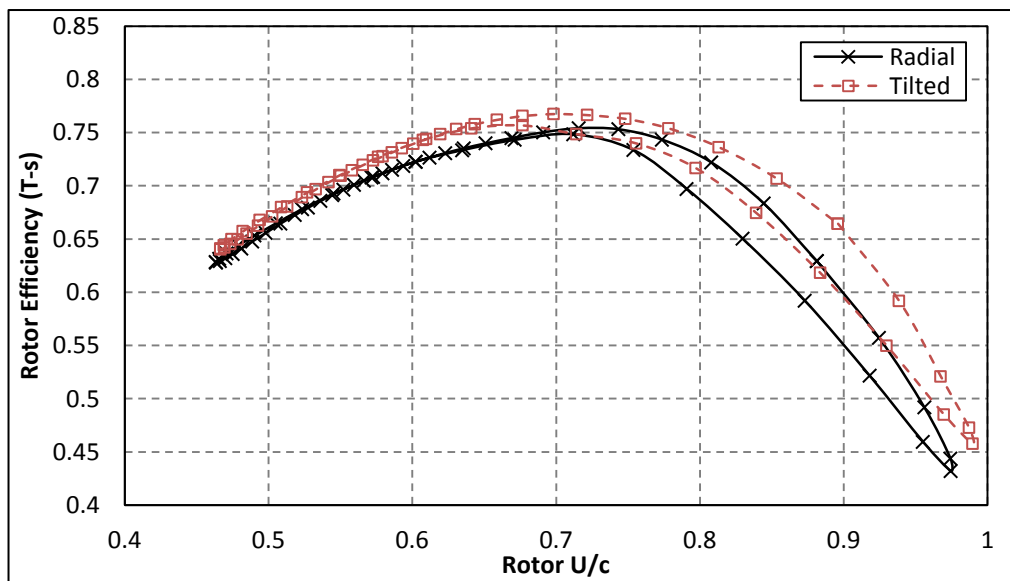


Figure 6.44: Rotor efficiency for radial and tilted volutes A/r=26

The resulting cycle averaged performance differences between the radial and tilted volute design at each of the A/r's is presented in table 6.4. An increase in cycle averaged stage and rotor efficiency was observed for the tilted design at each A/r. The improvement for the tilted design increased with volute A/r resulting in a peak improvement of 2.36% and 2.17% in rotor and stage efficiency respectively in the A/r=26 case.

The trend of stage and rotor efficiency with changing A/r is plotted in figure 6.45. The difference between rotor and stage efficiency varied over the range of A/r's. This is caused by the relative increase in total pressure loss in the tilted volute, reducing as volute A/r is increased. This results in more of the rotor efficiency improvement being carried forward into stage performance improvements.

| | A/r | | |
|---|--------|--------|--------|
| | 20 | 23 | 26 |
| Δ Cycle AVG Rotor eff increase (TV-RV) | 1.291% | 1.421% | 2.356% |
| Δ Cycle AVG Stage eff increase (TV-RV) | 0.835% | 1.145% | 2.171% |

Table 6.4: Cycle averaged performance difference between radial (RV) and tilted volute (TV) designs over a range of volute A/r's

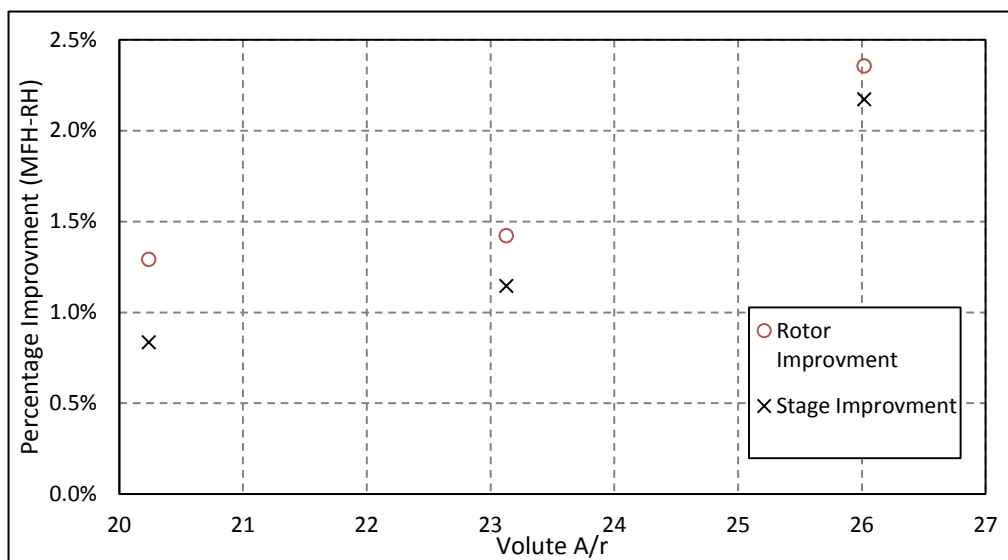


Figure 6.45: Comparison of rotor and stage efficiency for the radial and tilted volute designs over a range of A/r's

Analysis of the entropy generation through the rotor region at the maximum incidence operating point is included in figures 6.46-6.48. The same rotor regions and entropy calculation method is used to that in show in figure 6.25.

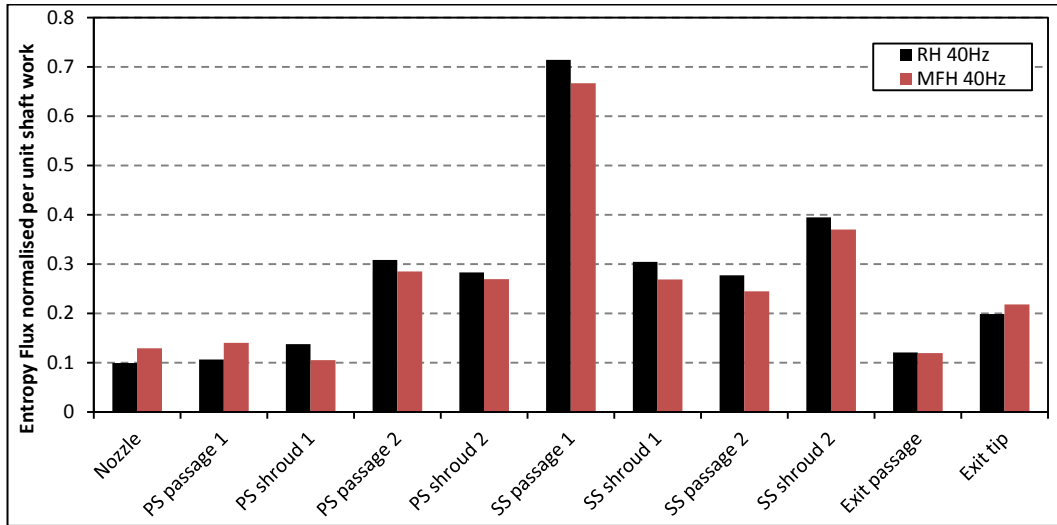


Figure 6.46: Entropy generation through rotor region for radial and tilted volute. A/r=20

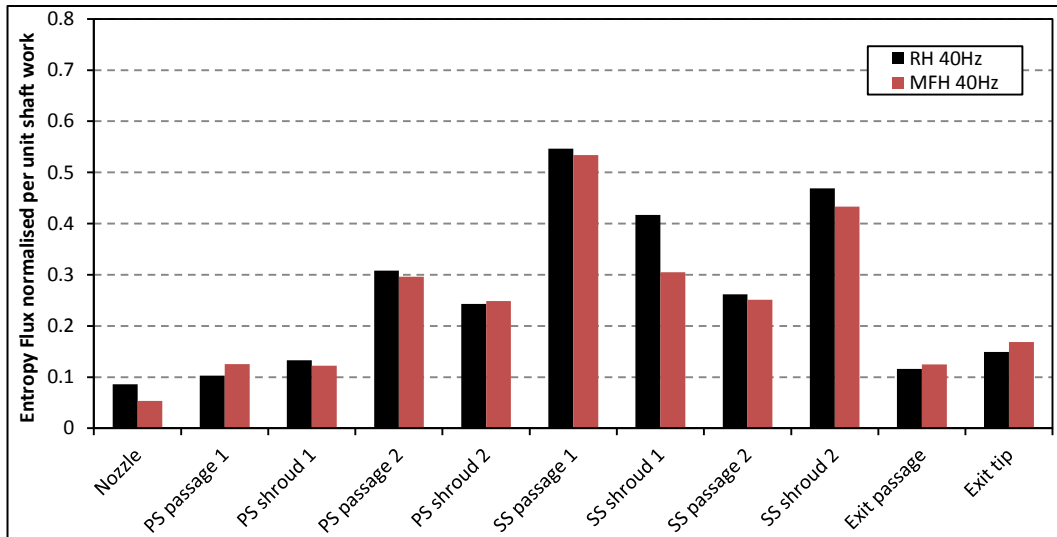


Figure 6.47: Entropy generation through rotor region for radial and tilted volute. A/r=23

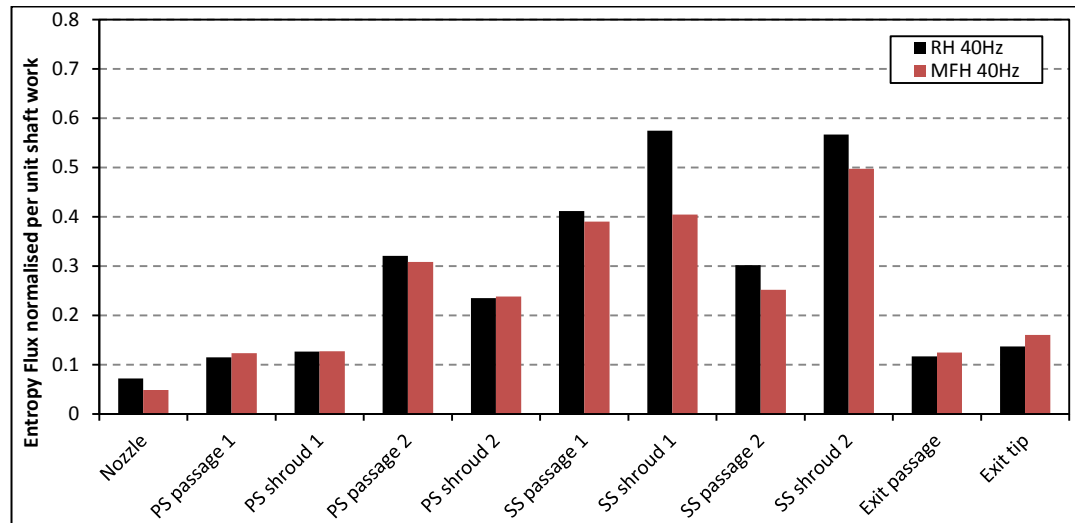


Figure 6.48: Entropy generation through rotor region for radial and tilted volute. $A/r=26$

A shift in the areas of loss in the rotor region occurs with changing volute A/r due to the change in degree of reaction. Therefore, a considerable change in the rotor flow physics and the energy extraction process of the turbine occurs. In the $A/r=20$ case the peak loss occurs in the SS passage 1 region which is mainly associated with LE separation. It will be shown in the following section that the smaller A/r results in a significant increase in LE incidence due to greater volute acceleration. This leads to greater LE separation and loss. The tilted housing results in a marginal reduction in LE incidence and entropy generation in the associated region.

With increasing volute A/r the loss in SS passage 1 reduces due to a reduction in LE incidence and the loss associated with SS shroud 1 and 2 increases. Losses in these regions are mainly attributed to shroud surface separation and the tip leakage losses. The volute tilt was shown to reduce the losses associated with these regions through reduced shroud surface separation and its impact on tip leakage. The improvement of the tilted design in these regions is, therefore, more beneficial in the larger volute A/r cases where these losses were more predominant. The increased loss in the SS shroud regions can be attributed to the greater blade loading associated with increasing volute A/r that occurs due to change in degree of reaction as shown by Roclawski et al., (2014). The larger acceleration in the rotor region results in greater loading of the blades and therefore, tip leakage increases.

6.5.1 VOLUTE SECONDARY FLOWS

Figures 6.49-6.54 shows streamlines and velocity contours plotted around the volute at minimum and maximum incidence running points for the three volute A/r's. At the smallest tested A/r, vortices only appear in the minimum incidence case in the titled volute design at the 90° plane. As the volute A/r increases the level of secondary flow activity increases due to lower operating pressure ratios and an increase in the Dean effect. In the A/r=23 volute, vortices occur in the radial case at the 72° plane and at the 90° plane in the tilted case. In the largest volute, vortices are evident in the 54°, 72° and 90° planes in the radial case at minimum incidence. In the tilted case vortices are only evident at the 72° and 90° planes. In the A/r=26 volute, vortices also appear at the maximum incidence running point in the 72° and 90° planes in the radial and tilted cases respectively. No vortex development was observed in the other volute sizes at the maximum incidence running point.

In all cases the vortices in the tilted volute occurred only on the shroud side of the volute. In this region two counter rotating vortices are formed. With increasing volute size, the vortices occurred earlier in the volute passage. In the A/r=26 case the vortices occurred in the 72° plane and formed closer together spanning across the volute passage as opposed to around the contour of the volute walls. In the radial cases, in regions of larger vortex activity four vortices form across the plane with two vortices forming high in the volute and two lower. This effect is most evident in the larger volute. As azimuth angle increase, the vortices higher in the volute passage breakdown quickly while the lower, strong vortices persist.

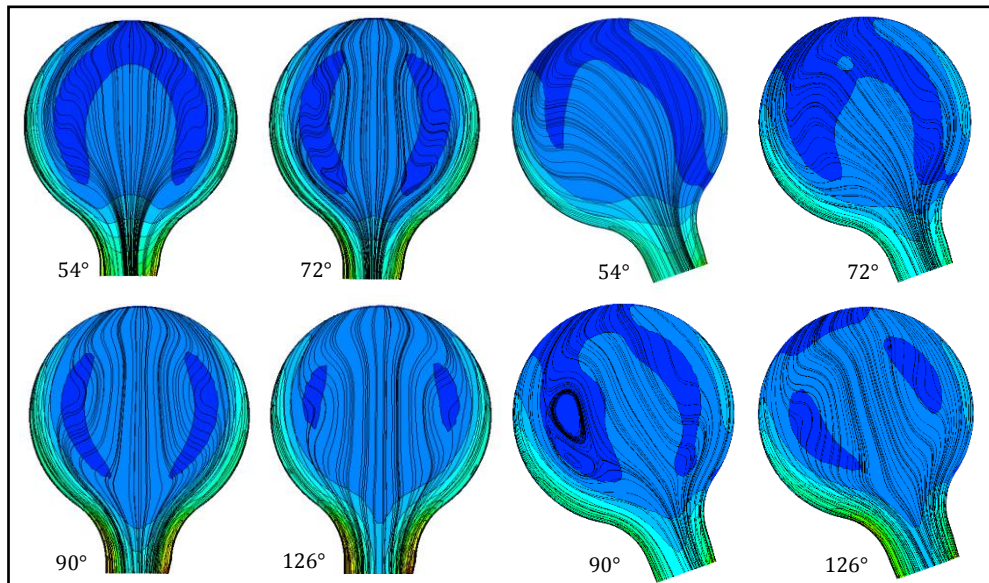


Figure 6.49: Meridional velocity contours and streamlines at Min Incidence. $A/r=20$, radial and 20° tilted volutes.

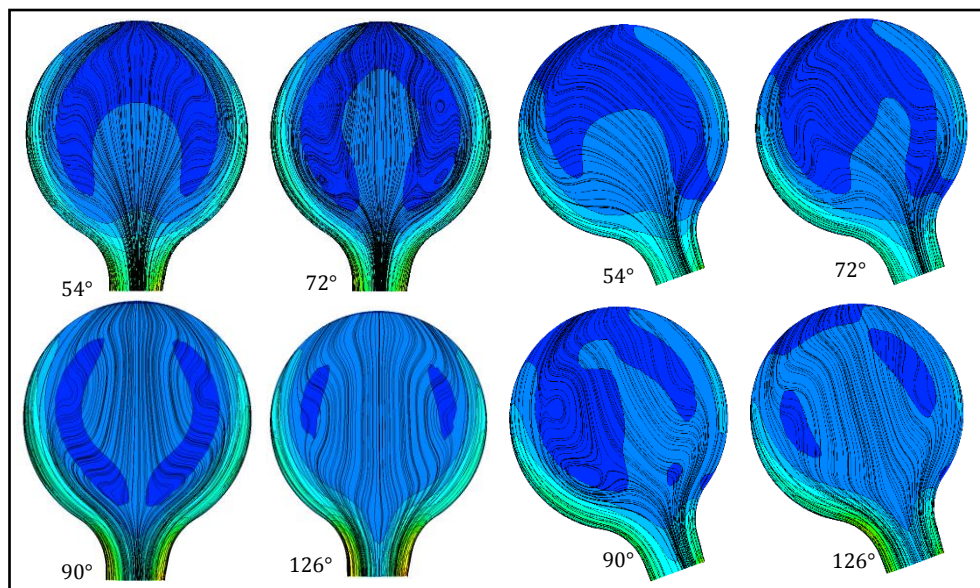


Figure 6.50: Meridional velocity contours and streamlines at Min Incidence. $A/r=23$ radial and 20° tilted volutes.

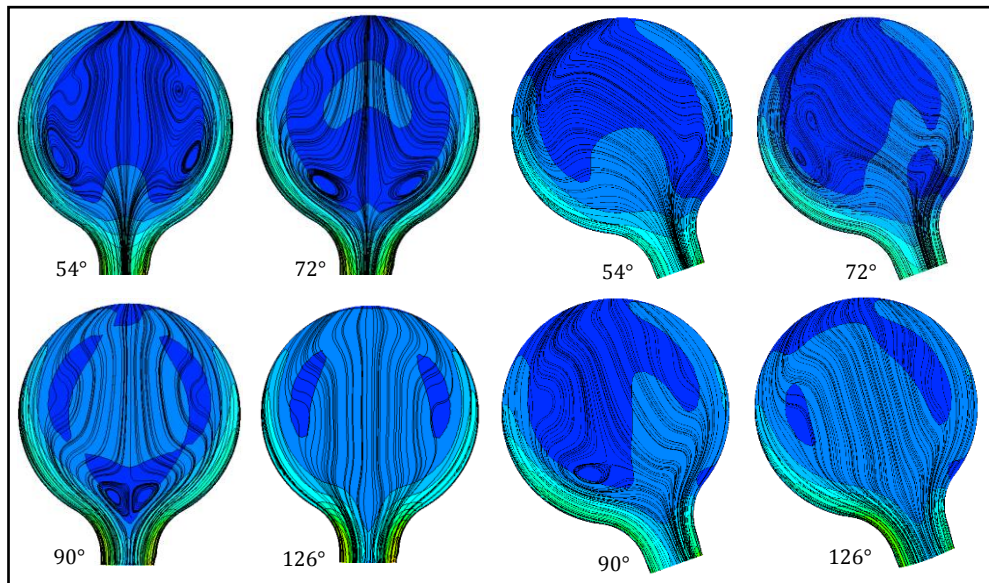


Figure 6.51: Meridional velocity contours and streamlines at Min Incidence. A/r=26 radial and 20° tilted volutes.

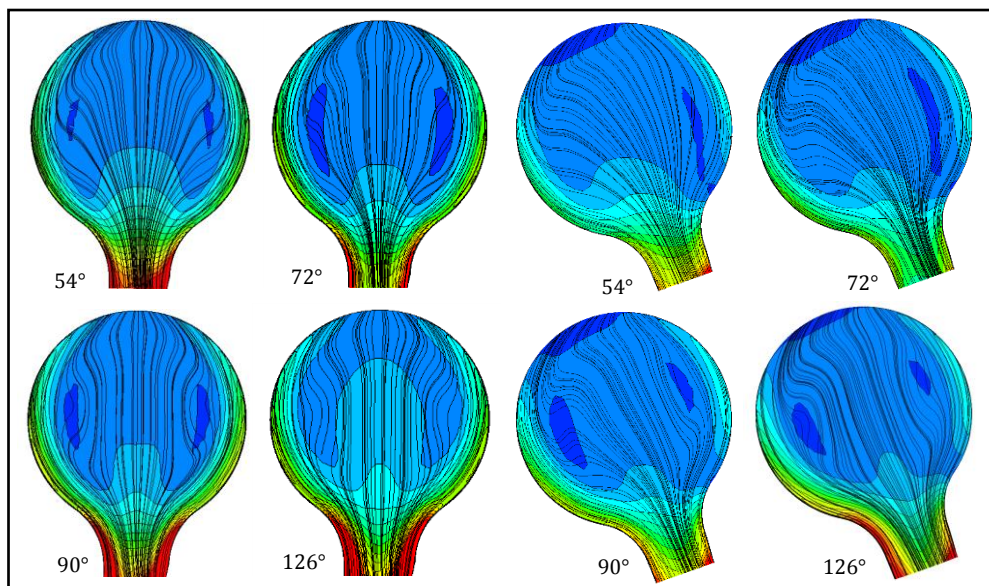


Figure 6.52: Meridional velocity contours and streamlines at Max Incidence. A/r=20 radial and 20° tilted volutes.

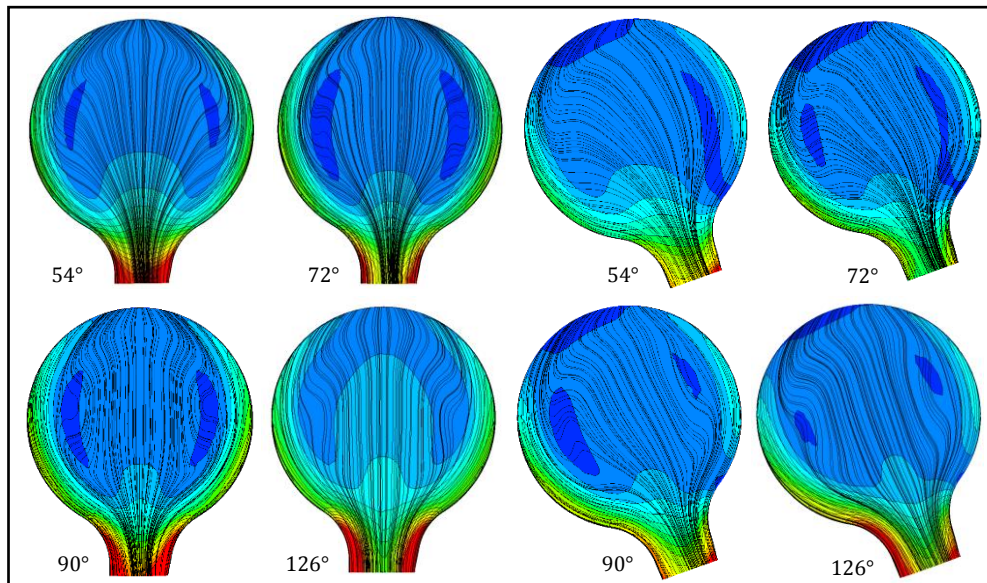


Figure 6.53: Meridional velocity contours and streamlines at Max Incidence. $A/r=23$ radial and 20° tilted volutes.

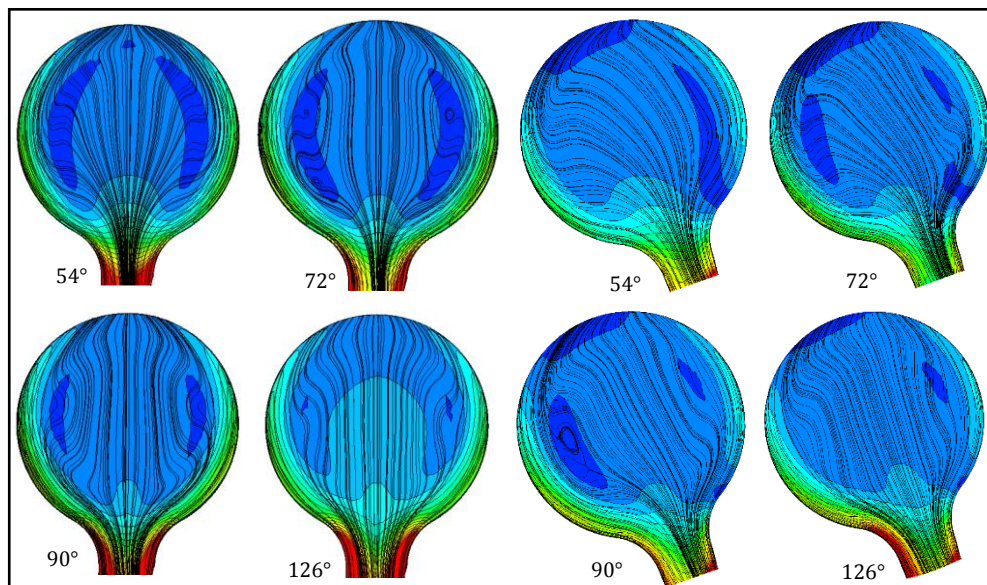


Figure 6.54: Meridional velocity contours and streamlines at Max Incidence. $A/r=26$ radial and 20° tilted volutes.

The resulting volute exit absolute flow angles are plotted in figures 6.55-6.60 for each of the volute A/r 's at maximum and minimum incidence for both the radial and tilted volutes. In all cases, the variation in absolute flow angle across the volute exit reduces from the minimum to maximum incidence running points. The variation with azimuth angle is also apparent in all cases with the peak variation occurring at 126° .

It is interesting to note that at this position no vortices exit in the passage, instead, it is around this position that the disturbed flow is situated at the volute exit.

It was observed that the variation in absolute flow angle was greater in the largest volute designs. It should be remembered that with changing volute size the MFP of the stage changes, hence the stages are not aerodynamically similar. It is therefore not fair to directly compare performance across A/r. However, it is interesting to note the impact of A/r on turbine operating environment as it is a vital turbine geometrical parameter.

In all cases the tilted housing results in a non-symmetrical span-wise variation. At minimum incidence, the peak absolute flow angle occurs at higher normalised span position in all cases in the tilted design. This effect also increased with increasing volute size and can be attributed to the greater level of volute secondary flow encountered in the larger volute. It was also observed that the asymmetry in the volute exit flow angle didn't develop until the 126° planes, but then persisted up to the 270° plane.

At maximum incidence, the shift in peak incidence to larger span-wise position is less noticeable. In the A/r=20 case the effect doesn't appear to occur but with increasing volute size the shift becomes increasingly noticeable. This observation can be attributed to the low level of secondary flow development at lower velocity ratio running points, as such the asymmetry of the flow does not develop. As volute size increased and volute secondary flows started to develop the asymmetry in volute exit flow then arose.

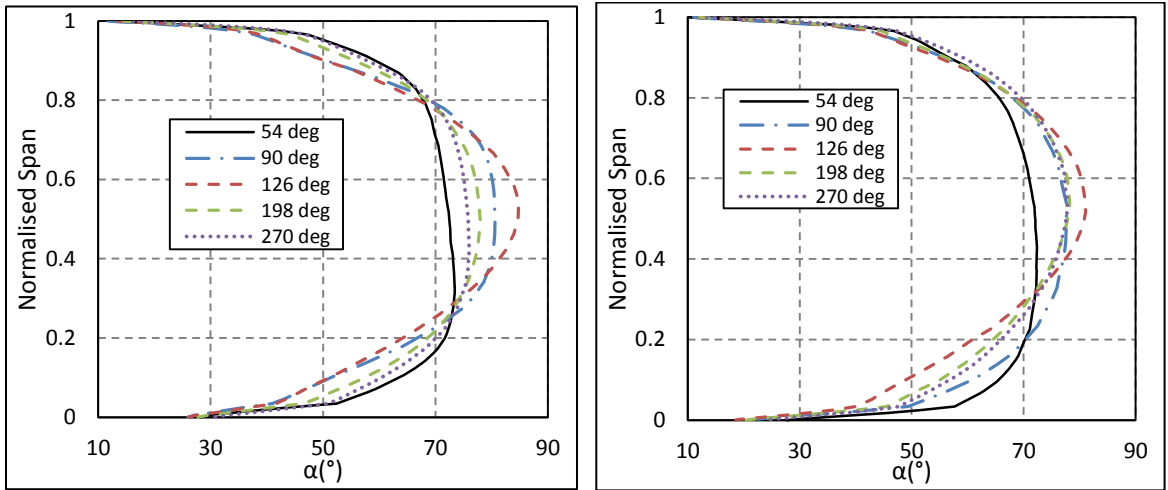


Figure 6.55: Volute exit absolute flow angle at min incidence A/r=20. Left - Radial housing. Right - Tilted housing.

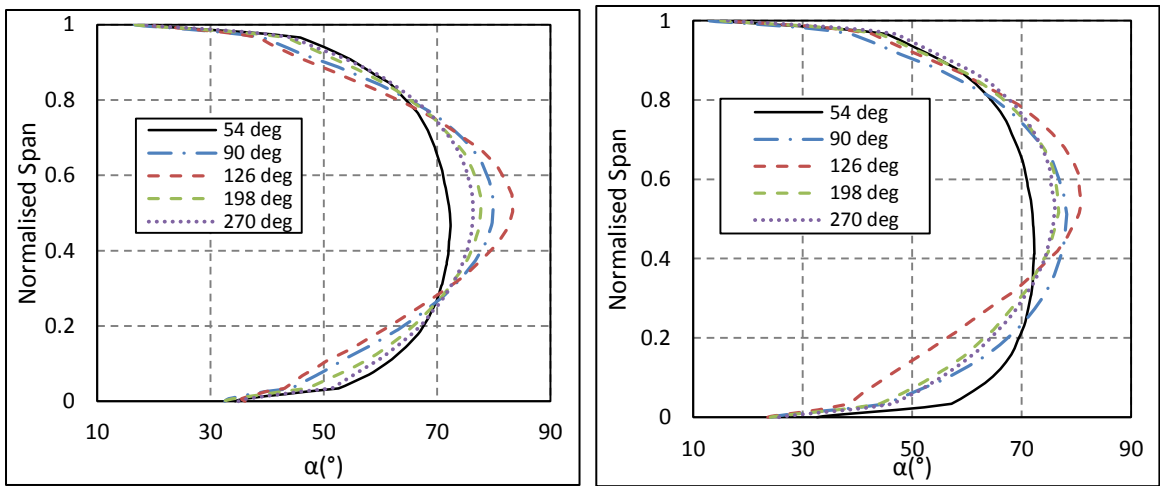


Figure 6.56: Volute exit absolute flow angle at min incidence A/r=23. Left - Radial housing. Right - Tilted housing.

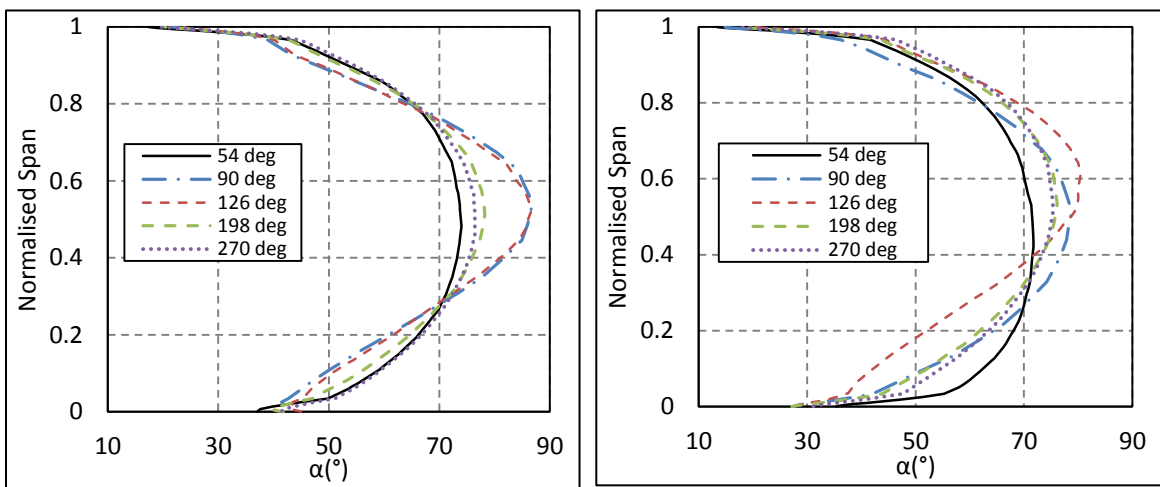


Figure 6.57: Volute exit absolute flow angle at min incidence A/r=26. Left - Radial housing. Right - Tilted housing.

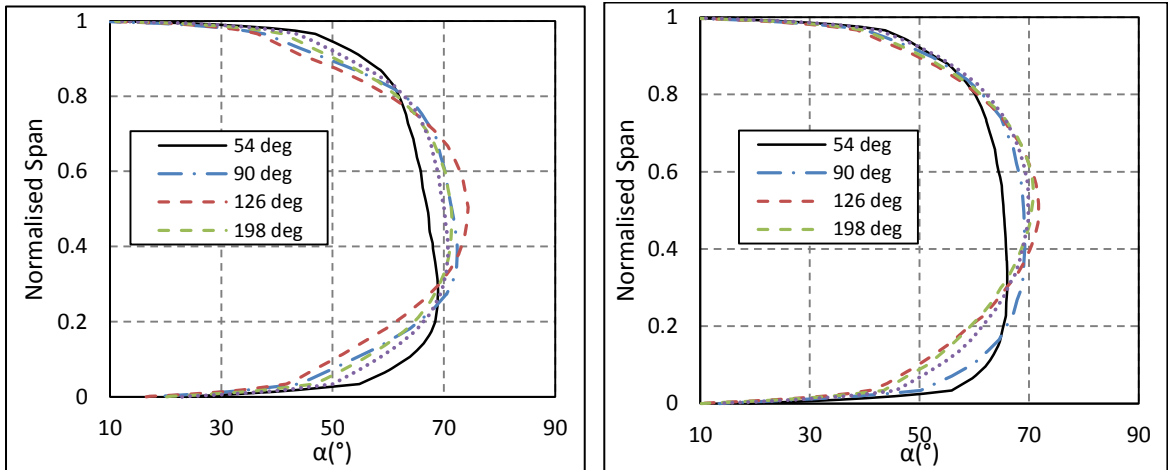


Figure 6.58: Volute exit absolute flow angle at max incidence A/r=20. Left - Radial housing. Right - Tilted housing.

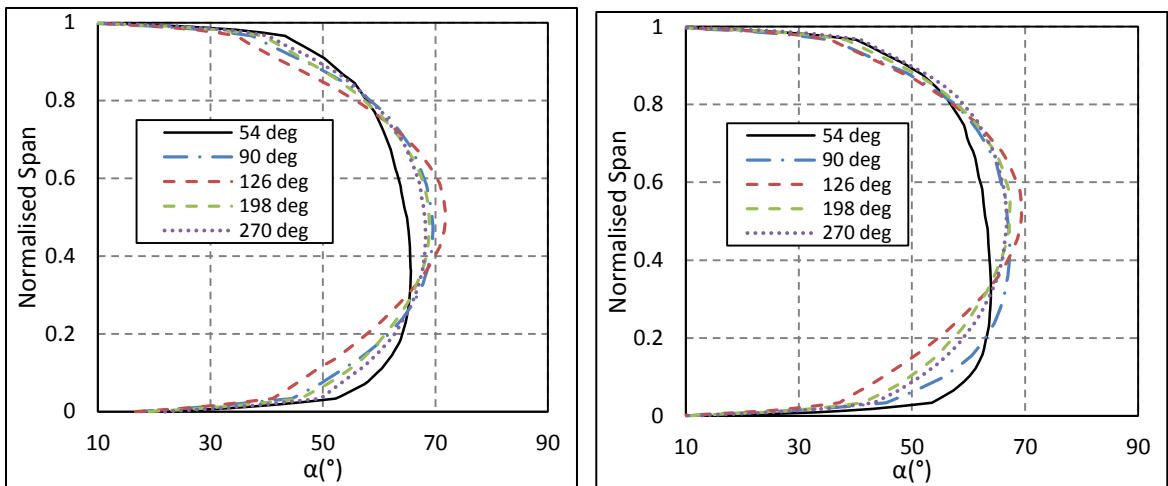


Figure 6.59: Volute exit absolute flow angle at max incidence A/r=23. Left - Radial housing. Right - Tilted housing.

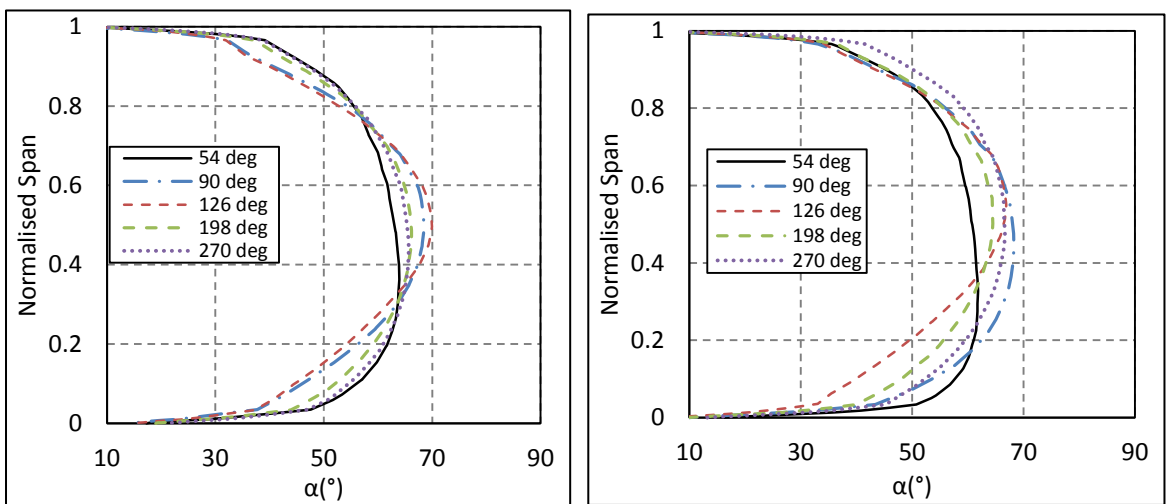


Figure 6.60: Volute exit absolute flow angle at max incidence A/r=26. Left - Radial housing. Right - Tilted housing.

The resulting circumferentially averaged LE incidence angles are plotted in figure 6.61-6.63 for each of the volute A/r's. With increasing volute size, the average incidence angles encountered reduced. This is due to the change in A/r and the impact on DoR and MFP. The reduction in LE incidence angle achieved in the tilted case increases in regions of extreme incidence. For instance, a greater reduction in incidence at the maximum incidence running point is observed in the A/r=20 case where the average LE incidence reduces by approximately 4°. At the minimum incidence running point the greatest reduction in the tilted case occurs in the A/r=26 case where the average variation between radial and tilted cases was approximately 3°.

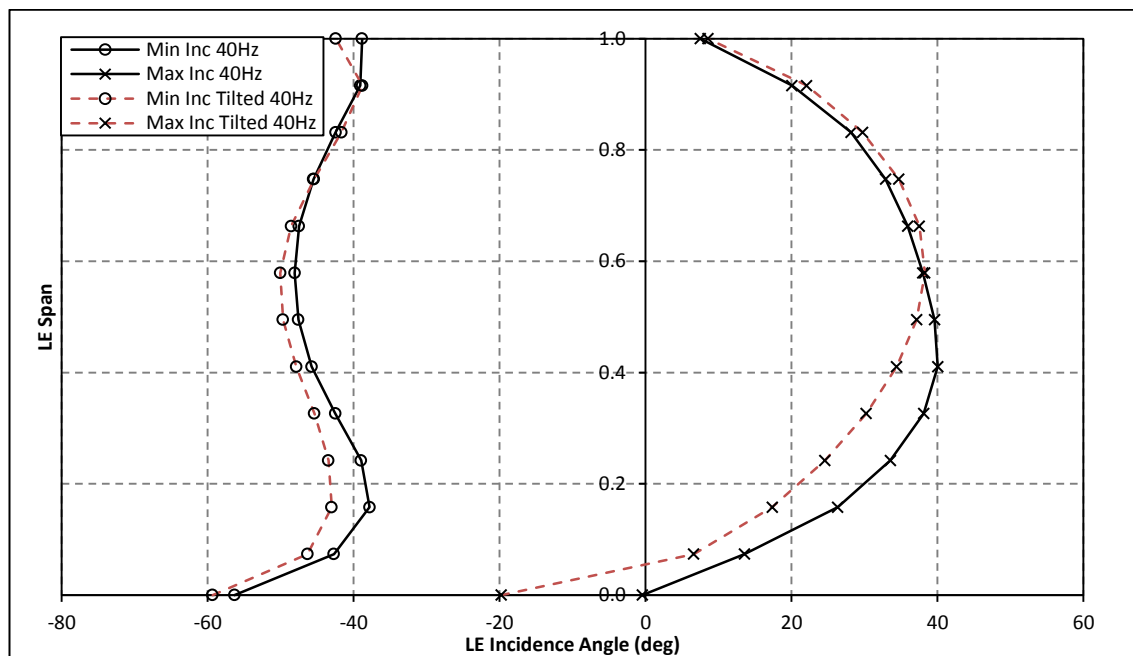


Figure 6.61: Span-wise incidence distribution at minimum and maximum incidence running points for radial and tilted volute. A/r=20

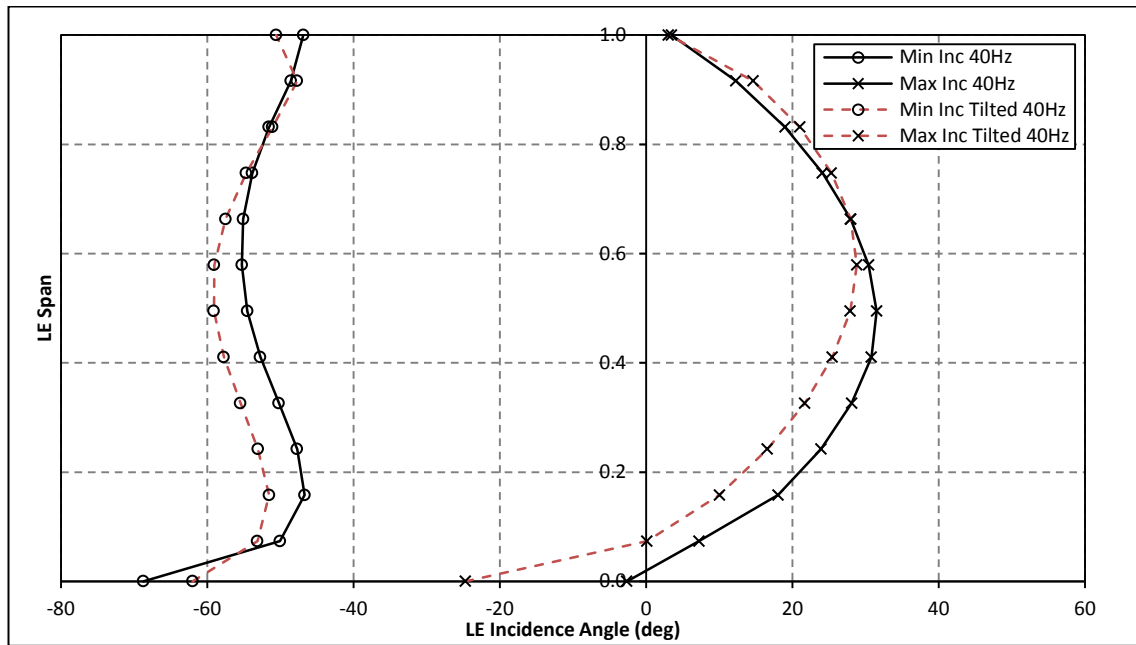


Figure 6.62: Span-wise incidence distribution at minimum and maximum incidence running points for radial and tilted volute. $A/r=23$

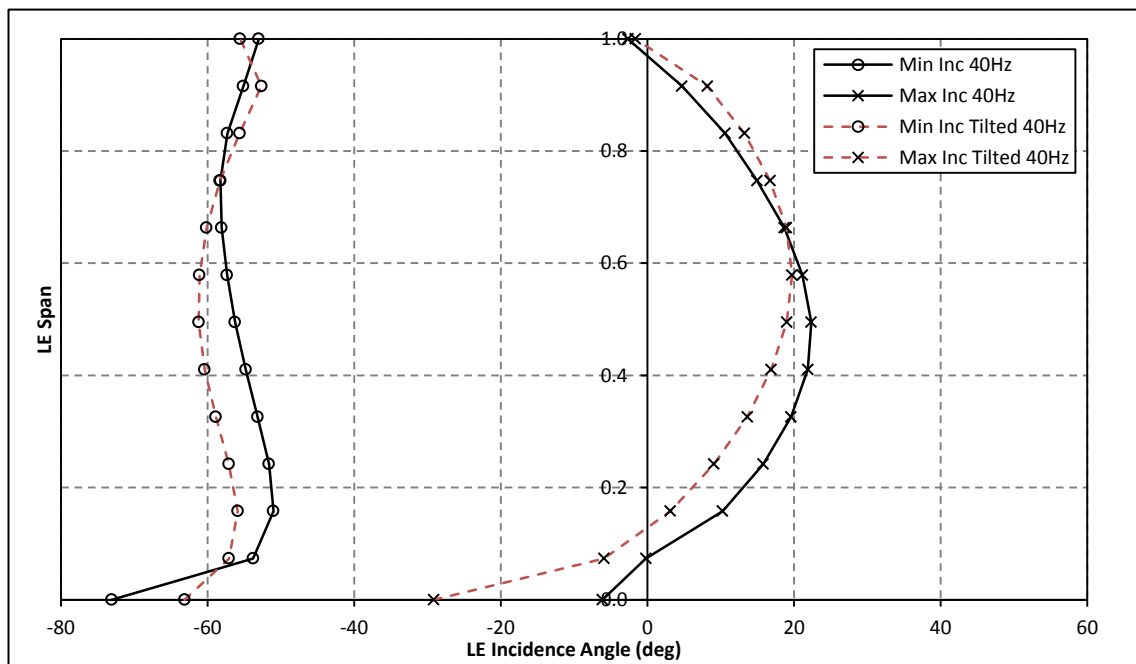


Figure 6.63: Span-wise incidence distribution at minimum and maximum incidence running points for radial and tilted volute. $A/r=26$

6.6 CHAPTER CONCLUSIONS

This chapter has shown the effect of mixed flow turbine housing tilt under steady state and pulsating inlet flows. The steady state results showed a peak stage efficiency improvement of up to 1.65% for the tilted housing over the radial design for the base size. The tilted housing design resulted in cycle average rotor efficiency improvements of up to 1.45% over the frequency range tested, 1.64% over the range of pulsation numbers tested and 2.13% over the range of tested loads. These corresponded to resulting stage efficiency improvements of 1.16%, 1.354% and 1.76% respectively. The reduction in cycle average performance improvement with respect to the rotor efficiency improvement was due to greater volute losses in the tilted design. In depth analysis of the volute and rotor flows revealed that the performance improvement achieved in tilted cases was the result of reduced shroud curvature.

The impact of volute A/r on the performance of tilt has also been assessed. It was observed that volute tilt was more beneficial in larger A/r cases. As the A/r was varied the loss mechanisms occurring within the rotor region shifted due to changes in degree of reaction and MFP. In the $A/r=26$ volute, the greatest level of loss occurred in the region associated with shroud separation and tip leakage. As the tilted volute was found to alleviate loss in this region most effectively, this led to greater performance improvements relative to the radial base line. The tilted volute design produced a 2.356% improvement in cycle averaged rotor efficiency and 2.171% improvement in cycle average stage efficiency in this case. This improvement reduced to only 1.291% and 0.835% for the rotor and stage efficiency in the $A/r=20$ volute case.

Analysis of the volute flows showed that secondary flow structures increase with increasing volute size under a constant inlet mass flow pulse. The secondary flow structures in the tilted volute showed asymmetrical flow structures, while symmetrical flows formed in the radial volute. The resulting volute exit flow angles were found to be impacted by this with the span-wise flow distribution shifting towards the shroud side of the LE.

7 THE IMPACT OF ROTOR LE FLOW DISTRIBUTION

In the previous section it was found that modifications to the volute can impact the LE span-wise flow distribution. These distributions were shown to be the result of the volute flow structures formed. This chapter attempts to gain an understanding of the impact of this flow variation. A range of LE flow distributions are simulated on a single passage model at a low velocity ratio running point. This running point was selected for the analysis as it was shown in chapter 4 that the available energy of the pulse is much greater at these operating points. Therefore, to improve pulse energy utilisation understanding turbine performance at these conditions is paramount. All simulations were conducted on the same mixed flow turbine described in section 4.1.

7.1 METHODOLOGY

A single blade passage was simulated to allow manipulation of the blade inlet span-wise flow distribution. The inlet boundary conditions applied were that of total pressure and temperature along with inlet velocity components. To assess the impact of LE span-wise distributions of flows, five velocity profiles were applied. These included a realistic distribution with radial, circumferential and axial velocity components varied over the span, the same distribution but with the range halved (named reduced realistic), a uniform velocity distribution with uniform axial, radial and circumferential velocity components over the span, a linearly varied circumferential velocity distribution increasing from hub to shroud (named positive linear distribution) and a linearly varied circumferential velocity decreasing from hub to shroud (named negative linear distribution). Although the circumferential span-wise velocity was varied in the two linear distributions, the axial and radial velocity components were kept constant. While the span-wise velocity profiles were varied the profiles were kept constant in the circumferential direction. In each case the passage total pressure and mass flow were kept constant to ensure constant mass flow parameter and therefore aerodynamic similarity. The span-wise average relative

flow angle was also kept constant so the focus of the comparison was on span-wise variation and not due to a shift in mean angle.

The single blade passage and outlet domain is shown in figure 7.1. The resulting mesh contained approximately 2 million cells.

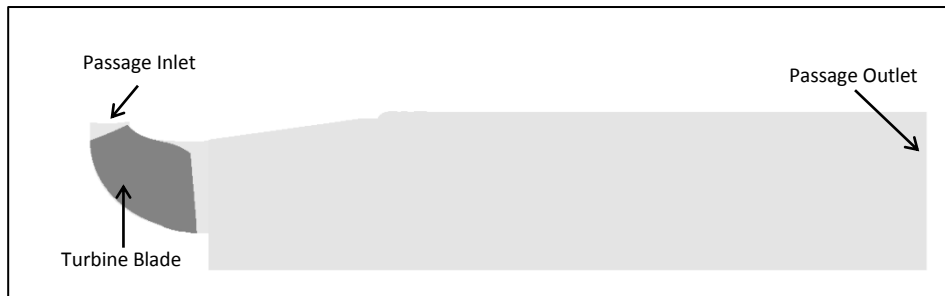


Figure 7.1: Single passage radial computational domain

The full stage simulations completed in chapters 5 and 6 provided the passage inlet boundary conditions for the realistic span-wise flow distribution implemented in this chapter.

As the maximum pulse energy is available at the peak pulse, this investigation is focussed on this running point. The volute outlet flow distribution is shown in figure 7.2. The range of absolute flow angle over the span is significant with a range of 35° over the central 95% of the span. The cause of this behaviour can be attributed to the complex flow development occurring in the volute resulting in varying radial flow over the passage also shown in figure 7.2. Figure 7.2 shows the flow distribution in radial housing design only. The analysis has been repeated to include the tilted housing design flow distribution which is discussed in section 7.3. Despite the significance of the variation, it is common practice to optimise blade geometries based on uniform LE flow distributions and not account for this span-wise variation.

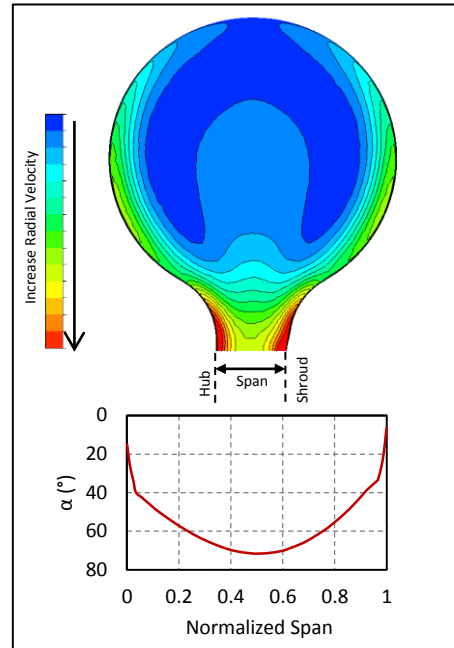


Figure 7.2: Volute radial velocity contours and exit absolute flow angle

7.2 THE IMPACT OF ROTOR INLET FLOW FROM THE RADIAL HOUSING

The resulting LE relative flow angles for each of the applied distributions is presented in figure 7.3 followed by the resulting LE incidence in figure 7.4. The uniform span-wise velocity case results in an approximately linear variation in LE relative flow angle decreasing from the maximum at the hub to a minimum at the shroud. The cause of this behaviour is the result of the variation in blade speed from hub to shroud due to the varying LE radius. The linear positive and linear negative distributions result in similar LE relative flow angle variations but the negative linear distribution increases the variation in relative flow angle over the span, while the positive linear distribution reduces the span-wise variation. The realistic distribution results in a parabolic type distribution in flow angle. In this case the relative flow angle range is greater than any other case ranging from approximately -9° at the hub to 34° at the centre of the LE. Not only does the range increase, but the parabolic distribution results in a larger gradient of incidence over the LE. Furthermore, the variation is dominated by the volute outlet flow distribution and the varying LE tip speed appears to have little impact. In the reduced variation case the impact of tip

speed can be seen as the parabolic distribution is no longer symmetrical and more positive flow angles occur towards the hub.

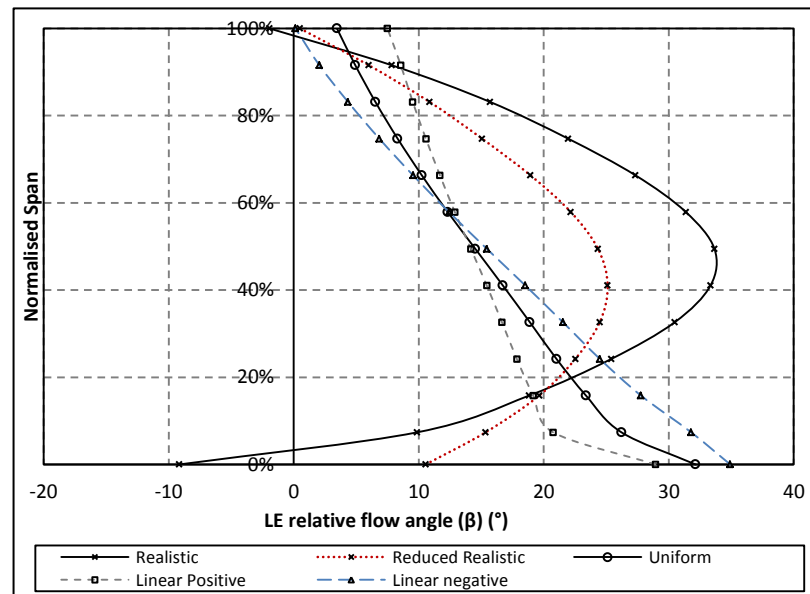


Figure 7.3: LE relative flow angle for all tested inlet span-wise distributions

Figure 7.4 shows the LE span-wise distribution of incidence. In this case the blade angle achieved due to the mixed flow effect is subtracted from the relative flow angle resulting in the LE incidence as per equation (2). The impact of the mixed flow effect is not constant over the blade LE due to the varying blade angle achieved as shown in figure 7.5. This variation is caused by varying blade camber (figure 7.6) and varying LE flow cone angle (figure 7.7) that is created due to the radial and axial flow components at the LE. The variation in blade camber angle was introduced in an attempt to reduce the impact of varying LE blade speed. However, the poor flow turning ahead of the LE shown in figure 7.7, particularly towards the hub, reduces the impact. The maximum blade angle magnitude achieved was 5.2° for the realistic case, this reduced for the linear distributions. While this is only a modest mixed flow effect, the impact on the incidence distribution is clear. In the uniform and linear variation cases the blade angle distribution acts to negate the impact of varying LE speed resulting in a reduction in incidence angle range compared to the relative flow angle range. In the positive linear distribution case, incidence remains almost constant from 40% blade span up to the shroud tip of the blade.

In the realistic and reduced realistic cases, the mixed flow effect reduced the peak incidence angle encountered but the variation in LE blade angle had a little impact on the span-wise distribution.

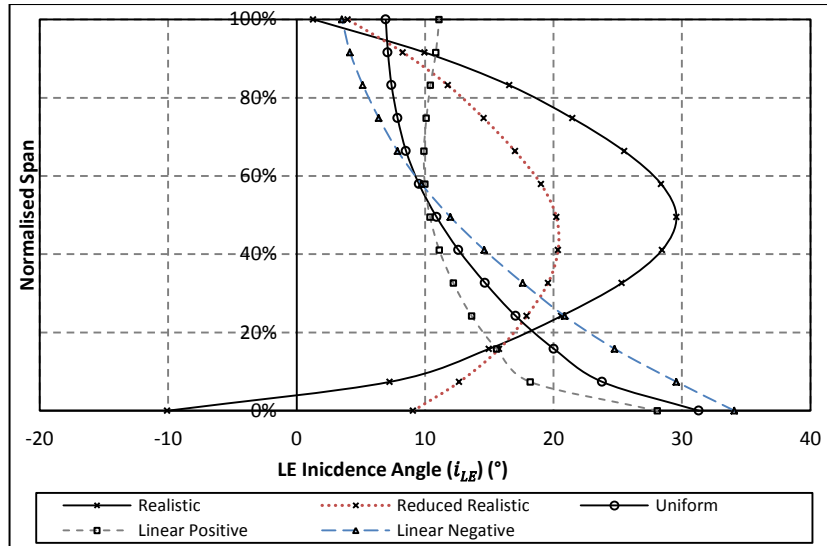


Figure 7.4: LE Incidence angle for all tested inlet span-wise distributions

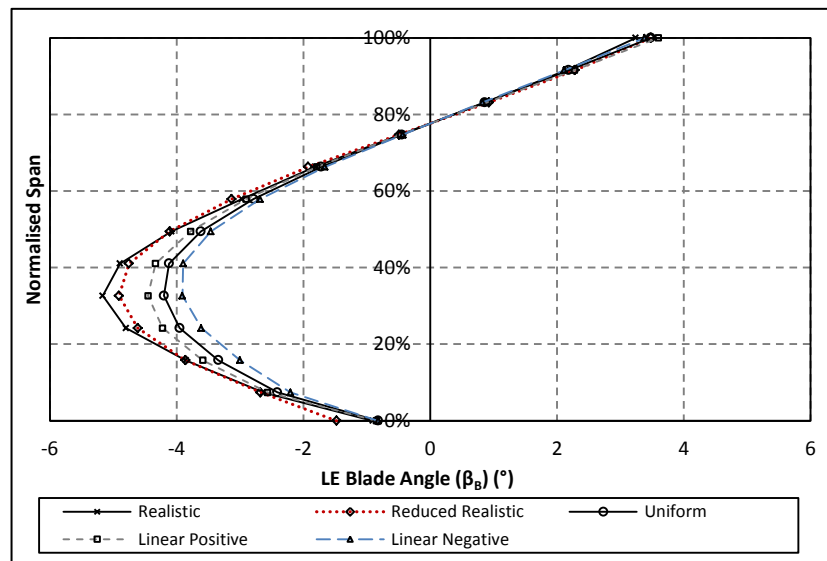


Figure 7.5: LE blade angle for all tested inlet span-wise distributions

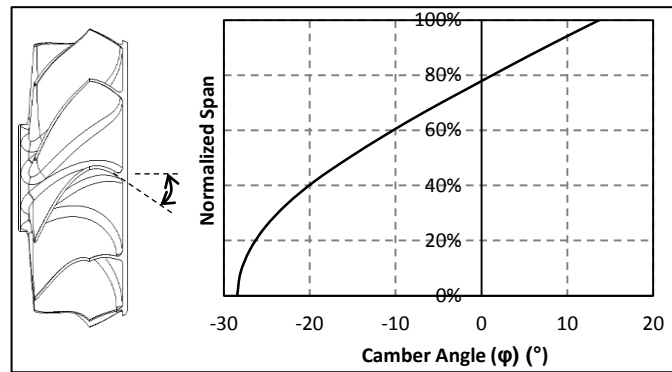


Figure 7.6: Blade LE camber angle

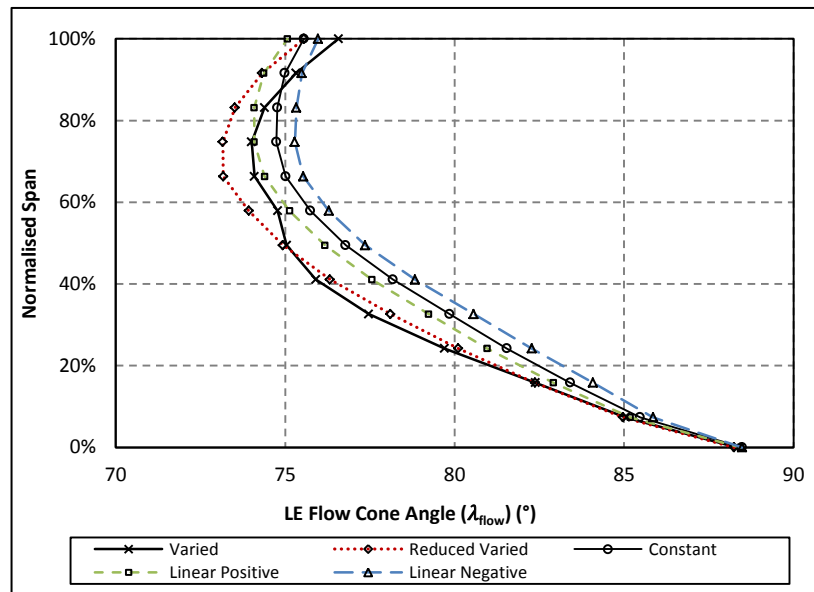


Figure 7.7: LE flow cone angle for all tested inlet span-wise distributions

Along with the span-wise variation in flow angle the span-wise mass flow was also found to vary significantly between cases. Figure 7.8 presents the normalised mass flow at the rotor LE for each of the cases. These values were extracted over circumferential bands covering the inlet span. As was the case with LE incidence, the realistic distribution results in the greatest variation in normalised mass flow. Here, the maximum mass flow occurs towards the hub and shroud sides of the passage. The cause of this distribution is the development of Dean type flows within the volute resulting in greater radial velocities around the volute walls as shown in figure 7.2. Each of the linear cases shows maximum mass flow towards the shroud but this effect reduced for the linear positive inlet distribution.

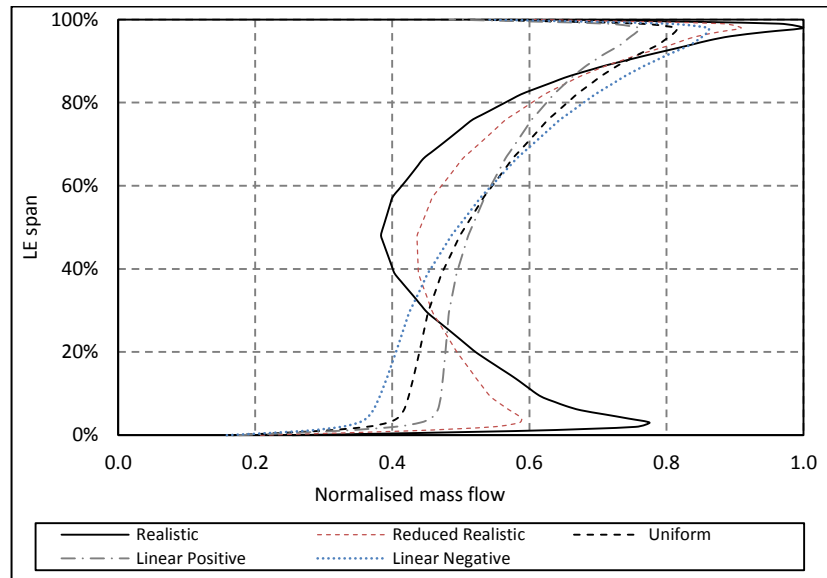


Figure 7.8: Normalised mass flow across LE span

Figure 7.9 shows static entropy contour plots on constant stream wise planes at 5%, 10%, 25% and 50% chord positions for the uniform and realistic flows. The tangential velocity vectors are also included overlaid on the contour plots. The planes are orientated to look downstream from the LE to the TE and the wheel is rotating in the clockwise direction with the suction surface of the blade (SS) on the left of the passage and the pressure surface of the blade (PS) on the right.

The impact of the incidence distribution on LE separation is evident in both the 5% and 10% planes as the shape and size of the separation region on the SS varies significantly. The realistic velocity distribution case results in the greater loss at the blade mid-span where incidence was most positive. The high entropy, separated region reduces towards both the hub and shroud side of the blade where incidence reduces to more optimal values. In the uniform inlet velocity case, the SS loss region is greatest at the hub. This is due to the increase in incidence towards the hub in this case. The 10% and 25% chord planes also show greater loss occurring on the shroud surface in the realistic distribution case. The cause of loss in this region is due to the relative motion of the shroud in the counter clockwise direction driving fluid across the passage, and shroud surface separation. This loss region is shown in the blade plot positioned 5% of the passage off the SS presented in figure 7.10. In the

varied case an increased loss region on the shroud is evident from shroud surface separation. The high mass flow in this region shown in figure 7.8 could be responsible for the increase in this loss in the realistic distribution case.

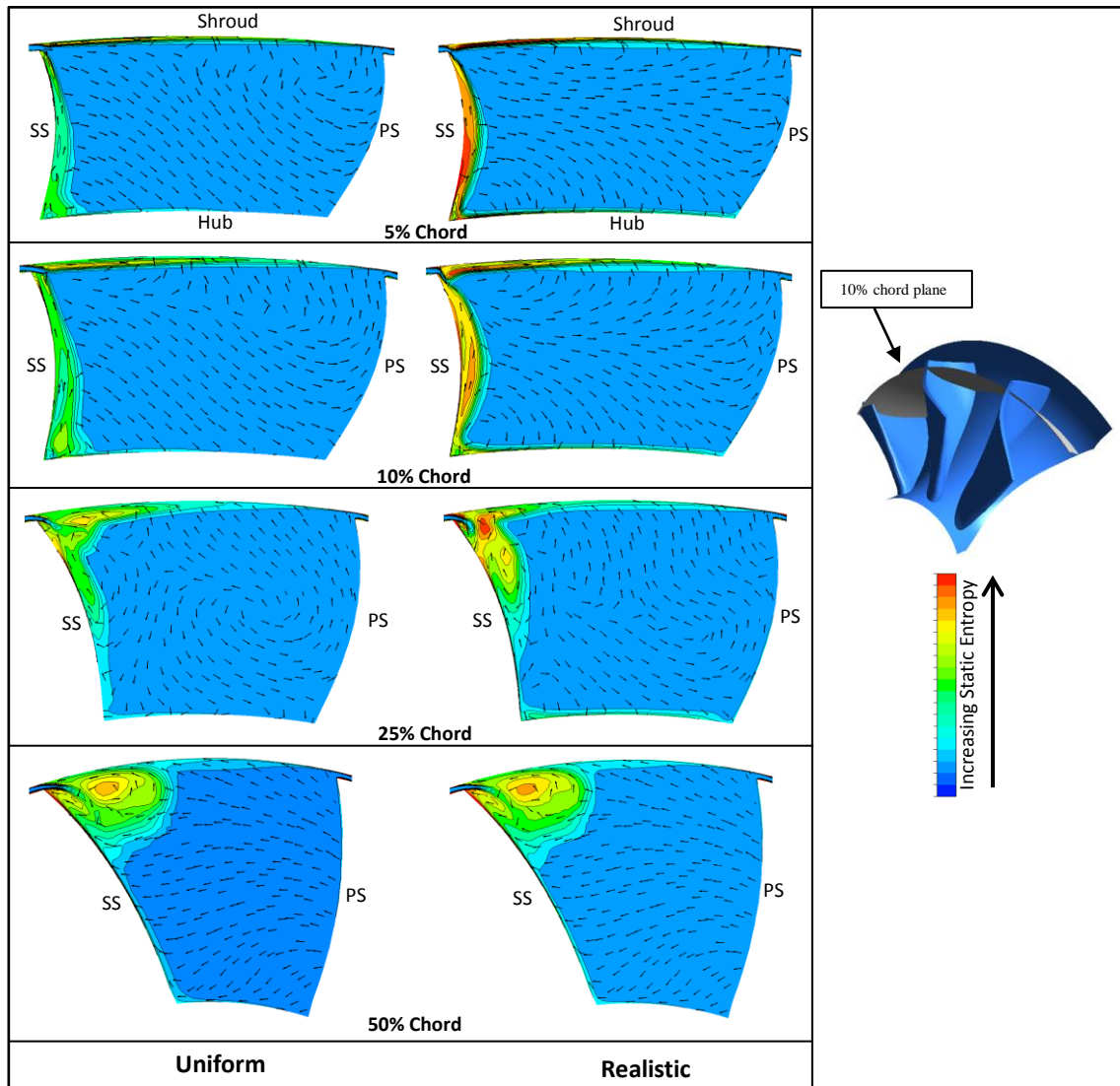


Figure 7.9: Static entropy contours and vectors plotted on constant streamwise planes in both the uniform inlet velocity distribution and realistic distribution models

The tangential velocity vectors on the constant streamwise planes in figure 7.9 show that the cross passage flows also differ between the two cases. At the 5% chord position in the uniform distribution case the flow moves from shroud to hub as well as from SS to PS. In the realistic distribution case the prominent flow is from the SS to PS and a notable reduction in flow from shroud to hub over the plane is evident. Moving down stream to the 10% and 25% chord positions the cross-passage flow continues to develop due to the Coriolis effect. In the uniform distribution case, the resulting counter clockwise rotation is more evident than that in the realistic distribution case. By the 50% chord plane, a uniform flow distribution from PS to SS has established in both cases. Only the top left corner shows significant secondary flow structures due to tip leakage.

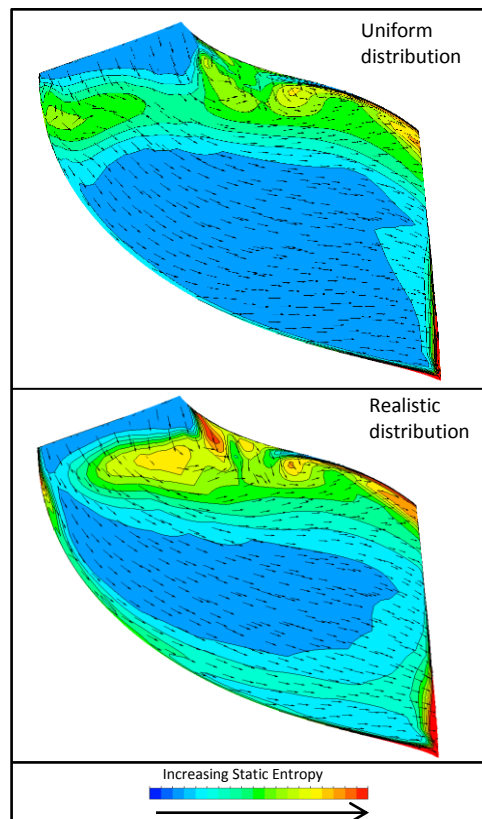


Figure 7.10: Between blade plot 5% of passage off suction surface

To assess the loss mechanisms within the rotor region, entropy generation through the passage was investigated using the same approach as implemented in chapter 6. The loss within each region can be attributed to a dominant mechanism giving a greater understanding of the physics behind the performance differences.

Figure 7.11 shows the control volumes in the blade passage used in the calculation of entropy generation.

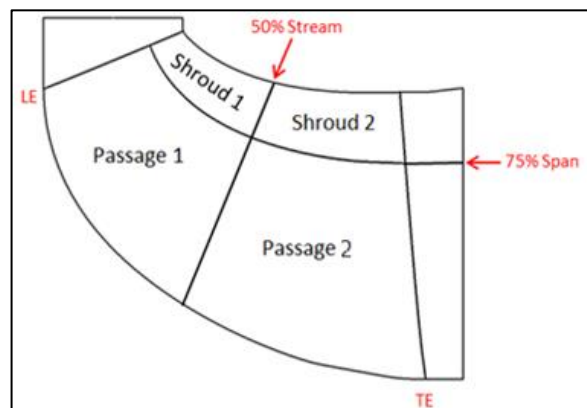


Figure 7.11: Rotor passage control volumes

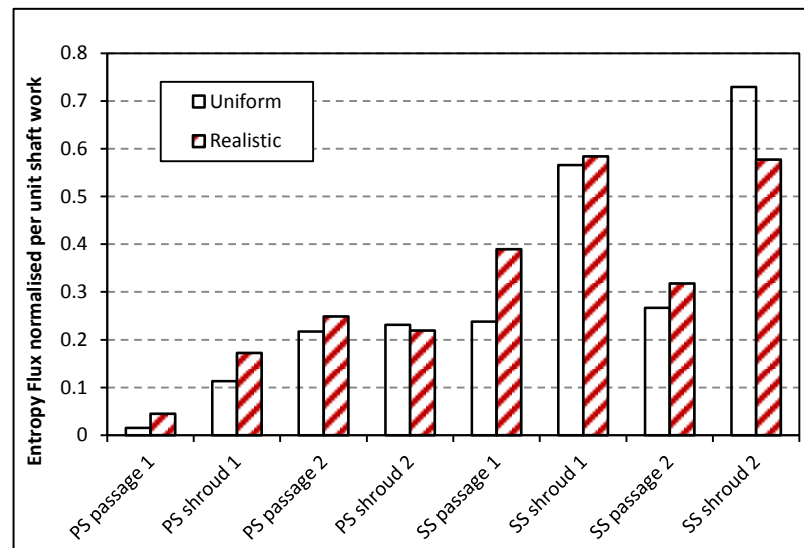


Figure 7.12: Entropy generation in rotor passage regions

The distribution of loss in the rotor region shown in figure 7.12 expresses noticeable differences in the loss generation in the two cases. The realistic distribution case shows a marked increase in entropy generation in the SS passage 1 region, and a decrease in the SS shroud 2 region when compared with the uniform distribution case. The main loss associated with SS passage 1 is LE loss due to excessive blade incidence. It is in this region that peak incidence occurs in the realistic distribution case leading to severe LE flow separation. SS shroud 2 is associated with tip leakage loss. An increase in loss in this region is the result of an increase in blade loading towards the tip in the uniform distribution case.

The resulting normalised efficiency for each of the five simulated cases is presented in table 7.1. The maximum difference observed was 2.17% for the reduced realistic case over the realistic component base case. Using the reduced realistic case would therefore overestimate the rotor efficiency. Of the linear distributions, the negative linear distribution resulted in a negative and hence conservative difference while both the uniform and positive linear distributions gave small positive differences. The difference for the uniform components was only 0.67% despite the substantial flow differences in flow and losses mechanisms highlighted.

| Distribution | Percentage change T-s Eff |
|------------------|------------------------------|
| Realistic | 0% |
| Halved Realistic | 2.17% |
| Uniform | 0.67% |
| Linear | 1.86% |
| Reversed Linear | -0.31% |

Table 7.1: Percentage efficiency change from the realistic variation span-wise distribution

7.3 TILTED PASSAGE PERFORMANCE

In addition to comparison of span-wise flow distribution in a standard radial passage, the work was extended to include the impact of the 20° volute tilt. In order to achieve this, the modified passage implemented with the tilted volute was used. This allowed the axial flow component to be added without misaligning the flow with the passage. The full stage tilted volute simulations were used as a base for this part of the study. The tilted full stage achieved the same mass flow at a slightly reduced inlet pressure ratio. The resulting inlet total pressure and temperature at the peak of the pulse, along with the LE flow velocity components in the span-wise direction were extract from this simulation and provided as inlet boundary conditions to the single passage model. This realistic distribution was then compared with a uniform inlet flow distribution with the same total pressure and temperature boundary conditions. The average LE relative flow angle was again kept constant and equal to that of the radial passage flow cases. The span-wise variations in relative flow angle are presented in figure 7.13. However, as previously stated the tilted passage

achieved equal mass flow to the radial passage at a pressure ratio approximately 1% lower. As a result, the two passage designs operate at slightly different MFP's and velocity ratios. Therefore, while aerodynamic similarity was maintained between the radial passage variants and the tilted passage variants individually, the radial and tilted passage efficiencies are not directly comparable.

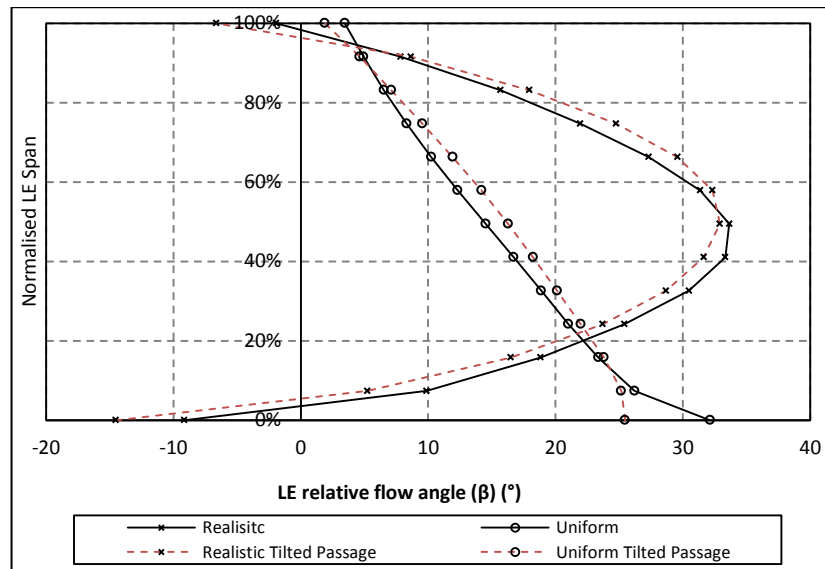


Figure 7.13: LE relative flow angle radial and titled passage

The LE blade angles and LE incidence angles are presented in figures 7.14, and 7.15 respectively for both the radial and tilted passages. From figure 7.14 it is clear that the tilted passage design results in a considerable increase in blade angle as a result of an increased axial flow component. Towards the hub the maximum blade angle achieved is approximately -10° . However, the increased axial flow component also means that the blade angle becomes increasingly positive towards the shroud where the blade camber angle is positive. The total range of blade angle in the tilted passage design is approximately 20° .

The resulting LE incidence distribution in the tilted case is notably different from the radial design for both the realistic and uniform distribution cases. The reduction in incidence in the tilted cases is greatest at the hub where the blade camber angle is greatest. Beyond the 60% span position the tilted passage incidence becomes more positive than the comparable radial passage due to the positive camber angle of the blade. The resulting span-wise incidence variation in the uniform distribution tilted passage case is considerably less than that of the radial passage case. The variation in

the realistic distribution case does not reduce for the tilted passage but the average incidence angle does show a reduction.

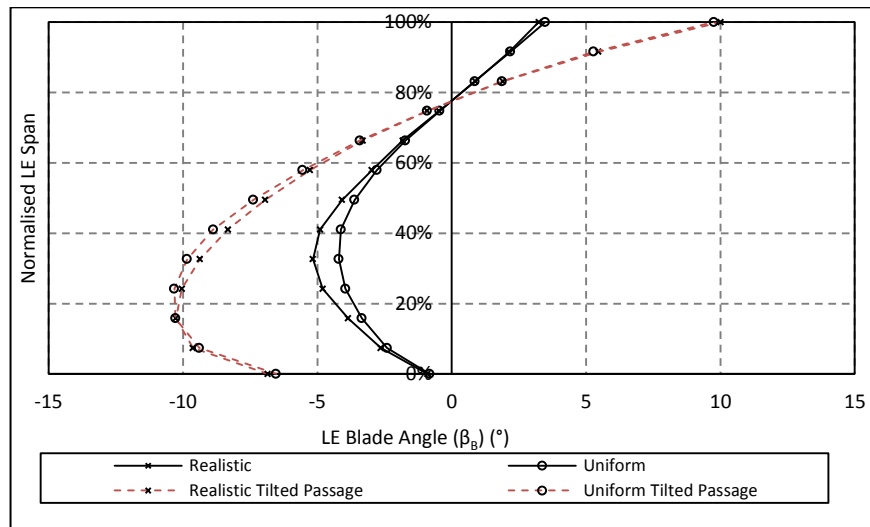


Figure 7.14: LE blade angle radial and titled passage

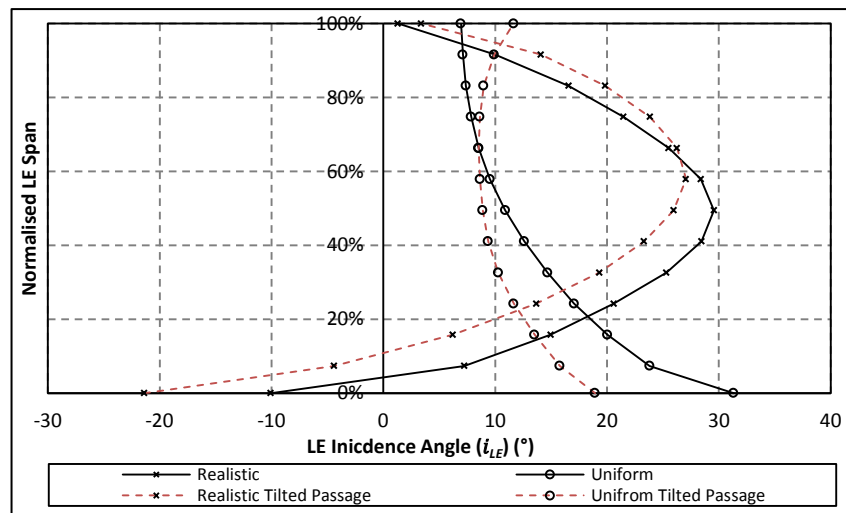


Figure 7.15: LE incidence radial and titled passage

Figure 7.16 shows contour plots through the tilted passage at constant chord positions with the same orientation as in figure 7.9. In the realistic distribution case at the 5% and 10% chord planes, SS separation is focused at the 60% span position. As shown in figure 7.15 the maximum incidence in this case occurs at a greater chord position than in the radial passage where the incidence distribution is centred at the middle of the span. The uniform distribution case sees an almost constant SS separation over the majority of the blade span, only a small increase in loss close to the hub, where incidence becomes increasingly positive was observed. Comparing

Figure 7.16 with figure 7.9 shows that in both the tilted passage cases the shroud surface separation reduced compared to that seen in the radial cases. This is further supported by figure 7.17 that shows the between blade plots 5% of the passage off the SS in the tilted passage case. Here a notable reduction in shroud surface separation occurs in the tilted passage due to reduced shroud curvature. The realistic distribution case in figure 7.17 does show an increased loss region at the blade hub which was not observed in any other cases.

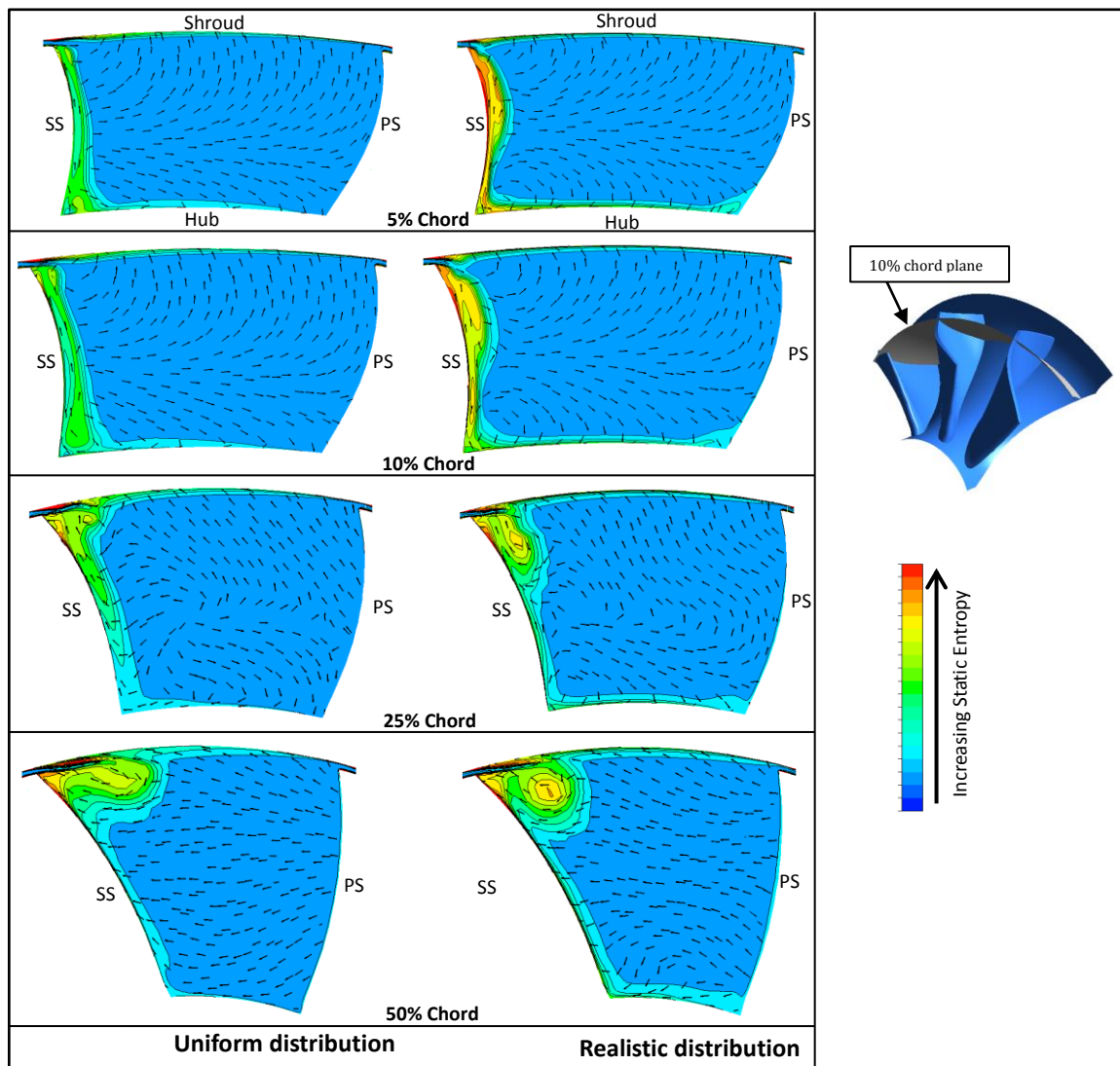


Figure 7.16: static entropy contours and vectors plotted on constant streamwise planes in both the uniform inlet velocity distribution and realistic distribution cases. tilted passage

The vector plot overlaid on the contours in figure 7.16 show flow moving from the hub to shroud at the 5% and 10% planes. This movement was not observed in the radial passage and was caused by the increase axial flow component at the blade LE

in the tilted passage. As a result, the counter clockwise rotation, clear in the uniform distribution radial case, is much less prevalent.

The uniform flow distribution in the tilted passage resulted in an increase of 0.7% in efficiency compared to that of realistic distribution. As was the case in the radial passage comparisons, the improvement in efficiency is small considering the significant change in rotor flows observed

Comparing the performance of the tilted passage with that of the radial passage shows approximately 1.8% improvement in terms of efficiency. However, the passage pressure ratio was not comparable between cases due to the increased swallowing capacity of the tilted passage. The resulting torque from the tilted passage design did show a small increase even though operating at a 1% lower pressure indicating improved performance in the tilted case.

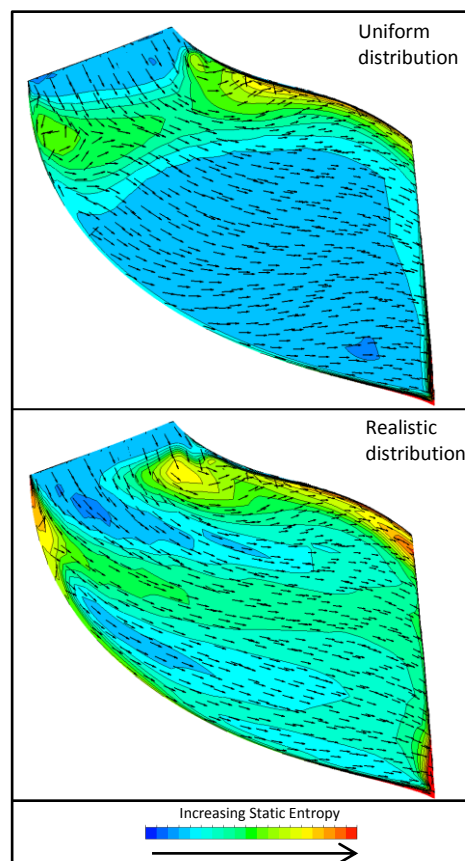


Figure 7.17: Between blade plot 5% of passage off ss. tilted passage

7.4 CHAPTER CONCLUSION

This chapter has investigated the impact of span-wise variation of incidence angle on turbine performance in a single passage. This allowed the domain complexity to be reduced and greater control over inlet flows to be achieved. It was observed that the rotor operates under highly varying span-wise flow in the presence of the turbine volute under pulsating flow in chapters 5 and 6. The variation resulting from the volute flow was applied as a boundary condition in this chapter to a single rotor passage. The results were compared with those of a uniform distribution, positive linear distribution, negative linear distribution and a reduced realistic distribution. The maximum efficiency difference observed was a 2.17% increase for the reduced realistic case when compared with that produced under the realistic distribution.

An in-depth analysis of the passage flow physics showed a significant difference in the effect of the realistic span-wise distribution and the uniform distribution. Not only did the incidence variation change significantly, but so did the mass flow distribution at the LE. Comparison of the entropy generation through the passage showed a shift in loss towards shroud region due to increased tip leakage in the uniform distribution case.

The tilted passage design, with an increased axial flow component, resulted in an increase in swallowing capacity over that of the radial passage. For a uniform inlet relative flow angle the incidence was found to decrease due to the greater mixed flow effect achieved. A reduction in shroud surface separation was evident along with a notable difference in passage secondary flows due to the added axial flow component.

In this chapter idealised boundary conditions were compared with realistic volute exit flows, although no volute was included. It is common practise in the rotor design process to assume such idealised inlet profiles. The findings presented show the inaccuracies of this approach, and the significant impact on rotor flow physics caused. Therefore, blade geometries designed under such conditions may be sub-optimal. As such it is recommended that future blade optimisation accounts for the realistic inlet flow conditions. This is particularly important in mixed flow turbine

design where the span-wise blade angle can be manipulated through blade cone and camber angles.

Furthermore, the work showed that changing the span-wise distribution of flows can increase performance. It is therefore of importance to address how volute design can be used to manipulate span-wise flow distributions.

8 IMPACT OF VOLUTE ASPECT RATIO

Chapter 7 discussed the impact of rotor inlet span-wise variation on turbine performance. The variation between the realistic and idealised distributions resulted in significant performance discrepancies.

This chapter investigates the impact of volute aspect ratio on performance. As the volute aspect ratio defines the cross-sectional shape of the volute, an impact on span-wise flow distribution can be expected. The aim was to assess how volute design can be used to improve secondary flow development and the resulting span-wise distribution.

8.1 TURBULENCE MODELLING APPROACH

Up to this point, the turbulence model implemented throughout this thesis has been the $k - \omega$ SST model. However, in an attempt to better capture the flow physics, the Shear Stress Transport Scale-Adaptive simulation (SST-SAS) method was employed in this chapter and chapter 9. This approach numerically solves the flow using the URANS approach but detects the resolved unsteady structures and adjusts them producing LES like results in the unsteady regions. This modelling approach can therefore result in more accurate predictions in highly unsteady separated or vortical regions. Full details of the turbulence computation can be found in Menter & Egorov, (2005).

8.2 ASPECT RATIO MODELS

Turbine design is often a compromise between performance and packaging requirements. In this study three turbine volute designs with varying aspect ratio were designed and analysed. The three volute designs are presented in figure 8.1. The volute aspect ratio is defined as -

$$AR = \frac{d_1}{d_2} \quad (81)$$

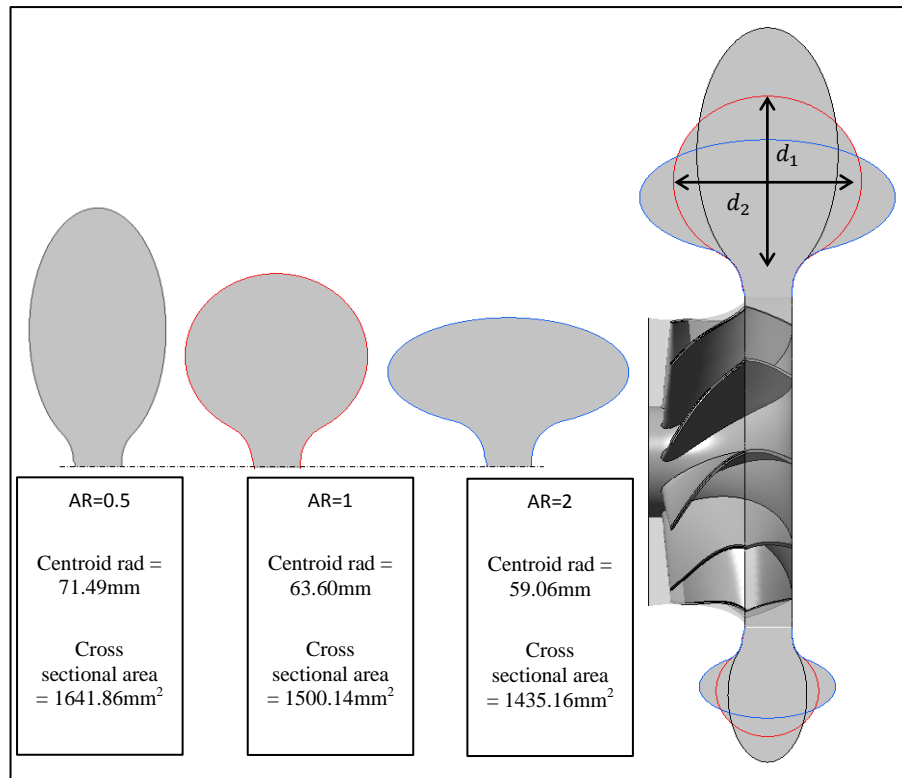


Figure 8.1: Aspect ratio designs, AR=0.5, AR=1 and AR=2

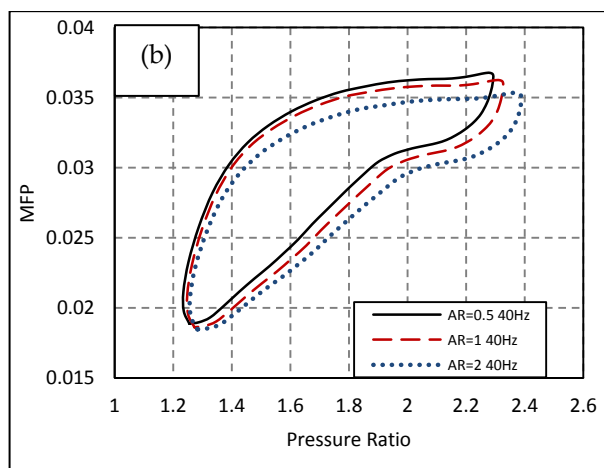
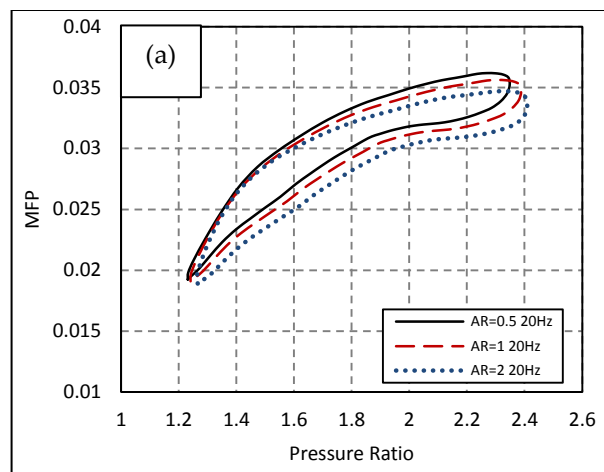
Where AR is Aspect Ratio, d_1 is the horizontal diameter and d_2 is the vertical diameter. The three tested volutes have aspect ratios of 0.5, 1 and 2. The volute A/r is defined as the ratio of volute cross sectional area to the volute centroid radius. Figure 8.1 includes the centroid radius and area values for each of the designs used to produce a constant MFP as used in section 8.3. This information is included to provide clarity on the volute designs as figure 8.1 is not exactly to scale.

8.3 4.1. IMPACT OF VOLUTE ASPECT RATIO ON MFP

Initial analysis of volute aspect ratio was completed at constant volute A/r . The volute A/r determines the rotor inlet flow angle and the swallowing capacity of the stage. Therefore, maintaining A/r is expected to maintain Mass Flow Parameter (MFP) and therefore ensure aerodynamic similarity. Analysis was conducted at 20Hz, 40Hz and 60Hz pulse frequencies under a pulse load of 100% and a pulsation number of 1, as defined in section 5.1.

Presented in figure 8.2 are the hysteresis loops for all three volute aspect ratios at 20Hz, 40Hz and 60Hz pulse frequencies. It is clear, that maintaining volute, A/r did

not ensure a constant MFP and that the volute aspect ratio has a significant impact on stage performance. At all three tested frequencies the MFP of the volute reduces with increasing aspect ratio. The maximum variation in cycle averaged MFP between the three designs at constant A/r was 4.3% under the 60Hz pulse frequency. This impact of volute aspect ratio is important as volute cross sectional shape is often compromised due to packaging requirements of the turbocharger. If the volute cross section shape is altered for such a design, ensuring constant A/r alone will therefore not ensure a constant MFP. A similar effect was observed by Yang et al. Yang et al., (2015). The variation observed in that study was approximately 2% and despite the discrepancy in MFP of the two volute designs, the authors still compared them in terms of performance.



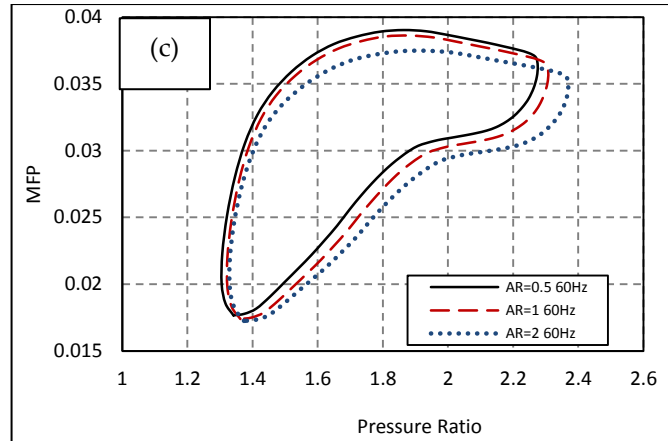


Figure 8.2: MFP vs pressure ratio for volute aspect ratio designs with constant A/r. (a) - 20Hz, (b) 40Hz and (c) 60Hz

Figure 8.3 presents the variation in LE incidence throughout the pulse for each of the volute aspect ratio's at 60Hz pulse frequency. Increasing the volute aspect ratio increases the mean incidence throughout the pulse. The variation between the three designs is approximately 6° . This observation, along with that of varying MFP with aspect ratio, indicates that reducing volute aspect ratio gives the same effect as increasing A/r and vice versa. More specifically, it is believed that increasing the centroid radius reduces the radial flow component of velocity due to less flow guidance from the volute outer wall.

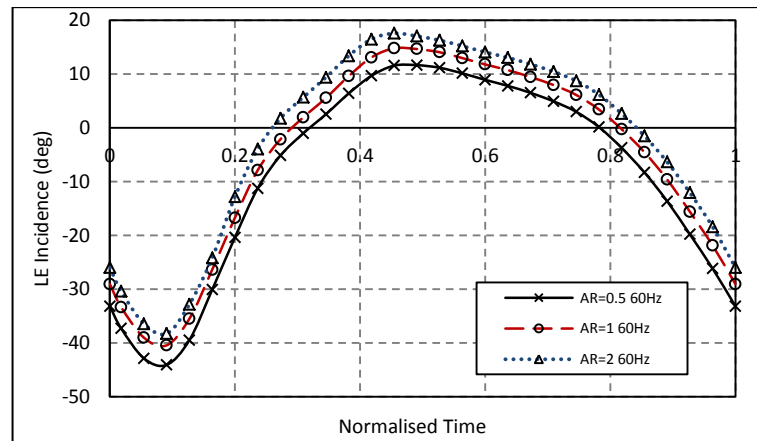


Figure 8.3: Variation in LE incidence between designs at constant A/r

8.4 4.2. ASPECT RATIO EFFECT WITH CONSTANT MFP

To ensure aerodynamic similarity between the designs, thereby giving a fair comparison of performance, stage MFP must be matched. To achieve this, the volute A/r's were modified. Figure 8.4 shows A/r as a function of azimuth angle for each volute design. The A/r ratio of the AR=1 and AR=2 volutes was increased slightly to enable constant MFP.

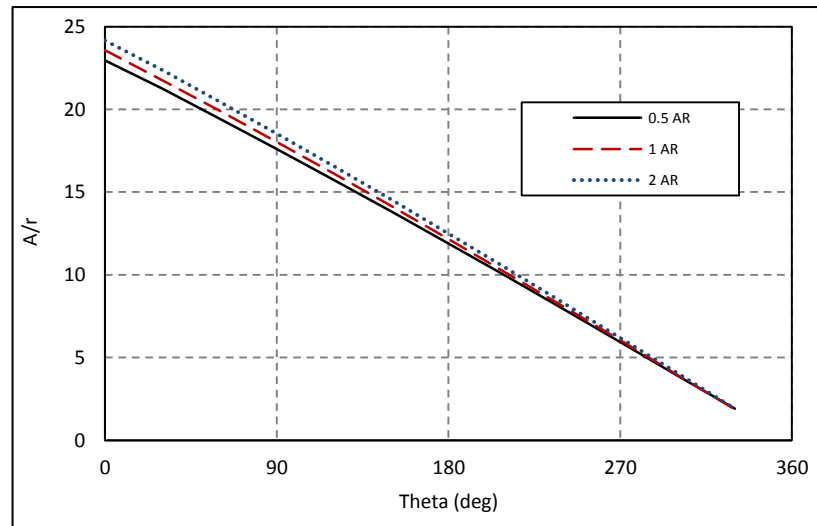


Figure 8.4: Volute A/r distributions to match MFP

The resulting MFP hysteresis loops are presented in figure 8.5 for the three designs at the three tested pulse frequencies. The resulting cycle averaged MFP varied by less than 0.5% between all three housing designs. The designs were judged to be aerodynamically similar for the purpose of analysing turbine performance.

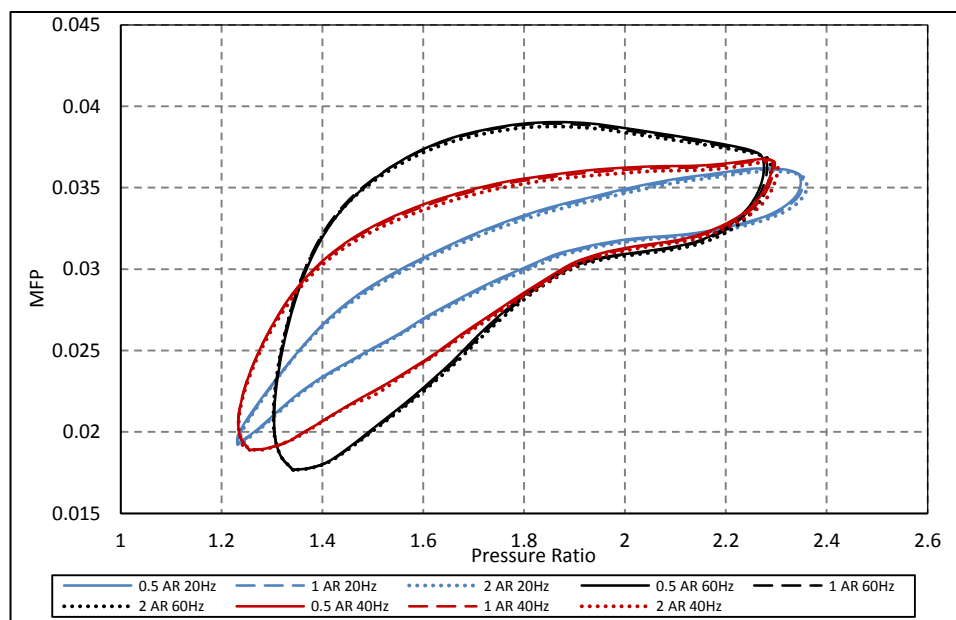


Figure 8.5: MFP vs pressure ratio for each of the volute aspect ratio design with modified A/r distributions

The rotor efficiencies achieved over the pulse cycle for each configuration, at the three tested pulse frequencies, are presented in figure 8.6. A clear reduction in the range of rotor operating velocity ratios with increasing frequency can be observed. This range reduction almost exclusively happens at the high U/c_s end of the

spectrum. The maximum U/c_s achieved at 60Hz was only 0.851 as appose to 0.994 at 20Hz. This effect was also observed in chapter 5 with increasing pulse frequency. The range of rotor efficiency measured also reduced with increasing frequency.

The variation in rotor efficiency between the tested designs is small, but at all frequencies the volute AR=0.5 design was less efficient across the range of operation. The AR=0.5 design also achieved greater maximum rotor U/c_s than the other two designs at all frequencies. This can be attributed to a greater volute loss occurring, resulting in a lower pressure ratio acting over the rotor. The efficiency of the AR=1 and AR=2 are similar over the range of rotor operation at all tested frequencies.

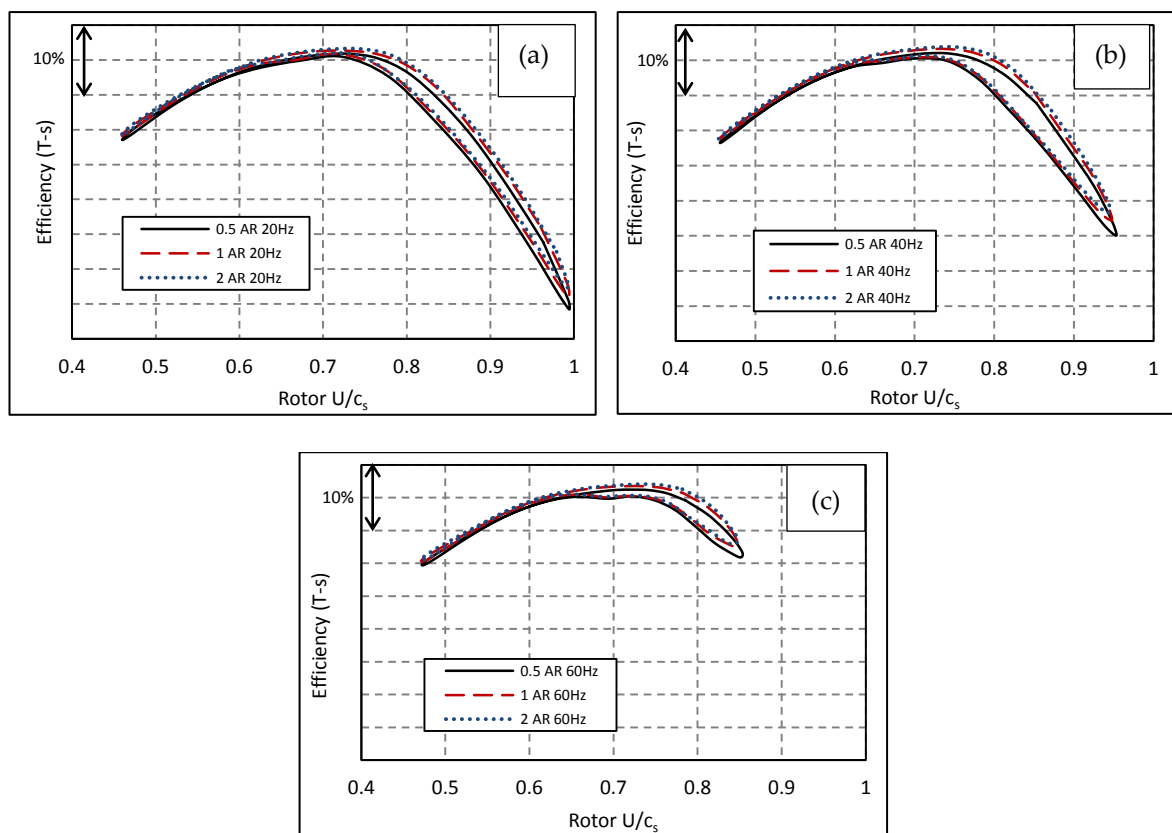


Figure 8.6: Turbine rotor efficiency. (a) - 20Hz, (b) - 40Hz and (c) - 60Hz

Table 8.2 presents the cycle averaged efficiencies for each design under the three tested frequencies. In all cases the values are normalised by the AR=2 case. The cycle averaged rotor performance of the largest aspect ratio design was consistently the greatest. The maximum improvement was 1.04% over the AR=0.5 design occurred at 20Hz. Increasing volute AR also resulted in an increase in cycle averaged stage efficiency with the greatest improvement over the AR=0.5 design being 1.47%, again at 20Hz pulse frequency. The larger improvement in stage efficiency between designs

was the result of the volute total pressure loss being significantly greater in the AR=0.5 design. The greatest difference in normalised volute loss coefficient between designs was 13.83%. In all cases the performance of the AR=1 design showed performance levels similar to that of the AR=2 design. The efficiency of the rotor at the minimum and maximum U/c_s running points is also presented. Consistently, the variation in efficiency between the three aspect ratio designs is greatest at the maximum velocity ratio point. The largest variation at this running point was 7.59% at 20Hz pulse frequency. At the minimum U/c_s running point the maximum variation in performance was only 1.17%. As the maximum amount of pulse energy is available at the minimum U/c_s running point, it is the performance here that has the largest contribution towards cycle averaged performance.

| Aspect Ratio | | 0.5 | 1 | 2 |
|--------------|----------------------------|--------|--------|--------|
| 20Hz | Eff Min U/c_s | 99.02% | 99.94% | 100% |
| | Eff Max U/c_s | 92.41% | 96.48% | 100% |
| | Cycle AVG Rotor Eff | 98.96% | 99.75% | 100% |
| | Cycle AVG Stage Eff | 98.53% | 99.57% | 100% |
| | Volute Pt loss Coefficient | 16.05% | 0.34% | 0.0% |
| 40Hz | Eff Min U/c_s | 99.12% | 100% | 99.99% |
| | Eff Max U/c_s | 93.85% | 97.96% | 100% |
| | Cycle AVG Rotor Eff | 99.00% | 99.77% | 100% |
| | Cycle AVG Stage Eff | 98.59% | 99.61% | 100% |
| | Volute Pt loss Coefficient | 15.54% | 0.0% | 0.14% |
| 60Hz | Eff Min U/c_s | 98.83% | 99.71% | 100% |
| | Eff Max U/c_s | 97.04% | 99.38% | 100% |
| | Cycle AVG Rotor Eff | 99.01% | 99.73% | 100% |
| | Cycle AVG Stage Eff | 98.60% | 99.59% | 100% |
| | Volute Pt loss Coefficient | 15.89% | 0.0% | 0.32% |

Table 8.1: Normalised performance of each aspect ratio housing design at 20hz, 40hz and 60hz pulse frequency

The rotor entropy generation method is used again to assess the loss mechanisms in the rotor regions of each of the designs. The breakdown of the control volumes within the rotor region is presented in figure 8.7.

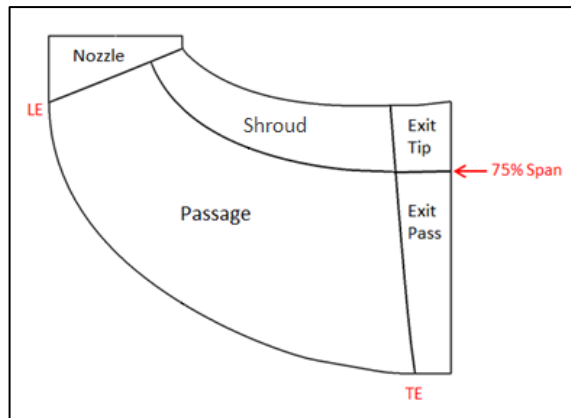


Figure 8.7: Breakdown of passage into section for loss analysis

The resulting entropy generation is plotted in figures 8.8 and 8.9 at the minimum and maximum running points respectively.

Comparing the losses at the minimum incidence running point shows that the maximum losses occur in the pressure surface (PS) shroud and passage regions. This can be attributed to the high level of PS separation occurring at the highly negative incidence. At this running point the level of PS loss was much greater in the AR=0.5 volute design. This result correlates with that presented in table 8.1 which shows a large efficiency difference between the AR=0.5 design and the other designs at this operating point. The AR=2 design showed only a small significant improvement over the AR=1 design.

At the maximum incidence running point, the major entropy generation occurred in the suction surface (SS) passage and shroud regions due to the LE losses associated with positive incidence. The variation between the three designs was smaller in this case. The most significant difference occurred in the SS shroud region where there are greater losses for the AR=0.5 design. The main loss contributions in this region was shroud tip leakage.

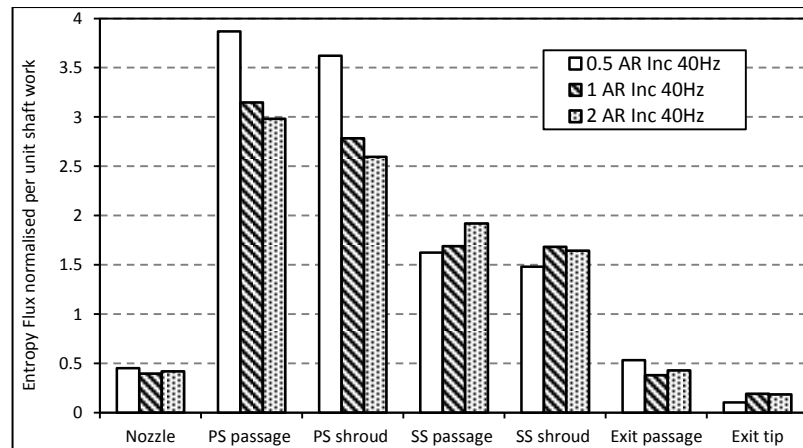


Figure 8.8: Entropy generation in rotor passage at minimum incidence

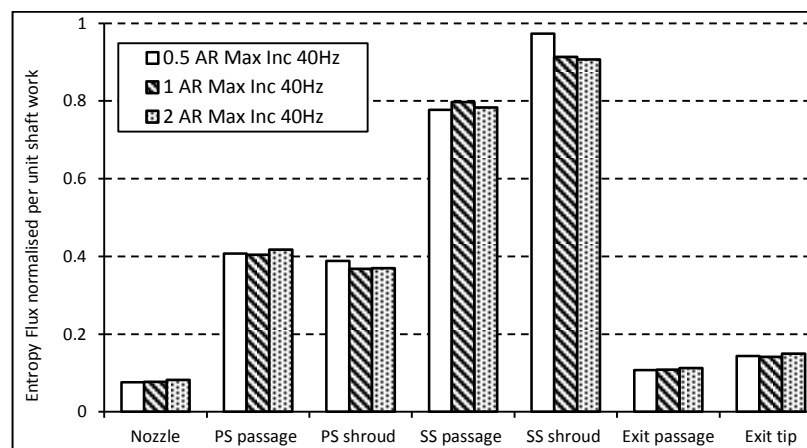


Figure 8.9: Entropy generation in rotor passage at maximum incidence

8.5 SECONDARY FLOW STRUCTURES

Understanding the impact of volute aspect ratio on turbine performance requires an understanding of the secondary flows within the volute passage. Figure 8.10 shows contours of radial velocity and streamlines at 7 planes around the volute for each design, at the minimum incidence running point at 40Hz pulse frequency. The angles of the planes are defined from the tongue in the direction of flow, as indicated in the figure. The planes are selected to sit directly between the blade LE's to reduce the impact of blade proximity. The exception is the 72° plane which is included to show the peak secondary flow activity.

A turbine volute is an example of a complex pipe, as both the radius of curvature and volute cross sectional area reduce with azimuth angle. Also, in the case of a turbine volute there is an added pressure force acting into the rotor which will resist flow reversal in the volute.

The development of the secondary flows within the volute can be attributed to the Dean effect. Dean vortices were first observed by Dean, (1927) and (Dean, 1928). These flow structures occur when the flow encounters a bend, with the low inertia flow at the walls turning readily into the radial direction within the pipe. In contrast, the higher inertia flow in the bulk of the passage does not turn as readily resulting in the development of counter rotation vortices with flow radially downwards at the walls and upwards in the passage centre creating two “D” shaped counter rotating vortices.

$$De = \sqrt{\frac{r}{R_c}} Re_D \quad (82)$$

Equation 82 defines the Dean number. Where: r is the pipe radius, R_c is the radius of curvature of the pipe bend and Re_D is the Reynolds number based on the pipe hydraulic diameter and is given by –

$$Re_D = \frac{\rho u D_H}{\mu} \quad (83)$$

Where μ is dynamic viscosity, ρ is density and u is bulk velocity and D_H is the hydraulic diameter. The Reynolds number expresses the ratio of inertial to viscous forces. The remaining term in equation 82, $\sqrt{\frac{r}{R_c}}$ expresses the centripetal force acting on the fluid. Therefore, as explained by Kalpakli Vester, (2014) the Dean number represents the impact of the inertia, viscous and centripetal forces acting on the fluid around the pipe bend. In the current study the volute radius (r) is given by $d_2/2$, therefore the radius ratio implemented accounts for the aspect ratio of the volute.

Figure 8.10 shows that the AR=0.5 volute results in a significant increase in the size of the counter rotating vortices present. The vortices are high in the volute passage at 18° and increase in size and move down the plane up to the 72° position. Between the 72° and 126° positions the vortices continue to move radially inwards but decrease in size ahead of the volute outlet. Beyond this point the vortices no longer exist even though clear variation in radial velocity across the plane still exists. In the AR=1 design, vortices are only visible at the 72° position and in the AR=2

design no vortex development occurs. Despite the lack of coherent vortex structures, the streamlines in both the AR=1 and AR=2 volutes show deviations from ideal flow through the volute. The variation in radial velocity over the cross section is also evident in all cases with the velocity around the volute walls noticeably greater due to the Dean effect. In the AR=0.5 case, the reduced volute width results in a greater shear between the wall and bulk passage flow and hence strong vortices develop. It should also be noted that increasing the volute AR, also increases the wall curvature. Therefore, the flow close to the walls in the AR=0.5 case is predominantly radial, whereas, the wall flow in the AR=2 case is only radial at the volute centre, beyond this the flow turns axially with the passage walls. The change in wall velocity components can be expected to effect secondary flow development as well as vortex shape and orientation. The effect of this can be seen in the relative orientation of the vortices in the AR=1 and AR=0.5 cases. In the former, vortices are positioned at a tangent to the local wall curvature (approximately 40° from the vertical). In the latter the vortices are orientated radially due to the reduced wall curvature.

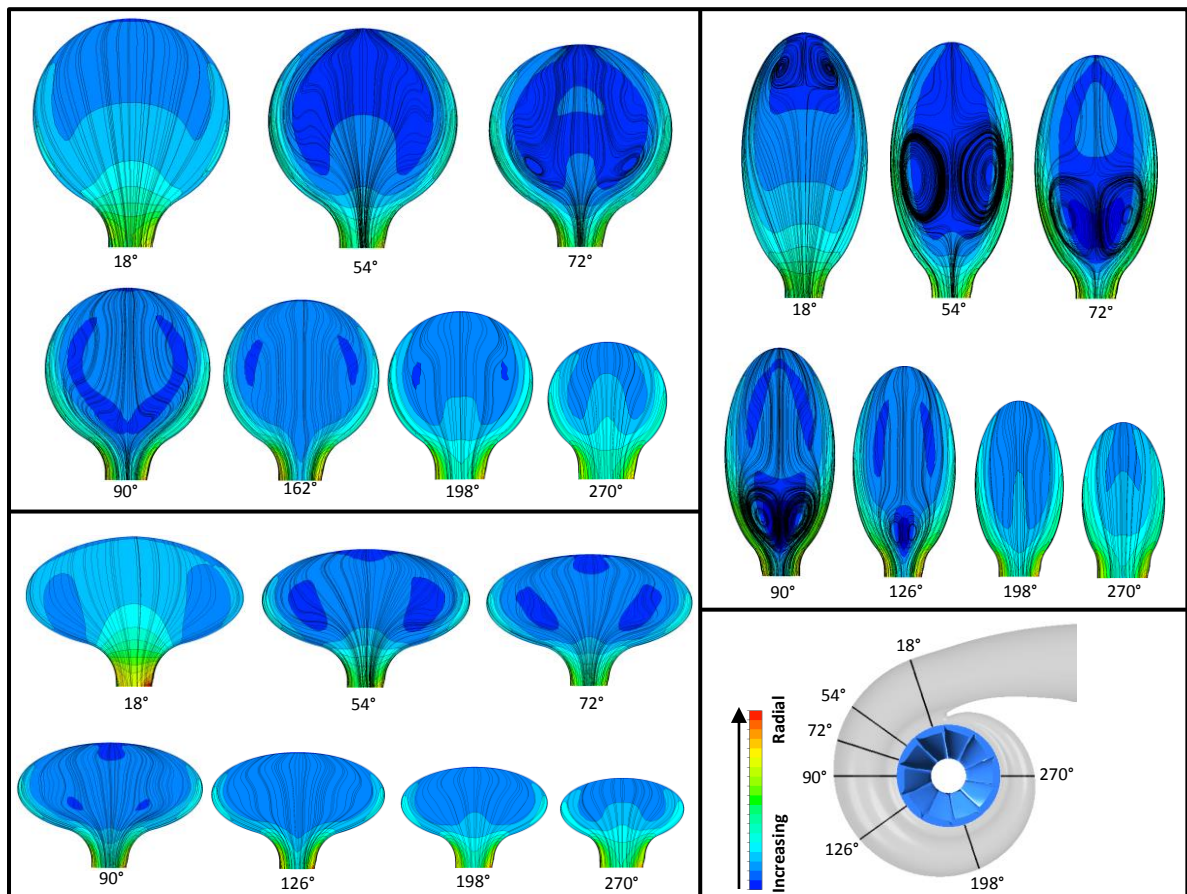


Figure 8.10: Surface streamlines at planes around the turbine volute and contours of radial velocity at 40Hz minimum incidence running point

The development of the vortex core present in the housing of aspect ratio 0.5 is presented in figure 8.11 using the lambda 2 criterion. This parameter shows the development of a vortex core and was used by Hellstrom & Fuchs, (2009) to show the development of vortices in the exhaust manifold ahead of a radial turbine. In the AR=0.5 volute, particularly at the maximum velocity ratio running point, a clear vortex can be seen to develop in figure 8.11 (a). The planes depicting streamlines are labelled with their angle from the volute tongue. The vortex region starts at around the 54° position where the streamlines shows strong secondary flows. With increasing azimuth angle, the vortex cores move radial inwards towards the rotor LE and in towards the passage centre. Just beyond the 126° plane the vortex core no longer exists. At the maximum incidence running point shown in figure 8.11 (b), the vortex core is much less distinct. Although vorticity exists in the same area of the volute, no clear core is established. The streamlines also show a large reduction in vortex size. Figures 8.12 (a) and (b) show the lack of clear vortex development in the AR=1 and AR=2 volutes at minimum incidence. In both cases, high levels of vorticity only exist close to the volute walls.

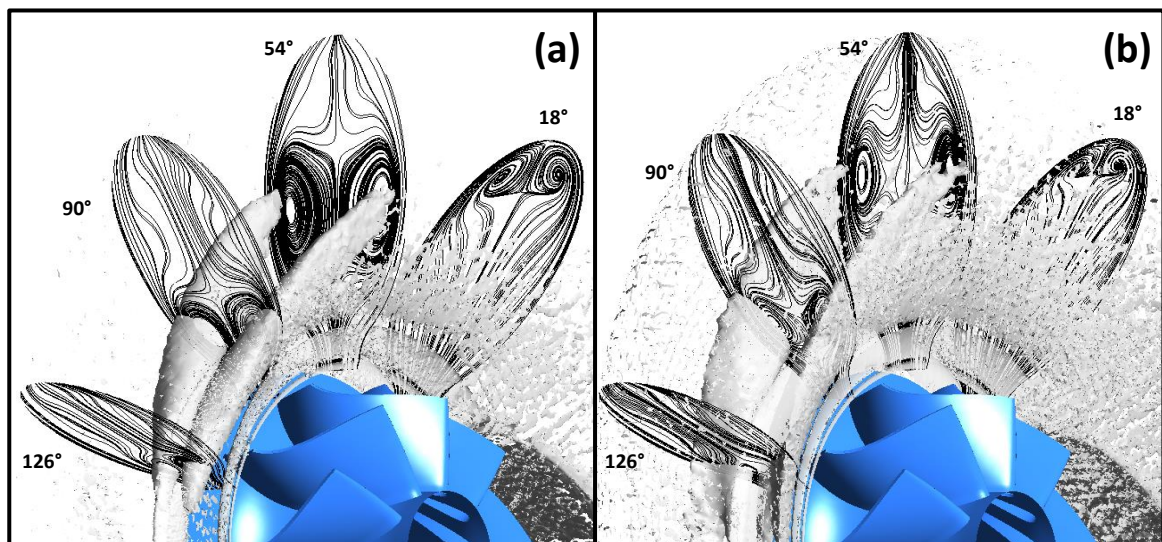


Figure 8.11: Lambda 2 parameter to show the vortex core development around AR=0.5 volute. (a) - Minimum incidence angle. (b) Maximum incidence angle.

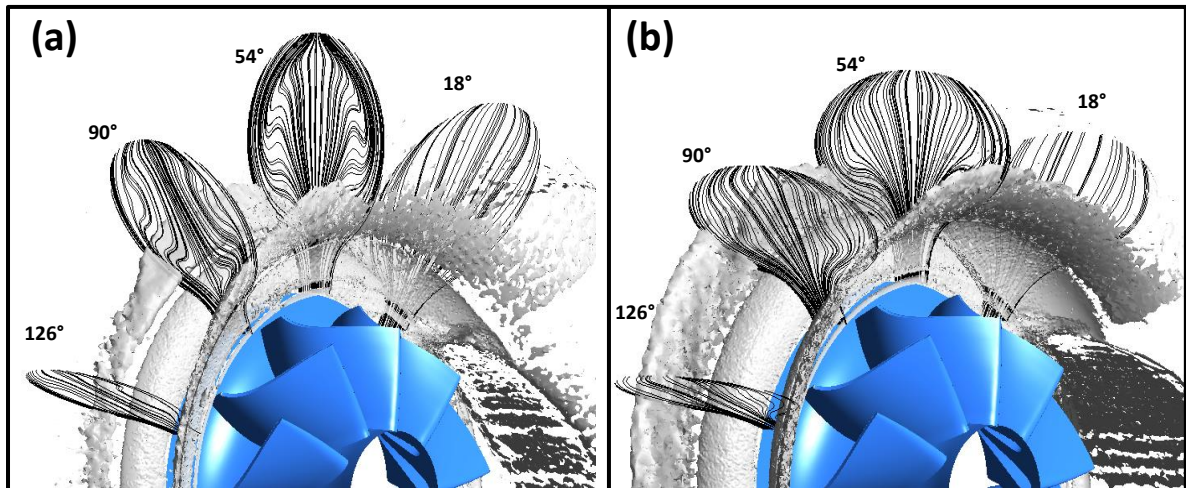


Figure 8.12: Lambda 2 parameter to show vortex core development around volute at minimum incidence (a) - AR=1. (b) AR=2.

The span-wise distribution of absolute flow angle at the volute exit, is presented in figure 8.13 for each of the volute aspect ratios at the 54°, 90°, 126° and 162° positions at both minimum and maximum incidence running points. The distance across the span of the volute exit has been normalised with the wheel hub being defined as 0 span and the shroud side as 1. The first observation to be made, is that the span-wise variation in absolute flow angle at the exit of the volute is significant at all azimuth angles presented in all designs. Secondly, the span-wise variation is greater at the minimum incidence running points, hence at the peak energy running points the variation in exit flow absolute angle over the span reduces. This change to the resulting absolute flow angle, is the product of both the radial and circumferential velocity distributions changing at the volute exit. Figure 8.13 also shows significant circumferential variation, with the absolute flow angle range peaking between the 90° and 126° positions reaching angles up to 85°. This position coincides with the angle at which the vortex core is close to the volute exit as shown in figure 8.11. At these two angular positions, variation in the three designs can be observed, which is greatest in the at 90° plane at minimum incidence. The variation at this point reaches approximately 8.5°. Beyond this position the variation reduces with all the housing designs resulting in similar distributions at the 162° plane. The similar span-wise distribution for the three designs continues around the remainder of the volute.

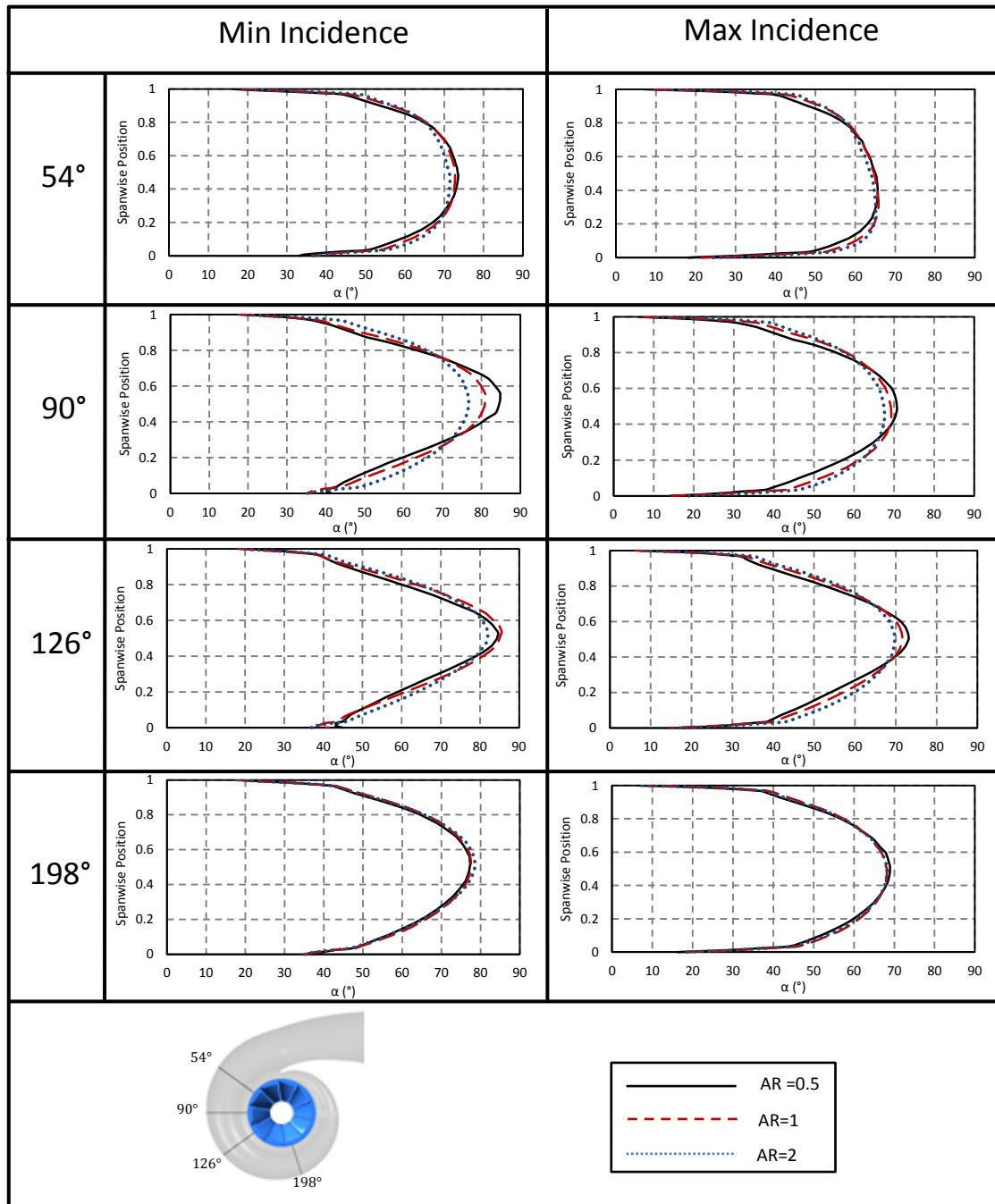


Figure 8.13: Variation in absolute flow angle across the volute exit span at the minimum and maximum incidence running points

The impact of volute exit variation on circumferentially averaged rotor LE incidence is presented in figures 8.14-8.16 at both the minimum and maximum incidence. The incidence is calculated from the circumferentially mass averaged velocities at the LE. This is therefore the variation in incidence averaged around the rotor inlet and not at specific positions as shown in figure 8.13.

At minimum incidence, the lowest flow angles are achieved at the rotor hub, increasing to a maximum between 15% and 20% span. Incidence reaches a local minima at the span centre in the 60Hz case, 60% span in the 40Hz case and 70% in the 20Hz case, before increasing again to a maximum at the shroud side. With increasing pulse frequency, a greater variation between the volute aspect ratio designs can be observed. In the 60Hz case a variation of approximately 4° in incidence was observed at the passage centre between the AR=0.5 and the other two larger aspect ratio designs which show similar incidence distributions at all frequencies. The notable variation in incidence between the frequencies can be attributed to the considerably different maximum rotor velocity ratio achieved under each tested pulse as shown in figure 8.6.

At the maximum incidence point, a distribution with a parabolic-like shape is formed at all pulse frequencies with the maximum incidence achieved in the centre of the LE. Between the tested frequencies, the distributions show little variation; only under the 60Hz pulse does the peak incidence achieved show a slight reduction. It was observed that the AR=0.5 volute design consistently results in an increase in maximum incidence measured at the LE centre of approximately 2° . Away from the centre of the LE, the AR=0.5 design achieved lower incidence angles by up to 3° when compared to the AR=1 and AR=2 designs which, again show similar distributions at maximum incidence under all pulse frequencies. This variation in LE incidence results in a greater range of incidence in the AR=0.5 case. However, the averaged incidence measure varies by less than 0.9° at all frequencies.

It should be noted that the change in LE axial flow component between the aspect ratio designs was negligible. Therefore, the change in incidence angle observed was not a result of changing blade angle but the result of relative flow angle variation.

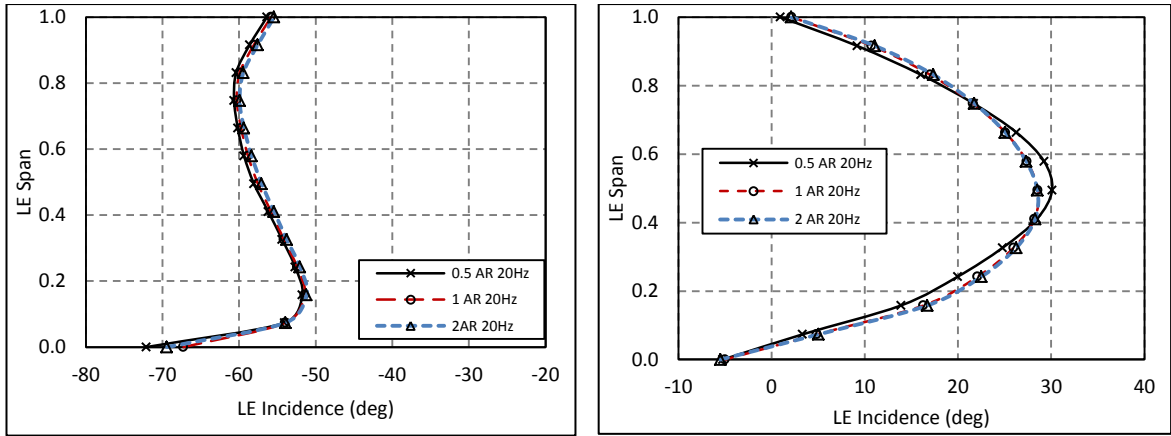


Figure 8.14: LE incidence at 20Hz frequency. Left - minimum incidence running point. Right - Maximum incidence running point

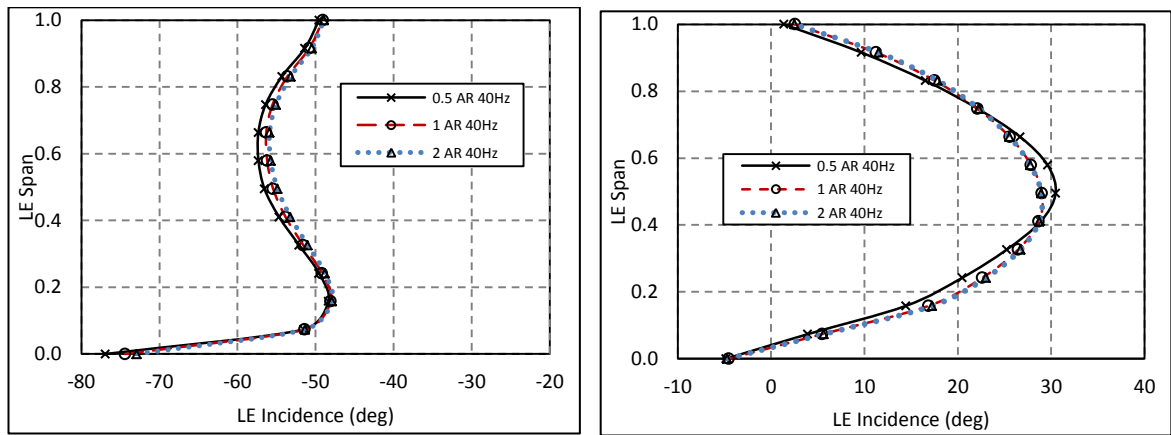


Figure 8.15: LE incidence at 40Hz frequency. Left - minimum incidence running point. Right - Maximum incidence running point

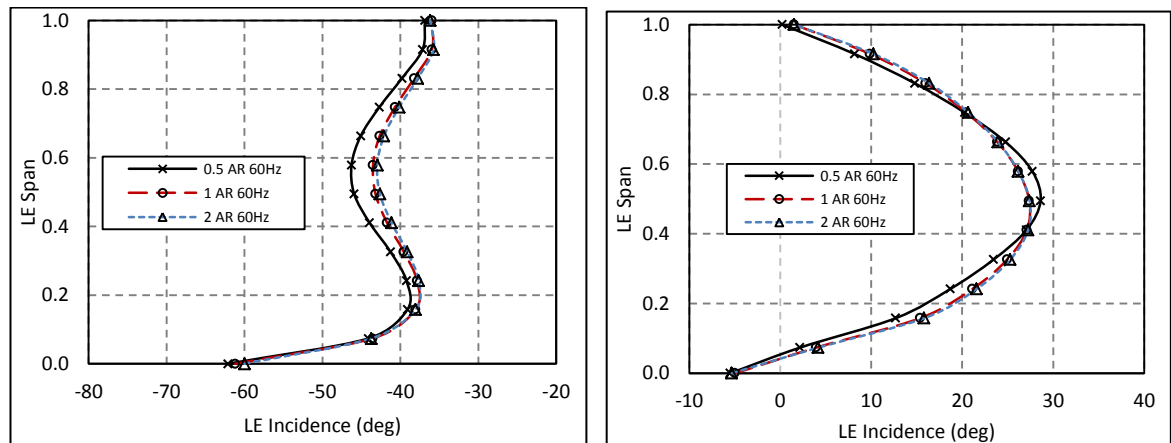


Figure 8.16: LE incidence at 60Hz frequency. Left - minimum incidence running point. Right - Maximum incidence running point

Figure 8.17 shows the development of volute secondary flows and volute outlet absolute flow angle for the AR=0.5 over the pulse period. Four points within the pulse are included, (1) – minimum mass flow, (2) – during the volute filling, (3) at maximum mass flow and (4) during the volute emptying. The vortices present at

points (2) and (4) are notable different, with the vortices larger in the volute emptying process. This shows that the volute flows are not quasi steady but are influenced by the flow hysteresis. Despite the change in vortex size between points (2), (3) and (4); the volute outlet absolute flow angle remains almost constant at both the 90° and 126° circumferential locations. At point (1) where the minimum volute exit mass flow occurs, the vortices are by far the greatest, encompassing the entire volute span. This is the only point which shows a substantial deviation in the volute exit absolute flow angle.

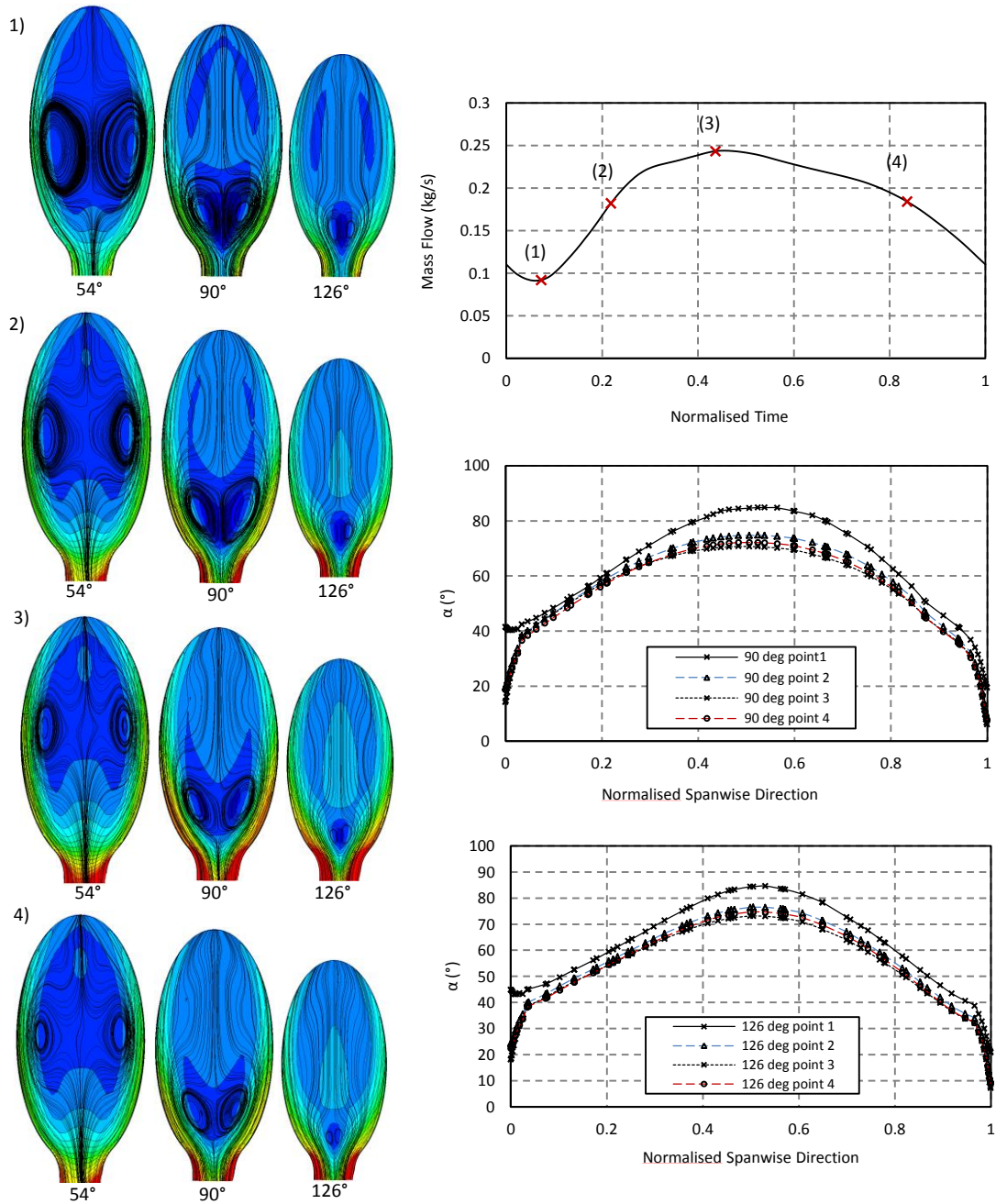


Figure 8.17: Vortex development and volute exit absolute flow angle distribution in AR=0.5 volute through pulse period

The variation in meridional velocity across the centre of the volute passage is presented in figures 8.18-8.22 at various locations around the volute. It should be noted, that as the values are taken at the passage centre, negative velocities are only present at low azimuth angles as the volute vortices traveling radial inwards with increasing angle. It was observed that greater peak meridional velocities occur as volute AR was reduced due to the increased Dean effect. However, this trend was

found to reduce as azimuth angle increased as the volute cross sectional area significantly reduces in all designs.

At the maximum incidence running points, the range of velocities across the volute span is greater than that occurring at minimum incidence in all cases, with the velocities at the walls reaching significantly higher speeds. However, the lower meridional velocities at the volute centre generally increase. In a standard pipe bend, as the Dean number increases the velocity towards the walls also increases, and to balance the forces, the central passage flow travels radial outward faster increasing vortex strength. In the volute, as the bulk flow velocity increases, the force acting into the rotor also increases due to the increased flow pressure. This driving pressure force suppresses flow reversal and increases the velocity towards the passage centre despite the greater Dean numbers and wall velocities.

With increasing azimuth angle, the variation in meridional velocity across the passage was found to reduce at both running points and in all volute AR's. However, the passage central velocity shows a greater variation as azimuth angle increases. This can be observed by comparing the 54° and 270° (figures 8.18 and 8.22 respectively) plots at the maximum incidence running point. From normalised span positions of 0.2-0.8, the variation in velocity at the 54° plane was $<10\text{m/s}$, at the 270° plane this increased to approximately 20m/s . This effect can be attributed to the reduction in cross sectional area, and hence absolute mid height span, as the azimuth angle increases, causing less distinction between the wall and central passage flows.

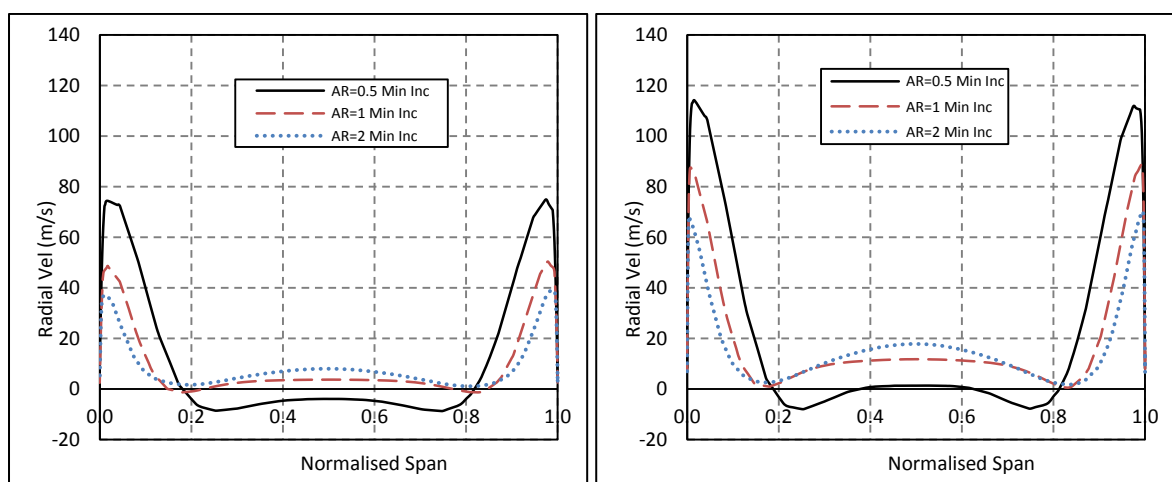


Figure 8.18: Meridional velocity across volute passage centre 54° . Left - Minimum incidence Right - Maximum incidence

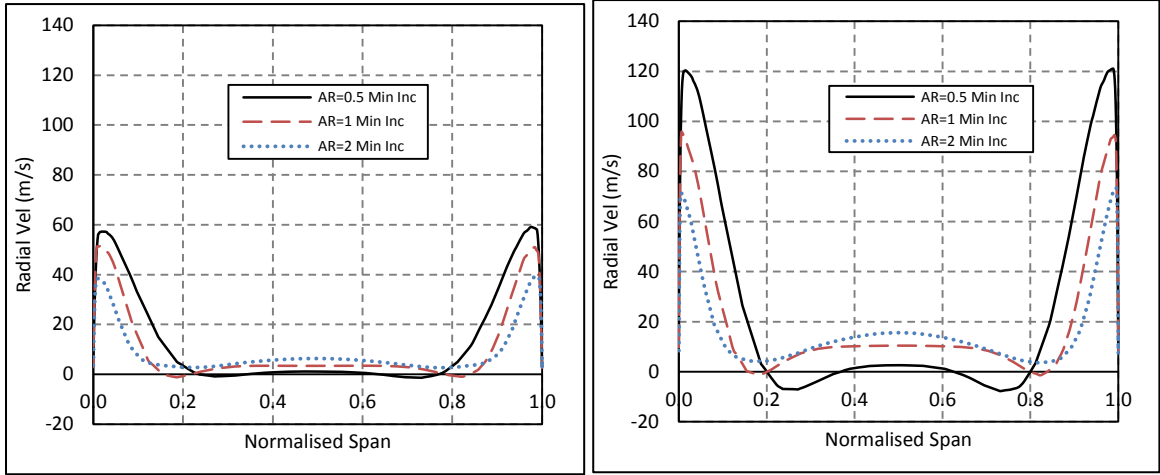


Figure 8.19: Meridional velocity across volute passage centre 72°. Left - Minimum incidence Right - Maximum incidence

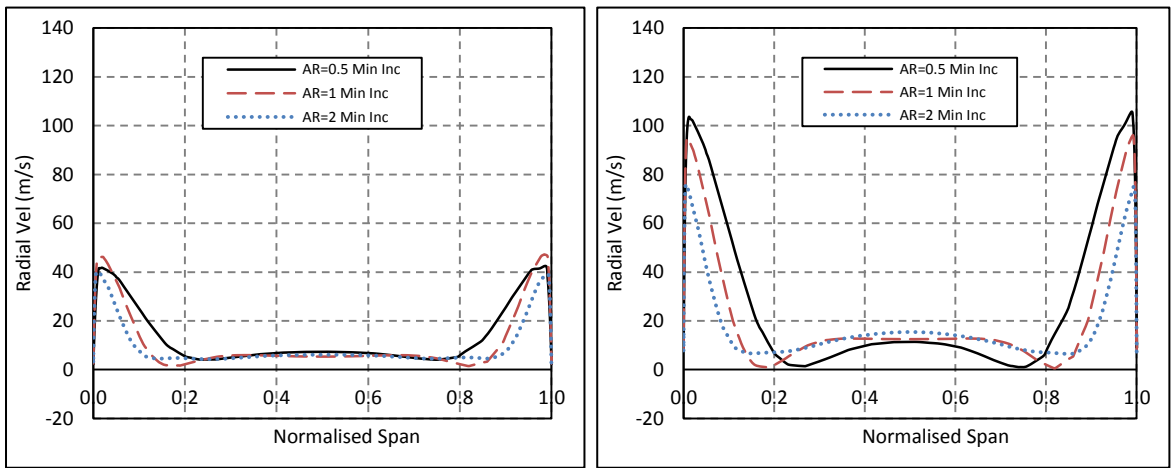


Figure 8.20: Meridional velocity across volute passage centre 90°. Left - Minimum incidence Right - Maximum incidence

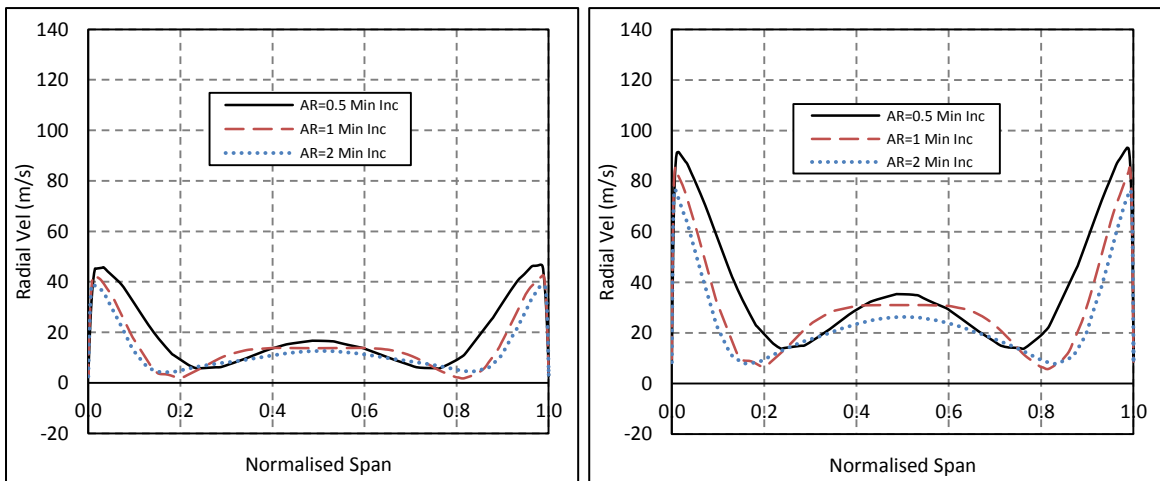


Figure 8.21: Meridional velocity across volute passage centre 180°. Left - Minimum incidence Right - Maximum incidence

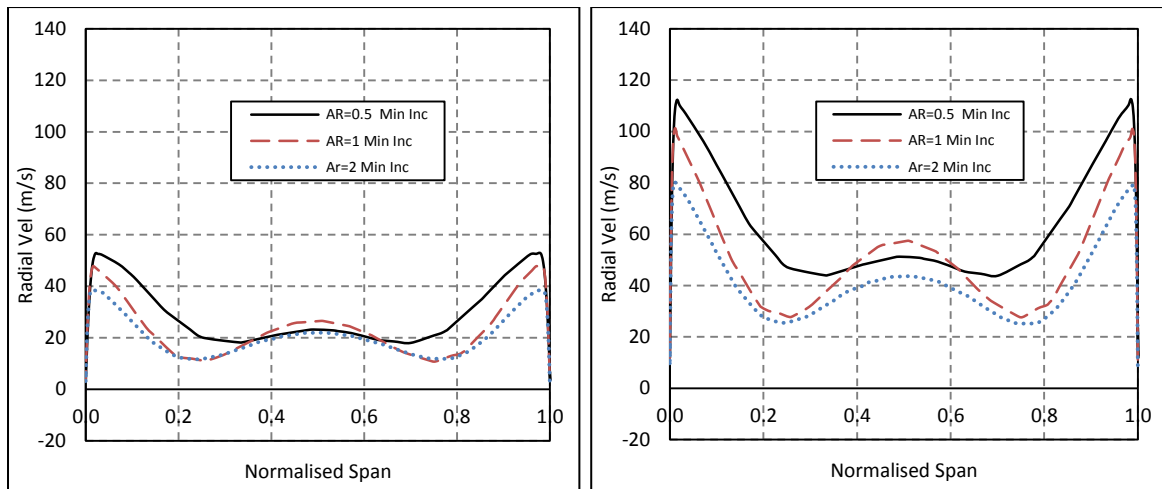


Figure 8.22: Meridional velocity across volute passage centre 270°. (Left - Minimum incidence Right - Maximum incidence)

The meridional velocity components at the volute exit are presented in figures 8.23-8.26 at the same locations around the volute azimuth angle as presented in figures 8.18-8.22. At the volute exit the variation in meridional velocity is much lower than at the volute mid plane and the mean is greater due to the fluid accelerating into the rotor through the volute. In all cases higher velocity towards the shroud side of the span is evident due to the non-symmetrical pressure acting into the rotor due to its mixed flow nature. At the maximum incidence running point, the average radial velocity is greater than at minimum incidence. However, the variation as a percentage of the average is greater in the minimum incidence case, see figure 8.27 and 8.29. It is this combined with absolute circumferential velocity that results in the increased variation in absolute flow angle at the volute exit at minimum incidence that is depicted in figure 8.17.

The variation in exit meridional velocity between the volute AR's is only noticeable at the 90° position, where the variation reduces with increasing AR. This effect is most significant as a percentage of the mean at the minimum incidence running point. This is again in keeping with the absolute flow angles presented in figure 8.17.

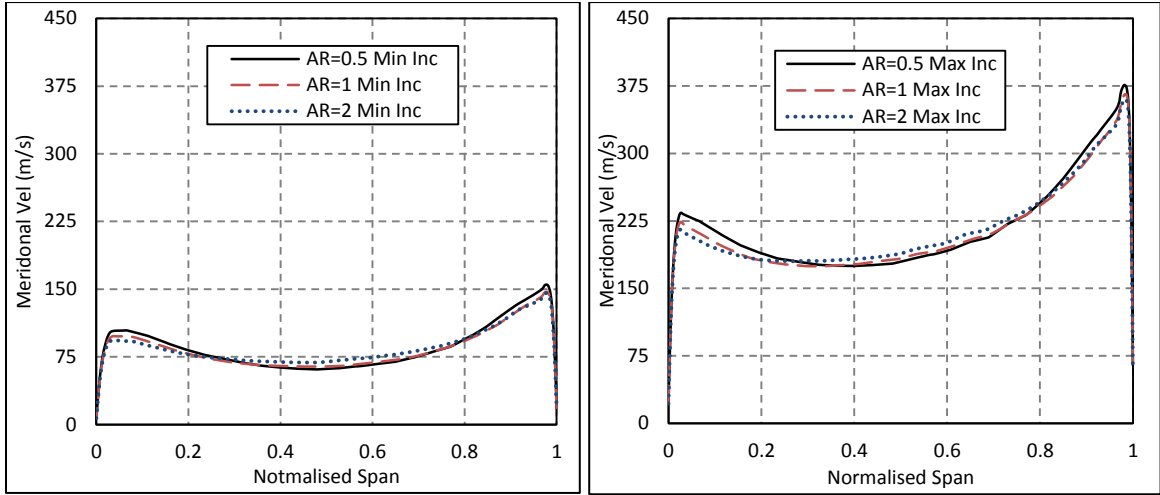


Figure 8.23: Meridional velocity at volute exit 54°. (a) - Minimum incidence (b) - Maximum incidence

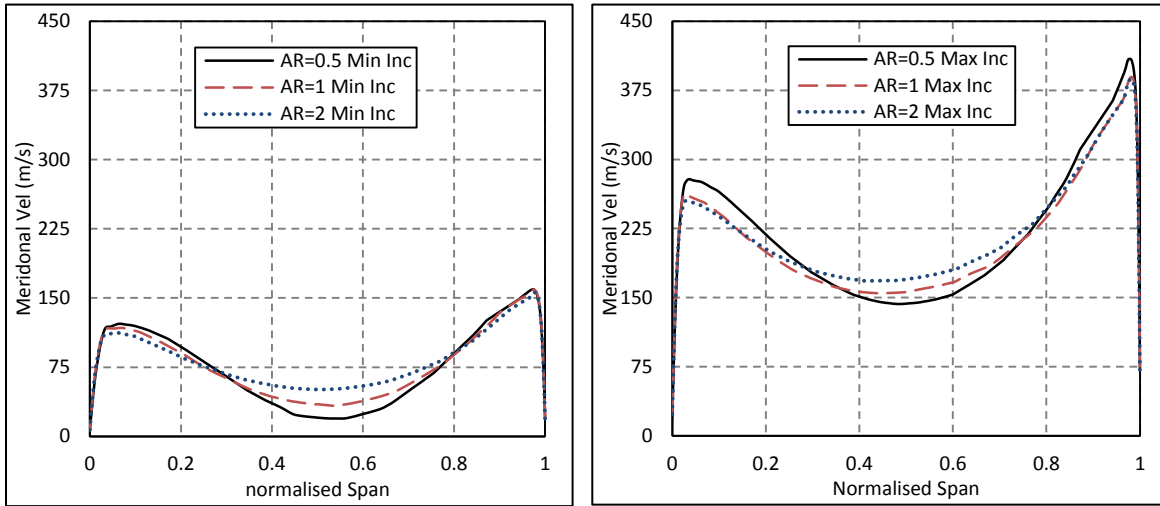


Figure 8.24: Meridional velocity at volute exit 90°. (a) - Minimum incidence (b) - Maximum incidence

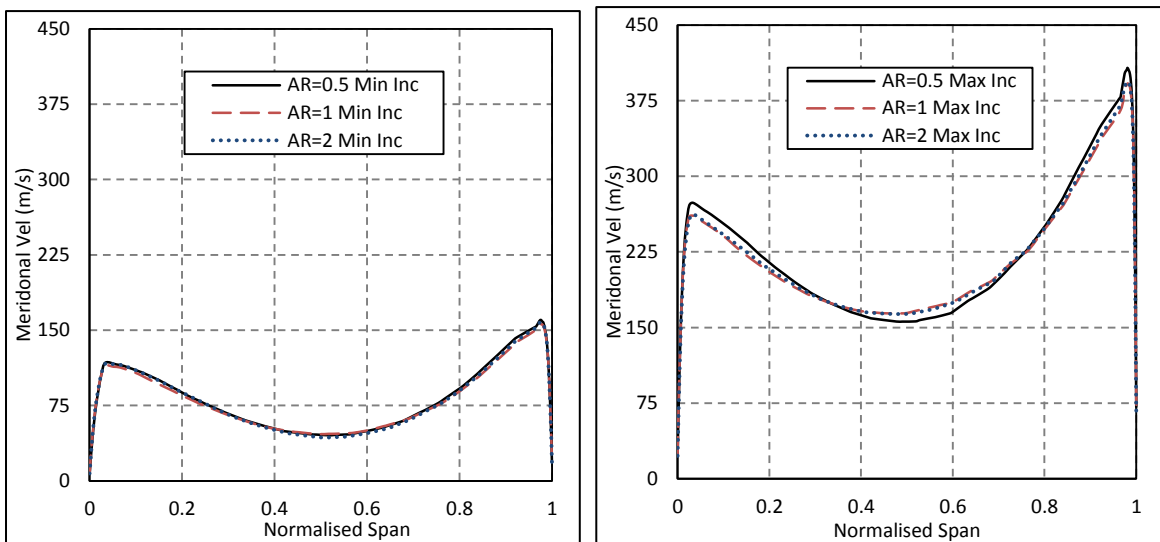


Figure 8.25: Meridional velocity at volute exit 198°. (a) - Minimum incidence (b) - Maximum incidence

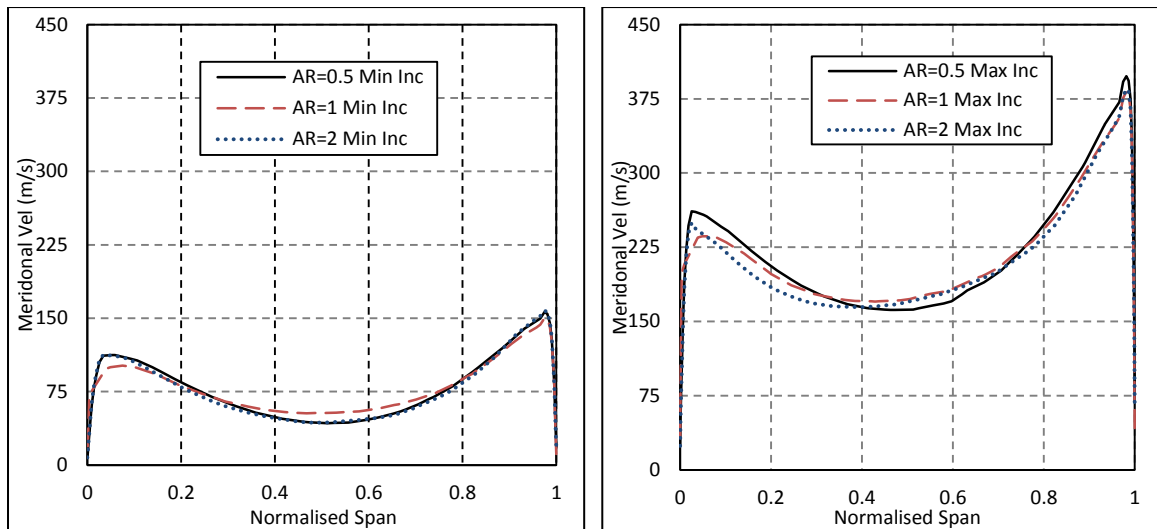


Figure 8.26: Meridional velocity at volute exit 270°. (a) - Minimum incidence (b) - Maximum incidence

Figures 8.27-8.31 shows the percentage variation of the meridional and circumferential velocity at the volute exit at 90° and 270°. The percentage variation of the meridional velocity is greater in the minimum incidence case at the volute exit especially at the 90° position. The greater pressure acting into the rotor at the higher incidence points, drives flow acceleration into the rotor and reduces span-wise velocity variation. The impact of AR is evident at the 90° position at minimum incidence with the smaller AR showing an increase in span-wise variation.

The observed variation in circumferential velocity is smaller in all cases with the plots showing a fully develop pipe flow trend with maximum velocity occurring at the passage centre. At the 90° position the AR=2 volute shows a notable reduction in this trend. Other than this effect the volute AR appears to have little impact on the circumferential velocity distribution.

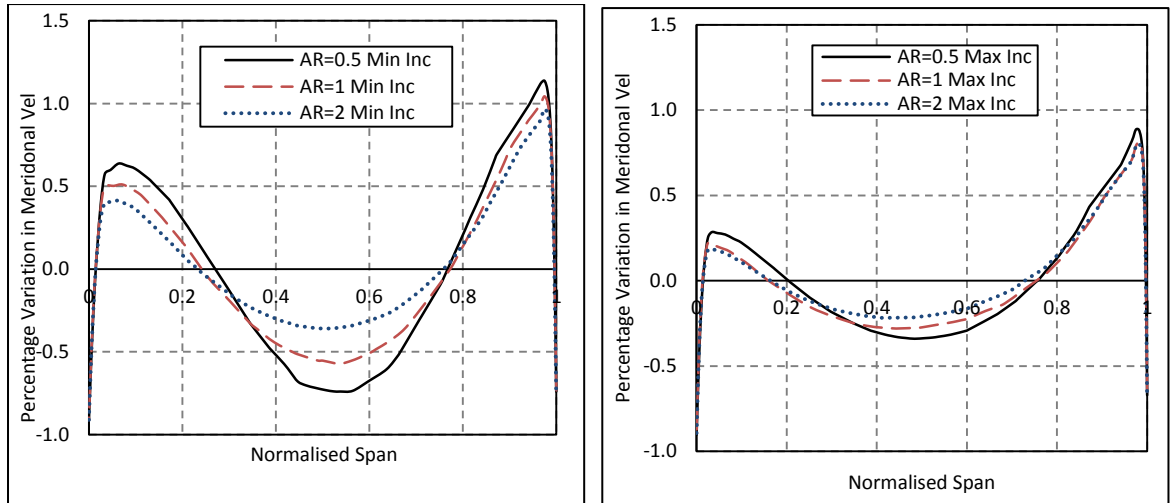


Figure 8.27: Meridional velocity percentage variation at volute exit 90° (a) - Minimum incidence (b) - Maximum incidence

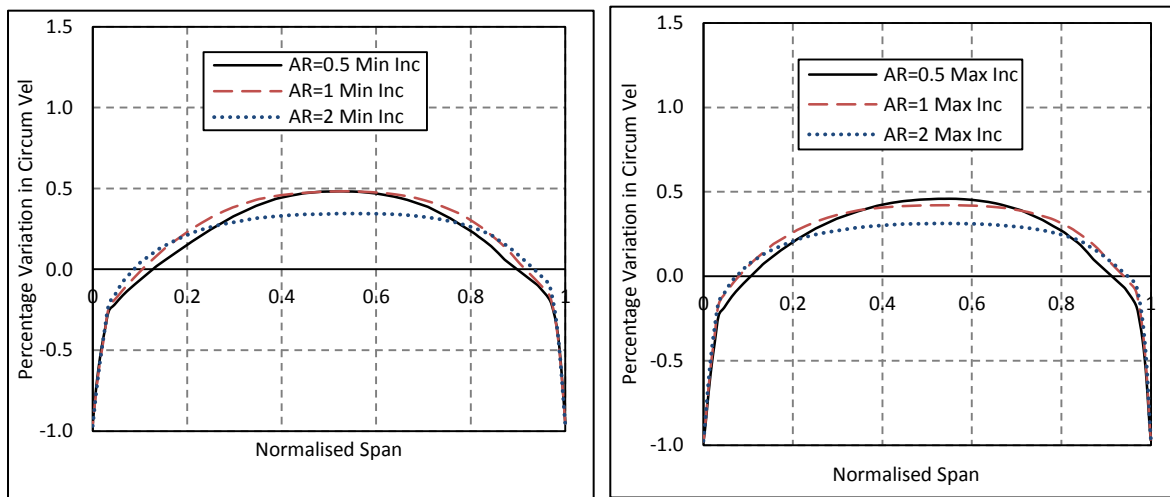


Figure 8.28: Circumferential velocity percentage variation at volute exit 90° (a) - Minimum incidence (b) - Maximum incidence

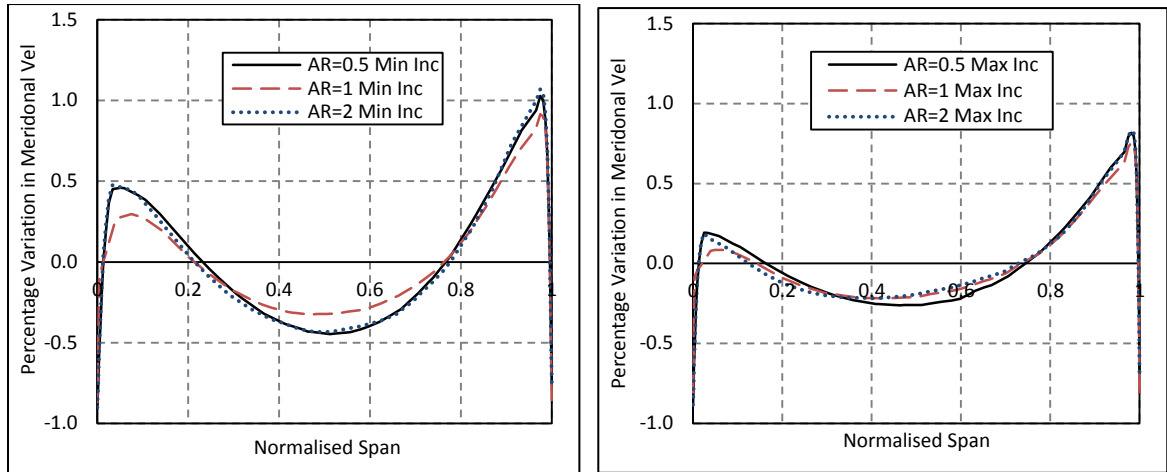


Figure 8.29: Meridional velocity percentage variation at volute exit 270° (a) - Minimum incidence (b) - Maximum incidence

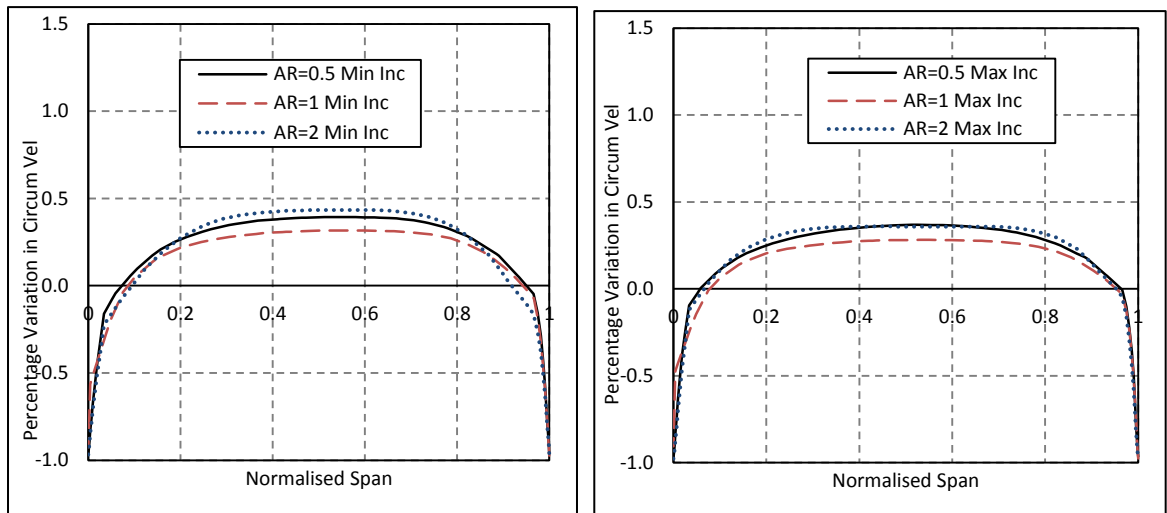


Figure 8.30: Circumferential velocity percentage variation at volute exit 270° (a) - Minimum incidence (b) - Maximum incidence

The Dean number in the current study was evaluated around the volute passage and is presented in figure 8.31. With increasing azimuth angle, the Dean number decreased in all designs as the volute cross sectional area and radius of curvature reduce. With reducing aspect ratio, the calculated local Dean number was found to increase. However, the variation in Dean number between the AR=0.5 and AR=1 cases is only marginal, while the secondary flow structures present are significantly different. This is because the Dean number calculation does not account for the volute shape but merely takes into account the ratio of outer wall radius to centroid radius.

The calculated Dean number was also greater at the maximum incidence running points which correspond to higher operating pressure ratios and reduced secondary

flows. This is caused by the increased Reynolds number. As seen in figures 8.18-8.22, at maximum incidence, the variation of velocity across the volute centre is greater at this running point. However, the development of secondary flows is impeded due to the higher pressure in the volute acting into the rotor. This limits the flows ability to recirculate. Therefore, the change in calculated Dean number matches the increased velocity variation across the volute central plane, but does not characterise the secondary flows. This is due to the added complexity of the volute passage that feeds the rotor which is not accounted for in the basic Dean number calculation. It can be concluded that the Dean number gives some measure of volute central passage variation in meridional velocity, but the resulting secondary flow structures are also dependent on the added pressure acting into the rotor and the volute cross sectional shape.

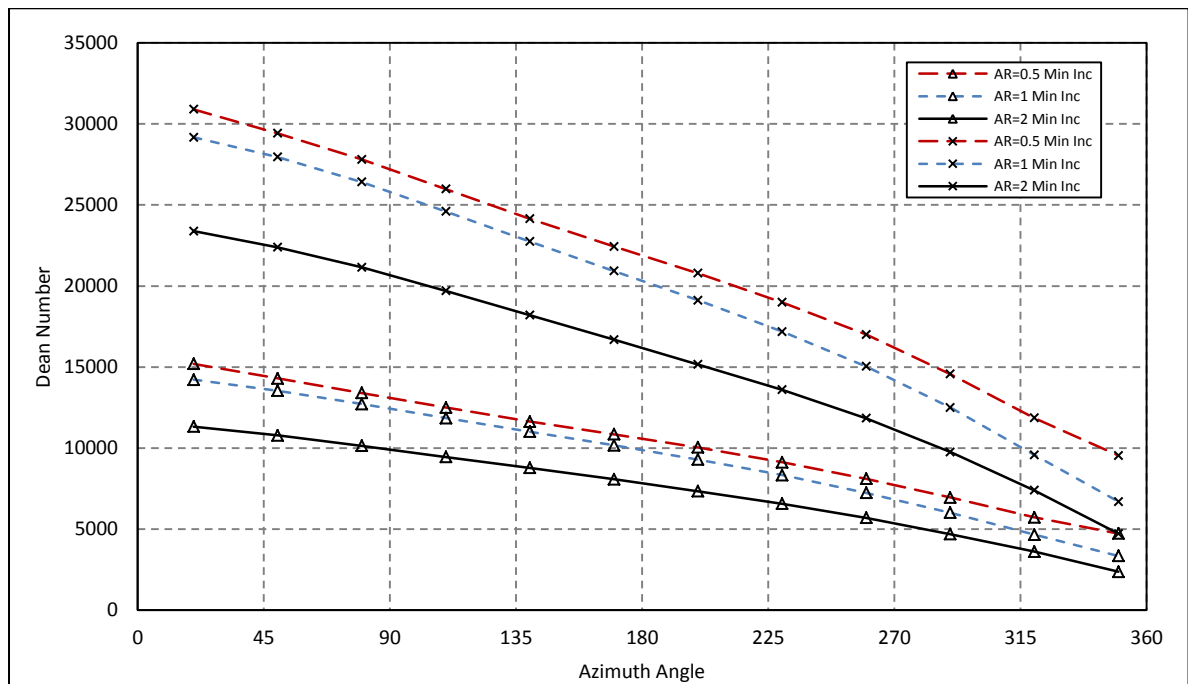


Figure 8.31: Dean number around the volute for the minimum and maximum incidence running points

8.6 SCALE RESOLVING TURBULENCE APPROACH

In addition to the SST SAS model, the stress blended eddy simulation (SBES) approach was used for comparison. This is a hybrid Large Eddy Simulation (LES) approach and was used to validate the application of the SAS model. The SBES model

uses the LES approach in the region of unsteadiness and a URANS approach in the more stable regions reducing the computational cost while ensuring that large scale turbulence is resolved rather than being mathematically modelled. The approach is detailed by Ansys, (2009a). Therefore, this model should show better flow predictions in regions of unsteadiness as the true turbulence is resolved. As the mesh used in the volute was already highly refined the mesh was not changed between the three tested methods. However, to ensure accurate convergence the time step used in the SBES approach was reduced to approximately half that required in the SST and SAS-SST approaches.

In this section the standard SST, SAS-SST and SBES approaches in the volute AR=0.5 are compared. This volute resulted in the largest amount of volute secondary flow activity and therefore, it was deemed the best design to compare the approaches.

Figure 8.32 shows the rotor efficiency for the SST, SAS-SST and SBES models at the 40HZ pulse frequency. The approaches show little deviation over the efficiency map. Only minor deviations between the three methods can be observed at the higher velocity ratios. At these higher velocity ratios the impact on cycle averaged performance is minimal. The resulting variation in cycle averaged stage performance between the three models was less than 0.15%.

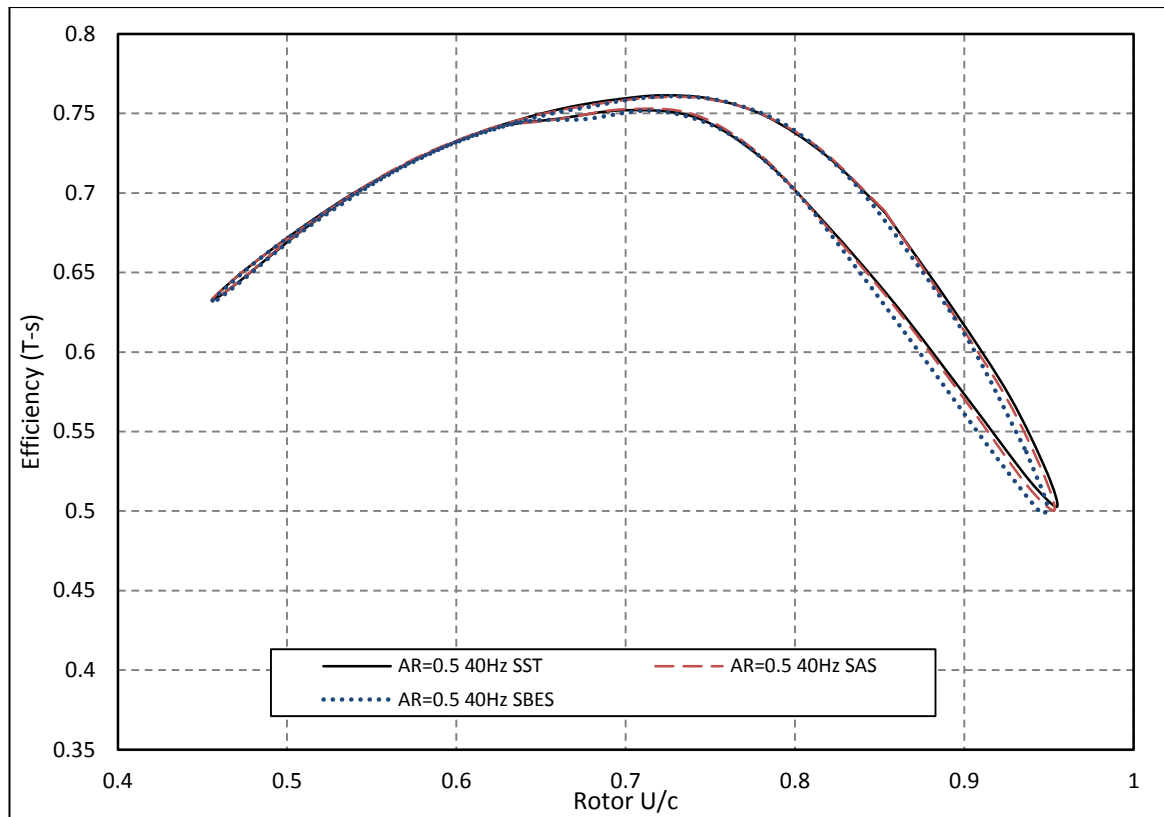


Figure 8.32: Rotor efficiency plot comparing SST, SAS-SST and SBES approaches

Figures 8.33 shows the lambda 2 criterion and streamlines within the volute at minimum and maximum incidence using the SST, SAS-SST and SBES approaches. The SST model results in taller vortices particularly at minimum incidence than the other two approaches. The vortex core region shown through the lambda 2 criterion also starts later in the SST case, were as the core region starts earlier in the other two approaches. This is particularly evident at the minimum incidence running point where the vortex core is more distinct. The deviation between the SAS and SBES approaches is much less notable.

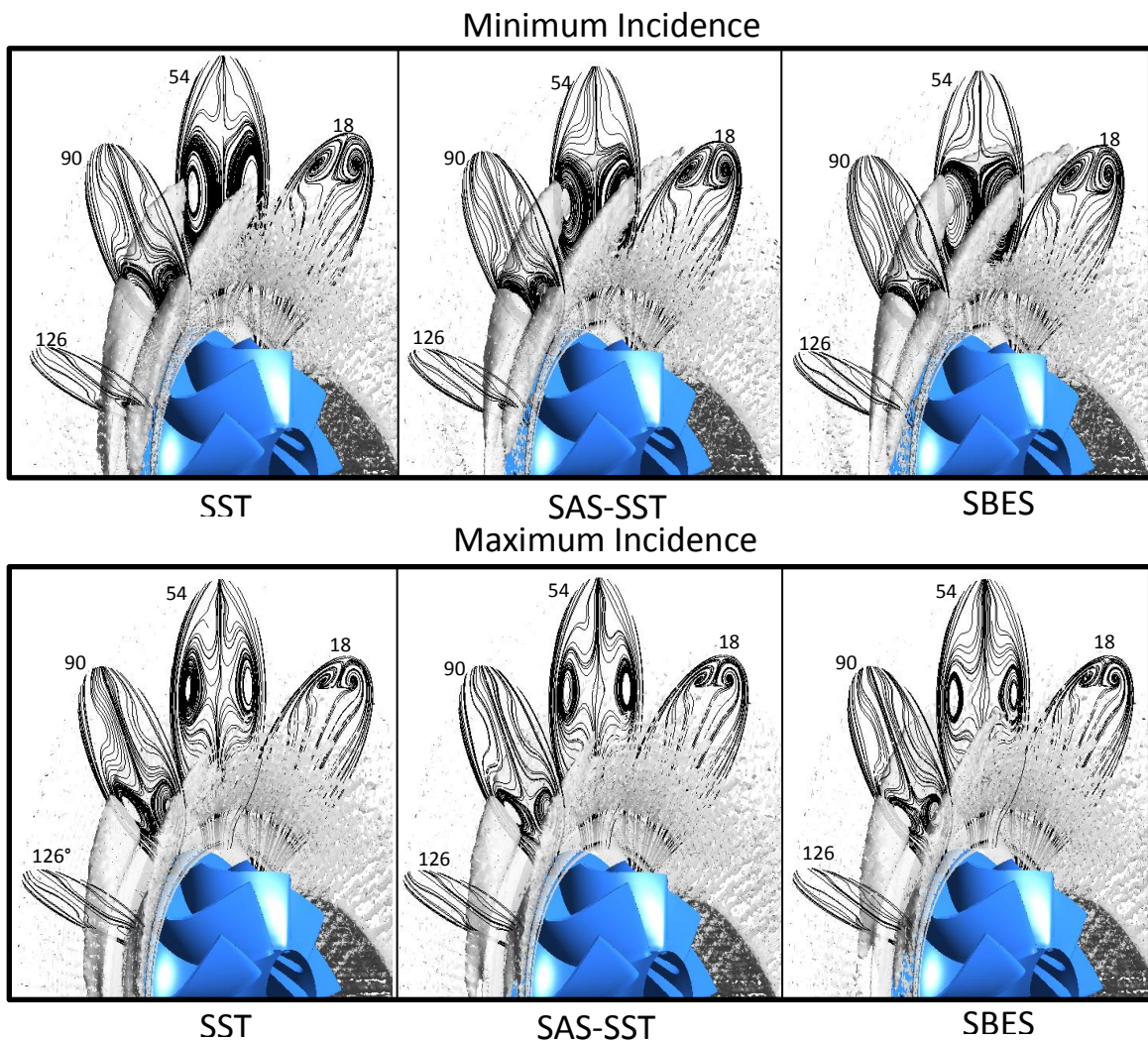


Figure 8.33: Streamlines and lambda 2 criterion through volute passage at minimum and maximum incidence for three approaches

Figure 8.34 shows the resulting LE incidence predicted at the minimum and maximum incidence running points using the SST, SAS-SST and SBES approaches. At either running point no noticeable difference in incidence over the LE span can be observed.

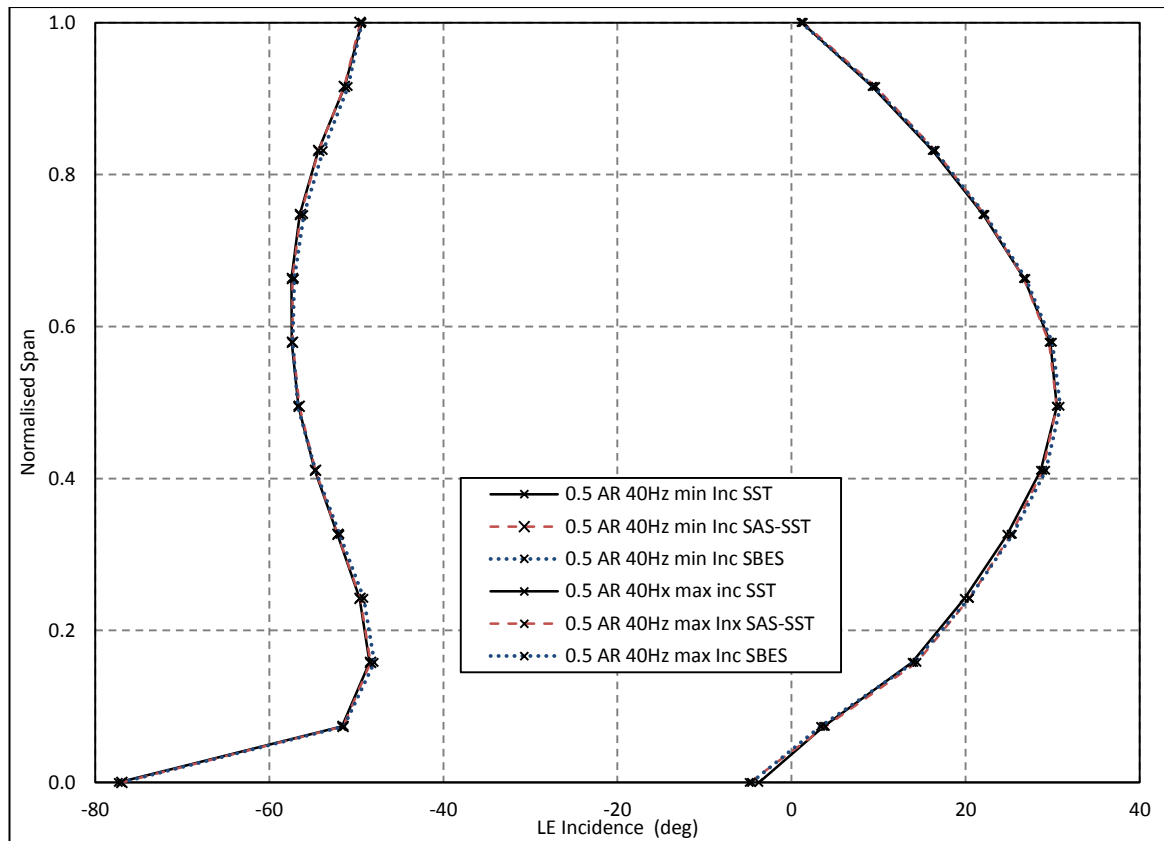


Figure 8.34: Comparison of LE incidence in AR=0.5 volute using SST, SAS-SST and SBES approaches

From the analysis it can be concluded that the basic SST model accurately predicts the performance and LE incidence of the turbine. However, the volute secondary flow structures show some small deviations. Meanwhile the SAS approach shows accurate replication of SBES results. While the SBES approach requires a considerable increase in computational time, the SAS model only requires a slight increase in time of the SST approach. For this reason, the SAS model was used throughout this chapter and chapter 9 to accurately capture the secondary flow structures in the volute.

8.7 CHAPTER CONCLUSIONS

This chapter has investigated the impact of volute AR on the performance of the mixed flow turbine over a range of pulse frequencies. Detailed analysis of the volute flow development has been included.

Comparing the rotor efficiencies at different points with-in the pulse across AR's showed that the performance at the highest velocity ratio is impacted more

significantly than that at minimum velocity ratios. However, at the high velocity ratio running points less pulse energy is available and therefore the cycle average performance sees a smaller improvement. Hence, only small changes in cycle averaged efficiency were observed across the investigated AR range.

Analysis of the secondary flow structures shows interesting interactions of the central and wall bound flows. The result is the development of a strong vortex core in the smallest aspect ratio design. The process that results in such secondary flow structures developing is also taken to be the cause of the significant span-wise variation observed in all designs. While the vortices are not present in all volutes, the span-wise variation persists in all cases. While Meghaine et al., (2017) stated that the volute passage contains one or more vortex, this work has shown for a symmetrical volute design, increasing the volute aspect removes vortex development completely.

The result of the study also shows that volute aspect ratio can significantly impact the MFP of the stage with a variation of 4.3% being observed when A/r was kept constant. However, AR was found to do little to improve the span-wise incidence distribution over the blade LE. The resulting change in stage efficiency observed was also small (1.47%) between the three designs. From a design perspective, this is an important result as it allows more freedom to designers to achieve package constraints, without a significant loss in stage efficiency as long as the housing is resized to ensure constant MFP. The limited effect of volute AR on the span-wise incidence distribution shows that even reducing volute secondary flows within the volute cannot reduce the severity of this variation. Alternately, incorporating such span-wise variation in to the rotor design process could yield new span-wise blade distributions and further performance benefits.

9 COMBINING HOUSING TILT AND ASPECT RATIO

9.1 INTRODUCTION

In chapters 6 and 8 the impact of both volute tilt and volute aspect ratio were investigated. The results show that both factors impact on turbine performance. This chapter brings together both aspects to investigate how the two factors interact.

Two new volute designs are introduced and analyzed in this chapter, a tilted volute with $AR=0.5$ and a tilted volute with $AR=2$. Both volutes are tilted to an angle of 20° the same as in the standard tilted housing introduced in chapter 6. Figure 9.1 shows the two further tilted volutes implemented in this chapter.

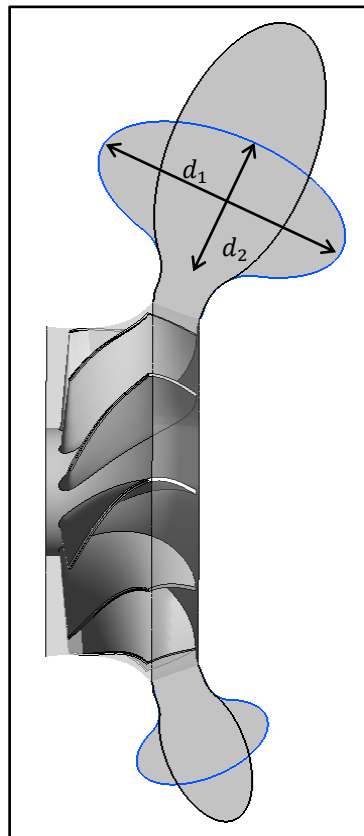


Figure 9.1: Tilt volute designs with $AR=0.5$ (black) and $AR=2$ (blue)

These two new volute designs were compared with the comparable radial volute design with $AR=0.5$ and $AR=2$ that were outlined in chapter 8. The computational approach is the same as that in chapter 8 with SAS-SST turbulence model implemented.

9.2 TURBINE PERFORMANCE RESULTS

Figure 9.2 compares the MFP for the four volutes compared in this chapter at 40Hz pulse frequency. These included the radial volute with AR=0.5 and AR=2 and the tilted volute with AR=0.5 and AR=2. The pulse shape used was the realistic form at a pulsation number of 1 and mid load, these parameters are fixed throughout this chapter. All volutes show good agreement with the MFP hysteresis. The cycle averaged MFP difference between all volutes is within 0.5% ensuring aerodynamic similarity.

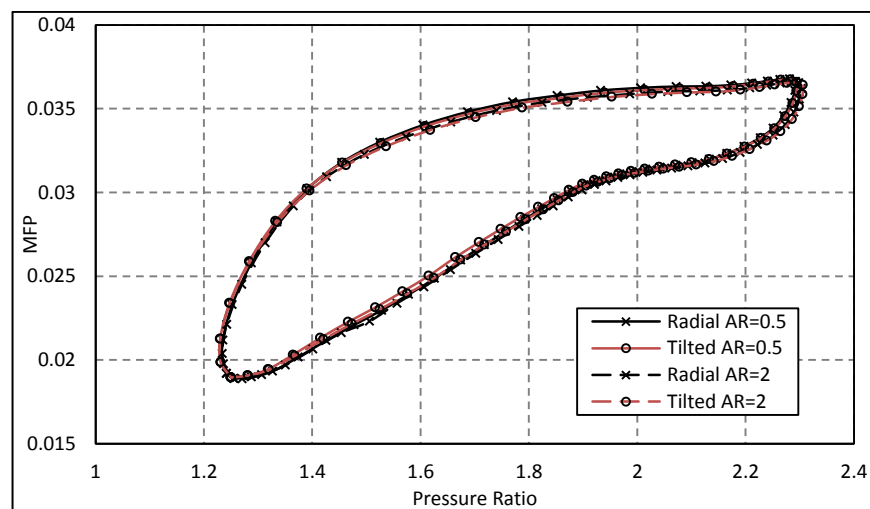


Figure 9.2: MFP hysteresis for radial and tilted housing at AR=0.5 and AR=2

Figures 9.3-9.5 present the rotor efficiencies for each of the volute designs at 20Hz, 40Hz and 60Hz respectively. In all cases the tilted volute results in an increase in efficiency, as was the case with the comparison of the radial and tilted volutes in chapter 6. This improvement in efficiency increases with velocity ratio. Furthermore, with increasing volute aspect ratio, the rotor efficiency also increases. However, the impact of volute aspect ratio on rotor performance is less than that caused by volute tilt. The combination of both features leads to a significant increase in efficiency.

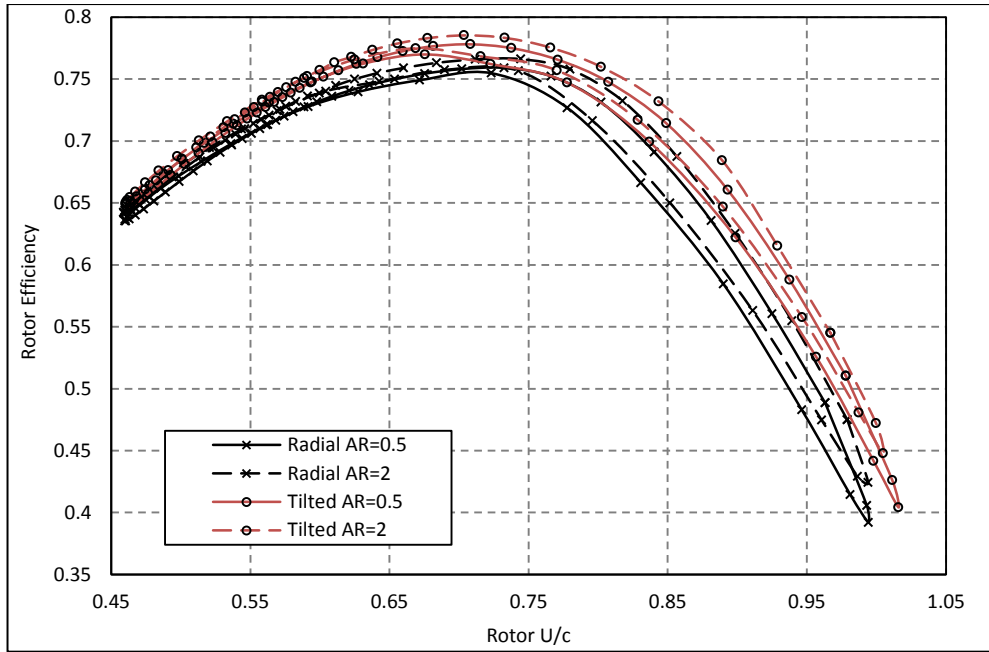


Figure 9.3: Rotor efficiency 20Hz

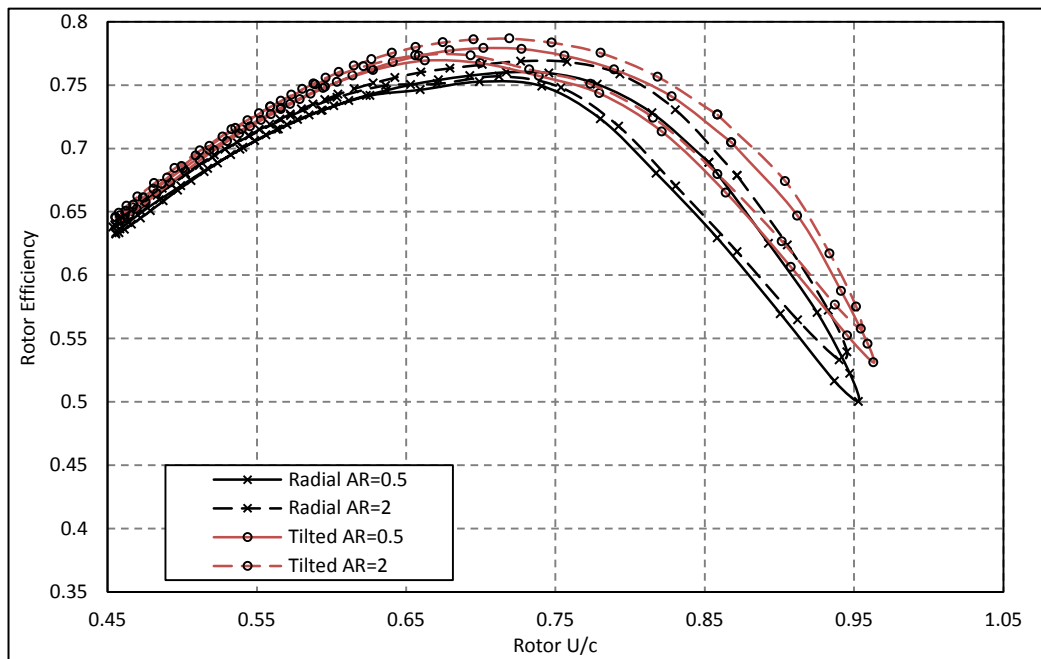


Figure 9.4: Rotor efficiency 40Hz

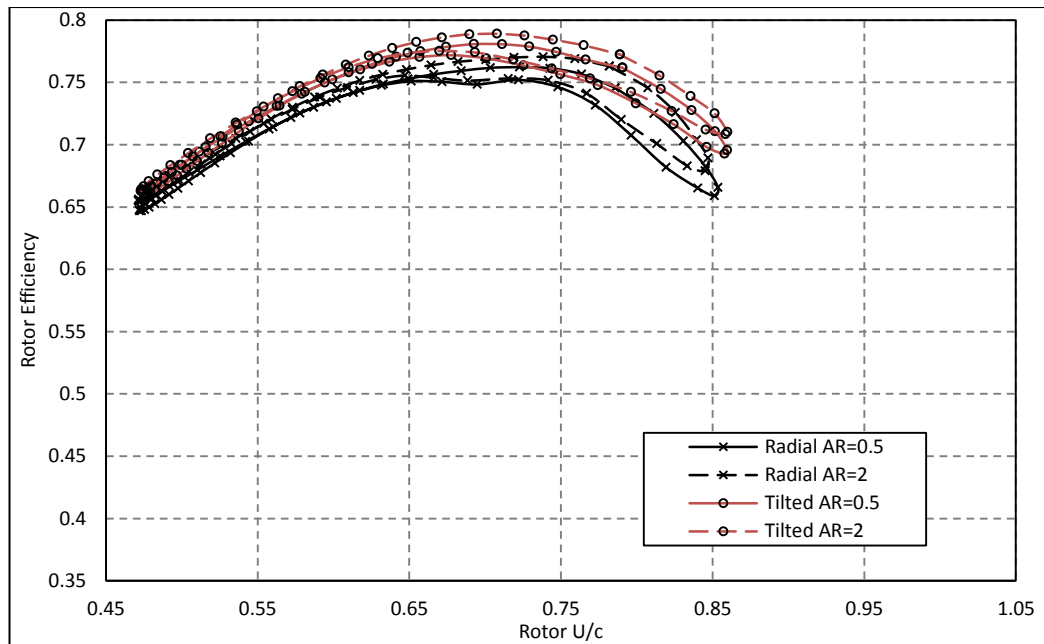


Figure 9.5: Rotor efficiency 60Hz

Table 9.1 compares the cycle averaged efficiencies for both the full stage and rotor only region for the investigated designs. The efficiency is normalised by the maximum achieved at each operating point which is the AR=2 design in all cases. Alongside the 100% efficiency of the AR=2 design, the absolute efficiency value is included of this design for clarity. The maximum improvements in rotor and stage cycle averaged efficiency observed were 3.00% and 2.87% respectively occurring at the 20Hz pulse frequency. The impact of frequency on this improvement was only small. The volute total pressure loss coefficient is also included in table 9.1, these are not normalised. This parameter shows that the volute AR=2 results in a large reduction in volute loss at all frequencies. Combining both volute tilt and AR=0.5 results in the greatest volute loss at all frequencies.

The impact of volute tilt is not constant across aspect ratios; this effect is better shown in table 9.2. This table compares the difference in absolute efficiency between the radial and tilted designs at both 0.5 and 2 AR. It was observed that the efficiency improvements achieved through the introduction of volute tilt were larger in the AR=0.5 volute design. This effect is particularly evident in the rotor region. The reduction in stage efficiency improvement relative to that achieved in the rotor region was the result of increased volute loss. The volute loss was greatest when both tilt and low AR were combined as shown in table 9.1, hence while the tilt resulted in

greater rotor efficiency improvement in the AR=0.5 than in the AR=2 case, the resulting stage efficiency improvements were only small.

Table 9.3 compares the impact of AR in both the radial and tilted cases. Consistently, increasing volute aspect ratio results in greater efficiency improvements in the radial volute case. This effect is particularly evident in the rotor region only. In the tilted case, the improvement in efficiency with increasing AR is much greater in the stage than in the rotor alone. This effect is due a significant reduction in volute loss between the two AR's in the tilted cases. Alternately the volute loss difference between the AR=0.5 and AR=2 cases in the radial configuration is much smaller.

| | | Radial | | Tilted | | Tilted |
|--------------|----------------------------|--------|--------|--------|---------|--------------|
| Aspect Ratio | | 0.5 | 2 | 0.5 | 2 | 2 - abs. eff |
| 20Hz | Cycle AVG Rotor Eff | 97.13% | 98.16% | 99.35% | 100.00% | 69.73% |
| | Cycle AVG Stage Eff | 97.00% | 98.45% | 98.67% | 100.00% | 67.60% |
| | Volute Pt loss Coefficient | 0.1231 | 0.1061 | 0.1282 | 0.1081 | |
| 40Hz | Cycle AVG Rotor Eff | 97.19% | 98.17% | 99.39% | 100.00% | 70.10% |
| | Cycle AVG Stage Eff | 97.08% | 98.47% | 98.71% | 100.00% | 68.50% |
| | Volute Pt loss Coefficient | 0.1221 | 0.1057 | 0.1282 | 0.1076 | |
| 60Hz | Cycle AVG Rotor Eff | 97.23% | 98.20% | 99.47% | 100.00% | 71.03% |
| | Cycle AVG Stage Eff | 97.13% | 98.51% | 98.75% | 100.00% | 69.74% |
| | Volute Pt loss Coefficient | 0.1195 | 0.1035 | 0.1267 | 0.1056 | |

Table 9.1: Radial and tiled volutes, AR=0.5 and AR=2, relative performance

| Aspect Ratio | | 0.5 | 2 |
|--------------|--------------------------------|-------|-------|
| 20Hz | Cycle AVG Rotor Eff (Tilt-Rad) | 1.54% | 1.29% |
| | Cycle AVG Stage Eff (Tilt-Rad) | 1.13% | 1.05% |
| 40Hz | Cycle AVG Rotor Eff (Tilt-Rad) | 1.54% | 1.28% |
| | Cycle AVG Stage Eff (Tilt-Rad) | 1.11% | 1.05% |
| 60Hz | Cycle AVG Rotor Eff (Tilt-Rad) | 1.60% | 1.28% |
| | Cycle AVG Stage Eff (Tilt-Rad) | 1.13% | 1.04% |

Table 9.2: Comparison of the impact of volute tilt on cycle averaged performance at aspect ratios of 0.5 and 2

| Volute | | Radial | Tilted |
|--------|-----------------------------------|--------|--------|
| 20Hz | Cycle AVG Rotor Eff (AR=2-AR=0.5) | 0.71% | 0.45% |
| | Cycle AVG Stage Eff (AR=2-AR=0.5) | 0.98% | 0.90% |
| 40Hz | Cycle AVG Rotor Eff (AR=2-AR=0.5) | 0.69% | 0.43% |
| | Cycle AVG Stage Eff (AR=2-AR=0.5) | 0.95% | 0.89% |
| 60Hz | Cycle AVG Rotor Eff (AR=2-AR=0.5) | 0.69% | 0.37% |
| | Cycle AVG Stage Eff (AR=2-AR=0.5) | 0.96% | 0.87% |

Table 9.3: Comparison of the impact of aspect ratio on cycle averaged performance in a radial and tilted volute

9.3 VOLUTE FLOW ANALYSIS

Figure 9.6 illustrates the secondary flow development around the volute in the AR=0.5 and AR=2 tilted volutes at both the minimum and maximum incidence running points. The surface streamlines are overlaid on contours of meridional velocity. Vortex development is evident in the AR=0.5 volute at both running points. The vortices take on a significantly different form to that observed in the radial AR=0.5 volute (see figure 8.15). As the volute tilt has removed the symmetry of the volute the vortices produced become asymmetric. The same effect was observed in chapter 6 when studying the impact of volute tilt. In this instance two main vortices develop at either side of the volute with the inner vortex (hub side) significantly larger than the one occurring on the outer (shroud side). At the minimum incidence running point this results in the inner vortex encompassing roughly 75% of the volute passage. At the maximum incidence running point, the development of a third vortex is evident in the 54° and 72° planes. This vortex rotates in the counter clockwise direction, opposite to the vortex forming on the outer wall of the volute. Development of a third vortex in this position was not observed in any other cases. Interestingly, of the symmetrical volutes tested, an even number of vortices were always observed; it wasn't until asymmetry was introduced to the volute that an odd number of vortices developed.

The tilted volute with AR=2 shows no signs of vortex development at any of the presented positions around the volute at either operating point. Despite this, a significant range of meridional velocity over the plane was still observed showing the development of the Dean type effect even though the flow does not reverse in the volute passage.

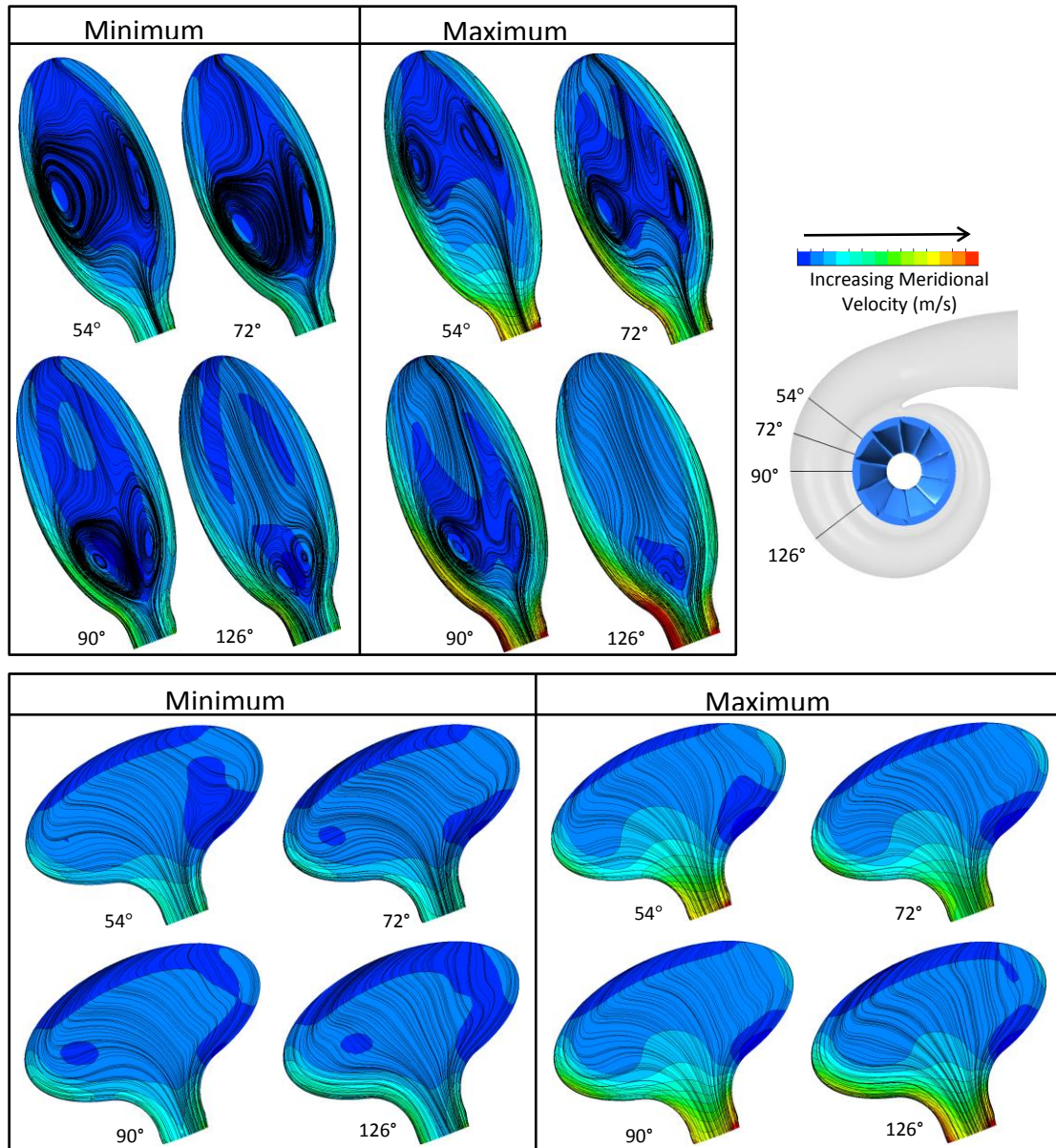


Figure 9.6: Surface streamlines and contours of meridional velocity at planes around the volute for the 20° tilted volute AR=0.5 and AR=2 at minimum and maximum incidence. (40Hz)

Figure 9.7 shows the development of the vortices around the volute using the lambda 2 criterion. At the minimum incidence running point, the vortex development is much more distinct than that at maximum incidence. In both cases the inner vortex shows a more distinct development and persists through the volute for longer. Again, the asymmetry of the vortex development can be compared to that of the radial volute with AR=0.5 (see figure 8.16). It is clear that the introduction of tilt results in asymmetry of the flow structures with the inner vortex increasing in strength while the outer vortex strength reduces.

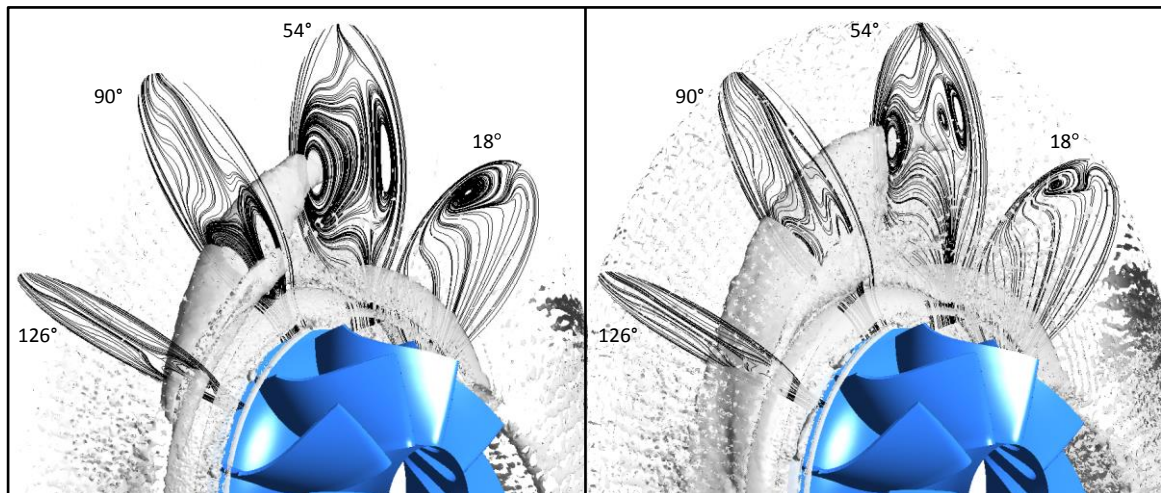


Figure 9.7: Lambda 2 criterion in the volute for the titled volute with AR=0.5. (a) - minimum incidence. (b) maximum incidence. (40Hz)

Figure 9.8 presents the development of the secondary flow vortices in the tilted volute with AR=0.5 through the pulse. This figure attempts to give greater insight into the development of the complex secondary flow structures occurring in the AR=0.5 volute.

At the minimum incidence and during the volute filling only two vortices develop within the volute. The vortex size decreases from minimum incidence (1) during the filling process (2) as the volute pressure increases reducing flow reversal. The development of a third vortex in the volute is first observed at the maximum incidence running point. This vortex still exists at the emptying point (4). Comparing the filling case (2) and emptying case (4) highlights the unsteady operation of the volute since the inlet mass flow is the same and yet the vortices present in case (2) encompass a much larger proportion of the passage area.

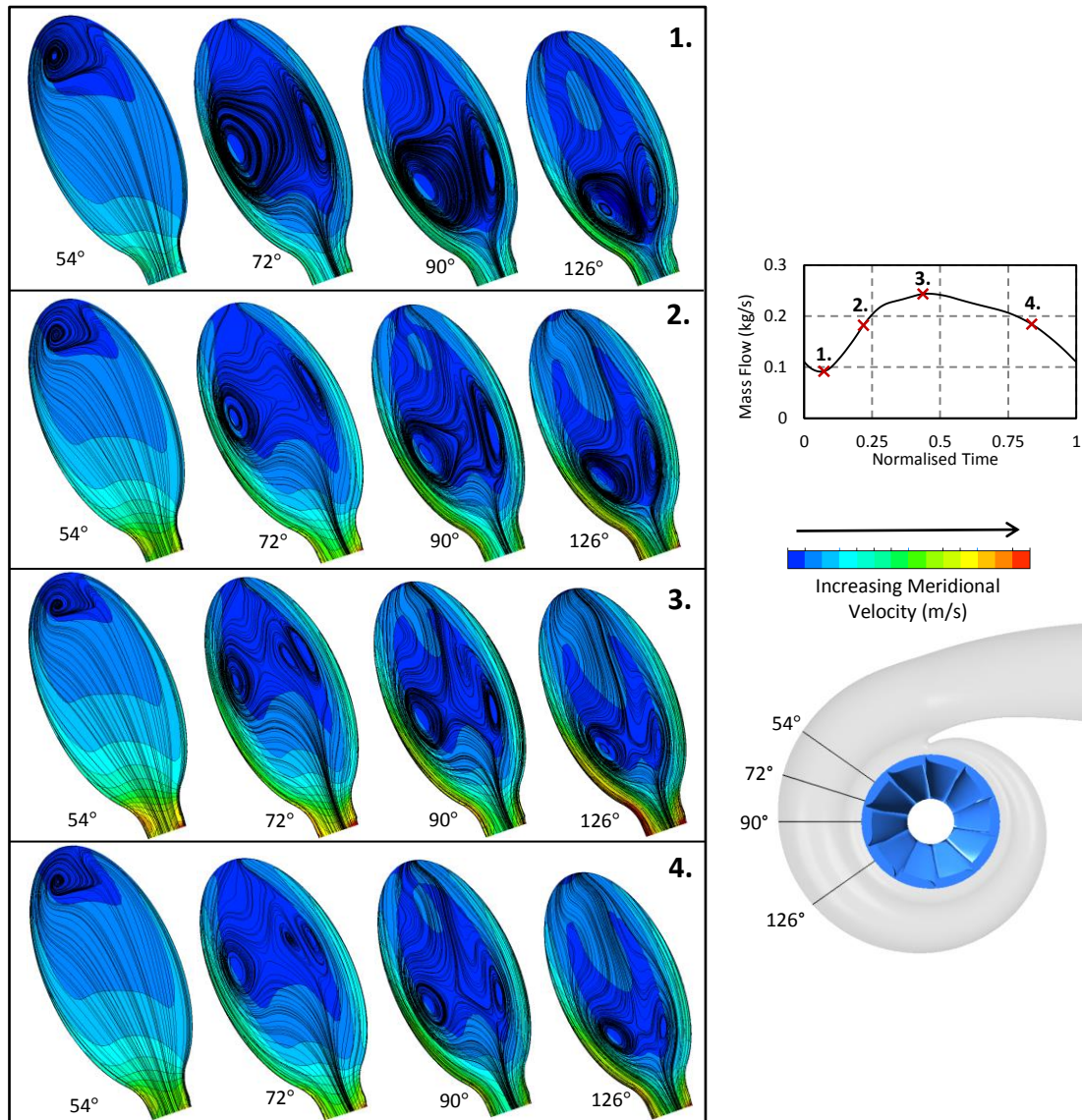


Figure 9.8: Vortex development in AR=0.5 20° tilted volute through pulse period (40Hz)

The meridional velocity across the centre of the volute cross sectional plane around the azimuth angle is plotted in figures 9.9-9.13 for the volutes with AR=0.5 and 2 in the radial and tilted cases. In the tilted volute case, the cross sectional plane is tilted to 20°; the same angle as the volute tilt to produce a plot normal to the meridional direction.

In the tilted case the results show an asymmetrical distribution of meridional velocity with higher velocities existing towards the hub side. The span-wise variation of velocity is greater in the AR=0.5 case in both the radial and tilted designs. Comparing the impact of volute tilt on both volute aspect ratios, it is clear that the volute tilt results in a great asymmetry in meridional velocity in the AR=2 case. At the

54°, 72° and 90° planes, the hub side velocity peak remains constant between the tilted and radial volute at AR=2 while at the shroud side a significant reduction in the peak is evident. Alternately the AR=0.5 volute shows a reduction in peak meridional velocity at both sides of the volute and therefore the asymmetry is not as severe. With increasing azimuth angle, the asymmetry of the meridional velocity in the tilted case tends to increase. This is particularly evident at the 270° position in the AR=2 case where the meridional velocity towards the shroud is very low and the span-wise distribution experienced is more asymmetric than anything experiences at other positions.

Negative meridional velocities (and hence reversed flow) only occur at the first 3 circumferential positions. Furthermore, it can be observed that the negative velocity in the tilted cases tends to start at a later circumferential position and ceases later around the volute. This indicates that the volute tilt delays the development of the vortices slightly and they move radial inwards at later positions. This effect was also observed and discussed in chapter 6.

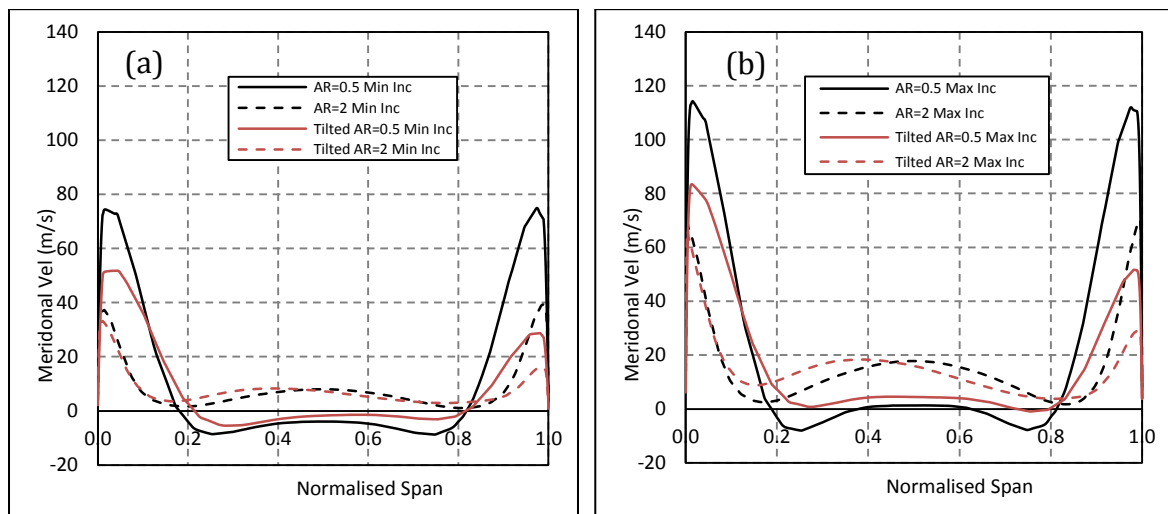


Figure 9.9: Meridional velocity across volute passage centre 54°. (a) - Minimum incidence (b) - Maximum incidence

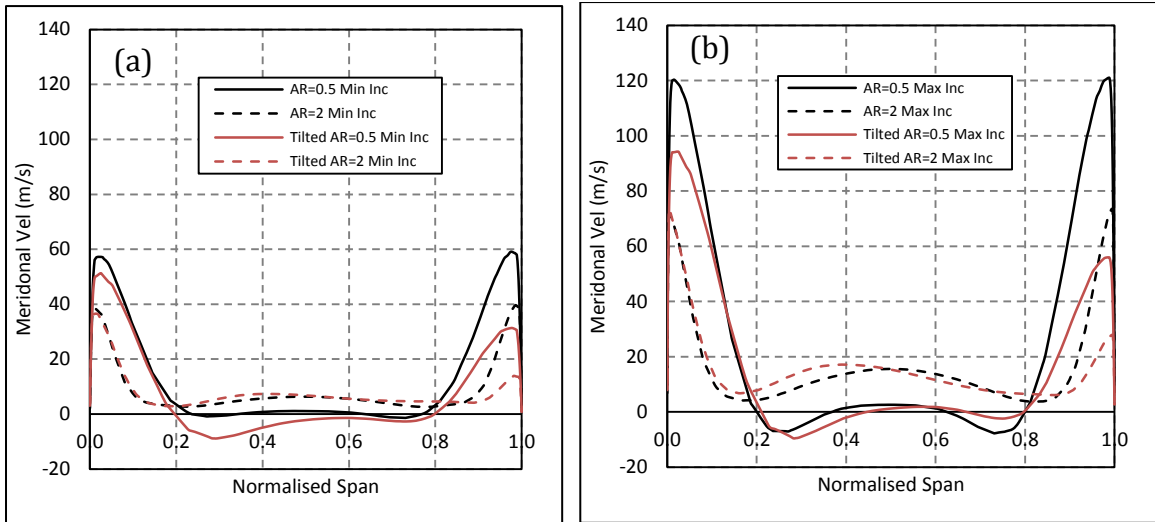


Figure 9.10: Meridional velocity across volute passage centre 72°. (a) - Minimum incidence (b) - Maximum incidence

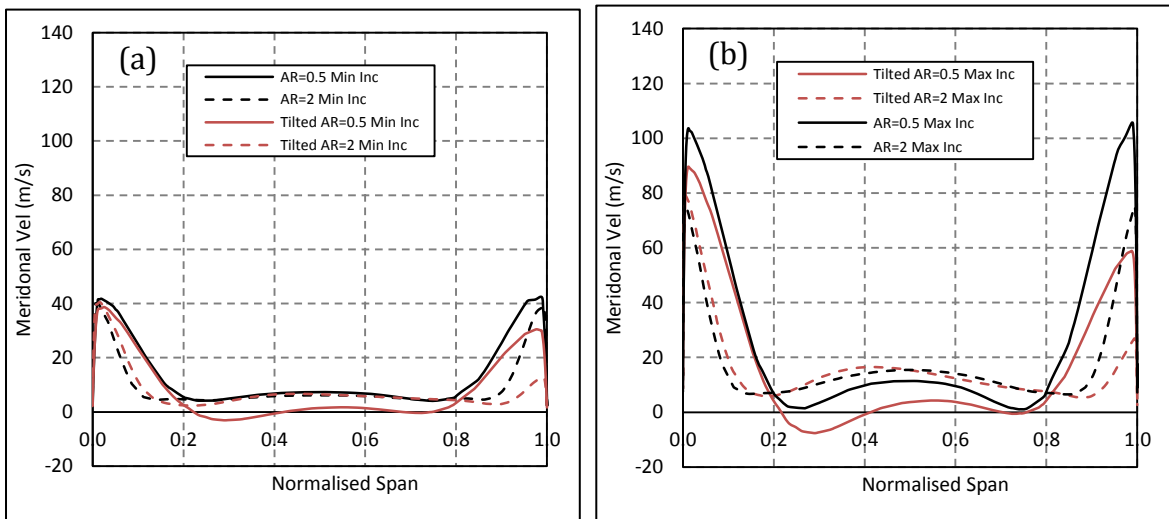


Figure 9.11: Meridional velocity across volute passage centre 90°. (a) - Minimum incidence (b) - Maximum incidence

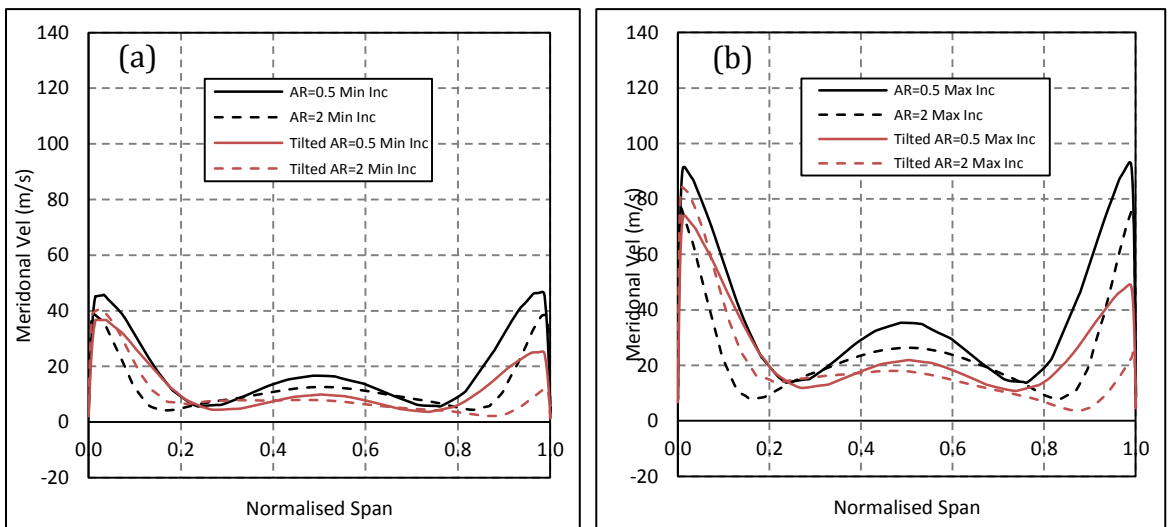


Figure 9.12: Meridional velocity across volute passage centre 180°. (a) - Minimum incidence (b) - Maximum incidence

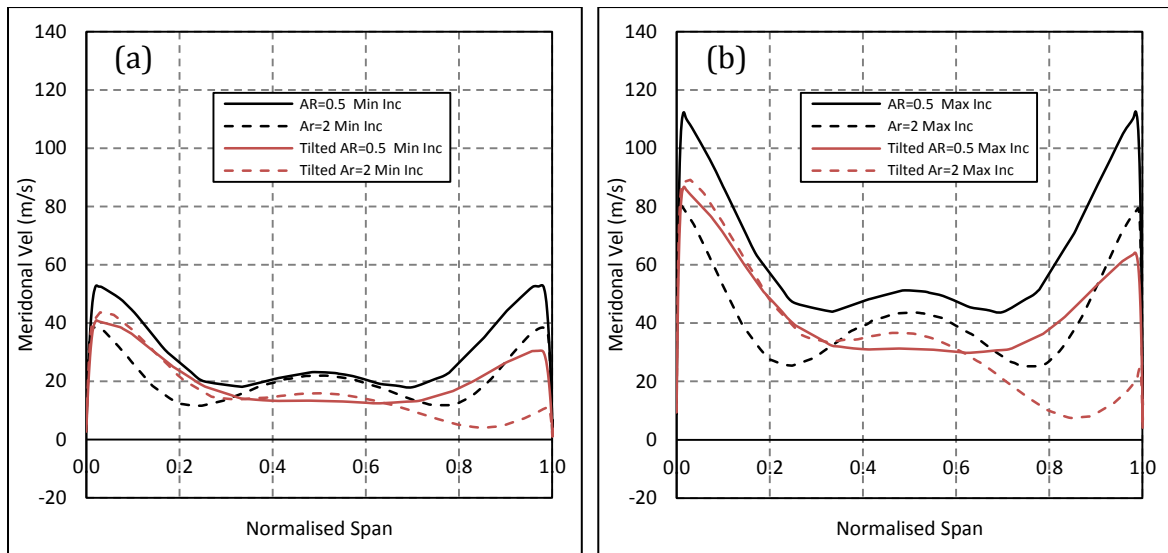


Figure 9.13: Meridional velocity across volute passage centre 270°. (a) - Minimum incidence (b) - Maximum incidence

Figures 9.14-9.17 present the resulting volute exit absolute flow angles around the volute circumference in both the radial and tilted volutes with AR=0.5 and 2. The circumferential positions are selected to lie equidistant from either blade LE to reduce any upstream effect.

Comparison of the radial and tilted, AR=0.5 volutes at the minimum incidence running point, shows a slight reduction in the span-wise variation in the tilted case compared with the radial case. The impact of the asymmetry is not constant around the circumference with the span-wise shift in absolute flow angle towards greater spans most distinct at the 126° position where the distribution in the tilted case is centered around 0.6 span. Beyond this point the shift reduces to produce almost symmetrical distributions. In the AR=2 case, at minimum incidence, the circumferential shift of peak absolute angle is more distinct but occurs predominantly at the 90° and 198° positions, while the other positions show the distribution centered. As observed for the radial volute in chapter 8, increasing the volute aspect ratio was observed to reduce the extent of the span-wise distribution at the volute exit. This effect can be observed at minimum incidence in both the radial and tilted volutes but is perhaps more prominent in the radial configuration.

At the maximum incidence running point, the span-wise distribution reduces in all cases as discussed in chapter 8. The same circumferential shift can be observed between the radial and tilted designs that was present at the minimum incidence

running point; with the peak shift occurring at 126° in the AR=0.5 case and at 90° and 198° in the AR=2 case. At other circumferential locations the absolute flow angle distribution shows no or little shift in the span-wise direction in the tilted case. At both running points the span-wise shift in the AR=2 case is interesting as the shift is largest on the 90° plane, before reducing at the 126° plane, only to increase again by the 198° plane. The impact of volute aspect ratio reducing the span-wise variation is evident in both the radial and tiled cases at both running points.

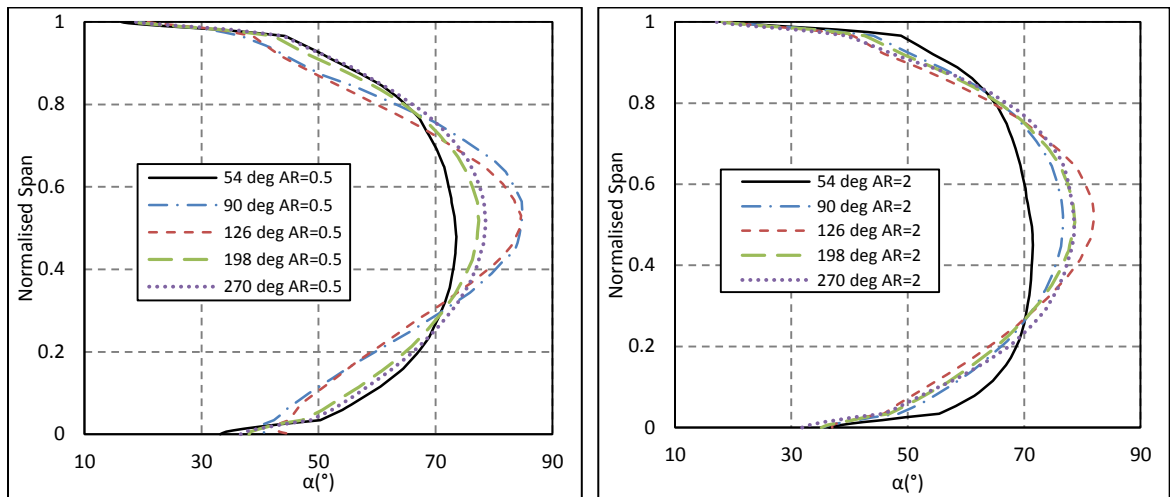


Figure 9.14: Volute exit absolute flow angle for the radial volute at minimum incidence. Left AR=0.5. Right AR=2.

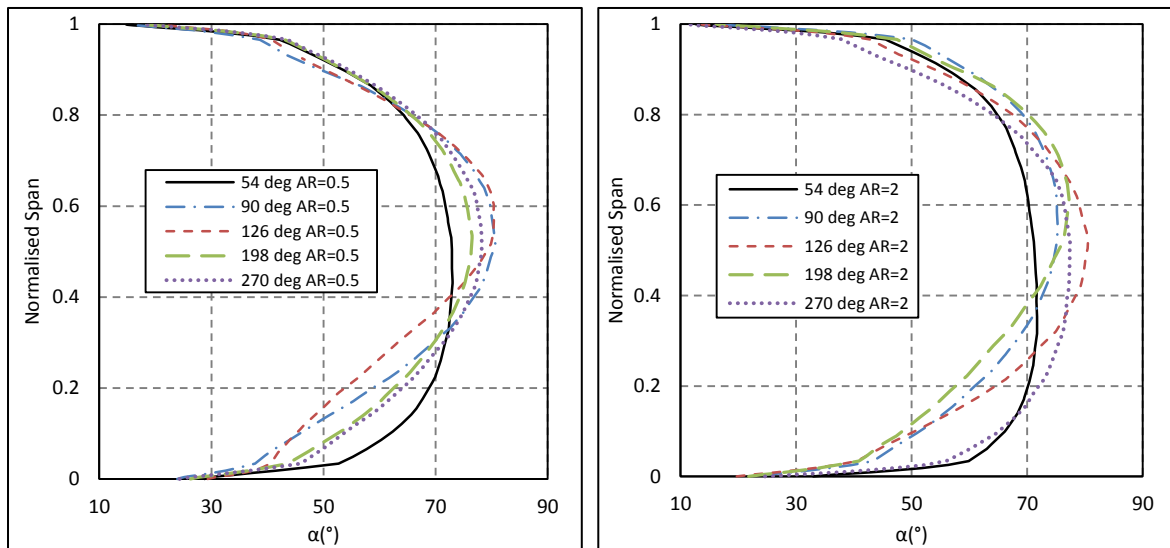


Figure 9.15: Volute exit absolute flow angle for the tilted volute at minimum incidence. Left AR=0.5. Right AR=2.

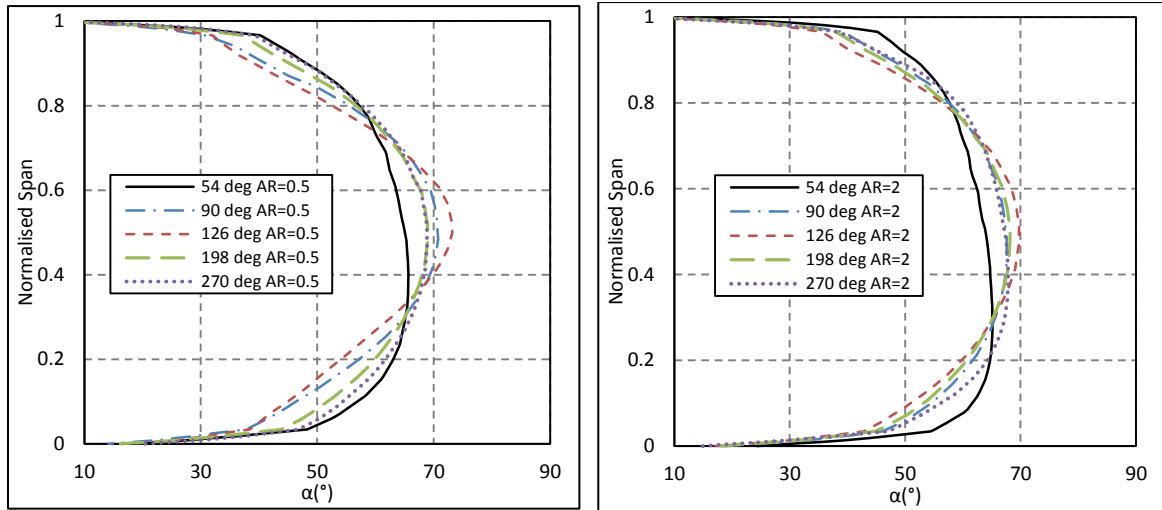


Figure 9.16: Volute exit absolute flow angle for the radial volute at maximum incidence. Left AR=0.5. Right AR=2.

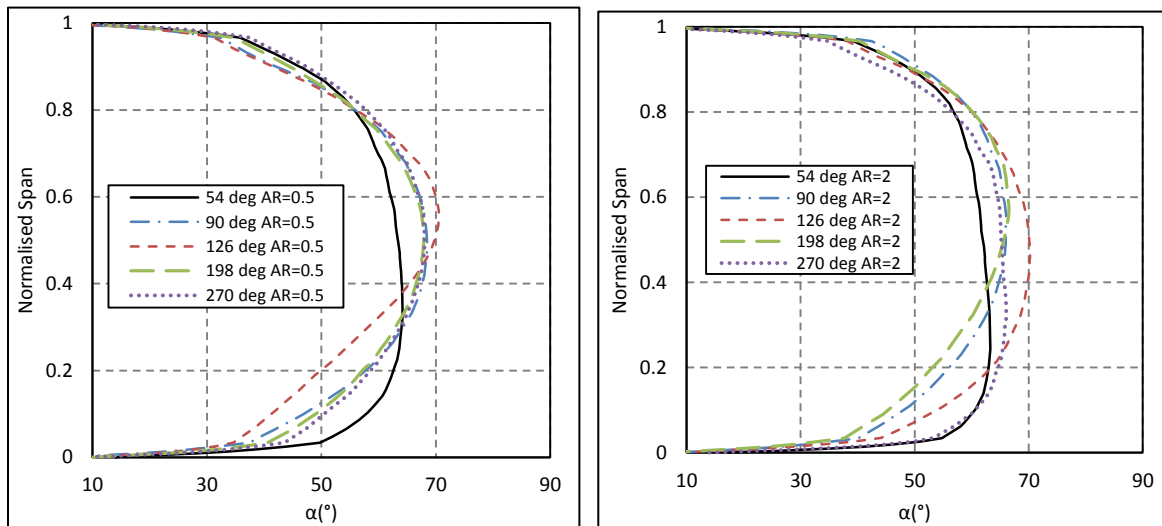


Figure 9.17: Volute exit absolute flow angle for the tilted volute at maximum incidence. Left AR=0.5. Right AR=2.

Figures 9.18 and 9.19 show the resulting circumferentially averaged LE incidence angles over the blade span at the minimum and maximum incidence running points respectively. It was observed that the tilted variants resulted in the span-wise distribution shifting to lower positions at the LE than their radial counterparts at minimum incidence. The opposite is true at the maximum incidence running point. This effect is the result of the achieved blade angle as explained in chapter 6. The blade angles achieved in the tilted design are greater and more negative towards the hub and become positive towards the shroud (figures 6.17). Therefore, the incidence distribution is shifted accordingly.

In all cases, increasing the aspect ratio reduces the LE incidence variation with the magnitude of the peak incidence angles reducing. At the maximum incidence running point, the AR=2 tilted volute results in the greatest span-wise shift of the distribution with the peak incidence occurring at approximately 0.65 span. The cause of this effect is the greater variation of meridional velocity in the tilted AR=2 case discussed above.

The clear impact of both tilt and AR on the LE spanwise variation is important to note in the rotor design process. The location of peak incidence over the blade LE span will impact the rotor flows and hence impact losses. Therefore, to achieve optimum performance the blade should be developed to best match these flow conditions being delivered by the volute.

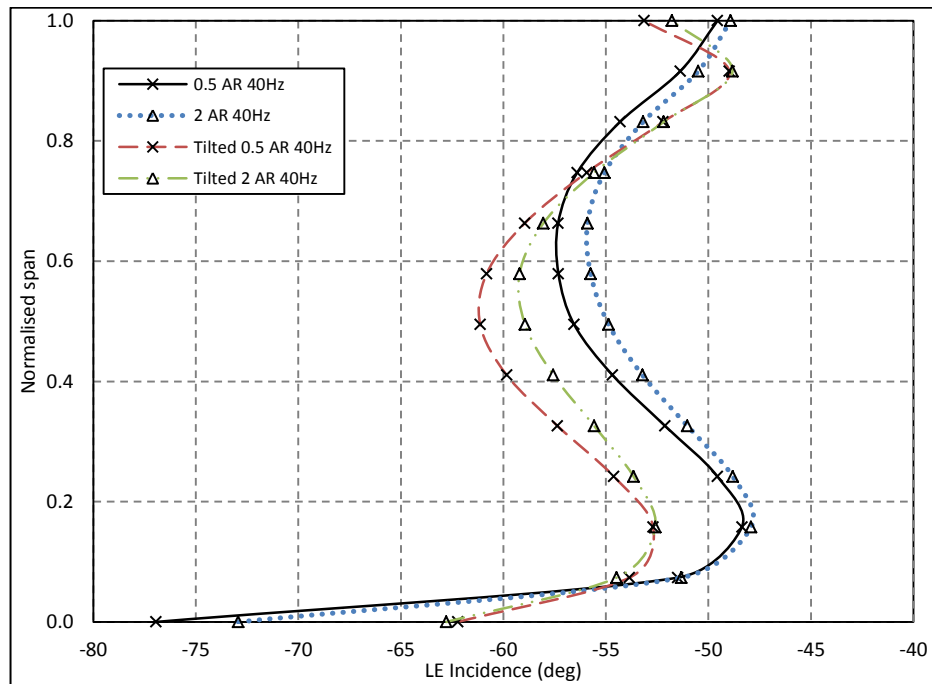


Figure 9.18: LE incidence at the minimum incidence running point in tilted and radial volute configurations with AR=0.5 and AR=2

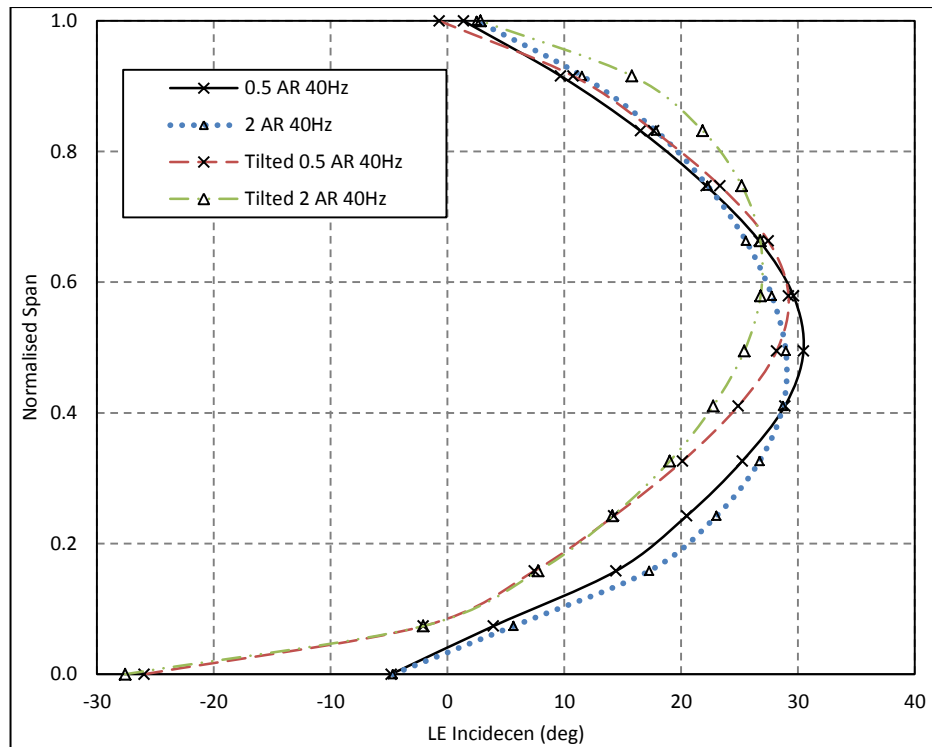


Figure 9.19: LE incidence at the maximum incidence running point in tilted and radial volute configurations with AR=0.5 and AR=2

9.4 CHAPTER CONCLUSIONS

This chapter has compared the impact of both volute tilt and volute aspect ratio by combining both parameters and comparing four volute designs.

It was found that volute tilt has a greater impact on turbine performance than aspect ratio but combining both aspects can result in sizable performance benefits. The maximum variation between the worst performing design, radial AR=0.5 and the best performing design tilted AR=2 was 3% in the rotor region and 2.87% over the entire stage. Introducing volute tilt was shown to produce a larger improvement in the AR=0.5 case. While increasing volute AR was more beneficial in the radial designs with the tilted design showing a smaller performance benefit particularly in the rotor region. It was also found that combining both tilt and small AR values results in the greatest volute loss.

The secondary flows showed that volute tilt has a significant impact on the development of secondary flow structures in the AR=0.5. The tilt resulted in asymmetric flow structures, and at certain points within the pulse, this resulted in the

development of a third vortex. The impact of these secondary flows on volute exit and rotor inlet flows shows that the combination of the volute parameters can shift the LE span-wise distribution across the LE as well as influencing the range of flow angles. The AR=2, tiled volute design resulted in the lowest peak incidence angles achieved of all the designs.

10 EXPERIMENTAL INVESTIGATION AND FURTHER VALIDATION

10.1 INTRODUCTION TO TEST SET-UP

To validate the computational finding with regards to volute tilt, both the radial and tilted volute designs were tested experimentally. This was done at the pulsating gas stand facility at Imperial College London. This cold flow test rig is capable of testing under both steady state and pulsating flow conditions. Both volutes were tested under steady state conditions at three turbine speeds (30krpm, 48krpm and 56krpm). Under pulsating conditions the two volute designs were tested across the three turbine speeds, at three pulse frequencies (20Hz, 40Hz and 60Hz) and three pulse loads resulting in 27 unsteady operating cycles for each design. An over view of the test rig layout is presented in figure 10.1.

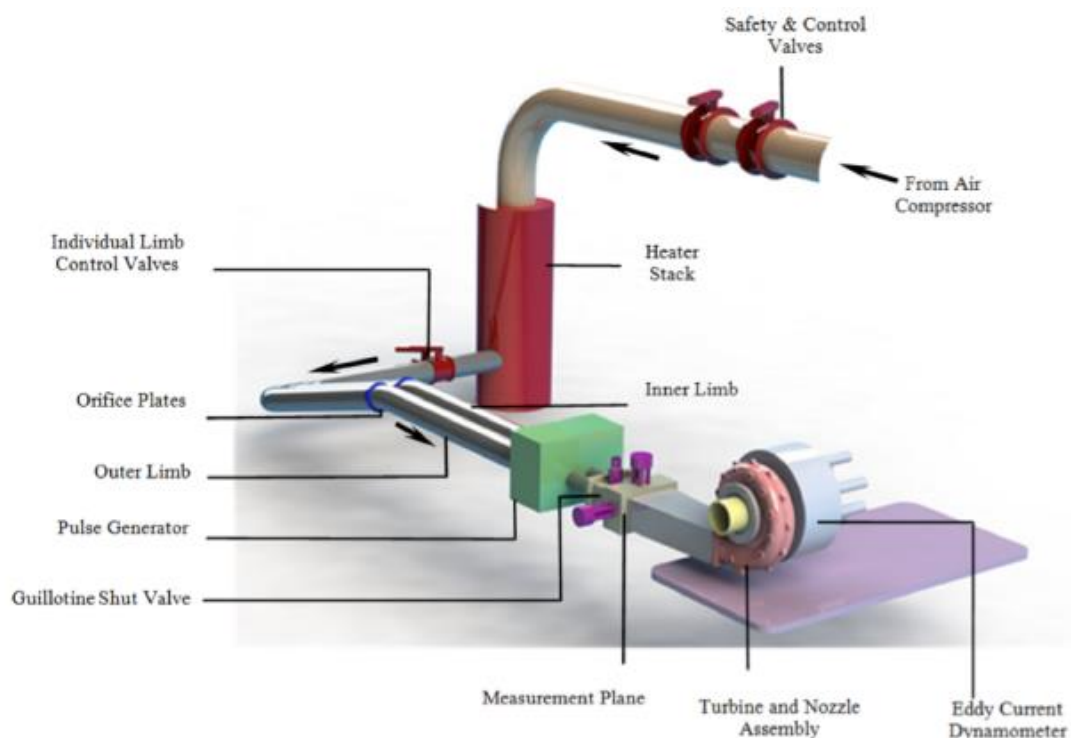


Figure 10.1: Imperial College test facility layout (Padzillah, 2014).

The test rig was supplied with compressed air from three Ingersoll Rand screw-type compressors which provide a maximum mass flow of 1Kg/s at a maximum pressure of 5 bar. Downstream of the inlet two valves were present, one for controlling the mass flow, the other, a safety valve. The flow then passed through the

heater stack. Although the test rig ran cold, the heater section was required to give some control of temperature and to prevent condensation occurring downstream of the turbine wheel after the flow had been expanded. The turbine tests are usually conducted between 300K - 340K. The passage then split into two parallel entries, namely the inner and outer limbs. This allows twin and double entry turbines to also be tested on the rig. In the current case the two limbs joined together as the volute under investigation was a single entry design. The flows then passed through the pulse generator which was originally designed by Dale & Watson, (1986). The pulse generator consisted of two chopper plates shown in figure 10.2. The cut outs in the plates produced the pulse characteristic as the plates were rotated. The rotation of the plates was computer controlled allowing the pulse frequency to be accurately controlled. Downstream of the pulse generator was the measurement plane where instantaneous parameters were recorded. This instrumentation included high response pressure transducers, static pressure tapings, thermocouples and a hotwire system for instantaneous mass flow measurement. Beyond the measurement plane the rig was connected to the test turbine stage inlet using a specifically designs connection. In this case the pipe work was designed to feed into the single-entry volute. The turbine assembly was connected to the permanent magnet eddy current dynamometer that was capable of extracting power up to 60kW and a maximum speed of 60krpm. The dynamometer created a load on the shaft as the magnetic rotor rotated relative to the stator. This induced an electrical current in the stator and therefore its own magnetic field which opposed the rotor rotation creating a load. To vary the shaft load the stator plates can be moved axial closer or further away from the rotor. Tests were therefore conducted over a specified range of gap distances (load) and a rotational speed target was set. The required inlet pressure and mass flow to achieve the target speed were measured along with the turbine torque from an optical speed sensor on the dynamometer.

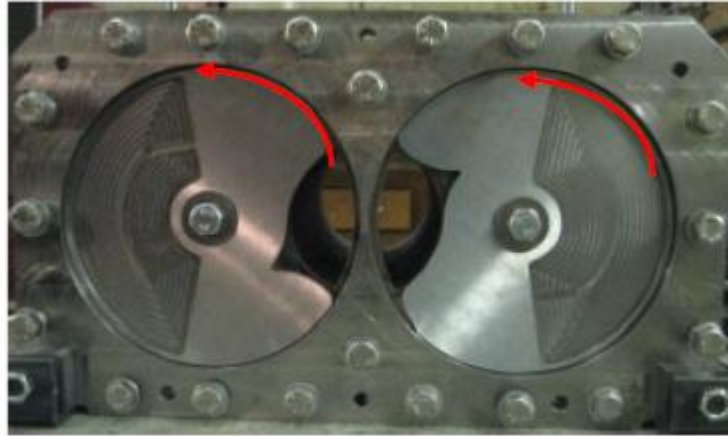


Figure 10.2: Imperial College test facility chopper plates (Newton, 2014)

10.2 EQUIVALENT PERFORMANCE PARAMETERS

Throughout this thesis several non-dimensional performance parameters have been introduced. Such parameters are important as they allow comparison between designs across scales and flow conditions. As the test rig at Imperial College runs cold (approximately 300K) it is important to ensure the cold flow tests are completed at comparable operation as that seen on engine.

Firstly, the turbine speed parameter needs to be equivalent to realistic engine conditions. Hence the speed parameter needs to be matched -

$$\frac{N}{\sqrt{T_{01}}} \quad (84)$$

Where N is rotational speed and T_{01} is total inlet temperature. It is important to scale the turbine speed to maintain a constant speed parameter under the reduced inlet temperatures.

$$\left(\frac{N}{\sqrt{T_{01}}} \right)_{Test} = \left(\frac{N}{\sqrt{T_{01}}} \right)_{Actual} \quad (85)$$

Assuming an inlet total temperature of 300K, the equivalent cold flow rpm for 90krpm hot flows (923K), would be approximately 51krpm.

In addition, it is important to ensure that the turbine is tested at equivalent mass flow parameters.

$$\left(\frac{\dot{m}\sqrt{T_{01}}}{P_{01}}\right)_{Test} = \left(\frac{\dot{m}\sqrt{T_{01}}}{P_{01}}\right)_{Actual} \quad (86)$$

Where \dot{m} is mass flow and P_{01} is total inlet pressure. As the turbine is likely to operate under similar pressure ratios on test to that on engine the lower inlet temperature means a greater inlet mass flow is required to account for the reduced temperature.

10.3 EXPERIMENTAL FACILITY INSTRUMENTATION

The overview given in section 10.1 discusses the instrumentation used in the pulsating flow test rig at Imperial College London. The measured parameters included mass flow rate, pressure, temperature, rotation speed and torque. These parameters were measured under both steady and unsteady conditions. The measurement of each of these parameters and the resulting errors are detailed in this section.

10.3.1 MASS FLOW STEADY STATE HARDWARE

Under steady state flow conditions the mass flow rate was measured using a McCrometer v-cone flow meter. The layout is shown in figure 10.3. This flow meter required measurements of the differential pressure between the high and low pressure ports. The gas temperature and absolute pressure were also required for the mass flow computation. The differential in pressure was measured using a Siemens Sitrans P DS111 differential pressure transmitter with an uncertainty of ± 120 Pa. The absolute pressure was measured using a Scanivalve system described in section 10.3.4 and the temperature using an E-type thermocouple with an uncertainty of ± 0.67 K. Equation 87 was used to calculate the final mass flow.

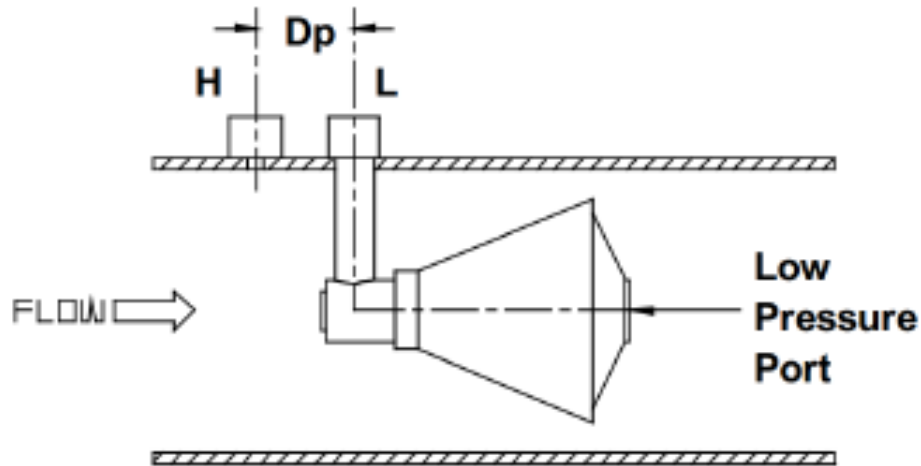


Figure 10.3: V-cone flow meter layout. Operation and maintenance manual, McCrometer 2013

$$\dot{m} = \sqrt{\rho} F_a C_d Y k_1 \sqrt{\Delta P} \quad (87)$$

Where ρ is density, F_a is the material thermal expansion factor, k_1 is the flow coefficient, Y is the gas expansion factor, C_d is the discharge coefficient and ΔP is the pressure differential.

The material thermal expansion factor depends on the flow temperature and the thermal expansion coefficient of the V-cone material which varies by less than 0.1% from unity. The gas expansion factor (Y) is given by -

$$Y = 1 - (0.649 - 0.696\beta^4) \frac{U_1 \Delta P}{\gamma P} \quad (88)$$

Where U_1 is a unit conversion factor constant given by McCrometer and β is the beta-ratio and is a function of the v-cone geometry and is given as -

$$\beta = \sqrt{1 - \frac{d^2}{D^2}} \quad (89)$$

Where D is the inside diameter of the pipe and d is the outside diameter of the v-cone. The flow coefficient k_1 in equation 87 is a function of both the pipe size and

beat ratio. Both v-cones used in the testing had flow coefficient of 0.0139. The discharge coefficient C_d was taken from the calibration sheets supplied with the v-cones (see Appendix A). Values of 0.8385 and 0.8472 were used for the two v-cones.

10.3.2 UNSTEADY MASS FLOW

Under unsteady flow conditions, the mass flow rate was measured using constant temperature hot wire anemometry (CTA) as the v-cones don't have the necessary responsiveness. Hot wire anemometry works by placing the very thin hot wire in the gas flow, and measuring the heat transfer of the wire. The hotwire itself makes up part of a Wheatstone bridge and the basic concept for the CTA operation is that the necessary current is supplied to the wire to balance the voltage of the bridge. This requires the wire resistance and hence temperature to remain constant. The CTA was equipped with a 10µm diameter platinum plated tungsten wire. The probes used were Dantec Dynamics 55P11 models along with CTA StreamLine hotwire control system also by Dantec Dynamics. Szymko, (2006) measured the frequency response of the hot wires to be 7.7kHz which is multiple orders of magnitude greater than the tested pulse frequency. The current was accurately controlled by a servo amplifier. Therefore, any changes to the air flow could be measure by the sensor due to the low thermal inertia of the sensor and the high gain of the servo loop amplifier. The required voltage to balance the bridge was then measured directly. Kings Law was then used to provide a relationship between the voltage and flow velocity through the use of the Nusselt number, Nu , and Reynolds number, Re . The relationship is expressed as –

$$Nu = a + bRe^{0.5} \quad (90)$$

10.3.2.1 HOT WIRE CALIBRATION

Initial calibration of the hot wire probes was done by Dantec Dynamics using a commercial calibration unit. A known velocity of air $\pm 0.5\%$ was supplied over a range of 5m/s - 300m/s and ten data points recorded. This process provided initial values for the constants a and b .

However, further calibration was necessary due to day to day changes in the test environment including fouling of the system or slight misalignments of the probe to the incoming air flow. This calibration was done under steady state flow by comparing the mass flow measured by the v-cone and that measured by the hot wire. The constants could then be updated from the calibration to produce improved alignment between the two mass flow measurements. The calibration points for both the radial and tilted volutes are shown in figure 10.4.

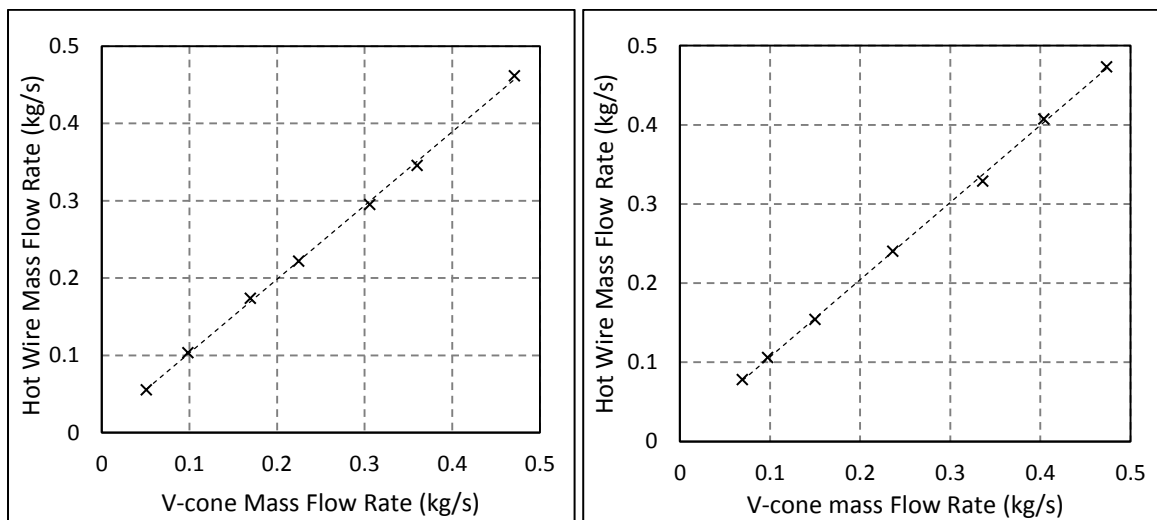


Figure 10.4: Hot Wire Calibration Data. Left - Radial Housing Right - Radial Housing

10.3.2.2 UNSTEADY MASS FLOW UNCERTAINTY

The uncertainty of the hot wire measurements can be obtained from the calibration data shown in figure 10.5. To achieve this a statistical approach was implemented using the calibration of different measurements. Calibration aims to link the actual measured value to that of the physical property through the use of a function –

$$y = f(x) \quad (91)$$

The calibration points will not match the function exactly due to numerous variables introducing inaccuracies to the measurements. The standard deviation (σ) of the recorded points from the function can therefore be obtained to give a measure of the uncertainty –

$$\sigma = \left[\frac{1}{n-v} \sum_{i=1}^n (y_i - f(x_i))^2 \right]^{1/2} \quad (92)$$

Where n is the number of data points, v is the number of restrictions placed on the possible value of y (as this is a linear function $v = 2$), y_i is the value of the hot wire reading and $f(x_i)$ is the calculated value of the hotwire reading using the linear function.

If it is assumed that the measured values follow a normal distribution the uncertainty can be given to a confidence interval. In this case the uncertainty will be given to $\pm 2\sigma$ giving a confidence level of 95.4%.

Using the statistical approach the standard deviation in mass flow for the radial and tilted housings was found to be 3.41g/s and 3.40g/s respectively. This gives an uncertainty of 6.82g/s and 6.80g/s for the radial and tilted housing respectively for a confidence level of 95.4%.

10.3.3 PRESSURE STEADY FLOW

The static pressure was measured at the measurement plane through tapings positioned perpendicular to the direction of flow. This data acquisition was achieved through a 24 channel Scanivalve system. The pressure ports were connected with a rotary valve system to one of two high accuracy strain gauge transducers. Each channel had two ports so that the pressure could be measured as a differential between two ports or by leaving the port open to measure the atmospheric pressure of the room providing the gauge pressure. The accuracy of the pressure transducers was $\pm 0.2\%$ over a range of 0.7bar -7bar. The atmospheric pressure in the room was measured using a dial barometer providing a measurement of the absolute ambient pressure. The accuracy of the measurements was $\pm 50\text{Pa}$.

10.3.4 UNSTEADY PRESSURE

Under unsteady operation the pressure was measured using two high response Schaevitz type P704-0001 strain gauge pressure transducers. These gauges are capable of measuring pressures over a range of 0.3-3.45 bar with a maximum deviation of $\pm 0.059\%$. To reduce the pulsating effects on the measurements, the

transducers were mounted close to the duct wall to minimise air passage length from the duct surface to the sensor. The Helmholtz frequency of this passage was measured by Szymko, (2006) and found to be approximately 2800Hz which is significantly greater than any tested pulse frequencies to ensure the impact of the resonance was negligible.

10.3.5 STEADY STATE TEMPERATURE

The inlet temperature was measured using a T-type thermocouple that was connected to a specific thermocouple module on the Field point system used. Further temperature measurements were taken to ensure safe operation of the test rig including temperature measurements of the bearings, stator plate and dynamometer cooling water. The accuracy of the thermocouples used was $\pm 0.5\text{K}$.

10.3.6 UNSTEADY TEMPERATURE

During unsteady operation the flow temperature was not measured directly as the thermal inertia of the thermocouple would not provide accurate values. Instead the temperature was obtained through equation 93.

$$T_{inst} \approx \bar{T} \left(\frac{P_{inst}}{\bar{P}} \right)^{\gamma - \frac{1}{\gamma}} \quad (93)$$

Where T_{inst} is the instantaneous temperature, \bar{T} is the time average temperature, P_{inst} is the instantaneous pressure, \bar{P} is the time average pressure and γ is the ratio of specific heats. The time averaged temperature required in equation 93 was measure using the same system as that used to measure the temperature in the steady state operation. Szymko, (2006) measured the uncertainty of the time averaged measurements using a duel hotwire probe to determine the temperature variation under pulsating conditions. The resulting accuracy of the time averaged temperature obtained was $\pm 3^\circ\text{C}$.

Although the test rig operates cold some heat loss will still occur and the calculation only provides an approximation of the temperature.

10.3.7 ROTATIONAL SPEED

The rotational speed of the turbine was measured using a Omron EE-SX4101 reflective optical switch with an integrated amplifier. An infra-red optical sensor was attached to the dynamometer that was triggered by a 20 tooth wheel on the turbine shaft. This produced 20 pulses per revolution of the wheel. The data acquisition system that measured the time between each produced pulse operated at 40MHz. The maximum speed of the test rig was 60krpm, or 1000 rotations a second giving 20 pulses per revolution. The uncertainty in the speed measurement was therefore 0.03rpm.

10.3.8 STEADY FLOW TORQUE

The torque was measured directly from the dynamometer through a load cell that measured the reaction force exerted by the dynamometer. A Tedea Huntleigh 1042 single point strain gauge load cell was used. This was connected to a National Instruments FP-SG-140 Fieldpoint strain gauge module. After each test the rotor was brought to rest removing all load and the system zeroed.

10.3.9 UNSTEADY FLOW TORQUE

Under unsteady conditions the instantaneous torque was necessary to calculate the performance of the turbine. The instantaneous torque was obtained by summing the mean and fluctuating torque values. The fluctuating torque (τ_{fluc}) is the product of the rotor angular acceleration (α) and the polar moment of inertia (I) of the turbine wheel.

$$\tau_{fluc} = I \cdot \alpha = I \cdot \frac{d\omega}{dt} \quad (94)$$

Where $\frac{d\omega}{dt}$ is the first derivative of angular speed and corresponds to the rotating acceleration. This is calculated numerically by –

$$\dot{\omega} = \frac{\omega_n - \omega_{n-1}}{t_n - t_{n-1}} = \frac{\delta\omega}{\delta t} \quad (95)$$

10.3.9.1 TORQUE UNCERTAINTY

The torque measured by the load cell was calibrated by attaching an arm of length 0.599m to the dynamometer producing a load parallel to the load cell. Known loads were then applied to the load cell over a range that might be expected to occur during testing. This calibration is regularly completed on the test rig to ensure consistency of the measurements. The calibration points suggest an uncertainty of $\pm 0.025\text{Nm}$. Under unsteady operation there is also an added error in the measured unsteady torque due to the error in the rotational speed measurement described in section 10.3.7.

10.4 UNCERTAINTY ANALYSIS

The measurement methods described in section 10.3 detail the potential errors introduced by the instrumentation. Each of these errors will have an impact on the measured turbine performance. Therefore, it is necessary to ascertain the impact of these errors on the important performance parameters. The method used here is the Root-Sum-Squares (RSS) approach. This methodology was originally proposed by Kline & McClintock, (1953) and developed further by Moffat, (1982). Stern et al., (1999) gave a full description of the method based on ASME and AIAA standards. The implementation of this approach for the current application was detailed by Szymko, (2006).

The RSS value for a given parameter, $\pm Par_{RSS}$, can be obtained from –

$$\pm Par_{RSS} = \sqrt{\sum_{i=1}^n \left(\pm var_i \cdot \frac{\partial Par}{\partial var_i} \right)^2} \quad (96)$$

Where $\pm var_i$ is the uncertainty of the individual variable and $\frac{\partial Par}{\partial var_i}$ is the sensitivity coefficient. The sensitivity coefficient for each of the parameters of interest are given in table 10.1 as suggested by Padzillah, (2014).

| | $\partial \dot{m}$ | ∂T_1 | ∂P_{01} | $\partial \tau$ | ∂N | ∂P_5 |
|----------------------|--------------------|----------------|-------------------|-----------------|--------------|----------------|
| $\partial \eta_{ts}$ | 44% | 7% | 15% | 30% | 0% | 4% |

| | | | | | |
|---------------------|-----|-----|-----|----|-----|
| $\partial U/c_{is}$ | 28% | 16% | 45% | 0% | 11% |
| ∂MFP | 72% | 6% | 21% | | |
| ∂PR | 39% | 3% | 44% | | 13% |

Table 10.1: Parameter sensitivity coefficients

The resulting RSS uncertainty equations for the total to static efficiency, mass flow parameter, pressure ratio and velocity ratio are given in equations 97-100.

$$\pm(\eta_{ts})_{RSS} = \sqrt{\left(\pm\dot{m} \cdot \frac{\partial\eta_{ts}}{\partial\dot{m}}\right)^2 + \left(\pm T_1 \cdot \frac{\partial\eta_{ts}}{\partial T_1}\right)^2 + \left(\pm P_1 \cdot \frac{\partial\eta_{ts}}{\partial P_1}\right)^2 + \left(\pm\tau \cdot \frac{\partial\eta_{ts}}{\partial\tau}\right)^2 + \left(\pm N \cdot \frac{\partial\eta_{ts}}{\partial N}\right)^2 + \left(\pm P_5 \cdot \frac{\partial\eta_{ts}}{\partial P_5}\right)^2} \quad (97)$$

$$\pm(MFP)_{RSS} = \sqrt{\left(\pm\dot{m} \cdot \frac{\partial MFP}{\partial\dot{m}}\right)^2 + \left(\pm T_1 \cdot \frac{\partial MFP}{\partial T_1}\right)^2 + \left(\pm P_1 \cdot \frac{\partial MFP}{\partial P_1}\right)^2} \quad (98)$$

$$\pm(PR)_{RSS} = \sqrt{\left(\pm\dot{m} \cdot \frac{\partial PR}{\partial\dot{m}}\right)^2 + \left(\pm T_1 \cdot \frac{\partial PR}{\partial T_1}\right)^2 + \left(\pm P_1 \cdot \frac{\partial PR}{\partial P_1}\right)^2 + \left(\pm P_5 \cdot \frac{\partial PR}{\partial P_5}\right)^2} \quad (99)$$

$$\pm(U/c_{is})_{RSS} = \sqrt{\left(\pm\dot{m} \cdot \frac{\partial U/c_{is}}{\partial\dot{m}}\right)^2 + \left(\pm T_1 \cdot \frac{\partial U/c_{is}}{\partial T_1}\right)^2 + \left(\pm P_1 \cdot \frac{\partial U/c_{is}}{\partial P_1}\right)^2 + \left(\pm T_1 \cdot \frac{\partial U/c_{is}}{\partial T_1}\right)^2 + \left(\pm N \cdot \frac{\partial U/c_{is}}{\partial N}\right)^2} \quad (100)$$

The calculated uncertainties of the performance parameters given above are dependent on the running point of the turbine. As the turbine inlet pressure, mass flow and temperature reduce, the relative errors of these parameters increases.

Under steady state operation this results in an uncertainty range of 1.01%-4.54% in turbine efficiency with the greater uncertainty occurring at high velocity ratios and low rotational speeds. The range of uncertainty of the MFP was 0.16%-1.29%, the uncertainty range of pressure ratio was found to be 0.13%-0.71% and the range of uncertainty in velocity ratio was 0.12%-0.52%. The impact of these uncertainties on the measured performance is shown in figures 10.9-10.14 through the error bars added to the plots. As stated in all cases the errors reduce as the turbine mass flow and pressure ratio increase giving a greater level of confidence in the measured values. Although the turbine efficiency shows the greatest level of uncertainty, the vast majority of points show a range of less than 1.5%.

Under unsteady operation, the uncertainties follow a similar trend of reducing with increasing mass flow and pressure ratio. There is an increased uncertainty in the mass flow measurement using the hot wire probe under pulsating conditions when compared to the approach used under steady state conditions. The resulting cycle averaged uncertainty of efficiency ranged from 1.26%-6.37% and the uncertainty in MFP ranged from 1.15%-6.24%. The cycle averaged pressure ratio uncertainty ranged from 0.63%-3.38% and the cycle averaged velocity ratio uncertainty ranged from 0.46%-2.43%. The larger uncertainties occurred under the low pulse load conditions that resulted in lower cycle average mass flows. Tables 10.2-10.4 shows the cycle averaged uncertainties for each of the 27 unsteady operating points tested for each volute configuration.

| Radial | | | | | | Tilted | | | | | |
|--------|------|-------------|-------------|------------|-------------|--------|------|-------------|-------------|------------|-------------|
| | | Eff error % | MFP error % | PR error % | U/c error % | | | Eff error % | MFP error % | PR error % | U/c error % |
| 20Hz | Low | 6.37% | 6.24% | 3.38% | 2.43% | 20Hz | Low | 5.76% | 5.54% | 3.00% | 2.16% |
| | Mid | 3.93% | 4.59% | 2.49% | 1.79% | | Mid | 3.80% | 4.31% | 2.34% | 1.68% |
| | High | 1.61% | 1.94% | 1.06% | 0.76% | | High | 1.55% | 1.84% | 1.00% | 0.72% |
| 40Hz | Low | 6.34% | 6.25% | 3.39% | 2.43% | 40Hz | Low | 5.43% | 5.61% | 3.04% | 2.19% |
| | Mid | 3.96% | 4.72% | 2.56% | 1.84% | | Mid | 4.00% | 4.69% | 2.54% | 1.83% |
| | High | 1.58% | 1.91% | 1.04% | 0.75% | | High | 1.60% | 1.92% | 1.04% | 0.75% |

| | | | | | | | | | | | |
|------|------|-------|-------|-------|-------|------|------|-------|-------|-------|-------|
| 60Hz | Low | 5.89% | 5.67% | 3.08% | 2.21% | 60Hz | Low | 5.90% | 5.72% | 3.10% | 2.23% |
| | Mid | 4.23% | 5.13% | 2.78% | 2.00% | | Mid | 3.90% | 4.29% | 2.33% | 1.67% |
| | High | 1.60% | 1.94% | 1.06% | 0.76% | | High | 1.60% | 1.93% | 1.05% | 0.76% |

Table 10.2: Experimental errors 30krpm

| Radial | | | | | | Tilted | | | | | |
|--------|------|-------------|-------------|------------|-------------|--------|------|-------------|-------------|------------|-------------|
| | | Eff error % | MFP error % | PR error % | U/c error % | | | Eff error % | MFP error % | PR error % | U/c error % |
| 20Hz | Low | 4.11% | 4.25% | 2.30% | 1.65% | 20Hz | Low | 4.02% | 4.39% | 2.38% | 1.71% |
| | Mid | 2.07% | 2.61% | 1.42% | 1.02% | | Mid | 2.01% | 2.50% | 1.36% | 0.98% |
| | High | 1.38% | 1.47% | 0.80% | 0.58% | | High | 1.40% | 1.52% | 0.83% | 0.60% |
| 40Hz | Low | 3.93% | 4.09% | 2.22% | 1.59% | 40Hz | Low | 4.00% | 4.17% | 2.26% | 1.63% |
| | Mid | 2.01% | 2.47% | 1.34% | 0.97% | | Mid | 2.07% | 2.60% | 1.41% | 1.02% |
| | High | 1.39% | 1.50% | 0.82% | 0.59% | | High | 1.42% | 1.56% | 0.85% | 0.61% |
| 60Hz | Low | 4.04% | 4.18% | 2.27% | 1.63% | 60Hz | Low | 4.14% | 4.23% | 2.29% | 1.65% |
| | Mid | 2.04% | 2.55% | 1.39% | 1.00% | | Mid | 2.11% | 2.67% | 1.45% | 1.04% |
| | High | 1.43% | 1.59% | 0.87% | 0.63% | | High | 1.43% | 1.58% | 0.86% | 0.62% |

Table 10.3: Experimental errors 48krpm

| Radial | | | | | | Tilted | | | | | |
|--------|------|-------------|-------------|------------|-------------|--------|------|-------------|-------------|------------|-------------|
| | | Eff error % | MFP error % | PR error % | U/c error % | | | Eff error % | MFP error % | PR error % | U/c error % |
| 20Hz | Low | 3.65% | 3.74% | 2.03% | 1.46% | 20Hz | Low | 4.04% | 3.96% | 2.15% | 1.54% |
| | Mid | 1.88% | 2.27% | 1.23% | 0.89% | | Mid | 1.91% | 2.33% | 1.27% | 0.91% |
| | High | 1.36% | 1.42% | 0.78% | 0.56% | | High | 1.35% | 1.41% | 0.77% | 0.56% |
| 40Hz | Low | 3.64% | 3.67% | 1.99% | 1.43% | 40Hz | Low | 3.57% | 3.42% | 1.85% | 1.33% |
| | Mid | 1.89% | 2.30% | 1.25% | 0.90% | | Mid | 1.92% | 2.33% | 1.27% | 0.91% |
| | High | 1.35% | 1.41% | 0.77% | 0.56% | | High | 1.35% | 1.41% | 0.77% | 0.56% |
| 60Hz | Low | 3.48% | 3.53% | 1.92% | 1.38% | 60Hz | Low | 3.52% | 3.67% | 1.99% | 1.43% |
| | Mid | 1.89% | 2.28% | 1.24% | 0.89% | | Mid | 1.91% | 2.30% | 1.25% | 0.90% |
| | High | 1.26% | 1.15% | 0.63% | 0.46% | | High | 1.39% | 1.49% | 0.82% | 0.59% |

Table 10.4: Experimental errors 56krpm

10.5 DATA PROCESSING OF UNSTEADY MEASUREMENTS

During unsteady testing it was not possible to measure time averaged parameters as is done in the steady state testing due to time varying boundary conditions. Therefore, the data recorded was influenced by random uncertainties, noise and vibrations. To overcome this the data acquisition system used ensemble averaging, and filtering methods developed by Rajoo, (2007) and (Szymko, 2006).

Ensemble averaging is a technique that averages repeat measurements into one output signal thereby reducing the impact of random noise and non-cyclic vibrations by a factor of \sqrt{n} , where n is the number of repeated measurements. In the tests

conducted all unsteady data was recorded over 30 pulse cycles. These cycles were then ensemble averaged producing one pulse for each measured parameter.

In addition to the ensemble averaging technique a filtering technique was also applied to further reduce the noise. The method was a low pass Finite Impulse Response filter as utilised by Rajoo, (2007). This filter was built into the LabVIEW set-up and smoothed the pulse trace without losing the primary features of the data. Details of the process are available in Rajoo, (2007).

One further issue with the unsteady data acquisition was due to the detection of the turbine rotational speed. As the speed was measured by recording the time required for the wheel to rotate through a fixed angular distance, the sampling rate was not constant. This resulted in a miss match between the rotor speed output and other measurement parameters that were acquired at 20kHz. To overcome this an analogue data resampling method used by (Szymko, 2006) was implemented. This method fitted a cubic spline through each of the unequally spaced data points.

10.6 TURBINE HARDWARE

10.6.1 VOLUTE

The turbine volutes used on test were rapid prototyped parts produced out of Inconel. Although the test rig at Imperial College runs cold, and prototypes capable of operating at high temperatures were not required, the aim was to compare two realistic designs capable of running at realistic engine conditions. The volutes were rapid prototyped with the aim of minimising variation between the components. Using normal production methods would mean the manufacturing tolerances would be greater and part to part variation could lead to significant variation in turbine performance. Although the produced volutes will still contain some level of uncertainty due to manufacturing inaccuracies, the errors should be minimal. The resulting radial and tilted volutes are shown in figure 10.5. The same mixed flow turbine wheel and shaft were used throughout all tests to ensure no variation in rotor characteristics. The rotor is shown in figure 10.6.



Figure 10.5: Radial and tilted volutes. Left - Radial. Right - tilted.



Figure 10.6: Mixed flow turbine wheel and shaft.

The resulting flow passages of both designs are shown in figure 10.7. The full geometry of the turbine is shown with the heat shield included. Small change to how

the wheel sits in the housing and the position of the heat shield were necessary to cater for the different volute designs. The bearing housing was shift back in the tilted case to allow space for the volute which encroached into this region. The resulting position of the heat shield relative to the volute walls and rotor were therefore slightly effected.

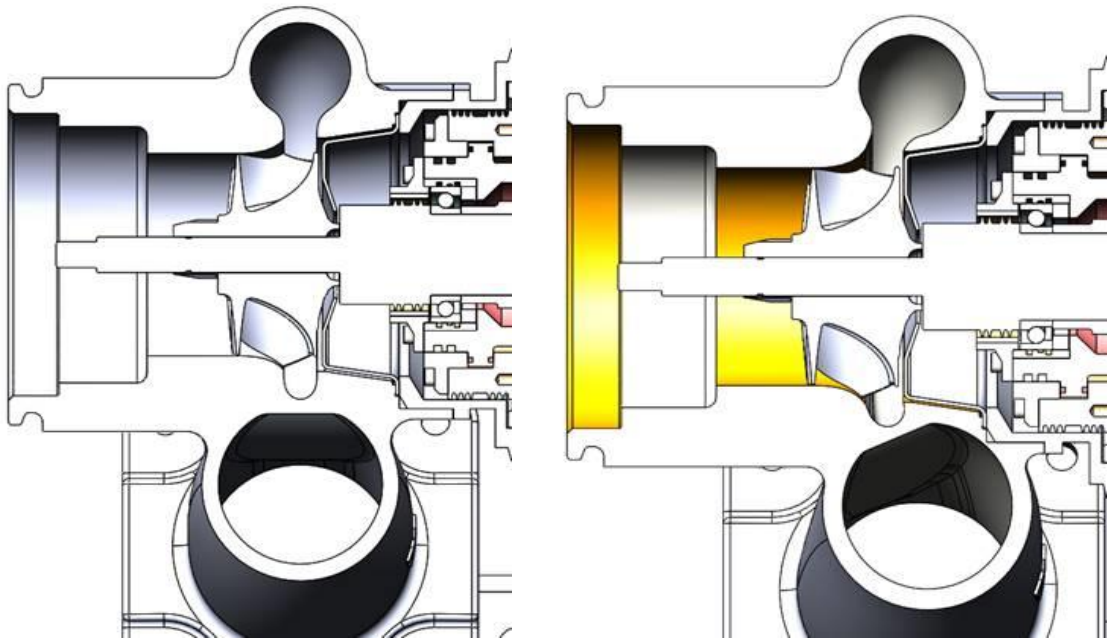


Figure 10.7: Schematic of the tested turbine geometries. Left -Radial Housing. Right - Tilted housing.

Figure 10.8 shows one of the assembled turbine geometries on test at Imperial College with major components labelled for clarity.

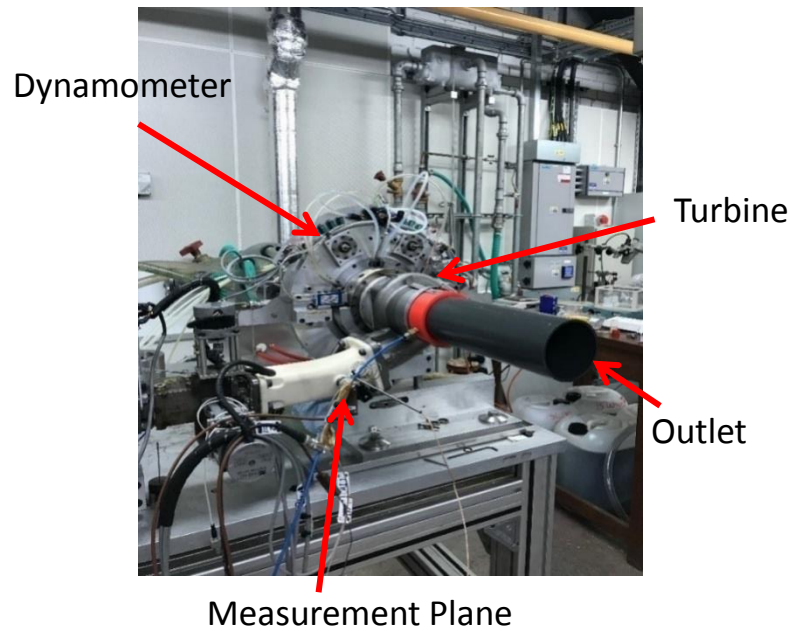


Figure 10.8: Test Layout

10.7 STEADY STATE RADIAL HOUSING VS TILTED

The steady state testing consisted of back to back comparisons of the two turbine housing designs at three turbine speeds, 30krpm, 48krpm and 56krpm. These correspond to hot flow speeds of 68.7krpm, 81.5krpm and 95.2krpm. The results are shown in figures 10.9-10.11 for MFP and in figures 10.12-10.14 for turbine efficiency (T-s). Error bars are included to show the uncertainty in the measured values. As discussed earlier the errors reduced as velocity ratio reduced and mass flow increased.

The MFP plots show that the two volute designs result in no noticeable differences in MFP at the lowest rotational speed of 30krpm. However, as the rotational speed increases, the tilted volute MFP was found to increase slightly with respect to the radial variant. At the maximum rotational speed of 56krpm, the tilted housing achieved an increase in MFP of up to 1.2% in the middle of the turbine map. This is larger than predicted in chapter 6, however it should be noted that the full experimental geometry included features not modelled in the previous CFD such as the step created where the turbine rotor backs up against the heat shield.

Comparing the measured efficiencies of the two designs over the speed range shows that the tilted housing results in efficiency improvements at the low velocity

ratio running points at 30krpm. It should be noted that at these operating points the experimental uncertainties were greater than the measured performance difference. As the velocity ratio reduced the performance of the two housings became identical. As the rotational speed was increased the performance of the tilted housing reduced relative to the base radial design. At 48krpm the tilted housing recorded a reduction in performance at velocity ratios of 0.718 and 0.876, but no noticeable difference was measured as velocity ratio reduced. At the highest tested speed of 56krpm, the tilted housing consistently underperformed compared to the radial design in terms of turbine efficiency. However, it is at this operating speed that the MFP's of the two designs deviated with the MFP of the tilted volute increasing. Therefore, the changes in MFP mean that aerodynamic similarity is not strictly maintained. Hence, comparing the turbine efficiencies can be misleading. However, these changing trends were not observed through the numerical modelling presented in chapter 6.

Although the computational work predicted that the tilted housing improvement would vary with rotational speed, and higher speed would result in smaller improvements, it was not predicted that the tilted housing would result in an efficiency drop, nor such a substantial MFP increase. It was therefore necessary to evaluate the performance of the full experimental flow domain in CFD to find the cause of the discrepancies between experimental and simulation results.

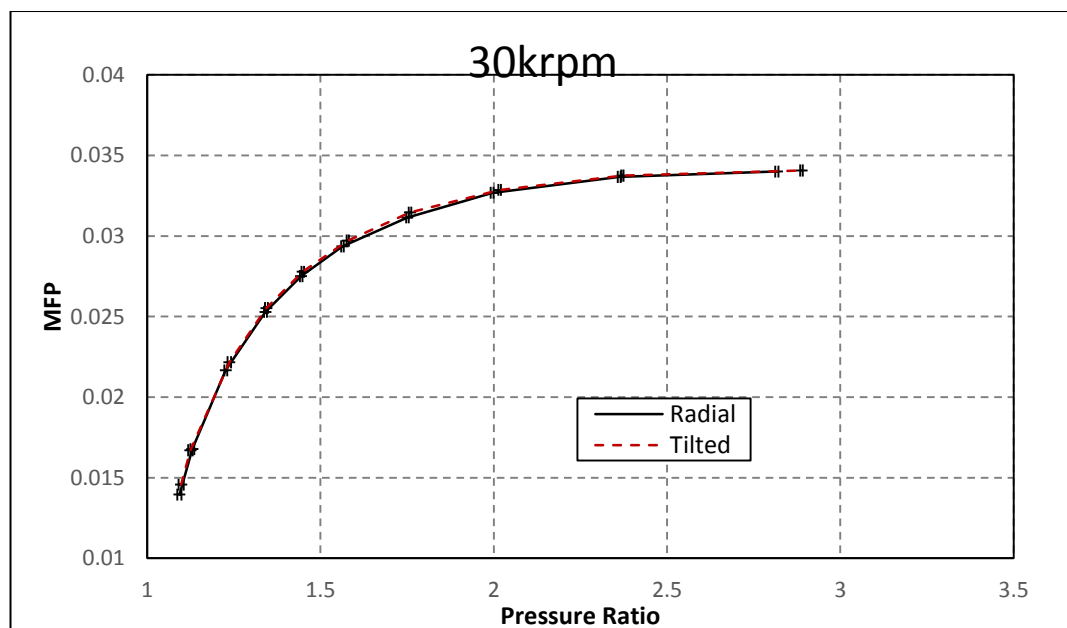


Figure 10.9: MFP comparison of radial and tilted volute designs at 30krpm

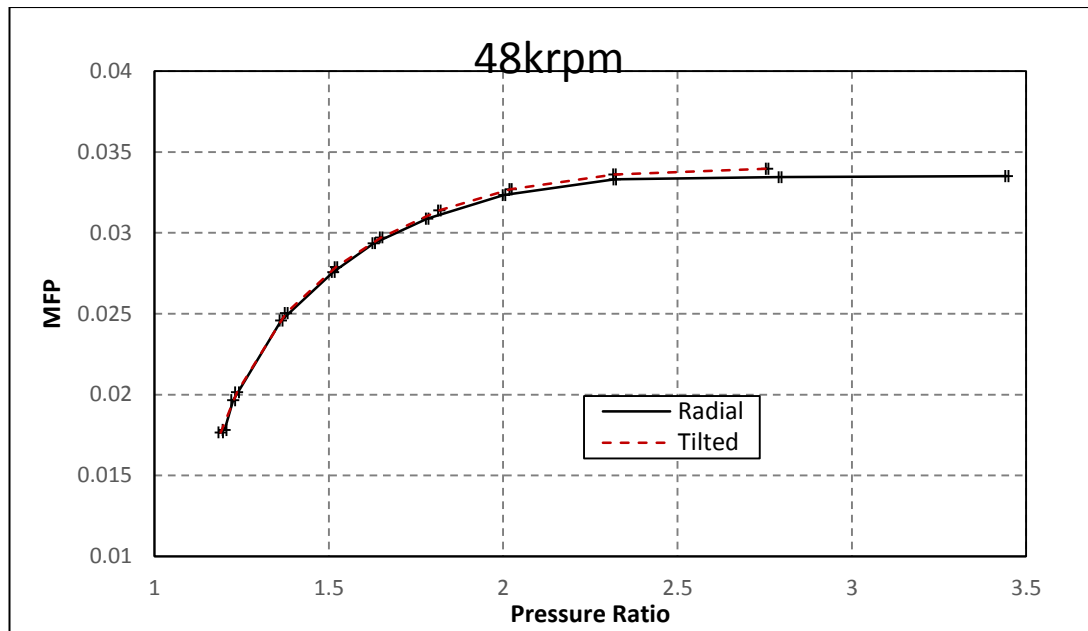


Figure 10.10: MFP comparison of radial and tilted volute designs at 48krpm

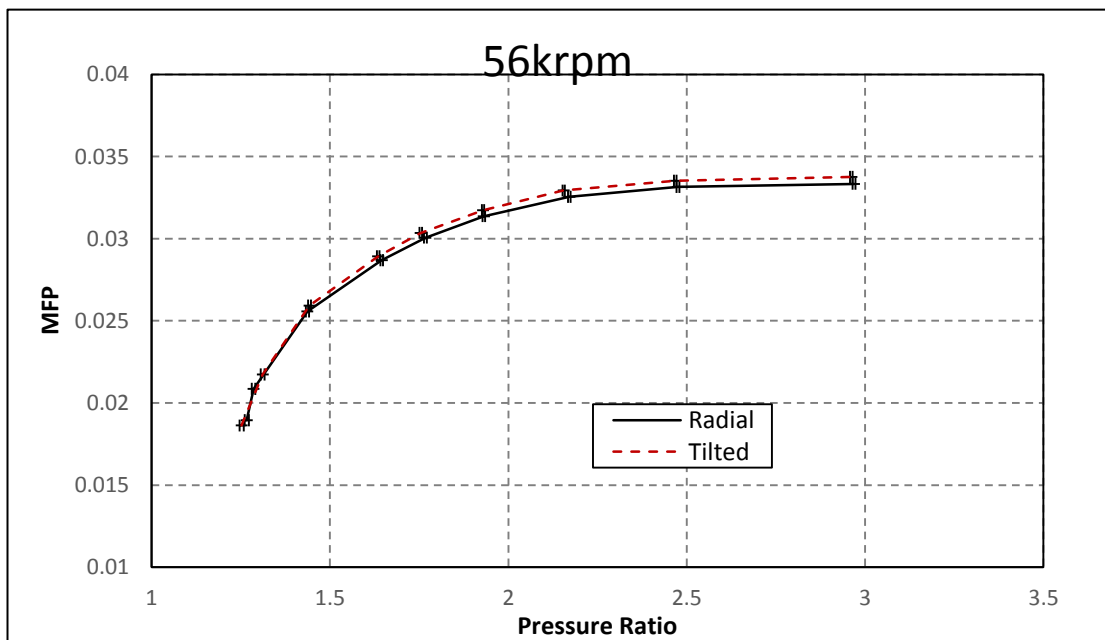


Figure 10.11: MFP comparison of radial and tilted volute designs at 56krpm

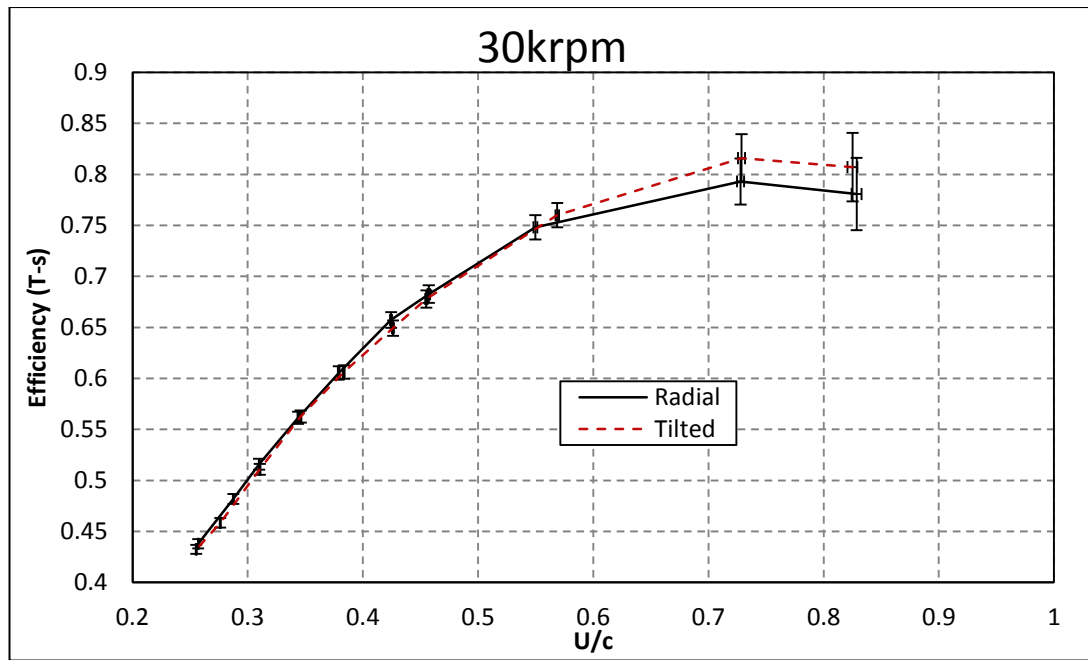


Figure 10.12: Efficiency comparison of radial and tilted volute designs at 30krpm

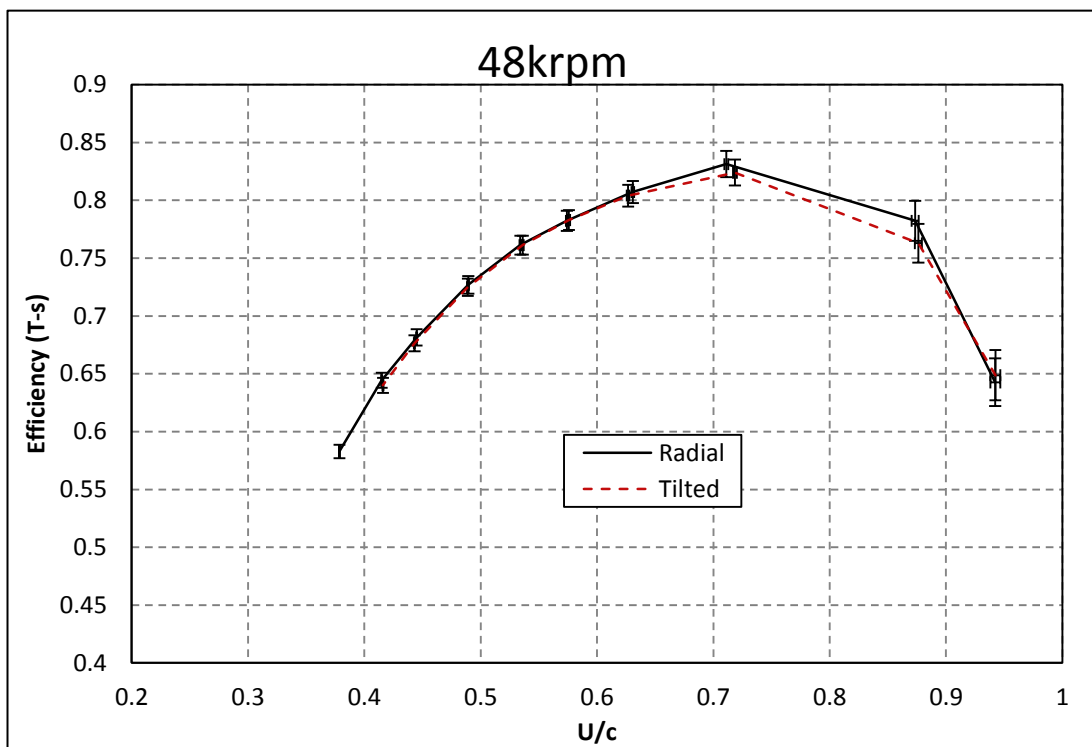


Figure 10.13: Efficiency comparison of radial and tilted volute designs at 48krpm

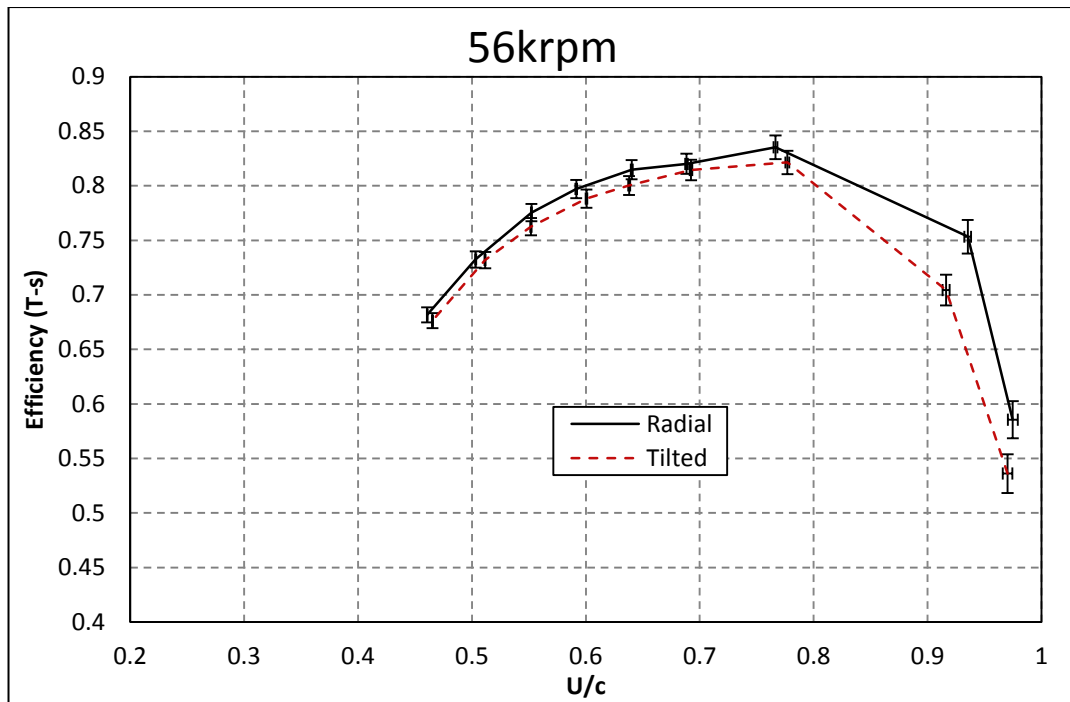


Figure 10.14: Efficiency comparison of radial and tilted volute designs at 56krpm

10.7.1 STEADY STATE COMPUTATIONAL VALIDATION AND ANALYSIS

To provide further validation for the computational approach used throughout this thesis the experimental test points were replicated in CFD. Furthermore, as the performance trends observed experimentally, were not predicted from the initial CFD analysis, further investigation was necessary to understand the root causes of the performance discrepancies.

Figures 10.15-10.17 show the comparison of experimental and computational efficiency results over the tested steady state maps. The computational results compare favorably with the experimental trends over the map range, particularly at lower velocity ratios. At higher velocity ratios the CFD consistently under predicts the experimental performance values. At these operating points the experimental uncertainties are greater due to larger relative errors. Furthermore, the unsteadiness in the stage increased due to reduced pressure ratio and therefore an increase in discrepancy can be expected.

While the overall performance trends are well replicated the tilted housing consistently out performs the radial design in CFD. However, the experimental data only shows an improvement at the lowest tested speed at high velocity ratios. At the

highest rotational speed, the experimental results show consistently better performance of the radial volute.

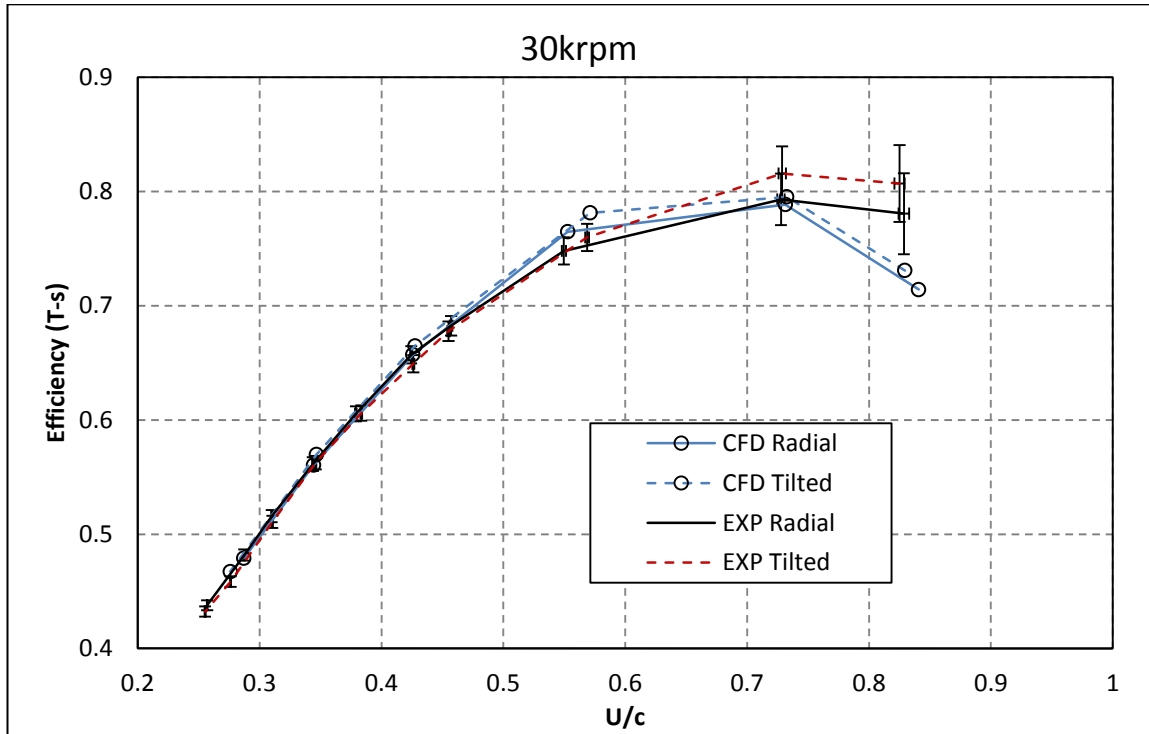


Figure 10.15: 30krpm steady state efficiency comparison experimental vs CFD

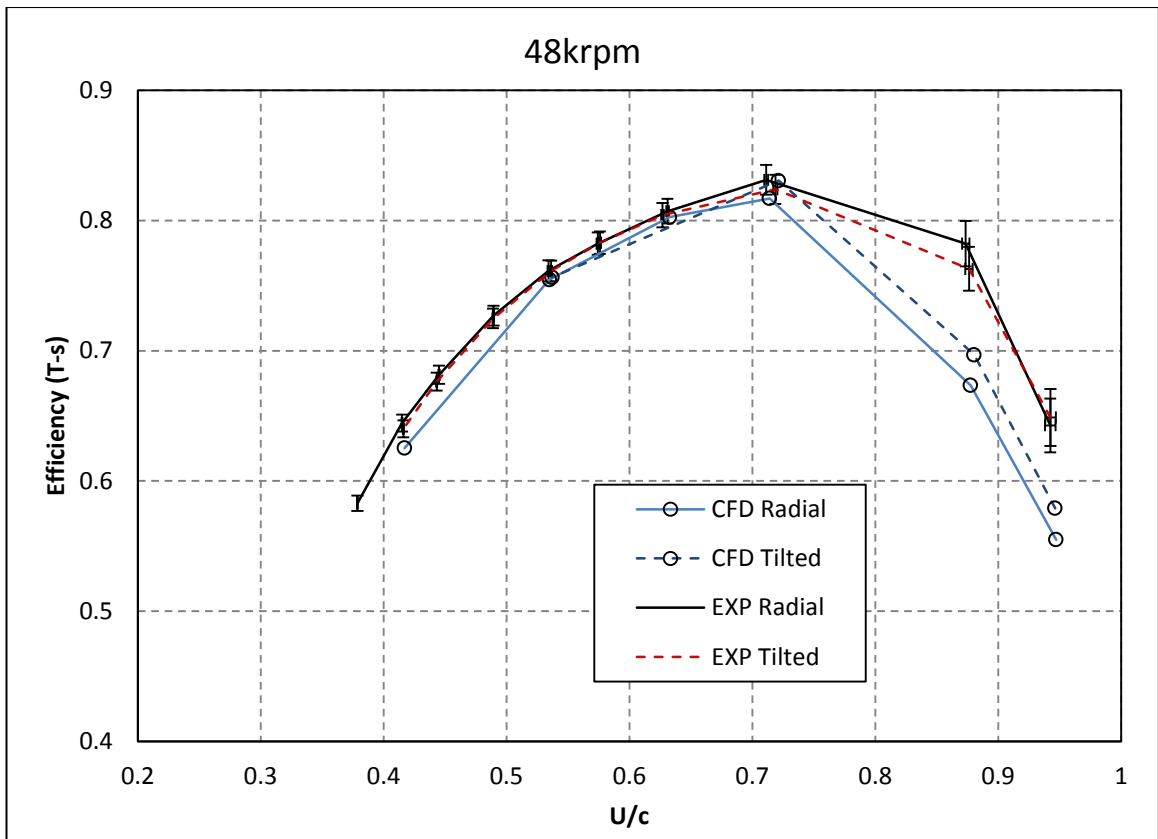


Figure 10.16: 48krpm steady state efficiency comparison experimental vs CFD

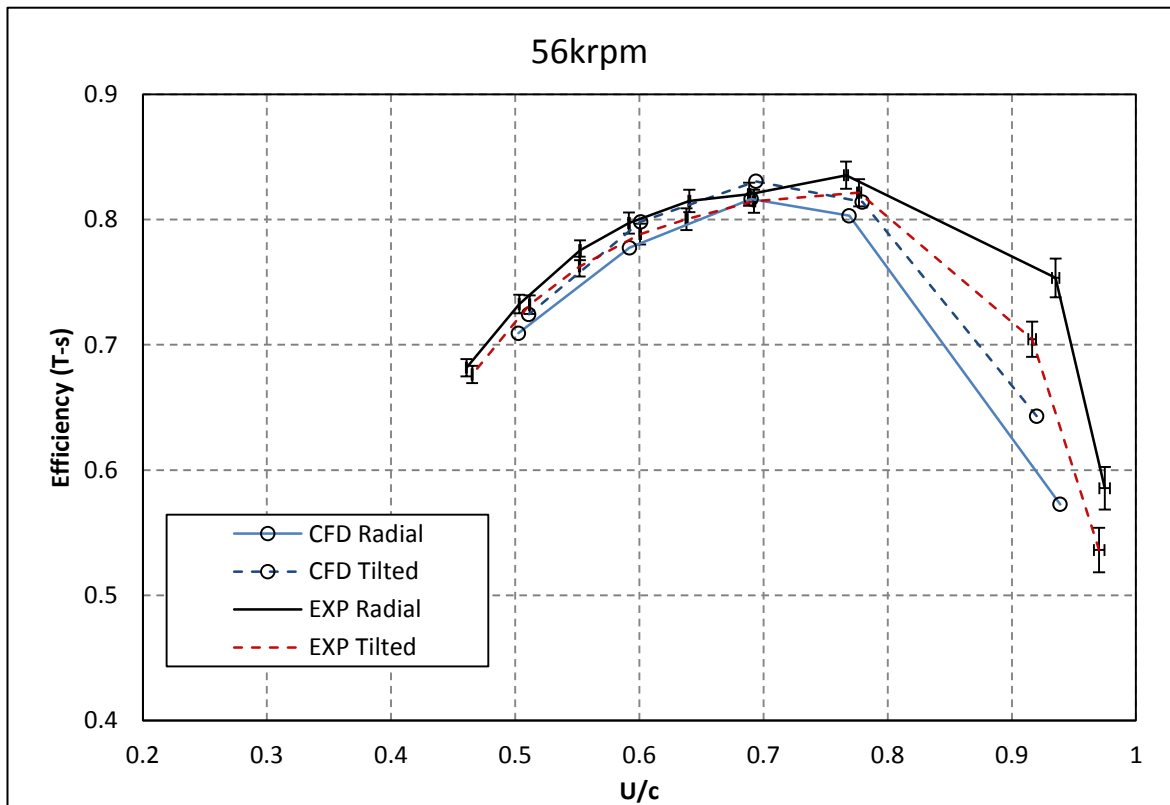


Figure 10.17: 56krpm steady state efficiency comparison experimental vs CFD

Shown in figures 10.18-10.20 are the experimental and computational MFP plots for each of the volute designs. Across all tested turbine speeds the CFD predicts the MFP with good accuracy. The CFD showed an increase in MFP of 0.96% for the tilted volute design in the middle of the map at the highest tested turbine speed. Although this prediction is not as large as that measured experimentally (1.2%), it is greater than previous CFD (chapter 6) showing that under the experimental running conditions the tilted housing produced a greater MFP variation than previously recorded.

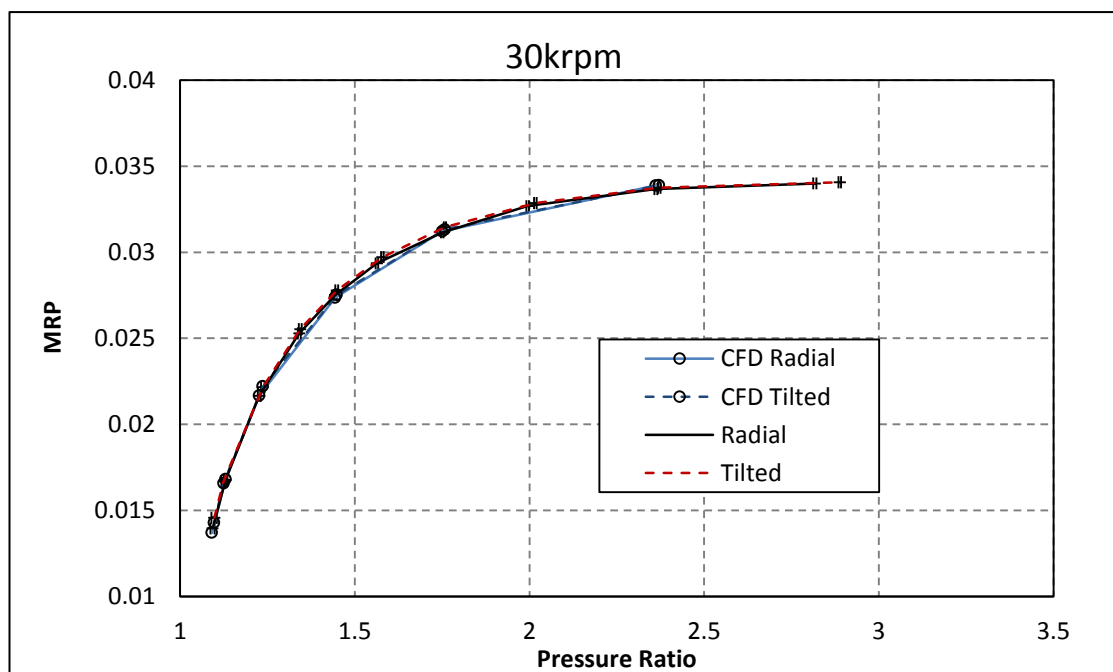


Figure 10.18: 30krpm steady state MFP comparison experimental vs CFD

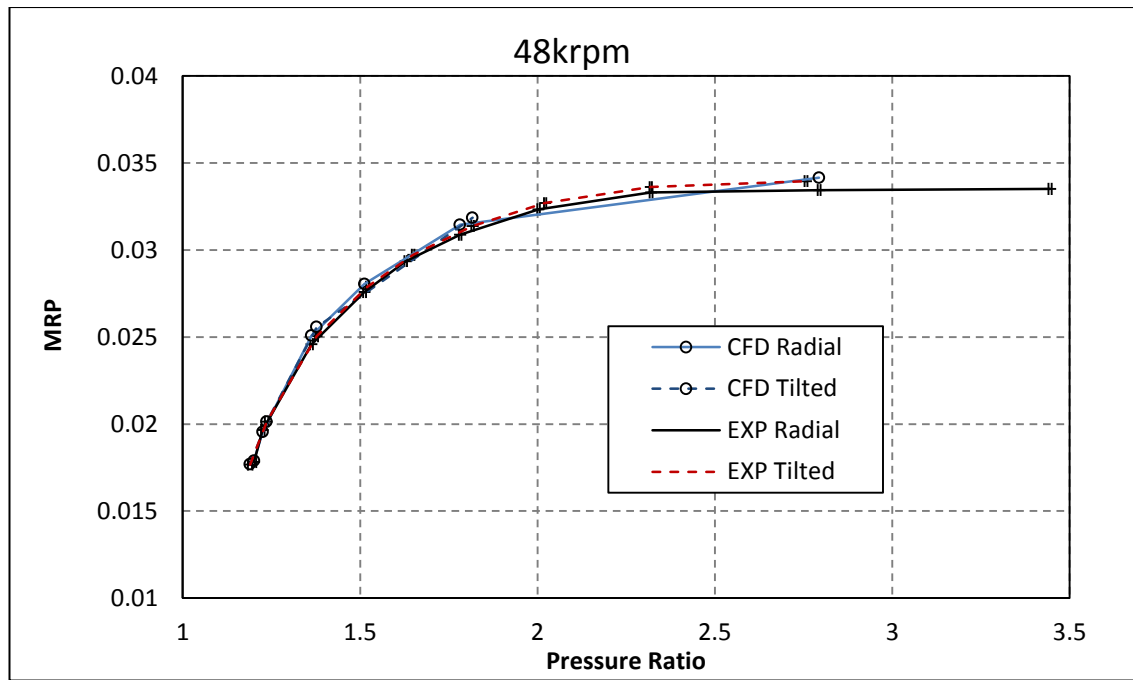


Figure 10.19: 48krpm steady state MFP comparison experimental vs CFD

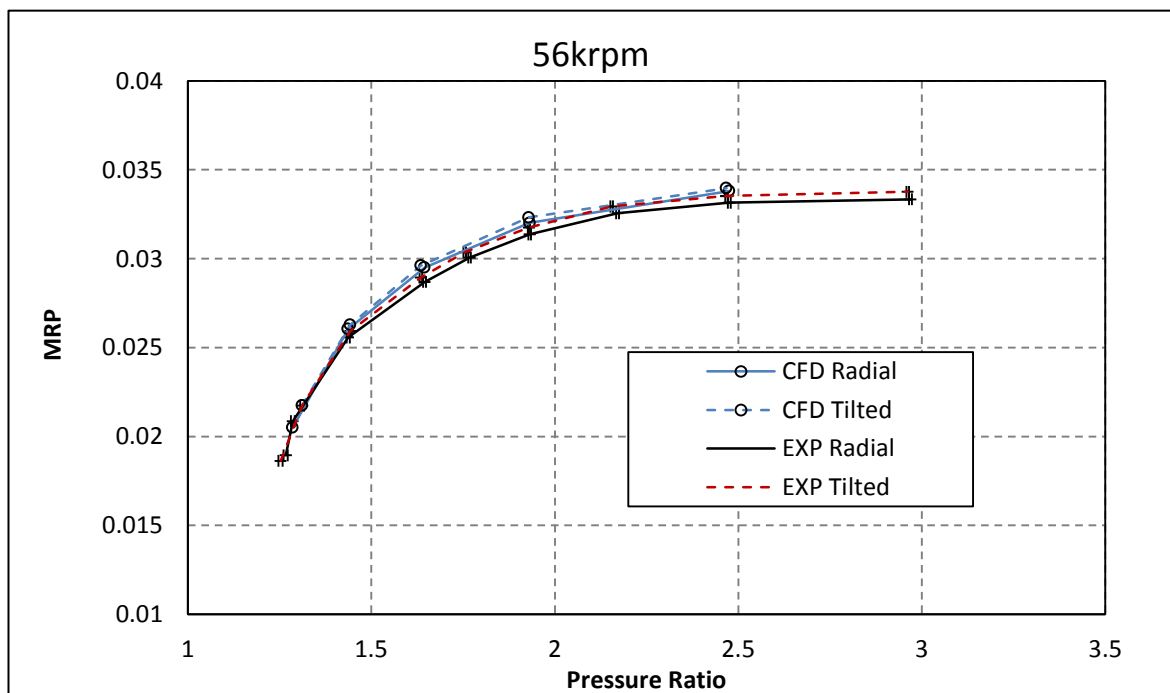


Figure 10.20: 56krpm steady state MFP comparison experimental vs CFD

As shown in figure 10.7 the full experimental domain is more complex than the simplified geometry simulated in CFD. The main difference between the two flow domains is the inclusion of the heat shield and resulting step introduced ahead of the rotor. It is common practice to omit this detail from CFD simulations as it is expected to have only a small impact on performance and is not expected to change between

turbine designs. Its inclusion also adds significant complexity to the meshing process and can be a source of bad quality elements.

To find the cause of the discrepancy between experimental and CFD results, the back step was included in the modeling process and compared with the experimental data. Figure 10.21 shows the experimental and computational results at 56krpm with the step included in the CFD domain. In both designs the inclusion of the step was found to have an adverse effect on the turbine efficiency. The resulting plot shows an increased deviation between computational and experimental results, with the CFD underestimating the turbine efficiency. The added loss incurred due to the inclusion of the step was greater in the tilted design with the tilted volute now showing a reduction in performance relative to its radial counterpart replicating the experimental trends.

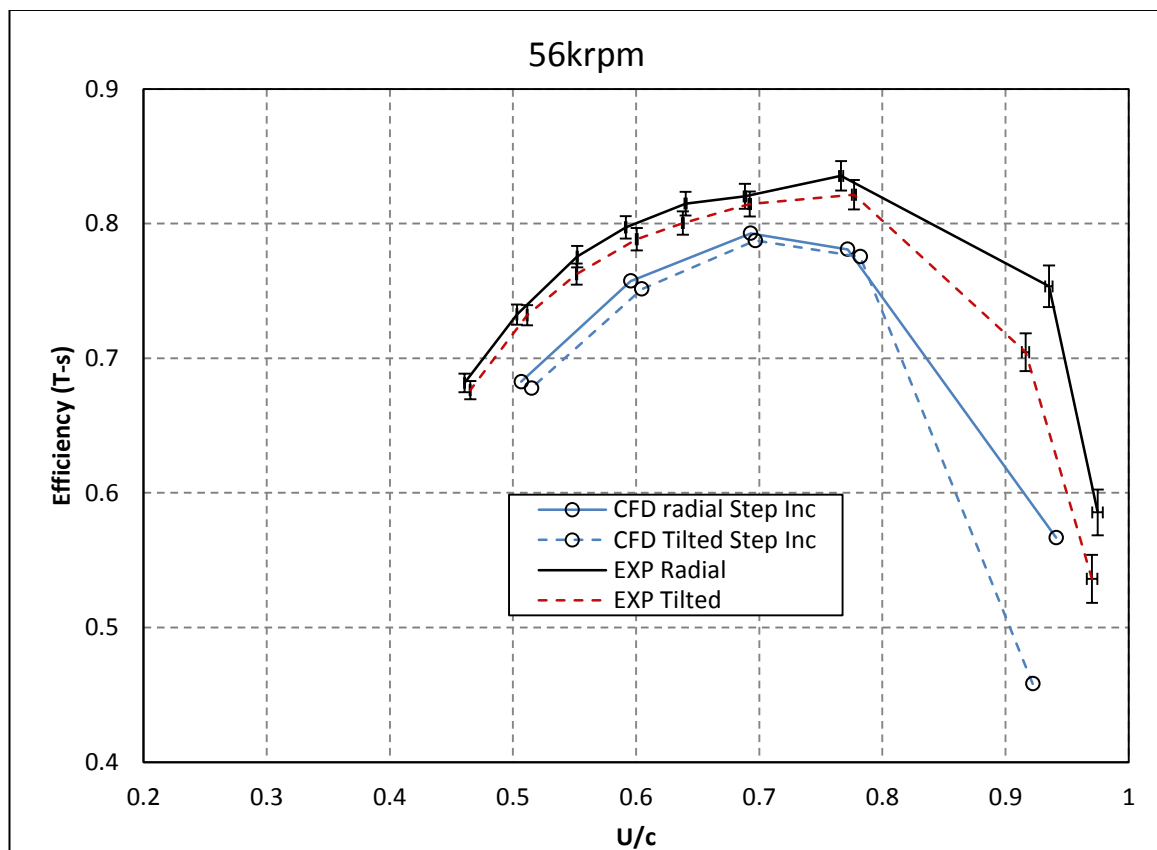


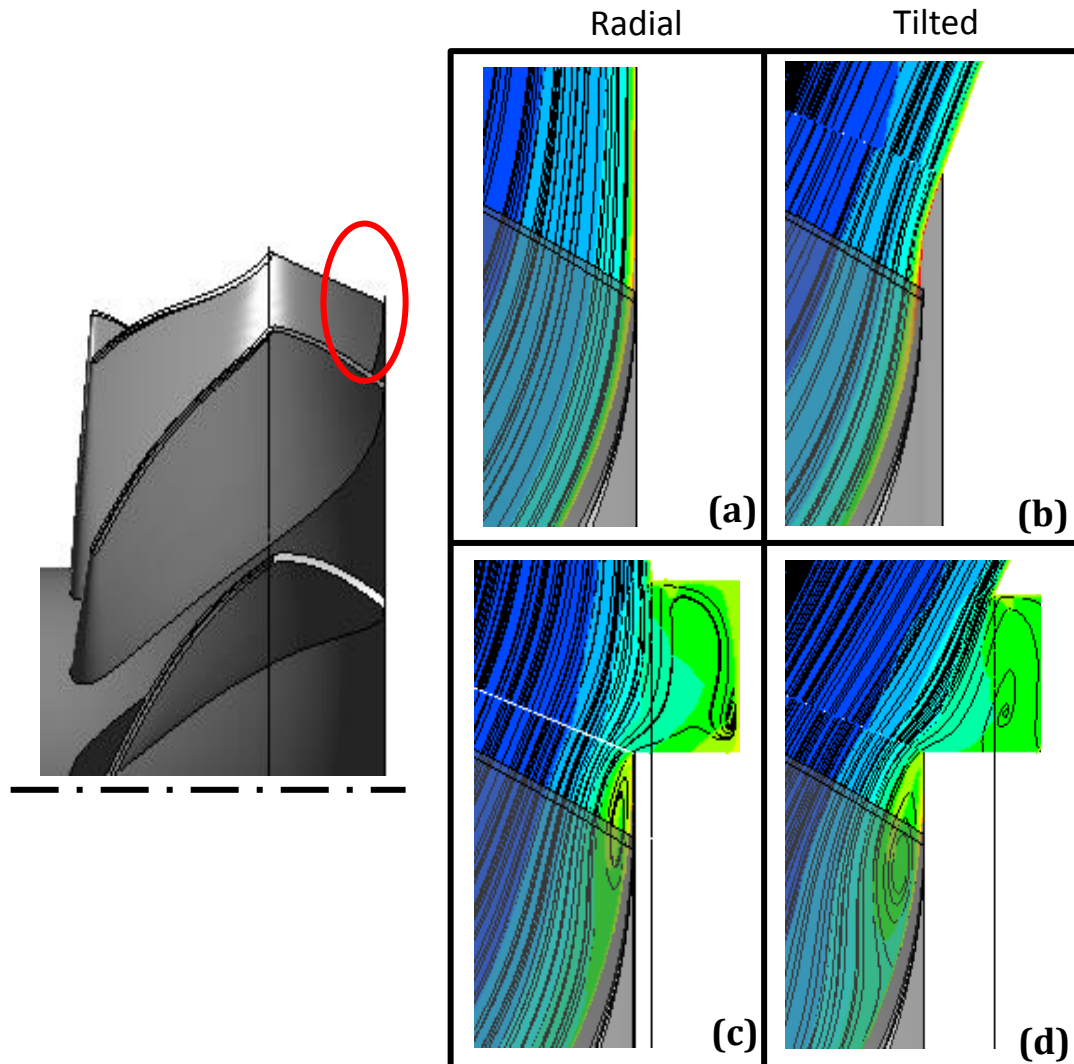
Figure 10.21: Comparison of turbine efficiency at 56krpm between CFD with step included and experimental

As previously discussed in chapter 6, the tilted housing was found to result in a small increase in hub surface loss (figure 6.29). Figure 10.22 compares this region of the rotor in both the radial and tilted volute designs with and without the inclusion of

the step. At the selected running point (56krpm $U/c_{is}=0.7$) no distinct hub surface separation is apparent in either design when the step is omitted, although a small increase in entropy generation can be observed along the titled volute hub surface. The inclusion of the step results in a significant change in flow physics within this region, with both designs showing distinct hub separation. The extent of this separation is notably greater in the tilted design. Hence, the inclusion of the step results in greater loss in the tilted volute design explaining the change in performance trends shown when the step is included in the computational domain.

It can be concluded that not only the application of volute tilt, but also the geometry in the rotor inlet region are vital to turbine performance. As a result, the introduction of any significant volute changes must also address the redesign of the secondary geometry that is necessary. This exercise has shown that while the step is usually omitted from CFD as its effect is expected to small and constant across designs, this is not the case in the current geometry as the step didn't not remain constant across the two variants. The change to the step size and location was the result of needing to relocate the heat shield to make space for the tilt. However, it is anticipated that further development could remove this change and the effect is not inherent of volute tilt performance.

This validation exercise has shown that the computational approach implemented throughout this thesis is capable of accurately predicting the experimental performance trends of both the radial and tilted volute designs.



10.8 UNSTEADY PERFORMANCE ANALYSIS

The unsteady testing was done at three turbine speeds of 30krpm, 48krpm and 56krpm, over a range of three pulse frequencies of 20hz, 40hz, and 60hz and three pulse loads (low, middle and high). The pulse loads tested experimentally were not the same as those simulated in CFD as the experimental load was applied through the specified gap between the stator and magnetic rotor. All of the resulting inlet pressure pulses are shown in appendix B.

10.8.1 UNSTEADY TURBINE MASS FLOW PARAMETER

Figures 10.23 – 10.31 present the unsteady cycle averaged MFP for both designs over the unsteady test range. The steady state curves are included in the plots with the three unsteady pulse loads. Generally, over the tested range of unsteady

conditions the cycle averaged unsteady flow characteristics do not differ substantially between designs although some level of deviation is expected due to the unsteady dynamics of the turbine operation. Importantly no substantial differences in trends arise between the two volute designs suggesting the cycle averaged unsteady operation of the two volutes is similar. However, some local deviation did occur resulting in substantial differences in measured MFP.

At 30krpm, 20Hz, the three tested pulse loads follow the steady state MFP trend closely. Differences between the unsteady operating pressure ratios of the two volute designs are apparent at constant turbine load. At the low and mid load operating point the deviation occurs in MFP as well as a small change in pressure ratios indicating the tilted volute operated at a slightly higher running point for a given load. At the high load operating point, cycle average pressure ratios of 1.54 and 1.59 for the radial and tilted volutes respectively were achieved. A discrepancy in MFP was also observed indicating that the two designs operated at different running points in this instance. Comparing the inlet pulses at 30krpm, 20Hz and high load in appendix B, shows a notable shift of the mean pressure of the inlet pulse supporting this observation. This behavior indicates that at high load, the tilted volute required a larger pressure ratio to match the turbine speed.

At the higher frequencies of 40Hz and 60Hz at 30krpm the MFP trends continue to follow the steady trends despite the increasing unsteadiness. However, two operating points show deviation from the steady trend line, the radial volute at 40Hz, high load and the tilted volute at 60Hz mid load. In both cases small differences in the cycle averaged pressure ratios occur that can also be observed from the pressure pulses in appendix B. The cycle averaged MFP in both cases shows deviation between the two designs and the steady state trend. Despite the discussed local deviations, no clear performance trends are apparent from the MFP plots at 30krpm.

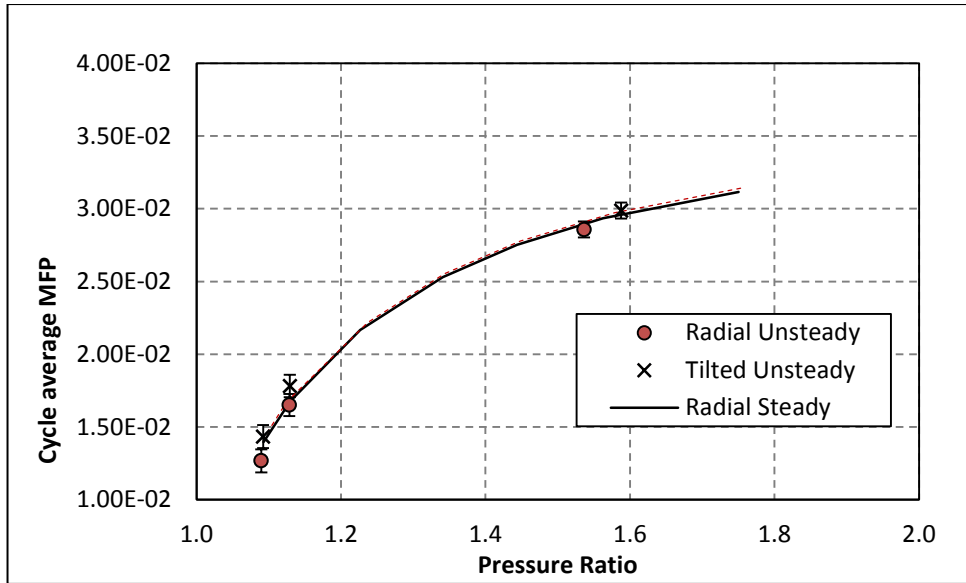


Figure 10.23: Cycle averaged MFP 30krpm 20Hz

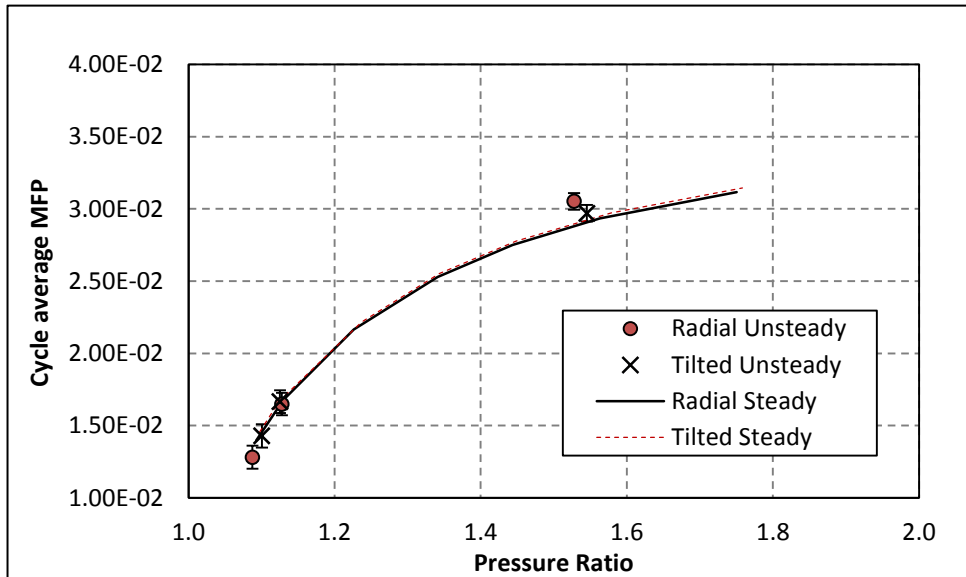


Figure 10.24: Cycle averaged MFP 30krpm 40Hz

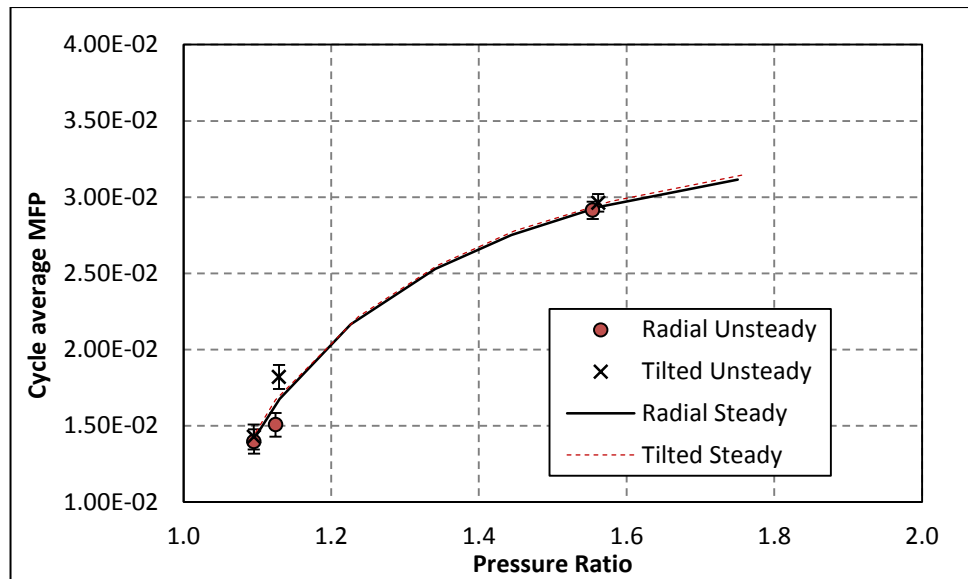


Figure 10.25: Cycle averaged MFP 30krpm 60Hz

At 48krpm, the unsteady data points generally follow the steady state plot but larger levels of local deviation can be observed than at 30krpm. Significant deviation in MFP between the two volute designs was measured at 20Hz high load, and 60Hz mid load. At 20Hz high load only a small difference in the cycle average pressure ratio was observed and from appendix B it can be observed that the pulse forms are closely matched. Despite this a reduction in the cycle averaged MFP is apparent for the tiled volute.

At 60Hz, mid load, the two designs again result in almost equal cycle averaged pressure ratios. However, comparing the pressure pulses in appendix B it can be seen that while the mean pressure ratio is constant the pulse amplitudes differ substantial. A pressure ratio range of 1.26-1.57 exists in the radial case while the tilted design range is only 1.31-1.50. Due to these changes in the inlet pulse, turbine performance at this operating point should not be compared. While changes in the pulse load are expected between the two designs as they are tasked with delivering the turbine work, substantial changes to the pulse form is undesirable as this adds an extra variable to the analysis. As shown in chapter 5, these factors can significantly effect turbine performance.

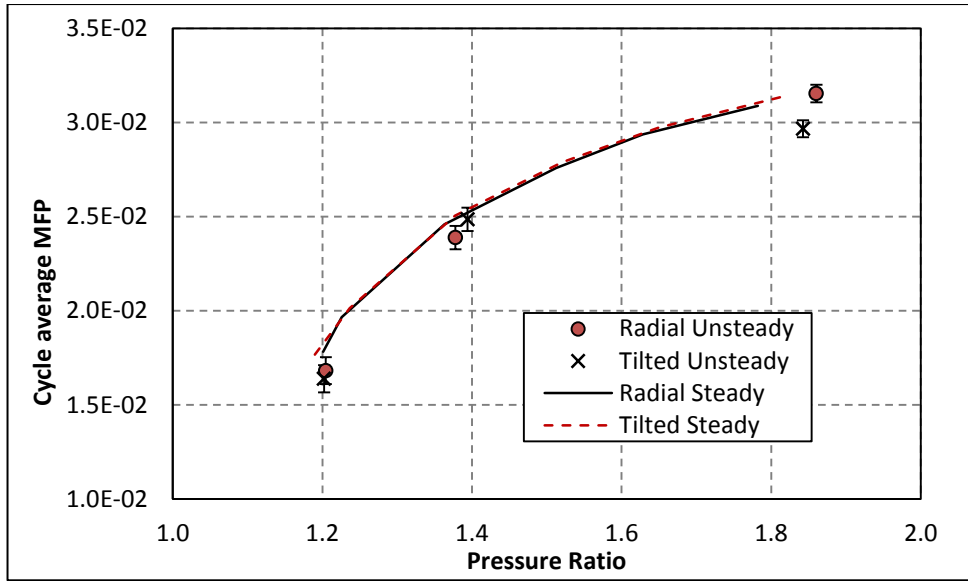


Figure 10.26: Cycle averaged MFP 48krpm 20Hz

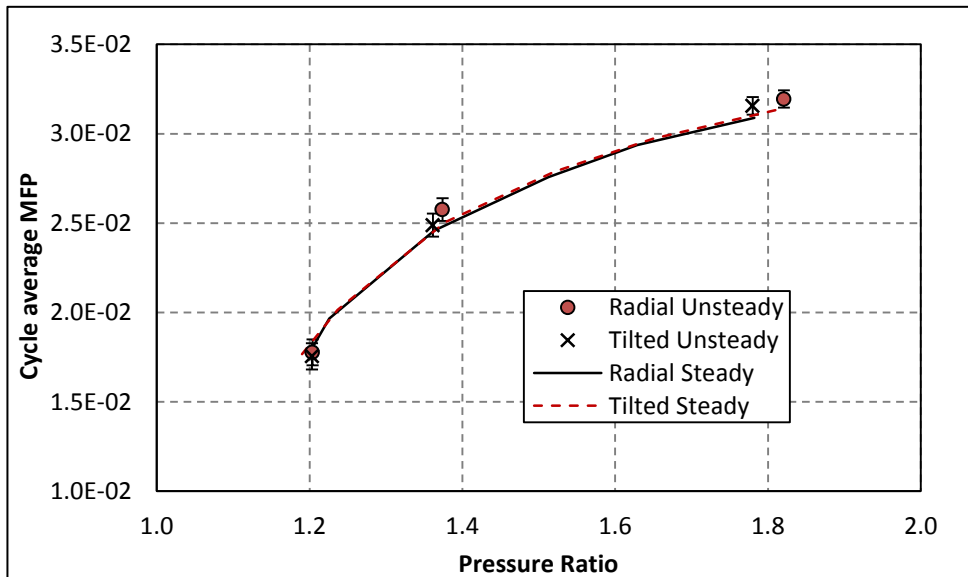


Figure 10.27: Cycle averaged MFP 48krpm 40Hz

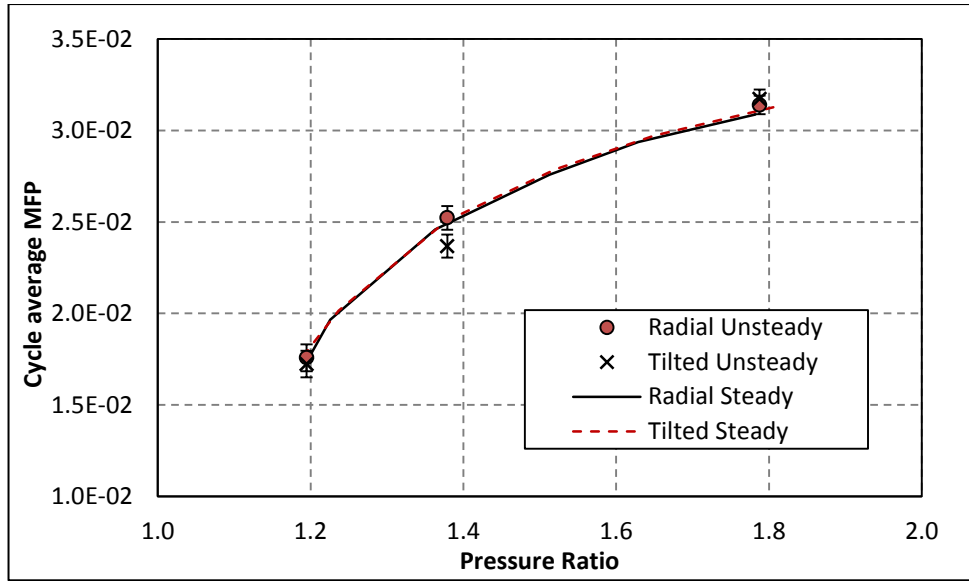


Figure 10.28: Cycle averaged MFP 48krpm 60Hz

At 56krpm the unsteady points again follow the steady state characteristics closely. Only at 60Hz high load does the performance show substantial deviation. At this point the radial volute shows a much greater cycle averaged MFP than the tilted variant. Comparing the inlet pressure plots in appendix B shows a small deviation in pulse load but no substantial change to the form that explains the sizable difference in MFP. As this operating point does not correlate with any other performance trends measured, the result at this point must be treated with scepticism.

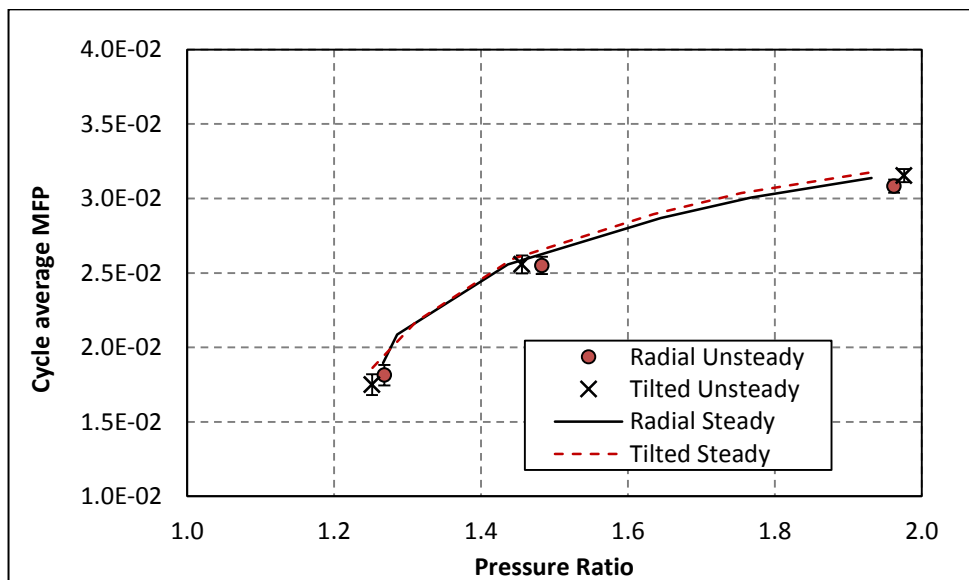


Figure 10.29: Cycle averaged MFP 56krpm 20Hz

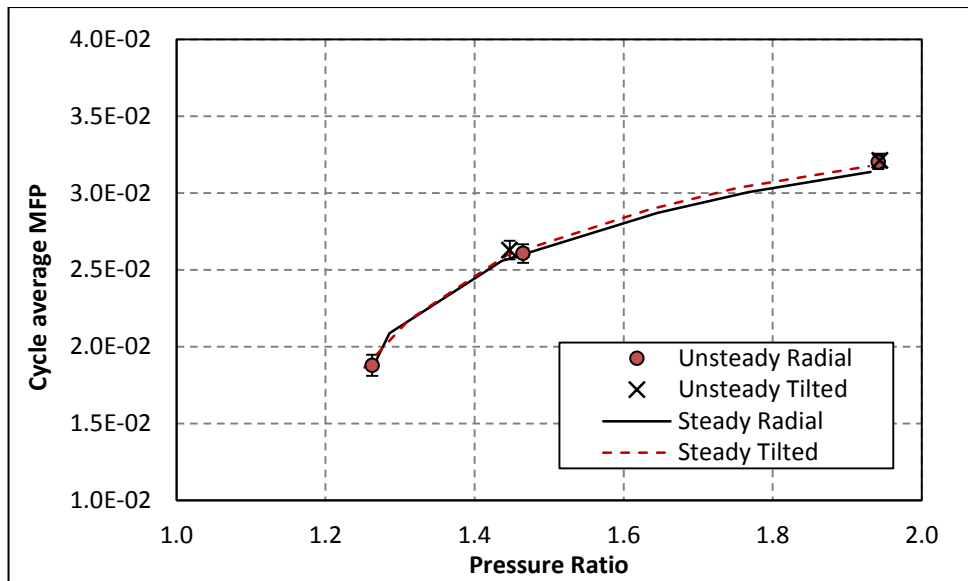


Figure 10.30: Cycle averaged MFP 56krpm 40Hz

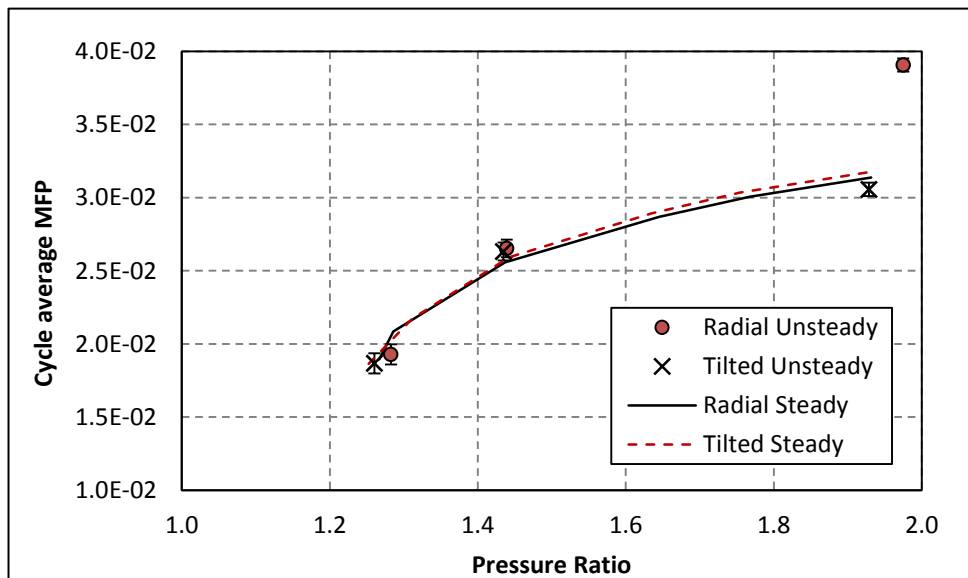


Figure 10.31: Cycle averaged MFP 56krpm 60Hz

10.8.2 UNSTEADY TURBINE EFFICIENCY ANALYSIS

As the turbine load is controlled by the specified gap between the stator and magnetic rotor, the load acting on the turbine is kept constant between the two volute tests. Therefore, by keeping turbine speed constant, turbine work will also be constant and provides a base to compare turbine performance. For this reason, Padzillah, (2014) used turbine work as the X axis variable to compare turbine efficiency results of a re-designed nozzle guide vane. The same method is used in figures 10.32–10.40 to compare turbine efficiency. Changes in efficiency are due to

the required work input to achieve the turbine speed. Slight differences in the actual work occur between the two tests as the turbine speed cannot be kept exactly constant from test to test.

Across the entire range of tested turbine speeds and pulse forms the unsteady efficiencies show a notable reduction compared to the steady state performance. This effect is caused by the inclusion of off design operating points within the unsteady operating envelope resulting in a reduction in cycle averaged performance.

At 30krpm the efficiency plots of the two volute designs show little difference at the lowest tested frequency of 20Hz (figure 10.32). As the frequency increases some local differences in measured efficiency become apparent but no distinct trends are expressed. At 60Hz mid load a significant difference between the performances of the two volutes can be observed. Referring to the MFP plot in figure 10.18, a notable discrepancy in MFP that did not follow the performance trends was found. It is clear from the efficiency plot that in the tilted volute case, the efficiency deviates substantially from the general turbine trend. Therefore, this operating point is not necessarily representative of the true performance.

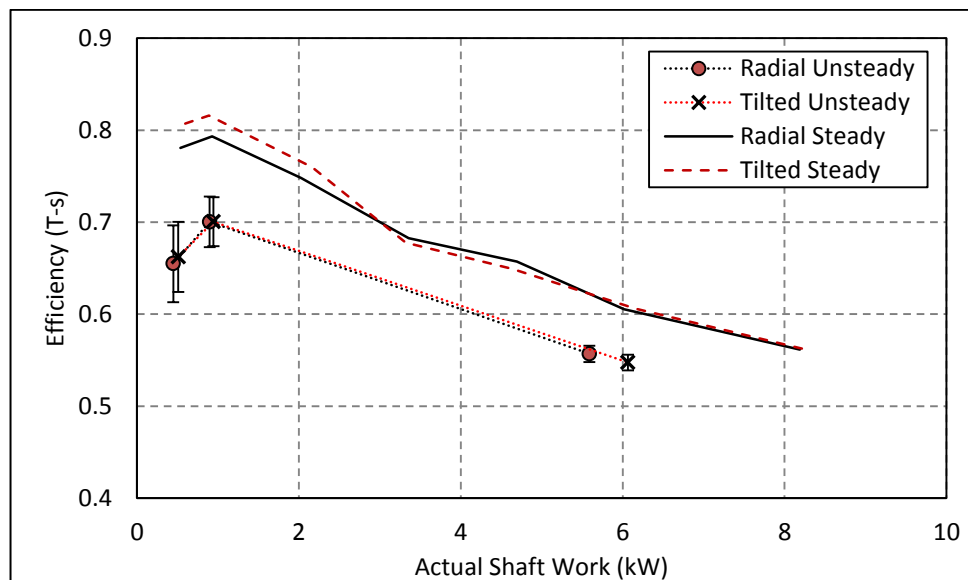


Figure 10.32: Cycle averaged Efficiency 30krpm 20Hz

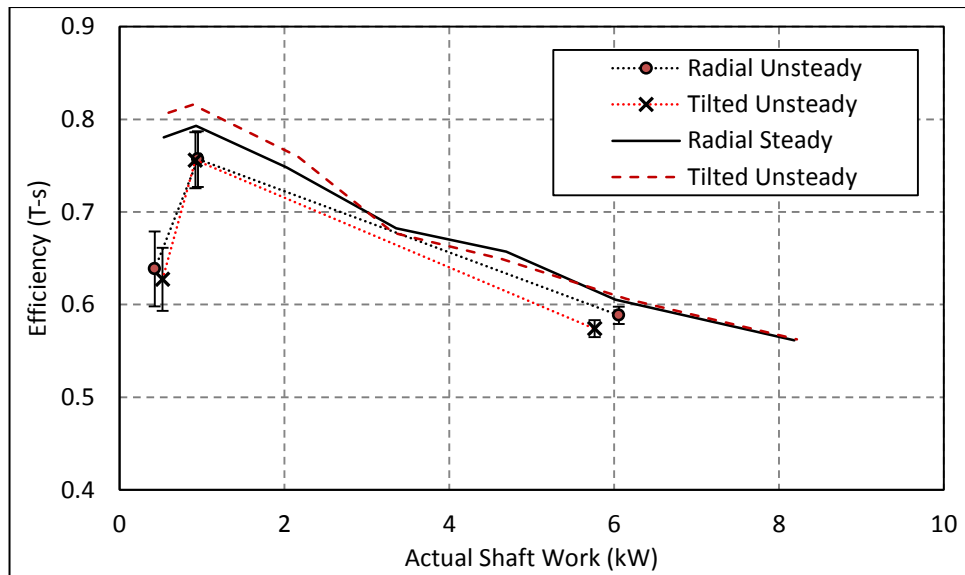


Figure 10.33: Cycle averaged Efficiency 30krpm 40Hz

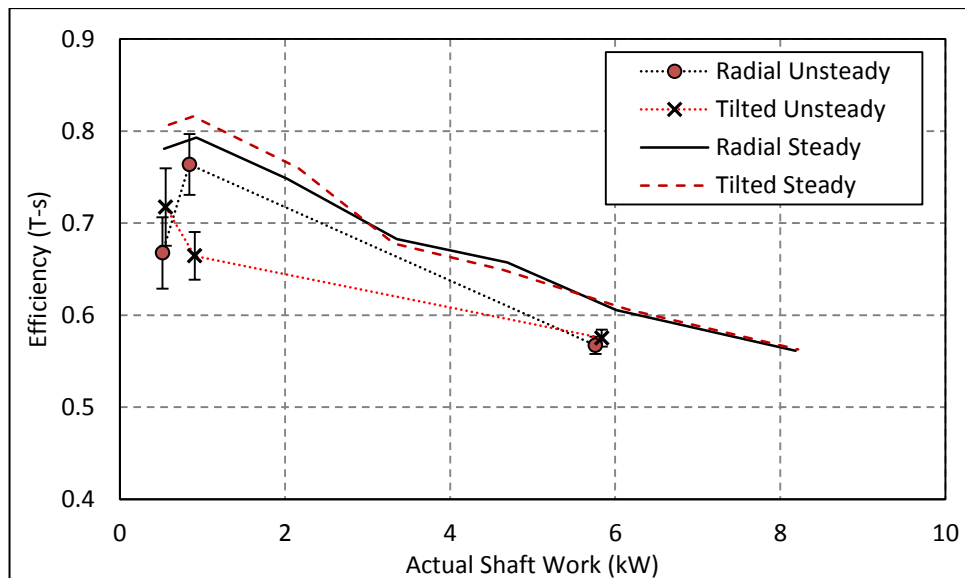


Figure 10.34: Cycle averaged Efficiency 30krpm 60Hz

At 48krpm, notable differences in the efficiency trends begin to arise. At 20Hz, while local difference in efficiency occur no distinct difference in trend over the pulse loads was observed. However, with increasing pulse frequency, the efficiency of the tilted volute increased relative to the radial base case, particularly at the low and mid pulse loads. At the highest tested frequency of 60Hz, this trend resulted in the tilted volute operating more efficiently over the entire range of tested loads, although the difference at high load is less than the uncertainty expressed by the error bars. At the low load operating point, a peak efficiency increase of 18% was measured. However, a small difference in the actual work output of the two designs at this point was also measured. Due to the significant efficiency drop off in this region, expressed by the

steady state characteristics, the difference in efficiency could be significantly impacted by this slight change of running point and is therefore not necessarily purely a result of the design change. Hence it is important to compare the experimental trends lines rather than absolute values. At the 60Hz mid load operating point, while the output shaft work was constant between the two designs it should be noted that a discrepancy in the MFP was observed in figure 10.28. As this was due to a change in pressure pulse amplitude between the cases, the resulting efficiency values cannot be taken to be representative of the volute tilt.

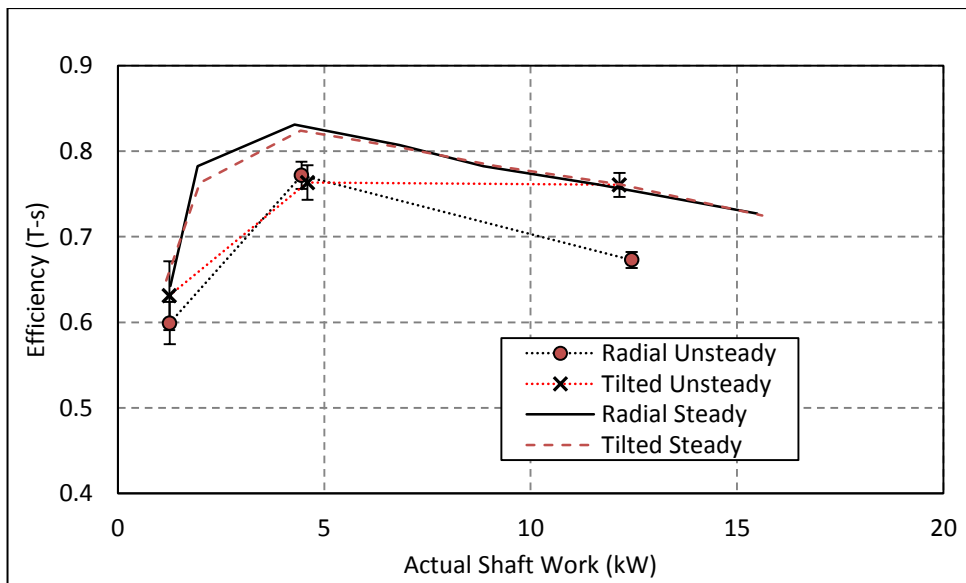


Figure 10.35: Cycle averaged Efficiency 48krpm 20Hz

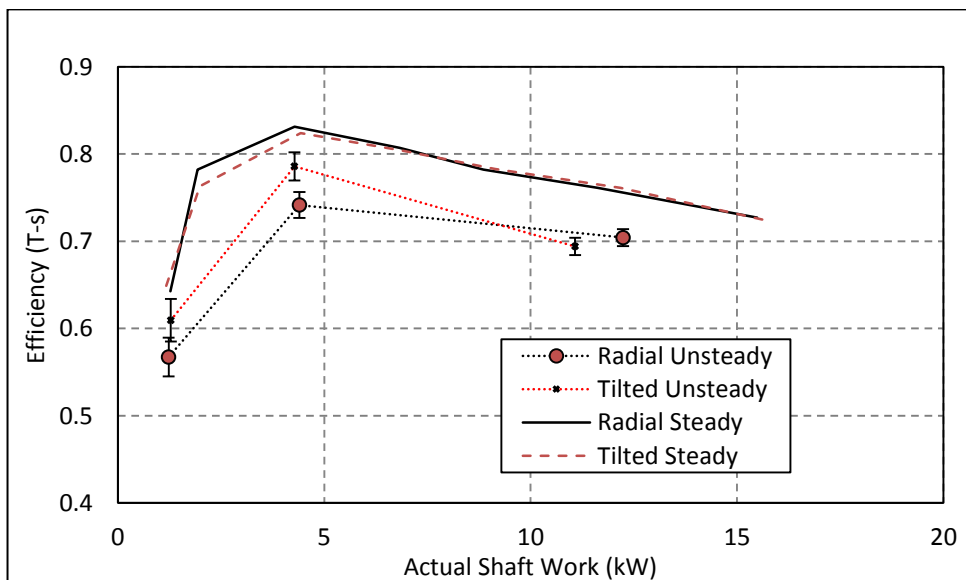


Figure 10.36: Cycle averaged Efficiency 48krpm 40Hz

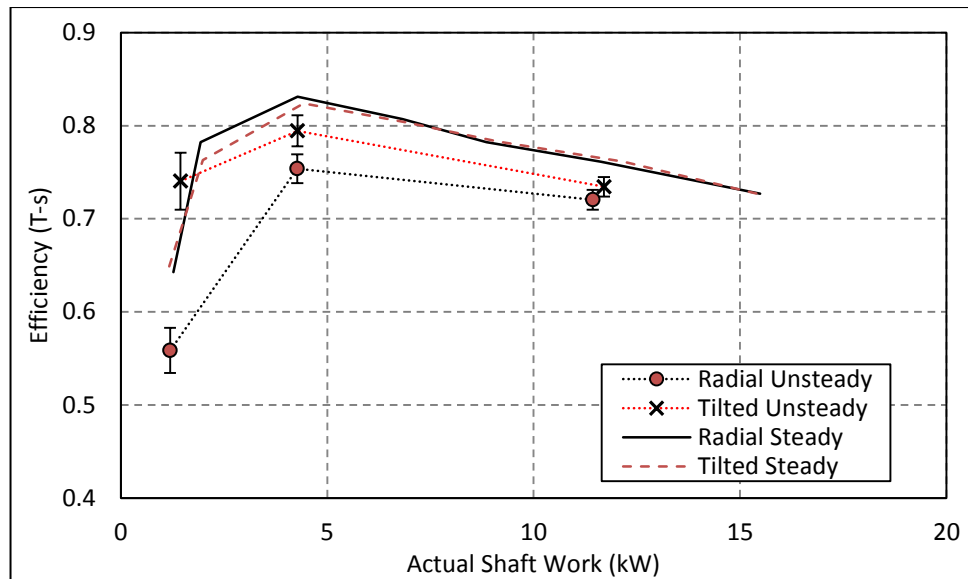


Figure 10.37; Cycle averaged Efficiency 48krpm 60Hz

At 56krpm, increasing pulse frequency also resulted in the development of notable differences in performance trends between the two designs. At this speed the tilted design showed improvements in efficiency at the mid and high load operating points. This shift in performance benefit with changing turbine speed, is due to a shift in optimal load performance, as increasing turbine speed increases velocity ratio. As such the velocity ratios experienced under each pulse increase, shifting the low loads towards increasingly large, off design, velocity ratios while the high loads move towards the more optimal range. At 40Hz, improvements of 2.5% and 2.0% were found in the tilted volute case at the mid and high load operating points. In both these cases the output shaft work was approximately equal, and as this region of the curve has a relatively flat efficiency trend, the small discrepancies are not expected to impact the efficiency greatly. However, it should be noted that these differences in efficacy are small relative to the uncertainty expressed by the error bars.

At 60Hz, low load, the tilted volute efficiency was 13% lower than that achieved by the radial design. However, a notable discrepancy in shaft work can be observed, and due the high sensitivity of efficiency to turbine work in this region, directly comparing the absolute efficiency values can be misleading. The mid load operating point shows a performance improvement of 6%. However, a small difference in shaft work again exists, with the radial design operating at a lower value. Again, the impact of this small deviation in shaft work at this point on the map could have a substantial impact on the measured efficiency. At the highest load, at 60Hz an efficiency

improvement of 19% was measured. However, referring to figure 10.31 shows that this operating point expresses significant MFP deviations that do not fit the turbine performance trends leading to questions about the reliability of this point.

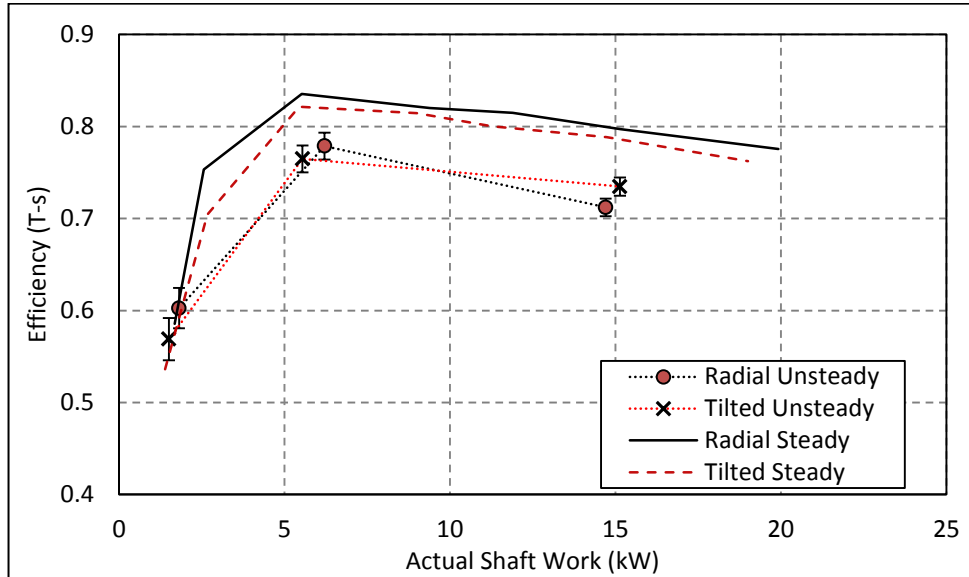


Figure 10.38: Cycle averaged Efficiency 56krpm 20Hz

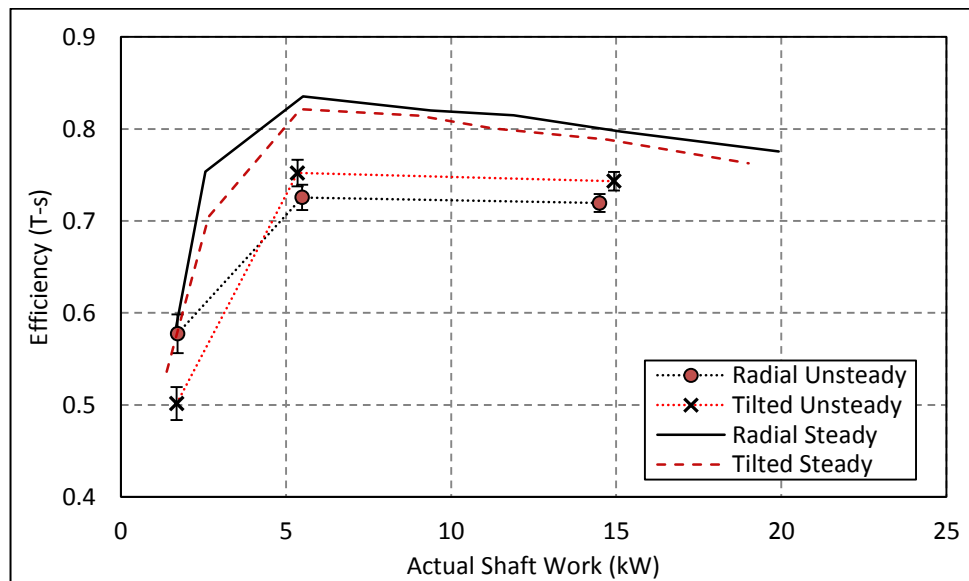


Figure 10.39: Cycle averaged Efficiency 56krpm 40Hz

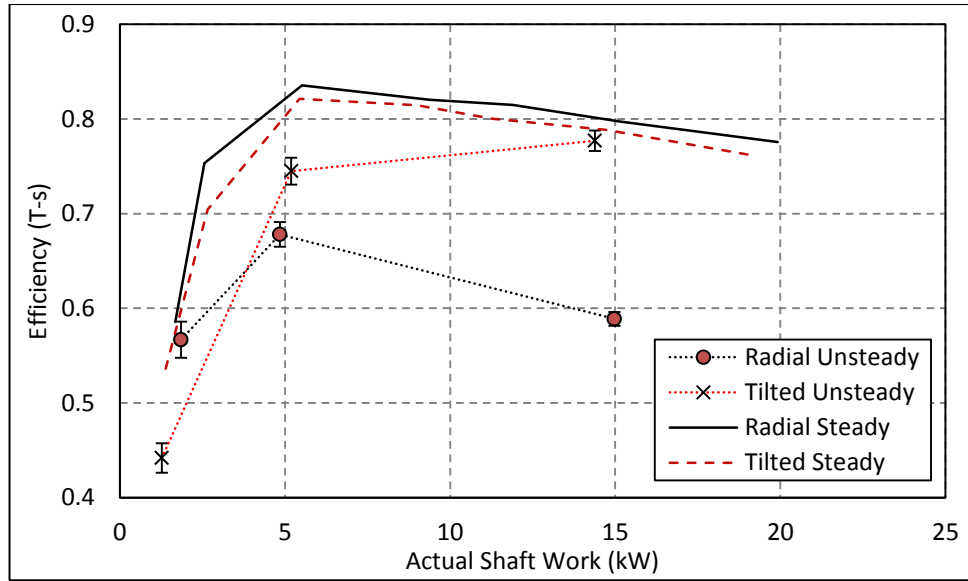


Figure 10.40: Cycle averaged Efficiency 56krpm 60Hz

10.8.3 LAMBDA PARAMETER

To assess the cycle averaged unsteadiness in the experimental tests, the lambda parameter (Λ) can be calculated that was introduced by Copeland et al., (2012). The definition of which is –

$$\Lambda = St \times \Pi \quad (101)$$

Where St is the Strhoul number and is defined as –

$$St = \frac{f_{ref} L_{ref}}{U_{ref}} \quad (102)$$

Where f_{ref} is frequency, L_{ref} is the domain length, and U_{ref} is the sum of the sonic and bulk velocities. And Π is defined as -

$$\Pi = \frac{2 \Delta P_{in}}{\lambda P_{ref}} \quad (103)$$

If the lambda parameter is equal to unity this indicates that rate of mass variation is equal to average mass moving in and out of the system. The parameter therefore provides a measure of the level of mass imbalance in stage.

Figures 10.41-10.43 compare the lambda parameter values for both designs over the tested unsteady range. It can be observed that the lambda parameter increases with both pulse load and frequency as the unsteadiness of the system increases. Over the tested range it can be noted that no substantial difference between the mass imbalance of the two volutes occurs and no obvious trends are apparent. However, some local discrepancies were observed due to the changes in pulse form from test to test. The most significant of which occurred at 48krpm, 60Hz mid load and 56krpm, 60hz high load where the cycle averaged performance of the two designs varied significantly.

These observations show that the stage unsteadiness measured in the two volute designs is very similar, despite the MFP hysteresis loops show local variations. This supports the observation of similar cycle averaged MFP performance between the designs. It should also be noted that the lambda parameter does not exceed 0.3 in any cases. This indicates that at no point did the unsteady mass variation exceed 30% of the average mass moving through the system.

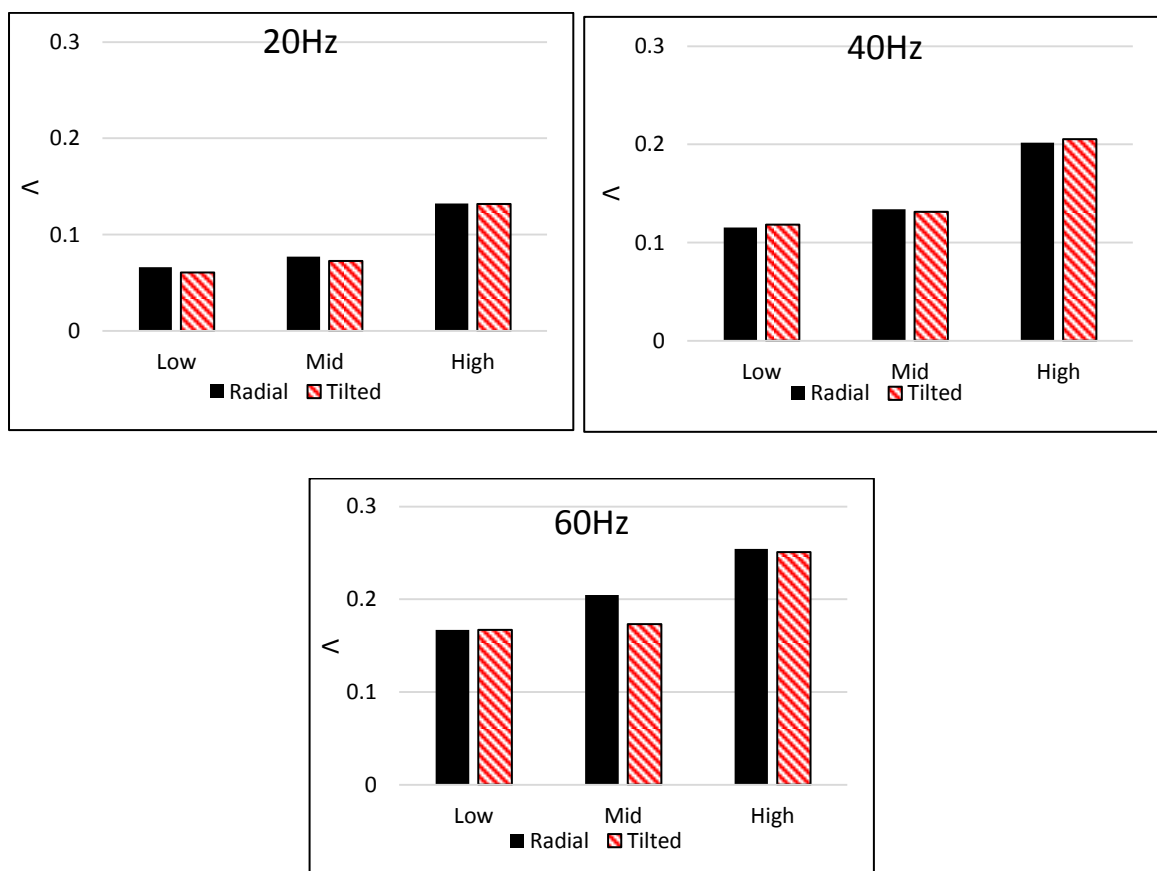


Figure 10.41: 30krpm Lambda parameter Radial vs Tilted volute design

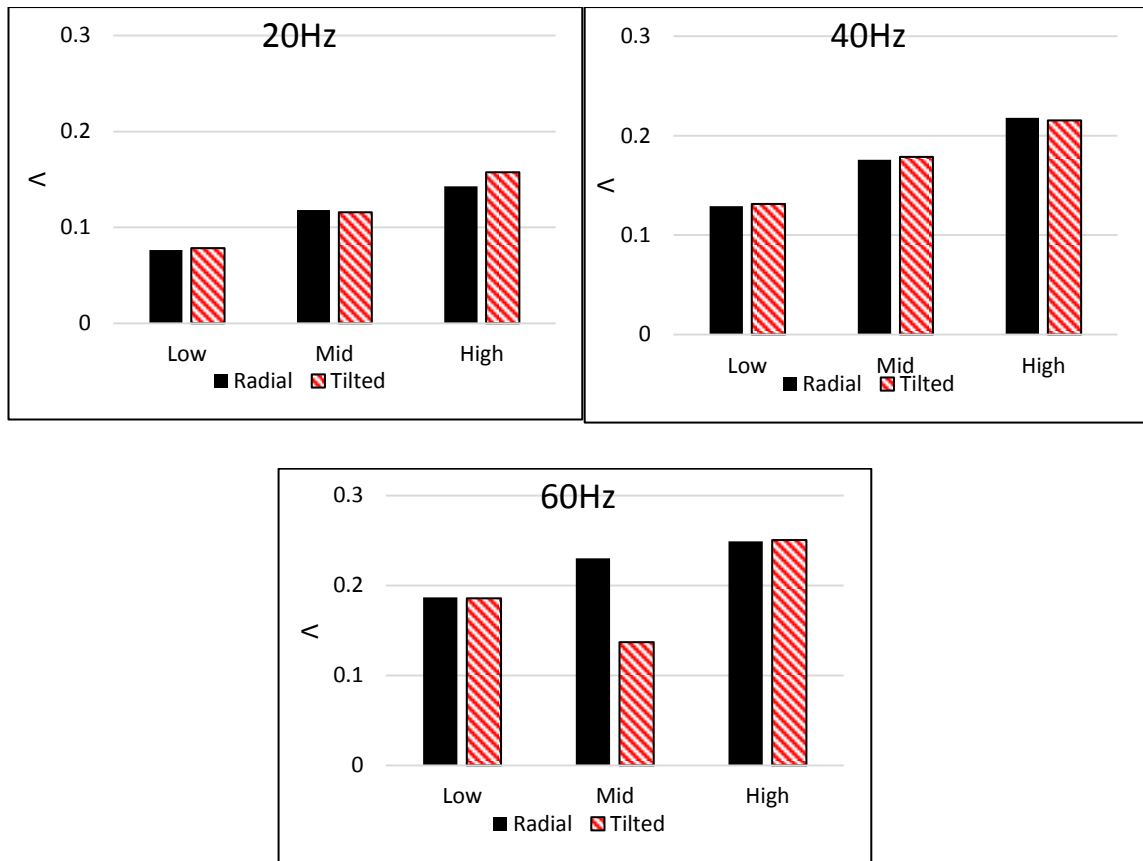
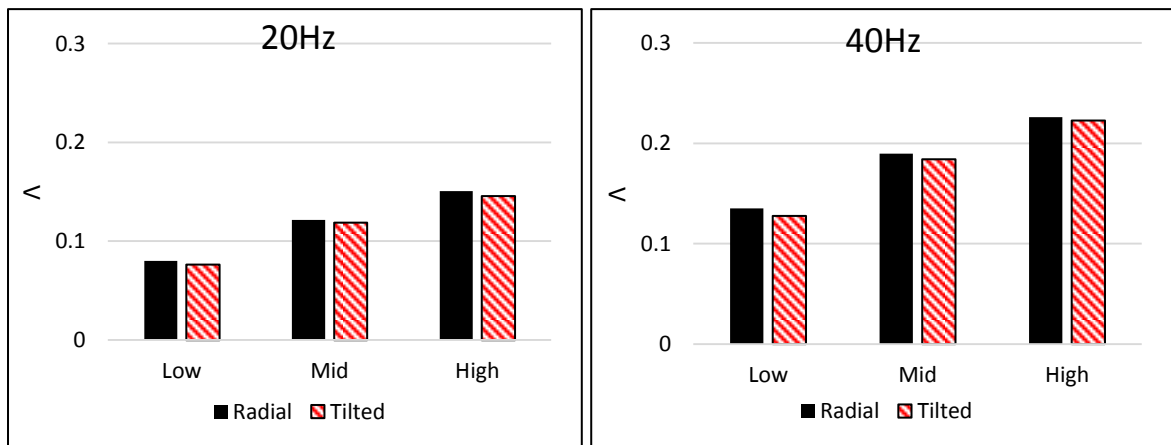


Figure 10.42: 48krpm Lambda parameter Radial vs Tilted volute design



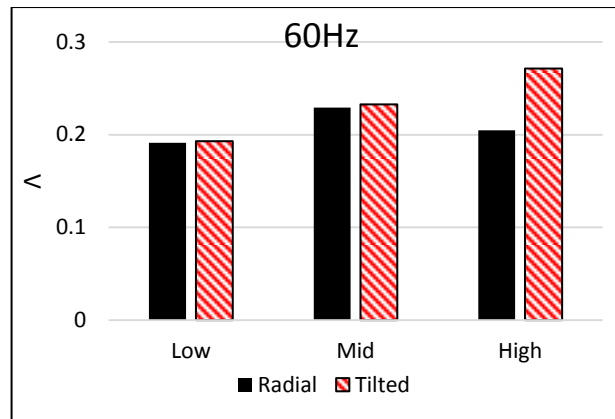


Figure 10.43: 56krpm Lambda parameter Radial vs Tilted volute design

10.8.4 PULSATING VALIDATION

To further validate the computational method used throughout this thesis, the pulsating experimental results were replicated in CFD and compared. Three pulse conditions were selected for validation: 20hz, 40hz and 60hz all at mid load and 48krpm. These pulse conditions were selected as it was deemed necessary to establish the accuracy of the computational approach over a range of frequencies.

Figures 10.44 and 10.45 compare the turbine isentropic work delivered to the turbine under unsteady operation in the radial and tilted designs respectively. In the radial volute the CFD traces follow the experimental values closely, albeit with the peak values consistently over predicted. It can be observed that at 20Hz pulse frequency, a low level of fluctuation was present in the experimental case that was not replicated computationally. This effect can be explained by the complex unsteady interactions occurring experimentally that are not replicated in the simplified computational domain.

In the tilted volute case, the experimental isentropic pulse at 20Hz frequency shows a greater level of secondary fluctuations particularly during the emptying phase. Again, this secondary unsteady effect is not captured by the CFD but the primary pulse shape is well replicated. A notable discrepancy arose at 60Hz frequency in the tilted volute. As discussed previously, the experimental measurements made at this point are not reliable. Therefore, this point was removed from further analysis.

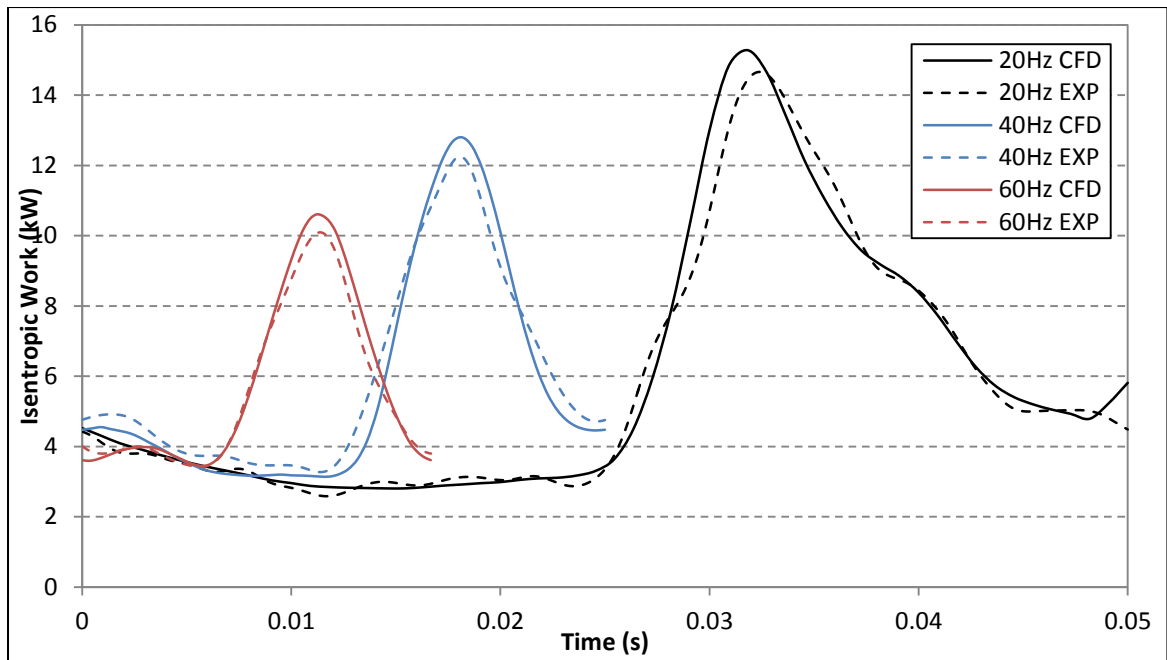


Figure 10.44: Unsteady isentropic work CFD vs experimental for the radial volute design

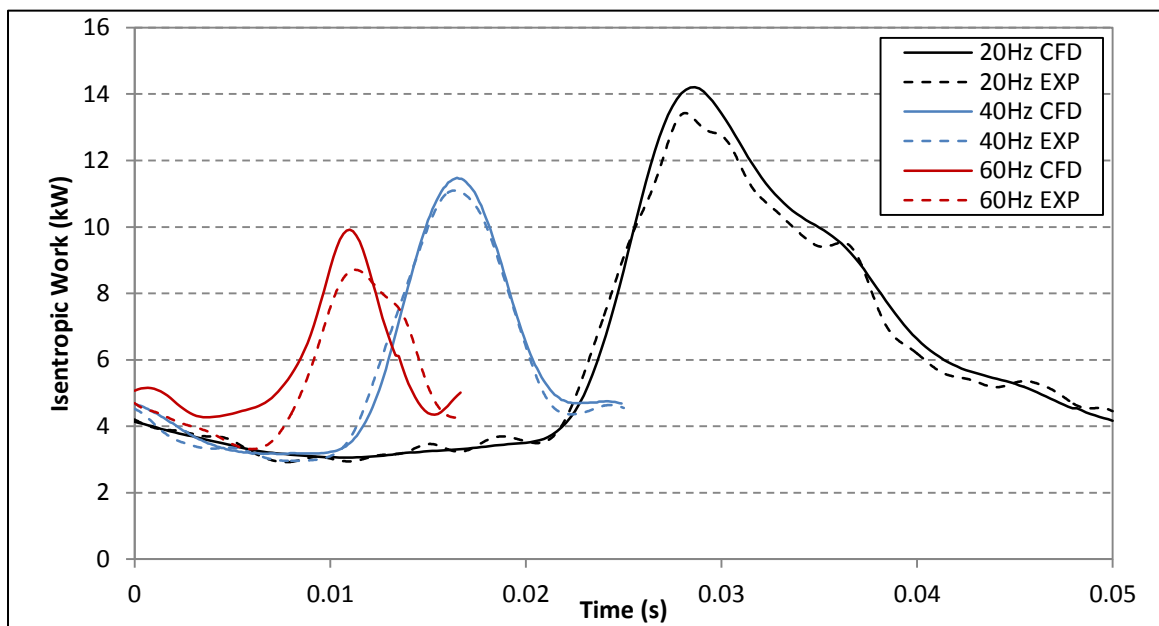


Figure 10.45: Unsteady isentropic work CFD vs experimental for the tilted volute design

The experimental and computational cycle averaged rotor torque, for both the radial and tilted volute designs are presented in figure 10.46 (a) and (b) respectively. Comparisons of rotor torque were deemed to be most appropriate, as the experimental uncertainties were smaller and not influenced by multiple variables.

The radial volute comparisons, show that CFD consistently under predicts the rotor torque across the range. In all cases the CFD values remains inside the

experimental uncertainties and the consistent difference means that the CFD captures the trend with changing frequency. In the tilted case, at 40Hz the CFD values shows the same under prediction expressed across all the radial tests. However, at 20Hz, the CFD and experimental values match closely. The change in this trend at the 20Hz, can in part be explained by the increased unsteadiness expressed in the experimental isentropic work pulse that was not achieved computationally. As a result, the computational torque shows an increase at this point relative to the other computational predictions. While this impacts the CFD results relative to the experimental values, it should be noted that this is secondary effect that is not the focus of the computational studies. The tilted 60Hz point, is omitted from the plot due to the reliability of the experimental values.

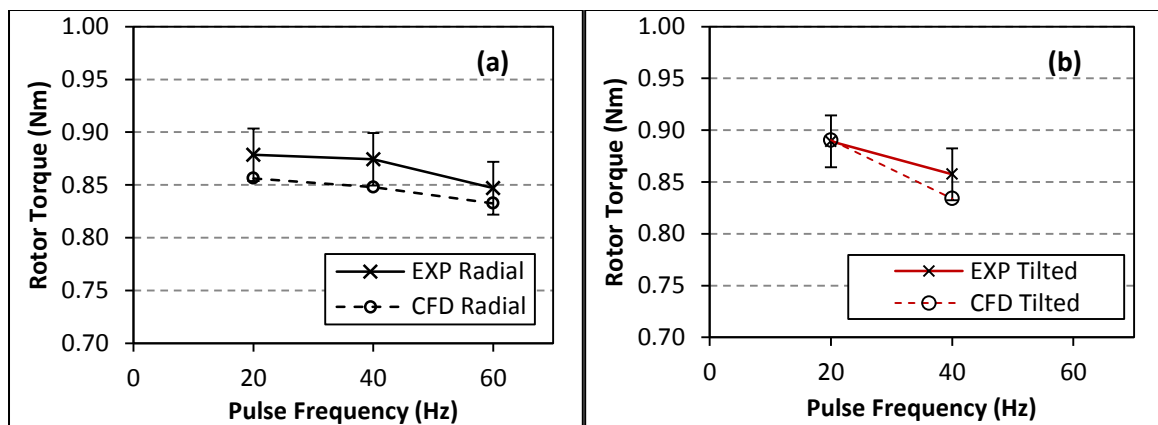


Figure 10.46: Comparison of rotor torque between experimental and CFD at 20Hz, 40Hz and 60Hz. (a) radial volute, (b) tilted volute.

In addition to the experimental validation, the frozen rotor method was compared against the fully sliding mesh approach under pulsating conditions to prove its capability. The same validation was presented in chapter 3 of this thesis for steady state inlet conditions. In this instance the comparison was done under pulsating inlet conditions in the radial housing at 48krpm, mid load at 40Hz frequency. Figure 10.47 presents the rotor torque generated by both methods. As can be seen the two methods show close alignment of the torque measurements with no significant deviation.

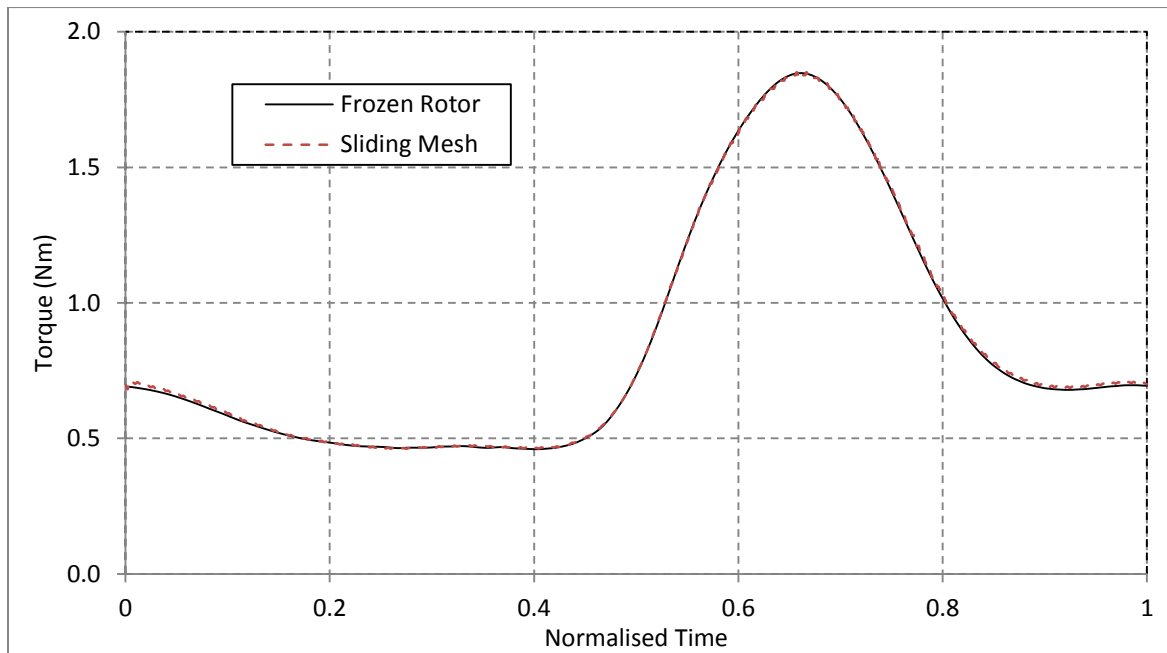


Figure 10.47: Generated rotor torque using frozen rotor and sliding mesh methods 40Hz

Figures 10.48 and 10.49 present the volute absolute flow angles around the rotor circumference at the pulse minimum and maximum mass flows. Static entropy contours and flow vectors are also included at 180° from the tongue at 10% chord. The flow angles show close agreement particularly at low mass flow. At high mass flow the flow angle distribution are still well matched but a small shift in the trend is apparent with the frozen rotor approach over predicting the angle by a maximum 2.5° . In both cases the rotor flow field shows close agreement with only small local variations.

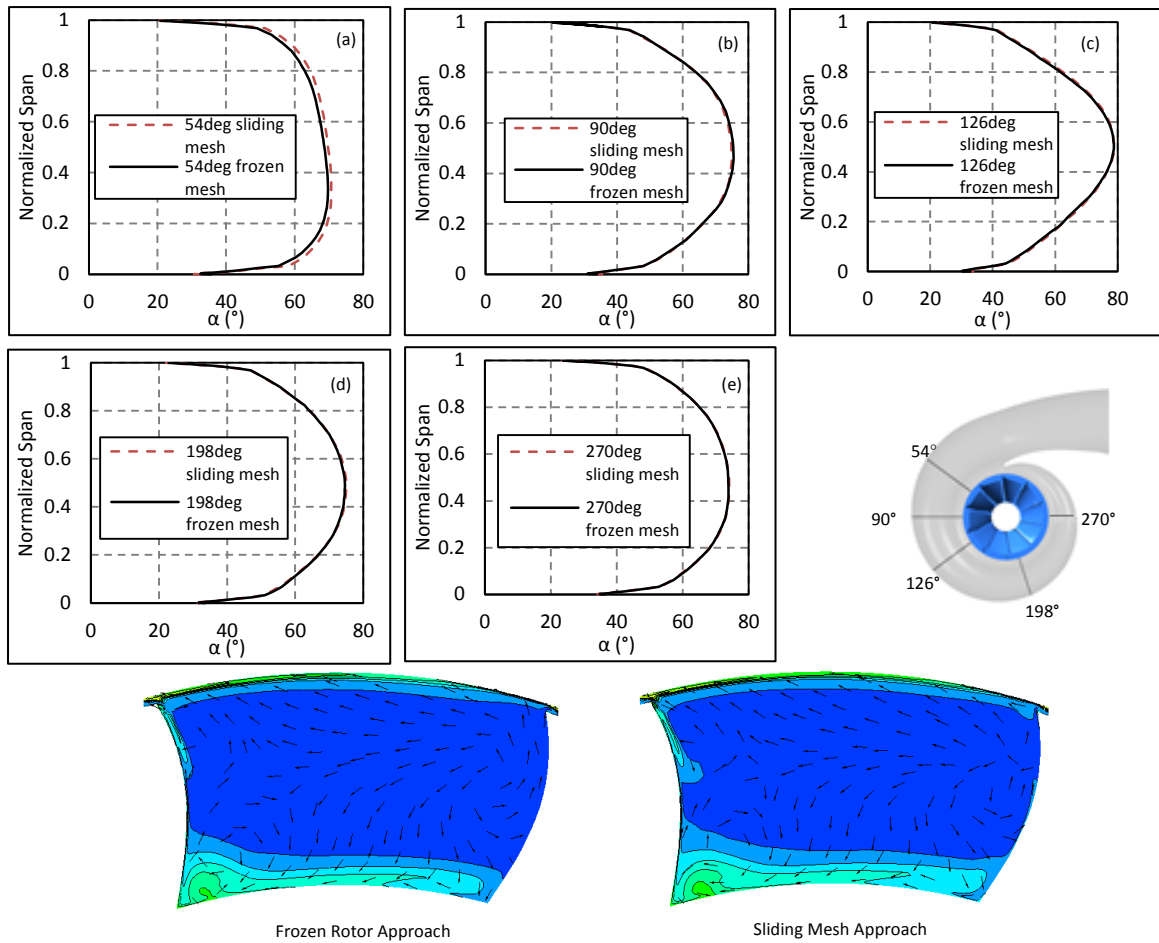


Figure 10.48: Volute exit absolute flow angle using frozen rotor and sliding mesh approach around azimuth angle at minimum mass flow point of pulse at 40Hz frequency

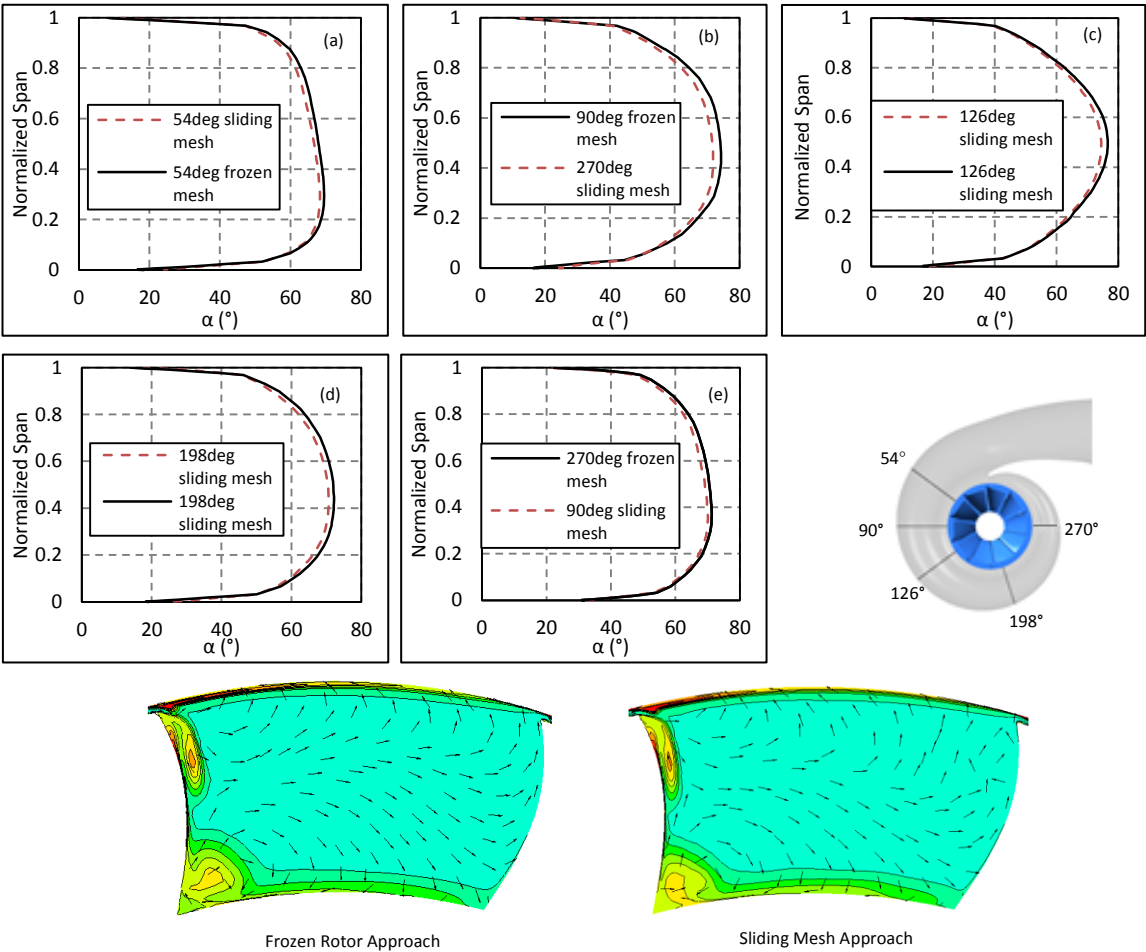


Figure 10.49: Volute exit absolute flow angle using frozen rotor and sliding mesh approach around azimuth angle at maximum mass flow point of pulse at 40Hz frequency

10.9 CHAPTER CONCLUSIONS

This chapter has shown the experimental comparison of the radial and tilted volute designs under both steady state and pulsating conditions. Further CFD validation has also been included showing the reliability of the methods used throughout this thesis.

The steady state experimental results showed that the tilted volute resulted in efficiency improvements only at high velocity ratios at the 30krpm. At 48krpm, both volutes showed similar efficiency values over the majority of the map, but a drop off in the tilted design at high velocity ratios was measured. At 56krpm the tilted volute operated at lower efficiencies over the entire map. However, the tilted volute was found to achieve larger MFP particularly at 56krpm. Follow up CFD showed this efficiency loss was the result of the step introduced by the heat shield having a greater impact on rotor hub separation in the tilted volute design.

Under pulsating conditions some notable performance trends were observed with the tilted design showing an improvement over the radial variant at 48krpm at low and mid loads as frequency was increased, and at 56krpm at mid and high load conditions as frequency was increased.

Overall, the computational model agrees with the experimentally measure values well. The computational approach implemented was capable of replicating the unsteady operation of the turbine. The output torque plots show that CFD predicts the performance trends across both frequency and the change in design. This supports the use of the computational model implemented throughout this thesis. Some discrepancies in the level of unsteadiness predicted by CFD were observed. However, as CFD is used throughout this thesis as a method of comparing turbine performance across designs and operation in back to back analysis, this secondary effect is not deemed vital to the validity of the method implemented.

The validation presented here is limited to global performance parameters. Further experimental validation of internal flows would be beneficial but would require significant modifications to the test facilities. This is outside the scope of this thesis but leaves potential for future investigation

11 CONCLUSIONS

In the literature review several gaps in the published knowledge were highlight –

1. The impact that pulsation shape may have on turbine performance requires more detailed analysis over a range of pulse shapes and operating conditions.
2. While tilted designs can be seen in the literature, no systematic investigation of the impact of these designs has been published.
3. The impact of volute design on volute flow structures and the subsequent impact on rotor inlet flow conditions appears to be a neglected area.

Each of these areas has been thoroughly investigated in this thesis leading to a number of contributions to knowledge in the field of mixed flow turbine performance and requiring the application of some novel techniques. The output of the work on each of these topics is summarised here –

Point 1 - Chapter 4 discusses the impact of pulse shape on the performance of a mixed flow turbine. Four pulse shapes were investigated including a sinusoidal, a triangular, a square and a realistic shape. Conclusions from this work were:

- The rate of change of a pulse results in notable changes to the performance of the turbine with the tested pulse shapes showing significant changes in instantaneous performance. This effect was illustrated through the changes in operating U/c range and the energy availability throughout the pulse period.
- The impact of pulse shape on cycle averaged turbine performance was found to only result in a 0.26% variation in cycle averaged efficiency and 0.5% in cycle average MFP for all but the square wave for the volute designs and pulse shapes investigated. For the square wave the cycle averaged performance showed a 1.37% variation in cycle averaged efficiency and 2.33% in cycle average MFP from the base line sinusoidal wave. This effect was explained due to the significant gradient changes and the resulting change to effective frequency.

- To accurately model the instantaneous operation of the turbine accurate modelling of the pulse is necessary. However, cycle averaged performance can be obtained with a high degree of accuracy using simplified pulse forms.

Point 2 –A novel tilted volute design was introduced and compared with that of a base radial design; the results of which were discussed in chapter 6 and 10. The performance of the tilted volute was analyzed over a range of pulse flow conditions and volute A/r's. The main conclusions from this work were:

- From the computational study in chapter 6 the tilted housing design resulted in cycle average rotor efficiency improvements of up to 1.45% over the frequency range tested, 1.64% over the range of pulsation numbers tested and 2.13% over the range of tested loads. These corresponded to resulting stage efficiency improvements of 1.16%, 1.354% and 1.76% respectively.
- Volute A/r was also found to have a substantial impact on the performance of the introduced tilt. As the volute A/r was increased, the tilted volute performed better with respect to the radial base line. The tilted volute design produced a maximum improvement of 2.356% in cycle averaged rotor efficiency and 2.171% improvement in cycle averaged stage efficiency in the largest volute case. This effect was found to be the result of the degree of reaction having a significant effect on the loss mechanism within the rotor region resulting in the improvement to the shroud curvature being more beneficial in the larger A/r volute case.
- Steady state experimental testing showed that the tilted volute produced marginal performance improvements at the lowest test turbine speed of 30krpm, the tilted volute under performed at higher rotational speeds. Subsequent CFD analysis showed that the impact of the volute heat shield step was greater in the tilted design leading to a performance reduction.

-
- Unsteady testing showed that the tilted volute produced performance improvements at higher rotational speeds and frequencies. At 48krpm performance improvements at lower turbine loads were evident while at 56krpm the higher load performance improved significantly.

Point 3 – The impact of volute flow structures and volute outlet flow conditions were focused on throughout the thesis. Initial work in chapter 5 discussed the impact of a range of pulsating conditions on the rotor inlet flows. The impact of said span-wise variation on rotor performance was then analyzed in chapter 7 by using a similar approach to that of Morrison et al., (2016). The effects of volute tilt and aspect ratio on span-wise flow distributions were then discussed in chapters 6 and 8 respectively. The main conclusions from this work were:

- The span-wise flow distributions were observed to varied substantial over the pulse cycle. Furthermore, with changing frequency, load and pulsation number the range of LE incidence was also impacted. The cause of this behavior was explained through the Dean effect in the volute by which the low inertia flow towards the volute walls turns readily in the radial direction while the higher inertia central passage flow does not. This is resulted in the development of vortices and significant flow variation across the volute exit span.
- Analysis of spanwise distributions on the rotor region only, presented in chapter 7, showed a variation in rotor efficiency of up to 2.17%. This work demonstrated a significant impact of the span-wise distribution on rotor performance and the need to include such variation in the rotor optimisation process.
- At a given volute A/r the volute aspect ratio (AR) was found to result in up to a 4.3% variation in cycle averaged MFP. As a result the volute A/r had to be modified to account for the changes to MFP with AR.
- A significant impact on volute secondary flows was also observed with changing aspect ratio with coherent vortices dominating the volute flow in the $AR=0.5$ case. As volute AR was increased these flows were removed from the volute passage. However, the resulting improvement on span-wise flow was found to be small.

Volute tilt was found to result in asymmetrical volute flows and resulted in a shift on the span-wise flow distributions towards the shroud.

- Combining the effects of both volute aspect ratio and tilt resulted in a maximum variation in efficiency between the worst performing design, radial AR=0.5, and the best performing, tilted AR=2, was 3% in the rotor region and 2.87% over the entire stage. The main conclusion from the work was the complex interaction between volute and rotor mean that correct matching is paramount for optimal aero-performance.

It is also important to note that from a turbocharger manufacture perspective the interaction between volute A/r , AR and tilt can result in several potential designs. Through manipulation of the three variables, the turbine space claim can be substantially affected. With current trends in engine downsizing, space within the engine bay is becoming more restricted. Understanding the impact of these parameters on performance allows designers to make an informed choice over the impact of geometrical changes to reduce package size. This also comes back to the initial argument that volute tilt could also be used to change volute A/r for a smaller cross sectional area. Although this effect was not studied in the current work it is something worthy of future investment.

11.1 CONTRIBUTIONS

The summary above compares the work output to that of the initial objectives of the project. It is also worth summarising the contributions to the field of turbomachinery aerodynamics and the research scholarly output. The major contributions claimed are:

- The analyse of the impact of pulse shape on turbine performance.
- Analysis into the impact of pulse characteristics on rotor LE characteristics over a wide range of pulsating conditions. The resulting distributions are also explained through thorough volute flow analysis.
- A novel tilted volute was designed and analysed. A significant contribution was made due to the exhaustive efforts to understand the fundamental cause of

performance benefits, from both computational and experimentally perspectives. Such knowledge is vital to future development of mixed flow turbines.

- Analysis of aspect ratio for symmetrical volute shapes showed the impact AR has on MFP and this must be accounted for in the turbine design process.
- The in depth analysis of volute secondary flow structures. The overall attempts to link these flow structures and the Dean effect to the rotor LE span-wise distribution is a major contribution to knowledge with in the field.

11.2 *Scholarly output*

Journal papers –

- Lee, S. P., Jupp, M. L., Barrans, S. M., & Nickson, A. K. (2018). Analysis of leading edge flow characteristics in a mixed flow turbine under pulsating flows. *Proceedings of the Institution of Mechanical Engineers, Part A: Journal of Power and Energy*, 0957650918778661.
- Lee, S. P., Barrans, S. M., Jupp, M. L., & Nickson, A. K. (2017). The Impact of Volute Aspect Ratio on the Performance of a Mixed Flow Turbine. *Aerospace*, 4(4), 56.
- Lee, S. P., Rezk, A., Jupp, M., & Nickson, K. (2017). The influence of pulse shape on the performance of a mixed flow turbine for turbocharger applications. *International Journal of Mechanical Engineering and Robotics Research*.

Conference papers –

- Lee, S. P., Barrans, S. M., Jupp, M. L., & Nickson, A. K. Investigation into the Impact of Span-wise flow Distribution on the Performance of a Mixed Flow Turbine (2018). In *ASME Turbo Expo 2018: Turbomachinery Technical Conference and Exposition*. American Society of Mechanical Engineers (ASME). In Press
- Lee, S. P., S. M., Jupp, M. L., Allport, J., & Nickson, A. K. Analysis of a tilted turbine housing volute design under pulsating inlet conditions. In *ASME Turbo Expo 2017: Turbomachinery Technical Conference and Exposition* (pp. V02CT44A016-V02CT44A016). American Society of Mechanical Engineers (ASME).

-
- Lee, S. P., S. M., Jupp, M. L., & Nickson, A. K. The influence of secondary flow structures in a turbocharger turbine housing in steady state and pulsating flow conditions. In Mechanical and Aerospace Engineering (ICMAE), 2016 7th International Conference on (pp. 154-159). IEEE.
 - Lee, S. P., S. M., Jupp, M. L., & Nickson, A. K. The introduction of a tilted volute design for operation with a mixed flow turbine for turbocharger applications. In Mechanical and Aerospace Engineering (ICMAE), 2016 7th International Conference on (pp. 165-170). IEEE.

11.3 FUTURE WORK

The current work only investigated the impact of one volute tilt angle. This was the angle equal to the cone angle of the blade to encourage optimal rotor inlet flow. However, increasing the scope to include further tilt angles would be useful to establish the full design envelope. Furthermore, investigation into the impact that volute tilt can have A/r would seek to establish the impact of tilt in A/r manipulation while maintain a constant turbine size.

The work included in this thesis has shown the effect of pulse shape on turbine performance in chapter 4 and the impact of various inlet parameter on performance over a range of pulse forms in chapter 5. The findings from this work, particularly the impact of out of phase parameters on performance would benefit from further investigation. This work utilised idealised pulse shapes to gain an understanding of the potential effects. However, experimentally measuring true pulse shapes over a range of engines and running conditions would allow for the true turbine operating environment to be established and the full interaction of the complex dynamics to be understood. Experimental measurements on engine are difficult due to necessity to capture data with high fidelity under high temperatures. While this was outside of the scope of the current work, developing techniques to accurately measures a full range parameters would be beneficial in understanding the true conditions experiences by the turbine.

While the impact of volute geometry on span-wise flow variation was analyzed in detail, rotor modifications were outside of the scope of this thesis. As the properties of mixed flow turbines allow span-wise variation of the LE, joint optimisation of both volute and rotor could yield significant benefits. While the effects of mixed flow blade angle has been investigated previously, no work has focused on the span-wise optimisation due to realistic volute flows. As such there is clear scope to optimise a mixed flow rotor for a specific volute design. Furthermore, due to the substantial inlet flow variation over the pulse period, it is important to establish how best to optimise the rotor for optimal energy extraction.

There is also potential to further investigate the development of volute secondary flow structures by increasing the range of volute cross sectional shapes. Further work into the impact of the Dean effect within the complex volute geometry could see a complete characterisation of the level of secondary flows expected within the volute due to this mechanism. Furthermore, it would be beneficial to experimentally capture the volute flow structures using an optical method under pulsating flows. The operating environment and geometry of the volute make this challenging and this was therefore outside of the scope of the current work. This would provide thorough validation for the computational method and allow further evaluation of the secondary flow development to fully understand the impact of the Dean effect.

Finally, further testing of the volute design on hot, steady state gas would be useful to further assess the performance of the tilted volute at realistic operating temperatures. Further inclusion of engine testing would also be beneficial to assess on engine benefits. The drawback of this is the difficult in accurately measuring instantaneous performance. Despite this, useful information can still be obtained from back to back testing.

12 REFERENCES

- Abidat, M., Baines, N., & Firth, M. (1992). Design of a highly loaded mixed flow turbine. *Proceedings of the Institution of Mechanical Engineers, Part A: Journal of Power and Energy*, 206(2), 95-107.
- Abidat, M., & Hachemi, M. (2005). Off design performance of a turbocharger mixed flow turbine. *European Conference on Turbomachinery*.
- Abidat, M., Hamidou, M., Hachemi, M., & Hamel, M. (2006). *Design and flow analysis of radial and mixed flow turbine volutes*. Paper presented at the European Conference on Computational Fluid Dynamics.
- Abidat, M., Hamidou, M. K., Hachemi, M., Hamel, M., & Litim, S. A. (2008a). Performance Prediction of a Mixed Flow Turbine. *EDP sciences*.
- Abidat, M., Hamidou, M. K., Hachemi, M., Hamel, M., & Litim, S. A. (2008b). Performance prediction of a mixed flow turbine. *Mechanics & Industry*, 9(1), 71-79.
- Ansys. (2009a). Ansys CFX-Solver Theory Guide.
- Ansys. (2009b). Fluent Users Guide.
- Arcoumanis, C., Hakeem, I., Khezzar, L., & Martinez-Botas, R. (1995). Performance of a mixed flow turbincharger turbine under pulsating flow conditions. *ASME Journal of Turbomachinery*.
- Arcoumanis, C., Martinez-Botas, R. F., Nouri, J. M., & Su, C. C. (1997). Performance and Exit Flow Characteristics of Mixed-Flow Turbines. *International Journal of Rotating Machinery*, 3(4), 227-293.
- Baines, N., Hajilouy-Benisi, A., & Yeo, J. (1994). *The pulse flow performance and modelling of radial inflow turbines*. Paper presented at the Institution of Mechanical Engineers Conference Publications.
- Baines, N., Wallace, F., & Whitfield, A. (1979). Computer aided design of mixed flow turbines for turbochargers. *Journal of Engineering for Power*, 101(3), 440-448.
- Baines, N. C. (2010). Turbocharger Turbine Pulse Flow Performance and Modelling - 25 years on.
- Baines, N. C., & Lavy, M. (1990). *Flows in vaned and vanless stators of radial inflow turbocharger turbines*.
- Baines, N. C., & Whitfield. (1990). *Design of Radial Turbomachines*: Longman Scientific and Technical
- Baines, N. C., & Yeo, J. H. (1991). Flow in a radial turbine under equal and partial admission conditions. *IMachE*.
- Benisek, E. S., W. (1987). Laser Velocimeter Measurements at the Rotor Inlet of a Turbocharger Radial Inflow Turbine *ASME*, 55.
- Benson, R. S. (1974). Nonsteady flow in a turbocharger nozzleless radial gas turbine: SAE Technical Paper.

- Benson, R. S., & Scrimshaw, K. H. (1965). An Experimental Investigation of Non-Steady Flow in a Radial Gas Turbine. *Proc Instn Mech Engrs*, 180 (10).
- Bhinder, F. S. (1969). Investigation of flow in the nozzle-less spiral casing of a radial inward-flow gas turbine. *IMachE*, 184, 66-71.
- Celik, I. B., Ghia, U., & Roache, P. J. (2008). Procedure for estimation and reporting of uncertainty due to discretization in {CFD} applications. *Journal of fluids {Engineering-Transactions} of the {ASME}*, 130(7).
- Cerdoun, M., & Ghenaiet, A. (2015). Analyses of steady and unsteady flows in a turbocharger's radial turbine. *Proceedings of the Institution of Mechanical Engineers, Part E: Journal of Process Mechanical Engineering*, 229(2), 130-145.
- Cerdoun, M., & Ghenaiet, A. (2016). *Analyse of flow structures through radial turbine twin- entry volute under pulsatile flows* Paper presented at the International Conference on Turbocharges and turbocharging
- Cerdoun, M., & Ghenaiet, A. (2018). Unsteady behaviour of a twin entry radial turbine under engine like inlet flow conditions. *Applied Thermal Engineering*, 130, 93-111.
- Chapple, P. M., Flynn, P. F., & Mulloy, J. M. (1980). Aerodynamic Design of Fixed and Variable Geometry Nozzleless Turbine Casings *Journal of Engineering for Power*.
- Chen, H. (1996). Design methods of volute casings for turbocharger turbine applications. *ImechE Journal of Power and Energy*.
- Chiong, M. S., Rajoo, S., Romagnoli, A., & Martinez-Botas, R. (2012). Single Entry Mixed Flow Turbine Performance Prediction With 1-D Gas Dynamics Code Coupled with Mean Line Model.
- Chou, C., & Gibbs, C. A. (1989). The design and testing of a mixed flow turbine for turbochargers. *SAE International*.
- Copeland, C., Newton, P., Martinez-Botas, R., & Seiler, M. (2012). A comparison of timescales within a pulsed flow turbocharger turbine. *Proc. Inst. Mech. Eng. C*, 1340, 389-404.
- Costall, A., & Martinez-Botas, R. F. (2007). *Fundamental characterization of turbocharger turbine unsteady flow behavior*. Paper presented at the ASME Turbo Expo 2007: Power for Land, Sea, and Air.
- Dale, A., & Watson, N. (1986). Vaneless radial turbocharger turbine performance *IMEchE C110*, 86.
- Dale, A. P. (1990). *Radial, vaneless, turbocharger turbine performance*. Imperial College London.
- Dean, W. R. (1927). Note on the Motion of Fluid in Curved Pipes. *Philosophical Magazine*.
- Dean, W. R. (1928). The Streamline Motion of Fluid in a Curved Pipe. *Philosophical Magazine*.
- Denton, J. D. (1993). The 1993 IGTI Scholar Lecture: Loss Mechanisms in Turbomachines *Journal of turbomachinery*, 115(4).

- Doorly, D., & Sherwin, S. (2009). *Geometry and Flow Cardiovascular Mathematics*: Springer.
- European-Commission. (2011). A Roadmap for moving to a competitive low carbon economy in 2050. *Communication from the commission to the european parliament, the council, the european economic and social committee and the committee of the regions*.
- Galindo, J., Hoyas, S., Fajardo, P., & R, N. (2014). Set-up Analysis and Optimisation of CFD Simulations for Radial Turbines. *Engineering Application of Computational Fluid Mechanics*.
- Gu, F., Engeda, A., & Benisek, E. (2001). A comparative study of incompressible and compressible design approaches of radial inflow turbine volutes. *Proceedings of the Institution of Mechanical Engineers, Part A: Journal of Power and Energy*, 215(4), 475-486. doi: 10.1243/0957650011538730
- Hakeem, I., Su, C.-C., Costall, A., & Martinez-Botas, R. F. (2007a). *Effect of Volute Geometry on the Steady and Unsteady Performance of Mixed-Flow Turbines*.
- Hakeem, I., Su, C. C., Costall, A., & Martinez-Botas, R. (2007b). Effect of volute geometry on the steady and unsteady performance of mixed-flow turbines. *Proceedings of the Institution of Mechanical Engineers, Part A: Journal of Power and Energy*, 221(4), 535-549. doi: 10.1243/09576509jpe314
- Hellstrom, F. (2010). *Numerical Computations of the Unsteady Pulsatile Flow in a Turbocharger*. (PhD), KTH Mechanics.
- Hellstrom, F., & Fuchs, L. (2008). Effects of inlet conditions on the turbine performance of a radial turbine. *Proceedings of the ASME Turbo Expo, Berlin, Germany, Paper No. GT2008-51088*.
- Hellstrom, F., & Fuchs, L. (2009). Numerical computation of the pulsatile flow in a turbocharger with realistic inflow conditions from an exhaust manifold. *ASME*.
- Hussain, M., & Bhinder, F. S. (1984). Experimental study of the performance of a nozzleless volute casing for a turbocharger turbine. *SAE International*.
- IEA, I. E. A. (2016). CO2 Emissions from Fuel Combustion Highlights.
- Japikse, D., & Baines, N. C. (1994). *Introduction to Turbomachinery*. Oxford: Oxford University Press.
- Kalpakli Vester, A. (2014). *Vortices in turbulent curved pipe flow-rocking, rolling and pulsating motions*. KTH Royal Institute of Technology.
- Karamanis, N., & Martinez-Botas, R. (2002). Mixed-flow turbines for automotive turbochargers: steady and unsteady performance. *International Journal of Engine Research*, 3(3), 127-138.
- Karamanis, N., Martinez-Botas, R., & Su, C. (2001). Mixed flow turbines: Inlet and exit flow under steady and pulsating conditions. *Journal of turbomachinery*, 123(2), 359-371.
- Kline, S., & McClintock, F. (1953). Analysis of Uncertainty in Single-Sample Experiments. *Mechanical Engineering*, 75.

- Kosuge, H., Yamanaka, N., Ariga, I., & Watanabe, I. (1975). *Performance of radial flow turbines under pulsating flow conditions*. Paper presented at the American Society of Mechanical Engineers, Gas Turbine Conference and Products Show, Houston, Tex.
- Lam, J. K.-W., Roberts, Q. D. H., & McDonnell, G. T. (2002). Flow modelling of a turbocharger turbine under pulsating flow. *IMachE*, 181-197.
- Lee, S., Jupp, M., & Nickson, A. (2016). *The influence of secondary flow structures in a turbocharger turbine housing in steady state and pulsating flow conditions*. Paper presented at the Mechanical and Aerospace Engineering (ICMAE), 2016 7th International Conference on.
- Leonard, T., Spence, S., Early, J., & Filsinger, D. (2013). A Numerical Study of Automotive Turbocharger Mixed Flow Turbine Inlet Geometry for Off Design Performance. *International Conference on Pumps and Fans with Compressors and Wind Turbines, 6th Proceedings*.
- Leonard, T., Spence, S., Early, J., & Filsinger, D. (2014). A Numerical Study of Inlet Geometry for a Low Inertia Mixed Flow Turbocharger Turbine. *ASME Turbo Expo*.
- Martinez-Botas, R., Pullen, K., & Shi, F. (1996). Numerical Calculations of a Turbine Volute Using a 3D Navier-Stokes Solver. *International Gas Turbine and Aeroengine Congress and Exhibition, ASME*.
- Meghaine, M. A., Hamidou, M. K., & Hamel, M. (2017). Influence of the volute cross-sectional shape on mixed inflow turbine performances. *Advances in Mechanical Engineering*, 9(7), 1687814017708174.
- Menter, F. (1992a). Performance of popular turbulence model for attached and separated adverse pressure gradient flows. *AIAA journal*, 30(8), 2066-2072.
- Menter, F., & Egorov, Y. (2005). A scale-adaptive simulation model using two-equation models. *AIAA paper*, 1095, 2005.
- Menter, F. R. (1992b). Improved two-equation k-omega turbulence models for aerodynamic flows.
- Menter, F. R. (1994). Two-equation eddy-viscosity turbulence models for engineering applications. *American Institute of Aeronautics and Astronautics*, 32.
- Menter, F. R. (1997). Eddy viscosity transport equations and their relation to the k- ϵ model. *Journal of Fluids Engineering*, 119(4), 876-884.
- Minegashi, H., Matsushita, H., & Sakakida, M. (1995). Development of a small mixed-flow turbine for automotive turbochargers. *Asme paper*(95-GT), 53.
- Moffat, R. (1982). Contributions to the theory of single-sample uncertainty analysis. *ASME, Transactions, Journal of Fluids Engineering*, 104(2), 250-258.
- Morrison, R., Spence, S., Kim, S., Filsinger, D., & Leonard, T. (2016). *Investigation of the effects of flow conditions at rotor inlet on mixed flow turbine performance for automotive applications*. Paper presented at the International Turbocharging Seminar, Tianjin China.
- Naguib, M. (1986). Experience With the Modern RR 151 Turbocharger for High-Speed Diesel Engines. *IMEchE Turbocharging and Turbochargers Transactions*.

- Newton, P. J. (2014). *An Experimental and Computational Study of Pulsating Flow within a Double Entry Turbine with Different Nozzle Settings*. (PhD), Imperial College London.
- Padzillah, M., Rajoo, S., Yang, M., & Martinez-Botas, R. (2015). Influence of pulsating flow frequencies towards the flow angle distributions of an automotive turbocharger mixed-flow turbine. *Energy Conversion and Management*, 98, 449-462.
- Padzillah, M. H. (2014). *Experimental and Numerical Investigation of an Automotive Mixed Flow Turbocharger Turbine under Pulsating Flow Conditions*. (PhD), Imperial College London.
- Palfreyman, D., & Martinez-Botas, R. (2002). Numerical study of the internal flow field characteristics in mixed flow turbines. *ASME*.
- Palfreyman, D., & Martinez-Botas, R. (2004). The pulsating flow field in a mixed flow turbocharger turbine: an experimental and computational study. *ASME Journal of Turbomachinery*.
- Pope, S. B. (2001). *Turbulent flows*: IOP Publishing.
- Rajoo, S. (2007). *Steady and pulsating performance of a variable geometry mixed flow turbocharger turbine*. (PhD), Imperial College London.
- Rajoo, S., & Martinez-Botas, R. (2008). Mixed Flow Turbine Research: A Review. *Journal of turbomachinery*, 130(4), 044001. doi: 10.1115/1.2812326
- Roach, P. J. (1997). Quantification of Uncertainty in Computational Fluid Dynamics. *Annual Review of Fluid Dynamics*, 29, 123-160.
- Roclawski, H., Bohle, M., & Gugau, M. (2012). Multidisciplinary Design Optimization of a Mixed Flow Turbine Wheel. *ASME Turbo Expo*.
- Roclawski, H., Gugau, M., Langecker, F., & Böhle, M. (2014). *Influence of Degree of Reaction on Turbine Performance for Pulsating Flow Conditions*. Paper presented at the ASME Turbo Expo 2014: Turbine Technical Conference and Exposition.
- Romagnoli, R., Martinez-Botas, R. F., & Rajoo, S. (2010). *Turbine performance studies for automotive turbochargers. Part 1: steady analysis*, London.
- Scrimshaw, K. H. (1981). *Scale effects in small geometrically similar radial gas turbines and particular reference to bladeless volute phenomena*. (PhD), University of London, London.
- Scrimshaw, K. W., T. (1984). Size Effects in Small Radial Turbines. *ASME*.
- Serrano, J. R., Gil, A., Navarro, R., & Inhestern, L. B. (2017). *Extremely Low Mass Flow at High Blade to Jet Speed Ratio in Variable Geometry Radial Turbines and its Influence on the Flow Pattern: A CFD Analysis*. Paper presented at the ASME Turbo Expo 2017: Turbomachinery Technical Conference and Exposition.
- Simpson, A. T., Spence, S., & Watterson, J. K. (2009). A comparison of the flow structures and losses within vaned and vaneless stators for radial turbines. *Journal of turbomachinery*.
- Slater, J. W. (2008). Examining Spatial (Grid) Convergence. *NASA*.

- Spence, S. W. T., Rosborough, R. S. E., Artt, D., & McGulloch, G. (2007). A direct performance comparison of vaned and vaneless stators for radial turbines. *Journal of Turbomachinery*, 129.
- Stern, F., Muste, M., Beninati, M.-L., & Eichinger, W. E. (1999). Summary of experimental uncertainty assessment methodology with example: IIHR Report.
- Szymko, S. (2006). *The development of an eddy current dynamometer for evaluation of steady and pulsating turbocharger turbine performance*. (PhD), Imperial College.
- Szymko, S., Martinez-Botas, R., & Pullen, K. (2005). *Experimental evaluation of turbocharger turbine performance under pulsating flow conditions*. Paper presented at the ASME Turbo Expo 2005: Power for Land, Sea, and Air.
- Szymko, S., Martinez-Botas, R., Pullen, K., McGlashan, N., & Chen, H. (2002). *C602/026/2002 A high-speed, permanent magnet eddy-current dynamometer for turbocharger research*. Paper presented at the IMECHE CONFERENCE TRANSACTIONS.
- Van Dyke, M., & Van Dyke, M. (1982). An album of fluid motion.
- Versteeg, H. K., & Malalasekera, W. (2007). *An introduction to computational fluid dynamics: the finite volume method*: Pearson Education.
- Walkingshaw, J., Iosifidis, G., Scheuermann, T., Filsinger, D., & Ikeya, N. (2015). A Comparison of a Mono-, Twin-, and Double-Scroll Turbine for Automotive Applications. *Journal of Engineering for Gas Turbines and Power*, 138(5), 052301-052301-052310. doi: 10.1115/1.4031449
- Wallace, F., & Blair, G. (1965). *The pulsating-flow performance of inward radial-flow turbines*. Paper presented at the ASME 1965 Gas Turbine Conference and Products Show.
- Watson, N., & Janota, M. S. (1982). *Turbocharging the internal combustion engine*. London: Macmillan.
- Whitfield, A., & Baines, N. (1990). Design of radial turbomachines. *Longman Scientific and Technical*.
- Whitfield, A., & Noor, A. M. (1994). Design and Performance of Vaneless Volute for Radial Inflow Turbines: Part 1: Non-Dimensional Conceptual Design Considerations. *Proceedings of the Institution of Mechanical Engineers, Part A: Journal of Power and Energy*, 208(3), 199-211.
- Winterbone, D. E., Nikpour, B., & Frost, H. (1991). A contribution to the understanding of turbocharger turbine performance in pulsating flow. *IMachE*.
- Yamaguchi, H., Nishiyama, T., Horiai, K., & Kasuya, T. (1984). High performance komatsu ktr150 turbocharger: SAE Technical Paper.
- Yang, B., Newton, P., & Martinez-Botas, R. (2017a). *UNSTEADY EVOLUTION OF SECONDARY FLOWS IN A MIXED TURBINE*. Paper presented at the Global Power and propulsion Forum.

- Yang, M., Martinez-Botas, R., Rajoo, S., Yokoyama, T., & Ibaraki, S. (2014). Influence of Volute Cross-Sectional Shape of a Nozzleless Turbocharger Under Pulsating Flow Condition *ASME Turbo Expo*.
- Yang, M., Martinez-Botas, R., Rajoo, S., Yokoyama, T., & Ibaraki, S. (2015). An investigation of volute cross-sectional shape on turbocharger turbine under pulsating conditions in internal combustion engine. *Energy Conversion and Management*, 105, 167-177.
- Yang, M., Martinez-Botas, R., Srithar, R., Ibaraki, S., Yokoyama, T., & Deng, K. (2017b). *UNSTEADY BEHAVIOURS OF A VOLUTE IN TURBOCHARGER TURBINE UNDER PULSATING CONDITIONS*. Paper presented at the Global Power and Propulsion Forum.
- Yeo, J. H., & Baines, N. C. (1990). Pulsating Flow Behavior in a Twin-Entry Vaneless Radial Inflow Turbine. *IMachE*.
- Zhang, Y., Chen, L., Zhuge, W., & Zhang, S. (2011). Effects of pulse flow and leading edge sweep on mixed flow turbines for engine exhaust heat recovery. *Science China Technological Sciences*, 54(2), 295-301.
- Zimmermann, R., Baar, R., Enghardt, L., & Hakensson, S. (2015). Investigation on Pulsating Turbine Flow Radial Turbines. *Aachen Colloquium Automobile and Engine Technology*.

Appendix A - V-CONE CALIBRATION DOCUMENT

V-Cone Application Sizing

| | | | |
|----------|-----------|-------------|------|
| Serial # | 09-1262 | Fluid State | GAS |
| Tag | | Fluid | AIR |
| Model | VW03UE14N | End User | ABLE |
| Job Ref. | Q#114652 | | |

| | | | |
|-------------|-----------|------------|--|
| Description | 3" V-CONE | Mtdg. Code | |
| Note | | | |

| | | | | | | |
|-------------|---------------------------|--------------------|-----------|------|------------------|------|
| C_d | 0.8472 | q max. Flowrate | .5 | kg/S | McCrometer Cal. | |
| P_f | 7 barG | Re max. Reynolds | 4.298e+05 | | Third Party Cal. | |
| T_f | 35 °C | V max. Velocity | 37.54 | fps | Dye. Pen. Exam. | |
| ρ | 0.5871 lb/ft ³ | ΔP max. Dp | 82.058 | inWC | Hydro. Test | |
| μ | 1.893e-02 cP | ΔP min. Dp | 0.12809 | inWC | X-Ray Exam. | |
| G | 1.000 | D Meter I.D. | 3.0810 | in | Mag. Part. | |
| Z | 0.9971 | d Cone O.D. | 2.7560 | in | PMI | |
| Y | 0.98770 | β Beta Ratio | 0.4470 | | CMTR Copies | |
| k | 1.402 | Turn Down | 25 | | McCrometer Eng. | RoLe |
| C_p | 6.932 | | | | | |
| M_w | 28.951 | | | | | |
| P_b | | | | | | |
| T_b | | | | | | |
| Z_b | | | | | | |
| $P_{b,bar}$ | 14.696 psiA | | | | | |
| P_c | 547.37 psiA | | | | | |
| T_c | 238.41 °R | | | | | |
| F_a | 1.000 | | | | | |
| aPE | D 6.7e-06 d 6.7e-06 | | | | | |
| P_v | | | | | | |
| P_{loss} | 2.195 psiA | | | | | |

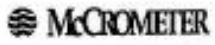
| | Re | C_d | Velocity fps | Gas. Exp. Y | ΔP inWC | Flowrate kg/S |
|----|-----------|--------|-----------------|----------------|--------------------|------------------|
| 1 | 4.298e+05 | 0.8472 | 37.543 | 0.9877 | 82.058 | 0.50000 |
| 2 | 3.839e+05 | 0.8472 | 33.539 | 0.9902 | 65.152 | 0.44667 |
| 3 | 3.381e+05 | 0.8472 | 29.534 | 0.9925 | 50.294 | 0.39333 |
| 4 | 2.923e+05 | 0.8472 | 25.530 | 0.9944 | 37.436 | 0.34000 |
| 5 | 2.464e+05 | 0.8472 | 21.525 | 0.9980 | 26.524 | 0.28667 |
| 6 | 2.006e+05 | 0.8472 | 17.520 | 0.9974 | 17.526 | 0.23333 |
| 7 | 1.547e+05 | 0.8472 | 13.516 | 0.9984 | 10.407 | 0.18000 |
| 8 | 1.089e+05 | 0.8472 | 9.5110 | 0.9992 | 5.1455 | 0.12667 |
| 9 | 6.304e+04 | 0.8472 | 5.5064 | 0.9997 | 1.7229 | 7.3333e-02 |
| 10 | 1.719e+04 | 0.8472 | 1.5017 | 1.0000 | 0.12809 | 2.0000e-02 |

Ⓔ Entered value.

Record Start Date: 4/6/2009

Print Date: 05-19-2009

Table based on one flow condition (P, T, Z, k ...) V40 Version 1.3
 Standard Gas Expansion Equation - Rev. Aug. 2001
 $k1 = 7.1764e-02$



Appendix B - EXPERIMENTAL INLET PRESSURE PULSE

